IHEP-CEPC-DR-2015-01

IHEP-EP-2015-01

IHEP-TH-2015-01

CEPC-SPPC

Preliminary Conceptual Design Report

Volume I - Physics & Detector

The CEPC-SPPC Study Group

March 2015

AUTHOR LIST

The CEPC-SPPC Study Group

Muhammd Ahmad[1] Daniele Alves[85] Haipeng An (安海鹏)[60]
Qi An (安琪)[6] Abdesslam Arhrib[124] Nima Arkani-Hamed[93]
Ijaz Ahmed[127] Yu Bai (白羽)[19] Rinaldo Baldini Ferroli[118]
Yong Ban (班勇)[8] Paolo Bartalini[39] Rachid Benbrik[125]
Xiaojun Bi (毕效军)[1] Ikaros Bigi[68] Yang Bai (白杨)[74]
Joseph Bramante[68] Vladislav Balagura[103] Vincent Boudry[103]
Jean Claude Brient[103] Yifu Cai (蔡一夫)[119] Hao Cai (蔡浩)[29]
Zhen Cao (曹臻)[1] Junjie Cao (曹俊杰)[41] Yu-Hsiang Chang (張祐祥)[56]
Yuan-Hann Chang (張元翰)[56] We-Fu Chang (張維甫)[58] Paoti Chang (張寶棣)[57]
Chiu-Ping Chang (張秋萍)[56] Ningbo Chang (畅宁波)[39] Qin Chang (常钦)[41]
Yuan Chao (趙元)[57] Jiunn-Wei Chen (陳俊瑋)[57] Shaolong Chen (陈绍龙)[39]
Ye Chen (陈晔)[1] Mingshui Chen (陈明水)[1] Guoming Chen (陈国明)[1]
Xuewen Chen (陈学文)[37] Shanzhen Chen[106] Zhenxing Chen (陈振兴)[8]
Shenjian Chen (陈申见)[21] Xurong Chen (陈旭荣)[2] Xun Chen (谌勋)[11]
Shaomin Chen (陈少敏)[9] Mingjun Chen (陈明君)[1] Shiyong Chen (陈时勇)[39]
Ning Chen (陈宁)[6] Gang Chen (陈刚)[1] Shi Chen (陈石)[7]
Hai-Yang Cheng (鄭海揚)[55] Shan Cheng (程山)[40] Tongguang Cheng (成曈光)[1]
Cheng-Wei Chiang (蔣正偉)[56] Kiwoon Choi[99] Wai Cheong Chu (朱偉昌)[51]
Chun-Khiang Chua (蔡俊謙)[59] Kris Chui (崔安欣)[52] Timothy Cohen[83]
Nathaniel Craig[62] David Curtin[67] Raffaele Tito D'Agnolo[93]
Jianping Dai (代建平)[11] Zhi Deng (邓智)[9] Weitian Deng (邓维天)[26]
Hengtong Ding (丁亨通)[39] Xuefeng Ding (丁雪峰)[29] Ran Ding (丁然)[8]
Yadong Ding (丁亚东)[1] Mingyi Dong (董明义)[1] Milos Dordevic[117]
Medhat ElSayed[1] Jens Erler[126] Rouven Essig[88]
Lisa Everett[74] Jiawei Fan (范嘉伟)[1] JiJi Fan (范吉吉)[87]
Jingzhou Fan (范荆洲)[9] Shuangshi Fang (房双世)[1] Yaquan Fang (方亚泉)[1]
Xin Fang (方馨)[6] Wenxing Fang (方文兴)[10] Cunfeng Feng (冯存峰)[16]
Oliver Fischer [82] Luis Roberto Flores Castillo [53] Zaiwei Fu (付在伟)
Michael A. Fedderke[79] Jamison Galloway [85] Yuanning Gao (高原宁)[9]

Xuyang Gao (高旭阳)[10] Yonggui Gao (高勇贵)[47] Jie Gao (高杰)[1]
Shaofeng Ge (葛韶锋)[116] Chaoqiang Geng (耿朝強)[58] Lisheng Geng (耿立升)[10]
Guanghua Gong (龚光华)[9] Li Gong (龚丽)[47] Lingling Gong (龚玲玲)[1]
Stefania Gori Alfred Goshaw [84] Quanbu Gou (苟全补)[1]
Jiayin Gu (顾嘉荫)[1] Yikun Gu (顾易坤)[29] Peihong Gu (顾佩洪)[11]
Lei Guo (郭磊)[36] Wanlei Guo (郭万磊)[1] Jun Guo (郭军)[11]
Yan Guo (郭雁)[41] Yacine Haddad [109] Jan Hajer[51]
Yanliang Han (韩艳良)[16] Ran Han (韩然)[28] Tao Han (韩涛)[72]
Liang Han (韩良)[6] shuang Han (韩爽)[29] Jinzhong Han (韩金钟)[48]
Michael Hance[63] Yongliang Hao (郝永亮)[11] Xiqing Hao (郝喜庆)[41]
Hongjian He (何红建)[9] Xiaogang He (何小刚)[57] Yuekun Heng (衡月昆)[1]
Ian Hinchliffe[63] Daojin Hong (洪道金)[34] Wei-Shu Hou (侯維恕)[57]
Zhilong Hou (侯治龙)[1] Kiel Howe[89] Yee Bob Hsiung (熊怡)[57]
Yu Hu (胡誉)[1] Qingli Hu (胡庆丽)[11] Tao Hu (胡涛)[1]
Chaoshang Huang (黄朝商)[3] Jinshu Huang (黄金书)[49] Yanping Huang (黄燕萍)[110]
Xingtao Huang (黄性涛)[16] Guangshun Huang (黄光顺)[6] Anson Hook[93]
Ahmed Ismail[94] Qingping Ji (姬清平)[22] Duojie Jia (贾多杰)[44]
Junji Jia (贾俊基)[29] Xuejun Jia (贾学军)[1] Yun Jiang (蒋贇)[64]
Lili Jiang (姜丽丽)[1] Luwen Jiang (姜鲁文)[29] Xingyu Jiang (蒋兴雨)[22]
Jianbin Jiao (焦健斌)[16] Shan Jin (金山)[1] Hongying Jin (金洪英)[25]
Sunghoon Jung[100] Susmita Jyotishmati[76] Markus Kaiser[110]
Xiaoshen Kang (康晓珅)[21] Xiaolin Kang (康晓琳)[1] Valentin V Khoze[109]
Felix Kling[75] Suman Koirala[57] Otto Kong (江祖永)[56]
Ashutosh Kotwal[84,95] Chia Ming Kuo (郭家銘)[56] Kevin Kwok (郭景炜)[52]
Shibei Kong (孔师碑)[1] Imad Laktineh[102] Andrew Larkoski[92]
Guo Lei (郭磊)[6] Shu Li (李数)[84] Ling-Fong Li (李灵峰)[81]
Qiang Li (李强)[8] Ying Li (李营)[33] Minxian Li (李敏贤)[1]
Kang Li (李康)[46] Yufeng Li (李玉峰)[1] Haibo Li (李海波)[1]
Zhao Li (李钊)[1] Xiaozhou Li (李晓周)[7] Bo Li (李波)[9]
Ye Li (李烨)[89] Haijun Li (李海军)[15] Liang Li (李亮)[11]
Xinqiang Li (李新强)[39] Weiguo Li (李卫国)[1] Xiaoling Li (李晓玲)[16]
Wenzhao Li (李文钊)[11] Fei Li (李飞)[1] Hengne Li (李衡讷)[77]
Junli Li (李军利)[7] Tianjun Li (李田军)[3] Cheng Li (李澄)[6]
Yijie Li (李一杰)[30] Honglei Li (李洪蕾)[32] Shiyuan Li (李世渊)[16]
Gang Li (李刚)[1] Huijing Li (李惠静)[1] Fengyun Li (李峰云)[8]
Lei Li (李蕾)[1] Ke Li (李科)[16] Cheng Li (李澄)[6]
Hsiangnan Li (李湘楠)[55] Guannan Li (李冠楠)[57] Qiyun Li (李启云)[16]
Yingying Li (李英英)[52] Xiaomei Li (李笑梅)[50] Dikai Li (李迪开)[15]
Zhijun Liang (梁志均)[65] Yi Liao (廖益)[22] Wei Liao (廖玮)[27]
Libo Liao (廖立波)[46] Jiajie Ling (凌家杰)[23] Hui Liu (刘绘)[18]
Bing Liu (刘冰)[11] Chuan Liu (刘川)[8] Zhen Liu (刘真)[72]
Landiao Liu (刘兰雕)[8] Yanlin Liu (刘彦麟)[6] Tao Liu (刘滔)[52]
Yilin Liu (刘一霖)[1] Zhongxiu Liu (刘钟秀)[1] Beijiang Liu (刘北江)[1]
Hongbang liu (刘宏邦)[34] Junyu Liu (刘峻宇)[6] Jia Liu (刘佳)[113]
Jinyan Liu (刘金艳)[22] Xin Liu (刘新)[45] Xiang Liu (刘翔)[24]
Jianbei Liu (刘建北)[6] Peilian Liu (刘佩莲)[1] Yanwen Liu (刘衍文)[6]
Fuhu Liu (刘福虎)[31] Zhaofeng Liu (刘朝峰)[1] Hu Liu (刘虎)[23]
Ning Liu (刘宁)[41] Rong Liu (刘熔)[1] Qian Liu (刘倩)[7]
Cheuk Yee Lo (勞卓義)[51] Xinchou Lou (娄辛丑)[1] Hou Keong Lou (盧濠強)[83]
Ian Low (羅亦安)[91] Matthew Low[79] Caidian Lu (吕才典)[1]
Weiguo Lu (陆卫国)[1] Yunpeng Lu (卢云鹏)[1] Shu Luo (罗舒)[35]
Xiaofeng Luo (罗晓峰)[39] Tao Luo (罗涛)[80] Lanchun Lyu (吕岚春)[9]
Xiaorui Lyu (吕晓睿)[7] Tongyan Lin[79] Guoliang Ma (马国亮)[4]
Ernest Ma[61] Lianliang Ma (马连良)[16] Wengan Ma (马文淦)[6]
Binsong Ma (马斌松)[1] Boqiang Ma (马伯强)[8] Hailong Ma (马海龙)[1]
Mingming Ma (马明明)[1] Yajun Mao (冒亚军)[8] Matthew McCullough[105]

Patrick Meade[88] Xiangwei Meng (孟祥伟)[1] Tianjue Min (闵天觉)[1]
Xin Mo (莫欣)[1] William Murray[107] Feipeng Ning (宁飞鹏)[1]
Sanjay Padhi[66] Stathes Paganis (裴思達)[57] Longgang Pang (庞龙刚)[39]
Emilie Passemar[86] Cong Peng (彭聪)[1] Klaus Peters[112]
Ronggang Ping (平荣刚)[1] Kirill Prokofiev[52] Gilad Perez[128]
Huirong Qi (祁辉荣)[1] Ming Qi (祁鸣)[21] Hongrong Qi (漆红荣)[47]
Jianming Qian (钱剑明)[69] Congfeng Qiao (乔从丰)[7] Nian Qin (覃拈)[29]
Guangyou Qin (秦广友)[39] Zhonghua Qin (秦中华)[1] Liqing Qin (秦丽清)[16]
Michael Ramsey-Musolf (任缪)[70] Matthew Reece[82] Jing Ren (任婧)[120]
Nikolaos Rompotis[71] Xifeng Ruan (阮熙峰)[123] Manqi Ruan (阮曼奇)[1]
Joshua Ruderman[85] Richard Ruiz[72] Joshua Sayre[72]
Sarmad Masood Shaheen[1] Jessie Shelton[73] Yuqiao Shen (沈玉乔)[1]
Chengping Shen (沈成平)[10] Jingge Shiu (徐靜戈)[57] Gary Shiu (萧文礼)[74]
Fu Hong John Shiu (蕭富康)[52] Jing Shu (舒菁)[3] Zongguo Si (司宗国)[16]
Weimin Song (宋维民)[1] Xinying Song (宋欣颖)[1] Huichao Song (宋慧超)[8]
Shufang Su (苏淑芳)[75] Akula Sujeet[121] Yueling Sun (孙俊峰)[41]
Sichun Sun[52] Yanjun Sun (孙艳军)[44] Hao Sun (孙昊)[14]
Xilei Sun (孙希磊)[1] Jusak Tandean[57] Zhicheng Tang (唐志成)[1]
Junquan Tao (陶军全)[1] Jesse Thaler[92] Arun Thalapillil[97]
Shihyen Tseng (曾師彥)[56] Yanjun Tu[51] Brock Tweedie[72]
Jay G. Wac ker[89] Minzu Wang (王名儒)[57] Bin Wang (王斌)[22]
Yong Wang (王勇)[5] Kechen Wang (王科臣)[1] Tianhong Wang (王天鸿)[13]
Mengmeng Wang (王蒙蒙)[8] Shaoming Wang (王少明)[36] Joseph Wang (王承宇)[54]
Zhe Wang (王喆)[9] Wei Wang (王为)[23] Yiwei Wang (王毅伟)[1]
Haiyun Wang (王海云)[1] Jin Wang (王锦)[1] Chi Wang (王驰)[6]
Xiaoping Wang (王小平)[113] Feng Wang (王峰)[29] Liantao Wang (王连涛)[79]
Zhiyong Wang (王至勇)[1] Yuchen Wang (王雨晨)[9] Xiaoyun Wang (王晓云)[2]
Qun Wang (王群)[6] Zheng Wang (王征)[1] Xinnian Wang (王新年)[39]
Yue Wang (王玥)[9] Wenyu Wang (王雯宇)[12] Fei Wang (王飞)[17]
Zongyuan Wang (王宗源)[1] Dayong Wang (王大勇)[8] Rongkun Wang (王融坤)[6]
Weiping Wang (王维平)[6] Binlong Wang (王滨龙)[7] Meng Wang (王萌)[16]
Zirui Wang (王子瑞)[11] Wei Wang (王伟)[11] Chengtao Wang (王呈涛)[1]
Xiongfei Wang (王雄飞)[9] Xueqiang Wang (王薛强)[1] Xiaolong Wang (王小龙)[96]
Siguang Wang (王思广)[8] Meifen Wang (王美芬)[1] Yuqian Wei (魏彧骞)[1]
Shuopin Wen (文硕频)[1] Susanne Westhoff[72] Sung Ching Sam Wong (黄崇清)[52]
Xinggang Wu (吴兴刚)[36] Xiaohong Wu (吴小红)[27] Wenjing Wu (伍文静)[1]
Lei Wu (武雷)[120] Linghui Wu (伍灵慧)[1] Yusheng Wu (吴雨生)[69]
Qianfei Xiang (向仟飞)[1] Zhong-Zhi Xianyu (鲜于中之)[9] Zhenjun Xiao (肖振军)[40]
Ming Xiao (肖铭)[1] Ruiqing Xiao (肖瑞卿)[9] Bowen Xiao (肖博文)[46]
Yuehong Xie (谢跃红)[39] Yuguang Xie (谢宇广)[1] Zhi-zhong Xing (邢志忠)[1]
Qinglei Xiu (修青磊)[1] Fanrong Xu (徐繁荣)[57] Qingjun Xu (徐庆君)[46]
Lailin Xu (徐来林)[6] Da Xu (徐达)[1] Nu Xu (许怒)[39]
Yin Xu (徐音)[22] Haojie Xu (徐浩洁)[6] Xunjie Xu (许勋杰)[9]
Lei Xia (夏磊)[94] Wenbiao Yan (鄢文标)[6] Qishu Yan (晏启树)[7]
Tian Yan (颜田)[1] Fang Yan (闫芳)[1] Yueling Yang (杨悦玲)[41]
Haijun Yang (杨海军)[11] Xuan Yang (杨轩)[16] Jinmin Yang (杨金民)[3]
Liu Yang (杨柳)[29] Bingfang Yang (杨炳方)[41] ZhongJuan Yang (杨中娟)[38]
Huan Yang (杨欢)[1] Weiming Yao (姚为民)[63] Weichao Yao (姚卫超)[1]
Mei Ye (叶梅)[1] Jingbo Ye (叶竞波)[90] Pengfei Yin (殷鹏飞)[1]
Zhongbao Yin (殷中宝)[39] Furong Yin (殷复荣)[9] Junhao Yin (殷俊昊)[1]
Zhengyun You (尤郑昀)[78] Fusheng Yu (于福升)[24] Tientien Yu (于秋恬)[88]
Felix Yu (游維和)[113] Chunxu Yu (喻纯旭)[22] Boxiang Yu (俞伯祥)[1]
Zhaohuan Yu (余钊焕)[1] Li Yuan (袁丽)[97] Changzheng Yuan (苑长征)[1]
Ye Yuan (袁野)[1] Chongxing Yue (岳崇兴)[42] Qian Yue (岳骞)[9]
Yue Zhang (张越)[60] Lei Zhang (张雷)[114] Jiawen Zhang (张家文)[1]
Renyou Zhang (张仁友)[6] Chen Zhang (张晨)[120] Yumei Zhang (张玉美)[23]

Yulian Zhang (张余炼)[1] Jianhui Zhang (张建辉)[115] Yu Zhang (张宇)[6]
Xiaomei Zhang (张晓梅)[1] Yi Zhang (张毅)[24] Wenchao Zhang (张文超)[43]
Zhiqing Zhang (张智庆)[104] Xueyao Zhang (张学尧)[16] Huaqiao Zhang (张华桥)[1]
Yujie Zhang (张玉洁)[10] Jianyong Zhang (张建勇)[1] Benwei Zhang (张本威)[39]
Hanzhong Zhang (张汉中)[39] Zhenyu Zhang (张振宇)[29] Yanxi Zhang (张艳席)[9]
Chi Zhang (张弛)[21] Jielei Zhang (张杰磊)[1] Bingxin Zhang (张丙新)[1]
Zhenghao Zhang (张正好)[39] Peng Zhang (张鹏)[1] Kai Zhang (张恺)[1]
Honghao Zhang (张宏浩)[23] Guoqing Zhang (张国庆)[1] Hao Zhang (张昊)[62]
Minggang Zhao (赵明刚)[22] Zhenhua Zhao (赵振华)[1] Zhengguo Zhao (赵政国)[6]
Jie Zhao (赵杰)[39] Ling Zhao (赵玲)[1] Wei Zhao (赵微)[1]
Hang Zhao (赵航)[1] Minshan Zheng (郑敏珊)[9] Liang Zheng (郑亮)[39]
Bo Zheng (郑波)[20] Yajuan Zheng (郑亚娟)[57] Yong Zhong (钟勇)[5]
Hang Zhou (周航)[11] Bing Zhou (周冰)[69] Shun Zhou (周顺)[1]
Yeling Zhou (周也铃)[1] Siyi Zhou (周思益)[52] Yufeng Zhou (周宇峰)[3]
Ning Zhou (周宁)[78] Xiang Zhou (周详)[29] Xiaorong Zhou (周小蓉)[6]
Zian Zhu (朱自安)[1] Hongbo Zhu (朱宏博)[1] Kai Zhu (朱凯)[1]
Chengguang Zhu (祝成光)[16] Ruilin Zhu (朱瑞林)[11] Jianhui Zhu (朱剑辉)[39]
Kejun Zhu (朱科军)[1] Junjie Zhu (朱俊杰)[69] Qianwen Zhu (朱倩雯)[28]
Xiangrong Zhu (朱祥荣)[8] Xuai Zhuang (庄胥爱)[1] Jure Zupan[98]

[1] Institute of High Energy Physics, Chinese Academy of Sciences, China (中科院高能物理研究所)
[2] Institute of Modern Physics, Chinese Academy of Sciences, China (中科院近代物理研究所)
[3] Institute of Theoretical Physics, Chinese Academy of Sciences, China (中科院理论物理研究所)
[4] Shanghai Institute of Applied Physics, Chinese Academy of Sciences, China (中科院上海应用物理研究所)
[5] Institute of Electronics, Chinese Academy of Sciences, China (中科院电子所)
[6] The University of Science and Technology of China, China (中国科学技术大学)
[7] University of Chinese Academy of Sciences, China (中国科学院大学)
[8] Peking University, China (北京大学)
[9] Tsinghua University, China (清华大学)
[10] Beihang University, China (北京航空航天大学)
[11] Shanghai Jiao Tong University, China (上海交通大学)
[12] Beijing University of Technology, China (北京工业大学)
[13] Harbin Institute of Technology, China (哈尔滨工业大学)
[14] Dalian University of Technology, China (大连理工大学)
[15] China University of Geosciences, China (中国地质大学)
[16] Shandong University, China (山东大学)
[17] Zhengzhou University, China (郑州大学)
[18] Jinan University, China (暨南大学)
[19] Southeast University, China (东南大学)
[20] University of South China, China (南华大学)
[21] Nanjing University, China (南京大学)
[22] Nankai University, China (南开大学)
[23] Sun Yat-sen University, China (中山大学)
[24] Lanzhou University, China (兰州大学)
[25] Zhejiang University, China (浙江大学)
[26] Huazhong University of Science and Technology, China (华中科技大学)
[27] East China University of Science and Technology, China (华东理工大学)
[28] North China Electric Power University, China (华北电力大学)
[29] Wuhan University, China (武汉大学)
[30] Liaoning University, China (辽宁大学)
[31] Shanxi University, China (山西大学)
[32] University of Jinan, China (济南大学)
[33] Yantai University, China (烟台大学)

[34] Guangxi University, China (广西大学)
[35] Xiamen University, China (厦门大学)
[36] Chongqing University, China (重庆大学)
[37] Chongqing university of science and technology, China（重庆科技大学）
[38] Henan Polytechnic University, China (河南理工大学)
[39] Central China Normal University, China (华中师范大学)
[40] Nanjing Normal University, China (南京师范大学)
[41] Henan Normal University, China (河南师范大学)
[42] Liaoning Normal University, China (辽宁师范大学)
[43] Shaanxi Normal University, China (陕西师范大学)
[44] Northwest Normal University, China (西北师范大学)
[45] Jiangsu Normal University, China (江苏师范大学)
[46] Hangzhou Normal University, China (杭州师范大学)
[47] Guangxi Normal University, China (广西师范大学)
[48] Zhoukou Normal University, China (周口师范学院)
[49] Nanyang Normal University, China (南阳师范学院)
[50] China Institute of Atomic Energy, China (中国原子能科学研究院)
[51] University of Hong Kong (香港大学)
[52] The Hong Kong University of Science and Technology (香港科技大学)
[53] The Chinese University of Hong Kong (香港中文大学)
[54] Bitquant Research Laboratories, Hong Kong
[55] Institute of Physics, Academia Sinica, Taipei (中央研究院物理研究所)
[56] National Central University, Taipei (中央大学, 新竹)
[57] National Taiwan University, Taipei (台湾大学, 台北)
[58] National Tsing Hua University, Taipei (清华大学, 新竹)
[59] Chung Yuan Christian University, Taipei (中原大学)
[60] CALTECH, Pasadena, USA
[61] University Calif Riverside, USA
[62] University Calif Santa Barbara, USA
[63] University Calif Berkeley, USA
[64] University Calif Davis, Davis, USA
[65] University Calif Santa Cruz, USA
[66] University Calif San Diego, USA
[67] University Maryland, USA
[68] University Notre Dame, USA
[69] University Michigan, USA
[70] University Massachusetts, USA
[71] University Washington, USA
[72] University Pittsburgh, USA
[73] University Illinois, USA
[74] University Wisconsin, USA
[75] University Arizona, USA
[76] University Texas Dallas, USA
[77] University Virginia, USA
[78] University Calif Irvine, USA
[79] University Chicago, USA
[80] University Hawaii, USA
[81] Carnegie Mellon University, USA
[82] Harvard University, USA
[83] Princeton University, USA
[84] Duke University, USA
[85] New York University, USA
[86] Indiana University, USA
[87] Syracuse University, USA
[88] Stony Brook University, USA
[89] Stanford University, USA

[90] Southern Methodist University, USA
[91] Northwestern University, USA
[92] MIT, Cambridge, USA
[93] Institute for Advanced Study, USA
[94] Argonne National Laboratory, USA
[95] Fermilab National Accelerator Laboratory, USA
[96] Virginia Polytech Inst and State University, USA
[97] Rutgers State University, USA
[98] University Cincinnati, USA
[99] Kobe University, Japan
[100] Korea Institute for Advanced Study, Korea
[101] Institute for Basic Science, Korea
[102] University Lyon 1, CNRS, IN2P3, France
[103] Ecole Polytechnique, CNRS, IN2P3, France
[104] University Paris 11, LAL, France
[105] CERN, Switzerland
[106] University Basel, Switzerland
[107] University Warwick, UK
[108] University Manchester, UK
[109] University Durham, UK
[110] DESY, Germany
[111] University Hamburg, Germany
[112] GSI Helmholtzctr Heavy Ion Res GmbH, Germany
[113] Johannes Gutenberg University Mainz, Germany
[114] University Freiburg, Germany
[115] University of Regensburg, Germany
[116] Max-Planck-Institut für Kernphysik, Germany
[117] University Belgrade, Serbia
[118] INFN Lab Nazl Frascati, Italy
[119] McGill University, Canada
[120] University Toronto, Canada
[121] Monash University, Australia
[122] University Sydney, Australia
[123] University Witwatersrand, South Africa
[124] Reseau University Phys Hautes Energies Univ Hassan II, Morocco
[125] University Cadi Ayyad, Morocco
[126] University Nacl Autonoma Mexico, Mexico
[127] COMSATS Institute of Information Technology, Pakistan
[128] Weizmann Institute of Science, Israel

ACKNOWLEDGMENTS

The CEPC-SPPC Preliminary Conceptual Design Report (Pre-CDR) was prepared and written by the CEPC-SPPC Study Group. The study was organised and led by scientists from the Institute of High Energy Physics (IHEP) of the Chinese Academy of Sciences (CAS), and from many universities and other institutes in China and abroad. The study was partially supported by the CAS/SAFEA International Partnership Program for Creative Research Teams and CAS and IHEP grants for the Thousand/Hundred Talent programs.

The current volume is on the physics case and the experiment at the CEPC collider. There will be a separate volume on the CEPC-SppC accelerators. This volume was authored by 480 scientists and engineers from 128 institutions in 17 countries. It has been reviewed by an International Review Committee before its release in April 2015.

CONTENTS

CHAPTER 1

INTRODUCTION

1.1 The CEPC-SPPC Study Group and the Preliminary CDR

A study group was formed in Beijing in September 2013 to investigate the feasibility of a high energy Circular Electron Positron Collider (CEPC) as a Higgs and/or Z factory, and a subsequent Super proton-proton Collider (SPPC). A provisional organization structure and a management team, consisted mostly of Chinese physicists, were established to guide the initial study [1]. The group aims at establishing an international collaboration on CEPC-SPPC after sufficient progress has been made in China or it has been given government funding for R&D on CEPC-SPPC.

The CEPC-SPPC study group undertook a preliminary Conceptual Design Report (preCDR) study, with an aim to address some of the critical questions about the CEPC-SPPC: identifying the most exciting and fundamental physics case, performing the initial design of the accelerator and of the detector, and selecting critical R&D projects for the Technical Design Report (TDR). The preCDR will be reviewed in early 2015 and in time for China's 13^{th} Five-Year Plan consideration, which dictated the time window for the preCDR study.

Since September 2013 a series of international workshops on CEPC-SPPC have been held to study their physics potentials, the designs and technologies of the accelerators and the detector, and the laboratory facilities in China.

This preCDR report contains two volumes: Volume 1 summarizes the theory, detector, software and simulation, and the physics potential of the CEPC-SPPC project; Volume 2 describes the CEPC accelerator design and SPPC consideration, and the associated civil engineering [2]. The contents presented are preliminary and are predominately focused on the CEPC. Formal CDR and TDR work will follow.

1.2 The Case for the CEPC-SPPC in China

The Beijing Electron Positron Collider II (BEPC II) [3] was commissioned in 2008 and is expected to be completed around 2022. The Chinese high energy physics community has been exploring options for the next accelerator based particle physics facility in China. High luminosity circular e^+e^- colliders, for which China has the expertise, operating at the τ-charm region (2 – 7 GeV) [4] and at the Z pole [5], have been under consideration.

The discovery of a Standard Model (SM) like Higgs boson at approximately 125 GeV at the LHC [6, 7] brought about the opportunity to investigate the feasibility of a circular e^+e^- collider (CEPC) operating at $\sqrt{s} \sim 240$ GeV, as a Higgs factory [8, 9], offering high luminosity at its nominal center-of-mass energy. Upgrading the CEPC to a high energy (70 – 100 TeV) super pp collider (SPPC) will be a natural next step which will complement the CEPC and further extend the discovery reach. The CEPC-SPPC distinguishes itself as the top priority collider project for particle physics to be explored in China.

In addition, the circular electron positron collider, CEPC, is likely to be economically affordable and technologically feasible, and the preCDR study will examine these aspects. Together with the upgrade from e^+e^- to pp option, it will cover a time span of several decades. Therefore, the CEPC-SPPC combination is an outstanding long term program for China.

1.3 The Science in the preCDR

As in the case of the International Linear Collider (ILC) [10], the CEPC provides a much cleaner environment than the LHC, and it is ideally suited for studying the Higgs. Another strong advantage of the CEPC experiment over the LHC is that the Higgs can be detected through the recoil mass method by reconstructing Z boson decay only without examining the Higgs decays. This method establishes the denominator for absolute measurement of branching fractions, and will consequently allow the incorporation of the LHC results to obtain the best world averages. The recoil mass method also provides the best probe into the Higgs invisible decays and search for dark matter and exotic particles produced in the Higgs decays.

The ATLAS and CMS experiments at the LHC will continue to improve the measurement of the Higgs boson properties including couplings to gauge bosons and Yukawa couplings, from current accuracies to future levels of a few percent achievable for some of the couplings. The Higgs physics program to be carried out at the CEPC have been be evaluated through the preCDR study and its extent of the precision of many of couplings are shown to percent or sub-percent levels. Mass and decay width of the Higgs boson will also be investigated. The production mechanism of the Higgs boson, an important probe into the nature of the Higgs, will also be examined.

The CEPC can also operate at the Z pole ($\sqrt{s} \sim 91$ GeV) and near the WW threshold ($\sqrt{s} \sim 160$ GeV) to allow for refined measurement of the SM parameters. Orders of magnitude of increase in luminosity at the Z pole compared to the LEP collider is expected, the Z line-shape and coupling measurements will benefit from the shorter time of operation with reduced systematic uncertainties. Many other electroweak parameters may also be better measured with CEPC operated at various energy points. Huge data sample from the Z pole will greatly improve our understanding of heavy flavor dynamics, namely the decays of beauty, charm hadrons and τ leptons and also about their productions.

This preCDR will also describe the physics potential of the SPPC. Although different options of SPPC have been proposed, the physics studies here used center of energy 100 TeV as a benchmark. At the same time, most studies are based on an integrated luminosity of 3 ab^{-1}, although higher ones have been considered in some cases.

1.4 The Accelerator and the Experiment

The CEPC e^+e^- collider is envisioned to operate with a center-of-mass energy of $\sqrt{s} \sim 240$ GeV where the Higgs events are produced primarily through the interaction $e^+e^- \to ZH$. With a nominal luminosity of $2 \times 10^{34}\ \mathrm{cm^{-2}s^{-1}}$ about 1 million clean Higgs events will be produced by CEPC over a period of 10 years at two interaction points.

This report will provide the accelerator machine configuration, the dimension of the tunnel and will consider the technology requirement for the colliders and the detector as well as identify the accelerator and detector R&D focuses for the next phase. A benchmark site in the city of Qinhuangdao has been identified and civil engineering consideration based on the site will be described.

The CEPC preCDR study has benefited from the progress in the ILC accelerator and detector designs, and the tools and know-hows achieved through the ILC projects [11, 12] and the LHC experiments. The CEPC study group, together with the FCC and ILC community, will contribute to the development of future high energy colliders and experiments which will ensure that the elementary particle physics remain a vibrant and exciting field of fundamental investigation for decades to come.

References

[1] CEPC project website. http://cepc.ihep.ac.cn.

[2] The CEPC-SPPC Study Group, *CEPC-SPPC Preliminary Conceptual Design Report, Volume II - Accelerator*, 2015. IHEP-CEPC-DR-2015-01, IHEP-AC-2015-01.

[3] M. Ablikim et al., *Design and construction of the BESIII detector*, Nucl. Instrum. Meth. **A614** (2010) 345 – 399.

[4] Workshop on Physics at Future High Intensity Collider @ 2 – 7 GeV in China. http://cicpi.ustc.edu.cn/indico/conferenceDisplay.py?confId=87.

[5] Z. Zhang, *The physics at a super Z-factory*, Sci. CHINA Phys. Mech. Astron. **53** (2010) 1947–2036.

[6] The ATLAS Collaboration, G. Aad et al., *Observation of a new particle in the search for the Standard Model Higgs boson with the ATLAS detector at the LHC*, Phys. Lett. B **716** (2012) 1–29, arXiv:1207.7214 [hep-ex].

[7] The CMS Collaboration, S. Chatrchyan et al., *Observation of a new boson at a mass of 125 GeV with the CMS experiment at the LHC*, Phys. Lett. **B716** (2012) 30–61, arXiv:1207.7235 [hep-ex].

[8] A. Blondel and F. Zimmermann, *A High Luminosity e^+e^- Collider in the LHC tunnel to study the Higgs Boson*, arXiv:1112.2518.

[9] A. Blondel, A. Chao, W. Chou, J. Gao, D. Schulte, et al., *Report of the ICFA Beam Dynamics Workshop 'Accelerators for a Higgs Factory: Linear vs. Circular' (HF2012)*, arXiv:1302.3318 [physics.acc-ph].

[10] T. Behnke et al., *The International Linear Collider Technical Design Report - Volume 1: Executive Summary*, arXiv:1306.6327 [physics.acc-ph].

[11] C. Adolphsen et al., *The International Linear Collider Technical Design Report - Volume 3.II: Accelerator Baseline Design*, arXiv:1306.6328 [physics.acc-ph].

[12] T. Behnke et al., *The International Linear Collider Technical Design Report - Volume 4: Detectors*, arXiv:1306.6329 [physics.ins-det].

CHAPTER 2

OVERVIEW OF THE PHYSICS CASE FOR CEPC-SPPC

With the discovery of the Higgs boson at the Large Hadron Collider [1, 2], fundamental physics finds itself at one of the most exciting crossroads in its history. The central questions today are the deepest ones that have been posed in decades, related to the ultimate origin of the elementary particles and even of space-time itself. Major new input from experiments is needed for progress. The future of fundamental physics on the 20-50 year timescale hinges on starting a huge new accelerator complex that can take us at least one order of magnitude beyond the ultimate reach in precision and energy of the LHC. This is the goal of the CEPC/SPPC project.

Many of the most profound mysteries are intimately connected with the Higgs particle, which is totally new, unlike anything we have seen before. In many ways the Higgs is the simplest particle imaginable, with no charge and no spin. This apparent simplicity is also what makes it so beguiling. All other scalar particles we have seen have been obviously composite, with a size close to their Compton radius. The Higgs is not like this, appearing to be more point-like than naturally expected on theoretical grounds.

The LHC will only provide a fuzzy picture of the Higgs, however, and will leave us in the dark as to whether it is truly “elementary". To settle this question it will be necessary to put the Higgs under a much more powerful microscope. The CEPC will do this by producing millions of Higgs particles and studying their interactions with exquisite precision.

The Higgs must also have a dynamical property we have never seen for any of the other fundamental particles: it should be to able to interact not only with other particles, but also with itself! Indeed, self-interaction is the most basic of all processes allowed by quantum field theory, but spin and charge forbids point-like self-couplings for all particles but the Higgs. The LHC will give us essentially no handle on this physics, but with the

data from the CEPC, and more crucially the SPPC, we will be able to unambiguously see this process, whose structure is deeply related to the origin and mass of the Higgs itself. These two points are sketched in Fig. 2.1, and represent the central physics questions the

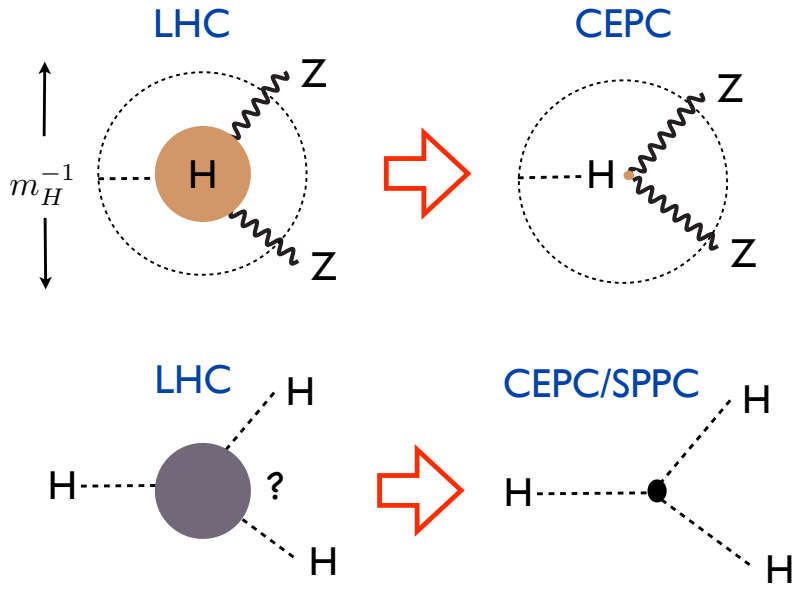

Figure 2.1 A sketch of two of the central goals of the CEPC and SPPC. The CEPC will probe whether the Higgs is truly “elementary", with a resolution up to a hundred times more powerful than the LHC. The SPPC will see, for the first time, a fundamentally new dynamical process — the self-interaction of an elementary particle — uniquely associated with the Higgs.

CEPC and SPPC are guaranteed to attack and resolve.

At an even more fundamental level, much of the excitement surrounding the CEPC and SPPC stems from the bold leap into the completely uncharted new territory that they offer, probing energy scales where we have long had reasons to expect fundamental new physical principles at play. The CEPC measurements of Higgs interactions with other particles, with an accuracy of nearly one part in a thousand, will provide a multitude of clues to its microscopic structure well beyond the capabilities of the LHC. The SPPC will allow us to hunt for new fundamental particles an order of magnitude heavier than we can possibly produce with the LHC, and new particles the LHC may produce in small numbers will be produced with up to a thousand times higher rate, giving us a new window into the quantum-mechanical vacuum of our universe with a hundred-fold greater resolution than ever before.

Over the past year, a large group of theorists around the world have embarked on detailed studies of the physics potential of the CEPC and SPPC, spanning a wide range of topics, resulting in dozens of papers [3–27]. Needless to say, these studies are all in early stages, and many years of intensive work is still needed to arrive at a complete picture of the capabilities of these machines. Our aim in this overview section is not to exhaustively review the wide array of results found to date, as these will likely be continuously improved in the near future. Instead, we will give a high-level summary of the central scientific issues at stake, and draw on the studies that have been carried out to show that the leap in precision and energy offered by the CEPC/SPPC project is just what is needed to robustly tackle many of the most profound mysteries that confront us. The main focus

will be on the nature of the electroweak phase transition, the origin and naturalness of the electroweak scale, and electroweakly interacting dark matter. More details and additional studies are provided in subsequent sections.

Before proceeding, let us define the parameters we will be using for the CEPC-SPPC studies in this report; further details are given in the companion accelerator pre-CDR volume. The CEPC will collide electrons and positrons. As a Higgs factory, the center of mass energy will be 250 GeV, with an instantaneous luminosity of 2×10^{34} cm^{-2}s^{-1}, giving 5 ab^{-1} of integrated luminosity over ten years of running with two detectors. The CEPC can also run at the Z pole, with a preliminary target of producing 10^{10} Z's in one year of running.

The baseline design of the CEPC is based on a 50 km tunnel, while a 100 km option has also been discussed. The same tunnel can house a proton-proton collider. With the 50 km option, center of mass energies can range from $70 - 100$ TeV, depending on the development of future superconducting magnet technology. A 100 km tunnel will allow center of mass energies from $100-140$ TeV. Given the longer timescale associated with the SPPC project, and the uncertainty associated with the development of magnet technology, for our SPPC studies we will take the ambitious view of exploring the physics capabilities of proton-proton collision at 100 TeV, and an integrated luminosity of 3 ab^{-1}.

2.1 New Colliders for a New Frontier

Fundamental physics began with the twin revolutions of Relativity and Quantum Mechanics. Much of the second half of the century was occupied with understanding the reconciliation of these principles within the framework of quantum field theory, and identifying a specific quantum field theory — the Standard Model of particle physics — describing all particles and interactions we know of to date.

Theoretical consistency with relativity and quantum mechanics places extremely strong constraints on theories of interacting masslesss particles, almost completely dictating the possible menu of spins and interactions. At low enough energies compared to some fundamental ultraviolet scale, physics is guaranteed to be described by Yang-Mills theories and gravity coupled to particles of spin 0, 1/2, and also possibly spin 3/2 with supersymmetry. The rigidity of this structure is striking. Of course, most elementary particles are not massless, but since the effects of mass are naively negligible at high energies, these rules fix what physics at very high energies can look like, at least until we hit the Planck scale where the usual notions of space-time itself break down.

For particles with nontrivial spins, there is a jump in the number of spin degrees of freedom between massless and massive particles. For instance, the massive W and Z bosons have spin one and three spin degrees of freedom, but only two helicity degrees of freedom. This discontinuous difference between “massless" and “massive" obstructs a smooth transition from the apparent complexity of low energy physics to the simplicity of the high energy world whose structure is almost entirely dictated by general principles.

Famously, in the Standard Model, the addition of a single particle—the Higgs boson—solves this problem, allowing us to reassemble the degrees of freedom of massive particles at low energies into the consistent high energy framework for massless particles.

The Higgs is certainly the simplest solution to the problem it solves—it is hard to imagine a simpler elementary particle, with no spin or charge. But this simplicity is actually extremely surprising and, in a literal sense, unprecedented, since we have never before

seen a point-like elementary particle of spin zero. Indeed, violent ultraviolet quantum fluctuations have the potential to generate huge masses for elementary particles, but this doesn't happen for particles with spin, where a change from "massless" to "massive" would change the number of spin degrees of discontinuously. However, the number of spin degrees of freedom for massless and massive particles of spin zero is the same, and so nothing shields the generation of huge scalar masses, near the highest ultraviolet (UV) scales of the theory.

This logic is strongly supported from analogous phenomena in condensed matter physics. Various materials can be engineered to be described by non-trivial long-distance effective theories at very low temperatures. Many of the key features of the Standard Model, like gauge fields and chiral fermions, can arise in a beautiful way as emergent collective excitations of the system. But interacting spin zero particles like the Higgs are not seen: the only light scalars that are ubiquitously present are Goldstone bosons — like phonons — which are non-interacting at low energy. This makes sense because the emergence of fermions and gauge fields can be robust and stable against small variations in the detailed properties of the material. Since this is not true for scalars, the only way to get light scalars to emerge from a condensed matter system is to finely adjust the microphysics of the material: for instance by putting it under high pressure, looking for the thin slivers in parameter space where a Higgs-like scalar becomes accidentally light. This expectation has been borne out by recent experiments which do indeed fine-tune to produce a particle resembling the Higgs boson of an (ungauged) $SO(3) \to SO(2)$ symmetry breaking pattern [28].

These good reasons for never having seen light scalars either in particle physics or condensed matter systems make it all the more remarkable to have finally found one with the Higgs! There is an irony here: the development of the Higgs mechanism was greatly inspired by the Landau-Ginzburg model of superconductivity. However, the Landau-Ginzburg model was never a real theory, only a phenomenological model, and was replaced by BCS theory a few short years later. Many theorists expected the same fate for the Higgs model of electroweak symmetry breaking, with technicolor being the particle physics analog of BCS theory. But it was the Higgs model that ended up being the right answer in particle physics!

So while an oft-heard desire of particle physicists for many years has been to find "new physics" beyond the Higgs, this is missing the essential point: the Higgs itself represents "new physics" in a much more more profound way than any more complex discoveries would have done. Its discovery closes the 20th century chapter of fundamental physics while simultaneously kicking the door open to entirely new questions that properly belong to the 21st century. These questions on the table now are not about details, but are deeper and more structural ones, leading back to the very foundations of quantum field theory. It is striking that very similar questions are forced on us in trying to reckon with the smallness of the cosmological constant and the discovery of the accelerating expansion of the universe.

Obviously, the experimental future of the field will importantly depend on results from the next run of the LHC. However, given what we have already seen — a light higgs, but no evidence yet for physics beyond the standard model — no matter what new physics the LHC does or does not discover, it is unlikely to provide us with a complete picture of the relevant physics. New machines beyond the LHC will be needed, not for cleaning up details, but in order to answer the big-picture questions that will set the direction of

fundamental physics for decades to come. The CEPC/SPPC program gives us the ideal combination of leaps in precision and energy needed to unravel the deep new mysteries opened up by the discovery of the Higgs.

Let us begin by giving a lightning tour of the raw physics capabilities of these machines.

The CEPC will produce millions of Higgs particles, measuring the Higgs couplings to the gauge bosons and fermions to exquisite accuracy, typically at the percent to sub-percent level, as shown in Fig. 2.2. Moreover, CP-violating Higgs couplings, which are

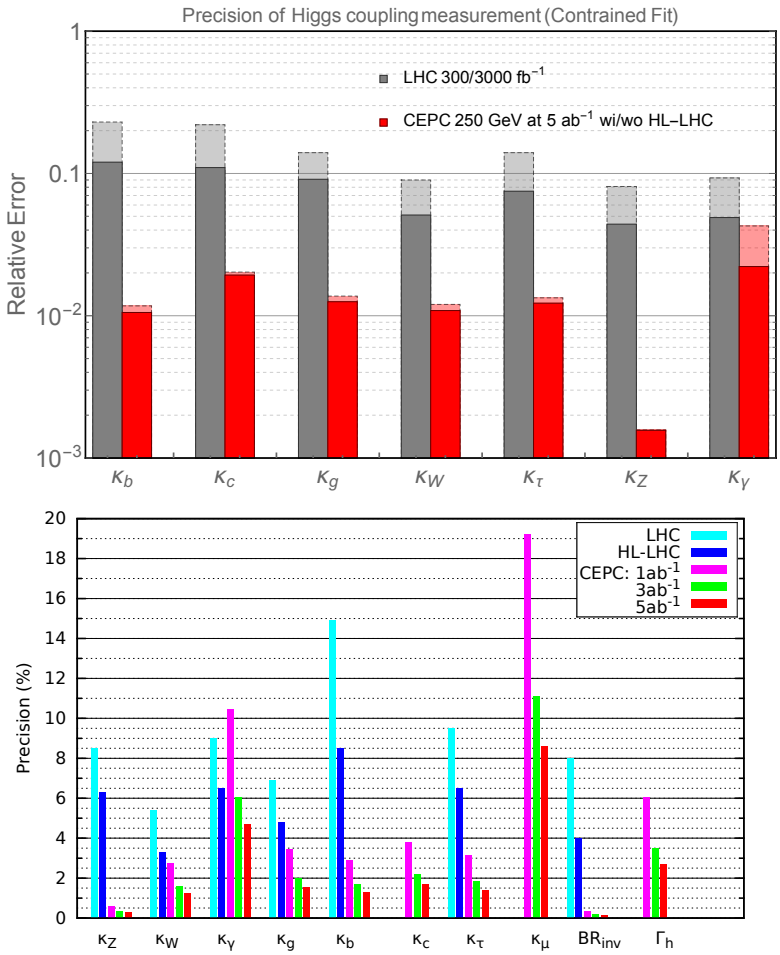

Figure 2.2 Top: The 7 parameter fit, and comparison with the HL-LHC, discussed in detail in Chapter 3. The projections for CEPC at 250 GeV with 5 ab^{-1} integrated luminosity are shown. The CEPC results without combination with HL-LHC input are shown with dashed edges. The LHC projections for an integrated luminosity of 300 fb^{-1} are shown in dashed edges. Bottom: Comparison between the LHC and several benchmark luminosities of the CEPC.

predicted in certain extensions of the Standard Model Higgs sector, can be seen at the percent level, and tiny branching ratios for invisible and exotic Higgs decays can be probed at the 10^{-4} level.

Furthermore, when running on the Z-pole, the CEPC can produce up to 10^{11} Z bosons, measuring the couplings of the Z to the 10^{-4} level, and improving the limits on precision electroweak observables by an order of magnitude or more [3], as shown in Fig. 2.3.

Most importantly, the leap in energy at the SPPC gives a huge increase in the reach for new physics. A seven-fold increase in center of mass energy relative to the LHC, with

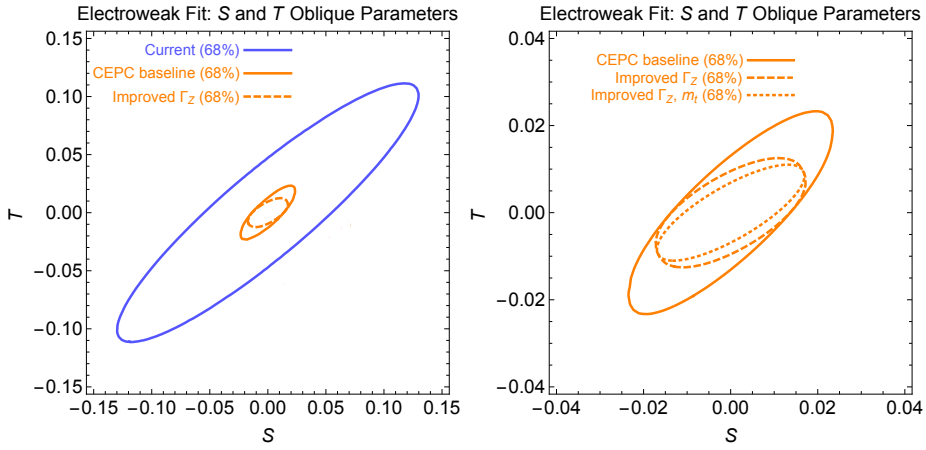

Figure 2.3 Left: CEPC constraints on the oblique parameters S and T, compared to the current constraints. Right: CEPC constraints on the oblique parameters S and T, for the baseline scenario and two possible improvements. Notice that the axes of this plot have zoomed in by a factor of 5 compared to those of left panel. For clarity we show only 1σ ($\Delta\chi^2 = 2.30$) constraints.

a luminosity comparable to that of the LHC, increases the mass reach for new particles by a factor of about five relative to the LHC. We illustrate this with typical production cross-sections for W', Z's, colored and uncolored particle pair production shown below in Fig. 2.4.

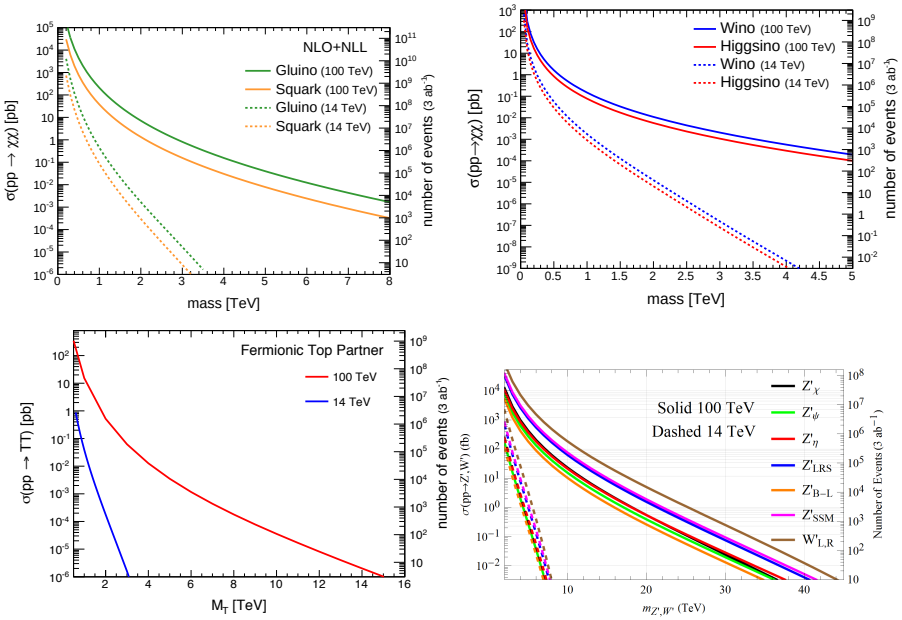

Figure 2.4 Production cross section of new physics particles. Top left: gluino and squark. Top right: higgsino and wino. Bottom left: fermionic T'. Bottom right: W' and Z'.

Due to rapidly falling parton luminosities, the rates for processes at fixed invariant masses also increases dramatically in going from 14 to 100 TeV, as illustrated in Fig. 2.5 [29]. This will allow several extremely rare standard model processes to be seen for the first time.

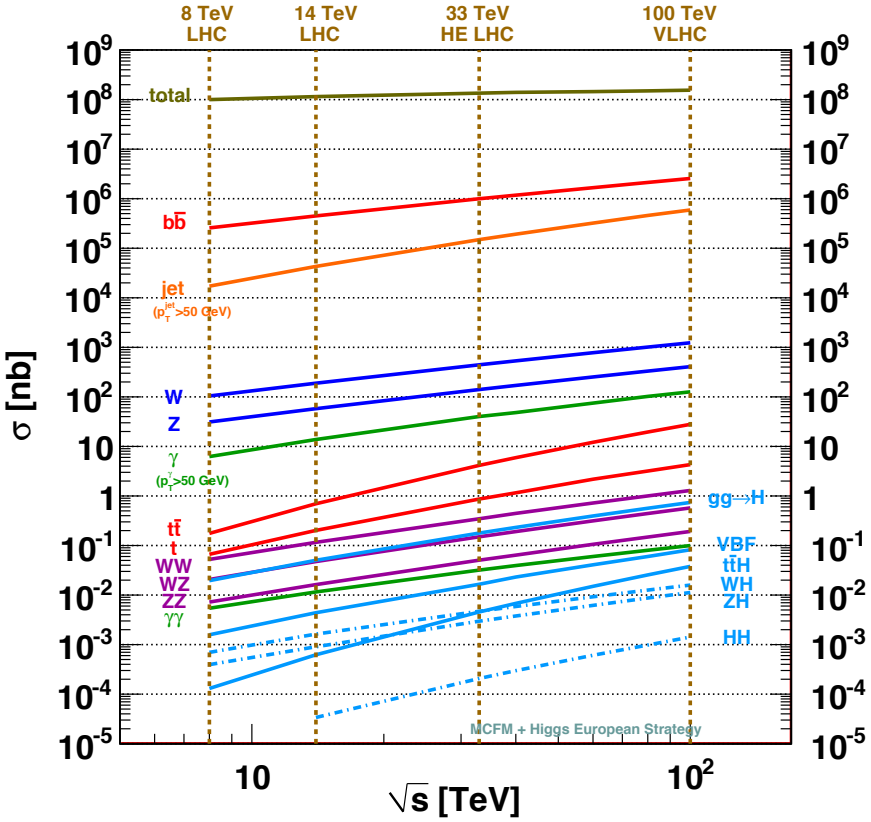

Figure 2.5 Rates of SM processes [29].

Collisions at 100 TeV experimentally probe the standard model in a regime where the electroweak symmetry is effectively restored. Numerically, a top quark at 100 TeV is as massless as the bottom quark at the Tevatron energy. An immediate consequence will be that the top quark, as well as the W, Z bosons, may be properly treated as partons in the proton when there is a heavy new physics scale involved. We illustrate this point in Fig. 2.6, where we show the partonic luminosities versus the averaged energy fraction $\sqrt{\tau}$ (lower scale) and the partonic CM energy $\sqrt{s}$ (top scale) for the top quark in Fig. 2.6 (left) [7] and the electroweak gauge bosons in Fig. 2.6 (right) [30]. We see that the top quark luminosity can be as large as a percent of the bottom quark in the relevant energy regime. For instance, at the 5 TeV partonic energy, the top quark luminosity is about 1. Incidentally, the electroweak gauge boson luminosities are comparable to that of the top quark. As expected, the luminosities of $W^{\pm}\gamma$ and $W_T^+ W_T^-$ are roughly the same, indicating the electroweak unification and the symmetry restoration. On the other hand, the luminosity for the longitudinally polarized gauge bosons is about two orders of magnitude lower, due to the lack of energy enhancement from a Goldstone-boson radiated off a quark.

For p_T's approaching ~ 10 TeV, the electroweak Sudakov factor $\sim 4\alpha_2 \log^2(p_T^2/m_W^2) \sim 0.1$, and we have "electroweak radiation" in complete analogy with electromagnetic and gluon radiation. At the very high energies $E \gg M_W$, EW gauge bosons are copiously produced by radiation. For instance, a W or Z gauge boson would be radiated off a light quark with 10 TeV of energy with a probability of 10% and off a gauge boson with a

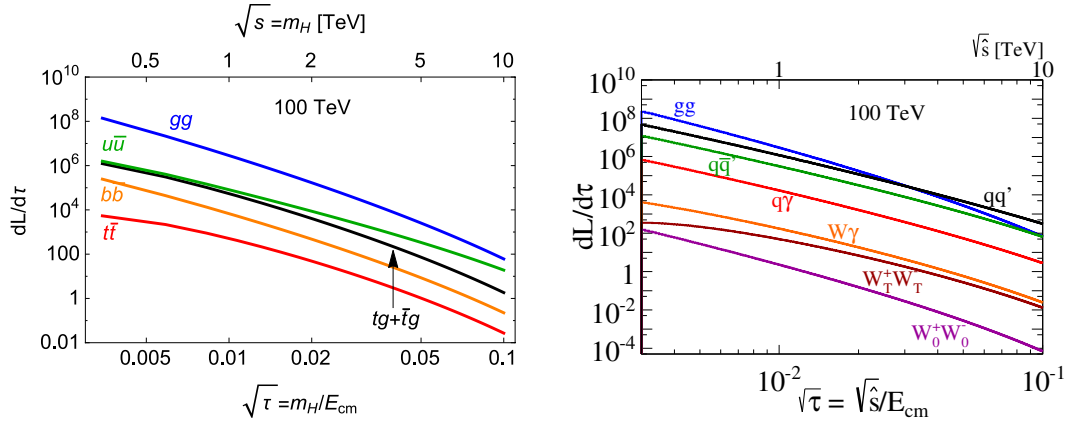

Figure 2.6 Parton luminosities at a 100 TeV pp collider, shown in particular are the top quark [7] and W^+W^- partonic luminosities [30] versus the averaged energy fraction $\sqrt{\tau}$ (lower scale) and the partonic CM energy $\sqrt{s}$ (top scale).

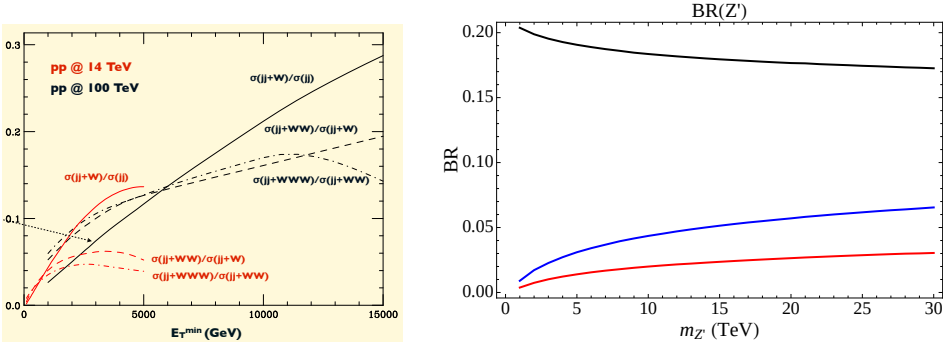

Figure 2.7 Left: Rates of SM W+jets processes [31]. Right: Branching ratios of a B-L gauge boson. We have the $\nu\bar{\nu}, \nu\bar{\nu}Z, \nu l^{\pm}W^{\mp}$ final states in black, red and blue respectively.

probability of 20%, yielding a rate that is order of magnitude higher than the perturbative production of a gauge boson. This is illustrated in the left panel of Fig. 2.7, where we see that nearly 20% of dijet events with $p_T \sim 10$ TeV contain a W or Z.

This phenomenon makes it easier to "see" traditionally invisible particles such as neutrinos (or even dark matter particles), through electroweak radiation. This can be nicely illustrated by probing the invisible decay of a $Z' \to \nu\nu$ at the SPPC. For heavy enough Z''s, there is a significant rate for radiating off W, Z's. The ratio $\Gamma(Z' \to \nu\bar{\nu})/\Gamma(Z' \to \nu\bar{\nu}Z/W)$ only depends on the mass of the Z', and so if this visible mode is abundant enough we can directly determine the invisible rate (and thereby also directly determine the Z' coupling to left-handed leptons). The total three-body branching ratio can be as large as a few percent for a heavy Z', as shown in the right panel of Fig. 2.7 [6].

It is worth emphasizing that the combination of Higgs and Z-pole measurements at the CEPC together with the SPPC give powerful and complementary probes of Higgs couplings. The leading deviations in Higgs couplings away from the Standard Model can be parametrized by a set of dimension six operators suppressed by a mass scale M:

$$\mathcal{L} = \mathcal{L}_{SM} + \sum_i \frac{c_i}{M^2}\mathcal{O}_{6,i} \tag{2.1}$$

These give corrections to Higgs couplings schematically of the form

$$\delta \sim c_i \frac{v^2}{M^2} \tag{2.2}$$

where the size of the c_i will typically be $O(1)$.

Probing new physics beyond the LHC's reach for directly produced new particles, with masses up to $M \sim 1$ TeV, requires the measurement of Higgs couplings at least at percent level accuracy. Current levels of precision are at the $\sim 15\%$ level in most cases, and precisions of a few percent are achievable for some of the couplings. The CEPC and SPPC can robustly improve this precision by an order of magnitude.

The dimension six Higgs operators are conveniently grouped into a few classes. Some involve inserting $(h^\dagger h)$ into the usual dimension 4 operators; these preserve custodial $SU(2)$ symmetry. Others, importantly including the standard precision electroweak operators, violate custodial $SU(2)$. Schematically we have

$$\begin{aligned} &(h^\dagger h)^3,\ (\partial_\mu h^\dagger h)^2, (h^\dagger h) h f f^c, (h^\dagger h) F_{\mu\nu}^2; \\ &h^\dagger \overleftrightarrow{D}_\mu h \bar{f} \bar{\sigma}^\mu f;\ (h^\dagger D_\mu h)^2, h^\dagger W^{\mu\nu} h B_{\mu\nu}, \end{aligned} \tag{2.3}$$

Since the operators on the first line preserve all the approximate global symmetries of the Standard Model, nothing stops them from being generated by integrating out new particles with masses near the TeV scale and with reasonable couplings to the Higgs . This is not necessarily the case for the operators on the second line.

The $(h^\dagger h)^3$ coupling, which leads to deviation in the triple Higgs coupling, is best probed at the SPPC, by looking for double-Higgs production. At the LHC, this process suffers a low production rate and large SM backgrounds. Moreover, one needs to disentangle different contributions, shown in Fig. 2.8, to the same scattering amplitude in order to achieve a desirable measurement of the triple Higgs coupling. This will probe the

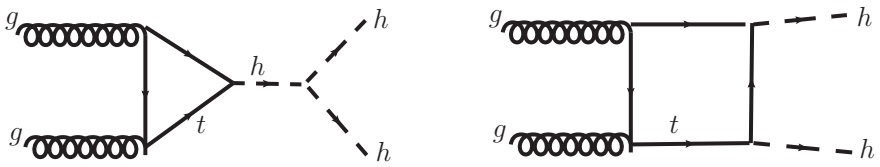

Figure 2.8 Left: dominant process for measuring triple Higgs coupling at SPPC. Right: a SM process which contributes to the same di-Higgs production process.

Higgs self-coupling at the ten percent level [4]. The SPPC will also directly probe the top Yukawa coupling via tth production, at the 1% level.

The CEPC is the best machine to probe the first set of operators on the top line — which give direct shifts of the coupling of the Higgs to the Z, fermions, and photons. The operators on the final two lines lead to modifications of the couplings of the Z to fermions, which are most powerfully probed in the Z factory mode of the CEPC.

In the coming sections, we will focus in more detail on a number of important cases of new physics — related to the nature of the electroweak phase transition, and to naturalness — which produce deviations at a level that can be detected by the CEPC/SPPC. Let us instead here use other examples of new physics, also generating sizable deviations, which further illustrate the complementarity between Higgs and Z-pole measurements.

Given that the only light scalars we have seen in particle physics — the pions — are pseudo-Goldstone bosons, it is natural to consider the possibility that the Higgs might also be a composite pseudo-Goldstone boson, non-linearly realizing an approximate underlying non-Abelian symmetry. Just as with pions, this gives rise to non-linear correction to the Higgs kinetic terms. This modifies the Higgs coupling to W^+W^- and ZZ by factors κ_W, κ_Z which deviate from unity by $O(v^2/f^2)$, where f is the decay constant for the PNGB Higgs. For example, in the minimal composite Higgs model [32] we have:

$$\kappa_W = \kappa_Z = \sqrt{1 - \frac{v^2}{f^2}} \tag{2.4}$$

Since the dominant Higgs production mechanism at the CEPC is Higgsstrahlung, $e^+e^- \to Z^* \to Zh$, κ_Z is measured at the per-mil level, powerfully constraining f. Composite Higgs models can also affect precision electroweak parameters albeit in a more model-dependent way, but a classic estimate for the S-parameter arising from an underlying theory with a large number N of colors is

$$S \sim \frac{N}{4\pi}\frac{v^2}{f^2} \sim \left(\frac{N}{3}\right)\frac{v^2}{4f^2} \tag{2.5}$$

Parametrically large N is disfavored on a number of phenomenological grounds, so we will take $N \sim 3$ and $S \sim v^2/(4f^2)$. From here we can see that the sizes of the shifts to the $Z - h$ coupling and S are essentially the same:

$$(\kappa_Z - 1) \sim S \sim \frac{v^2}{f^2} \tag{2.6}$$

We can also see such correlations in supersymmetric theories. Taking as a simple example the case where all but the left-handed stop squark $\tilde{t}_L$ are decoupled, at 1-loop we induce a shift in the higgs–gluon–gluon coupling, as well as a contribution to the T parameter:

$$(\kappa_g - 1) \sim \frac{m_t^2}{4m_{\tilde{t}_L}^2},\ T \sim \left(\frac{m_t^2}{4\pi \sin^2\theta_W m_W^2}\right) \times \frac{m_t^2}{4m_{\tilde{t}_L}^2} = \left(\frac{m_t^2}{4\pi \sin^2\theta_W m_W^2}\right) \times (\kappa_g - 1) \tag{2.7}$$

The reach in f and $m_{\tilde{t}_L}$ from Higgs factory and Z-pole measurements is shown in Table 2.1 [3]. For a composite Higgs, the most powerful probe is the very well-measured coupling of the Higgs to the Z which dwarfs those from the S and T parameters. On the other hand, bounds on the left-handed stops from the T parameter and from Higgs coupling measurements are very similar, with the T parameter bound generally being slightly stronger.

Note also that since custodial $SU(2)$ is broken by hypercharge, the custodial invariant operators will induce the precision electroweak operators under RG evolution; this alone gives some correlation between deviations in Higgs and Z couplings. For instance consider the case of the ubiquitous “oblique" Higgs operator $[\partial_\mu(h^\dagger h)]^2$, which leads to a shift in the $Z - h$ coupling after electroweak symmetry breaking:

$$\frac{1}{2}\frac{c_H}{M^2}[\partial_\mu(h^\dagger h)]^2 \to (1 + 2c_H\frac{v^2}{M^2}) \times \frac{1}{2}(\partial_\mu H)^2 \to \delta Z_h = \frac{2v^2 c_H}{M^2} \tag{2.8}$$

Under RG evolution from the scale M down to the Z, this coupling also induces the S and T parameters; keeping the logarithmically enhanced term gives us

$$S = \frac{1}{6\pi}\log\frac{M}{m_W} \times \frac{2v^2 c_H}{M^2} = .06 \times \delta Z_h \tag{2.9}$$

Experiment	κ_Z (68%)	f (GeV)	κ_g (68%)	$m_{\tilde{t}_L}$ (GeV)
HL-LHC	3%	1.0 TeV	4%	430 GeV
ILC500	0.3%	3.1 TeV	1.6%	690 GeV
ILC500-up	0.2%	3.9 TeV	0.9%	910 GeV
CEPC	0.2%	3.9 TeV	0.9%	910 GeV
TLEP	0.1%	5.5 TeV	0.6%	1.1 GeV

Experiment	S (68%)	f (GeV)	T (68%)	$m_{\tilde{t}_L}$ (GeV)
ILC	0.012	1.1 TeV	0.015	890 GeV
CEPC (opt.)	0.02	880 GeV	0.016	870 GeV
CEPC (imp.)	0.014	1.0 TeV	0.011	1.1 GeV
TLEP-Z	0.013	1.1 TeV	0.012	1.0 TeV
TLEP-t	0.009	1.3 TeV	0.006	1.5 TeV

Table 2.1 Interpreting the Higgs coupling and the bounds on the oblique S and T parameters in terms of new physics reach [3]. CEPC (imp.) is assuming the improvement in both $\sin^2\theta^\ell_{\rm eff}$ and Γ_Z.

and similarly

$$T = \frac{3}{8\pi\cos^2\theta_W}\log\frac{M}{m_W} \times \frac{2v^2 c_H}{M^2} = .2 \times \delta Z_h \tag{2.10}$$

where we have chosen $M \sim 300$ GeV as a reference. The projected CEPC sensitivity to S, T on the Z poles is $\Delta S, \Delta T \sim .01$, but we see that this is significantly weaker than the direct reach in δZ_h.

The CEPC also has some sensitivity to Higgs self-interactions arising from the $(h^\dagger h)^3$ operator. Amusingly, this operator does not induce any of the other dimension 6 operators involving the Higgs under 1-loop RG evolution. But there is infrared calculable correction to the Z-Higgs coupling at 1-loop, which probes deviations in the triple Higgs coupling at the 50% level [5].

Of course dimension six operators for the Higgs also give rise to a quadratically rising amplitude for longitudinal WW scattering $\mathcal{A}(W_L W_L \to W_L W_L) \sim c\frac{s}{M^2}$, which is a clear target of study for the SPPC; any deviation in Higgs couplings seen at CEPC should be correlated with WW scattering at SPPC. It is however difficult to make a sharp correlation in a model-independent way: a visible effect at the CEPC means that scale M can't be much larger than the TeV scale, but then partonic scatterings at the SPPC can take place at scales above M. The falling parton luminosities do not compensate for the rising amplitudes, so the prediction for the SPPC is dominated by the physics of the UV completion. For instance in composite Higgs modes, we expect that the Higgs couples to a new massive ρ-like spin-one particle. Detailed studies of the SPPC reach for such states are under way, but a rough estimate of the reach extends to ρ masses up to ~ 8 TeV:

We have largely focused on deviations in the largest Higgs couplings to the gauge bosons and the third generation, but the study of Higgs couplings to the light fermions could be equally interesting, and has the potential to shed significant new light on the origin of flavor. The "big" couplings to the Higgs are already constrained by the Higgs doing its job of unitarizing scattering amplitudes amongst longitudinal W's and top quarks. On the other hand, the small masses of the lighter generation fermions allow the Unitarity

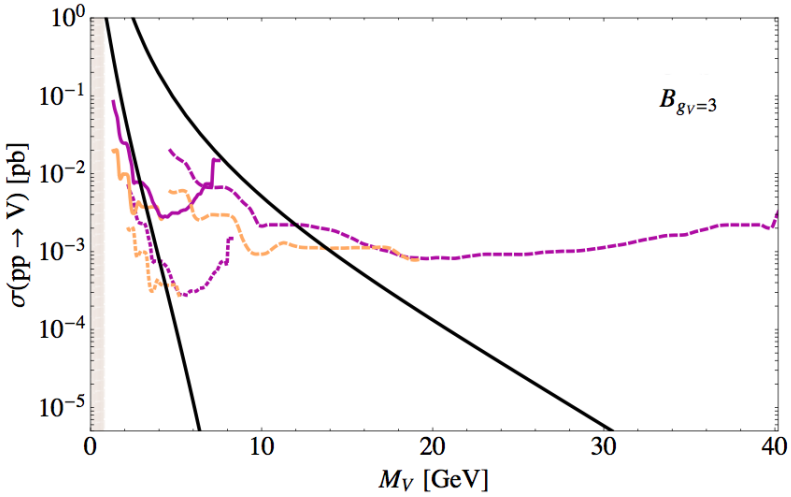

Figure 2.9 Reach for vector resonances, ρ, at the SPPC [33]. The purple lines are extrapolated from searches for leptons and neutrinos and the orange lines are extrapolated from decays to $W^{\pm}Z$.

bound to be pushed to much higher scales, and it is possible to imagine significant deviations in Higgs couplings to the light generations. To take an extreme limit, we can imagine that the Yukawa couplings to the physical Higgs are simply shut off. Interestingly, the analysis of [34] shows unitarity violation for first-generation quarks already for energies $\Lambda_F < 100$ TeV. Another way of understanding this is to assume corrections to the

$\xi_1\xi_2$	V_LV_L	$t\bar{t}$	$b\bar{b}$	$c\bar{c}$	$s\bar{s}$	$d\bar{d}$	$u\bar{u}$	$\tau^-\tau^+$	$\mu^-\mu^+$	e^-e^+	$\nu_L\nu_L$
Mass (GeV)	80.4	178	4.85	1.65	0.105	0.006	0.003	1.777	0.106	5.11×10^{-4}	5×10^{-11}
n_s	2	2	4	6	8	10	10	6	8	12	22
$E^{\star(\min)}_{2\to n}$ (TeV)	1.2	3.49	23.4	30.8	52.1	77.4	83.6	33.9	56.3	107	158
$E^{\star}_{2\to 2}$ (TeV)	1.2	3.49	128	377	6×10^3	10^5	2×10^5	606	10^4	2×10^6	1.1×10^{13}

Figure 2.10 Summary [34] of the strongest unitarity limit $E^{\star\,\min}_{2\to n}$ for each scattering $\xi_1\xi_2 \to nV_L^a$ ($\xi_{1,2} = V_L, f, \bar{f}, \nu_L$) and the corresponding number of final state particles $n = n_s$, in comparison to the classic $2 \to 2$ limit $E^{\star}_{2\to 2}$.

Higgs-Yukawa couplings from higher-dimension operators of the form, say for up quarks,

$$\left(\lambda_u + \frac{h^\dagger h}{\Lambda^2}\right) Q h u^c \to m_u \sim \left(\lambda_u + \frac{v^2}{\Lambda^2}\right) v \tag{2.11}$$

Indeed, precisely because the up mass is so small, we could even imagine that the usual Yukawa coupling vanishes ($\lambda_u \to 0$), and that needed up mass arises from $(m_u/v) \sim 10^{-5} \sim v^2/\Lambda^2$ for $\Lambda \sim 50$ TeV. In this case the physical Higgs coupling would be $(3m_u/v)$, larger than its Standard Model value by a factor of 3. We can also adjust this coupling to vanish; this allows us to see the origin of the 100 TeV strong coupling scale in [34] as simply being the scale associated with the higher-dimension operator. Of course in the absence of any other new physics, this picture is unnatural: the chiral symmetry on the up is badly broken at the scale Λ, so one would actually expect a large Yukawa coupling; this is also indicated by closing two higgses into a loop with this operator, which with a

cut-off Λ would again generate a large Yukawa coupling. This problem can be avoided in supersymmetric theories, which also provide a natural rationale for this structure, if the light fermions are charged under a Peccei-Quinn symmetry, so that the superpotential interactions giving Yukawa couplings involve extra factors of the up- and down- type Higgs fields (H_u, H_d). Of course since in such theories the couplings of the Higgs are inevitably flavor-violating, any complete model will have to ensure the absence of large FCNC's. It is fascinating to find the 100 TeV scale arising in connection with the fermion mass hierarchy in this way. This physics will be a natural target for studies at the SPPC.

Energy and luminosity of the SPPC

In this discussion of machine capabilities, some brief comments about the energy and luminosity requirements of the SPPC are in order. The center of mass energy and luminosity of a proton proton collider are crucial in determining its physics potential. Perhaps the most obvious question is how energy and luminosity impact mass reach for the production of new particles. Many of the studies quoted in this document are based on studies using $E_{\rm CM} = 100$ TeV, with integrated luminosities ranging from 3 ab^{-1} to 30 ab^{-1}. The reach will roughly scale with the $E_{\rm CM}$ if other options are considered.

At the same time, larger integrated luminosity leads to sensitivity to smaller signal cross section, which in turn enhance the new physics mass reach. To be concrete, let us compare the reach of the LHC and a 100 TeV pp collider for the production of massive particles with different two-parton initial states, using estimates of reach based on scaling of the parton luminosity. First, we focus on the highest possible reach in mass. For LHC, we

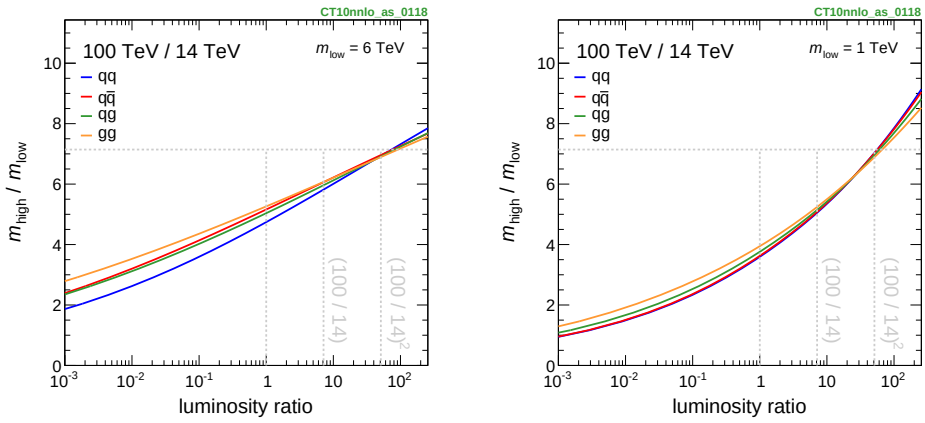

Figure 2.11 Ratio of the reach of new physics scale from the LHC and 100 TeV pp collider, shown as a function of the ratio of luminosity. New physics produced from different partonic initial states are considered. The limit of LHC is assumed to be 6 TeV (left) and 1 TeV (right).

assume the reach for the scale certain type of new physics is 6 TeV, shown in the left panel of Fig. 2.11. This could be the case for a 6 TeV Z', or about 3 TeV gluino since they are pair produced. While this is a crude estimate, it has been demonstrated to be a reasonable approximation in a wide variety of examples and suffices for our discussion here.

Even with 3 ab^{-1}, the same as the target luminosity of the HL-LHC, the 100 TeV pp collider can enhance the new physics reach by a factor of 5. This is a huge step and a large portion of the ratio of the center of mass energy ~ 7. Of course, given that partonic cross-sections drop as E^{-2}, an increase of a factor of 50 would be needed to extend the

reach by the full factor of ~ 7. We see that the much larger increase in luminosity only gives us a very modest gain in mass reach: this well known fact is a direct consequence of the steeply falling parton luminosity as a function of parton center of mass energy. This is especially true when we consider the highest reach in mass, which involves a regime where the parton density falls off very fast and the ultimate reach is typically limited by the production rate.

For the search of lower mass particles, the parton density falls off slower in the relevant regime and simple scaling suggests a larger luminosity is necessary to achieve the same enhancement in the mass reach, as demonstrated in the right panel of Fig. 2.11. However, we note that making a sharp statement in this case is much harder, since this is usually the case with weak signal and large background. We need to identify particular highly motivated cases to set the luminosity target. The most important example is probably the measurement of the triple Higgs coupling discussed earlier. The target here is to reach the 10% level accuracy, which is crucial in distinguishing qualitatively different characters of the Higgs potential. Preliminary studies of this process have reached somewhat different conclusions, partly due to differing assumption about systematic uncertainties. The study of [35] claims that an 8% measurement is possible with only 3 ab^{-1}, while [4] claims that 30ab^{-1} is needed for a 12% measurement. The ball-park luminosity is therefore likely in the neighborhood of 10 ab^{-1}. However, given the fundamental importance of this question for setting an objective target for the luminosity, future studies should be undertaken to settle it decisively.

We have given an overview of the impressive raw capabilities of the CEPC and SPPC. Of course, given that we can extrapolate the Standard Model alone to ultra-high energies, there is no guarantee that CEPC/SPPC will see new particles. But the production of new particles has never been an aim in itself: our driving ambition has always been to uncover *new principles* of physics, as they are needed. And as we have stressed, with the discovery of the Higgs we are fortunate to find ourselves in an era where such fundamentally new principles are called for, the character of which will be illuminated by direct studies of the Higgs itself. Nonetheless, in thinking about physics that may exist beyond the Higgs, it is important to ask whether the reaches of the CEPC/SPPC are the right ones: is there anything special about per-mille level precision on Higgs couplings at CEPC, or the 100 TeV scale for SPPC? Can any of the major open questions be effectively attacked in this way, or must we have an order of magnitude or more precision and energy?

Our goal in the rest of the remainder of this summary is to address this issue, identifying fundamental physics questions which are squarely within the cross-hairs of the CEPC/SPPC project: the nature of the electroweak phase transition, the deeper origin and naturalness of the electroweak scale, and the production of electroweak charged dark matter particles.

2.2 The Electroweak Phase Transition

For decades, particle physics has been driven by the question of what breaks the electroweak symmetry. With the discovery of the Higgs, we have discovered the broad outlines of the answer to this question: the symmetry breaking is associated with at least one weakly coupled scalar field. However, this gives us only a rough picture of the physics, leaving a number of zeroth order questions wide open that must be addressed experimentally, but cannot be definitively settled at the LHC. These questions include what is the

shape of the symmetry breaking potential, and how is electroweak symmetry restored at high scales.

The Standard Model picture for electroweak symmetry breaking follows the Landau-Ginzburg parametrization of second-order phase transitions,

$$V(h) = m^2 h^\dagger h + \frac{1}{2}\lambda (h^\dagger h)^2 \tag{2.12}$$

with $m^2 < 0$ and $\lambda > 0$. This is the simplest picture theoretically, and the one we would expect on the grounds of effective field theory, in which we include the leading relevant and marginal operators to describe low energy physics. On the other hand, as we will review in more detail in our discussion of naturalness, this picture is far from innocuous or "obviously correct" — for instance it is precisely this starting point that leads to the all vexing mysteries of the hierarchy problem!

The central scientific program directly continuing from the discovery of the Higgs must thus explore whether this simplest parametrization of electroweak symmetry breaking is actually the one realized in Nature. And while we have discovered the Higgs, we are very far from having confirmed this picture experimentally. As illustrated in Fig.2.12, the LHC will only probe the small, quadratic oscillations around the symmetry breaking vacuum, without giving us any idea of the global structure of the potential. For example, the potential could trigger symmetry breaking by balancing a negative quartic against a positive sextic [36–38], i.e.

$$V(h) \to m^2 (h^\dagger h) + \frac{1}{2}\lambda (h^\dagger h)^2 + \frac{1}{3!\Lambda^2}(h^\dagger h)^3, \tag{2.13}$$

with $\lambda < 0$. The potential might not even be well-approximated by a polynomial function, and may instead be fundamentally non-analytic, as in the early Coleman-Weinberg proposal for symmetry breaking [39]:

$$V(h) \to \frac{1}{2}\lambda (h^\dagger h)^2 \log\left[\frac{(h^\dagger h)}{m^2}\right]. \tag{2.14}$$

These possibilities are associated with totally different underlying dynamics for electroweak symmetry breaking than the Standard Model, requiring new physics beyond the Higgs around the weak scale. They also have radically different theoretical implications for naturalness, the hierarchy problem and the structure of quantum field theory.

The leading difference between these possibilities show up in the cubic Higgs self-coupling. In the standard model, minimizing the potential gives $v^2 = 2|m|^2/\lambda$. Expanding around this minimum $h = (v+H)/\sqrt{2}$ gives $V(H) = \frac{1}{2}m_H^2 H^2 + \frac{1}{6}\mu H^3 + \cdots$, with $m_H^2 = \lambda v^2$ and $\mu_{SM} = 3(m_H^2/v)$. Consider the example with the quartic balancing against a sextic, for the sake of simplicity to illustrate the point, let's take the limit where the m^2 term in the potential can be neglected. The potential is now minimized for $v^2 = 2|\lambda|\Lambda^2$, and we find $m_H^2 = \lambda v^2, \mu = 7m_H^2/v = (7/3)\mu_{SM}$, giving an $O(1)$ deviation in the cubic Higgs coupling relative to the Standard Model. In the case with the non-analytic $(h^\dagger h)^2 \log(h^\dagger h)$ potential, the cubic self-coupling is $\mu = (5/3)\mu_{SM}$.

The LHC will not have the sensitivity to the triple Higgs coupling to distinguish these possibilities. Even larger departures from the standard picture are possible — we don't even know whether the dynamics of symmetry breaking is well-approximated by a single light, weakly coupled scalar, as there may be a number of light scalars, and not all of them need be weakly coupled!

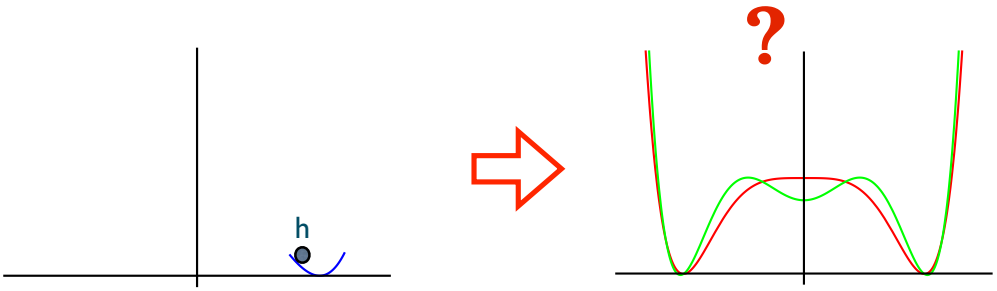

Figure 2.12 Question of the nature of the electroweak phase transition.

Understanding this physics is also directly relevant to one of the most fundamental questions we can ask about *any* symmetry breaking phenomenon, which is what is the order of the associated phase transition. How can we experimentally decide whether the electroweak phase transition in the early universe was second order or first order? This question is another obvious next step following the Higgs discovery: having understood what breaks electroweak symmetry, we must now undertake an experimental program to probe how electroweak symmetry is restored at high energies.

A first-order phase transition is also strongly motivated by the possibility of electroweak baryogenesis [40]. While the origin of the baryon asymmetry is one of the most fascinating questions in physics, it is frustratingly straightforward to build models for baryogenesis at ultra-high energy scales, with no direct experimental consequences. However, we aren't forced to defer this physics to the deep ultraviolet: as is well known, the dynamics of electroweak symmetry breaking itself provides all the ingredients needed for baryogenesis. At temperatures far above the weak scale, where electroweak symmetry restored, electroweak sphalerons are unsuppressed, and violate baryon number. As the temperature cools to near the electroweak transition, bubbles of the symmetry breaking vacuum begin to appear. CP violating interactions between particles in the thermal bath and the expanding bubble walls can generate a net baryon number. If the phase transition is too gradual (second order), then the Higgs vacuum expectation value (VEV) inside the bubbles turns on too slowly, so the sphalerons are still active inside the bubble, killing the baryon asymmetry generated in this way. However, if the transition is more sudden (first order), the Higgs VEV inside the bubble right at the transition is large, so the sphalerons inside the bubble are Boltzmann suppressed and the baryon asymmetry can survive. This requires $\exp(-\Delta E_{sph}/T_c) < \exp(-10)$, and can be translated to a rough criterion on the size of the Higgs expectation value at the transition:

$$\frac{\langle h \rangle (T_c)}{T_c} > 0.6 \to 1.6 \tag{2.15}$$

In the Standard Model with $m_h = 125$ GeV, the electroweak phase transition is not strong enough to satisfy this condition. The CP violation in the Cabibbo-Kobayashi-Maskawa (CKM) quark mixing matrix is not large enough to generate the asymmetry. Hence, in order to make this beautiful idea work, we have to go beyond the Standard Model. Getting the needed amount of CP violation is easy with the addition of new particles and interactions near the weak scale, without being in conflict with the stringent limits from electric dipole moments for the electron and neutron. However, while we can

probe for new CP phases indirectly, by the continued search for electric dipole moments, it is both difficult and highly-model dependent to probe CP violation at colliders. On the other hand, the physics needed for a sufficiently first-order phase transition are a perfect target for future colliders. We will use the requirement in Eq. (2.15) as our benchmark for probing an "interestingly" strong first order transition.

Colliders can not replicate the high-temperature conditions of the early universe at the electroweak scale. However, the CEPC/SPPC can provide an extremely powerful probe of any physics that could alter electroweak symmetry breaking dynamics enough to make the phase transition first-order. A large change in the structure of the Higgs potential leads to an $O(1)$ deviation in the triple Higgs self-coupling relative to the Standard Model, which will be probed to the 10% level at the SPPC. Furthermore, there must be additional particles beyond the Higgs, with mass not too much heavier than the weak scale, and relatively strongly coupled to the Higgs, in order to be able to qualitatively change the order of the transition relative to the minimal Standard Model. While such particles can escape detection at the LHC, they are a perfect target for the CEPC/SPPC. If these particles dominantly affect the Higgs potential at tree-level, their virtual exchange gives rise to percent-level deviations in the ZZh coupling visible at the CEPC, and the particles are light enough to be produced directly at the SPPC to produce them directly. Even in the most difficult scenario in which the new particles only affect the phase transition at loop-level, the combination of deviations in the Higgs triple coupling and direct production of the new states at the SPPC cover most of the allowed parameter space in the examples studied to date.

Of course, we are not claiming a "no-go" theorem, and it may be possible to engineer models which change the order of the phase transition while suppressing the CEPC/SPPC signals. However, such scenarios would appear to need some contrivance. Our aim in this section is to show that the CEPC/SPPC robustly cover the space of possibilities for simple models generating a first-order phase transition.

The simplest toy model for a first-order transition simply augments the Standard Model with a higher-dimension operator as in Eqn. 2.13 [36–38, 41, 42]. At leading order (which suffices for our purposes here) finite temperature effects merely add the usual quadratic shift to the quadratic part of the potential $m^2(T) \to m^2 + cT^2$ for a positive constant c determined by the top Yukawa and gauge couplings. A first-order phase transition can be achieved if the quartic terms is negative ($\lambda < 0$). As we saw earlier, in this example we have an $O(1)$ deviation in the Higgs self-coupling, and this is a general expectation for any theory where the first-order phase transition is driven by a large change in the (zero-temperature) Higgs potential.

Purely by effective field theory rules, it is consistent to have a theory where $(h^\dagger h)^3$ is the only dimension 6 operator at leading order. It is amusing that this choice is even radiatively stable at leading order: $(h^\dagger h)^3$ does not induce any of the other dimension 6 operators involving the Higgs under 1-loop RG evolution. However, in any reasonable UV completions we can expect other higher-dimension operators in addition to $(h^\dagger h)^3$. While the UV physics may preserve custodial $SU(2)$ and give suppressed contributions to the precision electroweak operators, there is no symmetry distinction between the $(h^\dagger h)^3$ operator and the operator $[\partial_\mu (h^\dagger h)]^2$, so they are expected to be generated as well, and affect the ZZh couplings.

We begin by considering the simplest example of a theory where these couplings are generated at tree-level by integrating out a massive singlet S coupled to the Higgs. As

we will see, this example represents the “easiest" case, where it is straightforward to get a first-order phase transition, with large associated signals for both the CEPC and SPPC. Since this is an “easy" case, we will use it largely to illustrate the important physics points parametrically. We will then move to the “hard" case, where the order of the transition is only affected at 1-loop.

The important interactions for this toy model are given by

$$m^2 h^\dagger h + \frac{\tilde{\lambda}}{2}(h^\dagger h)^2 + \frac{1}{2}m_S^2 S^2 + a m_S S h^\dagger h + \frac{b}{3!}m_S S^3 + \frac{\kappa}{2}S^2 h^\dagger h + \frac{1}{4!}\lambda_S S^4 \qquad (2.16)$$

The dimensionless couplings a, b can be set to zero by a Z_2 symmetry under which $S \to -S$, but in the absence of such a symmetry they should be present. We'll concentrate on the limit where the $b m_S S^3$ interaction is negligible. Integrating S out at tree-level gives rise to both the modified Higgs potential as well the oblique Higgs operator as

$$m^2 h^\dagger h + \frac{\lambda}{2}(h^\dagger h)^2 + \frac{\kappa a^2}{2m_S^2}(h^\dagger h)^3 \; + \; \frac{a^2}{2m_S^2}(\partial_\mu (h^\dagger h))^2 \qquad (2.17)$$

Here $\lambda = \tilde{\lambda} - a^2$. Neglecting the m^2 term as above, the first-order transition is driven with $\lambda < 0$, $k > 0$, and we can determine the electroweak scale and Higgs masses as $v^2 = (4/3)m_S^2|\lambda|/(\kappa a^2), m_H^2 = |\lambda| v^2$. We can also find the shift in the ZZh coupling as $\delta Z_h = (4/3)a^2 v^2/m_S^2 = (4/3)(|\lambda|/\kappa)$. In order not to avoid an unwanted $O(1)$ shift to the ZZh coupling, we must have $\kappa \gg \lambda$. This is perfectly consistent since λ is highly perturbative. It is interesting that despite the presence of a relatively strong coupling of the Higgs to a new massive state, there are no difficulties whatsoever with large precision electroweak corrections; this is closely related to the fact that the $O(1)$ deviation in the Higgs cubic couplings associated with the $(h^\dagger h)^3$ term does not radiatively induce precision electroweak operators at one-loop. Now, for the couplings to be self-consistently perturbative, we must have $(\kappa^2/16\pi^2) \lesssim |\lambda|$, $a^4/(16\pi^2) \lesssim |\lambda|$. Since κ can't become too large, the correction $\delta Z_h = (4/3)(|\lambda|/\kappa)$ can't be too small and the singlet mass $m_S = \sqrt{\frac{3\kappa a^2}{4|\lambda|}} v$ can't be too heavy, and we find

$$\delta Z_h \gtrsim \frac{4}{3}\frac{\sqrt{|\lambda|}}{4\pi} = 0.05, \qquad m_S \lesssim \frac{\sqrt{3}}{2} 4\pi v = 2.7\text{TeV} \qquad (2.18)$$

A similar conclusion holds even if the $b m_S S^3$ term is included and dominates; the parametrics changes slightly and we find instead

$$\delta Z_h \gtrsim 4\left(\frac{\sqrt{|\lambda|}}{4\pi}\right)^{3/2} = 0.03, \qquad m_S \lesssim 2\pi v \left(\frac{4\pi}{\sqrt{|\lambda|}}\right)^{1/4} = 3.4 \text{ TeV} \qquad (2.19)$$

This quantifies the intuitive expectation that any new physics giving a first-order phase transition can not be too heavy and too weakly coupled to the Higgs — in this model we find deviations in the ZZh coupling that can be seen at the CEPC. Note that as mentioned in our general discussion of Higgs couplings, while this correction also induces a radiative shift in the S, T parameters that can be probed on the Z pole, this is a weaker probe than what we get from the direct Z-Higgs measurement.

We also get an associated $O(1)$ deviation in the Higgs triple coupling, and a singlet mass in the range of at most a few TeV, both of which are easily accessible to the SPPC.

Since the singlet mixes significantly with the Higgs, the singlet is produced just as heavy Higgses would be, and its significant decays are $S \to hh, ZZ, W^+W^-, t\bar{t}$. A rough estimate of the SPPC reach for $pp \to S \to hh$ in these modes is shown in Fig. 2.13. Here c is a measure of the mixing between the singlet S and the Higgs; we have $c \sim (av)/m_S \sim (m_H/m_S)$, so this mixing is expected to be sizable.

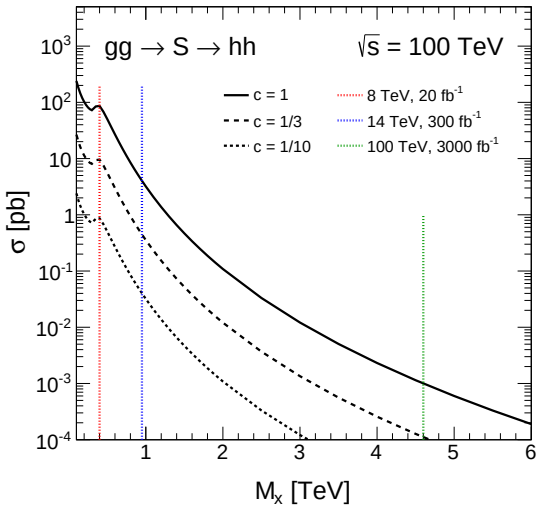

Figure 2.13 Estimate of reach in the $gg \to S \to hh$ channel at HL-LHC and SPPC extrapolating from an ATLAS search [43]. The reach lines assume that one Higgs decays to $\bar{b}b$ and the other to $\gamma\gamma$.

In the above analysis we have assumed that $m_S^2 > 0$, so that the singlet is localized to the origin throughout the phase transition. There is also a qualitatively different possibility with $m_S^2 < 0$. Here, we can imagine that it is really the phase transition for S that dominates the physics, and drags the Higgs along with it, since the effective Higgs mass term depends on $\langle S \rangle$ as $m_{h,eff}^2 = m_h^2 + a m_S \langle S \rangle + \kappa \langle S \rangle^2$. The dynamics in the S-sector can make the S phase transition strongly first-order, at a temperature $T_c \sim \langle S \rangle$. Thus if we wish to have $\langle h \rangle / T_c \sim 1$, we should have $\langle h \rangle \sim \langle S \rangle$. This again gives us the obvious upper bound to the mass m_S, $m_S < 4\pi \langle S \rangle \sim 4\pi v \sim 2$ TeV, and S easily accessible to direct production at the SPPC. We can also expect observable δZ_h over a wide range of the parameter space. In the case where the a term dominates $m_{h,eff}^2$ (we will shortly consider the opposite case in detail), it is easy to see that parametrically $\delta Z_h \sim \frac{m_h^4}{m_S^4}$, and the CEPC will have sensitivity for m_S up to around 700 GeV, moving well into the regime of strong self-coupling for S. Note however that the reach here is not as strong as the first case we considered with $m_S^2 > 0$. The reason is simple: in this example, we are affecting the nature of the electroweak transition at high-temperatures, without (at leading order) affecting the zero-temperature Higgs potential at all! Relatedly, in this case the deviation in the Higgs cubic couplings will not be large.

Having discussed the “easy" cases for new physics giving a first-order electroweak phase transition, let us consider what appears to be the most difficult possible case, where a first-order electroweak phase transition is driven entirely by radiative effects, coupling the Higgs to Standard Model singlet fields. This case is realized in our singlet model, if we further impose a Z_2 symmetry so that $a, b = 0$. This makes S exactly stable, and it

could indeed be a component of Dark Matter. However this aspect is not relevant to our discussion; we may always assume a minuscule amount of Z_2 breaking giving a small a, b which allow S to decay on cosmological timescales.

As with our tree-level example, there are two qualitatively different cases to consider. When $m_S^2 > 0$, and the role of the singlet is to give a large deformation to the Higgs potential at 1-loop, enabling a first-order phase transition directly in the Higgs direction. This will require κ to be large, but can be accomplished within a consistent weak-coupling approximation. In this case we expect a large correction to the zero-temperature Higgs potential and so an $O(1)$ deviation in the Higgs triple coupling. On the other hand if $m_S^2 < 0$, we can have a two-step phase transition, where a first-order transition in S forces a first-order transition for h.

A detailed analysis of the model parameter space allowing a strong first-order phase transition has recently been given in [11], as shown in Fig. 2.14. The two-step transition

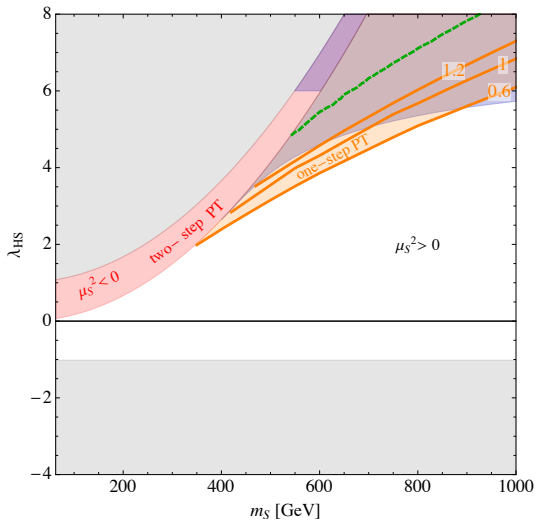

Figure 2.14 Parameter space with first order phase transition in the Z_2 model [11]. Red shaded region: for $m_S^2 < 0$ it is possible to choose λ_S ($= \kappa/2$ in Eq. 2.16) to get tree-induced two-step first-order electroweak phase transition. Orange contours: value of v_c/T_c for $m_S^2 > 0$. The orange shaded region indicates $v_c/T_c > 0.6$, where a one-step transition can be sufficiently first-order for electroweak baryogenesis. Above the green dashed line, singlet loop corrections generate a barrier between $h = 0$ and $h = v$ even at zero temperature, but results in the dark shaded region might not be reliable.

operates for smaller values of the singlet masses and couplings, while larger masses and couplings can give rise to the modified Higgs potential giving the one-step transition along the Higgs direction.

In all cases, the singlet S is lighter than ~ 1 TeV, and so certainly kinematically accessible to the SPPC. In this worst-case scenario, since S only couples in pairs to the Standard Model via the Higgs, as long as $m_S > m_h/2$ we must produce it via off-shell Higgses. Furthermore if S is collider-stable, we are looking for missing energy signals very much like standard invisible Higgs decay searches, the main difference being the much smaller, non-resonant SS production cross-section. The dominant channels for SS production are in Vector-Boson-Fusion (VBF) $qq \to qqSS$, as well as in associated production $qq \to VSS$ for $V = W^{\pm}, Z$. The cross-sections for these processes at the SPPC are shown in the right panel of Fig. 2.15. These cross-sections are very small, between

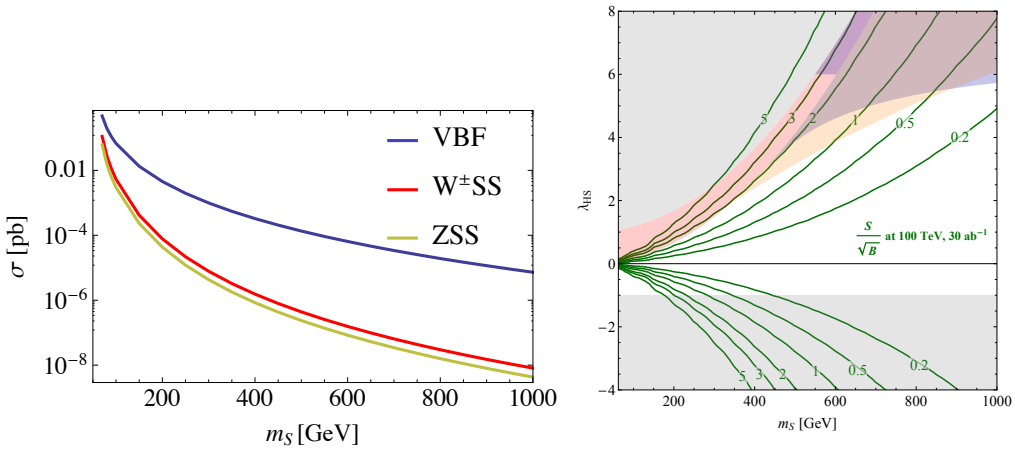

Figure 2.15 Left: Production rate for the VBF process at the SPPC. Right: $S/\sqrt{B}$ of VBF process at the SPPC for an integrated luminosity of 30 ab^{-1} [11].

$10^{-2} \to 10^{-4}$ pb. There is also a large background, in the VBF production of $Z \to \nu\nu$, which is $\sim 10^3$pb at 100 TeV. The authors of [11] imposed a simple set of cuts to isolate the signal, demanding exactly two forward jets with $p^T_{1,2} > 40$ GeV and $\eta_{1,2} < 5$, a missing energy cut $/E_T > 150GeV$, jet separation $|\eta_1 - \eta_2| > 3.5$ and $|\eta_{1,2}| > 1.8$, and M_{jj} >800 GeV, while rejecting leptons with $|\eta| < 2.5$ and p_T >15 GeV. The contours for $S/\sqrt{B}$ in the (m_S, κ) plane resulting from their analysis are shown in right panel of Fig. 2.15.

Already this simple analysis suggests that the entire region of the two-step transition can be probed by direct SS production at the SPPC. Note that this is a rough first pass at studying this signal, and one may expect to do significantly better. The main limiting factor is the huge $Z \to \nu\nu$ background, but this may be measured directly from the data in the familiar way, from the kinematically identical $Z \to ll$ process, which should give a sharp handle on the systematic error. In the part of parameter space giving the one-step transition, the direct production of SS is swamped by the $Z \to \nu\nu$ background. However, this is exactly the case in which we expect an $O(1)$ deviation to the Higgs cubic coupling, as shown in the left panel of Fig. 2.16 We see that even pushing to the limit of $\langle h \rangle / T_c \to .6$, we must have a deviation in the triple Higgs coupling of at least 20%, which is visible at the SPPC.

Finally, we can consider the fractional change in the ZZh coupling induced at one-loop in this model

$$\frac{\delta\sigma_{Zh}}{\sigma_{Sh}} = \frac{1}{4\sqrt{x(x-1)}} \log\left(\frac{1-2x-2\sqrt{x(x-1)}}{1-2x+2\sqrt{x(x-1)}}\right) \tag{2.20}$$

where $x = m_h^2/(4m_S^2)$. In much of the region with a strong first-order phase transition, this is within reach of the CEPC, though it can be as small as .1%, shown in the right panel of Fig. 2.16. This is at the absolute edge of CEPC sensitivity.

We conclude that, even in this very worst case scenario, the SPPC allows us to probe the physics giving us a first-order phase transition, and in much of the relevant parameter space, the CEPC should see hints of deviations in the Higgs couplings. Needless to say, even small modifications from this worst-case scenario can make detection much easier.

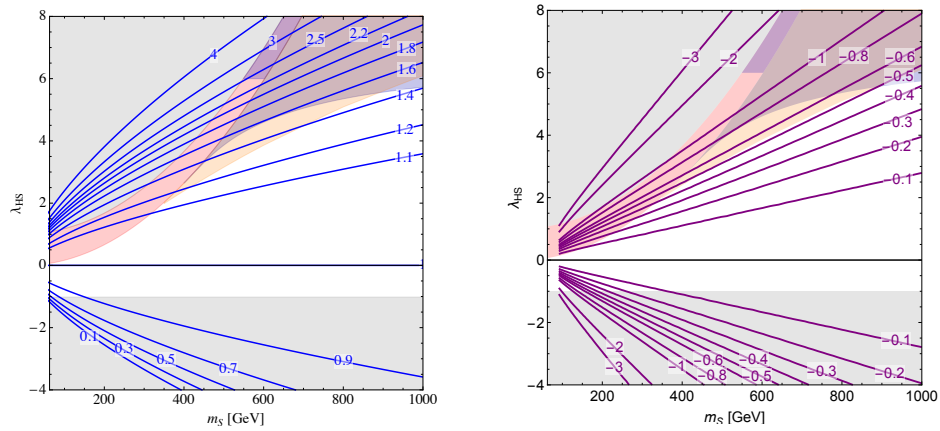

Figure 2.16 Left: Shift in triple Higgs coupling in the Z_2 singlet model. Right: Percentage shift in the $e^+e^- \to Zh$ cross section. Zh coupling.

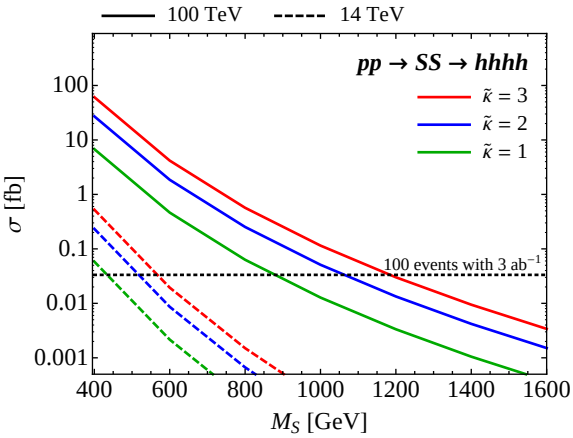

Figure 2.17 Rate of process $pp \to SS \to hhhh$ at the LHC and SPPC.

For instance, if the Z_2 symmetry is broken by an even tiny amount so that $a > 10^{-10}$, then S will decay as $S \to hh$ inside the detector. Direct S production will be much easier to see, giving a spectacular signal $pp \to SS \to hhhh$. This should allow the SPPC to cover the allowed range of m_S up to 1 TeV. While a detailed study is left for future work, an estimate of the reach for producing 100 events is shown in Fig. 2.17. Note that while at fixed mass, the SPPC cross-section is ~ 100 times larger than at the LHC, the mass reach is ~ 2.5 times greater, compared to the typical factor of ~ 5 we are accustomed to. This is because both the production and decay vertices of the off-shell Higgs are suppressed by factors of (v/E) at high energies, and the cross-section scales as v^4/E^6 rather than the usual $1/E^2$. These suppressions would be absent with more physical Higgses in the final state. It would be interesting to see whether such high-Higgs multiplicity final states could be seen at the SPPC.

We have seen in our simple examples something we expect to hold for models which drive a first-order phase transition more generally: percent to per-mille deviations in the ZZh coupling at the CEPC, coupled with large signals at the SPPC, either through the direct production of new states, or via an $O(1)$ deviation in the cubic Higgs self-coupling.

Probing the electroweak transition does not need 10^{-4} level precision on the Higgs couplings, nor does it need a 10^3 TeV pp collider. The parameters of the CEPC and SPPC are just right to robustly probe this physics.

It is interesting that even the qualitative pattern of signals between the CEPC and SPPC has information that can distinguish first-order phase transition physics from other ways of modifying the Higgs potential. A nice example is provided by theories where higher-dimension operators involving the Higgs are interpreted as non-standard interactions of the Higgs and gravity, via the coupling to the Ricci scalar

$$\xi \int d^4x\sqrt{-g}h^\dagger h\mathcal{R} \tag{2.21}$$

A Weyl transformation with conformal factor $\Omega^2 = (1+2\xi\frac{h^\dagger h}{M_{\rm Pl}^2})$ takes us to Einstein frame and corrections to the action

$$\int \sqrt{-g}\frac{3\xi^2}{M_{\rm Pl}^2\Omega^4}(\partial_\mu(h^\dagger h))^2 + \frac{1}{\Omega^2}(D_\mu h)^\dagger(D_\mu h) - \frac{1}{\Omega^4}V(h) \tag{2.22}$$

Expanding around flat space, this gives a tower of higher-dimension operators. Keeping only dimension six operators, we have only the oblique and sextic potential operators with fixed relative size

$$\frac{3}{\Lambda^2}(\partial_\mu(h^\dagger h))^2 - \frac{4\lambda}{\xi\Lambda^2}(h^\dagger h)^3 \tag{2.23}$$

where $\Lambda = M_{\rm Pl}/\xi$. The CEPC probes of Λ near the TeV scale is sensitive to $\xi \sim 10^{14}$ [44], bringing the cutoff Λ near the TeV scale. A possible motivation for such a huge ξ could be dark matter: a new singlet with a similar-size coupling to curvature would have $1/\Lambda$ suppressed interactions with the Standard Model leading to a correct thermal relic abundance [45].

It is interesting that in this example the pattern of deviations in Higgs couplings is qualitatively different than what we have seen with first-order phase transitions. The sextic Higgs operator is enormously suppressed by an extra factor of $1/\xi$ at tree-level. A small deviation from the oblique Higgs operator visible at CEPC will therefore not translate to any observably large deviations at SPPC. And there are no new light states beneath a TeV to be produced at SPPC either: we simply have the growing cross-section for W_LW_L scattering associated with the oblique operators, which become strong at energies far above the TeV scale as shown in Fig. 2.18. This is quite distinct from the pattern of signals forced on us by new physics responsible for a first-order electroweak phase transition.

2.3 Naturalness of the Electroweak Scale

The notion of naturalness, as introduced by Ken Wilson and Gerard 't Hooft in the late 1970's, is deeply connected to our understanding of the structure of effective field theory, strongly supported by analogies with condensed matter physics. Naturalness has been the dominant force driving our thinking about physics beyond the Standard Model for the past four decades, suggesting a rich spectrum of new physics at the weak scale.

However, there have also been reasons to question this doctrine throughout this period. Most glaringly, naturalness seems to fail spectacularly for the cosmological constant,

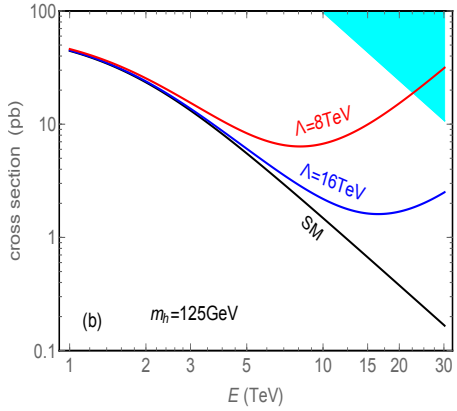

Figure 2.18 Cross sections of $W_L^{\pm}W_L^{\pm} \to W_L^{\pm}W_L^{\pm}$ with Higgs-gravity coupling for the SPPC, as in [44]. The label $\Lambda(= M_{\rm Pl}/\xi)$ on each curve denotes our input of the effective cutoff, while the label "SM" corresponds to the SM prediction with $\xi = 0$ (or $\Lambda = \infty$).

though this involves mysteries of gravity and cosmology that may not be relevant for particle physics. Within particle physics, there have also been a number of counter-indications to naturalness, from the lack of indirect signals that might have been induced by new physics at the weak scale in low energy flavor and CP violation to the absence of new states going back to LEP and the Tevatron. The absence of new physics at LHC8 continues this trend and appears to put naturalness under further pressure. Settling the ultimate fate of naturalness is perhaps the most profound theoretical question of our time that is amenable to to experimental tests, and will largely dictate the future development of fundamental physics in this century.

We will begin with a brief overview of this set of ideas to put them in context and elucidate their importance. As we will see, regardless of what we learn from LHC14, the CEPC/SPPC is certain to play a decisive role in unraveling this physics.

A good place to begin a discussion of naturalness is to look at the name of the Standard Model itself, which has an apt moniker, since it gives us a *model*, rather than a deeper *theory*, for electroweak symmetry breaking. This is most obviously seen by the fact that m_h^2 is a parameter of the theory; its value is not predicted, but must be taken from experiment. Even the most qualitative property of the Higgs potential — the negative sign of m_h^2, leading to symmetry breaking — is not predicted. The Standard Model allows us to *model and parametrize* symmetry breaking, but it certainly does not give us a real *understanding* of its origin.

The famous quadratically divergent radiative corrections to the Higgs mass, dominantly from top quark at 1-loop

$$\delta m_h^2 \sim \frac{3y_t^2}{8\pi^2}\Lambda_{\rm UV}^2 \sim (0.3\Lambda_{\rm UV})^2 \tag{2.24}$$

is one indication of the fact that the Higgs mass parameter can not be computed in the Standard Model. Note that purely within the Standard Model, nothing obliges us to think about "UV sensitivity", "fine-tuning" or the "hierarchy problem" — since there is no computation of the Higgs mass in the Standard Model, these notions are not precise. There is no well-defined computation of the Higgs mass to complain about "fine-tuning", and there is certainly no theoretical inconsistency with taking the value of the weak scale

from experiment. However, we will immediately confront these issues in attempting to find a real theory where we can actually *calculate* the Higgs mass.

What should such a theory look like? Especially over the past century, we have been driven by the reductionist paradigm, in which explanations for mysterious low energy phenomena are to be found in a more fundamental high energy theory. Following this tradition, there should be an UV scale Λ_h, above which we find the theory in which the Higgs mass becomes calculable. Unlike the Standard Model, in this theory there will be a concrete formula for the Higgs mass, which should take the form

$$m_h^2 = a\Lambda_h^2 + b\frac{3\lambda_t^2}{8\pi^2}\Lambda_h^2 + \dots \tag{2.25}$$

with $a, b, \dots$ dimensionless constants that are calculable in the theory.

There are then two possibilities: (A) $\Lambda_h \sim m_h$ with $a, b, \dots$ of $O(1)$. In this case we say the physics is "natural", and the physics at the scale Λ_h gives a complete account of electroweak symmetry breaking. Otherwise (B) $\Lambda_h \gg m_h$; this entails an extreme correlation between deep UV and IR physics. While such a correlation is a logical possibility, we have never seen anything like this before, anywhere else in physics.

Let's illustrate these possibilities with a concrete example, to show how the naturalness issues are forced upon us as soon as we find a theory in which the Higgs mass becomes calculable. Let's start with a toy model of a light scalar Φ with mass m_Φ^2, which is in the adjoint representation of an $SU(2)$ gauge group with coupling g. This mass m_Φ^2 is incalculable just as the Higgs mass is incalculable in the Standard Model. But there is a simple UV completion where it can be unambiguously computed: consider a five-dimensional gauge theory with gauge coupling g_5 compactified on a circle of radius R. The gauge field is obviously massless in the UV, but at energies much smaller than $1/R$ and at tree-level, we have a massless four-dimensional gauge field with coupling $g^2 = g_5^2/R$, and a massless scalar in the adjoint representation. The scalar will pick up a mass at 1-loop, and the radiative corrections in the full theory is calculable:

$$m_\Phi^2 = \frac{3\zeta(3)}{\pi^2} \times \frac{3g_4^2}{4\pi^2} \times \frac{1}{R^2} \tag{2.26}$$

Now, $1/R$ also sets the mass of the new states in the theory — the Kaluza-Klein excitation of the gauge boson. Thus, in this UV completion where the scalar mass becomes calculable, it is simply impossible to keep the scalar much lighter than the new KK states: there must be "new physics" in the model, parametrically at exactly the energy scale predicted from the classic back-of-the-envelope estimates following from the quadratic divergence in the low energy theory, cut-off at the scale $1/R$.

Simple variants of this model, where the extra dimension is an interval, are used in various guises of realistic theories for the Higgs as a pseudo-Nambu-Goldstone boson, interpreted in either extra-dimensional or four-dimensional terms. Of course the realistic theories include a top quark with an adjustable Yukawa coupling y_t. Once again, the Higgs mass can be completely calculated as $m_h^2 = [a(g^2/8\pi^2) - b(3y_t^2/8\pi^2)] \times 1/R^2$, where $a, b > 0$ are calculable, and the masses of the KK excitations of the gauge fields and fermions also calculable multiples of $1/R$. Even the signs of these contributions are fixed; remarkably, one can compute that when the top Yukawa is large, electroweak symmetry is necessarily broken. This beautifully explains one qualitative fact — why is electroweak symmetry broken? — as a consequence of the seemingly unrelated qualitative fact — that the top Yukawa is larger than gauge couplings.

Note that in this UV completion, it is possible to make the Higgs much lighter than the KK excitation set by $1/R$, but only if the couplings g, y_t happen to be adjusted to be extremely close to a particular ratio. Absent supersymmetry, there is nothing relating these couplings, and indeed they vary with scale, so the needed coincidence at just the right scale would be completely accidental. To say this more vividly, if as theorists we wished to simulate this model on a computer, we would have to very delicately move around in parameter space in order to make the scalar very light, giving an operational meaning to "fine-tuning" in a concrete calculation. Of course it logically possible that if such a model were realized in nature, the couplings would happen to be arranged in just a way as to yield a light scalar. But then the explanation for the generation of the weak scale would be deferred to the higher-energy theory which predicts the seemingly random choices of y_t and g needed to make this happen, entailing the extreme correlation between UV and IR physics we alluded to.

If we discount the possibility of extreme UV/IR correlations, this logic predicts that light scalars with non-derivative gauge and Yukawa interactions can never be "lonely" — they must always be within a weak-coupling loop factor of heavier new physics. This conclusion has been borne out in all examples we have seen in Nature to date. For instance the charged pion is just an electromagnetic loop factor lighter than the ρ meson. And we have a nice understanding for the striking absence of non-derivatively coupled scalars in condensed matter systems.

There is of course a famous example from condensed matter physics, however, where we do see light scalars, and where the word "fine-tuning" has direct experimental relevance. This is the Landau-Ginzburg description of a system very close to a second-order phase transition, say in a metal. Within the reductionist paradigm, one might naively imagine that the detailed microphysics of the material would provide the explanation for the lightness of the scalar field in this system. However, this assumption is incorrect, because in this system, it is not the physics of the material itself that controls the mass of the scalar, but rather the fact that the system is coupled to an external heat bath with a temperature that can be dialed by an experimentalist. In this example, the experimentalist must "fine-tune" the temperature to make the scalar very light. However, from the point of view of an observer within the material itself, the reductionist paradigm breaks down, since the explanation for macroscopic phenomena is not simply given by specifying the microphysics of the system, but also crucially depends on the presence of a "multiverse" outside it. The much discussed picture of an enormous landscape of vacua, populated by eternal inflation, is one possible analog of this scenario for particle physics.

Given the experimental observation of a light elementary Higgs scalar, we are confronted with three qualitatively different possibilities: if the reductionist paradigm continues to be the correct guide—as it has been for centuries—we must either discover physics to make the Higgs mass natural, or we must allow a possibility we have never seen before, of an extreme correlation between the physics of the deep UV and IR. While concrete examples of the latter possibility have not been found, it is possible that such a correlation may be associated with new symmetries or dynamics (as in for instance [46]), or cosmological adjustment mechanisms, of a sort that have been often contemplated for the cosmological constant problem [47]. Alternately we must acknowledge the failure of the reductionist paradigm altogether, and admit that the explanation for the lightness of the Higgs is not to be found in our microphysics. *Any* of three of these conclusions would have monumental implications for the future of fundamental physics.

The most conservative possibility is that naturalness holds. Even this conservative possibility involves major extensions to our picture of physics. Only a few theoretical possibilities for solving the hierarchy problem have emerged over the past few decades, starting from the early proposals of technicolor [48, 49] and variants with the Higgs as a pseudo-Goldstone boson [32, 50, 51]; the supersymmetric Standard Model [52]; and the proposals of large [53] and warped [54] extra dimensions, the latter of which are in fact holographically dual [55] to versions of technicolor and composite Higgs models. Technicolor was in many ways the most conservative, simplest and most beautiful of these possibilities, but has been conclusively ruled out by the discovery of a light Higgs. Supersymmetry remains the best studied and most attractive possibility, especially given the striking success of supersymmetric gauge-coupling unification, precise at the percent level [52, 56].

However, with the continued absence of both indirect and direct evidence for new physics to date, it is also conceivable that we will come to see that naturalness is not a good guide to TeV scale physics, as it has perhaps already been seen to fail for the cosmological constant. The two alternatives to naturalness represent much more radical paradigm changes; it is true that without further positive clues from experiment we won't know which of the options is correct, but being forced into either of these directions would be an epochal shift, akin to the move away from the aether triggered by the null result of aether-drift experiments over a century ago.

Given the magnitude of the stakes involved, it is vital to get a clear verdict on naturalness from experiment, and the CEPC/SPPC will be necessary to make this happen. To this end, we will be maximally conservative, and with a few exceptions will operate under the assumption that LHC14 sees no evidence for physics beyond the Standard Model. Let us recall why this would be surprising from the usual perspective of naturalness. Consider the top-loop contribution to the Higgs mass $\delta m_h^2 \sim (3\lambda_t^2/8\pi^2)\Lambda_{UV}^2 \sim (0.3\Lambda)^2$. Asking for δm_h^2 not to be larger than m_h^2 tells us that there must be some new state lighter than ~ 400 GeV, related to the top by some new symmetry that makes allows it to cancel the UV sensitivity. The couplings of this new state must be determined by λ_t; in addition, since the "3" in the expression for m_h^2 arises from the number of colors, the simplest possibility is that the "top-partner" is also colored. This is what happens in most well-studied natural theories. The top partner in supersymmetric theories is the (colored) stop, while the fermionic top-partners in Little Higgs and composite Higgs theories are also colored. This is the way in which naturalness predicted a bonanza of new physics for the LHC, since *colored* 400 GeV particles could have been copiously produced even at LHC8.

Of course this has not happened, and if the LHC continues to see nothing but the Higgs, any colored top partners will be pushed to being heavier than ~ 1 TeV, indicating a level of fine-tuning of typically a few percent for electroweak symmetry breaking. As a canonical example, consider the case of supersymmetric theories, in which stop loops generate a contribution to the Higgs mass, logarithmically enhanced starting from the scale Λ where supersymmetry (SUSY) breaking is first communicated to the minimal supersymmetry Standard Model (MSSM). This leads to a rough measure for the degree of fine-tuning, Δ^{-1} [57] as

$$\Delta^{-1} \sim 10^{-2} \left(\frac{1\text{TeV}}{m_{\tilde{t}}}\right)^2 \left(\frac{5}{\log(\Lambda/\text{TeV})}\right) \tag{2.27}$$

and $m_{\tilde{t}} \sim 1$ TeV is tuned at the percent level.

The question then becomes, how bad is percent-level tuning? Certainly it seems qualitatively different than the 10^{-30} levels of tuning usually discussed if Λ_{UV} is close to the Planck scale. Furthermore, we have seen accidents of order a few percent elsewhere in physics, ranging from the surprisingly large nucleon-nucleon scattering length, to the accident that the moon can nearly perfectly eclipse the sun! We don't tend to associate deep significance with these accidents at this level. Thus, while a failure to discover colored top-partners would be a major blow to the most popular natural theories of the weak scale, given the relative ubiquity of percent-level tunings in physics, it would perhaps not be a completely decisive blow. It is logically possible that the LHC might have just been a bit unlucky, and the new states could be a little heavier, slightly beyond its reach. The SPPC will then play a critical role to settle the issue. If the new particles are indeed "just around the corner", then the SPPC will produce them in enormous abundance. On the other hand, the SPPC reach for colored top partners will be able to discover them up to masses 5 times higher than the LHC, pushing the fine-tuning to the $10^{-3} - 10^{-4}$ level, a degree we have never seen before anywhere else in particle physics.

But one may justifiably ask: if the LHC sees nothing beyond the Higgs, doesn't this already kill the possibility of a completely natural theory for electroweak symmetry breaking? Would the only role of future colliders be to further clinch an already clear case? The answer to this question is an emphatic "No". What is true is that in all the natural theories for the weak scale developed over twenty years ago, we might have already expected to see new colored top-partners at the LHC. However this does not prove that the idea of naturalness itself is wrong, only that the particular natural scenarios theorists invented through the 1990's are not realized in Nature. As we've emphasized already, this is not a new surprise delivered to us by the LHC, since there were already indirect indications that these theories could not be fully natural going back to the absence of indirect signals for new physics in low energy experiments and at LEP. Motivated by these considerations, in the mid 2000's new classes of natural theories of EWSB were developed, where the top partners are not colored, but are charged under mirror gauge groups. These includes variations on the "Twin Higgs" [58], which realizes this idea with the Higgs as a pseudo-Goldstone boson, and "Folded SUSY" [59], where supersymmetry is ultimately responsible for the naturally light scalars. These "color-neutral natural" theories are much less constrained by LHC searches, and indeed, *completely natural* regions of parameter space for these theories could be completely missed by the LHC. They provide an existence proof that the idea of naturalness can survive the LHC era entirely unscathed, and there may be further ideas along these lines that have yet to be unearthed. Thus no new physics at the LHC will not decide the fate of naturalness, even at zeroth order: the final verdict awaits the CEPC and SPPC.

We begin with a discussion of more conventional theories with colored top partners, and for concreteness, we will discuss these issues mostly in the context of supersymmetric theories; a detailed investigation of other scenarios is left for future studies.

If the MSSM is just mildly tuned we should be able to produce all the superpartners at the SPPC. The reach for stops in particular will be critical; any gain in mass reach relative to the LHC is squared in the measure of tuning. Another interesting possibility is minimally split supersymmetry [60–65]. Here, the spectrum has one-loop splitting between the gauginos (and perhaps higgsinos) compared to the scalars, as typically happens in the simplest models of SUSY breaking. The gauginos/higgsinos are at the TeV scale for reasons of dark matter, while the scalars have a mass $m_S \sim 10^2 - 10^3$ TeV, entailing

a "meso-tuning" of $O(10^{-6})$ for electroweak symmetry breaking, while preserving gauge coupling unification and removing all flavor and CP difficulties of the MSSM. The usual SUSY boundary conditions for the Higgs quartic coupling is then easily compatible with the observed $m_h = 125$ GeV for heavy scalar masses in this range. Interestingly this tells us that the gluino can't get heavier than $\sim$ 20 TeV, quite apart from any constraints on the electroweak part of the spectrum from dark matter. So for mini-split SUSY, the SPPC should be able to produce the gluino, and the electroweak-inos as well.

An investigation of the SUSY reach for the SPPC was carried out in [66] for a number simplified models of SUSY production and decay, covering most of the qualitatively interesting scenarios. We summarize their findings here, referring to [66] for details of their analysis.

The first simplified model is of gluino pair production, with gluinos decaying to neutralino + light flavors, $\tilde{g} \to q\bar{q}\tilde{\chi}^0$. This process will dominate if the squarks are heavier than the gluino, and is particularly well-motivated in the case of split SUSY. The reach is obviously most powerful if there is a large splitting between the gluino and neutralino masses, and is shown in left panel of Fig. 2.19, comparing also to 33 TeV and the LHC at 14 TeV. The SPPC discovery reach goes up to $m_{\tilde{g}} = 11$ TeV, about 5 times the reach of LHC at 14 TeV. If the gluino and neutralino are instead relatively degenerate, the decay

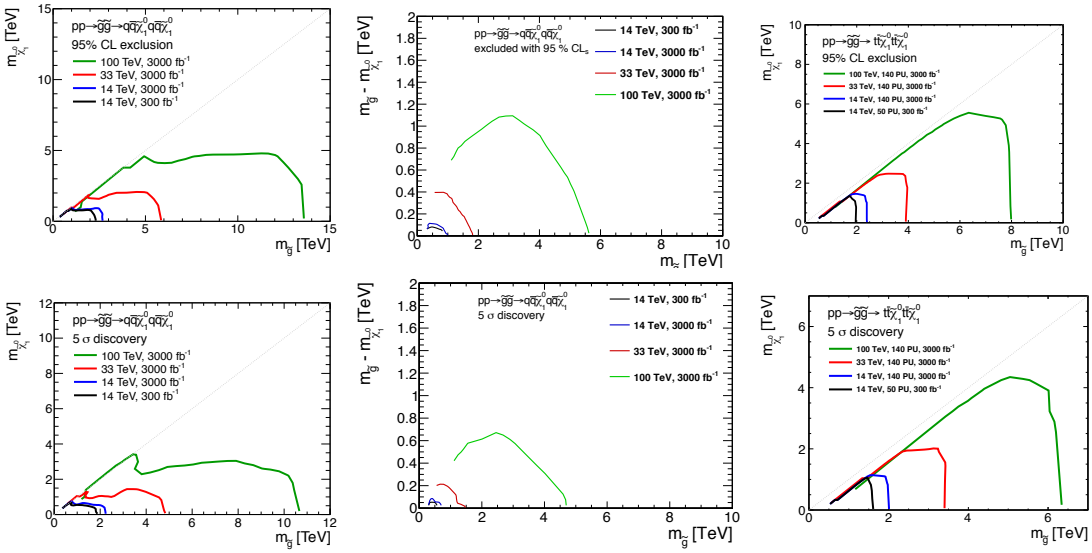

Figure 2.19 Reach for gluino at 100 TeV pp collider for separated (left column) and compressed (center column) spectrum. The reach for gluino decay dominated by $\tilde{g} \to t\bar{t}\chi_0$ is shown in the right column. The 95% exclusion reach and 5σ discovery potential are shown in the top and bottom rows, respectively.

products will be too soft to see and one will have to rely on the emission of initial or final state radiation to tag the events. The mass reach still goes up to an impressive $\sim$ 5 TeV in this case, as shown in the middle panel of Fig. 2.19. It is also interesting to consider that gluinos decay dominantly to top quarks and the neutralino as , $\tilde{g} \to t\bar{t}\tilde{\chi}^0$. This can easily arise from top-down theories, since stops are typically driven to be lighter than the first two generations of squarks, under RG evolution, and is again particularly well-motivated in split SUSY. In this case, the reach is shown in the right panel of Fig. 2.19:

A much more challenging case with smallest production cross-section for colored particles, is the pair production of the first-two generation squarks, which are taken to be

degenerate, followed by the decay to the lightest neutralino as $\tilde{q} \to q\tilde{\chi}^0$. The gluino is taken to be much heavier than the scalars. It is not easy to realize such a scenario from a top-down point of view, since a heavy gluino will quickly drag up the squarks under RG evolution. The reach for the case with the squarks significantly split from the neutralino is shown in the left panel of Fig. 2.20, while the case with more nearly degenerate squarks and neutralino is shown in the middle panel of Fig. 2.20.

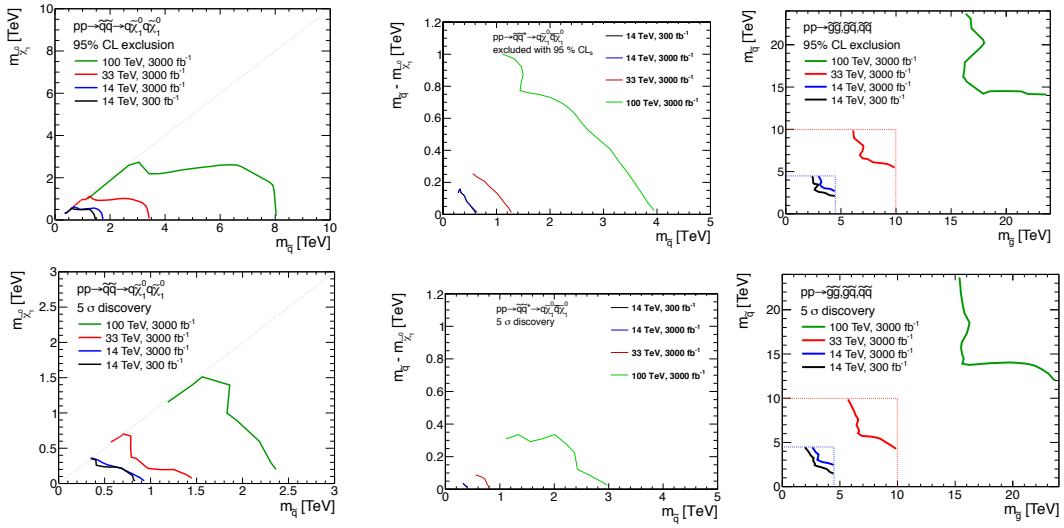

Figure 2.20 Reach of squark with separated (left column) and compressed (middle column) spectrum. The reach in the case of gluino and squark with comparable mass is shown in the right column. The 95% exclusion reach and 5σ discovery potential are shown in the top and bottom rows, respectively

Since the production cross-section is so small, it is difficult to see the signal over the background, so the improvement of the discovery reach at the SPPC relative to the LHC is not as pronounced here as in the previous examples. Nonetheless the exclusion reach is very impressive in both cases, again representing a factor ~ 5 improvement relative to the LHC.

The final simplified model is closest to a “typical" supersymmetric spectrum, where both the gluino and first-two generation squarks are light enough to be produced at the SPPC, via pair-production of $\tilde{g}\tilde{g}, \tilde{q}\tilde{q}$, and also associated production $\tilde{g}\tilde{q}$. If the gluino is heavier than the squark, it decays to the squark and neutralino as $\tilde{g} \to \tilde{q}\tilde{\chi}^0$, while if the gluino is lighter than the squark, it decays to light flavors + neutralino as $\tilde{g} \to q\bar{q}\tilde{\chi}^0$, and similarly for the squark, which decays as $\tilde{q} \to q\tilde{g}$ if heavier than the gluino, and $\tilde{q} \to q\tilde{\chi}^0$ if lighter than the gluino. The neutralino is taken to be much lighter than the gluinos and squarks. The SPPC reach is shown in right panel of Fig. 2.20. This shows an amazing reach up to $m_{\tilde{g}}, m_{\tilde{q}} \sim 15$ TeV.

We now turn to the SPPC reach for stops, which will probe masses up to the $5 - 10$ range, pushing the fine-tuning measure to the 10^{-4} level. It is interesting to note that with moderately large tanβ, stops in the $5 - 10$ TeV range can also be easily responsible for pushing the Higgs mass up to 125 GeV. To be conservative, we look at the simplified model with all particles but the stop and the lightest neutralino decoupled, considering the QCD production of $\tilde{t}\tilde{t}^*$, followed by $\tilde{t} \to t\tilde{\chi}^0$. The same search is of course being carried out at the LHC, but an interesting novelty arises at the SPPC. With heavy enough stops, the top quarks produced in the decay are so highly boosted, that it becomes more

difficult to identify the individual top decay decays products as compared to the LHC. Thus simply scaling up the LHC analysis to the SPPC is suboptimal, and identifying highly boosted tops becomes an important challenge for SPPC detectors. It is possible to use a strategy less dependent on unknown detector response: when a highly boosted top decays hadronically, the muons from the resulting b decays will be collinear with the top jet; thus requiring a lepton inside a jet can be used to effectively tag the boosted tops [15].

The SPPC reach for direct stop production is shown in the left panel of Fig. 2.21, for the two usual cases of a separated and compressed spectrum: The gain from using the

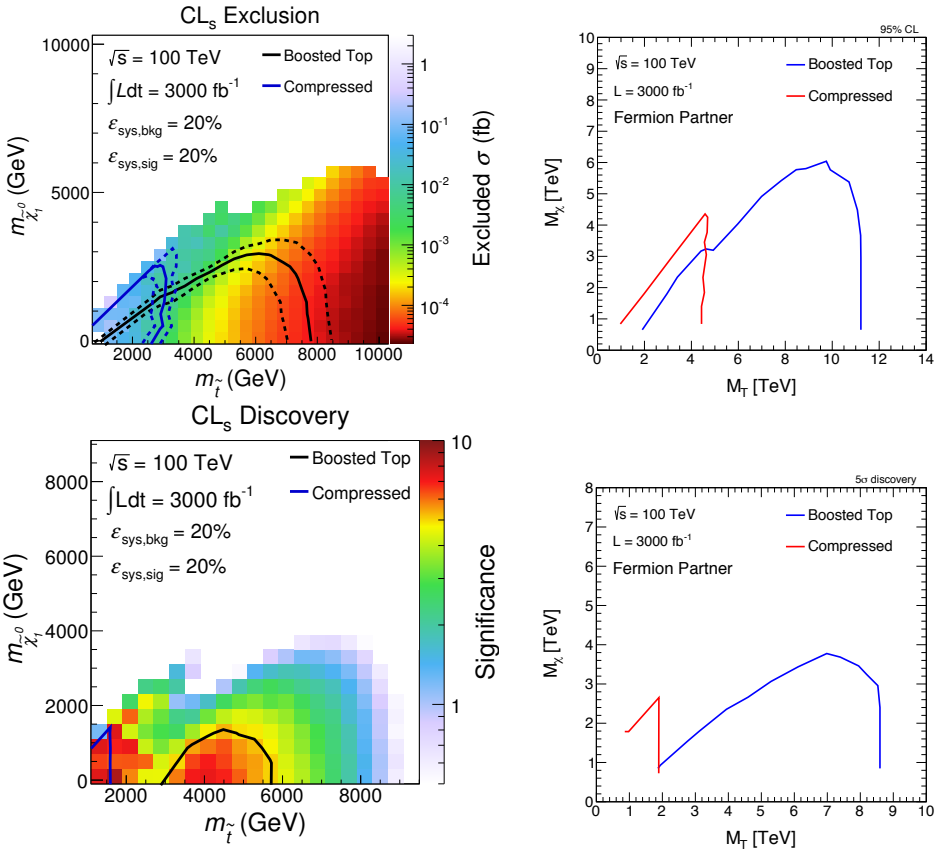

Figure 2.21 Reach for stops (left column) and fermonic top partners (right column) at a 100 TeV pp collider.

boosted top tagging can be clearly seen. Stops can be discovered (excluded) up to ~ 6 (8) TeV with this method.

Similar reaches are possible for non-supersymmetric theories. For instance in composite Higgs models, we have fermionic top partners T'. Depending on whether we have the "T-parity" analog of R-parity, these may decay to tops + missing energy, or via $T' \to tZ, T' \to th$. A dedicated SPPC search for these models has not yet been done. However, in the case with T-parity, the signal is very similar to that of the stop. Therefore, we can use the stop reach and get a rough estimate of the reach of T' by matching the production rate and mass splitting. The result is shown in the right panel of Fig. 2.21.

All of this discussion has assumed no signals for new physics at the LHC. In the more optimistic case that LHC *does* produce e.g. superpartners, the need to proceed to the higher energies of the SPPC is even more urgent, for two obvious reasons. First, given that

we haven't seen any superpartners at LHC8, while LHC14 could be powerful enough to discover them, it is unlikely to produce them in high enough numbers for the more detailed study needed to ascertain what the particles are trying to tell us about TeV scale physics. As a simple example, consider a gluino with mass of 1.5 TeV, just at the LHC8 limit. Roughly 10^4 of these particles will be produced through the LHC14 program, certainly enough to be able to claim a discovery, but not much else. The careful examination of its properties, necessary to even hope for a zeroth order claim that supersymmetry has been discovered, will need the SPPC, producing $\sim 10^7 - 10^8$ gluinos of the same mass. Second, the fact that we haven't seen any new physics at LHC8 also makes it very unlikely that the entire spectrum of new states will be produced at LHC14. Consider the example of "natural SUSY", where the stops and gluinos are light, but the first two generations scalars are heavy. The first two generation should plausibly be heavier than ~ 5 TeV, enough to eliminate their dangerous contribution to electric diploe moments. But they can't get too heavy, as they induce a logarithmically enhanced negative mass for the (light) third-generation squarks, [67, 68], and so can't be pushed higher than at most ~ 30 TeV. Finding these heavier scalars will be critical for a zeroth-order understanding of the spectrum, which entangles the physics of flavor and supersymmetry breaking in a fascinating way. While these scalars are well outside the reach of the LHC, they will be easily accessible to the SPPC. The most powerful production channel is the associated production of the gluino and first-two generation squarks, as shown in Fig. 2.22. The reach for squarks

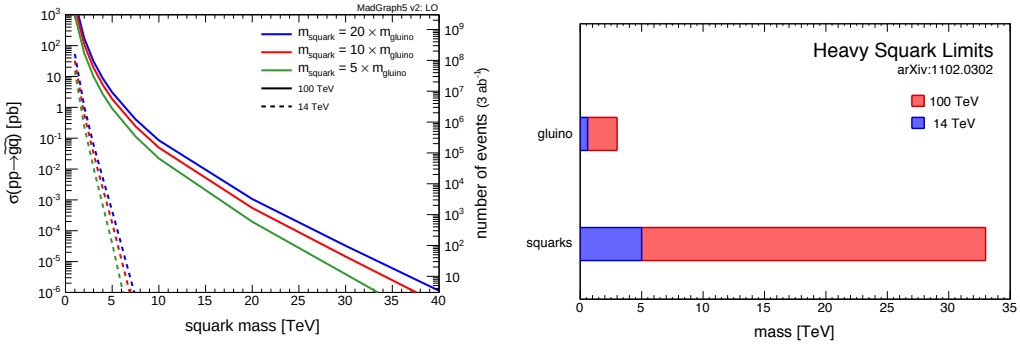

Figure 2.22 Cross section (left) and reach (right) for a heavy squark produced in association with a light gluino at 100 TeV pp collider.

goes up to an incredible ~ 35 TeV, covering the entire range of masses for the first-two generation scalars of natural SUSY.

We now move on to consider the possibility that natural physics was missed at the LHC, starting with another comment about SUSY. The most constraining searches for SUSY at the LHC involve looking for leptons or missing energy; it is thus conceivable that small changes to the theory, such as R-parity violation, can lead to decays with all hadronic final states that would be buried in the hadron collider environment. Indeed stops as light as 200 GeV may well escape LHC detection in this way. It is therefore important to have a complementary handle on the presence of stops, independent of any complicated decays it might decay. As mentioned in our earlier discussion of Higgs couplings, this can be provided by the deviations induced by stop loops to Higgs couplings—predominantly $h \to gg$—as well as Z-pole precision observables. These will be sensitive to the majority of the natural range for stop masses, as shown in Fig. 2.23.

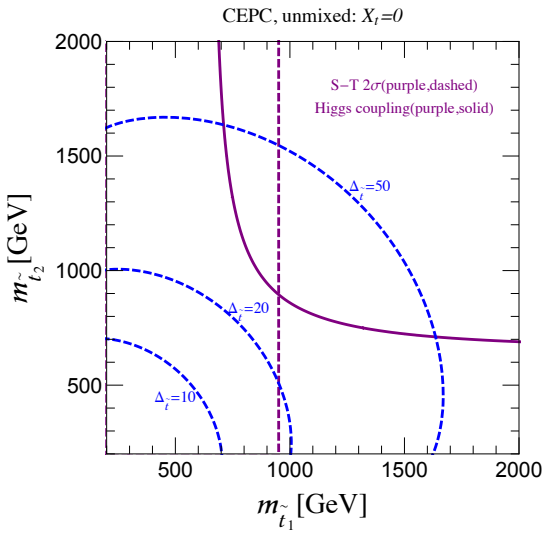

Figure 2.23 CEPC sensitivity to stops, through the shifts in the hgg coupling (solid purple line), and the S-T parameters (dashed purple line). The blue lines indicate the level of tuning.

Let's now turn to theories of neutral naturalness. We can begin with the earliest version of this idea in the "twin Higgs" [58]. Since the top partners are uncolored, they will not be easily produced at the LHC but will be accessible at the SPPC; we will defer discussing this phenomenology since it is similar to the case scalar top partners which we shortly cover. Instead, the largest signals are in the ZZh coupling shift at the CEPC. This is because in these models the Higgs is a pseudo-goldstone boson of some approximate global symmetry breaking pattern at the TeV scale, kept light by the "collective symmetry" breaking phenomenon [51, 69]. For perfect naturalness, the associated decay constant must be $f \sim 100$'s GeV. Since the Higgs is part of a non-linear sigma model multiplet, there are non-linear corrections to its kinetic term including necessarily the oblique Higgs operator $1/f^2(\partial(h^\dagger h))^2$. As in our earlier discussion of the electroweak phase transition from tree-level effects, this gives large δZ_h, which is shown as a function of f in Fig. 2.24. The scale f translates directly related to the degree of tuning $1/\Delta$ of the model, which is also indicated. If the degree of tuning is even just at 10%, the CEPC will see a huge 15% shift in the ZZh coupling; the ultimate reach of the CEPC will probe up to $f \sim 3$ TeV, corresponding to a 10^{-3} degree of tuning. Note that this signal is not directly related to the masses of top partners; it is rather that with uncolored top partners it is possible for highly natural regions of parameter space for such models to completely evade LHC detection, leaving a large signal that will first be seen at the CEPC.

The supersymmetric implementations of neutral naturalness do not generate this large oblique Higgs operator at tree-level. In the simplest cases, the top partners are scalars like the stop, but charged under a mirror SU(3), with six states in total. We can parametrize all the interesting possibilities from the bottom up: we imagine that there is some number N_ϕ of new scalars ϕ_I, and a quartic interaction with the Higgs

$$\frac{1}{2} c_\phi (\phi_I \phi_I) h^\dagger h \tag{2.28}$$

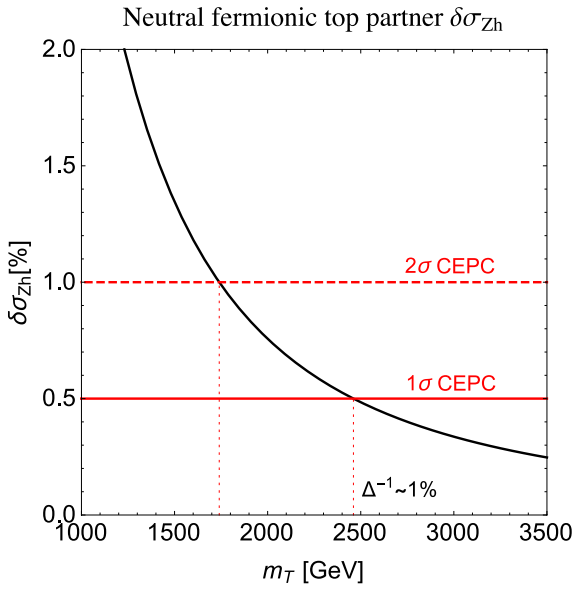

Figure 2.24 Tree level correction to Zh coupling in twin Higgs model.

Some or all of the global symmetries acting on the ϕ_I might be gauged, either by the Standard Model electroweak interactions, or mirror interactions. There must be an underlying symmetry that relates c_ϕ to the top Yukawa coupling, so as to guarantee

$$c_\phi \times N = \lambda_t^2 \times 6 \to c_\phi = \frac{6\lambda_t^2}{N} \tag{2.29}$$

In the simplest case of "folded SUSY" [59], the ϕ are uncolored but still carry the usual electroweak quantum numbers, so that there are 6 states and $c_\phi = \lambda_t^2$. The ϕ in this case will affect the Higgs and Z couplings at 1-loop just like the usual stop. Since they aren't colored the shift in the $h \to gg$ coupling is absent; instead the leading CEPC probe on these states is through the shift of the T-parameter, as shown in Fig. 2.25. This can

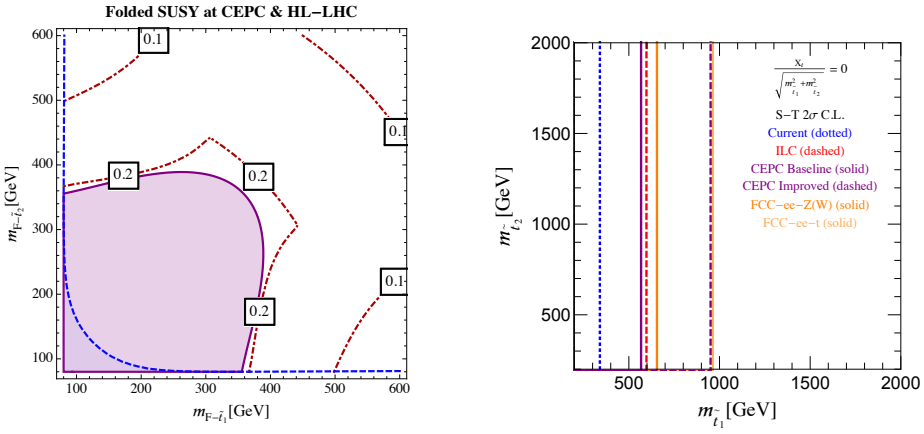

Figure 2.25 Constraints on the top partner in the folded SUSY model from $h \to \gamma\gamma$ (left) and Electroweak precision tests.

reach to folded stop masses of almost 1 TeV, fully covering the natural region of mass-

es. Furthermore, since the top-partners are electroweak charged, they can be produced through Drell-Yan production at the SPPC. Detailed studies of this are underway, but the mass reach is expected to reach into the TeV scale, well above the mass scale relevant for naturalness.

It is also interesting that in all known examples, there is also the possibility to probe the particles relevant to stabilizing the Higgs at *two* loop level. For instance folded supersymmetry, in either its extra-dimensional or "deconstructed" versions, has new colored particles amongst its "kaluza-klein" modes, whose masses are set by a loop factor above the top-partner scale, $\sim$ multi-TeV at most. These states can also be copiously produced at the SPPC.

In all the models of neutral naturalness that have been proposed to date, the top partners at least have electroweak charge. But taking a bottom-up point of view, the most minimal and (and experimentally most difficult to probe) possibility we can envision is when the ϕ_I are all Standard Model singlets. Even in this case, there is an inevitable 1-loop shift in δZ_h, which is the same as Eq.(2.20) in the previous section, with coefficient $c_\phi^2 N$. Fig. 2.26 shows this shift for the cases $N = 6$ and $N = 1$. For $N = 6$, the CEPC will

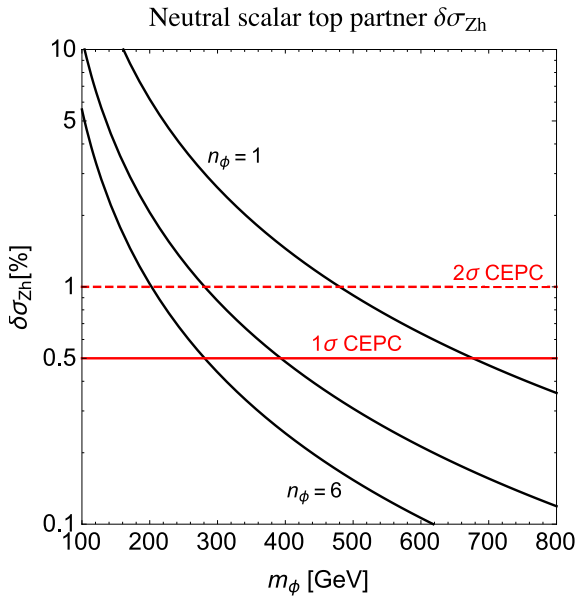

Figure 2.26 One loop correction to ZZh coupling from singlet top partner.

have sensitivity to masses close to $\sim$ 200 GeV. This covers much though not all of the relevant parameter space. Since $c_\phi \propto 1/N$, $\delta Z_h \propto 1/N$, so the effect is much larger for $N = 1$, and the entire natural range can be probed in this way.

It is also possible to directly produce the ϕ_I at the SPPC, again the discussion is analagous to the production of the S singlets in our discussion of the electroweak phase transition. There, the phase-transition requirement forced S to be light enough and sufficiently strongly coupled, for the ϕ_I naturalness plays the same role. For simplicity the ϕ_I are taken to be degenerate. The signals is just as we had before, vector-boson fusion production of the ϕ_I, which escape the detector (or decay invisibly). The SPPC reach is shown in fig. 2.27, along with the effective $|c_\phi|$ for associated with the case $N = 6$.

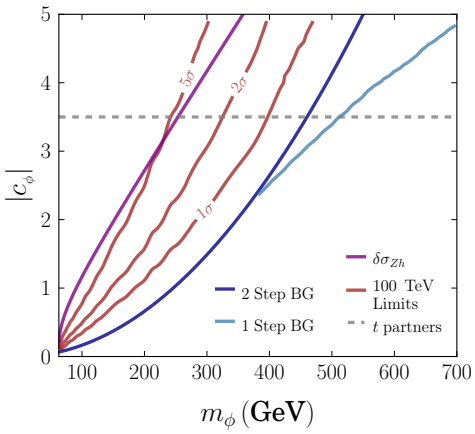

Figure 2.27 The SPPC reach for neutral top partners produced through Higgs portal.

We see that the SPPC has a reach for 5 sigma discovery up to ~ 250 GeV, and a 2 sigma exclusion up to ~ 350 GeV, pushing to the boundaries of the natural region. Note that the SPPC has a uniformly stronger reach in these cases than the CEPC; a 2 sigma hint of a deviation in δZ_h at the CEPC can be confirmed with a 5 sigma discovery of the ϕ_I at the SPPC.

2.4 Dark Matter

The existence of cold dark matter is one of the most direct and powerful pieces of evidence for physics beyond the Standard Model. There are a huge range of possibilities for what the dark matter might be, since for any mass we can simply adjust the number density to get the needed energy density today, with $\Omega_{DM}h^2 \sim 0.1$. Even if the new particle physics is completely specified, the main uncertainty is cosmological: what determines the abundance of the new particles in the early universe?

Weakly Interacting Massive Particles (WIMPs) remain the best motivated and well-studied possibility for dark matter by giving a clear answer to this question: the dark matter particles interact with the Standard Model and are thermalized in the early universe. Assuming a standard cosmological history, the present abundance of dark matter can be unambiguously computed once the underlying particle physics is fixed, in much the same way as the abundance of light elements is predicted in big bang nucleosynthesis.

The relic abundance of dark matter particles is set by their annihilation cross-section in the early universe: in order to avoid overclosure, we must have [70–72]

$$\Omega h^2 = 0.11 \times \left(\frac{\langle \sigma v \rangle_{\text{freeze}}}{2.2 \times 10^{-26}\ \text{cm}^3/\text{s}} \right)^{-1}, \tag{2.30}$$

with $\sigma \propto g_{\text{eff}}^4 / M_{\text{DM}}^2$. This leads us to a limit on the dark matter mass of

$$M_{\text{DM}} < 1.8\ \text{TeV} \left(\frac{g_{\text{eff}}^2}{0.3} \right). \tag{2.31}$$

As has been long appreciated, it is quite remarkable that the TeV scale emerges so naturally in this way, assuming dark matter couplings comparable in strength to the electroweak

gauge interactions. This gives a strong, direct argument for new physics at the TeV scale, independent of any theoretical notions of naturalness.

Compellingly, dark matter often falls out of theories of physics beyond the Standard Model without being put in by hand. Indeed, if the Standard Model is augmented by new physics, not even necessarily close to the weak scale, but far beneath the GUT scale, the interactions with new states should respect baryon and lepton number to a very high degree. Since all Standard Model particles are neutral under the discrete symmetry $(-1)^{B+L+2S}$, any new particles that are odd under this symmetry will be exactly stable. This is the reason for the ubiquitous presence of dark matter candidates in BSM physics. It is thus quite plausible that the dark matter is just one part of a more complete sector of TeV-scale physics; this has long been a canonical expectation, with the dark matter identified as e.g. the lightest neutralino in a theory with TeV-scale supersymmetry. The dominant SUSY processes at hadron colliders are of course the production of colored particles—the squarks and gluinos—which then decay, often in a long cascade of processes, to Standard Model particles and the LSP, resulting in the well known missing energy signals at hadron colliders. This indirect production of dark matter dominates, by far, the direct production of dark matter particles through electroweak processes.

However, as emphasized in our discussion of naturalness, it is also worth preparing for the possibility of a much more sparse spectrum of new particles at the TeV scale. Indeed, if the idea of naturalness fails even slightly, the motivation for a very rich set of new states at the hundreds of GeV scale evaporates, while the motivation for WIMP dark matter at the TeV scale still remains. This is for instance part of the philosophy leading to models of split SUSY: in the minimal incarnation, the scalars and second Higgs doublet of the MSSM are pushed to $\sim 10^2 - 10^3$ TeV, but the gauginos (and perhaps the higgsinos) are much lighter, protected by an R-symmetry. The scalars are not so heavy as to obviate the need for R-parity, so the LSP is still stable, and must be set at the TeV scale in order not to overclose the universe, thereby making up some or perhaps all of the dark matter.

In exploring dark matter at colliders, therefore, it is most prudent to first look for direct production of dark matter, rather than dark matter arising in the decay products of other states that may not be accessible. We will therefore explore the reach of the SPPC for the production of new states with only electroweak quantum numbers, which also certainly give the simplest possible picture for what the dark matter could be. The simplest case of all would be a single new state: a real triplet or vector-like doublet adds the fewest possible number of degrees of freedom to the Standard Model, and no new interactions, so the only free parameters are the particle masses. We can be slightly more general and allow for the presence of additional singlet states. Including just singlets, doublets, and triplets gives a minimal “module" for dark matter, which we will consider, described by the Lagrangian

$$\begin{aligned}\Delta L = \; & M_1 \tilde{B}\tilde{B} + M_2 \tilde{W}\tilde{W} + \mu \tilde{H}_u \tilde{H}_d \\ & + \sqrt{2}\kappa_1 h^\dagger \tilde{W} \tilde{H}_u + \sqrt{2}\kappa_2 h \tilde{W} \tilde{H}_d + \frac{\kappa_1'}{\sqrt{2}} h^\dagger \tilde{B} \tilde{H}_u + \frac{\kappa_2'}{\sqrt{2}} h \tilde{B} \tilde{H}_d .\end{aligned} \tag{2.32}$$

Since the quantum numbers are the same as binos ($\tilde{B}$), winos ($\tilde{W}$), and higgsinos ($\tilde{H}_{\rm u,d}$) of supersymmetric theories, we will use this notation and language in referring to these states, as “charginos", “neutralinos", “the LSP", and so on. Much of our analysis is, however, free of supersymmetric assumptions: supersymmetry only relates the new Yukawa

couplings to the Standard Model gauge couplings as $\kappa \sim g$ and $\kappa' \sim g'$, but this won't play an essential role in most of our discussion.

Given this spectrum of electroweak states, we can consider two obvious limits. One of these states can be significantly lighter than the others; if it is also significantly heavier than M_Z, then the dark matter is close to being a "pure" electroweak state, so we can have a "pure wino" or "pure higgsino" (a "pure bino" has no interactions at leading order and so isn't relevant to our discussion). Alternately, the lightest state can be a significant admixture of different electroweak states.

For both the higgsino and wino, the electroweak multiplet contains charged and neutral states that would be degenerate in the absence of electroweak symmetry breaking; however, a small splitting between these states arises after electroweak symmetry is broken. There is a calculable radiative correction to the splitting, that can be thought of as the difference between the "electrostatic" energy of the photon and Z fields for the charged and neutral components, giving $\Delta m \sim \alpha_{\rm EM} M_Z$. This irreducible splitting is Δm = 166 MeV for winos [73] and Δm = 355 MeV for higgsinos [74]. Further splittings can also arise from UV effects, through integrating out heavier particles (for instance the heavier electroweak states). For the higgsino, the leading dimension 5 operator $(\kappa^2/M)(h^\dagger \tilde{H}_u)(h\tilde{H}_d)$ generates a splitting between the charged and neutral states of order $\Delta m \sim m_Z^2/M$. For the wino, the leading dimension 5 operator does not split the two states, and we have to go to the dimension 7 operator $(\kappa^4/M^3)(h^\dagger \tilde{W} h)^2$, which generates an even smaller splitting $\Delta m \sim m_Z^4/M^3$. Comparing the radiative and UV splittings, if there is just an $\mathcal{O}(1)$ difference in mass between the wino and the rest of the states, the UV splittings become much smaller than the radiative splitting.

Since the wino and higgsino have sizable electroweak gauge interactions, they annihilate very efficiently; this is why their masses have to be pushed to $1 - 3$ TeV to be thermal relics. By contrast, the bino has no electroweak couplings at all. Therefore it is interesting to consider the dark matter as having a sizable admixture of bino together with wino or higgsino. Since the mixing between the states arises through electroweak symmetry breaking, in the limit where the masses M_1, M_2, μ are large compared to M_Z, the mixing angles will be very small, suppressed by powers of (M_Z/M), unless some pair of the diagonal masses are close to degenerate, as with the case of "well-tempered" neutralinos [63]. For the case where the bino/higgsino are nearly degenerate, the mixing terms are parametrically $\sim M_Z$, and this also sets the size of the splitting between the charged and neutral states, which can be typically $\sim 20 - 50$ GeV. For the bino/wino case, the mixing terms are parametrically $\sim M_Z^2/M$, and we expect somewhat smaller splittings.

Thermal relic pure winos and higgsinos must have a mass of 3.1 TeV and 1.1 TeV respectively to account for all the dark matter. At smaller masses they can still account for a significant fraction of the dark matter, for instance a 2 TeV wino can account for half of the dark matter. Mixed dark matter can be lighter but masses around ~ 500 GeV are typical.

The direct detection of pure winos and higgsinos is extremely challenging. The leading dark matter-nucleon interaction arises at 1-loop, and gives rise to a tiny spin-independent cross-section $\sigma_{\rm SI} = 10^{-47}$ cm^2 for winos and $\sigma_{\rm SI} \leq 10^{-48}$ cm^2 for higgsinos [75, 76]. These cross-sections are just at the border of the irreducible neutrino scattering floor for direct detection experiments, and with TeV masses the rates are also too low to be seen in any of the planned experiments. Mixed dark matter is a much more promising target for

direct detection, and is already tested by current limits, but a sizable region of parameter space continues to be viable.

We can also consider indirect detection of high energy particles resulting from dark matter annihilation near the center of our galaxy. Of course predictions for indirect detection rates are fraught with astrophysical uncertainties, and it is difficult to get robust limits in this way. Nonetheless, pure winos are constrained in an interesting way, since their annihilation cross-section has a significant Sommerfeld enhancement [77]. The absence of any signals in the HESS experiment for high energy gamma photons from the galactic center [78] sets limits on the fraction of dark matter a wino of a given mass can comprise. A 3 TeV wino making up all the dark matter is excluded for a standard NFW dark matter distribution, though it is allowed for more "cored" profiles [79–83]. The current limits are summarized in Fig. 2.28.

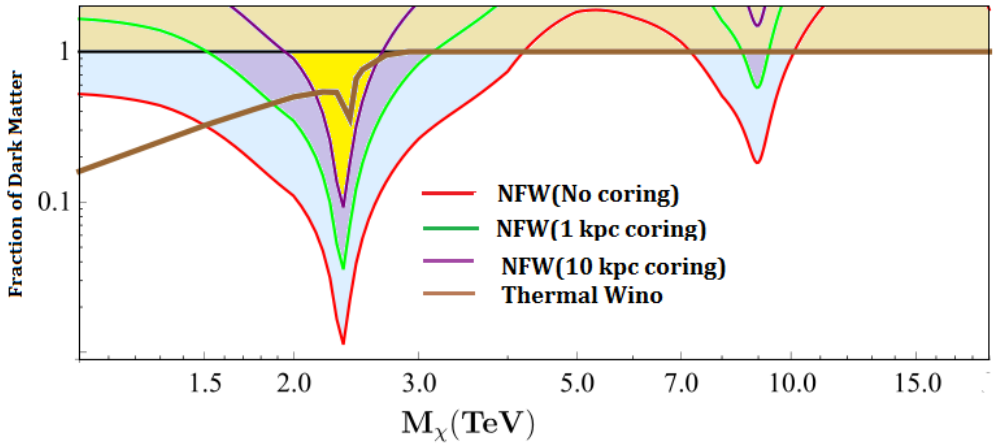

Figure 2.28 Exclusion plot for an NFW profile with the wino making up only some fraction of the wino dark matter [83].

Future indirect detection experiments, such as CTA, could move the wino bounds down to 1 TeV, subject to the same astrophysical uncertainties. But we can see that thermal relic winos making up an $\mathcal{O}(1)$ fraction of dark matter are certainly still consistent. For both pure higgsinos as well as mixed dark matter, the annihilation is not significantly Sommerfeld enhanced, and there are no interesting limits from indirect detection,

It is striking that the very simplest models of dark matter—pure winos and higgsinos—could be completely inaccessible to direct detection experiments, while astrophysical uncertainties make it hard to interpret indirect detection limits. We are left with directly producing the dark matter at accelerators. Relic winos and higgsinos forming a significant component of dark matter, which have masses in few TeV scale, are hopelessly out of reach for direct production at the LHC, which has an ultimate reach up to $\sim 300 - 400$ GeV for pure wino and ~ 200 GeV for pure higgsino production. Moreover, only a fraction of the parameter space for mixed dark matter is accessible to direct production at the LHC.

As we will see shortly, however, the huge increase of rate at the SPPC will allow a much larger range of the relevant parameter space to be explored. The most basic process we will first consider is dark matter pair production. Since the dark matter escapes the detector without leaving a trace, we need to look for additional hard radiation of Standard

Model particles from the process—quarks or gluons, photons, W/Z's, and Higgses. Of these, the "monojet" channel where a quark or gluon is radiated typically gives the best sensitivity. For mixed states we can have a mass splitting $m_{\chi^\pm} - m_{\chi^0} \sim 20 - 50$ GeV between the chargino and neutralino states. In this case, in addition to a hard jet, it is possible to search for low p_T leptons resulting from a chargino or neutralino which decays to the LSP and leptons. We call this the soft lepton channel. On the other hand when the lightest state is pure, the radiative mass splitting is tiny and the decay length is long, leaving a striking signature of high p_T charged track abruptly ending when the chargino decays to the LSP and very soft, likely undetected, Standard Model particles. We also include this disappearing tracks search in our considerations as well.

Monojets: Our first analysis looks for a single hard jet produced in association with a pair of dark matter particles, the classic monojet plus missing energy search. Monojet searches for dark matter and large extra dimensions have been carried out both at the Tevatron and the LHC. The backgrounds for this channel include Standard Model processes with a hard jet and neutrinos. Processes with leptons also comprise part of the background because leptons can fail to be tagged if they are outside the detector acceptance, not isolated, or too soft. This is a very challenging channel with the uncertainty dominated by systematic uncertainty on the background.

Soft Leptons: In the case of mixed dark matter, where we have splittings of $\Delta m \sim 20-50$ GeV, the heavier states can also be pair produced and decay to the dark matter via off-shell gauge bosons, which then decay hadronically or into low p_T leptons. The hadronic decays are difficult to extricate from the noisy hadronic environment, but it is possible to tag the soft leptons. This is different from the standard multilepton searches where there are both more and harder leptons. It has been noted that triggering on a hard jet, as in the monojet search, is advantageous in a soft lepton search.

Disappearing Tracks: The third analysis leverages the near degeneracy of charginos and the LSP for pure electroweak states. Due to the tiny mass splitting, the dominant decay $\chi^\pm \to \pi^\pm \chi^0$ can have a long enough lifetime – $c\tau \sim 6$ cm for winos – to leave a track in the inner detector. This chargino track disappears within the inner detector when it decays to a neutralino and soft pion. This is a promising search channel with no obvious physics background. Searches can also be done when the charginos have a shorter or longer lifetime and look for displaced vertices and stable charged massive particles, respectively.

Multi-Lepton Finally when one moves away from the compressed region of parameter space, any mass splitting between the NLSP's and LSP can be generated and it is most natural to cast limits in the NLSP-LSP mass plane. For these searches, there are multiple leptons from the NLSP to LSP decays whose energies scale with the NLSP-LSP splitting. They are energetic enough that the hard jet required for triggering in the soft lepton search is unnecessary. These searches can be categorized by the particular combination of leptons for which they are looking. Here we consider the three lepton ($3l$), the opposite-sign di-lepton (OSDL), and the same-sign di-lepton (SSDL) signatures, although the $3l$ is always the most sensitive. Multi-lepton searches are based on the observation that while the signal has large mass splittings and heavy invisible particles, the background has neither and so has harder jets that are more back-to-back with leptons than the signal.

As the optimal search strategy strongly depends on the splittings, it would be interesting to look at the overlap and transitions between the approaches discussed above. This more detailed analysis deserves focus in future studies.

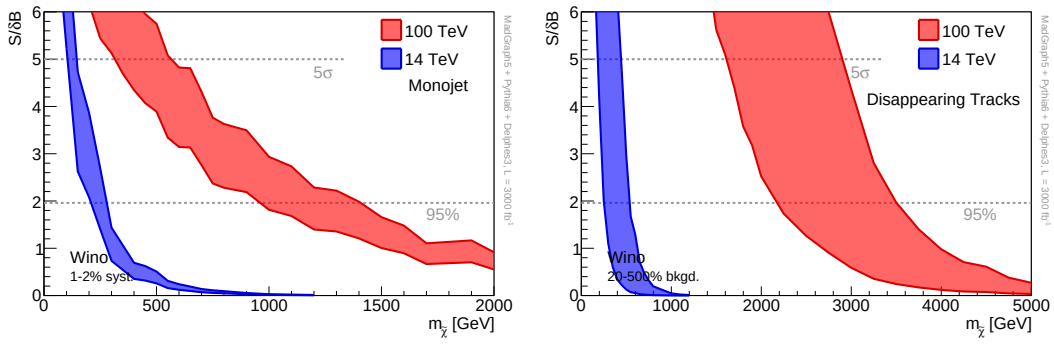

Figure 2.29 Left: The mass reach for the pure wino in the monojet channel with $\mathcal{L} = 3000\ \text{fb}^{-1}$ for the 14 TeV LHC (blue) and the SPPC (red). The bands are generated by varying the background systematics between $1-2\%$ and the signal systematic uncertainty is set to 10% [17]. Right: The mass reach in the pure wino scenario in the disappearing track channel with $\mathcal{L} = 3000\ \text{fb}^{-1}$ for the 14 TeV LHC (blue) and the SPPC (red). The bands are generated by varying the background normalization between $20-500\%$ [17].

Pure Wino

The pure wino has nearly degenerate charged and neutral states. The pair production of the chargino proceeds via Drell-Yan production through an s-channel Z/γ^*, while the production of a chargino/neutralino proceeds through an s-channel W. The charginos decay to to the neutralino and a soft pion.

The mass reach in the monojet channel for a pure wino is shown in Fig. 2.29. The dominant uncertainty in the reach comes from the systematical error of the background, which is varied between $1-2\%$, generating the bands in the plot. Naively scaling the systematics from current ATLAS studies [84] (see Ref. [85] for the CMS study) with luminosity would yield 0.5% for $3000\ \text{fb}^{-1}$, but this is clearly overly optimistic. Choosing the systematic error $\sim 1-2\%$ as we have done may also be optimistic, but it sets a reasonable benchmark, and underscores that minimizing these systematics should be a crucial factor taken into account in the design of the SPPC detectors. Given the same integrated luminosity, the monojet search increases the reach relative to the LHC by nearly a factor of 5, as shown in the left panel of Fig. 2.29 .

Due to the tiny mass splitting $\Delta m = 166$ MeV between the chargino and the neutralino, the decay lifetime can be long. The resulting disappearing track is a very distinctive signal in this case. Since the dominant background for a disappearing track search would be mis-measured low p_T tracks, we cannot accurately predict the backgrounds in the not-yet-designed SPPC detectors. Nonetheless, we can calibrate against the present ATLAS searches for disappearing tracks [86] (see Ref. [87] for the CMS search). For example, we can require that $d^{\text{track}} > 30$cm, with ~ 10's of signal events passing all cuts. The resulting mass reach is shown in the right panel of Fig. 2.29, and the bands result from varying the background normalization upwards and and downwards by a factor of 5. The disappearing tracks could be extremely powerful, with the potential to both convincingly rule out, or discover, thermal wino dark matter.

Pure Higgsino

Pure higgsinos are also produced through s-channel Z's and W's, and the analysis is similar to the pure wino case. The reach of the monojet search is shown in the left panel of Fig. 2.30. As for winos, the search improves by nearly a factor of 5 in mass relative to

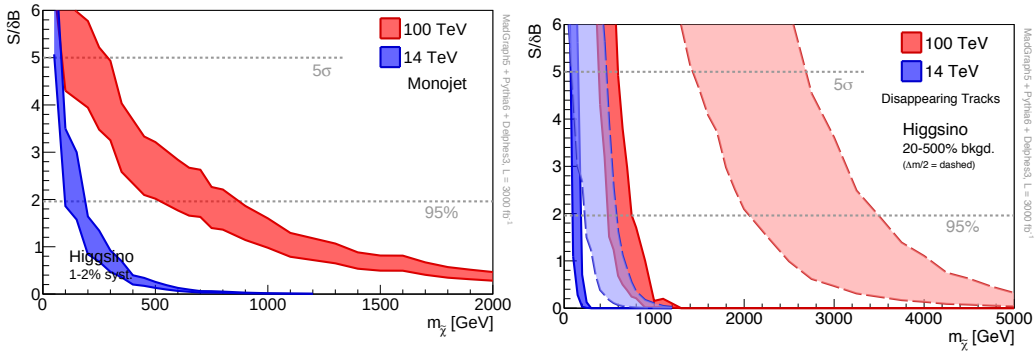

Figure 2.30 Left: The mass reach for the pure higgsino in the monojet channel with $\mathcal{L} = 3000$ fb^{-1} for the 14 TeV LHC (blue) and the SPPC (red). The bands are generated by varying the background systematics between $1-2\%$ and the signal systematic uncertainty is set to 10% [17]. Right: The mass reach for the pure higgsino in the disappearing track channel with $\mathcal{L} = 3000$ fb^{-1} for the 14 TeV LHC (blue) and the SPPC (red). The bands are generated by varying the background normalization between $20-500\%$ [17].

the LHC; the weaker reach relative to winos is due to the smaller production cross-section. With optimistic systematics, higgsinos can be excluded up to 800 GeV.

We can next look at the disappearing tracks search. If the splitting between the states is purely radiative, the lifetime for the higgsino is much shorter than for the wino, since the lifetime scales as $\tau \propto \Delta m^{-5}$. This makes the disappearing track search less effective than the monojet search for higgsinos; the reach is shown in the right panel (solid contour) of Fig. 2.30.

However it is worth recalling that unlike for the pure wino, the splitting for the higgsino states can more easily be affected by the presence of heavier states which can generate $\Delta m \sim M_Z^2/M$ — which could be comparable to the radiative splittings if the heavier electroweak states are near $M \sim 5$ TeV. If these splittings are comparable, resulting in a reduction of the width by a factor of 2, the decay length increases by a factor of $\sim 10-30$, and the higgsino reach becomes comparable to that for winos as shown in the right panel (dashed contour) of Fig. 2.30.

This could be extremely exciting — not only discovering the higgsino, but giving direct evidence for new multi-TeV electroweak states needed to reduce the higgsino mass-splittings in order to account for its anomalously long lifetime.

Mixed Dark Matter

In the case of mixed dark matter we can expect mass splittings of $\sim$ 10's of GeV, and so the search is dominated by looking for the soft leptons from chargino decays via off-shell W's and Z's. This will give us a more powerful reach than with monojet alone. On the other hand, with these splittings the decays are prompt and we lose the advantages of the disappearing tracks search. We will focus on two representative examples, with mass splittings of 20 GeV. The first is a bino/higgsino mixture and the second is a bi-

no/wino(/higgsino) mixture, obtained by dialing all three of $|M_1|, |M_2|, |\mu|$ close to each other. The mass reach for these scenarios is shown in Fig. 2.31.

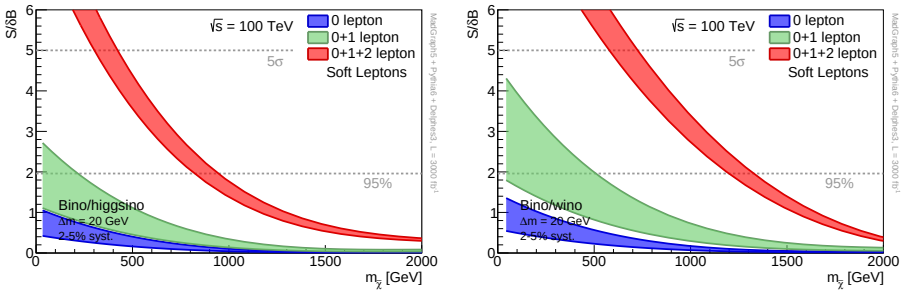

Figure 2.31 The mass reach in the mixed bino/higgsino ($\Delta = 20$ GeV) scenario in the soft lepton channel at 100 TeV with $\mathcal{L} = 3000$ fb^{-1} at 100 TeV looking for 0 leptons (blue), 0 or 1 leptons (green), and 0, 1, or 2 leptons (red). The bands are generated by varying the background systematics between $2 - 5\%$ and the signal systematic uncertainty is set to 10% [17].

Note that in all cases the tagging of soft leptons is very important to maximize the mass reach. The 2-lepton bin is most important: while the 0 and 1 lepton bin backgrounds are dominated by single gauge-bosons, the 2-lepton backgrounds are controlled by diboson production with a much smaller cross-section. We find exclusions reaching up to ~ 1 TeV masses, and discovery up to several hundred GeV.

Electroweak Cascades

We have so far focussed on the most difficult cases for dark matter production, where the lightest electroweak states are produced and their decays contain only soft particles. The mass reach can be considerably higher if there is an electroweak spectrum with sizable splittings. If the heavier states can be produced, they will decay to the dark matter state, emitting hard W's, Z's, and Higgses. This leads to the familiar signals of multi-lepton plus missing energy, and searches for events with leptons, such as 4 leptons, opposite- and same-sign di-leptons. A study of the SPPC reach for electroweak cascades has recently been carried out in [18], for four representative cases of the production of NLSP's decaying to the LSP:

- Wino NLSP and higgsino LSP ($M_1 \gg M_2 > \mu$)
- Higgsino NLSP and wino LSP ($M_1 \gg \mu > M_2$)
- Higgsino NLSP and bino LSP ($M_2 \gg \mu > M_1$)
- Wino NLSP and bino LSP ($\mu \gg M_2 > M_1$)

The heaviest electroweakino in all cases is fixed to 5 TeV. Bino NLSP's have too small a production cross-section to be relevant, so they are never considered as the NLSP.

The reach for the final case, with wino NLSP and bino LSP, depends importantly on the wino branching ratios: for very heavy higgsinos, the decay $\tilde{W} \to \tilde{B}h$ dominates, but it is also possible to have sizable branching ratios for emitting $W's, Z's$ as well. The SPPC reach for these four scenarios are summarized in Fig. 2.32.

This represents a major gain over the reach of the LHC. Most notably, the entire interesting range for higgsino masses can be probed in this way, provided the wino is lighter than 3 TeV, and not too degenerate with the higgsino.

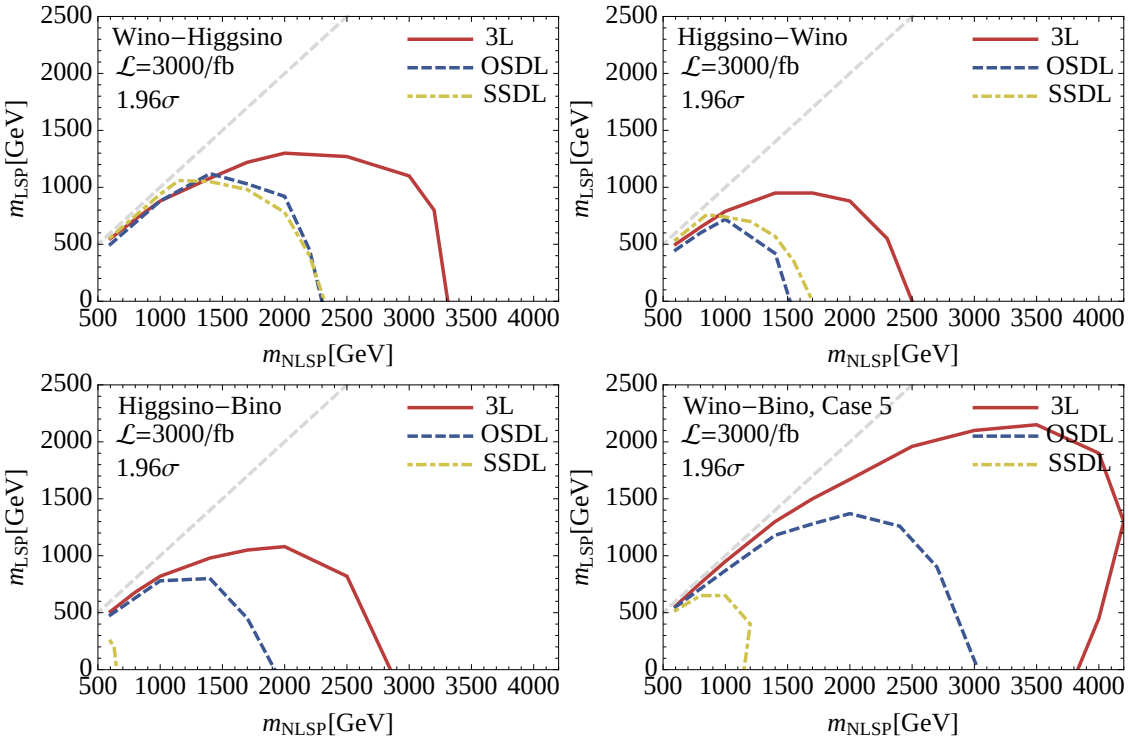

Figure 2.32 95 % CL limits for wino-NLSP and higgsino-LSP (top left), Higgsino-NLSP and wino-LSP (top right), Higgsino-NLSP and bino LSP (bottom left) and wino-NLSP and bino-LSP (bottom right) [18].

Co-Annihilation with Bino Dark Matter

So far we have only briefly considered the case of bino dark matter. Due to its small couplings, the bino does not annihilate efficiently as it freezes out, and typically overcloses the universe unless it is extremely light. Bino dark matter can be made viable in a supersymmetric context, if there are other superpartners with a mass nearly degenerate with it. Their presence can enhance the bino annihilation rate and give the correct relic abundance for heavier bino masses. If the co-annihilators are gluinos, stops, or squarks, the bino masses giving the correct relic abundance are in the multi TeV region, ~ 7 TeV for gluino co-annihilation, and ~ 2 TeV for stop or squark co-annihilation. Since the colored states are very close in mass to the bino, they can have large production rates at the SPPC. They will then decay to the bino and soft Standard Model particles, resulting in the monojet signal. Due to the colored production, however, these rates will be much higher than with electroweakino monojet signals.

The SPPC reach for gluino and stop annihilations, as obtained by [17], are shown in left and right panels of Figs. 2.33, respectively. For gluino co-annihilation the gluino-bino splitting required to get the right relic abundance is shown on the bottom x-axis of left panel of Fig. 2.33. We see that the SPPC covers most of this parameter space. It is worth recalling too, that we have presented the most conservative search as we assume that whatever accompanies the LSP from the co-annihilator decay is undetectable. In practice, the searches can be augmented by looking for the possibly soft decay products.

The mass splitting for the correct relic abundance in stop co-annihilation has also been computed and is displayed on the bottom x-axis of the right panel of Fig. 2.33. Here, the

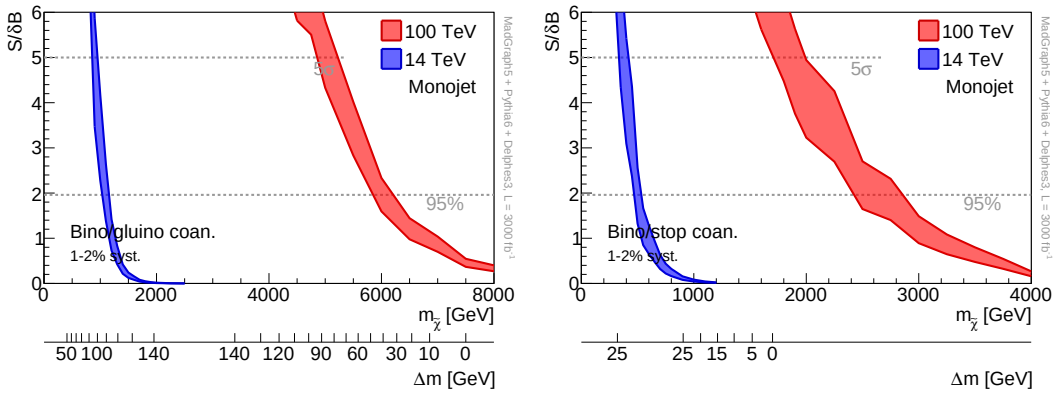

Figure 2.33 Left: The mass reach in the gluino coannihilation scenario in the monojet channel with $\mathcal{L} = 3000$ fb^{-1} for the 14 TeV LHC (blue) and the SPPC (red). The bands are generated by varying the background systematics between $1 - 2\%$ and the signal systematic uncertainty is set to 10%. The lower x-axis displays the gluino-bino mass splitting Δm for a given bino mass which is required to saturate the relic density [88, 89]. A tick is placed every 10 GeV with the exception of the consecutive $\Delta m = 140$ GeV ticks [17]. Right: The mass reach in the stop coannihilation scenario in the monojet channel with $\mathcal{L} = 3000$ fb^{-1} for the 14 TeV LHC (blue) and the SPPC (red). The bands are generated by varying the background systematics between $1 - 2\%$ and the signal systematic uncertainty is set to 10%. The lower x-axis displays the stop-bino mass splitting Δm for a given bino mass which is required to satisfy the relic density [89]. A tick is placed every 5 GeV with the exception of the consecutive $\Delta m = 25$ GeV ticks [17].

SPPC can make strong statements about this spectrum. Both exclusion and discovery is possible even in the degenerate stop-bino limit.

Summary

A broad summary of the dark matter reaches we have discussed is given in Fig. 2.34. While the LHC can look for electroweak states up to a few hundred GeV, it will not

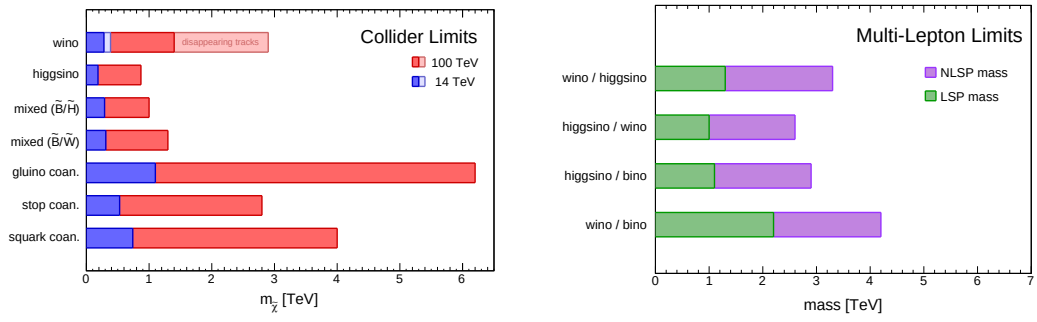

Figure 2.34 Summary of collider reach for neutralino dark matter [17] and in electroweakino cascades [18].

probe the TeV mass range which is most natural for thermally saturating dark matter. By contrast the jump to 100 TeV at the SPPC allows us to go deep into this territory, with a great potential to discover WIMP dark matter.

References

[1] The ATLAS Collaboration, G. Aad et al., *Observation of a new particle in the search for the Standard Model Higgs boson with the ATLAS detector at the LHC*, Phys.Lett. **B716** (2012) 1–29, arXiv:1207.7214 [hep-ex].

[2] The CMS Collaboration, S. Chatrchyan et al., *Observation of a new boson at a mass of 125 GeV with the CMS experiment at the LHC*, Phys.Lett. **B716** (2012) 30–61, arXiv:1207.7235 [hep-ex].

[3] J. Fan, M. Reece, and L.-T. Wang, *Possible Futures of Electroweak Precision: ILC, FCC-ee, and CEPC*, arXiv:1411.1054 [hep-ph].

[4] A. J. Barr, M. J. Dolan, C. Englert, D. E. F. de Lima, and M. Spannowsky, *Higgs Self-Coupling Measurements at a 100 TeV Hadron Collider*, arXiv:1412.7154 [hep-ph].

[5] M. McCullough, *An Indirect Model-Dependent Probe of the Higgs Self-Coupling*, Phys.Rev. **D90** (2014) 015001, arXiv:1312.3322 [hep-ph].

[6] A. Hook and A. Katz, *Unbroken $SU(2)$ at a 100 TeV collider*, JHEP **1409** (2014) 175, arXiv:1407.2607 [hep-ph].

[7] T. Han, J. Sayre, and S. Westhoff, *Top-Quark Initiated Processes at High-Energy Hadron Colliders*, arXiv:1411.2588 [hep-ph].

[8] S. Dawson, A. Ismail, and I. Low, *A Redux on "When is the Top Quark a Parton?"*, Phys.Rev. **D90** (2014) no. 1, 014005, arXiv:1405.6211 [hep-ph].

[9] N. Craig, H. K. Lou, M. McCullough, and A. Thalapillil, *The Higgs Portal Above Threshold*, arXiv:1412.0258 [hep-ph].

[10] N. Craig, M. Farina, M. McCullough, and M. Perelstein, *Precision Higgsstrahlung as a Probe of New Physics*, arXiv:1411.0676 [hep-ph].

[11] D. Curtin, P. Meade, and C.-T. Yu, *Testing Electroweak Baryogenesis with Future Colliders*, JHEP **1411** (2014) 127, arXiv:1409.0005 [hep-ph].

[12] A. Katz and M. Perelstein, *Higgs Couplings and Electroweak Phase Transition*, JHEP **1407** (2014) 108, arXiv:1401.1827 [hep-ph].

[13] S. Profumo, M. J. Ramsey-Musolf, C. L. Wainwright, and P. Winslow, *Singlet-Catalyzed Electroweak Phase Transitions and Precision Higgs Studies*, arXiv:1407.5342 [hep-ph].

[14] B. Henning, X. Lu, and H. Murayama, *What do precision Higgs measurements buy us?*, arXiv:1404.1058 [hep-ph].

[15] T. Cohen, R. T. D'Agnolo, M. Hance, H. K. Lou, and J. G. Wacker, *Boosting Stop Searches with a 100 TeV Proton Collider*, JHEP **1411** (2014) 021, arXiv:1406.4512 [hep-ph].

[16] J. Fan, M. Reece, and L.-T. Wang, *Precision Natural SUSY at CEPC, FCC-ee, and ILC*, arXiv:1412.3107 [hep-ph].

[17] M. Low and L.-T. Wang, *Neutralino dark matter at 14 TeV and 100 TeV*, JHEP **1408** (2014) 161, arXiv:1404.0682 [hep-ph].

[18] S. Gori, S. Jung, L.-T. Wang, and J. D. Wells, *Prospects for Electroweakino Discovery at a 100 TeV Hadron Collider*, JHEP **1412** (2014) 108, arXiv:1410.6287 [hep-ph].

[19] V. V. Khoze, *Perturbative growth of high-multiplicity W, Z and Higgs production processes at high energies*, arXiv:1411.2925 [hep-ph].

[20] S. A. R. Ellis, G. L. Kane, and B. Zheng, *Superpartners at LHC and Future Colliders: Predictions from Constrained Compactified M-Theory*, arXiv:1408.1961 [hep-ph].

[21] B. S. Acharya, K. Bozek, C. Pongkitivanichkul, and K. Sakurai, *Prospects for observing charginos and neutralinos at a 100 TeV proton-proton collider*, arXiv:1410.1532 [hep-ph].

[22] D. S. M. Alves, J. Galloway, J. T. Ruderman, and J. R. Walsh, *Running Electroweak Couplings as a Probe of New Physics*, arXiv:1410.6810 [hep-ph].

[23] M. Cirelli, F. Sala, and M. Taoso, *Wino-like Minimal Dark Matter and future colliders*, JHEP **1410** (2014) 033, arXiv:1407.7058 [hep-ph].

[24] W. Altmannshofer, P. J. Fox, R. Harnik, G. D. Kribs, and N. Raj, *Dark Matter Signals in Dilepton Production at Hadron Colliders*, arXiv:1411.6743 [hep-ph].

[25] G. G. di Cortona, *Hunting electroweakinos at future hadron colliders and direct detection experiments*, arXiv:1412.5952 [hep-ph].

[26] J. Bramante, P. J. Fox, A. Martin, B. Ostdiek, T. Plehn, et al., *The Relic Neutralino Surface at a 100 TeV collider*, arXiv:1412.4789 [hep-ph].

[27] D. Curtin, R. Essig, S. Gori, and J. Shelton, *Illuminating Dark Photons with High-Energy Colliders*, arXiv:1412.0018 [hep-ph].

[28] M. Endres, T. Fukuhara, D. Pekker, M. Cheneau, P. Schauss, et al., *The 'Higgs' Amplitude Mode at the Two-Dimensional Superfluid-Mott Insulator Transition*, Nature **487** (2012) 454–458, arXiv:1204.5183 [cond-mat.quant-gas].

[29] J. Campbell, K. Hatakeyama, J. Huston, F. Petriello, J. R. Andersen, et al., *Working Group Report: Quantum Chromodynamics*, arXiv:1310.5189 [hep-ph].

[30] J. Chen, T. Han, R. Ruiz, and B. Tweedie. In preparation.

[31] M. Mangano. Talk at 1st CFHEP Symposium on Circular Collider Physics.

[32] K. Agashe, R. Contino, and A. Pomarol, *The Minimal composite Higgs model*, Nucl.Phys. **B719** (2005) 165–187, arXiv:hep-ph/0412089 [hep-ph].

[33] D. Pappadopulo, A. Thamm, R. Torre, and A. Wulzer, *Heavy Vector Triplets: Bridging Theory and Data*, JHEP **1409** (2014) 060, arXiv:1402.4431 [hep-ph].

[34] D. A. Dicus and H.-J. He, *Scales of fermion mass generation and electroweak symmetry breaking*, Phys.Rev. **D71** (2005) 093009, arXiv:hep-ph/0409131 [hep-ph].

[35] W. Yao, *Studies of measuring Higgs self-coupling with $HH \to b\bar{b}\gamma\gamma$ at the future hadron colliders*, arXiv:1308.6302 [hep-ph].

[36] X.-m. Zhang, *Operators analysis for Higgs potential and cosmological bound on Higgs mass*, Phys.Rev. **D47** (1993) 3065–3067, arXiv:hep-ph/9301277 [hep-ph].

[37] X. Zhang, B. Young, and S. Lee, *Electroweak sphaleron for effective theory in the limit of large Higgs boson mass*, Phys.Rev. **D51** (1995) 5327–5330, arXiv:hep-ph/9406322 [hep-ph].

[38] C. Grojean, G. Servant, and J. D. Wells, *First-order electroweak phase transition in the standard model with a low cutoff*, Phys.Rev. **D71** (2005) 036001, arXiv:hep-ph/0407019 [hep-ph].

[39] S. R. Coleman and E. J. Weinberg, *Radiative Corrections as the Origin of Spontaneous Symmetry Breaking*, Phys.Rev. **D7** (1973) 1888–1910.

[40] V. Kuzmin, V. Rubakov, and M. Shaposhnikov, *On the Anomalous Electroweak Baryon Number Nonconservation in the Early Universe*, Phys.Lett. **B155** (1985) 36.

[41] D. Bodeker, L. Fromme, S. J. Huber, and M. Seniuch, *The Baryon asymmetry in the standard model with a low cut-off*, JHEP **0502** (2005) 026, arXiv:hep-ph/0412366 [hep-ph].

[42] C. Delaunay, C. Grojean, and J. D. Wells, *Dynamics of Non-renormalizable Electroweak Symmetry Breaking*, JHEP **0804** (2008) 029, arXiv:0711.2511 [hep-ph].

[43] The ATLAS Collaboration, G. Aad et al., *Search For Higgs Boson Pair Production in the $\gamma\gamma b\bar{b}$ Final State using pp Collision Data at $\sqrt{s} = 8$ TeV from the ATLAS Detector*, arXiv:1406.5053 [hep-ex].

[44] J. Ren, Z.-Z. Xianyu, and H.-J. He, *Higgs Gravitational Interaction, Weak Boson Scattering, and Higgs Inflation in Jordan and Einstein Frames*, JCAP **1406** (2014) 032, arXiv:1404.4627 [gr-qc].

[45] J. Ren and H.-J. He, *Probing Gravitational Dark Matter*, arXiv:1410.6436 [hep-ph].

[46] S.-h. Zhu, *A New Paradigm: Role of Electron-positron and Hadron Colliders*, arXiv:1410.2042 [hep-ph].

[47] S. Weinberg, *The Cosmological Constant Problem*, Rev.Mod.Phys. **61** (1989) 1–23.

[48] S. Weinberg, *Implications of Dynamical Symmetry Breaking*, Phys.Rev. **D13** (1976) 974–996.

[49] L. Susskind, *Dynamics of Spontaneous Symmetry Breaking in the Weinberg-Salam Theory*, Phys.Rev. **D20** (1979) 2619–2625.

[50] D. B. Kaplan and H. Georgi, *SU(2) x U(1) Breaking by Vacuum Misalignment*, Phys.Lett. **B136** (1984) 183.

[51] N. Arkani-Hamed, A. G. Cohen, and H. Georgi, *Electroweak symmetry breaking from dimensional deconstruction*, Phys.Lett. **B513** (2001) 232–240, arXiv:hep-ph/0105239 [hep-ph].

[52] S. Dimopoulos and H. Georgi, *Softly Broken Supersymmetry and SU(5)*, Nucl.Phys. **B193** (1981) 150.

[53] N. Arkani-Hamed, S. Dimopoulos, and G. Dvali, *The Hierarchy problem and new dimensions at a millimeter*, Phys.Lett. **B429** (1998) 263–272, arXiv:hep-ph/9803315 [hep-ph].

[54] L. Randall and R. Sundrum, *A Large mass hierarchy from a small extra dimension*, Phys.Rev.Lett. **83** (1999) 3370–3373, arXiv:hep-ph/9905221 [hep-ph].

[55] J. M. Maldacena, *The Large N limit of superconformal field theories and supergravity*, Int.J.Theor.Phys. **38** (1999) 1113–1133, arXiv:hep-th/9711200 [hep-th].

[56] P. Langacker and M.-x. Luo, *Implications of precision electroweak experiments for M_t, ρ_0, $\sin^2\theta_W$ and grand unification*, Phys.Rev. **D44** (1991) 817–822.

[57] R. Barbieri and G. Giudice, *Upper Bounds on Supersymmetric Particle Masses*, Nucl.Phys. **B306** (1988) 63.

[58] Z. Chacko, H.-S. Goh, and R. Harnik, *The Twin Higgs: Natural electroweak breaking from mirror symmetry*, Phys.Rev.Lett. **96** (2006) 231802, arXiv:hep-ph/0506256 [hep-ph].

[59] G. Burdman, Z. Chacko, H.-S. Goh, and R. Harnik, *Folded supersymmetry and the LEP paradox*, JHEP **0702** (2007) 009, arXiv:hep-ph/0609152 [hep-ph].

[60] J. D. Wells, *Implications of supersymmetry breaking with a little hierarchy between gauginos and scalars*, arXiv:hep-ph/0306127 [hep-ph].

[61] N. Arkani-Hamed and S. Dimopoulos, *Supersymmetric unification without low energy supersymmetry and signatures for fine-tuning at the LHC*, JHEP **0506** (2005) 073, arXiv:hep-th/0405159 [hep-th].

[62] G. Giudice and A. Romanino, *Split supersymmetry*, Nucl.Phys. **B699** (2004) 65–89, arXiv:hep-ph/0406088 [hep-ph].

[63] N. Arkani-Hamed, A. Delgado, and G. Giudice, *The Well-tempered neutralino*, Nucl.Phys. **B741** (2006) 108–130, arXiv:hep-ph/0601041 [hep-ph].

[64] A. Arvanitaki, N. Craig, S. Dimopoulos, and G. Villadoro, *Mini-Split*, JHEP **1302** (2013) 126, arXiv:1210.0555 [hep-ph].

[65] N. Arkani-Hamed, A. Gupta, D. E. Kaplan, N. Weiner, and T. Zorawski, *Simply Unnatural Supersymmetry*, arXiv:1212.6971 [hep-ph].

[66] T. Cohen, T. Golling, M. Hance, A. Henrichs, K. Howe, et al., *SUSY Simplified Models at 14, 33, and 100 TeV Proton Colliders*, JHEP **1404** (2014) 117, arXiv:1311.6480 [hep-ph].

[67] S. Dimopoulos and G. Giudice, *Naturalness constraints in supersymmetric theories with nonuniversal soft terms*, Phys.Lett. **B357** (1995) 573–578, arXiv:hep-ph/9507282 [hep-ph].

[68] N. Arkani-Hamed and H. Murayama, *Can the supersymmetric flavor problem decouple?*, Phys.Rev. **D56** (1997) 6733–6737, arXiv:hep-ph/9703259 [hep-ph].

[69] N. Arkani-Hamed, A. Cohen, E. Katz, and A. Nelson, *The Littlest Higgs*, JHEP **0207** (2002) 034, arXiv:hep-ph/0206021 [hep-ph].

[70] B. W. Lee and S. Weinberg, *Cosmological Lower Bound on Heavy Neutrino Masses*, Phys.Rev.Lett. **39** (1977) 165–168.

[71] H. Goldberg, *Constraint on the Photino Mass from Cosmology*, Phys.Rev.Lett. **50** (1983) 1419.

[72] G. Steigman, B. Dasgupta, and J. F. Beacom, *Precise Relic WIMP Abundance and its Impact on Searches for Dark Matter Annihilation*, Phys.Rev. **D86** (2012) 023506, arXiv:1204.3622 [hep-ph].

[73] M. Ibe, S. Matsumoto, and R. Sato, *Mass Splitting between Charged and Neutral Winos at Two-Loop Level*, Phys.Lett. **B721** (2013) 252–260, arXiv:1212.5989 [hep-ph].

[74] S. D. Thomas and J. D. Wells, *Phenomenology of Massive Vectorlike Doublet Leptons*, Phys.Rev.Lett. **81** (1998) 34–37, arXiv:hep-ph/9804359 [hep-ph].

[75] J. Hisano, K. Ishiwata, and N. Nagata, *A complete calculation for direct detection of Wino dark matter*, Phys.Lett. **B690** (2010) 311–315, arXiv:1004.4090 [hep-ph].

[76] R. J. Hill and M. P. Solon, *WIMP-nucleon scattering with heavy WIMP effective theory*, Phys.Rev.Lett. **112** (2014) 211602, arXiv:1309.4092 [hep-ph].

[77] J. Hisano, S. Matsumoto, M. M. Nojiri, and O. Saito, *Non-perturbative effect on dark matter annihilation and gamma ray signature from galactic center*, Phys.Rev. **D71** (2005) 063528, arXiv:hep-ph/0412403 [hep-ph].

[78] H.E.S.S. Collaboration, A. Abramowski et al., *Search for Photon-Linelike Signatures from Dark Matter Annihilations with H.E.S.S.*, Phys.Rev.Lett. **110** (2013) 041301, arXiv:1301.1173 [astro-ph.HE].

[79] T. Cohen, M. Lisanti, A. Pierce, and T. R. Slatyer, *Wino Dark Matter Under Siege*, JCAP **1310** (2013) 061, arXiv:1307.4082.

[80] J. Fan and M. Reece, *In Wino Veritas? Indirect Searches Shed Light on Neutralino Dark Matter*, JHEP **1310** (2013) 124, arXiv:1307.4400 [hep-ph].

[81] A. Hryczuk, I. Cholis, R. Iengo, M. Tavakoli, and P. Ullio, *Indirect Detection Analysis: Wino Dark Matter Case Study*, JCAP **1407** (2014) 031, arXiv:1401.6212 [astro-ph.HE].

[82] G. Ovanesyan, T. R. Slatyer, and I. W. Stewart, *Heavy Dark Matter Annihilation from Effective Field Theory*, arXiv:1409.8294 [hep-ph].

[83] M. Baumgart, I. Z. Rothstein, and V. Vaidya, *Constraints on Galactic Wino Densities from Gamma Ray Lines*, arXiv:1412.8698 [hep-ph].

[84] The ATLAS Collaboration, *Search for New Phenomena in Monojet plus Missing Transverse Momentum Final States using 10fb-1 of pp Collisions at sqrts=8 TeV with the ATLAS detector at the LHC*, .

[85] The CMS Collaboration, *Search for new physics in monojet events in pp collisions at sqrt(s)= 8 TeV*, .

[86] The ATLAS Collaboration, G. Aad et al., *Search for charginos nearly mass degenerate with the lightest neutralino based on a disappearing-track signature in pp collisions at $\sqrt{s}$=8 TeV with the ATLAS detector*, Phys.Rev. **D88** (2013) no. 11, 112006, arXiv:1310.3675 [hep-ex].

[87] The CMS Collaboration, *Search for disappearing tracks in proton-proton collisions at $\sqrt{s}$ = 8 TeV*, arXiv:1411.6006 [hep-ex].

[88] K. Harigaya, K. Kaneta, and S. Matsumoto, *Gaugino coannihilations*, Phys.Rev. **D89** (2014) 115021, arXiv:1403.0715 [hep-ph].

[89] A. De Simone, G. F. Giudice, and A. Strumia, *Benchmarks for Dark Matter Searches at the LHC*, JHEP **1406** (2014) 081, arXiv:1402.6287 [hep-ph].

CHAPTER 3

HIGGS PHYSICS AT THE CEPC

3.1 Introduction

The historic discovery of a Higgs boson in 2012 by the ATLAS and CMS collaborations [1, 2] at the Large Hadron Collider (LHC) has opened a new era in particle physics. Subsequent measurements of the properties of the new particle have indicated compatibility with the Standard Model (SM) Higgs boson [3]. While the SM has been remarkably successful in describing experimental phenomena, with the discovery of the Higgs boson completing the last missing piece of the puzzle, it is likely that the SM is only an effective theory at the electroweak scale. In particular, the SM does not *predict* the parameters in the Higgs potential, nor does it provide an explanation for the nature of electroweak phase transition. Furthermore, the vast difference between the Planck scale and the weak scale still remains a mystery. In addition, there is no particle candidate for dark matter in the SM. The discovery of a spin zero Higgs boson, the first elementary particle of its kind, only sharpens these questions. It is clear that any attempt to address them will involve new physics beyond the SM; see Ref. [4] for a more detailed discussion. Therefore, the Higgs discovery marks the beginning of a new era of theoretical and experimental explorations.

A precision Higgs physics program will be a critical component of any roadmap for high energy physics in the coming decades. Potential new physics beyond the SM could lead to observable deviations in the Higgs couplings from the SM expectations. Typically, such deviations can be parameterised as

$$\delta = c\frac{v^2}{M_{\rm NP}^2}, \tag{3.1}$$

where v and $M_{\rm NP}$ are the vacuum expectation value of the Higgs field and the typical mass scale of new physics, respectively. The size of the proportionality constant c depends on the model, but it should not be much larger than $\mathcal{O}(1)$. The current and upcoming LHC runs will directly search for new physics from a few hundred GeV to at least a TeV. Eq. (3.1) implies that probing new physics beyond the LHC reach would require the measurement of the Higgs couplings to at least percent level accuracy. The current level of precision in the Higgs coupling measurements are at about $\mathcal{O}(15\%)$ in most cases. This will be significantly improved in the coming decades through the on-going LHC program, as documented in several studies, see, e.g., Ref [5]. Precisions of a few percent are achievable for some of the couplings. To achieve sub-percent level precision will need new facilities. A lepton collider operating as a Higgs factory is a natural next step.

The Circular Electron-Positron Collider (CEPC), proposed by the Chinese particle physics community, is one such possible facility. CEPC will operate at a center-of-mass energy of $\sqrt{s} \sim 250$ GeV that maximises the Higgs production cross section through the $e^+e^- \to ZH$ process. At the CEPC, in contrast to the LHC, Higgs candidate events can be identified through the recoil mass method without tagging its decays. Therefore, Higgs production can be disentangled from Higgs decay in a model-independent way. Moreover, the cleaner environment at a lepton collider allows much better exclusive measurement of Higgs decay channels. All of these give CEPC impressive reach in probing Higgs properties. For example, with an integrated luminosity of 5 ab^{-1}, over one million Higgs bosons will be produced. With this sample, CEPC will be able to measure the Higgs coupling to Z at an accuracy level of 0.25%, more than a factor 10 better than the HL-LHC. Such a precise measurement gives the CEPC unprecedented reach into interesting new physics scenarios which are very difficult to probe at the LHC. The CEPC also has strong capability in detecting Higgs exotic decays. For example, with 5 ab^{-1}, it can improve the reach of invisible decay branching ratios to 0.28% at 95% confidence level. It is also expected to have good sensitivity to exotic decay channels which are swamped by the backgrounds at the LHC. It is also important to stress that an e^+e^- Higgs factory can perform *model-independent* measurement of the Higgs width. This unique feature in turn allows for model-independent determination of the Higgs couplings.

After the completion of the CEPC program, a Super Proton-Proton Collider (SPPC) will be installed in the same tunnel, following the successful LEP-LHC model. SPPC is expected to achieve a center-of-mass energy between $70 - 100$ TeV, far exceeding that of the LHC. SPPC will search directly for new physics particles which could affect electroweak symmetry breaking and Higgs physics. It is complementary to the searches at the CEPC, and the combination of the two experiments will maximise the physics potential. In the following, the focus is on the physics capabilities of the CEPC.

This chapter summarises the first studies of a precision Higgs physics program at the CEPC. It is organised as following: Section 3.2 briefly summarises the collider and detector performance parameters assumed for the studies, then Section 3.3 describes individual Higgs measurements, including the methodology and results from simulation studies.

3.2 Simulation and Reconstruction

3.2.1 Detector Simulation and Software Chain

The CEPC conceptual detector design takes the International Large Detector (ILD) design [6, 7] as a reference. ILD is one of the two baseline detectors proposed for the International Linear Collider (ILC) [8]. To adapt the ILD to the CEPC collision environment, some necessary changes have been made, leading to the CEPC conceptual detector geometry.

The simulation of the CEPC detector makes use of the ILC software chain. CEPC uses iLCSoft [9], the standard software chain for the linear collider studies, as the software framework for its simulation studies. iLCSoft provides a uniform data format [10]), common data management services and rich reconstruction/analysis functionalities. Dedicated software tools have also been developed, including the CEPC fast simulation tool [11] and a general physics analysis framework. In addition, GuineaPig [12] is used to study the beam background and beam energy spectrum. The CEPC detector simulation studies follow three major steps: generation of physics events, simulation of detector response and reconstruction of physics objects.

Higgs signal and SM background processes are simulated with a dedicated event generator, WHIZARD [13]. In addition, MADGRAPH [14] and PYTHIA [15] have been used to generate samples for Higgs exotic decay studies. Detailed information for the available sample can be found at [16]. The event generators are interfaced to MOKKA [17]/ GEANT4 [18] for detector simulation. The CEPC conceptual detector geometry has been fully implemented and validated [19], as shown in Fig. 3.1.

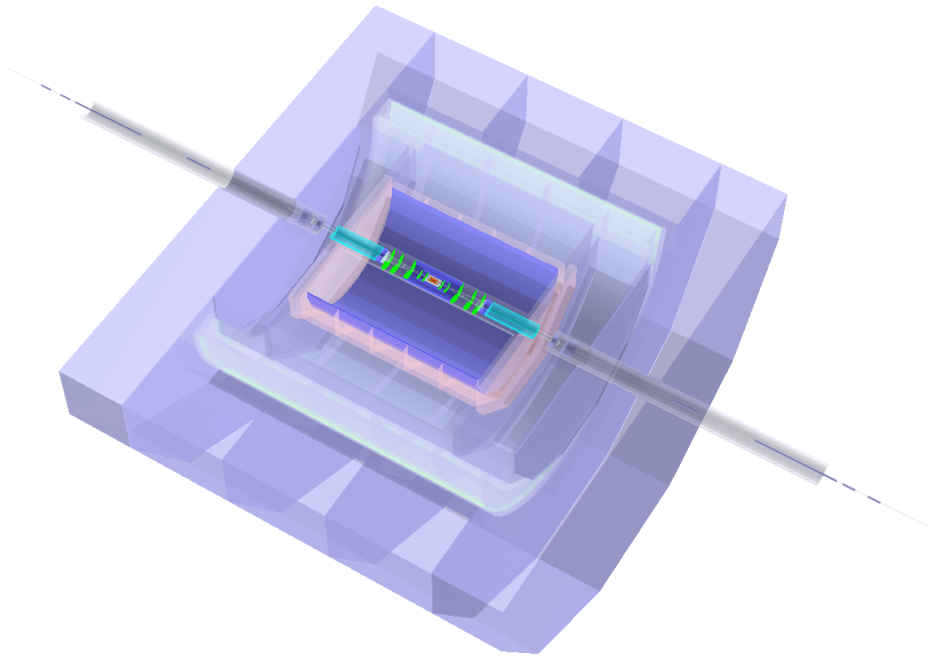

Figure 3.1 Geometry of the conceptual CEPC detector implemented in MOKKA and GEANT 4.

The full simulation is followed by digitisation. A full digitisation should provide appropriate modelling/parametrisation of the electronics response to the incident particles. Effects such as noise, dead time/dead zones and inhomogeneous detector response should also be taken into account. The current CEPC studies use the default digitisation modules in iLCSoft. More realistic digitisation should be pursued in future studies. The digitised hits are then reconstructed into physics objects. CEPC adopts the standard ILC reconstruction tools for tracking [20], Particle Flow Algorithm (PFA) [21], jet clustering and jet flavour tagging [22]. Meanwhile, it also uses a newly developed PFA framework, the Arbor PFA [23].

3.2.2 Detector Performance

PFA is not only an indispensable component of the CEPC event reconstruction, but also provides the guideline for its detector design. PFA is a general reconstruction concept originating from the LEP experiments [24]. It attempts to identify and reconstruct all the final-state particles in the most suitable sub-detector systems. Explicitly, PFA reconstructs charged particles in the tracking system (whose momentum resolution is significantly better than calorimeter energy resolution), photons in the electromagnetic calorimeter (ECAL) and neutral hadrons in the whole calorimeter. The PFA algorithm gives a significant improvement in jet energy resolution. It has been proven to be very efficient in both pp collisions [25, 26] and e^+e^- collisions [24] for lepton identification, tau reconstruction and jet energy measurement. Fig. 3.4 shows the identification efficiencies of simultaneous identification of different charged particles.

The key requirement of PFA is the separation and identification of calorimeter clusters deposited by different incident particles. In the CEPC studies, Arbor PFA [23] has been used as the default and its performance has been cross-checked with that of PandoraPFA. Inspired by the fact that shower spatial development follows a tree topology, Arbor PFA organises calorimeter hits into trees where branches represent the trajectories of the charged shower particles, as illustrated in Fig. 3.2. In the ideal case, each incident particle is reconstructed as one tree. With the current configuration, Arbor PFA has slightly worse performance for jet energy resolution than PandoraPFA, see Fig. 3.3.

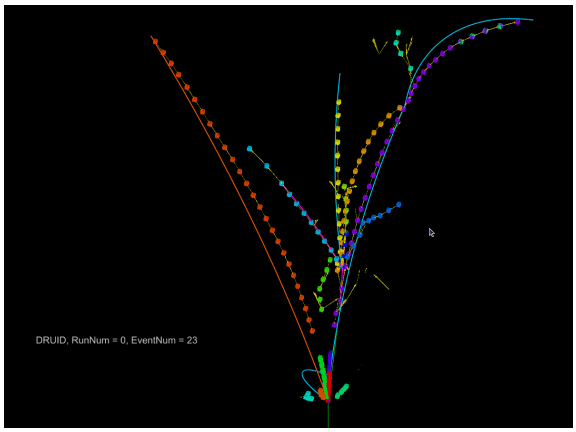

Figure 3.2 20 GeV K_L^0 shower simulated at ILD calorimeter and reconstructed with Arbor. The trajectories of charged shower particles are reconstructed as the tree branches, and the whole shower is represented by a tree.

Table 3.1 Expected performance of CEPC detector at object level (within geometry acceptance). For flavor tagging, the *b*/*c* tagging efficiency should preserve a purity of 80% in Z pole samples with hadronic final states

Charged particle reconstruction efficiency ($E > 10$ GeV)	99.5%
Muon identification efficiency ($E > 10$ GeV)	98.5%
Electron identification efficiency ($E > 10$ GeV)	99.5%
Photon tagging efficiency ($E > 1$ GeV)	98%
Neutral hadron tagging efficiency ($E > 5$ GeV)	90%
Jet energy resolution	3 - 4%
b-tagging efficiency	90%
c-tagging efficiency	60%

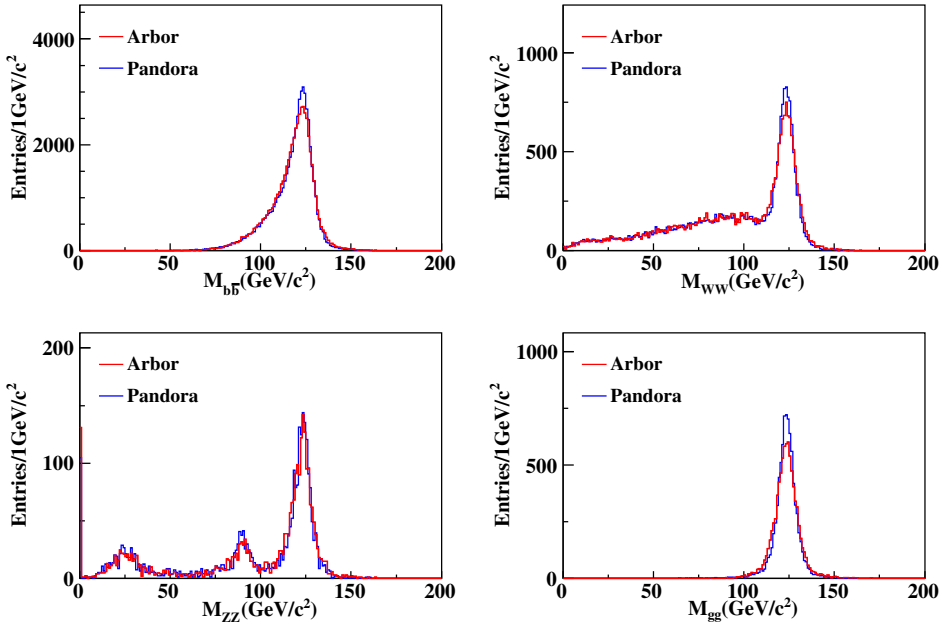

Figure 3.3 Invariant mass of all reconstructed particles of $\nu\bar{\nu}H$ events, with Higgs decay into different final states.

The expected performance of the CEPC detector is summarised in Table. 3.1. Using current reconstruction tools, the reconstruction of charged particles and identification of leptons already meets these goals. The plot shown in Fig 3.4 shows the identification efficiency of simultaneous identification of different charged particles.

Identification of b-quark and c-quark jets is crucial for the Higgs measurement and Z pole physics. The LCFIPlus algorithm has been applied directly to the final state particles reconstructed by Arbor PFA. The right-hand plot in Fig 3.5 shows the signal rates of b quark jets against the rejection power of the background contaminations of c quarks and

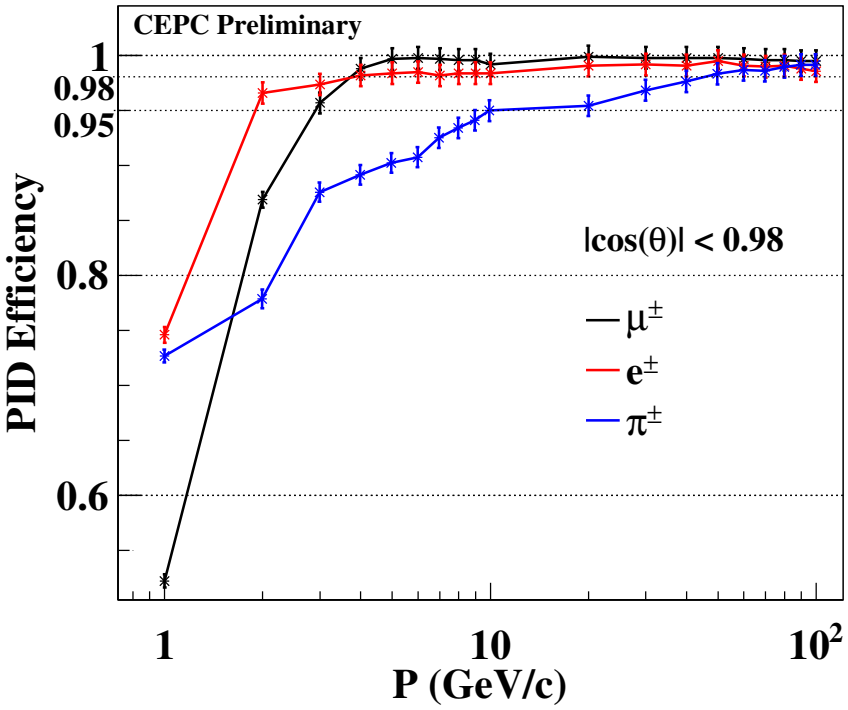

Figure 3.4 Lepton identification performance.

uds quarks. The b-tagging performance is close to that expected, while the c-tagging efficiency is worse by about 20%. Detailed adjustments and optimisation are needed.

3.3 Higgs Boson Measurements

The software tools introduced above have been applied to centrally produced CEPC samples and the subsequence physics analyses. A SM sample set at 250 GeV center-of-mass energy, including both Higgs signals and all 2-fermion and 4-fermion backgrounds, has been generated [27]. All the Higgs signal and part of the SM background have been processed to full simulation and reconstruction. Limited by the computing resources, the rest of the SM backgrounds are simulated with CEPCFS, which has been validated with full simulation at key physics distributions such as the Higgs recoil mass spectrum.

Samples simulated for the ILC studies [28] are used for cross-checks. It should be pointed out that the beam spot size at CEPC is much larger than that at ILC or CLIC, resulting in a much weaker beamstrahlung effect at single collision. Therefore, the beamstrahlung effect is ignored in the current set of CEPC samples.

3.3.1 Production Cross Sections of Signal and Background Processes

The leading production processes for the SM Higgs boson (mass = 125 GeV) at CEPC operating at $\sqrt{s} \sim 240 - 250$ GeV are: $e^+e^- \to ZH$ (Higgsstralung or ZH), $e^+e^- \to \nu\bar{\nu}H$ (WW fusion) and $e^+e^- \to e^+e^-H$ (ZZ fusion), as illustrated in Fig. 3.6. WW and ZZ fusion are collectively referred to below as vector boson fusion (VBF) production.

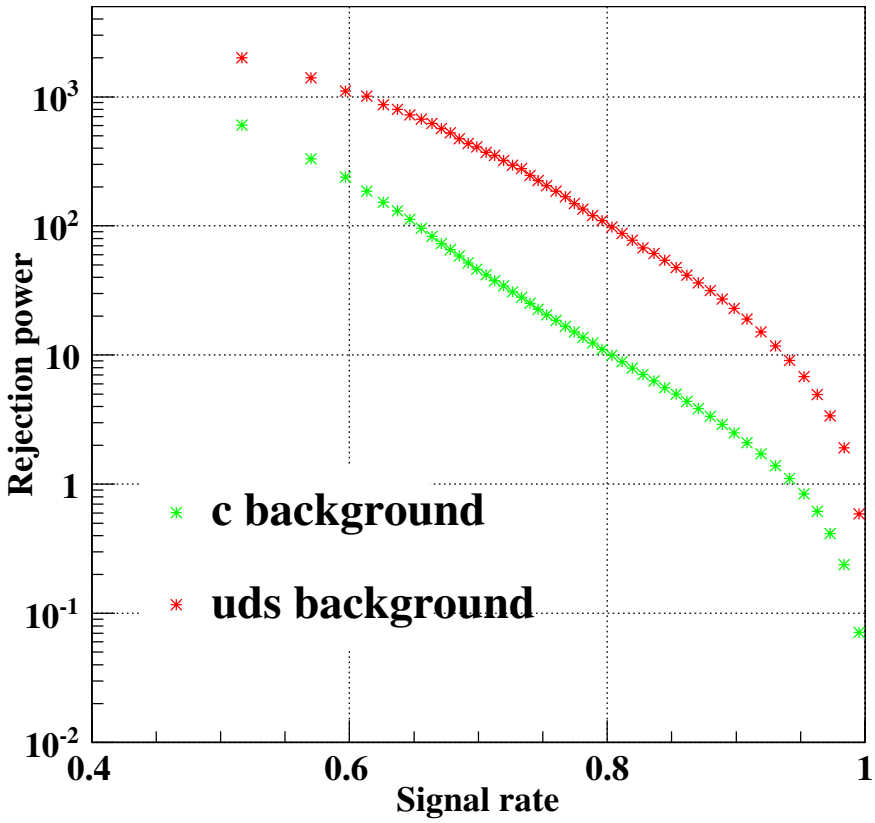

Figure 3.5 Signal rate of b jets vs. rejection power of c and light jets backgrounds with $Z \to q\bar{q}$ sample at 91 GeV. The rejection power is defined as $(1/\epsilon - 1)$.

The total and individual production cross sections for the SM Higgs boson with mass of 125 GeV, as functions of center-of-mass energy, are plotted in Fig. 3.7 (a); its decay branching ratios are shown in Fig. 3.7 (b). As an s-channel process, the cross section of the Higgsstrahlung process reaches its maximum at $\sqrt{s} \sim 250$ GeV, and then decreases with increasing $\sqrt{s}$. The VBF cross sections increase logarithmically with $\sqrt{s}$, with a dominant contribution from the WW fusion process.

CEPC is designed to deliver a total of 5 ab^{-1} integrated luminosity to two detectors over 10 years. Over 10^6 clean Higgs events will be produced during this period. The large statistics of this Higgs sample will enable CEPC to measure the Higgs boson production cross sections and most of its properties with precisions far beyond achievable at the LHC. Compared with hadron collisions, e^+e^- collisions are not affected by underlying events and pile-up effects. The tagging of $e^+e^- \to ZH$ events through the recoil mass method is independent of the Higgs boson decay. It is unique to lepton colliders and provides a powerful tool for model-independent measurements of Higgs boson production cross sections and decay branching ratios. Combinations of these measurements will determine the total Higgs boson decay width and the Higgs boson couplings to fermions and vector bosons, providing sensitive probes to potential new physics beyond the SM.

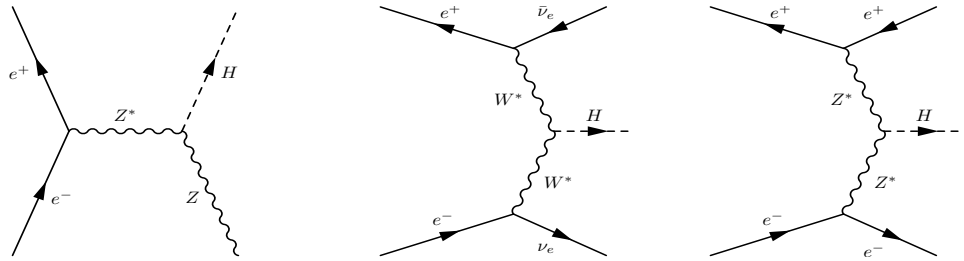

Figure 3.6 Feynman diagrams of the $e^+e^- \to ZH$, $e^+e^- \to \nu\bar{\nu}H$ and $e^+e^- \to e^+e^-H$ processes.

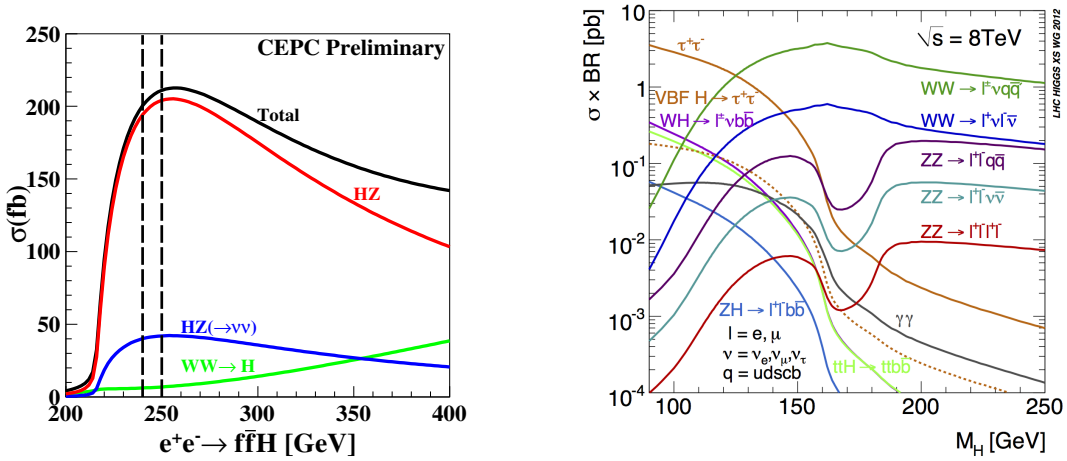

(a) (b)

Figure 3.7 (a) Production cross sections of $e^+e^- \to ZH$ and $e^+e^- \to \nu\bar{\nu}H$, e^+e^-H as functions of $\sqrt{s}$ for a 125 GeV Higgs boson. (b) Higgs boson decay branching ratios as functions of m_H, taken from [29].

Table 3.2 summarise the cross sections for the signal and background processes at $\sqrt{s} = 250$ GeV and the corresponding numbers of events expected for an integrated luminosity of 5 ab^{-1}. Along with the 10^6 Higgs events, 5×10^6 ZZ, 8×10^7 WW and 2.5×10^8 $q\bar{q}(\gamma)$ events will be produced. These events are the main backgrounds for Higgs analyses. On the other hand, they are important for SM measurements and studies of systematic uncertainty of the Higgs measurements.

3.3.2 $\sigma(ZH)$ and m_H Measurements

Unlike hadron colliders, the center-of-mass energy at an e^+e^- collider is precisely measurable and adjustable. In a ZH event, where the Z boson decays to a pair of visible fermions ($Z \to f\bar{f}$), the Higgs boson mass can be reconstructed with the recoil mass method:

$$m^2_{\text{recoil}} = (\sqrt{s} - E_{f\bar{f}})^2 - p^2_{f\bar{f}} = s - 2E_{f\bar{f}}\sqrt{s} + m^2_{f\bar{f}} \tag{3.2}$$

where $E_{f\bar{f}}$, $p_{f\bar{f}}$ and $m_{f\bar{f}}$ are, respectively, the total energy, momentum and invariant mass of the fermion pair. The m_{recoil} distribution should exhibit a peak at m_H for the signal process of $e^+e^- \to ZH$ (with a small contribution from ZZ fusion), and is expected to be smooth for background processes. The reconstructed width of the peak will be dominated by the detector resolution and the beam energy spread, while the effect of the

Table 3.2 Production cross sections of signal and background processes at $\sqrt{s} = 250$ GeV, and numbers of events expected in 5 ab^{-1}. The cross sections are calculated using the WHIZARD program [13]. Note that cross sections do not include potential interference effects between the same final states from different processes after W and Z bosons decay.

Process	Cross section	Events in 5 ab^{-1}
Higgs boson production, cross section in fb		
$e^+e^- \to ZH$	212	1.06×10^6
$e^+e^- \to \nu\bar{\nu}H$	6.72	3.36×10^4
$e^+e^- \to e^+e^-H$	0.63	3.15×10^3
Total	219	1.10×10^6
Background processes, cross section in pb		
$e^+e^- \to e^+e^-$ (Bhabha)	25.1	1.3×10^8
$e^+e^- \to q\bar{q}$	50.2	2.5×10^8
$e^+e^- \to \mu\mu$ (or $\tau\tau$)	4.40	2.2×10^7
$e^+e^- \to WW$	15.4	7.7×10^7
$e^+e^- \to ZZ$	1.03	5.2×10^6
$e^+e^- \to eeZ$	4.73	2.4×10^7
$e^+e^- \to e\nu W$	5.14	2.6×10^7

Higgs physical width (about 4 MeV) can be ignored. The best mass precision can be achieved with the $Z \to \ell\ell$ ($\ell = e, \mu$) decays.

With the m_{recoil} spectrum, the $e^+e^- \to ZH$ event yield can be extracted independently of the Higgs decays. The $e^+e^- \to ZH$ production cross section, σ_{ZH}, or equivalently the Higgs-Z boson coupling $g(HZZ)$, can be derived in a totally model-independent way. Higgs boson decay branching ratios can then be measured by identifying the Higgs decay final states in the selected $e^+e^- \to ZH$ candidate events. $g(HZZ)$ and Higgs decay branching ratios can be used to derive the total Higgs boson decay width. The recoil mass spectra have been investigated for both leptonic and hadronic Z boson decays as presented below.

3.3.2.1 Recoil Mass with Leptonic Z Decays

Events with leptonic Z decays are ideal to reconstruct the $e^+e^- \to ZH$ recoil mass spectrum, since $Z \to \ell^+\ell^-$ decays can be easily identified and the lepton momenta can be precisely measured. Fig. 3.9 shows the reconstructed recoil mass spectrum in the $Z \to \mu^+\mu^-$ and $Z \to ee$ channels. These analyses are based on the full simulated ZH signal and fast simulated backgrounds. Strict model independent analyses have been performed for both channels with event selection entirely based on the information of the two leptons. The SM processes with at least 2 leptons in their final states are considered as backgrounds.

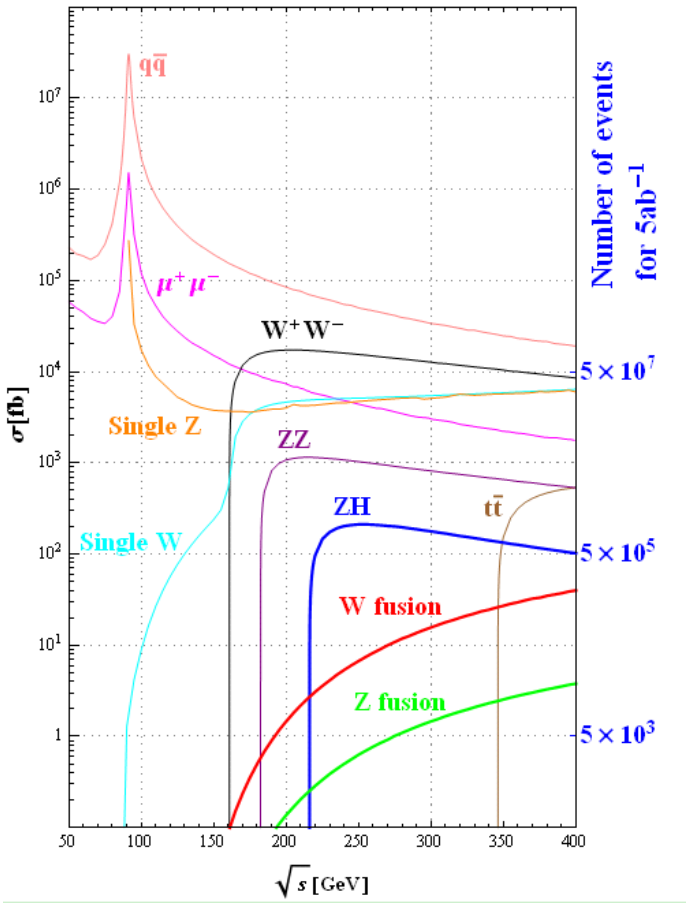

Figure 3.8 Cross sections of main standard model processes of e^+e^- collisions as functions of center-of-mass energy $\sqrt{s}$, where ISR effect is included. Calculated with WHIZARD.

The event selection in $Z \to \mu^+\mu^-$ starts with requiring a pair of identified muons. A multi-variate analysis (MVA) discriminant constructed with the invariant mass, transverse momentum, polar angle and acollinearity of the di-muon system is employed to enhance the separation between signal and background. About 22k signal events (selection efficiency of 62%) and 48k background events pass the event selection. The leading backgrounds after event selection are ZZ, WW and $Z\gamma$ (ISR return) events. The left-hand plot of Fig. 3.9 shows the fitted result; the signal is modelled by a Crystal Ball function and the background by a polynomial. A relative precision of 0.9% for the inclusive cross section has been achieved. The Higgs mass can be measured with a precision of 6.5 MeV. The precision is limited by the beam energy spread, radiation effect and detector resolution.

The $Z \to \mu^+\mu^-$ and $Z \to ee$ channels use different event selection methods. The resulting recoil mass spectra are shown in Fig. 3.9. Both channels have a significant high-mass tail resulting mainly from initial state radiation. In addition, the $Z \to ee$ channel has much stronger bremsstrahlung and FSR radiation, leading to a much wider recoil mass distribution.

In addition to the discriminating variables used in the $Z \to \mu^+\mu^-$ analysis, the polar angle and energy of the electron and positron are also used in the $Z \to e^+e^-$event selection. In the $Z \to e^+e^-$ channel, there are additional backgrounds from $e^+e^- \to$

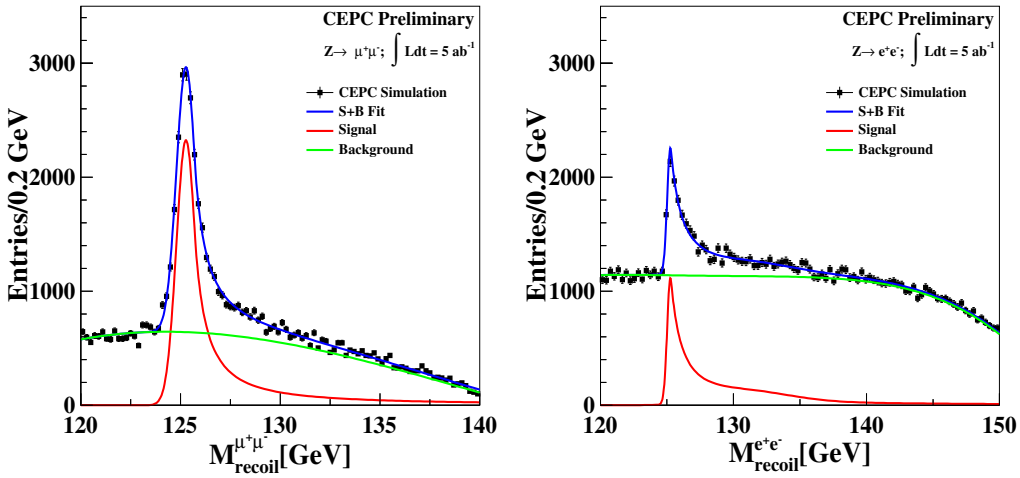

Figure 3.9 Recoil mass spectrum of $e^+e^- \to ZX$ candidates with the Z boson decaying to a pair of leptons, for an integrated luminosity of 5 ab^{-1}, for $Z \to \mu\mu$ (left) and $Z \to ee$ (right).

$e^+e^-(\gamma), e\nu W, eeZ$ production. These become the dominant backgrounds after event selection. This simple-cut based event selection results in 10k signal events (27% selection efficiency) and 147k background events.The right-hand plot of Fig. 3.9 shows the recoil mass spectrum. A relative precision of 2.4% for the inclusive cross section has been achieved, and an accuracy of 14 MeV is expected for the Higgs boson mass measurement. To take into account the energy loss due to bremsstrahlung and FSR, the momentum of the electron/positron track can be corrected by adding the energy carried by the photons located inside a small cone around the track. With this correction, the accuracy of the ZH cross section measurement can be improved to 2.1% in the $Z \to e^+e^-$ channel.

Model-independent event selection is necessary for the absolute cross section measurement. However, additional cuts which might break this requirement can be used to improve the Higgs mass measurement. For instance, in the $Z \to e^+e^-$ channel, the main backgrounds (Bhabha, single W and single Z events) can be suppressed more effectively.

3.3.2.2 Recoil Mass with Hadronic Z Decays

The recoil mass technique can also be applied to the hadronic decay channels ($Z \to q\bar{q}$). This analysis benefits from the larger $Z \to q\bar{q}$ decay branching ratio, but suffers from poorer jet energy resolution and random combinatorics of jet-pairing with additional jets. This measurement is highly dependent on the performance of the PFA, jet clustering and jet flavour tagging algorithms.

An analysis based on fast simulation has been performed. After event selection, the main backgrounds arise from WW and $Z\gamma$ production. Fig. 3.10 (left) shows the reconstructed recoil mass distribution. A relative precision of 0.65% for the inclusive cross section has been achieved [30]. Jets from Higgs decays can lead to mis-pairing in reconstructing the $Z \to q\bar{q}$ decay, which may further violate the model-independence of event selection. Thus it is crucial to understand and to control the event selection efficiency homogeneity of different Higgs decay modes. As shown in the right-hand plot of Fig. 3.10, average signal efficiency is 33.9%, with a relative variation of 6.5%.

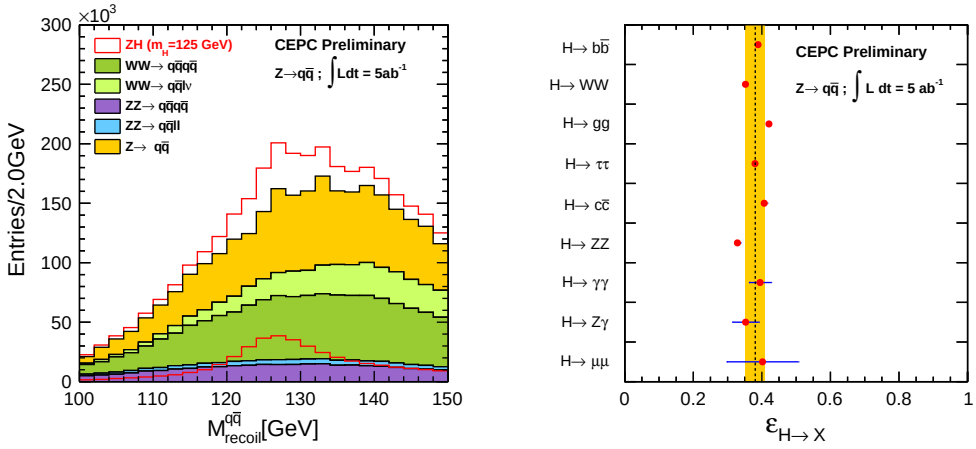

Figure 3.10 Left: recoil mass spectrum of $e^+e^- \to ZX$ candidates assuming $Z \to q\bar{q}$ decay, for 5 ab^{-1} of integrated luminosity. Right: selection efficiency for different Higgs boson decay modes.

3.3.2.3 Combined Results

Table 3.3 summarises the expected precisions on $\sigma(ZH)$ and m_H in different channels. For an integrated luminosity of 5 ab^{-1}, an uncertainty of 5.9 MeV on the Higgs boson mass can be achieved by combining $Z \to e^+e^-$ and $Z \to \mu^+\mu^-$ channels, and a relative precision of 0.51% on $\sigma(ZH)$ by combining all three channels. In the SM, $g(HZZ)$ can be extracted from $\sigma(ZH)$ with a relative precision of 0.25%, free of assumptions on Higgs boson width or its couplings to fermions and other vector bosons. This model-independent determination of $g(HZZ)$ allows for the measurement of the Higgs boson total width, which will be detailed in Sec. 3.3.5.

Table 3.3 Estimated precisions of the Higgs boson mass, $\sigma(ZH)$ and Higgs-Z boson coupling with 5 ab^{-1} integrated luminosity.

Z decay mode	ΔM_H (MeV)	$\Delta\sigma(ZH)/\sigma(ZH)$	$\Delta g(HZZ)/g(HZZ)$
ee	14	2.1%	
$\mu\mu$	6.5	0.9%	
$ee + \mu\mu$	5.9	0.8%	0.4%
$q\bar{q}$		0.65%	0.32%
$ee + \mu\mu + q\bar{q}$		0.51%	0.25%

3.3.3 Production Rates of Individual Higgs Boson Decay Modes

Different decay modes of the Higgs boson can be identified through their specific decay products. Some of these measurements are discussed below.

3.3.3.1 $H \to b\bar{b}, c\bar{c}, gg$

For a SM Higgs boson with a mass of 125 GeV, nearly 70% of Higgs bosons decay into a pair of jets: b-quarks (57.8%), c-quarks (2.7%) or gluons, gg (8.6%). Measurements of

these three branching ratios require efficient reconstruction of the hadronic decays of the Higgs boson. Flavor tagging is essential for the separation of $H \to b\bar{b}, c\bar{c}, gg$.

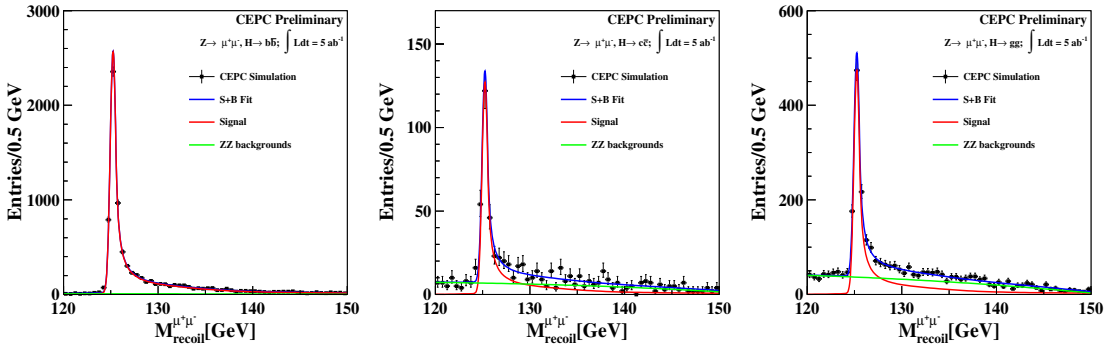

Figure 3.11 Recoil mass spectra for the bb, cc and gg categories of the $\mu^+\mu^-$ channel

Based on the decay final states of the Z boson in the ZH events, the signal events are classified into di-lepton channel, neutrino channel and di-jet channel. The W fusion events are counted in the neutrino channel and Z fusion events in the e^+e^- channel. Full simulation analysis of the di-lepton channel has been performed.

The di-lepton channel analyses (both the di-muon channel and di-electron channel) are based on fully simulated signal samples and fast simulated 4 fermion $llqq$ background. After selecting the two leading leptons with opposite charge, the rest of the reconstructed particles are clustered to two jets.

Event selection is based on the lepton and jet kinematics. Explicitly, the transverse momentum of the lepton pair is required to be within $10-90$ GeV. The di-lepton invariant mass is required to be within $70-110$ GeV in the e^+e^- channel and $81-101$ GeV in the $\mu^+\mu^-$ channel. The recoil mass must lie in the range $120-150$ GeV. In addition, a cut on the polar angle of the Higgs candidate, $|\cos\theta_H| < 0.8$, is applied.

The remaining events are classified by the flavour tagging algorithm. With the flavor tagging algorithm, the remaining events are classified into six categories: bb, cc, gg, bc, cg and gg. In each category, the signal and background yields are extracted from the recoil mass spectrum, from which the numbers of events of $H \to b\bar{b}, c\bar{c}, gg$ can be derived [31]. The recoil mass spectra for the bb, cc and gg categories of the $\mu^+\mu^-$ channel are shown in Fig. 3.11.

In the $\nu\bar{\nu}H$ and $q\bar{q}H$ channels, results are extrapolated from ILC studies [32]. Assuming the same signal and background selection efficiencies, the expected yields for signal events and different backgrounds are calculated according to the beam polarisation conditions and scaled to integrated luminosity. The individual and combined results are listed in Table 3.4 for an integrated luminosity of 5 ab^{-1}; the relative precisions of $\sigma(ZH)\times \mathrm{BR}$ are expected to be 0.28%, 2.2% and 1.6% for $H \to b\bar{b},\ c\bar{c}$ and gg respectively.

3.3.3.2 $H \to WW^*$

In the SM, the branching ratio of a Higgs boson with mass 125 GeV decaying to WW^* is about 21.5%. The measurement of $\sigma(ee \to ZH) \times \mathrm{BR}(H \to WW^*)$ determines one of the largest branching ratios of the Higgs boson decay and provides insight into the details of the electroweak symmetry breaking mechanism. In addition, this measurement provides necessary input for the Higgs width measurement.

Table 3.4 Expected precision of $\sigma(ZH) \times BR$ for $H \to b\bar{b}/c\bar{c}/gg$, normalised to 5 ab^{-1}.

	$\Delta(\sigma \times \mathrm{BR})/\sigma \times \mathrm{BR}$		
Channel	$H \to b\bar{b}$	$H \to c\bar{c}$	$H \to gg$
$\mu^+\mu^- H$	0.9%	12.6%	3.8%
eeH	1.1%	14.6%	5.6%
$\nu\bar{\nu}H$	0.45%	3.2%	2.8%
$q\bar{q}H$	0.4%	3.0%	2.6%
Combined	0.28%	2.2%	1.6%

The CEPC performance for this measurement is examined with a study based on fully simulated signal samples and fast simulated backgrounds. The final state under study contains a $Z \to \mu^+\mu^-$ decay and $WW^* \to \ell\nu\ell\nu$ (leptonic) or $\ell\nu qq$ (semi-leptonic), where $\ell = e,\ \mu$. The distributions of the mass of the system recoiling against the $\mu\mu$ pair for this analysis are shown in Fig. 3.12 for an integrated luminosity of 5 ab^{-1}. The event selection uses the number of isolated leptons, jets, kinematic variables of the lepton system, total energy, missing energy and the impact parameter of lepton tracks (introduced to remove tau-related background). In the semi-leptonic channel, a cut on Boost Decision Tree (BDT) output has been applied to suppress the ZZ background. More details can be found in Ref. [33]. Combining these two channels, the expected precision for the measurement of $\sigma(ZH) \times \mathrm{BR}(H \to WW^*)$ is 4.9%.

Following the same approach as described in Section 3.3.3.1, the expected precision in the $\nu\bar{\nu}H$ and $q\bar{q}H$ channels are extrapolated from ILC studies [34]. This extrapolation covers two channels: $Z \to \nu\bar{\nu}, H \to WW^* \to qqqq$ and $Z \to qq, H \to WW^* \to \ell\nu qq$. The individual and combined results for an integrated luminosity 5 ab^{-1} are summarised in Table 3.5.

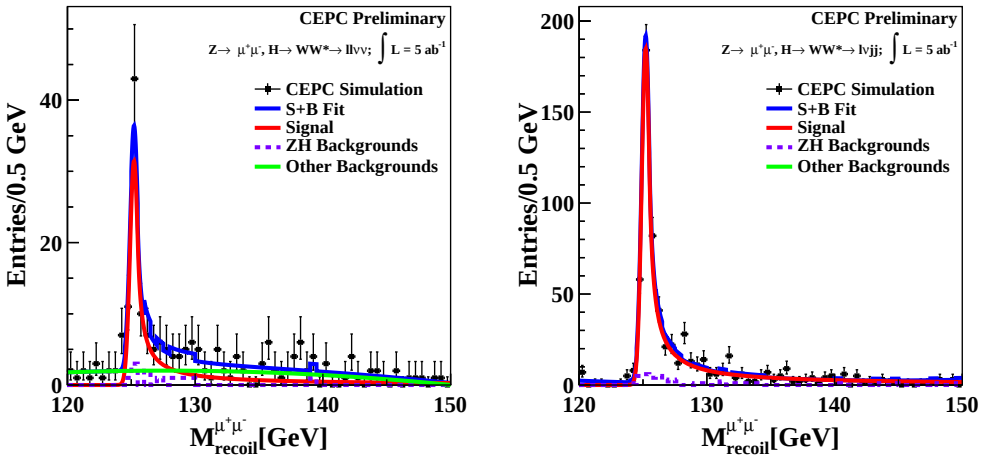

Figure 3.12 Distributions of recoil system mass against the $\mu^+\mu^-$ pair (a) for the $WW* \to \ell\ell\nu\nu$ ($\ell = e, \mu$) channel and (b) for the $WW* \to \ell\nu qq$ ($\ell = e, \mu$) channel.

Table 3.5 Expected precision of the $\sigma(ee \to ZH) \times \mathrm{BR}(H \to WW^*)$ measurement, assuming an integrated luminosity of 5 ab^{-1}.

Channel	Precision	Comment
$Z \to \mu\mu, H \to WW^* \to \ell\nu qq, \ell\ell\nu\nu$	4.9%	CEPC Full Simulation
$Z \to ee, H \to WW^* \to \ell\nu qq,\ \ell\ell\nu\nu$	7.0%	Scaled from $\mu^+\mu^-$ channel
$Z \to \nu\bar{\nu}, H \to WW^* \to qqqq$	2.3%	Extrapolated from ILC result
$Z \to qq, H \to WW^* \to \ell\nu qq$	2.2%	Extrapolated from ILC result
Combined	1.5%	

3.3.3.3 $H \to ZZ^*$

The branching ratio of a SM Higgs boson at 125 GeV decaying to ZZ^* is about 2.64%. Similar to $H \to WW^*$, the $H \to ZZ^*$ branching ratio provides insight into electroweak symmetry breaking and is crucial for the Higgs boson width measurement.

$e^+e^- \to ZH$ production with $H \to ZZ^*$ has 3 Z bosons in its final state, with one of them being off-shell. Consequently, this channel has a very rich variety of topologies that requires very different data analysis techniques. The final state under examination in this study assumes that the Z boson, which is produced in association with the Higgs boson, decays to neutrinos and the Higgs boson decays to $ZZ^* \to \ell^+\ell^- q\bar{q}$. The total branching ratio in the SM for this final state is $\mathrm{BR}(Z \to \nu\bar{\nu}) \times \mathrm{BR}(H \to ZZ^*) \times \mathrm{BR}(ZZ^* \to \ell\ell q\bar{q}) = 0.05\%$.

A fast simulation analysis has been performed in order to assess the expected performance of this measurement. The invariant mass distribution of the $\ell^+\ell^- q\bar{q}$ system, after event selection, is shown in Fig. 3.13. The events from processes other than Higgs boson production are negligible. However, there are backgrounds from ZH events where the Z boson decays into a pair of quarks, and the Higgs boson into WW^* which subsequently decay to $\ell\ell\nu\nu$. A relative precision of 6.9% can be achieved for the quantity $[\sigma(ZH) \times \mathrm{BR}(Z \to \nu\bar{\nu}) + \sigma(\nu\bar{\nu}H)] \times \mathrm{BR}(H \to ZZ)$. More information about this analysis can be found in Ref. [35]. This result is expected to be significantly improved when other $H \to ZZ^*$ final states are considered.

Since the current CEPC simulation study is not complete, an estimated precision of combined results from all channels has been obtained by extrapolating the FCC-ee full simulation study [36]. This yields a relative precision of 4.3% at 5 ab^{-1} integrated luminosity. This value is used as the expected precision for the Higgs boson coupling fit presented in Sec. 3.4.

Table 3.6 Expected relative precision for the $\mathrm{BR}(H \to ZZ^*)$ measurement, normalised to 5 ab^{-1}.

Channel	Precision	Comment
$\sigma(Z(\nu\bar{\nu})H + \nu\bar{\nu}H) \times \mathrm{BR}(H \to ZZ)$	6.9%	CEPC Fast Simulation
$\mathrm{BR}(H \to ZZ^*)$	4.3%	Extrapolation from FCC-ee [36]

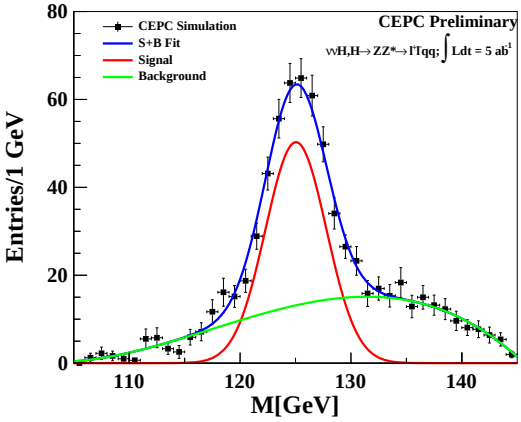

Figure 3.13 Invariant mass spectrum of the $\ell\ell q\bar{q}$ system for the $H \to ZZ^*$ performance study. It is assumed that the Higgs boson is produced in association with a Z boson, which decays to neutrinos. The Higgs boson is assumed to decay to $ZZ^* \to \ell\ell q\bar{q}$.

3.3.3.4 $H \to \gamma\gamma$

The Higgs boson decay to a photon pair proceeds through loops of massive charged particles, like the W boson and top quark. It can therefore be a sensitive probe of new particles that may come into the loop and interfere with the SM particles. The loop-induced nature of this process leads to a low branching fraction which is around 0.23% for a SM Higgs at 125 GeV. Hence, the performance required in photon reconstruction and energy resolution is a challenge for the electromagnetic calorimeter (ECAL) design.

Four sets of final states are considered in this measurement, based on the decay modes of the Z associated with the Higgs boson: $q\bar{q}\gamma\gamma$, $\nu\bar{\nu}\gamma\gamma$, $\mu\mu\gamma\gamma$ and $\tau\tau\gamma\gamma$. Suffering from the huge Bhabha background, the $ee\gamma\gamma$ channel does not have the sensitivity to access this measurement. After event selection, the main background is the $e^+e^- \to Z\gamma\gamma$ process where the photons arise from initial state radiation.

The events are mainly selected by requiring two energetic ECAL clusters. The mass of the system recoiling against the $\gamma\gamma$ pair is required to be close to the Z peak. A constraint on the smallest ℓ-γ angle is implemented in the $\ell\ell\gamma\gamma$ channel to suppress final state radiation. More details of the event selection are given in Ref. [37].

For the $\mu\mu H$ or $\tau\tau H$ channel, a kinematic fit has been used. With an integrated luminosity of 5 ab^{-1}, the expected numbers of signal events after selection are 62, 56, 339, and 582 for $\mu\mu H$, $\tau\tau H$, $\nu\bar{\nu}H$ and $q\bar{q}H$ final states respectively. The corresponding numbers of background events are 831, 757, 7053 and 12831.

Assuming an ECAL energy resolution of $16\%/\sqrt{E} \oplus 1\%$, a relative precision of 9.0% can be obtained for the $\sigma(ZH) \times \mathrm{BR}(H \to \gamma\gamma)$ measurement. By varying the stochastic term of the ECAL energy resolution, its impact on the expected precision has been evaluated. The results are summarized in Table 3.7.

3.3.3.5 $H \to \mu\mu$

The Higgs boson decay to $\mu^+\mu^-$ is a rare process with a branching ratio of 0.022% for a Higgs boson mass of 125 GeV. This measurement provides a performance benchmark for the tracking system design. A full simulation study has been performed to estimate the expected accuracy of the $Br(H \to \mu\mu)$ measurement. The event selection includes

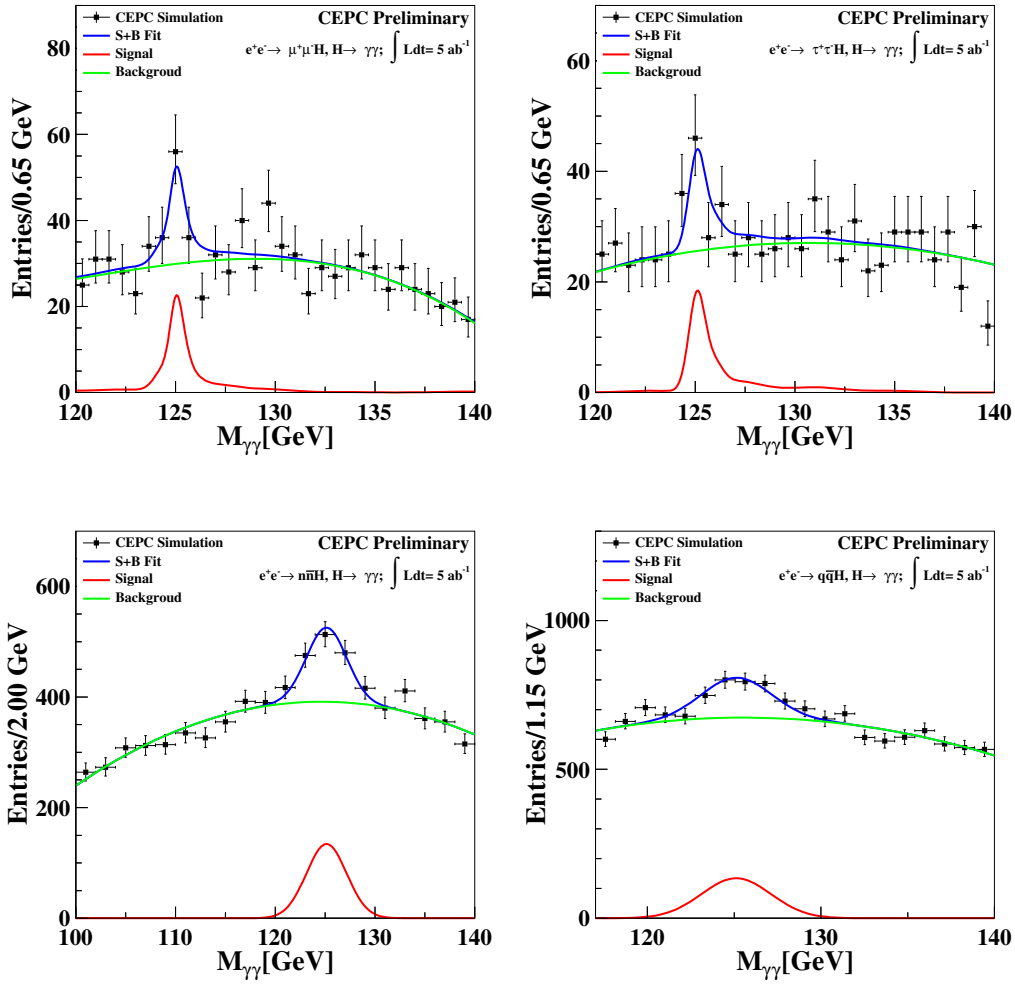

Figure 3.14 Invariant mass distributions of di-photons measured from $\mu\mu H$, $\tau\tau H$, $\nu\bar{\nu}H$ and qqH candidate events with the nominal ECAL energy resolution.

requirements on the number of muons and their kinematic properties. The reconstructed $\mu^+\mu^-$ invariant mass after event selection is shown in Fig. 3.15. The expected relative precision of $\sigma(f\bar{f}H) \times Br(H \to \mu\mu)$ is about 17% for 5 ab^{-1}. More information can be found in Ref. [38].

3.3.3.6 WW Fusion Process

The measurement of $\sigma(\nu\bar{\nu}H) \times \mathrm{BR}(H \to b\bar{b})$ is a crucial input for Higgs width measurement. The main background includes ZZ production and more importantly, ZH events with $Z \to \nu\bar{\nu}$ and $H \to b\bar{b}$. The latter is irreducible background and it interferes with the signal production. This interference effect is small and is ignored in this study.

The CEPC performance for this measurement is estimated with a fast simulation study. The ZH events can be distinguished from W fusion events by the recoil mass against the $b\bar{b}$ system. However, at a center-of-mass energy of 250 GeV, the discriminating power is limited. This recoil mass distribution is shown in Fig. 3.16. The analysis based on fast simulation leads to a relative accuracy of 2.8% for $\sigma(\nu\bar{\nu}H) \times \mathrm{BR}(H \to b\bar{b})$. Details can be found in Ref. [39].

Table 3.7 Expected yields for signal and backgrounds in the $H \to \gamma\gamma$ channel, normalised to 5 ab^{-1}.

		Resolution assumption: $\frac{\delta E}{E} = \frac{R}{\sqrt{E}} \oplus 1\%$		
Channel		$R = 10\%$	$R = 16\%$	$R = 20\%$
$Z \to \mu^+\mu^-$	Signal/efficiency	62 ± 18/42.2%	62 ± 19	59 ± 19
	Background	832 ± 33	831 ± 34	826 ± 33
	$\Delta(\sigma \times BR)/\sigma \times BR$	29.0%	30.6%	32.2%
$Z \to \tau^+\tau^-$	Signal/efficiency	58 ± 18/41.9%	56 ± 18	54 ± 19
	Background	760 ± 32	757 ± 32	762 ± 32
	$\Delta(\sigma \times BR)/\sigma \times BR$	31.0%	32.1%	35.2%
$Z \to \nu\bar{\nu}$	Signal	334 ± 40/57.5%	339 ± 46	342 ± 51
	Background	7059 ± 91	7053 ± 94	7047 ± 96
	$\Delta(\sigma \times BR)/\sigma \times BR$	12.0%	13.6%	14.9%
$Z \to qq$	Signal	594 ± 67/34.3%	582 ± 83	575 ± 94
	Background	13053 ± 130	12831 ± 138	12566 ± 144
	$\Delta(\sigma \times BR)/\sigma \times BR$	11.3%	14.3%	16.4%
Combined	$\Delta(\sigma \times BR)/\sigma \times BR$	7.7%	9.0%	10.0%

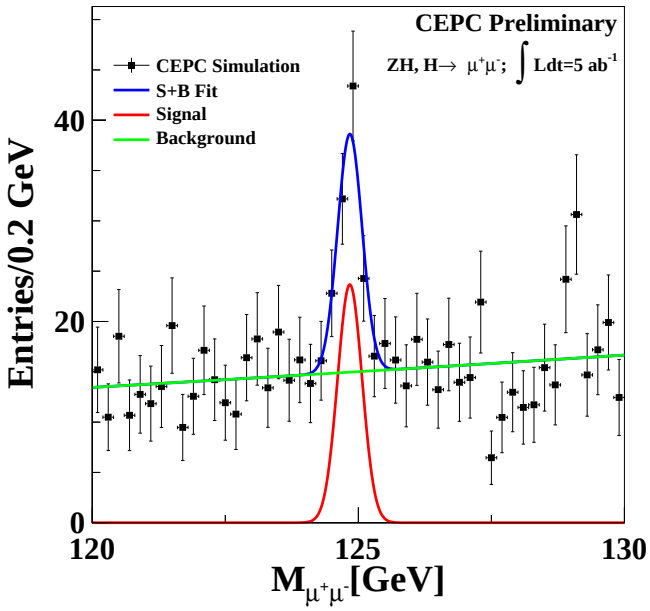

Figure 3.15 The $\mu\mu$ invariant mass after full selection criteria for the $H \to \mu\mu$ measurement with 5 ab^{-1} integrated luminosity at the CEPC.

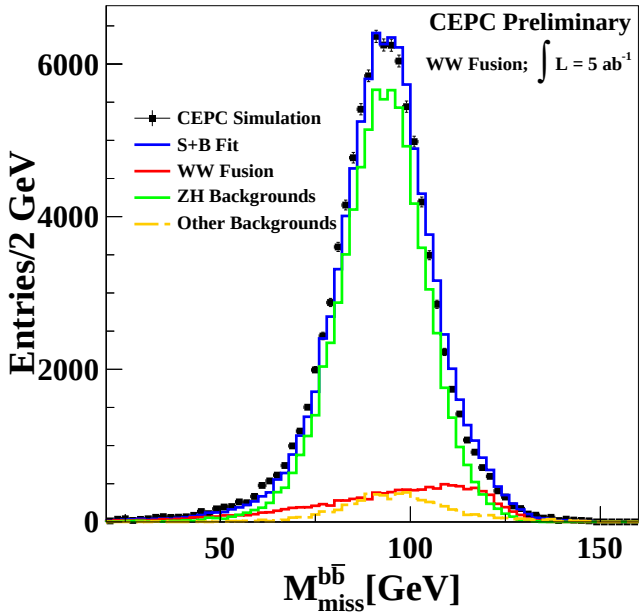

Figure 3.16 Missing mass spectrum for WW fusion process with ZH events and SM background.

3.3.3.7 Exotic Higgs Decays

The current precision with which the Higgs boson branching ratios and couplings have been measured at the LHC could still cover a significant fraction of invisible or exotic decays. At the CEPC, these measurements can fully benefit from the recoil mass method. The Higgs invisible decay is well motivated in many new physics models with dark matter candidates. The left-hand side of Fig. 3.17 shows an example Feynman diagram of a Higgs boson decaying to $\chi_1\chi_1$, the lightest SUSY particle that exists in many SUSY models.

A full simulation study in the leptonic channel has been made to investigate the achievable precision on $\mathrm{BR}(H \to \mathrm{inv})$ at the CEPC. $\sigma(ZH) * Br(H \to inv)$ is assumed to be 200 fb in this analysis. An event selection similar to that used in the $\sigma(ZH)$ measurement has been applied. After event selection, the dominant backgrounds are $ZZ \to \ell\ell\nu\nu$ and $WW \to \ell\ell\nu\nu$ events. The recoil mass spectrum is shown in the right-hand plot of Fig. 3.17. A precision of 0.65% can be achieved using the Z to e^+e^- $\mu^+\mu^-$ channel.

The sensitivity of searching for $(H \to \mathrm{inv})$ decays can be greatly improved by including the $Z \to q\bar{q}$ decay mode. The precision, extrapolated from ILC studies, is 0.14%, see Ref. [40]. The individual and combined result is presented in Table. 3.8. The 95% CL upper limit of $\sigma(ZH) * Br(H \to inv)$ is 0.56 fb (0.28% of the $\sigma(ZH)$).

The recoil mass method on di-lepton channels can also be used for the measurement of the exotic Higgs boson decay branching ratios. Two exotic decay modes have been considered: a semi-invisible decay and a fully visible decay [41].

In the semi-invisible decay, the final decay state of the Higgs boson is a pair of b quarks, and missing energy/momentum is carried by the dark matter candidate. Such decay modes can be realized in the context of the NMSSM and currently there are no constraints from LHC searches. The dominant background processes for this channel are $ZZ \to \ell\ell\tau\tau$, $ZH \to \ell\ell\tau\tau$, $ZH \to \ell\ell ZZ \to \ell\ell\nu\nu b\bar{b}$ and $ZH \to \ell\ell b\bar{b}$. The probability of misidentifying a τ jet as a b jet is assumed to be 1% in this analysis, which is why processes

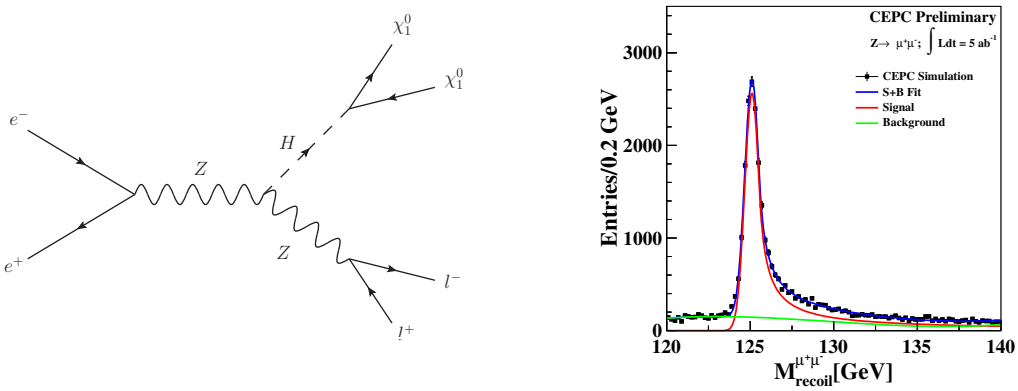

Figure 3.17 Left: Feynman diagram of Higgs invisible decay. Right: Higgs recoil mass spectrum for $Br(H \to inv)$ measurement, assuming $\sigma(ZH) * Br(H \to inv) = 200fb^{-1}$

.

Table 3.8 Expected accuracy for the $\mathrm{BR}(H \to \mathrm{inv})$ measurement, normalized to 5 ab^{-1}.

Channel	Accuracy	Methods
$Z \to \mu\mu, H \to \mathrm{inv}$	0.8%	CEPC Full Simulation
$Z \to ee, H \to \mathrm{inv}$	1.1%	Estimation
$Z \to q\bar{q}, H \to \mathrm{inv}$	0.14%	Extrapolated from ILC result
Combined	0.14%	

with τ in the final state are also regarded as background. The event selection is based on the invariant mass and recoil mass of the di-lepton system, b-tag flag, and total missing energy.

In the fully visible exotic decay, Higgs boson decays to lighter Higgs bosons are considered, and the lighter Higgs bosons subsequently decay to four b-quarks: $H \to h_1h_1, a_1a_1 \to b\bar{b}b\bar{b}$. The dominant background process is $ZH \to \ell\ell ZZ \to \ell\ell b\bar{b}b\bar{b}$. For both semi-invisible and fully visible exotic decays, a 5σ discovery is expected for $\mathrm{Br}(H \to \mathrm{exo})$ of 0.1% [42].

3.3.4 Measurements of Branching Ratios

With the measurements of inclusive cross section $\sigma(ZH)$ and the cross sections of individual Higgs boson decay mode $\sigma(ZH) \times \mathrm{BR}$, the Higgs boson branching ratio BR can be extracted. Most of the systematic uncertainties associated with the measurement of $\sigma(ZH)$ cancel out. A maximum likelihood fit is used to estimate the precisions of the BRs. For a given Higgs decay channel, the likelihood has the form:

$$L(\mathrm{BR}, \theta) = \mathrm{Poisson}\left[N^{\mathrm{obs}} \middle| N^{\mathrm{exp}}(\mathrm{BR}, \theta)\right] \cdot G(\theta), \tag{3.3}$$

where BR is the parameter of interest and θ represent nuisance parameters. N^{obs} is the number of observed events in the channel, $N^{\mathrm{exp}}(\mathrm{BR}, \theta)$ is the expected number of events,

and $G(\theta)$ is a set of Gaussian constraints on the nuisance parameters within their estimated uncertainties.

The number of expected events is the sum of signal and background events. The number of signal events is calculated from the integrated luminosity, the $e^+e^- \to ZH$ cross section $\sigma(ZH)$ measured from the recoil method, Higgs boson branching ratio BR and event selection efficiency ϵ. The number of expected background events, N^b, is estimated from Monte Carlo samples. Thus:

$$N^{\exp}(\mathrm{BR}, \theta) = \mathrm{Lumi}(\theta^{\mathrm{lumi}}) \times \sigma_{ZH}(\theta^{\sigma}) \times \mathrm{BR} \times \epsilon(\theta^{\epsilon}) + N^b(\theta^b) \tag{3.4}$$

where θ^X ($X = \mathrm{lumi}, \sigma$ and ϵ) are the nuisance parameters of their corresponding parameters or measurements. For the current study, θ^{lumi} and θ^{ϵ} are fixed to their nominal values, as the uncertainties in luminosity and selection efficiency are negligible.

The estimated precisions of BR for the different Higgs boson decay modes are shown in Table 3.9. The uncertainty used in inclusive ZH production cross section is 0.5%, from Table 3.3.

3.3.5 Measurement of Higgs Boson Width

The Higgs boson width (Γ_H) is of special interest, as it is sensitive to physics beyond SM. Because of the limited detector resolution, the 4 MeV width predicted by the SM is too small to be measured directly. However, the width can be indirectly derived from the measured Higgs boson production cross sections and its decay branching ratios at e^+e^- colliders:

$$\Gamma_H = \frac{\Gamma(H \to ZZ^*)}{\mathrm{BR}(H \to ZZ^*)} \propto \frac{\sigma(ZH)}{\mathrm{BR}(H \to ZZ^*)}. \tag{3.5}$$

Here $\Gamma(H \to ZZ^*)$ is the partial width of the $H \to ZZ^*$ decay. Because of the small $\mathrm{BR}(H \to ZZ^*)$ for a 125 GeV Higgs boson (2.3% in the SM), the precision of Γ_H is limited by the statistics of $H \to ZZ^*$ events.

Alternatively, the Higgs width can be also determined using four measured quantities: $\sigma(ZH)$, $\sigma(ZH) \times Br(H \to bb)$, $\sigma(ZH) \times Br(H \to WW^*)$ and $\sigma(vvH) \times Br(H \to bb)$.

$$\Gamma_H = \frac{\Gamma(H \to bb)}{BR(H \to bb)}, \tag{3.6}$$

where $\Gamma(H \to bb)$ can be extracted from the cross section of the WW fusion process $e^+e^- \to \nu\bar{\nu}H \to \nu\bar{\nu}bb$:

$$\sigma(\nu\bar{\nu}H \to \nu\bar{\nu}bb) \propto \Gamma(H \to WW^*) \cdot \mathrm{BR}(H \to bb) = \Gamma(H \to bb) \cdot \mathrm{BR}(H \to WW^*). \tag{3.7}$$

Thus, the Higgs boson total width can be determined with

$$\Gamma_H \propto \frac{\Gamma(H \to bb)}{\mathrm{BR}(H \to bb)} \propto \frac{\sigma(\nu\bar{\nu}H \to \nu\bar{\nu}bb)}{\mathrm{BR}(H \to bb) \cdot \mathrm{BR}(H \to WW^*)}. \tag{3.8}$$

Here $\mathrm{BR}(H \to bb)$ and $\mathrm{BR}(H \to WW^*)$ are measured from the $e^+e^- \to ZH$ process. At the CEPC, the precision that can be achieved with this method is limited by the small

$e^+e^- \to \nu\bar{\nu}H \to \nu\bar{\nu}bb$ cross section. The precisions obtained with Eq. 3.5 and Eq. 3.8 are 4.4% and 3.3% respectively.

A combined result, after taking the correlations into account, yields a precision of 2.7% with 5 ab^{-1} integrated luminosity. Precise knowledge of the Higgs boson total width will lead to much better understandings of Higgs boson properties in a model-independent way, as discussed in Sec. 3.4.

3.3.6 Summary of the Higgs Measurements

Table 3.9 summarises the estimated precisions of Higgs measurements presented above. Percentage level precisions can be achieved for the branching ratio measurements of $H \to b\bar{b}, c\bar{c}, gg, WW^*, ZZ^*$.

Table 3.9 Estimated precisions of Higgs boson measurements at the CEPC. All numbers refer to relative precisions except for m_H and $\mathrm{BR}(H \to \mathrm{inv})$, for which Δm_H and 95% CL upper limit are quoted respectively.

ΔM_H	Γ_H	$\sigma(ZH)$	$\sigma(\nu\bar{\nu}H) \times \mathrm{BR}(H \to b\bar{b})$
5.9 MeV	2.8%	0.51%	2.8%

Decay mode	$\sigma(ZH) \times \mathrm{BR}$	BR
$H \to b\bar{b}$	0.28%	0.57%
$H \to c\bar{c}$	2.2%	2.3%
$H \to gg$	1.6%	1.7%
$H \to \tau\tau$	1.2%	1.3%
$H \to WW$	1.5%	1.6%
$H \to ZZ$	4.3%	4.3%
$H \to \gamma\gamma$	9.0%	9.0%
$H \to \mu\mu$	17%	17%
$H \to \mathrm{inv}$	–	0.28%

All the $\sigma \times BR$ measurements are based on a simple counting method. The best achievable precision at the CEPC is 0.28% for $\sigma(e^+e^- \to ZH) \times \mathrm{BR}(H \to b\bar{b})$. In this measurement, the precision is limited by the statistical uncertainties. Systematic uncertainties from the efficiency/acceptance of the detector, the luminosity and the beam energy determination are expected to be small. The integrated luminosity can be measured with a precision of 0.1% level, as achieved at LEP [43]. The center-of-mass energy will be known to better than 1 MeV, resulting in negligible uncertainties on the recoil mass measurements.

The CEPC results are statistically consistent with the ILC and the FCC-ee studies [28, 36]. Limited by computing resources, manpower and time, the Higgs measurements are not completely based on full simulation, but will be pursued in future studies. Emphasis shall be given to $\sigma(ZH) \times Br(H \to b\bar{b}, c\bar{c}, gg)$ measurements, as they give critical requirements for the flavour tagging algorithms and vertex/inner tracking system design,

Table 3.10 Status of Higgs measurements at the CEPC

Observable	Sub-channel	Status
m_H	$Z \to ee, \mu\mu$	Full Simulation
$\sigma(ZH)$	$Z \to ee, \mu\mu$	Full Simulation
	$Z \to q\bar{q}$	Fast Simulation [30]
$\sigma(ZH) \times Br(H \to b\bar{b}, c\bar{c}, gg)$	$Z \to ee, \mu\mu$	Full Simulation
	$Z \to \nu\bar{\nu}, q\bar{q}$	Extrapolated from ILC study [32]
$\sigma(ZH) \times Br(H \to WW^*)$	$Z \to \mu\mu$	Full Simulation of $H \to WW^* \to lvqq, llvv$
	$Z \to ee$	Scaled from $Z \to \mu\mu$ result
	$Z \to \nu\bar{\nu}$	Extrapolated from ILC study of $H \to WW^* \to qqqq$ [34]
	$Z \to q\bar{q}$	Extrapolated from ILC study of $H \to WW^* \to lvqq$ [34]
$\sigma(ZH) \times Br(H \to ZZ^*)$	inclusive	Extrapolated from FCC-ee study [36]
	$Z \to \nu\bar{\nu}$	Fast Simulation of $H \to ZZ^* \to llqq$
$\sigma(ZH) \times Br(H \to \tau\tau)$	$Z \to ee, \mu\mu, q\bar{q}$	Extrapolated from ILC study [44]
$\sigma(ZH) \times Br(H \to \gamma\gamma)$	$Z \to ee, \mu\mu$	Fast Simulation and Full Simulation with Kinematic fit
	$Z \to \nu\bar{\nu}, q\bar{q}$	Fast Simulation and Full Simulation
$\sigma(ZH) \times Br(H \to \mu\mu)$	inclusive	Full Simulation
$\sigma(\nu\bar{\nu}H) \times Br(H \to b\bar{b})$		Fast Simulation
$\sigma(ZH) \times Br(H \to invisible)$	$Z \to \mu\mu$	Full Simulation
	$Z \to ee$	Scaled from $Z \to \mu\mu$ result
	$Z \to q\bar{q}$	Extrapolated from ILC study [40]
$\sigma(ZH) \times Br(H \to exotic)$	$Z \to ll$	Fast Simulation on several target case

and the latter may be significantly different from ILD geometry. It is important to explore further the inclusive Higgs generation cross section measurement via the $Z \to q\bar{q}$ channel, which requires a carefully designed jet clustering algorithm and accurate jet energy resolution. $\sigma(ZH) \times Br(H \to ZZ^*, WW^*)$ measurements will be carefully studied, not only because they provides essential input for the Higgs width measurement, but also because their various final states pose critical requirements for the detector performance. Special attention will be paid to searches for exotic Higgs decay modes. A brief summary of the status of these analyses is presented in Table. 3.10.

Simulation studies are indispensable for the demonstration of CEPC physics potential, the optimisation of detector geometry design and the effective planning of the operational program. Simulation is composed of three pillars: the detector geometry design and full simulation, the reconstruction algorithm development/optimisation and the physics analysis. In the coming CDR phase, more detector models will be implemented in simulation, which will include a realistic design for the MDI. Dedicated reconstruction software will be developed and optimised. With the new detector models, all the measurements will be revisited and the precision will be re-evaluated. These studies will be iterated until they converge to an optimized detector design and eventually an effective planning of the operational program.

3.4 Coupling Extractions and Combinations

3.4.1 Coupling Fits

In order to understand the implications of the predicted measurement precision shown in Table 3.9 on possible new physics models, constraints on additional contributions to Higgs couplings are derived. The Standard Model makes specific predictions for the Higgs couplings to the SM fermions, $g(hff;\mathrm{SM})$, and to the SM gauge bosons $g(hVV;\mathrm{SM})$ [1]. The deviation from the Standard Model couplings will be parameterised using:

$$\kappa_f = \frac{g(hff)}{g(hff;\mathrm{SM})},\ \kappa_V = \frac{g(hVV)}{g(hVV;\mathrm{SM})} \tag{3.9}$$

In addition to couplings which are present at tree level, the Standard Model also predicts effective couplings $h\gamma\gamma$ and hgg in terms of other SM parameters. Change can be induced by the possible shifts in the Higgs couplings described above. In addition, they can also be altered by loop contributions from new physics states. Hence, they will be introduced as two independent couplings, with their ratios to the SM predictions denoted as κ_γ and κ_g.

Furthermore, it is possible that the Higgs can decay directly into new physics particles. In this case, two type of new decay channels will be distinguished:

1. Invisible decay. This is a specific channel in which the Higgs decays into invisible particles. This can be searched for and, if detected, measured.

2. Exotic decay. This includes all the other new physics channels. Whether they can be observed, and, if so, to what precision, depends strongly on the particular final states. At one extreme, they could be very distinct and could then be measured very well. At the other extreme, they could be in a form which is completely swamped by the background. Whether postulating a precision for the measurement of the exotic decay or treating it as an independent parameter (essentially assuming it cannot be measured directly) is an assumption one has to make. Results in both cases will be presented. In the latter case, it is common to use the total width Γ_h as an equivalent free parameter.

In general, possible deviations of all Standard Model Higgs couplings should be considered. However, in the absence of obvious light new physics states with large couplings to the Higgs boson and other SM particles, a very large deviation ($> \mathcal{O}(1)$) is unlikely. In the case of smaller deviations, the Higgs boson phenomenology will not be sensitive to the deviations κ_e, κ_u, κ_d and κ_s. Therefore, they will not be considered here.

CEPC will not be able to directly measure the Higgs coupling to top quarks. A deviation of this coupling from its SM value does affect $h\gamma\gamma$ and hgg amplitudes. However, this can be viewed as already parameterised by κ_γ and κ_g. Therefore, there will be no attempt to include κ_t as an independent parameter. In summary of the previous discussions, the following set of 10 independent parameters is considered:

$$\kappa_b,\ \kappa_c,\ \kappa_\tau,\ \kappa_\mu,\ \kappa_Z,\ \kappa_W,\ \kappa_\gamma,\ \kappa_g,\ \mathrm{BR}_{\mathrm{inv}},\ \Gamma_h. \tag{3.10}$$

In this 10-parameter list, the relation $\Sigma_i\Gamma_i = \Gamma_h$ is used to replace the exotic decay branching ratio with the total width. Several assumptions can be made that can lead to a

[1] For the discussion of coupling fits and their implications, h is used to denoted the 125 GeV Higgs boson.

reduced number of parameters (see also [29, 45]). For instance, a 9-parameter fit can be defined assuming lepton universality:

$$\kappa_b,\ \kappa_c,\ \kappa_\tau = \kappa_\mu,\ \kappa_Z,\ \kappa_W,\ \kappa_\gamma,\ \kappa_g,\ \mathrm{BR}_{\mathrm{inv}},\ \Gamma_h. \tag{3.11}$$

This can be further reduced to 7 parameters, by assuming the absence of exotic and invisible decays (excluding $h \to ZZ \to \nu\bar{\nu}\nu\bar{\nu}$) [5, 45]:

$$\kappa_b,\ \kappa_c,\ \kappa_\tau = \kappa_\mu,\ \kappa_Z,\ \kappa_W,\ \kappa_\gamma,\ \kappa_g. \tag{3.12}$$

In addition to the previously mentioned assumptions, which reduce the number of parameters, there are also several classes of parameter-space constraining assumptions, which can be combined in various ways with the former. These assumptions could also lead to possible extraction of coupling strengths from the LHC and enhancement of coupling precision projections for lepton colliders in a more model-dependent manner. One such example is to assume $\kappa_W,\ \kappa_Z \leq 1$ [46, 47]. This assumption on the κ_V ratios is valid for a large class of Higgs sector extensions, including MSSM, 2HDM, NMSSM, etc. [48].

A remark should be made here on the rationale for considering a variety of fits with different assumptions. Different fits achieve different goals. In practice, their relative usefulness depends on the scenario and the goal. For example, in a specific and complete model, the Higgs couplings can be determined by a smaller number of more fundamental parameters. This leads to relations among the Higgs couplings. One can set the strongest limit by taking full advantage of these relations. Deviations produced by such an underlying model can be detected most sensitively in such a constrained fit.

At the other extreme, a model-independent fit gives a model-independent limit on the broadest possible model space. It helps to capture deviations that could be missed by a constrained fit. At the same time, it produces the weakest limits. In practice, it is likely that something in between these two extremes will be the most useful. As was previously mentioned, there are many ways of imposing constraints, and even stronger ones than those discussed above can be considered. However, the purpose of this note is not to assess the reach in all possible models, which is an impossible task. It aims to give an overall picture of the capability of CEPC. Similar problems have been encountered in all previous studies of Higgs factories. A relatively common set of assumptions have been used as benchmarks, such as the ones discussed above. Therefore, for comparison purposes, this note focuses on a 10-parameter model-independent fit and a 7-parameter constrained fit recommended by the LHC Higgs cross section group [45].

The LHC and especially the HL-LHC will provide valuable and complementary information about the Higgs boson properties. For example, the LHC is capable of directly measuring the top Yukawa coupling through the tth process [49, 50]. In addition, the LHC could use differential cross sections to differentiate top-loop contributions and other heavy particle-loop contributions to the Higgs to gluon coupling [51–54], and similarly to separate the dimension-four and dimension-six (with higher momentum dependence) operator contributions to the Higgs to vector boson couplings [55]. For the purpose of the coupling fit in our framework, the LHC, with its large statistics, helps to improve precision in rare processes such as Higgs to di-photon couplings. Note that a large portion of the systematics intrinsic to a hadron collider would be cancelled by taking ratios of measured cross sections. For example, combining the ratio of the rates of $pp \to h \to \gamma\gamma$ and $pp \to h \to ZZ^*$ and the measurement of hZZ coupling at the CEPC can signifi-

cantly improve the measurement of κ_γ. These are the most useful inputs from the LHC to combine with CEPC. Similar studies with the ILC can be found in Refs. [40, 56, 57].

The 10-parameter fit and the 7-parameter fit for several integrated luminosities are shown in Tables 3.12 and 3.11, respectively. In addition, the combinations with expectations (with theoretical uncertainties included) from HL-LHC from Ref. [58] are shown in the same tables.[2] It is assumed that the HL-LHC will operate at 14 TeV center-of-mass energy and accumulate an integrated luminosity of 3000 fb^{-1}.

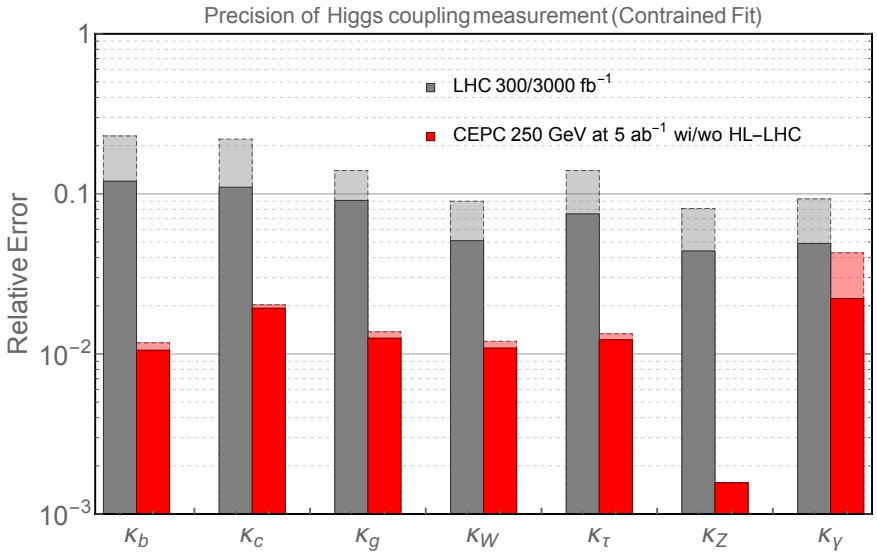

Figure 3.18 The 7 parameter fit result, and comparison with the HL-LHC. The projections for CEPC at 250 GeV with 5 ab^{-1} integrated luminosity are shown. The CEPC results without combination with HL-LHC input are shown with dashed edges. The LHC projections for an integrated luminosity of 300 fb^{-1} are shown with dashed edges.

The CEPC Higgs properties measurements mark a giant step beyond the HL-LHC. First of all, in contrast to the LHC, a lepton collider Higgs factory is capable of measuring the absolute width and coupling strengths of the Higgs boson. A comparison with the HL-LHC is only possible with model-dependent assumptions. One such comparison is within the framework of a 7-parameter fit, as shown in Fig. 3.18. The details of combination with HL-LHC with several benchmark CEPC luminosities is shown in Table 3.11. Even with this set of restrictive assumptions, the advantage of the CEPC is still significant. The measurement of κ_Z is more than a factor 10 better. The CEPC can also significantly improve a set of channels which suffer from large background at the LHC, such as κ_b, κ_c, and κ_g. It should be emphasised that this is comparing with the HL-LHC projection, with aggressive assumptions about systematics. Such uncertainties are typically under much better control at lepton colliders. Within this 7 parameter set, the only coupling for which HL-LHC can give a competitive measurement is κ_γ, for which the CEPC's accuracy is limited by statistics. This is also the most valuable input that the HL-LHC can give to the Higgs coupling measurement at the CEPC, which underlines the importance of combining the results of these two facilities.

[2]It noted that LHC and CEPC have different sources of theoretical uncertainties; for detailed discussion, see Refs. [5, 29, 59–61].

Table 3.11 Coupling measurement precision in percent from the 7 parameter fit described in the text for several benchmark integrated luminosities of CEPC, and corresponding results after combination with the HL-LHC.

	CEPC				CEPC+HL-LHC			
Luminosity (ab^{-1})	0.5	2	5	10	0.5	2	5	10
κ_b	3.7	1.9	1.2	0.83	2.3	1.5	1.1	0.78
κ_c	5.1	3.2	1.6	1.2	4.0	2.3	1.5	1.1
κ_g	4.7	2.3	1.5	1.0	2.9	1.9	1.3	0.99
κ_W	3.8	1.9	1.2	0.84	2.3	1.6	1.1	0.80
κ_τ	4.2	2.1	1.3	0.94	2.9	1.8	1.2	0.90
κ_Z	0.51	0.25	0.16	0.11	0.49	0.25	0.16	0.11
κ_γ	15	7.4	4.7	3.3	2.6	2.5	2.3	2.0

A remark should be made on the couplings which are left out in this fit. The most obvious omission is BR_{inv}. The CEPC with 5 ab^{-1} can measure this to a high accuracy of 0.25%, as shown in Table 3.12. The HL-LHC can only manage a much lower accuracy of $6-17\%$ [5].

As discussed above, one of the greatest advantages of a lepton collider Higgs factory is the capability of determining the Higgs coupling model-independently. The projection of such a determination at the CEPC is shown in Fig. 3.19. The details of combination with HL-LHC for several benchmark luminosities of CEPC are shown in Table 3.12. In the top panel of Fig. 3.19, a comparison with the LHC (7 parameter fit) is shown. For comparison, it also includes the projection from the combination ILC 250 GeV and 500 GeV runs in the bottom panel of Fig. 3.19, based on the baseline designed luminosities. The advantage of the higher integrated luminosity at a circular lepton collider is apparent. The CEPC has a clear advantage in the measure of κ_Z. It is also much stronger in κ_μ and BR_{inv} measurements. A more complete comparison, including several ILC upgrade options, is shown in Table 3.13.

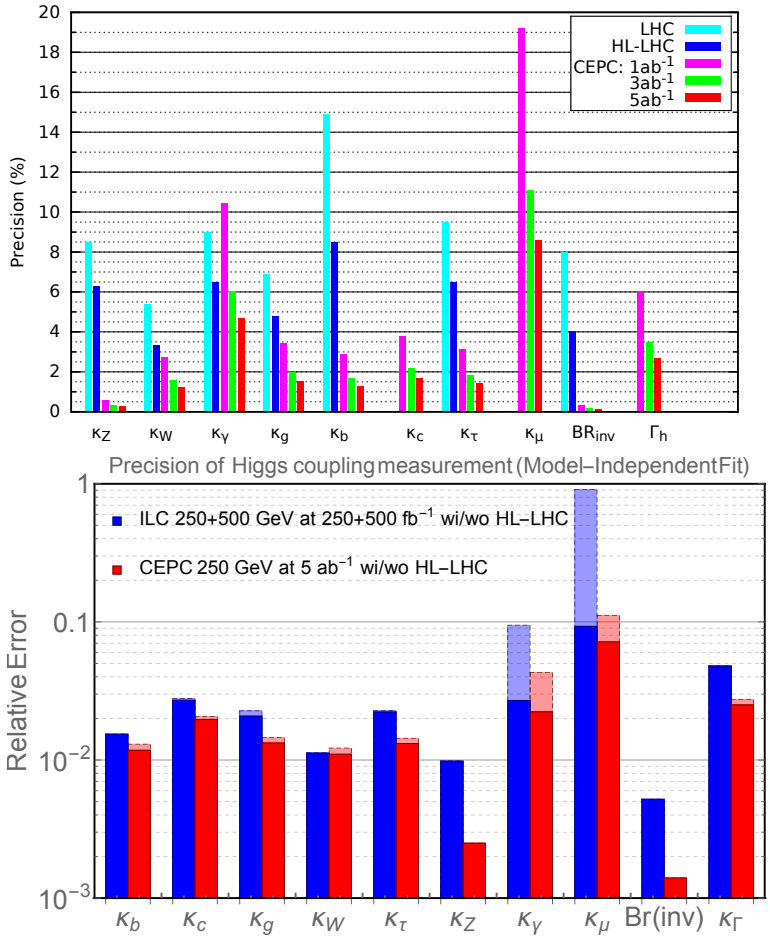

Figure 3.19 Top: Comparison between LHC, HL-LHC and several benchmark luminosities of the CEPC. Bottom: The 10 parameter fit result and comparison with the ILC. The CEPC at 250 GeV with 5 ab^{-1} integrated luminosity and the ILC 250+500 GeV at 250+500 fb^{-1} are shown. The CEPC and ILC results without combination with HL-LHC input are shown with dashed edges.

3.4.2 Higgs Self-coupling

The Higgs self-coupling, $\lambda(hhh)$, is a critical parameter governing the dynamics of electroweak symmetry breaking. It does not enter the CEPC phenomenology directly, but it affects the hZZ coupling at 1-loop level. Therefore, a limit on κ_Z can be interpreted as a limit on $\kappa_{\lambda(hhh)}$ with some model assumptions [62]. Of course, other new physics can also alter κ_Z. Unless in the case of a cancellation, the limit on $\kappa_{\lambda(hhh)}$ should be regarded as a reasonable estimate.

The correction to the SM hZ production cross section induced by a shift in λ_{hhh} is given by [62]

$$\Delta\sigma_{Zh} = \frac{\sigma_{Zh}}{\sigma_{Zh}^{\mathrm{SM}}} - 1 = 2\Delta_{\kappa_Z} + 0.014\Delta_{\lambda_{hhh}}. \tag{3.13}$$

The sensitivities of measuring σ_{Zh} and κ_Z at CEPC have been analysed in the previous section. The result from such a constraint on the SM λ_{hhh} is summarised in Fig. 3.20.

Table 3.12 Coupling measurement precision in percent from the 10 parameter fit described in the text for several benchmark integrated luminosities of CEPC, and corresponding results after combination with the HL-LHC. All the numbers given are relative precision, except for $\mathrm{BR}_{\mathrm{inv}}$ for which 95% CL upper limit is quoted.

	CEPC				CEPC+HL-LHC			
Luminosity (ab^{-1})	0.5	2	5	10	0.5	2	5	10
Γ_h	8.7	4.4	2.8	1.9	6.2	3.7	2.5	1.8
κ_b	4.1	2.1	1.3	0.92	2.8	1.7	1.2	0.87
κ_c	5.4	2.7	1.7	1.2	4.2	2.4	1.6	1.2
κ_g	4.8	2.4	1.5	1.1	3.2	2.0	1.4	1.0
κ_W	3.9	1.9	1.2	0.87	2.4	1.6	1.1	0.82
κ_τ	4.5	2.3	1.4	1.0	3.2	1.9	1.3	0.97
κ_Z	0.81	0.40	0.26	0.18	0.81	0.40	0.26	0.18
κ_γ	15	7.4	4.7	3.3	2.7	2.5	2.3	2.0
κ_μ	28	14	8.6	6.1	8.9	7.7	6.3	5.1
$\mathrm{BR}_{\mathrm{inv}}$	0.88	0.44	0.28	0.20	0.88	0.44	0.28	0.20

Table 3.13 Comparison of the projections between CEPC and various luminosity upgrades of the ILC. The ILC luminosity upgrade assumes an extended running period on top of the low luminosity program and cannot be directly compared to CEPC numbers without accounting for the additional running period. ILC numbers include a 0.5% theory uncertainty. For invisible decays of the Higgs, the number quoted is the 95% confidence upper limit on the branching ratio.

Facility		ILC		ILC(LumiUp)	CEPC (2 IP)	
$\sqrt{s}$ (GeV)	250	500	1000	250/500/1000	240–250	
$\int \mathcal{L}dt$ (ab^{-1})	0.25	+0.5	+1	+1.15+1.6+2.5	0.5	5
$P(e^-, e^+)$	$(-.8, +.3)$	$(-.8, +.3)$	$(-.8, +.2)$	(same)	$(0, 0)$	$(0, 0)$
Γ_H	12%	5.0%	4.6%	2.5%	8.7%	2.8%
κ_γ	18%	8.4%	4.0%	2.4%	15%	4.7%
κ_g	6.4%	2.3%	1.6%	0.9%	4.8%	1.5%
κ_W	4.9%	1.2%	1.2%	0.6%	3.9%	1.2%
κ_Z	1.3%	1.0%	1.0%	0.5%	0.80%	0.25%
κ_μ	91%	91%	16%	10%	28%	8.6%
κ_τ	5.8%	2.4%	1.8%	1.0%	4.5%	1.4%
κ_c	6.8%	2.8%	1.8%	1.1%	5.4%	1.7%
κ_b	5.3%	1.7%	1.3%	0.8%	4.1%	1.3%
κ_t	–	14%	3.2%	2.0%	–	–
BR_{inv}	0.9%	$< 0.9\%$	$< 0.9\%$	0.28%	0.89%	0.28%

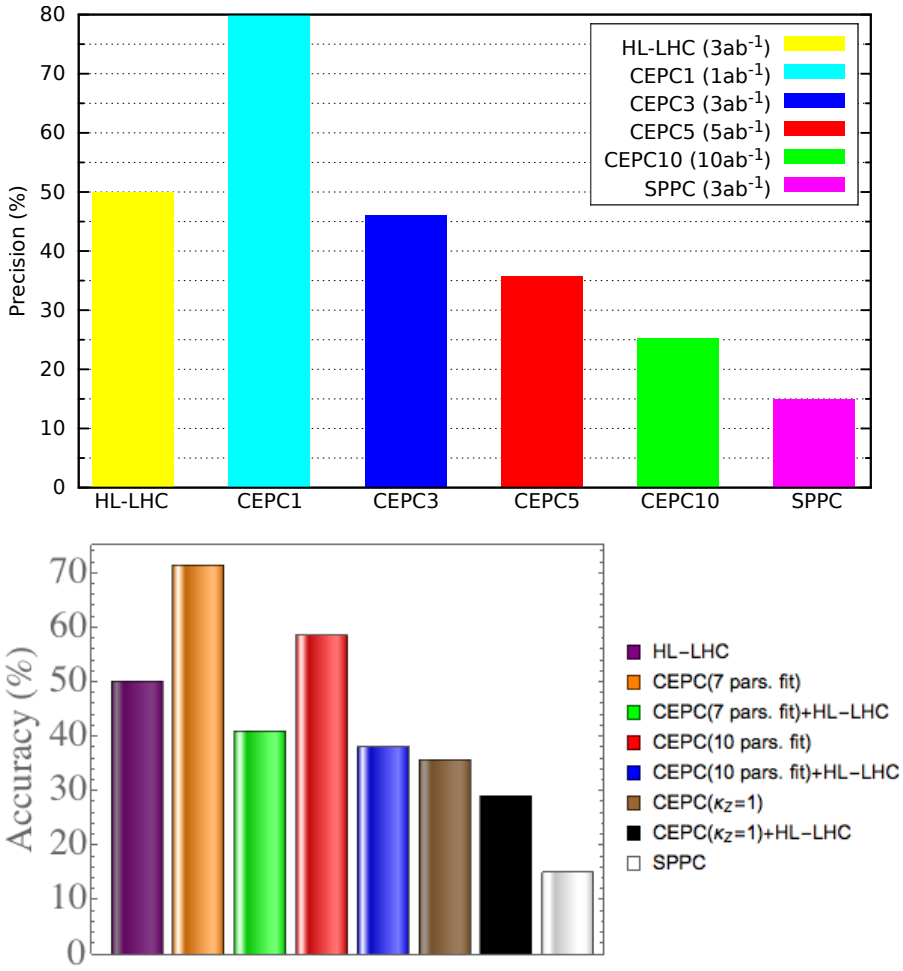

Figure 3.20 Higgs self-coupling constraint inferred from the shift in hZZ coupling. Top: Higgs self-coupling measurement at HL-LHC, several luminosity options at the CEPC, and the SPPC. Bottom: 7 and 10 parameter fits are considered. The combinations of HL-LHC and CECP are also shown. The CEPC results refer to a luminosity of 5 ab^{-1}. The HL-LHC and SPPC results are taken from Ref. [63], with an integrated luminosity of 3 ab^{-1} assumed. In the latter case, the impact of the uncertainties in measuring the Higgs top Yukawa coupling is not incorporated.

3.5 Implications

In this section, the most important physics implications of the Higgs property measurements at the CEPC will be briefly discussed. These topics have already been mentioned in the overview section and are recapitulated here briefly so that readers only reading this section may have a self-contained account of the important theoretical implications of Higgs couplings measurements at the CEPC.

Many theories for physics beyond the Standard Model (BSM) have been proposed over the past four decades. A central theme motivating the construction of these models has been to address the question of electroweak symmetry breaking. In most of these models, the Higgs couplings to the SM particles are typically modified, either by new particles propagating in loops, or by mixtures of the SM-like Higgs boson with other states. With its significant improvement on the sensitivities to the deviations in the Higgs couplings

from their SM predictions, the CEPC will offer an excellent opportunity to probe a wide variety of BSM scenarios. A number of important cases are mentioned, guided by the crucial questions about EWSB to be addressed.

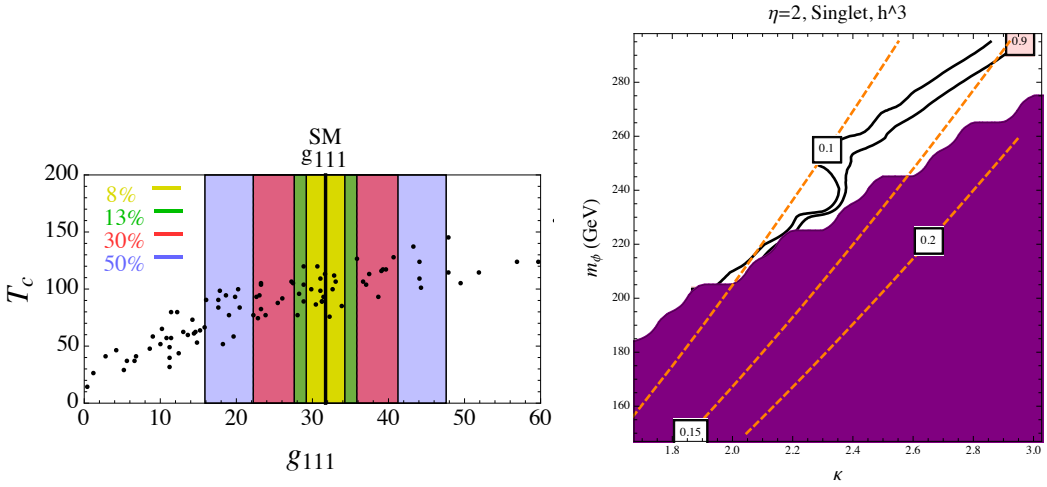

Figure 3.21 Higgs self-coupling deviation and first order electroweak phase transition. Left panel: A generic singlet model. Black dots are points where the phase transition is of first order. g_{111} is the triple Higgs coupling [64]. Right panel: A singlet model with a Z_2 symmetry [65]. Orange dashed lines are contours of fractional deviation. The region within the thick black curves has first order electroweak phase transition. In the shaded region, there is phase transition into a wrong vacuum.

Since its discovery, the image of a SM-like Higgs boson has gradually emerged from the suite of LHC measurements. At the same time, the nature of the electroweak phase transition remains a mystery. With the assumption of a minimal Higgs potential and the Higgs sector of the SM, it is well known that the phase transition is not of first order. However, this conclusion can be easily modified by new physics with sizeable couplings to the Higgs boson. Many such examples have been proposed. All of them predict deviations in the Higgs couplings from the Standard Model prediction. CEPC has the capability to robustly probe these models.

The minimal model that has been well studied in this class is to introduce an additional singlet which couples to the Higgs [64–69]. Generically, if the electroweak phase transition is of first order, a significant deviation in the triple Higgs coupling is expected. This is shown in the left-hand panel of Fig. 3.21, where the deviation can vary as much as $\sim 100\%$. A more restricted scenario, in which a discrete Z_2 symmetry is imposed on the singlet, has also been considered [65, 69]. A first order electroweak phase transition is significantly harder in this scenario. It requires stronger couplings between the Higgs boson and the singlet, which is limited at least by perturbativity. In this case, the expected loop induced deviation in the triple Higgs coupling is generically smaller, about $10 - 15\%$, as shown in the right-hand panel of Fig. 3.21. From the projections of the accuracy of Higgs self-coupling measurement shown in Fig. 3.20, CEPC has excellent reach in the more general case. For the case with Z_2 symmetry, SPPC will be needed to make a more decisive determination based on the self-coupling measurement and direct production of the additional singlet.

New physics affecting the nature of the electroweak phase transition will also modify the coupling between the SM-like Higgs and other SM states. It is here where the CEPC has the greatest strength. For example, in the general singlet model, the correction to

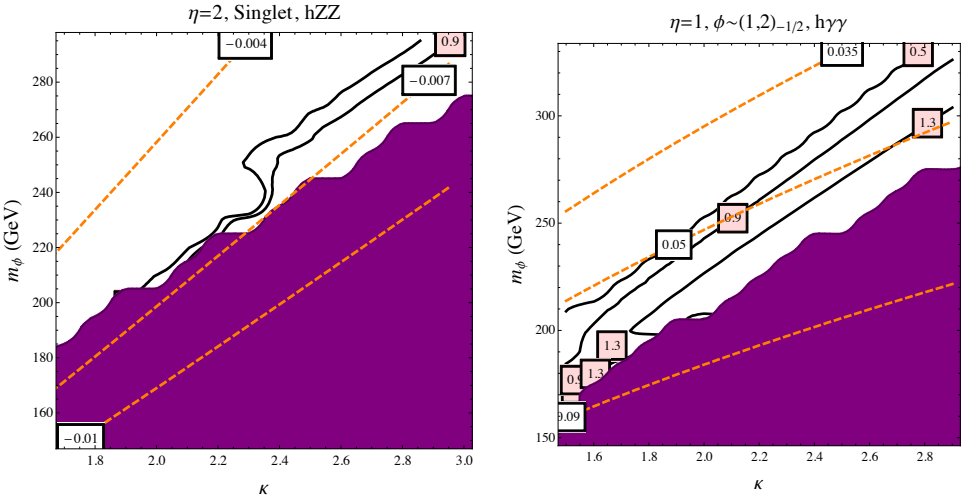

Figure 3.22 Left: The fractional deviation of σ_{Zh} at the Higgs factory, in singlet model with Z_2 symmetry [65]. Right: Fractional deviation of the hgg coupling in singlet model with Z_2 symmetry [65]. The new physics particle is a colour triplet with electric charge $-1/2$. In both figures, η is the coupling constant of interaction $H^\dagger H \phi^\dagger \phi$.

the Higgs-Z coupling, parameterised by κ_Z, is of the order of v^2/M_S^2, for M_S being the typical new physics scale. The projection on the accuracy of measuring this coupling at the CEPC is about 0.25%. Therefore, generically, κ_Z measurement at CEPC will allow us to probe a singlet as heavy as 5 TeV. At the same time, for first order phase transitions, the singlet mass is typically hundreds of GeV. Therefore, CEPC can completely cover the possible parameter space just by measuring κ_Z in this case.

Even in the difficult case of the singlet model with a Z_2 symmetry, the expected deviation of the cross section σ_{Zh} (κ_Z) is about 0.6% (0.5%), as shown in the left-hand panel of Fig. 3.22. Therefore, CEPC will see the first evidence of new physics even in this very difficult case. In more general classes of models, the new physics which modifies the Higgs coupling can carry other SM gauge quantum numbers, such as electric charge and/or colour. In such cases, there will be significant change in the $h \to gg$ and $h \to \gamma\gamma$ couplings. One such example is shown in the right-hand panel of Fig. 3.22, with 6% deviation in $h\gamma\gamma$ coupling expected. From the projection shown in Fig. 3.19, it is demonstrated that the CEPC can have sensitivity to such new physics.

Another important question associated with the electroweak symmetry breaking is naturalness. The discovery of a spin-0 Higgs boson only deepens this mystery. Naturalness arguments lead to the expectation that new physics should be around the TeV scale, and the level of fine-tuning grows $\propto m_{\rm NP}^2$. It has been a main motivation for postulating the existence of TeV-scale new physics. Such new physics has been a main part of the ongoing LHC physics program. By definition, any new physics which helps address the naturalness problem must have sizeable couplings to the Higgs boson. For example, if the Higgs boson is composite, it is typically implemented as a pseudo-Nambu-Goldstone boson with new dynamics at scale f. In this case, it is expected that Higgs boson would not unitarize the WW scattering amplitude completely, and its coupling to W and Z will

be shifted by

$$\kappa_W,\ \kappa_Z \simeq \sqrt{1 - \frac{v^2}{f^2}}. \tag{3.14}$$

Therefore, the measurement of κ_Z at the CEPC can push f to about 4-5 TeV and gives an interesting test of the idea of naturalness in the composite Higgs models.

Due to the large Higgs coupling to the top quark, arguably the most important particle in addressing the naturalness problem is the top partner. For example, in SUSY, the most important new physics particle responsible for the naturalness of the electroweak scale is the scalar top or stop, $\tilde{t}$. The presence of a stop will shift both hgg and $h\gamma\gamma$ couplings. The dominant effect is

$$\kappa_g - 1 \simeq \frac{m_t^2}{4m_{\tilde{t}}^2}. \tag{3.15}$$

The measurement of κ_g at the CEPC, up to 1% accuracy, will allow us to probe stop mass up to 900 GeV [70]. This gives another interesting test of the idea of naturalness. It should be noted that, in favourable cases, searches for stops at LHC run 2 can set a stronger limit on the stop mass. However, this limit depends on the assumption of the mass spectrum of the other superpartners, and the relevant decay modes of the stop. As a result, similar to the result of the stop search at LHC run 1, there will be significant gaps remaining after the upcoming runs of the LHC, even for light stops. On the other hand, the search for the stop by measuring the hgg coupling is complementary, and completely independent of the decay modes of the stop.

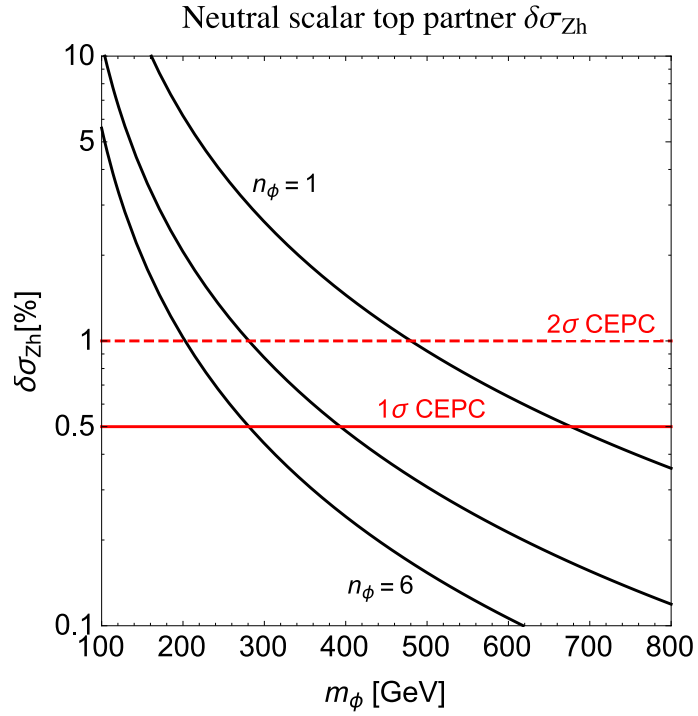

Figure 3.23 Fractional deviation of σ_{Zh} at the Higgs factory, in the model with scalar singlet top partner, coupling through $H^\dagger H \phi_t^\dagger \phi_t$ [71].

It is also possible that the top partner does not have the same SM gauge quantum numbers as the top quark - it could conceivably be a SM singlet! Such models are quite special.

Nevertheless, they represent perhaps the most difficult case in the search of top partners. For example, the only coupling the top partner has with the SM fields could be of the form $H^\dagger H \phi_t^\dagger \phi_t$, where ϕ_t is the scalar top partner [71, 72]. This coupling will induce a shift in the Higgs coupling to Z at one-loop level, which in turn can be probed by the precision measurement of κ_Z at the CEPC. As shown in Fig. 3.23, the CEPC will be able to probe the top partner mass up to 1 TeV, giving an non-trivial test of naturalness even in this very difficult scenario.

In general, the newly discovered Higgs particle can also be a new gateway to new physics. One generic form of the Higgs coupling to new physics is the so called Higgs portal, $H^\dagger H \mathcal{O}_{\rm NP}$, where $\mathcal{O}_{\rm NP}$ is an operator composed out of new physics fields. Since $H^\dagger H$ is the lowest dimensional operator that is consistent with all the symmetries in the Standard Model, it is easy to imagine scenarios in which such Higgs portal couplings are the most relevant ones for the low energy phenomenology of new physics. The singlet extended Higgs sector and the scalar top partner, discussed earlier, are special examples of this coupling. In general, such couplings will shift the Higgs couplings, which can be tested at the CEPC. Moreover, if the new physics is lighter than $m_H/2$, the Higgs portal coupling will lead to new Higgs decay channels. The CEPC has excellent capability for probing such decays. For example, it can detect invisible decays to the level of BR$\sim 0.2\%$. For comparison, HL-LHC can only measure the invisible decay branching ratio down to about 6%.

The Higgs boson plays a unique role in Electroweak Symmetry Breaking and is the only scalar particle in the Standard Model. The discovery of such a particle at the LHC is a major triumph on both the theoretical and experimental sides. However, the Standard Model is likely only an effective theory at the electroweak scale. To explore potential new physics at the electroweak scale and beyond, the complementary approaches of direct searches at the energy frontier as well as precision measurements will be needed. The current LHC and the planned HL-LHC have the potential to significantly extend its new physics reach and to measure many of the Higgs couplings with precisions of a few percent.

However, many new physics models predict Higgs coupling deviations at a sub-percent level, beyond those achievable at LHC. CEPC complements LHC and will be able to study the properties of the Higgs boson in great detail and with unprecedented precision. It is therefore capable of unveiling the true nature of this particle. At CEPC, most Higgs couplings can be measured with precisions at a sub-percent level. More importantly, CEPC will able to measure many of the key Higgs properties such as the total width and decay branching ratios model-independently, greatly enhancing the coverage of its search for potential new physics. Furthermore, the clean event environment of CEPC will allow the detailed study of known decay modes and the identification of potential unknown decay modes that are impossible at LHC.

A snapshot has been provided of the current studies. Many of these are ongoing and more analyses are needed to fully understand the physics potential of CEPC. Nevertheless, the results presented here have already built a strong case for CEPC as a Higgs factory. CEPC has the potential to "undress" the Higgs boson as LEP has already done for the Z boson, and possibly shed light on the direction of new physics.

References

[1] The ATLAS Collaboration, G. Aad et al., *Observation of a new particle in the search for the Standard Model Higgs boson with the ATLAS detector at the LHC*, Phys. Lett. B **716** (2012) 1–29, arXiv:1207.7214 [hep-ex].

[2] The CMS Collaboration, S. Chatrchyan et al., *Observation of a new boson at a mass of 125 GeV with the CMS experiment at the LHC*, Phys. Lett. B **716** (2012) 30–61, arXiv:1207.7235 [hep-ex].

[3] The ATLAS and CMS Collaboration, G. Aad et al., *Combined Measurement of the Higgs Boson Mass in pp Collisions at $\sqrt{s} = 7$ and 8 TeV with the ATLAS and CMS Experiments*, arXiv:1503.07589 [hep-ex].

[4] N. Chen et al., *Higgs Physics at the CEPC-SPPC*, (Paper in preparation).

[5] S. Dawson et al., *Working Group Report: Higgs Boson*, arXiv:1310.8361 [hep-ex].

[6] The ILD Concept Group, T. Abe, et al., *The International Large Detector: Letter of Intent*, arXiv:1006.3396 [hep-ex].

[7] T. Behnke et al., *The International Linear Collider Technical Design Report - Volume 4: Detectors*, arXiv:1306.6329 [physics.ins-det].

[8] T. Behnke et al., *The International Linear Collider Technical Design Report - Volume 1: Executive Summary*, arXiv:1306.6327 [physics.acc-ph].

[9] *ilcsoft home page*, http://ilcsoft.desy.de/portal.

[10] *LCIO home page*, http://lcio.desy.de/.

[11] Z. Chen, *CEPCFS, A Fast Simulation Tool for the CEPC Studies* , (CEPC Note in preparation).

[12] D. Schulte, *Beam-beam simulations with GUINEA-PIG*, In 5th International Computational Accelerator Physics Conference. 1999. CLIC-NOTE-387.

[13] W. Kilian, T. Ohl, and J. Reuter, *WHIZARD: Simulating Multi-Particle Processes at LHC and ILC*, Eur. Phys. J. C **71** (2011) 1742, arXiv:0708.4233 [hep-ph].

[14] J. Alwall et al., *MadGraph 5 : Going Beyond*, JHEP **1106** (2011) 128, arXiv:1106.0522 [hep-ph].

[15] T. Sjöstrand, S. Mrenna, and P. Z. Skands, *PYTHIA 6.4 Physics and Manual*, JHEP **0605** (2006) 026, arXiv:hep-ph/0603175 [hep-ph].

[16] X. Mo, *Generator Sample Stauts for CEPC Simulation Studies* , (CEPC Note in preparation).

[17] P. Mora de Freitas and H. Videau, *Detector simulation with MOKKA / GEANT4: Present and future*, pp. 623–627. 2002. LC-TOOL-2003-010.

[18] The GEANT4 Collaboration, S. Agostinelli et al., *GEANT4: A simulation toolkit*, Nucl. Instrum. Meth. A **506** (2003) 250–303.

[19] Y. Xu, *CEPC detector model CEPC_v1 and its validation*, (CEPC Note in preparation).

[20] F. Gaede, *Clupatra, TPC pattern recognition*, Presented at AIDA meeting at CERN, 2011.

[21] M. Thomson, *Particle Flow Calorimetry and the PandoraPFA Algorithm*, Nucl.Instrum.Meth. **A611** (2009) 25–40, arXiv:0907.3577 [physics.ins-det].

[22] T. Tanabe and T. Suehara, *LCFIPlus*, Presented at ILD workshop at Kyushu University, 2012.

[23] M. Ruan and H. Videau, *Arbor, a new approach of the Particle Flow Algorithm*, arXiv:1403.4784 [physics.ins-det].

[24] P. Janot, *Particle Flow Event Reconstruction from LEP to LHC*, Presented at Excellence in Detectors and Instrumentation Technologies workshop, CERN, 2011.

[25] The CMS Collaboration, *Particle-Flow Event Reconstruction in CMS and Performance for Jets, Taus, and MET*, CMS-PAS-PFT-09-001, 2009.

[26] The CMS Collaboration, F. Beaudette, *The CMS Particle Flow Algorithm*, arXiv:1401.8155 [hep-ex].

[27] Y. Wei, *Stauts for CEPC Full Simulation Sample Generation* , (CEPC Note in preparation).

[28] D. Asner et al., *ILC Higgs White Paper*, arXiv:1310.0763 [hep-ph].

[29] The LHC Higgs Cross Section Working Group, S. Heinemeyer, et al., *Handbook of LHC Higgs Cross Sections: 3. Higgs Properties*, arXiv:1307.1347 [hep-ph].

[30] Y. Haddad, *Feasibility of a minimum bias analysis of* $e^+e^- \to ZH \to q\bar{q} + X$ *at a 250 GeV ILC*, arXiv:1404.3164 [hep-ph].

[31] J. Dai and ohters, *Higgs to bb, cc, gg Branching ratio measurement at CEPC*, (CEPC Note in preparation).

[32] H. Ono and A. Miyamoto, *Higgs Branching Fraction Study in ILC*, arXiv:1202.4955 [hep-ex].

[33] Z. Chen, *Higgs to WW* Branching ratio measurement at CEPC*, (CEPC Note in preparation).

[34] H. Ono and A. Miyamoto, *Higgs Branching Fraction Study in ILC*, 2012. arXiv:1202.4955 [hep-ex].

[35] X. Yang et al., *Higgs to ZZ* Branching ratio measurement at CEPC*, (CEPC Note in preparation).

[36] The TLEP Design Study Working Group, M. Bicer, et al., *First Look at the Physics Case of TLEP*, JHEP **1401** (2014) 164, arXiv:1308.6176 [hep-ex].

[37] F. Wang, G. Li, and M. Ruan, *Higgs to di-photon Branching ratio measurement at CEPC*, (CEPC Note in preparation).

[38] B. Wang, *Higgs to di-muon Branching ratio measurement at CEPC* , (CEPC Note in preparation).

[39] Z. Chen, *Measurement of* $\sigma(WW^* \to ZH) \times Br(H \to b\bar{b})$ *at CEPC*, (CEPC Note in preparation).

[40] T. Han, Z. Liu, and J. Sayre, *Potential Precision on Higgs Couplings and Total Width at the ILC*, Phys. Rev. D **89** (2014) 113006, arXiv:1311.7155 [hep-ph].

[41] J. Huang et al., *Supersymmetric Exotic Decays of the 125 GeV Higgs boson*, Phys. Rev. Lett **112** (2014) 221803, arXiv:1309.6633 [hep-ph].

[42] Z. Chen et al., *Higgs to invisible and exotic Branching ratio measurement at CEPC* , (CEPC Note in preparation).

[43] The ALEPH, DELPHI, L3 and OPAL Collaboration, S. Schael et al., *Electroweak Measurements in Electron-Positron Collisions at W-Boson-Pair Energies at LEP*, Phys. Rept. **532** (2013) 119–244, arXiv:1302.3415 [hep-ex].

[44] K. Shin-ichi, K. Fujii, et al., *Higgs to di tau branching ratio study at 250 GeV center of mass energy at the ILC with the ILD detector* , LC-REP-2013-001, 2013.

[45] The LHC Higgs Cross Section Working Group, A. David, et al., *LHC HXSWG interim recommendations to explore the coupling structure of a Higgs-like particle*, arXiv:1209.0040 [hep-ph].

[46] M. Duhrssen et al., *Extracting Higgs boson couplings from CERN LHC data*, Phys. Rev. D **70** (2004) 113009, arXiv:hep-ph/0406323 [hep-ph].

[47] B. A. Dobrescu and J. D. Lykken, *Coupling spans of the Higgs-like boson*, JHEP **1302** (2013) 073, arXiv:1210.3342 [hep-ph].

[48] J. F. Gunion et al., *The Higgs Hunter's Guide*, Front.Phys. **80** (2000) 1–448.

[49] The CMS Collaboration, V. Khachatryan et al., *Search for the associated production of the Higgs boson with a top-quark pair*, JHEP **1409** (2014) 087, arXiv:1408.1682 [hep-ex].

[50] The ATLAS Collaboration, G. Aad et al., *Search for* $H \to \gamma\gamma$ *produced in association with top quarks and constraints on the Yukawa coupling between the top quark and the Higgs boson using data taken at 7 TeV and 8 TeV with the ATLAS detector*, Phys. Lett. B **740** (2015) 222–242, arXiv:1409.3122 [hep-ex].

[51] A. Banfi, A. Martin, and V. Sanz, *Probing top-partners in Higgs+jets*, JHEP **1408** (2014) 053, arXiv:1308.4771 [hep-ph].

[52] A. Azatov and A. Paul, *Probing Higgs couplings with high* p_T *Higgs production*, JHEP **1401** (2014) 014, arXiv:1309.5273 [hep-ph].

[53] C. Grojean et al., *Very boosted Higgs in gluon fusion*, JHEP **1405** (2014) 022, arXiv:1312.3317 [hep-ph].

[54] M. Buschmann et al., *Resolving the Higgs-Gluon Coupling with Jets*, Phys. Rev. D **90** (2014) 013010, arXiv:1405.7651 [hep-ph].

[55] J. Ellis, V. Sanz, and T. You, *Complete Higgs Sector Constraints on Dimension-6 Operators*, JHEP **1407** (2014) 036, arXiv:1404.3667 [hep-ph].

[56] M. Klute and ohters, *Measuring Higgs Couplings at a Linear Collider*, Europhys. Lett. **101** (2013) 51001, arXiv:1301.1322 [hep-ph].

[57] M. E. Peskin, *Estimation of LHC and ILC Capabilities for Precision Higgs Boson Coupling Measurements*, arXiv:1312.4974 [hep-ph].

[58] The ATLAS Collaboration, *Projections for measurements of Higgs boson signal strengths and coupling parameters with the ATLAS detector at a HL-LHC*, ATL-PHYS-PUB-2014-016, CERN, Geneva, Oct, 2014.

[59] A. Denner et al., *Standard Model Higgs-Boson Branching Ratios with Uncertainties*, Eur. Phys. J. C **71** (2011) 1753, arXiv:1107.5909 [hep-ph].

[60] L. G. Almeida et al., *Study of the standard model Higgs boson partial widths and branching fractions*, Phys. Rev. D **89** (2014) no. 3, 033006, arXiv:1311.6721 [hep-ph].

[61] G. P. Lepage, P. B. Mackenzie, and M. E. Peskin, *Expected Precision of Higgs Boson Partial Widths within the Standard Model*, arXiv:1404.0319 [hep-ph].

[62] M. McCullough, *An Indirect Model-Dependent Probe of the Higgs Self-Coupling*, Phys. Rev. D **90** (2014) 015001, arXiv:1312.3322 [hep-ph].

[63] W. Yao, *Studies of measuring Higgs self-coupling with $HH \to b\bar{b}\gamma\gamma$ at the future hadron colliders*, arXiv:1308.6302 [hep-ph].

[64] S. Profumo et al., *Singlet-catalyzed electroweak phase transitions and precision Higgs boson studies*, Phys. Rev. D **91** (2015) no. 3, 035018, arXiv:1407.5342 [hep-ph].

[65] A. Katz and M. Perelstein, *Higgs Couplings and Electroweak Phase Transition*, JHEP **1407** (2014) 108, arXiv:1401.1827 [hep-ph].

[66] A. Noble and M. Perelstein, *Higgs self-coupling as a probe of electroweak phase transition*, Phys. Rev. D **78** (2008) 063518, arXiv:0711.3018 [hep-ph].

[67] B. Henning, X. Lu, and H. Murayama, *What do precision Higgs measurements buy us?*, arXiv:1404.1058 [hep-ph].

[68] S. Profumo, M. J. Ramsey-Musolf, and G. Shaughnessy, *Singlet Higgs phenomenology and the electroweak phase transition*, JHEP **0708** (2007) 010, arXiv:0705.2425 [hep-ph].

[69] D. Curtin, P. Meade, and C.-T. Yu, *Testing Electroweak Baryogenesis with Future Colliders*, JHEP **1411** (2014) 127, arXiv:1409.0005 [hep-ph].

[70] J. Fan, M. Reece, and L.-T. Wang, *Precision Natural SUSY at CEPC, FCC-ee, and ILC*, arXiv:1412.3107 [hep-ph].

[71] N. Craig, C. Englert, and M. McCullough, *New Probe of Naturalness*, Phys. Rev. Lett. **111** (2013) no. 12, 121803, arXiv:1305.5251 [hep-ph].

[72] N. Craig et al., *Precision Higgsstrahlung as a Probe of New Physics*, JHEP **1503** (2015) 146, arXiv:1411.0676 [hep-ph].

CHAPTER 4

ELECTROWEAK PRECISION PHYSICS AT THE CEPC

4.1 W, Z Measurements at the CEPC

The Z boson factories LEP 1 at CERN and SLC at SLAC observed about 2×10^7 Z-decays, and could determine Z boson properties with a precision reaching the 10^{-3} level. This allowed to test the SM at the electroweak loop level and constrained new particles from possible new physics beyond the SM provided these were not very much heavier than the electroweak symmetry breaking scale of 246 GeV. However, many theories addressing the naturalness of the SM or the hierarchy problem introduced by an elementary Higgs sector predict or are consistent with new physics mass scales of the order of one or several TeV. To observe quantum fluctuations associated with such scales one needs to improve the precision in at least some electroweak observables by about another order of magnitude, which in turn requires the production of 10^9 Z bosons or more.

This level of precision can be achieved by the CEPC with its large integrated luminosity and the production of the order of 10^{10} Z bosons already assuming a basic design. Beyond that various design options, including polarized beams, a dedicated WW threshold scan, or yet higher luminosities would increase the precision and therefore the reach in mass scale even further. Precise measurements of the W and Z boson masses, widths, and couplings at the CEPC could thus discover deviations from the SM and reveal indirectly the existence of new particles even before they may have been produced directly [1].

Very significant improvements are expected from the CEPC for most of the observables. Table 4.1 compares the expected precisions from a basic CEPC design to achieved precisions from the LEP experiments for various measurements. Some details regarding the estimation of these uncertainties are described in this section. These are conservative expectations with an ILC type detector in mind. Future studies assuming a detector de-

sign and beamtime allocation optimized for the CEPC can be expected to yield even more favorable projections.

Table 4.1 The expected precision in a selected set of EW precision measurements and the comparison with the precision from LEP experiments. The current precisions for $\sin^2\theta_W^{\text{eff}}$ and R_b include the measurements at the SLC.

Observable	LEP precision	CEPC precision	CEPC runs	$\int \mathcal{L}$ needed in CEPC
m_Z	2 MeV	0.5 MeV	Z lineshape	> 150 fb^{-1}
m_W	33 MeV	3 MeV	ZH (WW) thresholds	> 100 fb^{-1}
A_{FB}^b	1.7%	0.15%	Z pole	> 150 fb^{-1}
$\sin^2\theta_W^{\text{eff}}$	0.07%	0.01%	Z pole	> 150 fb^{-1}
R_b	0.3%	0.08%	Z pole	> 100 fb^{-1}
N_ν (direct)	1.7%	0.2%	ZH threshold	> 100 fb^{-1}
N_ν (indirect)	0.27%	0.1%	Z lineshape	> 150 fb^{-1}
R_μ	0.2%	0.05%	Z pole	> 100 fb^{-1}
R_τ	0.2%	0.05%	Z pole	> 100 fb^{-1}

Preliminarily, the CEPC is expected to collect 10^{10} Zs. For the studies presented here, 100 fb^{-1} is used as a more conservative estimate of the total integrated luminosity, corresponding to about 2×10^9 Zs. With this amount of statistics, the precision of most of the observables here, with the possible exception of $\sin\theta_W^{\text{eff}}$, are already dominated by systematical uncertainties.

4.1.1 Z Pole Measurements

The CEPC offers the possibility of dedicated low-energy runs at the Z pole with a large integrated luminosity (> 100 fb^{-1}) and a Z lineshape scan around the pole (from 88 GeV to 94 GeV). These runs allow ultra-high precision electroweak measurements of the Z boson decay partial widths, e.g. the parameters $R_b = \Gamma_{Z\to b\bar{b}}/\Gamma_{\text{had}}$ and $R_\ell = \Gamma_{\text{had}}/\Gamma_{Z\to \ell\bar{\ell}}$. (Notice that R_ℓ is defined as the ratio to any *one* charged lepton flavor, not the ratio to the sum of all lepton flavors.) It will also perform high precision measurements of the forward-backward charge asymmetry (A_{FB}), the effective weak mixing angle ($\sin^2\theta_W^{\text{eff}}$), number of light neutrino species (N_ν), and the mass of the Z boson (M_Z). These runs will also be important for the calibrations of leptons and jets. It is also possible to perform some measurements of Z boson properties without these dedicated low-energy runs near or at the Z pole. For example, the direct measurement of the number of light neutrino species can be performed in ZH runs intended for Higgs boson measurements.

4.1.1.1 R_b

The width of the Z boson into each of its decay channels is proportional to the sum of squares of fundamental Z-fermion couplings. The partial width R_b is sensitive to electroweak radiative corrections from new physics particles. For example, the existence of the scalar tops or charginos in supersymmetry could lead to a visible change of R_b from the SM prediction.

Precise measurements of R_b have been made by the LEP collaborations [2] and by the SLD collaboration [3] at SLAC using hadronic Z events. Decays of b-hadrons were tagged using tracks with large impact parameters and/or reconstructed secondary vertices, complemented by event shape variables. The combination of LEP and SLD measurements yields a value of 0.21629 ± 0.00066 for R_b. The relative statistical uncertainty of R_b is 5×10^{-4}. The main systematic uncertainty includes the uncertainty due to hemisphere tag correlations for b events (0.2%), the uncertainty due to gluon splitting (0.15%), the uncertainty due to charm physics modeling (0.1%) and the uncertainty due to light quark modeling (0.1%).

A precision of 0.08% can be achieved for the measurement of R_b at CEPC, improving the current precision in experimental measurement by a factor of 4. Assuming the CEPC will collect a total integrated luminosity of 100 fb^{-1} at the Z pole, the statistical uncertainty improves by at least a factor of 10 and the systematic uncertainties will reduce also. The uncertainty due to hemisphere tag correlations for b events will be reduced to a level of 0.05% due to the expected improvement in the b-tagging performance of the CEPC detector. The improvement of b-tagging efficiency is important to reduce the correction in C_b since the correlation becomes irrelevant in the limit of 100% b-tagging efficiency.

Due to that fact that a next-generation vertex detector will be used in the CEPC detector, the b-tag efficiency is expected to be around 80% with a b-jet purity of 90%, which is about 15% higher than the efficiency in the SLD experiment. The impact of C_b to R_b will reduce by at least a factor of four with respect to previous measurements.

The CEPC measurement is thus expected to have a 5-10% purer b-tagged sample at the 90% tagging efficiency compared to previous measurements. Therefore the uncertainty due to the modeling of the light quarks in the CEPC measurement can be reduced to a level of 0.05% using a tighter b-tagging working point.

More precise gluon splitting measurements are expected at the CEPC, reducing the uncertainty due to gluon splitting to the 0.08% level.

The uncertainty due to charm physics modeling can be reduced to 0.05% by reducing the mis-b-tag rate for charm jets. Typical working points at LEP measurements have a b-tagging efficiency of 60% and a charm mistag rate of 1.3%. The b-tag efficiency of charm jets can be reduced to less than 0.5% compared to LEP measurements in the 65% b jet purity working point.

4.1.1.2 The Partial Decay Width of $Z \to \mu^+\mu^-$

The $\mu^+\mu^-$ channel provides the cleanest leptonic final state. Combining the measurements from all four LEP experiments [4–7], the overall uncertainty of R_μ is 0.2%. The statistical uncertainty of R_μ is 0.15%. Main systematic uncertainties from the ALEPH measurement come from the uncertainty in muon momentum scale (0.009%) and in muon momentum resolution (0.005%), the uncertainty in the modeling of $Z \to \mu^+\mu^-\gamma$ events (0.05%), and the uncertainty of photon energy scale (0.05%) in the $Z \to \mu^+\mu^-\gamma$ process.

A precision of 0.05% can be achieved at the CEPC. Benefitting from the excellent CEPC tracking detector, the uncertainties due to muon momentum scale and resolution will be negligible. The energy resolution in the EM calorimeter of the CEPC detector is expected to be at least 10 times better than the resolutions at LEP experiments. Therefore, the uncertainty due to photon energy scale and resolution in $Z \to \mu^+\mu^-\gamma$ process can be reduced to 0.02%. The main challenge in this measurement is to reduce the systematics due to QED ISR events. More detailed studies of radiative events in Z threshold scan

runs are expected. Benefitting from high statistics in Z threshold scan runs, the source of uncertainty can be reduced to a level of 0.03%.

4.1.1.3 The Forward-backward Asymmetry A_{FB}^{b} at the Z Pole

The measurement of the forward-backward asymmetry in $e^+e^- \to b\bar{b}$ events at the Z pole, $A_{FB}^{b,0}$, gives an important test of the Standard Model. $A_{FB}^{b,0}$ offers the most precise determination of the weak mixing angle. The measurements have been made at LEP [4–7] using about 10^6 hadronic Z events.

$Z \to b\bar{b}$ events were identified by tagging two b jets. Each event was divided into forward and backward categories by the plane perpendicular to the thrust axis which contains the interaction point. The combination of the LEP and SLD measurements gives a measured value of $A_{FB}^{b,0} = 0.1000 \pm 0.0017$. The statistical uncertainty is 1.2% and the main systematic uncertainties come from hemisphere tag correlations for b events (1.2%), tracking resolution and vertex detector alignment (0.8%), charm physics modeling (0.5%), and QCD and thrust axis correction (0.7%).

A precision of 10^{-4} can be achieved for the measurement of $A_{FB}^{b,0}$ at the CEPC, improving the current precision by more than a factor of 10. The expected statistical uncertainty is at a level of 0.05%. The uncertainty due to hemisphere tag correlations for b events can be reduced to 0.1% due to high b-tagging efficiency. The uncertainty due to charm physics modeling can be reduced to 0.05% by choosing a tighter b-tagging working point. The uncertainty due to tracking resolution and vertex detector alignment can be reduced to 0.05%. The expected tracking momentum resolution in the CEPC detector is $\sigma/p_T = 2 \times 10^{-4} \times p_T + 0.005$, which is 10 times better than the resolutions of the LEP detectors. The uncertainty due to QCD and thrust axis correction can be reduced to 0.1% due to at least 10 times better granularity in the CEPC calorimeters. Overall, the expected systematics at CEPC measurement can be reduced to a level of 0.15%.

4.1.1.4 Prospects for the Effective Weak Mixing Angle Measurement

The weak mixing angle $\sin^2\theta_W^{\text{eff}}$ is a very important parameter in the electroweak theory of the SM. It is the only free parameter that fixes the relative couplings of all fermions to the Z. It describes the rotation of the original W^0 and B^0 vector boson states into the observed γ and Z bosons as a result of spontaneous symmetry breaking. The weak mixing angle is very sensitive to electroweak radiative corrections, and it can be used perform a precise test of the SM theory. Furthermore, if there is any new heavy gauge boson Z', the weak mixing angle is expected to deviate from the SM prediction due $Z - Z'$ mixing, therefore $\sin^2\theta_W^{\text{eff}}$ is very sensitive to new physics as well.

A centre-of-mass energy dependence of the forward-backward asymmetry arises from the interference of Z boson and virtual photon exchange. Thus, while the asymmetry can be extracted precisely from data to be taken on top of the Z resonance, off-peak data may provide additional leverage, and dedicated studies for optimized beamtime allocation between on-peak and off-peak running are required.

The effective weak mixing angle has been extracted at LEP [4–7] from $Z \to b\bar{b}$, $Z \to c\bar{c}$, and $Z \to \ell^+\ell^-$ decays, and from final state τ polarization asymmetries. The current experimental result is $\sin^2\theta_W^{\text{eff}} = 0.23153 \pm 0.00016$. The expected precision in the effective weak mixing angle measurement at the CEPC from $Z \to b\bar{b}$ events alone is expected to be 0.01%. In addition, there would be several other independent determinations which can be expected to average to a similar precision.

4.1.1.5 Z Mass Measurement

The Z mass, m_Z, is a fundamental parameter in the SM and was determined with an overall uncertainty of 2 MeV by the four LEP experiments. m_Z was extracted from fits to hadronic cross section measurements in dedicated Z lineshape scans from 88 GeV to 94 GeV, together with the Z width, Γ_Z, and the total hadronic peak cross section. The dominant uncertainties in m_Z were LEP beam energy related, and the statistical uncertainty contributed about another MeV.

Table 4.2 Example of a Z lineshape scan including six off-peak energies and their integrated luminosity.

$\sqrt{s}$(GeV)	88.2	89.2	90.2	91.1876	92.2	93.2	94.2
$\int \mathcal{L}$(fb)	10	10	10	100	10	10	10

A precision of 0.5 MeV can be achieved at the CEPC, provided a mass scan around the Z peak will be performed. For example, the six off-peak runs and one on-peak run listed in Table 4.2 would reduce the statistical uncertainty to about 0.1 MeV. The beam energy uncertainty at the CEPC is expected to be accurate to the 10 ppm level, which is about five times better than LEP yielding an uncertainty of less than 0.5 MeV. The uncertainty due to the jet energy scale and resolution results in about 0.1 MeV in m_Z. There would be sufficient data at the CEPC to utilize the cleaner lepton final states in addition to hadrons.

4.1.1.6 Neutrino Species Counting

Two different methods have been used to determine the number of neutrino species (N_ν) at LEP.

The first is an indirect method using the analysis of the Z lineshape, and it uses the data collected by the Z threshold scan runs. The second method is a direct measurement, which is based on the measurement of the cross section for the radiative process $e^+e^- \to \nu\nu\gamma$. At the CEPC, this method will be used in the ZH runs.

These two methods use different theoretical inputs from the Standard Model and also use completely different datasets, therefore they are independent and complementary. The sensitivity to new physics will be different for these two methods. In the direct method, one can measure N_ν as a function of $\sqrt{s}$. This is very sensitive to new physics at high energy scales. Possible contributions include WIMP dark matter particles, and other weakly coupled particles such as exotic neutrinos, gravitinos, or KK gravitons in theories with large extra dimensions. Thus, when we refer to the number of neutrino species, we actually include any number of possible invisible particles other than neutrinos.

Indirect Method from Z Line Shape The indirect method assumed all contributions from invisible channels are coming from the $Z \to \nu\bar{\nu}$. This method used the analysis of Z lineshape, subtracting the visible partial widths of the hadrons ($\Gamma_{\rm had}$), and the partial widths of the leptons (Γ_ℓ) from the total width Γ_Z. The invisible width $\Gamma_{\rm inv}$ can be written as:

$$\Gamma_{\rm inv} = N_\nu \Gamma_\nu = \Gamma_Z - \Gamma_{\rm had} - 3\Gamma_\ell. \tag{4.1}$$

We take as our definition of the number of neutrinos $N_\nu = \Gamma_{\rm inv}/\Gamma_\nu$, i.e. the ratio of the invisible width to the Standard Model expectation for the partial width to a single neutrino species.

Using the input from the SM model, we can rewrite equation (4.1) as the following:

$$N_\nu = \frac{\Gamma_\ell}{\Gamma_\nu}\left(\sqrt{\frac{12\pi R_\ell}{M_Z^2\sigma^0_{\rm had}}} - R_\ell - 3\right). \tag{4.2}$$

As shown in equation (4.2), the precision of N_ν depends on the lepton partial width R_ℓ measurement, the Z mass measurement, and the hadronic cross section of the Z boson on its mass peak ($\sigma^0_{\rm had}$). The precision of $\sigma^0_{\rm had}$ gives the largest impact to N_ν measurement, and it is very sensitive to the precision of the luminosity. Therefore the precise luminosity measurement is the key to determine N_ν.

Precise measurements of N_ν have been made by LEP collaborations [8], and they obtained a precision of 0.27% using this indirect method. The main systematics of the N_ν measurement is coming from the uncertainty in the luminosity measurement (0.14%) and the theory uncertainty in the predicted cross section of the small angle Bhabha process (0.11%).

The precision of 0.1% in N_ν measurement with the indirect method can be achieved in CEPC measurement, which improves the current precision by a factor of three. Benefitting from the recent development of luminosity detector technology, the uncertainty due to luminosity can be reduced to 0.05%. The uncertainty from the small angle Bhabha process can be reduced to 0.05% due to recent progress in studying this process[9].

Direct Method Using $e^+e^- \to \nu\bar{\nu}\gamma$ Events The most precise direct N_ν measurements at LEP were carried out by the L3 and DELPHI collaborations [10, 11]. By combining the direct measurements at LEP, the current experimental result is $N_\nu = 2.92 \pm 0.05$. The statistical uncertainty of N_ν in the previous measurement is 1.7%. The main systematic uncertainty from the L3 measurement includes the uncertainty in single photon trigger efficiency (0.6%), and photon identification efficiency (0.3%), and the uncertainty in identifying the converted photons (0.5%).

A precision of 0.2% can be achieved for the direct measurement of N_ν at CEPC, and it will improve the current precision by a factor of 10. Due to the excellent performance of the CEPC inner tracker, the uncertainty due to converted photons' selection efficiency is expected to be negligible. The granularity of the CEPC EM calorimeter is expected to be 10 to 100 times better than the detectors at LEP. Therefore photons can be identified with high purity with loose EM shower shape based selection. The uncertainty of the photon efficiency can be reduced to less than 0.05%.

4.1.1.7 Rare Z Decays

CEPC may have the opportunity to probe rare Z decays, including exclusive processes like $Z \to J/\psi\,\gamma$ or $Z \to \Upsilon\,\gamma$. These processes are predicted to have small branching ratios in the Standard Model [12, 13]. For example, [13]

$$\begin{aligned} {\rm Br}(Z^0 \to J/\psi\,\gamma) &\approx 8\times 10^{-8} \\ {\rm Br}(Z^0 \to \Upsilon(nS)\,\gamma) &\approx 1.0\times 10^{-7}. \end{aligned} \tag{4.3}$$

Given these expectations, CEPC's sample of order 10^9 to 10^{10} Z bosons could allow the branching ratio to these decays to be measured to better than 10% statistical accuracy. The

LHC has set upper bounds at the level of 10^{-6} for these branching ratios, still far from the Standard Model prediction [14]. CEPC will have the opportunity to explore a new frontier of the Standard Model in these channels, putting high-precision theoretical calculations to the test.

Even more importantly, observation of Z decays that are forbidden or quasi-forbidden in the SM would be a clear signal of new physics. For example, the limits on lepton-flavor violating decays such as $Z \to \mu^{\pm}e^{\mp}$ could be improved by three orders of magnitude reaching the 10^{-9} level or better. This will test the flavor structure of theories beyond the SM up to scales of tenth or hundreds of TeV.

4.1.2 W Mass Measurement

In e^+e^- collisions, W bosons are produced mainly through the $e^+e^- \to W^+W^-$ process. The cross section of this process at the WW production threshold is very sensitive to m_W. m_W can be measured from threshold scans.

At centre-of-mass energies above the W^+W^- production threshold, the mass of the W bosons can be determined by measuring the momentum of its decay products. This is called the direct measurement approach in this section.

The measurements have been made at LEP using both the threshold scan method and a direct measurement approach. The threshold scan method suffered from large statistical uncertainty (about 200 MeV). The direct measurement approach using $\ell\nu qq$ and $qqqq$ channels at LEP provides a better measurement. The uncertainty due to limited data statistics in the direct measurement was found to be about 30 MeV [15–18] . The main systematic uncertainties from the measurement include the modeling of hadronization (13 MeV) and radiative corrections (8 MeV), and the energy scale of lepton and missing energy (10 MeV).

Using the threshold scan method, a precision of 2.5 MeV can be achieved for the measurement at the CEPC. We assume that the CEPC can provide a 6-point threshold scan with 500 fb^{-1} integrated luminosity. The $\sqrt{s}$ values of the threshold scan runs are assumed to be 160.6, 161.2, 161.4, 161.6, 162.2 and 170.0 GeV. The $\ell\nu qq$ channel suffers from statistics uncertainty using the threshold scan method. The $\ell\nu qq$ and $qqqq$ channels can be used to measure the $e^+e^- \to W^+W^-$ cross section as a function of $\sqrt{s}$. Assuming that the momentum scale uncertainty in the CEPC accelerator can be at the 10 ppm level, the systematic uncertainty of the W mass measurement has the potential to be reduced to 1 MeV. The list of systematic uncertainties is summarized in Table 3.

Using the direct measurement method, a precision of 3 MeV can be achieved for the measurement at CEPC. The main advantage of the direct measurement method is that no dedicated run is needed: all the measurements can be performed in ZH runs with $\sqrt{s} = 250$ GeV. Another advantage is that this method has a lower requirement for accelerator performance. The main challenge of this method is to handle the uncertainty due to QED radiation. The energy spread from beamstrahlung is proportional to the square of the beam energy. The uncertainty due to the beamstrahlung effect can be reduced to the 1 MeV level using 1000 fb^{-1} data. Other systematic uncertainties include the lepton momentum scale and the modeling of hadronization. The list of systematic uncertainties are summarized in Table 4.4.

Table 4.3 Using the threshold scan measurement method in dedicated WW threshold scan runs, the expected precision in the m_W measurement with CEPC detectors is shown together with the comparison with LEP experiments.

ΔM_W(MeV)	LEP	CEPC	CEPC
$\sqrt{s}$(GeV)	161	250	250
$\int \mathcal{L}$(fb^{-1})	3	1000	1000
channel	$\ell\nu qq, qqqq$	$\ell\nu qq$	$qqqq$
beam energy	13	1.0	1.0
background	13	0.5	1.5
efficiency	8	0.5	0.1
luminosity	10	1.0	1.0
jet energy scale	—	0.5	1.0
statistics	20	1.0	0.5
total	36	2.5	3.0

Table 4.4 Using the direct measurement method in ZH runs, the expected precision in the m_W measurement with CEPC detectors is shown together with the comparison with the LEP experiments.

ΔM_W(MeV)	LEP	CEPC	CEPC
$\sqrt{s}$(GeV)	161	250	250
$\int \mathcal{L}$(fb^{-1}	3	1000	1000
channel	$l\nu qq, qqqq$	$l\nu qq$	$qqqq$
beam energy	9	1.0	1.0
hadronization	13	1.5	1.5
radiative corrections	8	1.0	2.0
lepton and missing energy scale	10	1.5	1.0
bias in mass reconstuction	3	0.5	1.0
statistics	30	1.0	2.5
overall systematics	21	2.5	3.0
total	36	3.0	4.0

4.2 CEPC Electroweak Oblique Parameter Fit

Based on the latest estimates of the experimental capabilities of CEPC, we estimate the precision that can be obtained in a fit of the electroweak parameters S and T [19, 20]. These parameters describe the gauge boson self-energies and are very sensitive to physics beyond the SM, especially when the new physics addresses the Higgs sector. Thus, one expects them to be affected in almost any TeV scale scenario. Table 4.5 presents the assumed experimental uncertainties that enter into the fit. The numbers in boldface represent measurements performed by CEPC. Other improvements between the current uncertainties and those that will be available when CEPC runs will result from LHC measurements of the top quark, lattice QCD calculations, and perturbative Standard Model calculations. A thorough discussion of the prospects for these improvements and the rationale behind the choices made in the table may be found in Ref. [21]. Readers seeking a more general review of the status of electroweak precision should consult Ref. [22].

	Present data	CEPC fit
$\alpha_s(M_Z^2)$	0.1185 ± 0.0006 [23]	$\pm 1.0 \times 10^{-4}$ [24]
$\Delta\alpha^{(5)}_{\rm had}(M_Z^2)$	$(276.5 \pm 0.8) \times 10^{-4}$ [25]	$\pm 4.7 \times 10^{-5}$ [26]
m_Z [GeV]	91.1875 ± 0.0021 [27]	$\pm\mathbf{0.0005}$
m_t [GeV] (pole)	$173.34 \pm 0.76_{\rm exp}$ [28] $\pm 0.5_{\rm th}$ [26]	$\pm 0.2_{\rm exp} \pm 0.5_{\rm th}$ [29, 30]
m_h [GeV]	125.14 ± 0.24 [26]	$< \pm 0.1$ [26]
m_W [GeV]	$80.385 \pm 0.015_{\rm exp}$ [23] $\pm 0.004_{\rm th}$ [31]	$(\pm\mathbf{3}_{\rm exp} \pm 1_{\rm th}) \times 10^{-3}$ [31]
$\sin^2\theta^\ell_{\rm eff}$	$(23153 \pm 16) \times 10^{-5}$ [27]	$(\pm\mathbf{2.3}_{\rm exp} \pm 1.5_{\rm th}) \times 10^{-5}$ [32]
Γ_Z [GeV]	2.4952 ± 0.0023 [27]	$(\pm\mathbf{5}_{\rm exp} \pm 0.8_{\rm th}) \times 10^{-4}$ [33]
$R_b \equiv \Gamma_b/\Gamma_{\rm had}$	0.21629 ± 0.00066 [27]	$\pm\mathbf{1.7} \times 10^{-4}$
$R_\ell \equiv \Gamma_{\rm had}/\Gamma_\ell$	20.767 ± 0.025 [27]	$\pm\mathbf{0.007}$

Table 4.5 Inputs to the electroweak fit of the oblique parameters S and T. The oblique parameters and the first five observables in the table float freely in the fit, and determine the values of the remaining five. We find that R_b and R_ℓ have minimal effect on the fit of oblique parameters. We quote the precisions of current and CEPC measurements as well as the current central values. Theory uncertainties are provided only when they are nonnegligible and are not already incorporated in the quoted experimental uncertainty. Boldface numbers represent measurements that will be performed at CEPC.

We have included $\sin^2\theta^\ell_{\rm eff}$ as an observable in the fit, although it will itself result from a fit of several other parameters, including $A^{0,b}_{\rm FB}$, $\mathcal{A}_\ell$, and $A^{0,\ell}_{\rm FB}$. A detailed assessment of each of these individual inputs has not yet been performed for CEPC, so we include only the estimated precision that can be achieved on the combination $\sin^2\theta^\ell_{\rm eff}$. Similarly, other observables like $\sigma_{\rm had}$ will ultimately play a role in CEPC precision tests, but we omit them until future experimental studies provide precise uncertainty estimates.

We have performed a fit to the oblique parameters S and T under the assumption that $U = 0$. Given that a weakly-coupled Higgs boson has been discovered, S and T result from dimension six operators,

$$\mathcal{O}_S \equiv h^\dagger W^{\mu\nu} h B_{\mu\nu}, \tag{4.4}$$

$$\mathcal{O}_T \equiv \left|h^\dagger D_\mu h\right|^2, \tag{4.5}$$

whereas U would arise from a dimension eight operator [34]. This provides a strong theoretical prior that $U \ll S, T$ and justifies our focus on only two oblique parameters. The fit presented here is a profile likelihood: the free parameters are varied to maximize the likelihood for given S and T. This differs from marginalizing, when various values of the free parameters are integrated with respect to some prior probability distribution. The profile likelihood gives slightly more conservative bounds.

The result of the fit for S and T is depicted in Fig. 4.1. For ease of comparison of the bounds, we have artificially displaced the input central values to agree with the predicted values so that $S = T = 0$ will be the best-fit point. Both 68% C.L. and 95% C.L. uncertainty contours are presented (i.e., $\Delta\chi^2 = 2.30$ and 6.18). Relative to the current electroweak precision results (dominated by LEP and the SLC together with the improved measurement of m_W from hadron colliders), the results of CEPC will shrink the error bars on S and T by a factor of about 3.

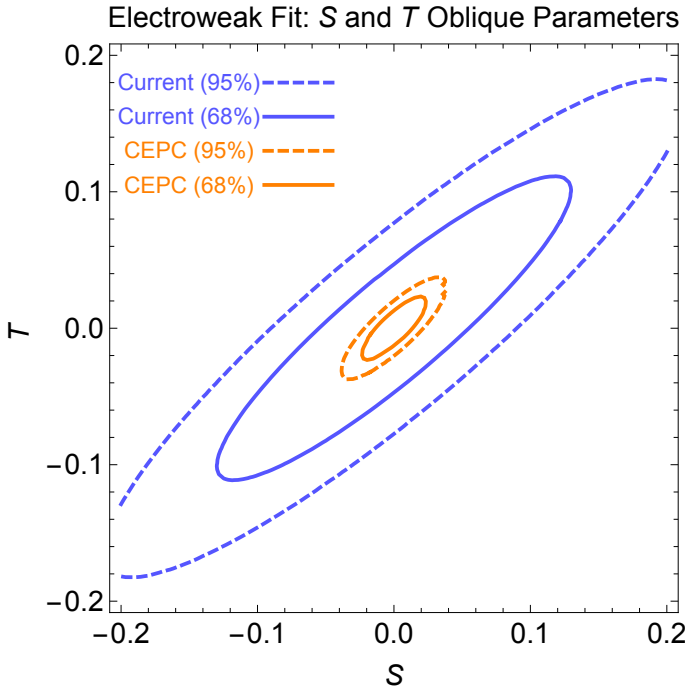

Figure 4.1 CEPC constraints on the oblique parameters S and T, compared to the current constraints.

CEPC	$\Gamma_Z(m_Z)$ [GeV]	m_t [GeV]
Improved Error	$(\pm 1_{\rm exp} \pm 0.8_{\rm th}) \times 10^{-4}$ (± 0.0001)	$\pm 0.03_{\rm exp} \pm 0.1_{\rm th}$

Table 4.6 Potential improvements for CEPC measurements. The Z width measurement (and the Z mass) may be improved by better energy calibration. A precise top mass measurement requires a scan of the $t\bar{t}$ threshold, and thus a larger collision energy than current CEPC plans.

It is possible that the current baseline plan for CEPC can be improved upon by higher luminosity runs, better calibration, or higher beam energy. Table 4.6 lists possible improvements. The Z width measurement will require a high-precision calibration of the beam energy, which is made possible at circular colliders by the technique of resonant spin depolarization [27]. The same technique could also improve m_Z's precision. We consid-

er the possibility that this width and mass can be measured to an experimental precision comparable to the theoretical uncertainty of about 0.1 MeV. The top mass improvement requires a significant experimental effort. It will either rely on input from another collider like the ILC with higher beam energy, or a significant boost in the CEPC energy to scan the top pair production threshold. Such an energy upgrade would significantly improve the ultimate bound attained on the T parameter. We show the result of such improvements in Fig. 4.2. The figure illustrates first the effect of improving Γ_Z together with m_Z (which improves the bounds on S and T comparably), and then the effect of additionally improving the top mass (which constrains T somewhat more strongly than S). From this plot it is apparent that upgrades to the initial CEPC plan potentially offer significant physics benefits and deserve further consideration.

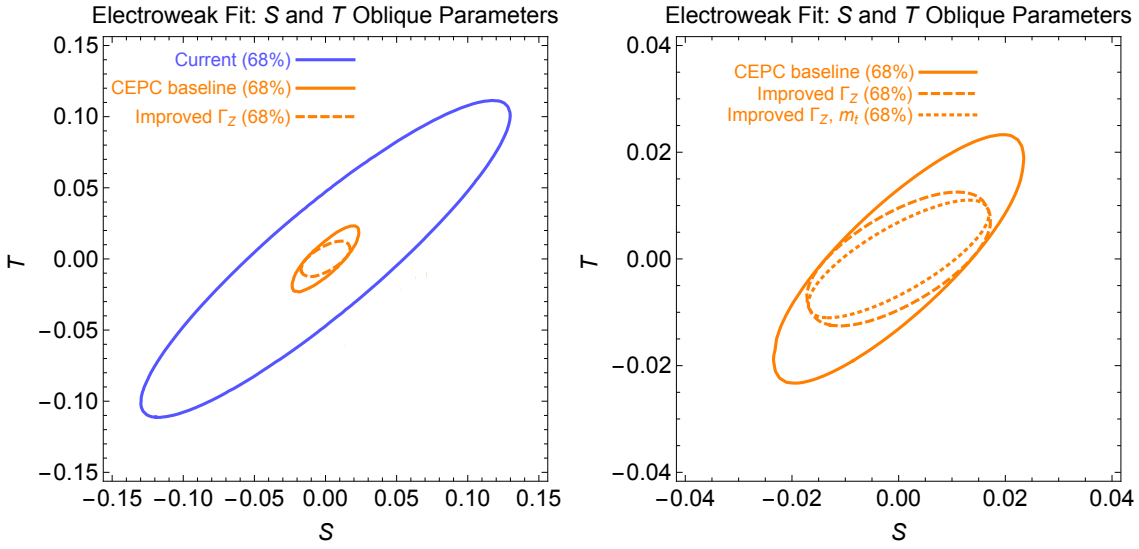

Figure 4.2 CEPC constraints on the oblique parameters S and T, for the baseline scenario and two possible improvements. At left we show the current bound, the CEPC baseline, and one improved scenario. At right we zoom in and show the CEPC baseline and two different improved scenarios. Notice that the axes of this plot have zoomed in by a factor of 5 compared to those of Fig. 4.1. For clarity we show only 68% C.L. ($\Delta\chi^2 = 2.30$) constraints.

Table 4.7 summarize the physics reach by quoting the 68% C.L. bound on S assuming that T is zero, and vice versa. These are one-parameter fits (corresponding to $\Delta\chi^2 = 1$).

Parameter	Current	CEPC baseline	Improved Γ_Z (and m_Z)	Also improved m_t
S	3.6×10^{-2}	9.3×10^{-3}	9.3×10^{-3}	7.1×10^{-3}
T	3.1×10^{-2}	9.0×10^{-3}	6.7×10^{-3}	4.6×10^{-3}

Table 4.7 Current and CEPC projected one-parameter bounds on S and T (in each case, assuming that the other is zero).

4.2.1 The Precision Challenge for Theorists

The estimates of CEPC prospects above assumed an improvement in theoretical uncertainties relative to the current status. Theory uncertainties quoted for m_W, $\sin^2\theta^\ell_{\rm eff}$, and Γ_Z in the "CEPC fit" column of Table 4.5 are based on the size of estimated four-loop

corrections from refs. [31–33], under the assumption that three-loop calculations will be completed in the future. Full use of the power of the CEPC collider thus relies on significant (but reasonable) advances in the state of the art of Standard Model calculations in the coming years.

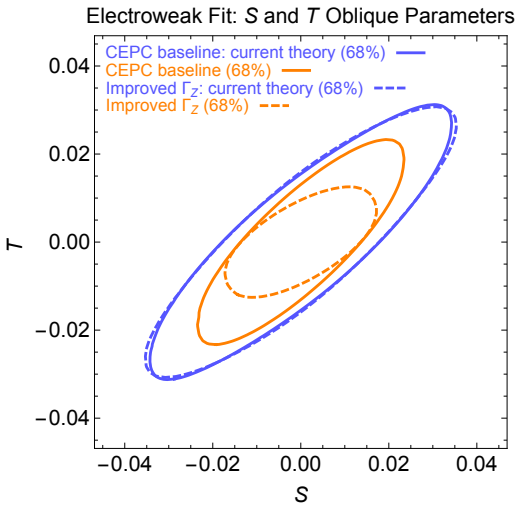

Figure 4.3 An illustration of the importance of improvements in theoretical predictions needed for CEPC to achieve its full potential. The orange solid and dashed curves are as in Fig. 4.2. The blue solid and dashed curves show the result of fitting the same projected experimental measurements, but with today's theory uncertainties (the blue dashed line should overlap with the solid line and it is slightly off the solid line due to numerical artifacts). We see that, especially for the case of improved precision in CEPC's measurement of Γ_Z, the completion of three-loop theoretical calculations will play a decisive role in allowing for precise constraints.

To emphasize the importance of these calculations, we have performed a fit including estimated CEPC experimental errors but *present-day* theoretical uncertainties. In addition to the theory uncertainties already quoted in the "Present data" column of Table 4.5, we also include $\delta_{\rm th} \sin^2\theta^\ell_{\rm eff} \approx 4.7 \times 10^{-5}$ [32] and $\delta_{\rm th}\Gamma_Z \approx 0.5$ MeV [33]. The resulting fits are shown in blue in Fig. 4.3. We see that for the baseline scenario, improving current theoretical predictions will make a modest improvement in the bounds derived from experimental data. For the scenario with improved measurements of Γ_Z, the improved theory calculations are decisive. If we do not improve over present-day theory, such improvements in experimental measurements will make little difference in the fit. The challenge for theorists is to provide sufficiently precise calculations to justify the pursuit of higher precision in experiment.

4.2.2 A General To Do List for a Successful Electroweak Program

So far we have presented the reach of the CEPC for new physics parametrized by S and T. In this section (which is directly extracted from ref. [21]) we want to address some general questions regarding Electroweak Precision Tests (EWPT): what are the most important observables whose precisions need to be improved to achieve the best sensitivity of EWPT? What levels of precision are desirable for these observables? The answers are already contained in the simplified fits of the CEPC electroweak programs with potential improvements but we want to make it clearer by decomposing the fit into three steps and

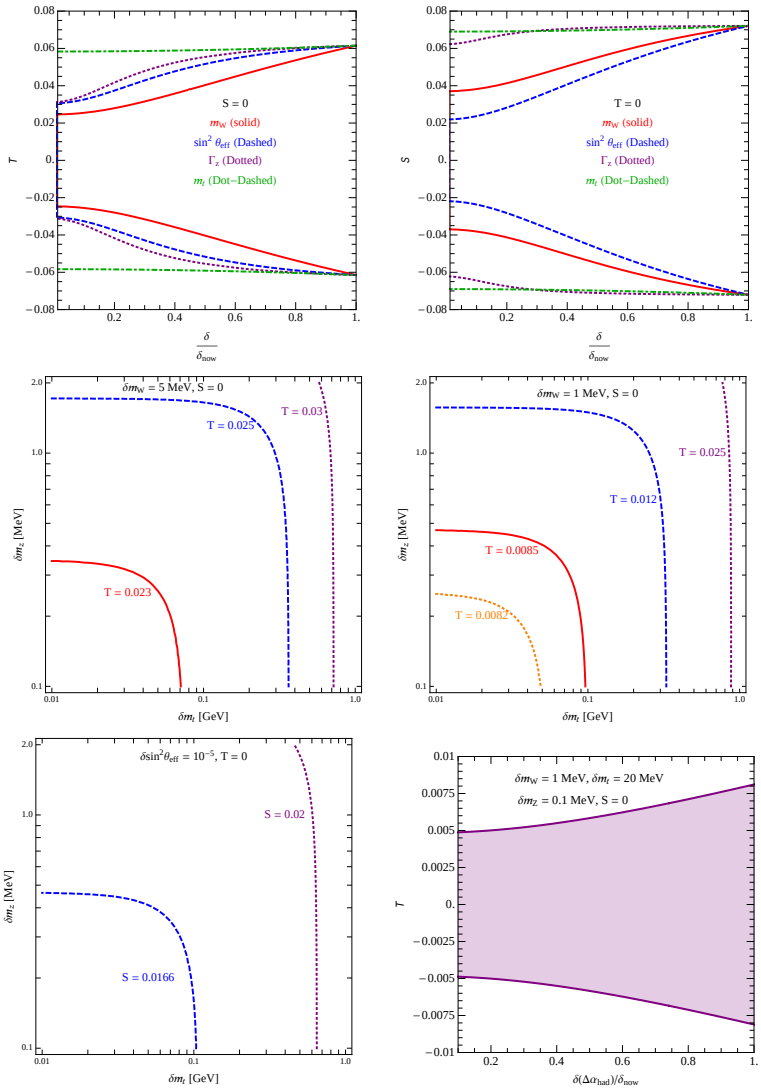

Figure 4.4 First row: allowed T (left) and S (right) at 95% C.L. as a function of error bar of one observable (normalized with respect to its current value) with the precisions of all the other observables in the fit fixed at current values. Second row: contours of allowed T at 95% C.L. in the $(\delta m_t, \delta m_Z)$ plane for $\delta m_W = 5$ MeV (left) and 1 MeV (right). Again the precisions of all other observables in the fit fixed at current values. Last row: left plot: contours of allowed S at 95% C.L. in the $(\delta m_t, \delta m_Z)$ plane for $\delta \sin^2\theta^\ell_{\rm eff} = 10^{-5}$ (left) ; right plot: allowed T at 95% C.L. as a function of the error bar of $\Delta\alpha^{(5)}_{\rm had}$ normalized to its current value fixing $\delta m_W = 1$ MeV, δm_t = 20 MeV and δm_Z = 0.1 MeV. (From ref. [21].)

changing the error bar of only one or two observables at each step. For this section, we will consider two limits with $S = 0$ or $T = 0$ and consider only the bound on T or S.

Among all electroweak observables, m_W is the one that is most sensitive to the T parameter and $\sin^2\theta^\ell_{\rm eff}$ is the one most sensitive to the S parameter. This is demonstrated by the plots in the first row of Fig. 4.4, where we presented the dependence of T setting $S = 0$ (left panel) and S setting $T = 0$ (right panel) on four observables: m_W, $\sin^2\theta^\ell_{\rm eff}$, Γ_Z and m_t. Keeping the other observables with the current precisions, the allowed T at 95% C.L. will decrease by a factor of 3 if the m_W error bar is reduced from the current value 15 MeV to 3 MeV, the CEPC projection, while the allowed S at 95% C.L. will decrease

by a factor of 3 if the $\sin^2\theta^\ell_{\rm eff}$ error bar is reduced from the current value to 2.3×10^{-5}, the CEPC projection. Thus the priority of all electroweak programs is to improve the measurements of m_W or $\sin^2\theta^\ell_{\rm eff}$ and reduce their theory uncertainties as well.

For m_W as well as the other derived observables, the errors of m_t and m_Z are the dominant sources of parametric uncertainties at the moment. Thus among all free observables in the fit, m_t and m_Z are the most important ones to improve the sensitivity to new physics further. The effect on T from reducing the error bars of m_t and m_Z for different choices of δm_W is presented in the middle row of Fig. 4.4. In these two plots, we fix the errors of all the other observables in the fit to their current values. For δm_W around or above 5 MeV, improving δm_t and δm_Z doesn't help much. When δm_W drops to around 1 MeV, reducing δm_Z by at least a factor of 4 and δm_t by at least a factor of 10 compared to their current values *simultaneously* could improve the constraint on T by a factor of about 3. This explains that CEPC with an improved m_t determination could improve the sensitivity to new physics by a factor of 10 compared to the current constraint along the T axis with a factor of 3 from shrinking $\sin^2\theta^\ell_{\rm eff}$ and δm_W and another factor of 3 from simultaneous reductions in δm_t and δm_Z. However, along the S axis, reducing δm_t and δm_Z doesn't help much as depicted in the right panel of the bottom row in Fig. 4.4.

Lastly once δm_t is reduced to be below 100 MeV and m_Z is reduced to be below 0.5 MeV, they are no longer the dominant sources of parametric uncertainties while the contribution from $\Delta\alpha^{(5)}_{\rm had}$ will become the most important one. The improvement of T as a function of the error bar of $\Delta\alpha^{(5)}_{\rm had}$ is depicted in the last row of Fig. 4.4 fixing $\delta m_W = 1$ MeV, δm_t = 20 MeV and δm_Z = 0.1 MeV. Reducing the error bar of $\Delta\alpha^{(5)}_{\rm had}$ by a factor of 5 or more may only buy us a mild improvement of allowed T range about 2.

In summary, the following observables are the most important ones for EWPT and they should be determined with precisions

- Determine m_W to better than 5 MeV precision and $\sin^2\theta^\ell_{\rm eff}$ to better than 2×10^{-5} precision.

- Determine m_t to 100 MeV precision and m_Z to 500 keV precision.

Notice that in the discussions of this section, we do not differentiate theory uncertainties from experimental ones. It should be understood that the precision goals apply to both experimental and theory uncertainties. This means that for m_W and $\sin^2\theta^\ell_{\rm eff}$, complete three-loop SM electroweak corrections computations are desirable.

4.3 Implications for New Physics

4.3.1 Natural Supersymmetry and EWPT

A detailed assessment of the consequences of CEPC measurements for "Natural SUSY," meaning scenarios with light stops and higgsinos [35–41], may be found in ref. [42]. Here we will summarize some of the main results. The loop effects of stops on the S and T parameters were first computed in ref. [43], and have more recently been studied from an effective field theory viewpoint (among many other dimension six operators) [44–46]. Some representative Feynman diagrams contributing to the electroweak precision corrections are displayed in Fig. 4.5 and 4.6.

Upon going to a minimal basis of operators [47], the S and T parameters can be read off from the effective Lagrangian

$$\mathcal{L}_{\text{oblique}} = \frac{\alpha}{4 \sin\theta_W \cos\theta_W v^2} S\mathcal{O}_S - \frac{2\alpha}{v^2} T\mathcal{O}_T. \tag{4.6}$$

The S parameter is sensitive to any form of electroweak symmetry breaking, arising whenever a heavy SU(2)$_L$ multiplet whose states do not have exactly the same mass is integrated out. On the other hand, the T parameter breaks the custodial symmetry of the Standard Model, i.e. the enhanced SO(4) symmetry present in the Higgs sector when the hypercharge coupling g' and Yukawa couplings are neglected. As a result, not all electroweak breaking physics will contribute to T, but in the case of supersymmetry there will be contributions proportional to powers of the top Yukawa coupling. Other operators like $i\partial^\nu B_{\mu\nu} h^\dagger \overleftrightarrow{D^\mu} h$ contribute to the S parameter but can be rewritten in the minimal basis using equations of motion [45–50]; eq. 4.6 is only valid after this operation. In the MSSM, diagrams contributing to the S parameter from stop and sbottom loops are depicted in Fig. 4.5, where the rightmost diagram illustrates the point that the operator generated from integrating out heavy fields is not necessarily one in the minimal basis. The correction derived from these diagrams is

$$S \approx -\frac{1}{6\pi} \frac{m_t^2}{m_{\tilde{Q}_3}^2} + \mathcal{O}\left(\frac{m_t^2 X_t^2}{4\pi m_{\tilde{Q}_3}^2 m_{\tilde{u}_3}^2}\right). \tag{4.7}$$

Notice that the right-handed stop affects the result only via mixing, because it has no direct coupling to W^μ.

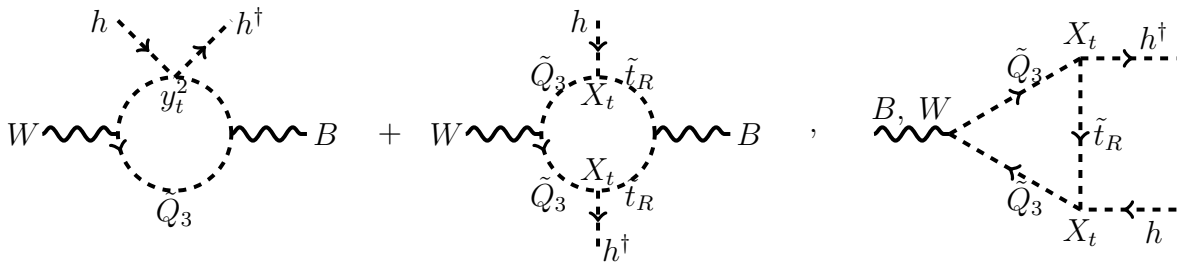

Figure 4.5 Loop diagrams contributing to the S parameter. The two diagrams at left generate the usual operator $h^\dagger W^{i\mu\nu} \sigma^i h B_{\mu\nu}$ when the left-handed stop/sbottom doublet $\tilde{Q}_3$ and the right-handed stop $\tilde{t}_R = (\tilde{u}_3^c)^\dagger$ are integrated out. The diagram at right generates the operators $i\partial^\nu B_{\mu\nu} h^\dagger \overleftrightarrow{D^\mu} h$ and $iD^\nu W^i_{\mu\nu} h^\dagger \sigma^i \overleftrightarrow{D^\mu} h$, which also contribute to S after being rewritten in terms of the minimal basis of dimension-six operators.

The T parameter also arises from integrating out the doublet of stops and sbottoms, and proves to be numerically dominant over the correction to S [43]. Because the T parameter involves four Higgs bosons, the diagrams that contribute are the same as the famous diagrams that raise the Higgs mass relative to m_Z in the MSSM [51–54]. Rather than extracting the Higgs quartic, we simply read off the first subleading momentum-dependent term. This calculation yields:

$$T \approx \frac{m_t^4}{16\pi \sin^2\theta_W m_W^2 m_{\tilde{Q}_3}^2} + \mathcal{O}\left(\frac{m_t^2 X_t^2}{4\pi m_{\tilde{Q}_3}^2 m_{\tilde{u}_3}^2}\right). \tag{4.8}$$

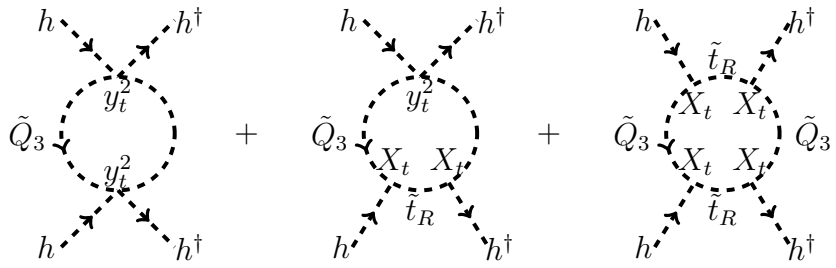

Figure 4.6 Loop diagrams contributing to the T parameter operator $\left(h^\dagger D_\mu h\right)^2$ when the left-handed stop/sbottom doublet $\tilde{Q}_3$ and the right-handed stop $\tilde{t}_R = (\tilde{u}_3^c)^\dagger$ are integrated out.

Again, the right-handed stops contribute only via mixing effects.

Loops of stops and higgsinos modify other observables that will be measured as part of the CEPC electroweak precision programme, such as the Z partial decay width to b quarks (R_b), but these turn out to give weak constraints. The coupling of Higgs bosons to photons and gluons are also modified by loops of stops, and these give important constraints summarized in the Higgs section of the CDR. In Fig. 4.7 we show the expected reach of CEPC electroweak precision constraints on the S and T parameter and of CEPC Higgs coupling measurements on stop masses. The two measurements are comparably strong and will probe stop masses near the TeV scale.

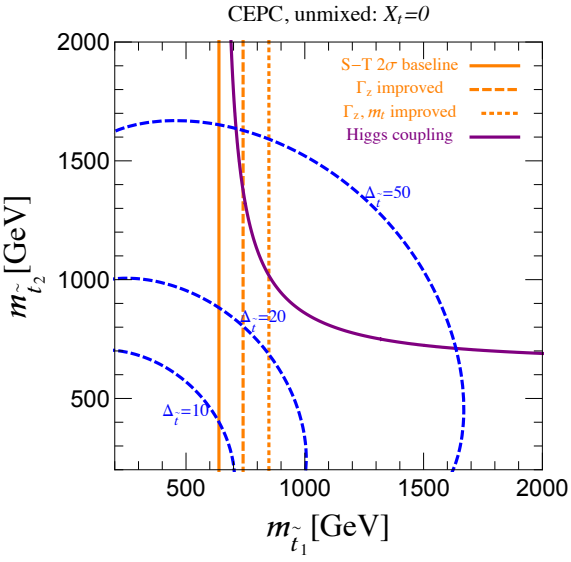

Figure 4.7 CEPC electroweak precision constraints on stops. Here we present the unmixed case, $X_t = 0$. The horizontal and vertical axes gives the mass of the left- and right-handed stops. The region to the left of the orange lines will be excluded by CEPC constraints on the S and T parameters. The solid, dashed, and dotted orange lines correspond to the three scenarios from Fig. 4.2. The region below and to the left of the purple curve is expected to be excluded by CEPC measurements of Higgs boson branching ratios. We see that electroweak precision tests and Higgs precision measurements are complementary and have comparable strength. Dashed blue lines display contours of fine-tuning, which will be probed at the few percent level.

The constraint on stop masses translates into a probe of fine-tuning through the quadratic sensitivity of the Higgs mass parameter to the stop mass,

$$\Delta_{\tilde{t}} \approx \frac{3y_t^2(m_{\tilde{t}_1}^2 + m_{\tilde{t}_2}^2 + A_t^2)\log(\Lambda/m_{\rm EW})}{4\pi^2 m_h^2}. \tag{4.9}$$

We plot this fine-tuning in Fig. 4.7 (for the choice $\Lambda = 30$ TeV) with blue dashed lines. CEPC constraints will translate into fine-tuning of a few percent. There is an exception in the "stop blind spot" region of parameter space, which occurs for a critical mixing $X_t^2 \approx \left|m_{\tilde{t}_1}^2 - m_{\tilde{t}_2}^2\right|$ at which the light stop mass eigenstate has zero coupling to the Higgs boson [42, 55]. Electroweak precision measurements are a powerful probe of tuning away from this small window of parameter space, which may be accessible to alternative probes like $b \to s\gamma$.

In the interesting case of Folded Supersymmetry [56], where the top partners that cancel divergences in the Higgs mass have Standard Model electroweak quantum numbers but not color quantum numbers, the T parameter constraint is a more effective precision probe than Higgs coupling measurements. This is because folded stops modify the Higgs coupling to photons but not to gluons, leading to weak bounds [42, 55, 57]. The oblique parameter bound depends only on electroweak couplings and goes through unscathed. Thus, for one of the scenarios that will be most difficult to probe at the LHC, a future circular collider can lead to novel and important constraints through measurements near the Z pole.

4.3.2 Composite Higgs scenarios

Supersymmetry is not the only possibility for natural new physics at the weak scale. The other leading contender is the case of a composite (pseudo-Nambu-Goldstone or PNGB) Higgs boson. Unlike the Standard Model Higgs, a PNGB Higgs generally will not completely unitarize the scattering of longitudinal W and Z bosons, because the exchange of heavier resonances (like the technirho meson) also play a role. The failure of the Higgs to unitarize the amplitude is associated with v^2/f^2 corrections to the coupling of the Higgs boson to SU(2)$_L$ gauge bosons, with f the PNGB decay constant. The minimal composite Higgs has, for instance, [58]:

$$\kappa_W = \kappa_Z = \sqrt{1 - \frac{v^2}{f^2}}, \tag{4.10}$$

Because the primary Higgs production mechanism at an e^+e^- collider is Higgsstrahlung, $e^+e^- \to Z^* \to Zh$, the coupling κ_Z is especially well-measured and provides a powerful constraint on the scale f. The details of how a composite Higgs theory modifies the S and T parameters are model-dependent. As a general guideline they receive corrections suppressed by the scale m_ρ, the mass of a technirho meson, i.e. a composite state sourced by the SU(2)$_L$ current. We expect contributions to the S parameter of order

$$S \sim \frac{4\pi v^2}{m_\rho^2} \sim \frac{N}{4\pi}\frac{v^2}{f^2}, \tag{4.11}$$

where we have used the NDA estimate $m_\rho \sim 4\pi f/\sqrt{N}$. The number of colors N in the composite sector is generally order one—rarely larger than 10 due to phenomenological

constraints like Landau poles and cosmological problems—and so we will take as our benchmark estimate

$$S \approx \frac{v^2}{4f^2}. \tag{4.12}$$

Comparing equations 4.10 and 4.12, we see that the parametric size of corrections to Higgs boson couplings and to the S parameter are linked. Numerically the reach for f is close to 4 TeV from Higgs measurement and 1 TeV from S parameter constraint at CEPC.

4.3.3 Fermionic Higgs Portal

The lowest dimension operators coupling new singlets to the SM are via the so-called Higgs portal, i.e., operators of the form $H^\dagger H \mathcal{O}_{\rm NP}$ where $\mathcal{O}_{\rm NP}$ is some SM-singlet set of fields. While singlet scalars have been discussed previously in this document, here the focus is on the "CP-even fermionic Higgs portal" operator $H^\dagger H \bar{\chi}\chi$, with χ a SM-singlet fermion. Studies of this operator have been carried out in recent literature (see, e.g., Refs. [59–61] and references therein). Since the new states are weakly coupled, precision electroweak and Higgs physics will be important to study this new physics, and test the possible UV-completions of the operator. Presented here is a summary of the constraints which high-precision measurements of the electroweak observables S and T, and of the Higgs-strahlung cross section σ_{Zh}, may place on two different UV completions of this scenario.

The simplest possible UV completion of the CP-even fermionic Higgs portal is to take the Standard Model (SM) augmented by the vector-like Dirac fermion SM-singlet χ, and add to it a SM-singlet scalar S, coupling via the following Lagrangian (see, e.g., Ref. [60])

$$\mathcal{L} = \mathcal{L}_{\rm SM} + i\bar{\chi}\partial\!\!\!/\chi - m_\chi \bar{\chi}\chi + \frac{1}{2}(\partial_\mu S)^2 - V(S) + a\, m_S S|H|^2 + \frac{\epsilon_S}{2} S^2 |H|^2 - \kappa_S S \bar{\chi}\chi, \tag{4.13}$$

where a, ϵ_S and κ_S are real parameters.

This model is just the renormalisable scalar Higgs portal model (see, e.g., Ref. [45] for detailed discussion), augmented with the singlet-χ Yukawa coupling. In the limit where the S has mass $m_S \gg v$, it can be integrated out at tree-level to give rise to the following operators

$$\mathcal{L}_{\rm EFT} \supset -\frac{a\kappa_S}{m_S} H^\dagger H \bar{\chi}\chi + \frac{a^2}{m_S^2}\frac{1}{2}(\partial_\mu |H|^2)^2 + \cdots . \tag{4.14}$$

Depending on the parameters, there can be one additional dimension-6 operator appearing in the Lagrangian [45]: $|H|^6$ which, taken together with the ability to change the sign of the $|H|^4$ operator in the SM-Higgs Lagrangian and yet maintain a stable minimum to the Higgs potential, can have interesting implications for the order of the electroweak phase transition (see, e.g., Ref. [45]).

The fermionic Higgs portal operator $H^\dagger H \bar{\chi}\chi$ leads to a variety of effects (see, e.g., Ref. [59] for a detailed analysis): upon EWSB, it contributes to the mass of the χ field, and allows both $h\bar{\chi}\chi$ and $h^2\bar{\chi}\chi$ couplings. Note also that it is possible for the χ field play the role of the (thermal relic) dark matter and saturate the relic density. However, due to the stringent LUX [62] direct detection bounds [59, 60], it is difficult to achieve this

with perturbative couplings. In particular, $m_S/(a\kappa_S) \sim 0.5$ TeV is required along with $m_\chi^{\text{physical}} \gtrsim 3$ TeV which, together with EFT validity, imply that the couplings must be fairly large, $a\kappa_S \gtrsim 2\pi$.

As has recently been emphasised in Ref. [63], and investigated further in, e.g., Refs. [45, 55], new-physics models such as this induce a modification to wave-function normalization of the Higgs (i.e., a modification of the momentum-dependent part of the Higgs 2-point function). This manifests itself in the EFT analysis at dimension-6 via the generation of the operator $\frac{1}{2}(\partial_\mu|H|^2)^2$. The resulting modifications of this "Higgs oblique" correction lead to corrections of all Higgs couplings, and in particular to modifications of the "Higgs-strahlung" process $e^+e^- \to Zh$, as mediated by an intermediate off-shell Z. As projections (see, e.g., Ref. [21] and references therein) for the CEPC indicate that a sub-percent accuracy is achievable on the measurement of σ_{Zh}, these limits are expected to be severely constraining. Taking the results of Ref. [55], it can be seen that for an estimate of $\Delta\sigma_{Zh}/\sigma_{Zh} \sim 0.5\%$, values of $m_S/a \lesssim 2.5$TeV could be ruled out at 95% confidence, with 5-σ discovery reach up to $m_S/a \sim 1.6$TeV; for a more aggressive estimate of $\Delta\sigma_{Zh}/\sigma_{Zh} \sim 0.1\%$, these values increase to 5.5TeV and 3.5TeV, respectively.

The Higgs portal can also be UV-completed by augmenting the SM with the same vector-like Dirac fermion singlet χ as before, along with a vector-like Dirac fermion $SU(2)$-doublet $F \sim (\mathbf{1}, \mathbf{2}, +1/2)$. These fields are coupled to the SM via the following Lagrangian:

$$\mathcal{L} = \mathcal{L}_{\text{SM}} + i\bar{\chi}\partial\!\!\!/\chi - m_\chi\bar{\chi}\chi + i\bar{F}D\!\!\!/F - M_F\bar{F}F - \kappa\bar{F}H\chi - \kappa\bar{\chi}H^\dagger F. \tag{4.15}$$

In the parameter region where $M_F \gg m_\chi$, the heavy doublet F can be integrated out, leading to the lowest-order effective operator being precisely the fermionic Higgs portal $H^\dagger H\bar{\chi}\chi$. The constraints on this UV completion will be discussed both in the regime where $M_F \gg m_\chi$, as well as in the more general mass parameter space, even though away from $M_F \gg m_\chi$, this model would not provide the UV completion to the fermionic Higgs portal operator. Further details on the results below can be found in Ref. [64].

Since the Yukawa-like coupling κ in (4.15) breaks the accidental global $SU(2)_V$ custodial symmetry [65] of the SM maximally, fairly large corrections to the precision electroweak T parameter [19, 20] are to be expected. Additionally, the mass-splitting (i.e., weak iso-spin breaking) in the F doublet which arises after electroweak symmetry breaking (EWSB), leads to the expectation that there will additionally be contributions to the electroweak S parameter.

Note that custodial symmetry could be restored—or broken in a controlled fashion—by augmenting the field content with an additional positively-charged vector-like fermion $\psi \sim (\mathbf{1}, \mathbf{1}, +1)$ with the same Yukawa-like coupling to the H and F fields; the mass-splitting $(m_\psi - m_\chi)^2$ then controls the degree to which the symmetry is broken.

Furthermore, this model also generates, at one-loop, both the Higgs oblique correction discussed above and other corrections to couplings, so that even if the large corrections to T were to be tuned away by, e.g., the method indicated in the previous paragraph, significant constraints would still be expected to remain on this model from precision measurement of, *inter alia*, the Higgs-strahlung cross section.

The precision electroweak observables predicted in this model can be extracted in a variety of ways, which are detailed in Ref. [64]: (1) assuming a hierarchy of scales $M_F \gg m_\chi \gg v \sim m_Z$, the F and χ can both be integrated out of the theory at the

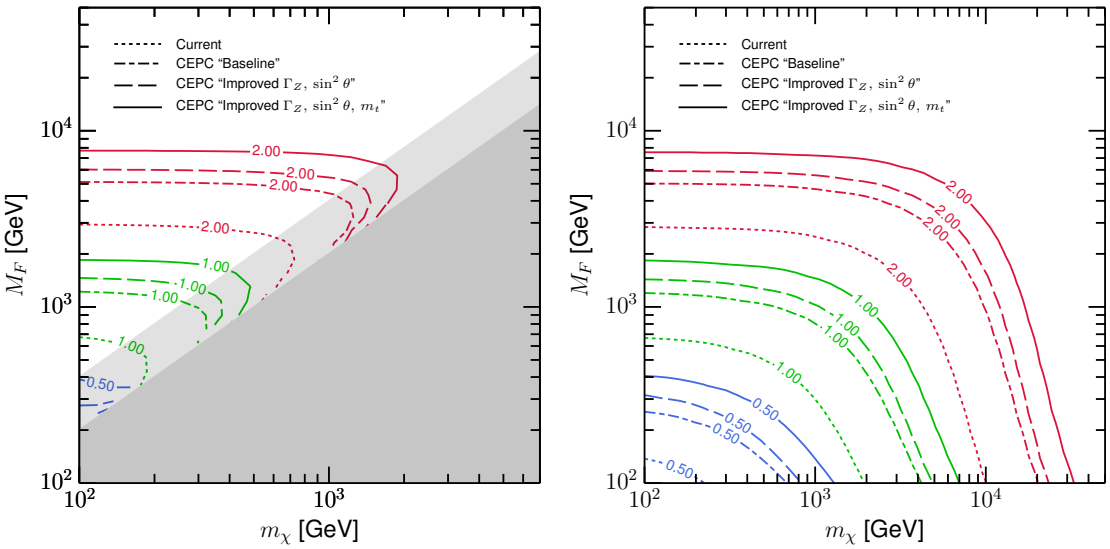

Figure 4.8 Approximate 95% confidence exclusion regions ($-2\ln[\mathcal{L}/\mathcal{L}_0] \gtrsim 5.99$) from measurement of the precision electroweak variables (S, T). These are presented as boundaries in the allowed mass parameter space for fixed representative values of κ, as annotated on each colored line; the unshaded region to the lower-left of these lines is excluded for the given value of κ. These results in the left plot are from the EFT computation of (S, T). The light shaded region, $M_F/4 \lesssim m_\chi \lesssim M_F/2$, denotes the region where the EFT begins to break down: the error in the EFT result for T compared to the v^2/M_F^2 piece of the full result (i.e., the "dimension-6 part of" the full result) is $\sim 20\%$ at $m_\chi \sim M_F/4$, reaches $\sim 50\%$ at $m_\chi \sim M_F/3$, and becomes $> 100\%$ before $m_\chi \sim M_F/2$. In the dark-shaded region, $m_\chi \gtrsim M_F/2$ and the results have consequently been masked as they are invalid. The results in the right plot are from the full one-loop computation are hence are valid for arbitrary masses. The various line styles correspond to current constraints and various projected constraints on (S, T) for the proposed CEPC collider. The underlying limits on (S, T) are extracted from Ref. [21] (and references therein): the current limits from Fig. 1 of that reference, and the CEPC limits from Fig. 4 of that reference.

appropriate mass scales, and the S and T parameters can be read off from the resulting set of dimension-6 operators in an appropriate basis [47, 48, 66, 67]. This approach requires a one-loop matching computation to find the Wilson coefficients of the relevant operators. Alternatively, (2) the one-loop computation of S and T can be carried out directly by evaluating the necessary vector-boson self-energy diagrams with closed loops of F and/or χ fermions.

The result of the EFT-based analysis is the following precision electroweak variables [64], correct to dimension-6 and one-loop:

$$S \approx \frac{2\kappa^2}{9\pi}\frac{v^2}{M_F^2}\left[1 - \frac{7}{4}\frac{m_\chi}{M_F} - \frac{3}{2}\frac{m_\chi^2}{M_F^2} + \cdots\right] \tag{4.16}$$

$$T \approx \frac{\alpha_\kappa}{\alpha_e}\frac{5\kappa^2}{24\pi}\frac{v^2}{M_F^2}\left[1 - \frac{2}{5}\frac{m_\chi}{M_F} - 3\frac{m_\chi^2}{M_F^2} + \cdots\right] \quad \text{where} \quad \alpha_\kappa \equiv \frac{\kappa^2}{4\pi} \tag{4.17}$$

$$U = 0 + (\text{dimension-8}). \tag{4.18}$$

The left plot of Fig. 4.8 shows the exclusion regions in the mass parameter space which, for the fixed representative values of κ, would yield electroweak precision variables (S, T) in conflict with the 95% confidence limits on the latter, as taken from Ref. [21]. These

results are as computed in the EFT, and are shown for both current limits (LEP+SLD) and for the proposed CEPC collider.

In this region of parameter space, the limits shown are driven almost exclusively by the size of the T parameter, which in this region is parametrically enhanced by $\sim \alpha_\kappa/\alpha_e$ compared to the S parameter.[1] In the regime where the EFT is valid, $m_\chi \lesssim \frac{1}{4}M_F$, the exclusion reach is largely insensitive to the value of m_χ. Already with current (LEP+SLD) constraints on S, T, masses M_F below about 675GeV can be ruled out for $\kappa \sim 1$; due to the κ^4 dependence of T, this lower limit increases to around 2.9TeV for a coupling $\kappa \sim 2$, but there is essentially no limit in the regime where the EFT is valid if $\kappa \sim 0.5$. With even with the "baseline" sensitivity for the CEPC [21], these lower limits increase by around a factor of 1.75 owing to the factor ~ 3.5 times stronger limits on S and T in this scenario as compared to the current bounds. For the CEPC scenario with improved measurements of Γ_Z, and $\sin^2\theta$ only [21], the lower limits on M_F increases by a factor of ~ 2 compared to the present limits (or 20% compared to the baseline scenario), rising to $M_F \sim 1.5(6)$ TeV for $\kappa \sim 1.0(2.0)$, in the limit where $m_\chi \ell^+\ell^- M_F$. This results from the tightening in the limit on S and T by factor of 4 compared to present limits. For best-case scenario for the CEPC, with improved measurements of Γ_Z, $\sin^2\theta$, and m_t [21], the lower limits on M_F are increased by a factor of ~ 2.7 compared to the present limits (or 30% over the previous scenario), raising them $\sim 1.8(7.7)$ TeV for $\kappa \sim 1.0(2.0)$, in the limit where $m_\chi \ell^+\ell^- M_F$.

The exclusion regions due to precision electroweak constraints arising from the full loop computation of S, T are shown in the right plot of Fig. 4.8. In the limit where $m_\chi \ell^+\ell^- M_F$ it is clear that the results agree well with the EFT computation, the small differences being ascribable to the neglect of dimension-8 and higher operators in the EFT.

Focussing here exclusively on the parameter space not covered by the EFT, the most obvious point is that a significantly larger region of the m_χ parameter space at small M_F is ruled out than *vice versa*. For example, the fully improved CEPC results indicate that if $M_F \sim 100$GeV, m_χ up to ~ 33TeV can be ruled out for $\kappa \sim 2.0$, compared to M_F being ruled out up to ~ 7.7TeV if $m_\chi \sim 100$GeV. This pattern is generic for all the results; it traces its origin to the fact that in this model for $m_\chi \ell^+\ell^- M_F$, S and T are both positive and, roughly speaking, $|S| \sim 0.1|T|$ near the exclusion limit, whereas for $M_F \ell^+\ell^- m_\chi$, T is positive and S is negative, with $|S| \sim |T|$ near the exclusion limit (indeed, $|S| > |T|$ is possible here) [64]. Clearly, the larger deviation from $(S, T) = (0, 0)$ in this region leads to the stronger limits. There is also a stronger dependence of the boundary of the exclusion region on M_F at small m_χ than vice versa.

Fig. 4.9 shows the regions in the mass parameter space (m_χ, M_F) which, for the given fixed value of κ, would yield a value of σ_{Zh} in conflict with the projected 95% CL limits on the latter, assuming that at the CEPC with 5/ab of data at $\sqrt{s} = 240$GeV, a sensitivity of $\Delta\sigma_{Zh}/\sigma_{Zh} \lesssim 0.5\%$ is obtained. Note that the limits on M_F from σ_{Zh} measurements, in the region where the EFT results are valid, are more sensitive to the value of m_χ than

[1] In this model, this arises because, for $M_F \gg m_\chi$, $\Pi_{W^+W^-}(0) - c_W^2\Pi_{ZZ}(0) \sim g^2(\kappa^2 v^2)(\kappa^2 v^2/M_F^2)$ while $\Pi'_{ZZ}(0) \sim (g^2 + (g')^2)(\kappa^2 v^2/M_F^2)$. Therefore, $T \sim \alpha_e^{-1} M_W^{-1}\left(\Pi_{W^+W^-}(0) - c_W^2\Pi_{ZZ}(0)\right) \sim (\kappa^2/\alpha_e)(\kappa^2 v^2/M_F^2)$ since $M_W^2 \sim g^2 v^2$ (the corrections to this tree-level SM relationship from the new physics, or SM loops, yield formally higher-order effects on T), while $S \sim c_W^2 s_W^2 \alpha_e^{-1}\Pi'_{ZZ}(0) \sim \kappa^2 v^2/M_F^2$.

the electroweak precision limits, with lower bounds on M_F lying around 590GeV, 1.9TeV, 4TeV, and 7TeV, respectively for $\kappa \sim 1.0$, 2.0 , 3.0, and 4.0 in the limit where $m_\chi \ell^+\ell^- M_F$. These lower limits rise to approximately 660GeV, 2.5TeV, 5.6TeV and 10TeV, respectively, for $m_\chi \sim M_F/4$, which is the validity of the EFT begins to be questionable.

In none of these cases are the limits from the precision Higgsstrahlung measurement competitive with the electroweak precision programs at these future colliders in imposing constraints on this specific model; nevertheless, these results do demonstrate that the σ_{Zh} measurement would provide a strong complimentary constraint on closely allied models where the T parameter is dialed away, as discussed above.

Although the full one-loop computation of σ_{Zh} has not been carried out in Ref. [64], the EFT results are indicative of the relative strengths of the constraints from precision electroweak measurements and from Higgsstrahlung measurements which one can expect at the CEPC.

An heuristic[2] understanding of the differences in the strength of the EWPO and σ_{Zh} limits can be obtained by examining a subset of the operators relevant for the generation of T and $\delta\sigma_{Zh}$: suppose $\mathcal{L} = \mathcal{L}_{\rm SM} + \frac{a}{2\Lambda^2}(H^\dagger D_\mu H - h.c.)^2 + \frac{b}{2\Lambda^2}(\partial_\mu |H|^2)^2$. It can then be easily shown that $T = (av^2)/(\alpha_e \Lambda^2)$, and a little more work shows that $\delta\sigma_{Zh}/\sigma_{Zh} \approx -(v^2/\Lambda^2)(b + a \cdot f(g, g'))$, where the $f(g, g')$ is a complicated function of the gauge couplings which evaluates to approximately 0.83, taking the approximate Z-pole values of the running gauge couplings ($g = 0.648, g' = 0.358$). The anticipated one-parameter 95% confidence measurement uncertainties on T (restricted to $S = U = 0$) as adapted from Ref. [21] are 2.0×10^{-2}, 1.5×10^{-2}, and 8.9×10^{-3} for the CEPC baseline,"Improved $\Gamma_Z, \sin^2\theta$", and "Improved $\Gamma_Z, \sin^2\theta, m_t$" scenarios, respectively. The resulting 95% confidence lower bounds on $\Lambda/\sqrt{|a|}$ are approximately 20TeV, 23TeV and 29TeV, respectively. On the other hand the 95% confidence measurement uncertainty on the Higgs-strahlung cross section at CEPC is projected to be $\sim 1\%$ (corresponding to the 68% confidence projection $\delta\sigma_{Zh}/\sigma_{Zh} = 0.5\%$ used above), which yields the limit $\Lambda/\sqrt{|b + 0.83a|} \gtrsim 2.5$TeV. It is clear that the latter bounds are significantly weaker than the EWPO constraints for roughly equally-sized Wilson coefficients, which is a scenario one might expect when these operators are generated at the same loop order (provided of course that custodial symmetry is broken). Parametrically, the relative strength of the limits can be traced to the enhancement of T by a factor of $1/\alpha_e$. The conclusion that, absent custodial symmetry protection, the EWPO limits are stronger than the Higgs-strahlung cross section limits is quantitatively weakened, but not qualitatively changed if the full set of operators [55] contributing to σ_{Zh} are considered.

References

[1] J. Erler, S. Heinemeyer, W. Hollik, G. Weiglein, and P. Zerwas, *Physics impact of GigaZ*, Phys.Lett. **B486** (2000) 125–133, arXiv:hep-ph/0005024 [hep-ph].

[2] The ALEPH , DELPHI , L3, OPAL and LEP Collaboration, J. Alcaraz et al., *A Combination of preliminary electroweak measurements and constraints on the*

[2]The full set of operators contributing to $\delta\sigma_{Zh}$ contains more operators than considered here, and these other operators are generated in this model [64]. See, e.g., Ref. [55] for a more complete discussion.

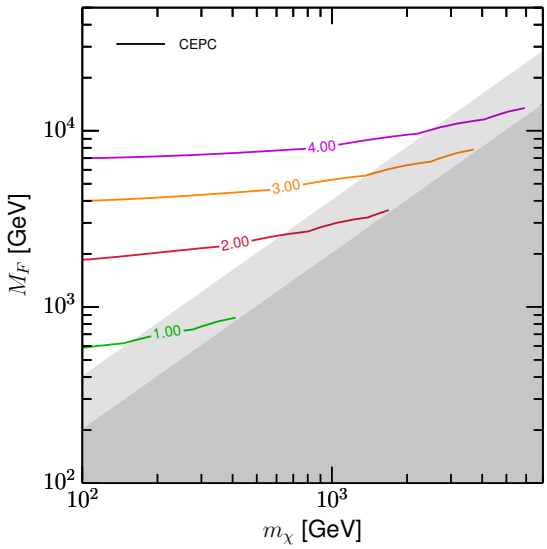

Figure 4.9 Approximate 95% confidence exclusion regions ($-2\ln[\mathcal{L}/\mathcal{L}_0] \gtrsim 3.84$) from precision measurements of σ_{Zh}. These are presented as boundaries in the allowed mass parameter space for fixed representative values of κ, as annotated on each colored line; the unshaded region to the lower-left of these lines is excluded for the given value of κ. These results are from the EFT computation of σ_{Zh}. Absent the full loop computation, it is not possible to quote an error in the EFT-based result, but based on the comparison of the EFT-based and full computations for the EWPO results, it is probable that the EFT results here are questionable in the light shaded region, $M_F/4 \lesssim m_\chi \lesssim M_F/2$, and are almost certainty invalid in the dark-shaded region, $m_\chi \gtrsim M_F/2$, where the results have consequently been masked. The precision assumed for the CEPC constraints is $\Delta\sigma_{Zh}/\sigma_{Zh} = 0.5\%$, the predicted sensitivity with 5/ab of data at $\sqrt{s} = 240$GeV.

standard model, arXiv:hep-ex/0612034 [hep-ex].

[3] The SLD Collaboration, K. Abe et al., *Measurement of the branching ratio of the Z0 into heavy quarks*, Phys.Rev. **D71** (2005) 112004, arXiv:hep-ex/0503005 [hep-ex].

[4] The ALEPH Collaboration, A. Heister et al., *Measurement of A^b(FB) using inclusive b hadron decays*, Eur.Phys.J. **C22** (2001) 201–215, arXiv:hep-ex/0107033 [hep-ex].

[5] The OPAL Collaboration, G. Abbiendi et al., *Measurement of the b quark forward backward asymmetry around the Z0 peak using an inclusive tag*, Phys.Lett. **B546** (2002) 29–47, arXiv:hep-ex/0209076 [hep-ex].

[6] The DELPHI Collaboration, J. Abdallah et al., *Determination of A^b(FB) at the Z pole using inclusive charge reconstruction and lifetime tagging*, Eur.Phys.J. **C40** (2005) 1–25, arXiv:hep-ex/0412004 [hep-ex].

[7] The L3 Collaboration, M. Acciarri et al., *Measurement of the $e^+e^- \to Z \to b\bar{b}$ forward–backward asymmetry and the B0 anti-B0 mixing parameter using prompt leptons*, Phys.Lett. **B448** (1999) 152–162.

[8] The DELPHI Collaboration, P. Abreu et al., *A Precise measurement of the partial decay width ratio $R_b^0 = \Gamma(b\bar{b})/\Gamma(\mathrm{had})$*, Eur.Phys.J. **C10** (1999) 415–442.

[9] R. Brinkmann, I. Ginzburg, N. Holtkamp, G. Jikia, O. Napoly, et al., *An Interaction region for gamma gamma and gamma - electron collisions at TESLA / SBLC*, Nucl.Instrum.Meth. **A406** (1998) 13–49, arXiv:hep-ex/9707017 [hep-ex].

[10] The L3 Collaboration, P. Achard et al., *Single photon and multiphoton events with missing energy in e^+e^- collisions at LEP*, Phys.Lett. **B587** (2004) 16–32, arXiv:hep-ex/0402002 [hep-ex].

[11] The DELPHI Collaboration, J. Abdallah et al., *Photon events with missing energy in e+ e- collisions at $\sqrt{s}$ = 130-GeV to 209-GeV*, Eur.Phys.J. **C38** (2005) 395–411, arXiv:hep-ex/0406019 [hep-ex].

[12] T.-C. Huang and F. Petriello, *Rare exclusive decays of the Z-boson revisited*, arXiv:1411.5924 [hep-ph].

[13] Y. Grossmann, M. König, and M. Neubert, *Exclusive Radiative Decays of W and Z Bosons in QCD Factorization*, arXiv:1501.06569 [hep-ph].

[14] The ATLAS Collaboration, G. Aad et al., *Search for Higgs and Z Boson Decays to $J/\psi\gamma$ and $\Upsilon(nS)\gamma$ with the ATLAS Detector*, arXiv:1501.03276 [hep-ex].

[15] The OPAL Collaboration, G. Abbiendi et al., *Measurement of the mass and width of the W boson*, Eur.Phys.J. **C45** (2006) 307–335, arXiv:hep-ex/0508060 [hep-ex].

[16] The DELPHI Collaboration, J. Abdallah et al., *Measurement of the Mass and Width of the W Boson in e^+e^- Collisions at $\sqrt{s}$ = 161-GeV - 209-GeV*, Eur.Phys.J. **C55** (2008) 1–38, arXiv:0803.2534 [hep-ex].

[17] The L3 Collaboration, P. Achard et al., *Measurement of the mass and the width of the W boson at LEP*, Eur.Phys.J. **C45** (2006) 569–587, arXiv:hep-ex/0511049 [hep-ex].

[18] The ALEPH Collaboration, S. Schael et al., *Measurement of the W boson mass and width in e^+e^- collisions at LEP*, Eur.Phys.J. **C47** (2006) 309–335, arXiv:hep-ex/0605011 [hep-ex].

[19] M. E. Peskin and T. Takeuchi, *A New constraint on a strongly interacting Higgs sector*, Phys.Rev.Lett. **65** (1990) 964–967.

[20] M. E. Peskin and T. Takeuchi, *Estimation of oblique electroweak corrections*, Phys.Rev. **D46** (1992) 381–409.

[21] J. Fan, M. Reece, and L.-T. Wang, *Possible Futures of Electroweak Precision: ILC, FCC-ee, and CEPC*, arXiv:1411.1054 [hep-ph].

[22] J. Erler and A. Freitas, *Electroweak Model and Constraints on New Physics*, Particle Data Group review . http://pdg.lbl.gov/2014/reviews/rpp2014-rev-standard-model.pdf.

[23] Particle Data Group, J. Beringer, et al., *Review of Particle Physics (RPP)*, Phys.Rev. **D86** (2012) 010001.

[24] G. P. Lepage, P. B. Mackenzie, and M. E. Peskin, *Expected Precision of Higgs Boson Partial Widths within the Standard Model*, arXiv:1404.0319 [hep-ph].

[25] S. Bodenstein, C. Dominguez, K. Schilcher, and H. Spiesberger, *Hadronic contribution to the QED running coupling $\alpha(M_Z^2)$*, Phys.Rev. **D86** (2012) 093013, arXiv:1209.4802 [hep-ph].

[26] M. Baak, J. Cuth, J. Haller, A. Hoecker, R. Kogler, et al., *The global electroweak fit at NNLO and prospects for the LHC and ILC*, arXiv:1407.3792 [hep-ph].

[27] The ALEPH , DELPHI , L3 , OPAL , SLD , LEP and SLD Collaboration, S. Schael et al., *Precision electroweak measurements on the Z resonance*, Phys.Rept. **427** (2006) 257–454, arXiv:hep-ex/0509008 [hep-ex].

[28] The ATLAS , CDF , CMS and D0 Collaboration, *First combination of Tevatron and LHC measurements of the top-quark mass*, arXiv:1403.4427 [hep-ex].

[29] The CMS Collaboration, *Projected improvement of the accuracy of top-quark mass measurements at the upgraded LHC*, CMS-PAS-FTR-13-017, 2013.

[30] J. Erler, *Status of Precision Extractions of α_s and Heavy Quark Masses*, arXiv:1412.4435 [hep-ph].

[31] M. Awramik, M. Czakon, A. Freitas, and G. Weiglein, *Precise prediction for the W boson mass in the standard model*, Phys.Rev. **D69** (2004) 053006, arXiv:hep-ph/0311148 [hep-ph].

[32] M. Awramik, M. Czakon, and A. Freitas, *Electroweak two-loop corrections to the effective weak mixing angle*, JHEP **0611** (2006) 048, arXiv:hep-ph/0608099 [hep-ph].

[33] A. Freitas, *Higher-order electroweak corrections to the partial widths and branching ratios of the Z boson*, JHEP **1404** (2014) 070, arXiv:1401.2447 [hep-ph].

[34] J. Wudka, *Effective Lagrangians (for electroweak physics)*, arXiv:hep-ph/9405206 [hep-ph].

[35] R. Barbieri and L. Maiani, *Renormalization of the Electroweak rho Parameter from Supersymmetric Particles*, Nucl.Phys. **B224** (1983) 32.

[36] S. Dimopoulos and G. Giudice, *Naturalness constraints in supersymmetric theories with nonuniversal soft terms*, Phys.Lett. **B357** (1995) 573–578, arXiv:hep-ph/9507282 [hep-ph].

[37] A. Pomarol and D. Tommasini, *Horizontal symmetries for the supersymmetric flavor problem*, Nucl.Phys. **B466** (1996) 3–24, arXiv:hep-ph/9507462 [hep-ph].

[38] A. G. Cohen, D. Kaplan, and A. Nelson, *The More minimal supersymmetric standard model*, Phys.Lett. **B388** (1996) 588–598, arXiv:hep-ph/9607394 [hep-ph].

[39] P. Meade and M. Reece, *Top partners at the LHC: Spin and mass measurement*, Phys.Rev. **D74** (2006) 015010, arXiv:hep-ph/0601124 [hep-ph].

[40] R. Kitano and Y. Nomura, *Supersymmetry, naturalness, and signatures at the LHC*, Phys.Rev. **D73** (2006) 095004, arXiv:hep-ph/0602096 [hep-ph].

[41] M. Perelstein and C. Spethmann, *A Collider signature of the supersymmetric golden region*, JHEP **0704** (2007) 070, arXiv:hep-ph/0702038 [hep-ph].

[42] J. Fan, M. Reece, and L.-T. Wang, *Precision Natural SUSY at CEPC, FCC-ee and ILC*, arXiv:1412.3107 [hep-ph].

[43] M. Drees, K. Hagiwara, and A. Yamada, *Process independent radiative corrections in the minimal supersymmetric standard model*, Phys.Rev. **D45** (1992) 1725–1743.

[44] J. R. Espinosa, C. Grojean, V. Sanz, and M. Trott, *NSUSY fits*, JHEP **1212** (2012) 077, arXiv:1207.7355 [hep-ph].

[45] B. Henning, X. Lu, and H. Murayama, *What do precision Higgs measurements buy us?*, arXiv:1404.1058 [hep-ph].

[46] B. Henning, X. Lu, and H. Murayama, *How to use the Standard Model effective field theory*, arXiv:1412.1837 [hep-ph].

[47] B. Grzadkowski, M. Iskrzynski, M. Misiak, and J. Rosiek, *Dimension-Six Terms in the Standard Model Lagrangian*, JHEP **1010** (2010) 085, arXiv:1008.4884 [hep-ph].

[48] W. Buchmuller and D. Wyler, *Effective Lagrangian Analysis of New Interactions and Flavor Conservation*, Nucl.Phys. **B268** (1986) 621–653.

[49] C. Grojean, W. Skiba, and J. Terning, *Disguising the oblique parameters*, Phys.Rev. **D73** (2006) 075008, arXiv:hep-ph/0602154 [hep-ph].

[50] Z. Han, *Effective Theories and Electroweak Precision Constraints*, Int.J.Mod.Phys. **A23** (2008) 2653–2685, arXiv:0807.0490 [hep-ph].

[51] H. E. Haber and R. Hempfling, *Can the mass of the lightest Higgs boson of the minimal supersymmetric model be larger than m(Z)?*, Phys.Rev.Lett. **66** (1991) 1815–1818.

[52] R. Barbieri, M. Frigeni, and F. Caravaglios, *The Supersymmetric Higgs for heavy superpartners*, Phys.Lett. **B258** (1991) 167–170.

[53] J. Casas, J. Espinosa, M. Quiros, and A. Riotto, *The Lightest Higgs boson mass in the minimal supersymmetric standard model*, Nucl.Phys. **B436** (1995) 3–29, arXiv:hep-ph/9407389 [hep-ph].

[54] M. S. Carena, J. Espinosa, M. Quiros, and C. Wagner, *Analytical expressions for radiatively corrected Higgs masses and couplings in the MSSM*, Phys.Lett. **B355** (1995) 209–221, arXiv:hep-ph/9504316 [hep-ph].

[55] N. Craig, M. Farina, M. McCullough, and M. Perelstein, *Precision Higgsstrahlung as a Probe of New Physics*, arXiv:1411.0676 [hep-ph].

[56] G. Burdman, Z. Chacko, H.-S. Goh, and R. Harnik, *Folded supersymmetry and the LEP paradox*, JHEP **0702** (2007) 009, arXiv:hep-ph/0609152 [hep-ph].

[57] J. Fan and M. Reece, *A New Look at Higgs Constraints on Stops*, JHEP **1406** (2014) 031, arXiv:1401.7671 [hep-ph].

[58] K. Agashe, R. Contino, and A. Pomarol, *The Minimal composite Higgs model*, Nucl.Phys. **B719** (2005) 165–187, arXiv:hep-ph/0412089 [hep-ph].

[59] M. A. Fedderke, J.-Y. Chen, E. W. Kolb, and L.-T. Wang, *The Fermionic Dark Matter Higgs Portal: an effective field theory approach*, JHEP **1408** (2014) 122, arXiv:1404.2283 [hep-ph].

[60] L. Lopez-Honorez, T. Schwetz, and J. Zupan, *Higgs portal, fermionic dark matter, and a Standard Model like Higgs at 125 GeV*, Phys.Lett. **B716** (2012) 179–185, arXiv:1203.2064 [hep-ph].

[61] A. De Simone, G. F. Giudice, and A. Strumia, *Benchmarks for Dark Matter Searches at the LHC*, JHEP **1406** (2014) 081, arXiv:1402.6287 [hep-ph].

[62] THe LUX Collaboration, D. Akerib et al., *First results from the LUX dark matter experiment at the Sanford Underground Research Facility*, Phys.Rev.Lett. **112** (2014) 091303, arXiv:1310.8214 [astro-ph.CO].

[63] N. Craig, C. Englert, and M. McCullough, *New Probe of Naturalness*, Phys.Rev.Lett. **111** (2013) no. 12, 121803, arXiv:1305.5251 [hep-ph].

[64] M. A. Fedderke, T. Lin, and L.-T. Wang. To appear, 2015.

[65] P. Sikivie, L. Susskind, M. B. Voloshin, and V. I. Zakharov, *Isospin Breaking in Technicolor Models*, Nucl.Phys. **B173** (1980) 189.

[66] K. Hagiwara, S. Ishihara, R. Szalapski, and D. Zeppenfeld, *Low-energy effects of new interactions in the electroweak boson sector*, Phys.Rev. **D48** (1993) 2182–2203.

[67] S. Willenbrock and C. Zhang, *Effective Field Theory Beyond the Standard Model*, Ann.Rev.Nucl.Part.Sci. **64** (2014) 83–100, arXiv:1401.0470 [hep-ph].

CHAPTER 5

FLAVOR PHYSICS AT THE CEPC

5.1 Introduction

As we have seen, the amazing precision with which the CEPC probes Higgs and Z boson couplings will allow an unprecedented probe of high energy physics up to the multi-TeV scale. In this section, we show that the CEPC will also allow a direct probe of an entirely different set of fascinating phenomena, associated with low-energy hadron spectroscopy and flavor physics.

We understand that the luminosity is not able to reach $1 \times 10^{35} cm^{-2} s^{-1}$ *with current accelerator design, however, we still expect to have opportunity to improve the design luminosity in the future. So for this chapter we assume instantaneous luminosity of* $1 \times 10^{35} cm^{-2} s^{-1}$*, and an integrated luminosity of 2.5* ab^{-1} *will be collected at CEPC with one-year running on Z pole at two collision points.*

We have a special situation in e^+e^- collisions: most data from a Z^0 factory are well described by two jets of hadrons. Most of beauty and charm hadrons come from energetic jets, and beauty & anti-beauty hadrons mostly appear on opposite sites and somewhat also for charm hadrons. It is rare that a pair of beauty baryon & beauty anti-baryon appear in the same Final States (FS). Instead we get the same probability for FS with $B_i\bar{B}_jX$ & $B_j\bar{B}_iX$, but also $\Lambda_b\bar{B}X$ & $\bar{\Lambda}_bBX$ with decent rates; likewise for FS with $D_i\bar{D}_jX$ & $D_j\bar{D}_iX$ and $\Lambda_c\bar{D}X$ & $\bar{\Lambda}_cDX$.

The PDG gives the ratio $\Gamma(Z^0 \to \bar{b}b)/\Gamma(Z^0) \simeq 0.15$. In Table 5.1 we show the numbers of different beauty hadrons produced based on direct rate measurements performed at LEP [1]. The SM produces at least the leading source of CP asymmetries in $\Delta B \neq 0$, which is large in B_d, B_u and B_s (except *in*direct CP violation in the latter). Therefore the real goal is to find non-leading source from the ND.

Table 5.1 The $b-$hadron fractions in Z decays are calculated by combining direct rate measurements performed at LEP from HFAG [1]. The B^+ and B^0 mesons are assumed to be produced in equal amount at Z^0 peak, and the sum of the fractions is constrained to unity. The expected numbers of $b-$hadrons are estimated by assuming an instantaneous luminosity of $1 \times 10^{35}\text{cm}^{-2}\text{s}^{-1}$ at Z^0 factory with one-year running at two collision points. For comparison, we also list the number of b-hadrons at the Belle-II with an integrated luminosity of about 50 ab^{-1} at $\Upsilon(4S)$ or $\Upsilon(5S)$ peak (about five-year running time). B_c production is neglected; in future studies one includes the latter.

b-hadron species	Fraction in decays of $Z^0 \to b\bar{b}$	Number of b-hadron at Z^0 peak	Fraction in $\Upsilon(4S)/(5S)$ decays	Number of b-hadron at $\Upsilon(4S)/(5S)$
B^0	0.404 ± 0.009	0.6×10^{10}	0.486 ± 0.006 ($\Upsilon(4S)$)	4.9×10^{10}
B^+	0.404 ± 0.009	0.6×10^{10}	0.514 ± 0.006 ($\Upsilon(4S)$)	5.1×10^{10}
B_s	0.103 ± 0.009	0.02×10^{10}	0.201 ± 0.030 ($\Upsilon(5S)$)	0.6×10^{10}
b baryons	0.089 ± 0.015	0.02×10^{10}	–	–

No CP asymmetries have been found in baryons transitions (except about our 'existence' in the universe). Therefore it would be an excellent achievement to find them with beauty (& charm) baryons, never mind if they come from the SM or not. With those numbers produced by beauty baryons one can probe CP asymmetries in Λ_b, $\Xi_b^{-,0}$ & Ω_b decays and even regional ones. Then there would be steps about impact of ND and its features. In particular there will be no competition from Belle II about the decays of beauty baryons.

For charm hadrons one gets similar numbers: $\Gamma(Z^0 \to \bar{c}c)/\Gamma(Z^0) \simeq 0.12$. The number of produced $D^0/\bar{D}^0/D^{\pm}/D_s/D^{*\pm}$ is about order of 10^9 at CEPC. No *indirect* CP violation has been found; it is close what one 'expects' from the SM. Also no *direct* CPV have been found in D^0, D^+, D_s^+, Λ_c etc. decays. There are two classes that can be differentiated in the SM, namely singly and doubly Cabibbo suppressed decays: in singly Cabibbo suppressed transitions (SCS) one expects a landscape of the order $\mathcal{O}(10^{-3})$ and basically zero in doubly Cabibbo suppressed ones (DCS). Re-scatterings are expected to produce large impacts as discussed below.

So far we have focus mostly on two-body hadronic FS for good reasons. Now we have to probe many-body FS in $\Delta B \neq 0 \neq \Delta D$; in particular we have a long history with tools to analyze Dalitz plots with three-body FS. Which is the best definition of 'regional' ones, it depends – and needs judgment. Furthermore it is crucial to measure FS with neutral hadrons.

Very rare decays from the class of $B \to \gamma X_s$, γX_d and $B \to l^+l^- X_s$, $l^+l^- X_d$ will be measured by LHCb collaboration with exclusive ones and by Belle-II with inclusive ones in the future. It seems that a Z^0 factory can measure many-body hadronic FS including $l = \tau$, since high reconstruction efficiency of τ decays at high energy (strong boost) is expected from experiences at LEP.

Furthermore we can probe dynamics of pairs of τ leptons. We talk about 6×10^9 of τ pairs that will been produced. Thus one can probe τ CP asymmetries in both decays and productions of τ leptons. Any CPV in τ sector will indicate physics beyond the SM (beyond CPV due to $K^0 - \bar{K}^0$ oscillations). Electric dipole moments (EDM) and weak dipole moments of τ can be studied with the processes $Z^0 \to \tau^+\tau^-(\gamma)$. In addition this Z^0 factory will definitely improve the measurements of anomalous magnetic moments of τ lepton.

In Sect. 5.2 we discuss CP asymmetries in the decays of beauty hadrons and charm hadrons; we talk about rare decays of B & D decays Sect. 5.3; we discuss CP violation in τ decays in Sect. 5.4 and charged lepton flavor violation in Sect. 5.5; we summarize in Sect. 5.6.

5.2 Beauty and Charm Transitions

Beauty Transitions The SM produces large CPV in the decays of B mesons [2]. Therefore we have to probe FS with non-leading source. We have some examples about the difference between averaged vs. regional ones as shown by LHCb data [3]. It is crucial to measure three- and four-body FS including neutral hadrons and also probe 'regional' asymmetries; the best definitions need 'judgment'.

There are a few competitions from both Belle-II and LHCb experiments on the tests of CKM unitarity. The Belle-II experiment will collect about 50 ab^{-1} at $\Upsilon(4S)$ peak, on which they will do excellent job for B_u and B_d cases and improve the triangle measurements by a factor 3-10. It seems that Belle II will spend some time to probe B_s for CPV in many-body FS and rare/very rare decays. However, Belle II would not be a strong competitor for this project, especially the time-dependent analysis in B_s sector will not be done at Belle-II. The LHCb experiment and its update will greatly improve the sensitivities in both B_s and B_c decays into charged final states. The CEPC project at Z^0 peak will not only have high statistics but also provide good performances for both charged and neutral final states for the B_s meson (even B_c meson). The most important thing is that both the $B_{d,s}$ and D mesons are strongly boosted in the rest frame of the Z^0 with the Lorentz boost factor of $(\beta\gamma)_{B,D} \sim 20$, so that the averaged decay length, for example, the D^0 meson at Z^0 peak, is about 2600 μm, while it is about 290 μm at Belle-II energy. Assuming the same impact parameter resolution of vertex detector as that in Belle-II, Z^0 factory will improve the proper time resolution by a factor of 10 times and measure the decay time of 10 times longer than that at Belle-II, therefore yield more precise measurements of D mixing and CPV parameters than these at Belle-II. This merit should be considered in the study of heavy flavor physics at CEPC when running at Z^0 peak.

For B_c decays Belle II will not be a competitor at all. Although the B_c meson production is small at Z^0 peak, however, according to the nonrelativistic QCD study [4], the B_c production cross-section will be reachable with huge dataset (about 10^7-10^8 B_c produced). Therefore, it will be very interesting to look for the B_c decays with neutral objects in the final states which cannot be reached by the LHCb experiment. Especially interesting is to look for the pure leptonic decays of $B_c \to \mu\nu$ and $B_c \to \tau\nu$. It provides opportunity to get $|V_{cb}|$ with mild theoretical uncertainties. More importantly it would open a gateway to find the impact of charged Higgs scalars.

Finding CPV in beauty *baryons'* decays would be a great achievement – never mind if it can be described by the SM or not. Later we can search for non-leading source. We list first and second classes that are CKM suppressed.

- In the first class of Λ_b decays one gets $p\pi^-$, $p\pi^-\pi^0$, pK^-K^0, ΛK^-, $p\pi^-\pi^+\pi^-$, $p\pi^-K^+K^-$, $p\pi^-\bar{K}^0K^0$, etc.

  In the second class one probes pK^-, $pK^-\pi^0$, $pK_S\pi^-$, ΛK^+K^- etc.

- Ξ_b^- decays lead to $\Lambda^0\pi^-$, $\Lambda^0\pi^-\pi^0$ etc. and Λ^0K^-, $\Lambda^0K^-\pi^0$, $\Lambda^0\bar{K}^0\pi^-$ etc.

For Ξ_b^0 decays one probes FS about $\Sigma^+\pi^-$, $\Lambda^0\pi^+\pi^-$ etc. and Σ^+K^-, $\Lambda^0\pi^+K^-$ etc.

- For obvious reasons we list only first class of Ω_b^-, namely $\Xi^0\pi^-$, Ω^-K^0.

We do not give predictions for these decays; instead we want to emphasize the rich landscapes of baryons' decays and the lessons we can learn about fundamental dynamics – and why a Z^0 factory would be an excellent opportunity to do that. The inclusive b-baryon production at CEPC will be order of 10^{10}, therefore the sensitivity of CPV in beauty baryon sector will be $10^{-4} - 10^{-3}$.

Charm Transitions An important reference for charm physics with many details can be found in 'Physics at BES-III' [5]. While $D^0 - \bar{D}^0$ oscillations have been established, still we have to measure x_D & y_D with accuracy including their differences. No CPV has been found yet anywhere in $D_{(s)}$ and charm baryons' decays. The SM gives very small CP asymmetries in SCS and basically zero.

One wants to probe the correlations of $D_{(s)}$ decays based on CPT and I-spin invariance. Again it is crucial to measure decays of charm hadrons with three-& four-body etc. in SM suppressed FS. Furthermore we have to use refined tools both on the experimental & theoretical sides. Here we focus on three-body FS to make our case mostly (but not totally). Data cover all parts of the Dalitz plots. We will not discuss the impact of $D^0 - \bar{D}^0$ oscillation; it is obvious how to include that in D^0 transitions.

With more data in the future one has to probe regional asymmetries:

- For SCS decays of mesons, where the SM gives averaged CPV on the level of $\mathcal{O}(10^{-3})$ we list:
  – $D^+ \to \pi^+\pi^+\pi^-, \pi^+\pi^0\pi^0, \pi^+K^+K^-, \pi^+K^0\bar{K}^0$ etc.;
  – $D^0 \to \pi^+\pi^-\pi^0$, $\pi^0\pi^0\pi^0$, $K^+\bar{K}^0\pi^-$, $K^+K^-\pi^0$, $K^0\bar{K}^0\pi^0$ etc.;
  – $D_s^+ \to K^+\pi^+\pi^-$, $K^+\pi^0\pi^0$, $K^0\pi^+\pi^0$, $K^+K^+K^-$, $K^+\bar{K}^0K^0$.
  The SM gives CPV basically zero for DCS decays; we list:
  – $D^0 \to K^+\pi^-\pi^0$, $K^+\pi^-\eta$;
  – $D^+ \to K^+\pi^+\pi^-$, $K^+\pi^0\pi^0$, $K^+\bar{K}^0K^0$;
  – $D_s^0 \to K^+K^+\pi^-$, $K^0K^0\pi^+$.
  Again, Belle II produces first competition, and one thinks about the impact of huge boosts at a Z^0 factory.

- The semi-inclusive decay of $Z^0 \to \Lambda_c X$ is listed as be $(1.53\pm0.33)\%$ in the PDG. We expect that about 3×10^9 Λ_c baryons will be produced at the Z^0 factory with two-year running at CEPC. It is much larger than expected size at a super-tau-charm factory or super-B factory [6]. For example, the data suggest $\mathrm{BR}(\Lambda_c \to p\pi^+\pi^-) \sim 3.5\times10^{-3}$. Therefore the SM could produce averaged CP asymmetry that would be measured with around 0.01% at Z^0 peak with 10^9 Λ_c baryons.
  For the DCS $\Lambda_c \to pK^+\pi^-$ we have only an upper limit $\leq 2.3\times10^{-4}$, where the SM practically gives no background; they can be calibrated by Cabibbo favored $\Lambda_c \to pK^-\pi^+$. These and other decays like $\Lambda_c \to \Lambda K^+K^0$ can well be studied with these huge data set.

- Again finding $C_T \neq -\bar{C}_T$ in Λ_c vs. $\bar{\Lambda}_c$ or D vs. $\bar{D}$ would establish CPV at a Z^0 factory.

In any cases, one has to probe the Dalitz plots about regional asymmetries. As mentioned above strong FS interactions have large impact on regional asymmetries, in particular by scalar resonances like σ and κ.

Production of Beauty & Charm Hadrons: While it is not the real goal of this project, one can measure the total & regional ratios of $\Gamma(Z^0 \to b\bar{b}b\bar{b})/\Gamma(Z^0 \to b\bar{b})$, $\Gamma(Z^0 \to c\bar{c})/\Gamma(Z^0 \to c\bar{c})$ and $\Gamma(Z^0 \to b\bar{b}c\bar{c})/\Gamma(Z^0 \to b\bar{b})$.

It would be very interesting to measure $Z^0 \to l^+l^-b\bar{b}$ or $Z^0 \to l^+l^-c\bar{c}$ ($l = e$, μ or τ) for several reasons, even for 'miracles'.

5.3 Very Rare Decays

One looks at transitions of beauty hadrons that the SM cannot produce with tree amplitudes, only by loops. Well known examples are $B \to \gamma X_s$, γX_d and $B \to l^+l^-X_s$, $l^+l^-X_d$ with $l = e, \mu$ and even $l = \tau$. The rare decays from the class of $B \to \gamma X_s$, γX_d and $B \to l^+l^-X_s$, $l^+l^-X_d$ can be studied at the Z^0 peak. We are able to not only probe the decays with electron/muon pairs but also the τ pairs. It is interesting to note that the LHCb Collaboration recently measured the ratio of decay rates for $B^+ \to K^+l^+l^-$ ($l = e$ or μ), obtaining [7]:

$$R_K = \frac{\mathrm{BR}(B^+ \to K^+\mu^+\mu^-)}{\mathrm{BR}(B^+ \to K^+e^+e^-)} = 0.745^{+0.090}_{-0.074}(stat) \pm 0.036(syst). \tag{5.1}$$

This result is a 2.6 sigma deficit from the SM expectation, $R_K = 1 + O(10^{-4})$ [8–10]. These decay rates were determined for $1 < q^2 = M_{ll}^2 < 6$ GeV^2 in order to be well below the radiative tail of the J/ψ. LHCb also measured the $B \to K\mu^+\mu^-$ branching ratio in this q^2-range [11]. The updated result, based on its full Run I dataset of 3 fb^{-1}, is [12],

$$\mathrm{BR}(B^+ \to K^+\mu^+\mu^-)_{[1<q^2<6]} = (1.19 \pm 0.03 \pm 0.06) \times 10^{-7}, \tag{5.2}$$

which is about 45% higher than that from the SM predictions [13–15]. Reference [16] argues that any possible non-universal lepton interactions is necessarily associated with the violation of lepton flavor conservation. Many ND will affect the $B \to K^{(*)}\tau^+\tau^-$ decay more. For this mode, only the weak limit $\mathrm{BR}(B \to K\tau^+\tau^-) < 3.3 \times 10^{-3}$ has been set by BaBar Collaboration [17]. The results reported by the LHCb Collaboration may indicate that $B \to K^{(*)}\mu^\pm e^\mp$ and $B \to K^{(*)}\mu^\pm\tau^\mp$ must occur at rates much larger than would occur in the SM due to tiny neutrino masses. The B_s decays to a pair of oppositely-charged leptons provide an interesting correlation with $B \to Kl^+l^-$. The only observed mode is

$$\mathrm{BR}(B_s \to \mu^+\mu^-)_{exp} = (2.8 \pm 0.7) \times 10^{-9} = (0.77 \pm 0.20) \times \mathrm{BR}(B_s \to \mu^+\mu^-)_{SM} \tag{5.3}$$

where the experimental value is an average of LHCb and CMS measurements with full Run I statistics [18], while the SM value is $\mathrm{BR}(B_s \to \mu^+\mu^-)_{SM} = (3.65 \pm 0.23) \times 10^{-9}$ [19]. More precision measurements for $B_s \to \mu^+\mu^-$ and search for $B^0 \to \mu^+\mu^-$ will be important to identify possible ND in the heavy flavor sector. It will be also possible to look for $B_{s,d} \to \tau^+\tau^-$, as well as $B_{s,d} \to \mu\tau$ and $e\tau$, which are much important for possible ND in both b and τ lepton sectors.

The FCNC processes in charm decays are strongly suppressed due to the GIM mechanism. The charm rare decay amplitudes are fully dominated by long distance dynamics, therefore the decay rate itself cannot reveal information on the size of short distance contribution in the SM. One has to construct new observables, such as differential rate, forward-backward asymmetries, T-odd asymmetries [20–23], which are sensitive to short distance contributions and ND in charm decays. In experiment, precision measurements of these new observables might help in distinguishing ND from the SM ones. For example, signals of new physics may arise from $D \to \rho(\omega)\gamma$, $D \to KK\gamma$, $\Lambda_b \to p\pi^-(pK^-/\Lambda\pi^0)\gamma$ and $\Lambda_c^+ \to p\gamma$, as well as in decays with the leptonic pair in the final state $D \to hl^+l^-$, $D \to h_1h_2l^+l^-$, $\Lambda_b \to l^+l^-p\pi^-/pK^-/\Lambda\pi^0$ and $\Lambda_c \to pl^+l^-$. In rare decays $D \to hl^+l^-$ the CP violating effects might arise due to the interference of resonant part of the long distance contribution and the new physics affected short distance contribution as discussed in Ref. [21]. With huge data sample at the Z^0 peak, we expect that one can reach not only long distance contributions but also short distances contributions to the rare charm decays.

5.4 CPV in τ Decays and Production

One has to probe CPV in τ dynamics in different ways. Global symmetries are mostly much more broken than local ones.

5.4.0.1 τ Decays

One needs to probe different final states – include three- and four-body ones to established its existence of ND. Furthermore it is very important to determine its features. We focus on the class of $\tau^- \to \nu X_{(S=-1)}$ decays that are CKM suppressed in the SM. We have a good chance to find the impact of ND without 'background' from SM amplitudes beyond the well-measured $K^0 - \bar{K}^0$ oscillations. Those can be calibrated by the Cabibbo favored FS $\tau^- \to \nu X^-_{(S=0)}$ transitions; there is hardly a chance that CP asymmetry can be found with ND.

With the huge data from a Z^0 factory one can measure the still rich landscapes of τ decays:

- $\tau^- \to \nu X^-_{(S=-1)}$ with $X^-_{(S=-1)} = K^-, K^-\pi^0, K^-\eta, K^0\pi^-, K^-\pi^+\pi^-, \bar{K}^0\pi^-\pi^0$ etc.
- $\tau^- \to \nu X_{(S=0)}$ with $X^-_{(S=0)} = \pi^-, \pi^-\pi^0, \pi^-\eta, K^-K^0, \pi^-\pi^+\pi^-, \pi^-\pi^0\pi^0$ etc.

Other symmetries and their violations connect same FS on different scales. In particular $\tau^- \to \nu\pi^-\pi^0[\eta]$ can combine with $\tau^- \to \nu 4\pi/\nu 2\pi K\bar{K}$ to get close to CPT symmetry and for $\tau^- \to \nu 3\pi$ with $\tau^- \to \nu\pi K\bar{K}$.
Three items have to be dealt with:
(1) One measures FS with K_S, K_L and their interferences. $K^0 - \bar{K}^0$ oscillation impacts CP asymmetries as expressed by $2\mathrm{Re}\,\epsilon_K$ in a global way for channels.
(2) Mixing between $\bar{K}^0\pi^- \Leftrightarrow K^-\pi^0$, $\bar{K}^0\pi^0 \Leftrightarrow K^-\pi^+$ and $K^-K^+ \Leftrightarrow K^0\bar{K}^0$ happen by FSI – like it does for $K\pi \leftrightarrow K\eta$, but on reduced level.
(3) Theoretical tools exist for $\pi\pi$, πK, $K\bar{K}$ non-perturbative interactions based on dispersion relations and others that use data in different ways.

To measure semi-hadronic decays of τ leptons like $\tau \to \nu K\pi$, $K\pi\pi$, $K\pi\eta$ etc. gives us important lessons about non-perturbative dynamics at least. The goal is to probe CPV first with averaged asymmetries and then with 'regional' ones.

It is very important to have the final state interactions under control. In the case of the CPV asymmetry in $\tau \to K\pi\nu_\tau$, the hadronic part is described by the scalar and vector $K\pi$ form factors that are constrained from the measurement of the $\tau \to K\pi\nu_\tau$ decay rate. Recently, to study this decay, some model-independent parametrizations for the form factors based on dispersion relations have been introduced [24]. They allow to take into account FS interactions. As in the case of the kaon decays [25], they would have to be used to treat correctly the hadronic part of the decays when one reaches a high-level of precision in the measurements. Moreover, in order to determine the hadronic part of these decays very accurately and to disentangle the scalar from the vector contribution, it would be very useful to measure of the forward-backward asymmetry [26]:

$$A_{FB} = \frac{d\Gamma(\cos\theta) - d\Gamma(-\cos\theta)}{d\Gamma(\cos\theta) + d\Gamma(-\cos\theta)} \; ; \tag{5.4}$$

θ denotes the angle between the momentum of the pion and the neutrino in the hadronic rest frame. Such a measurement would also give us some insights on non-perturbative QCD and hadrodynamics for the Kπ (& Kπ's) system. Combining this asymmetry with the measurement of the CP violating, one would allow to disentangle the hadronic contribution from the possible new sources of CP violation. The τ forward-backward asymmetry has never been measured. The CEPC running at the Z pole could offer the first measurement of this forward-backward asymmetry and the first model-independent determination of the CP violating Kπ asymmetry by combining both results.

g-2 and EDM of τ

Anomalous Magnetic Moment of the τ The experimental discrepancy with the Standard Model prediction for the muon anomalous magnetic moment at a 3σ level has triggered huge interest in measuring also the anomalous magnetic moment of the τ (a_τ).

In a large class of theories beyond the Standard Model, the g-2 of the tau should be more sensitive to ND than the muon one since the new contributions to the anomalous magnetic moment of a lepton ℓ of mass m_ℓ are proportional to m_ℓ^2 giving an enhancement by a factor of $m_\tau^2/m_\mu^2 \sim 283$.

The Standard Model prediction for the g-2 of the tau relies on the same ingredients as the prediction for the g-2 of the muon and has been evaluated to be [27]:

$$a_\tau^{\rm SM} = 1177.21(5) \times 10^{-6}. \tag{5.5}$$

However, the very short lifetime of the τ lepton (2.9×10^{-13} s) makes impossible the determination of a_τ by measuring the τ spin precession in a magnetic field like in the electron and muon cases. The best current experimental limit: $-0.052 < a_\tau < 0.013$ at 95% confidence level [28] has been derived from the DELPHI measurement at LEP 2 of the total cross section for $e^+e^- \to e^+e^-\tau^+\tau^-$ as proposed in Ref. [29]. This is well above the Standard Model prediction but nevertheless this bound provides a model-independent bound on new physics contribution $a_\tau^{\rm NP} = -0.018(17)$. A reanalysis using various measurements of the $e^+e^- \to \tau^+\tau^-$ cross section, the transverse τ polarization asymmetry at LEP and SLD as well as the $W \to \tau\nu_\tau$ decay width from LEP and Tevatron in an effective field theory framework has led to a much stringent constraint on ND: $-0.007 < a_\tau^{\rm NP} < 0.005$ at 95 % level [30].

As recently shown [31], the prospects of more precise measurements of $e^+e^- \to e^+\gamma^*\gamma^*e^- \to e^+\tau^+\tau^-e^-$ at a machine such as CEPC will certainly allow for a remarkable improvement in the existing experimental bound on a_τ.

Several new methods have also been suggested to improve the determination of a_τ. For instance, one can use the precise measurements of $\tau^- \to \nu_\tau \ell^- \bar{\nu}_\ell \gamma$ ($\ell = e, \mu$) decays [32] or takes advantage of a radiation zero of the differential decay rate which occurs when, in the τ rest frame, the final lepton ℓ and the photon are back-to-back, and ℓ has maximal energy [33]. This requires very good resolution, high statistics and a very good control of systematic uncertainties [27]. For all these reasons, among the future flavor experiments, CEPC running as a Z factory will provide the best experimental set-up to drastically improve the measurement of a_τ through radiative τ decays. However, the feasibility studies remain to be done.

A similar method to determine a_τ through radiative W decays: $W^- \to \tau^- \bar{\nu}_\tau \gamma$ has been proposed [34]. One can make use of the very high data samples of LHC but CEPC should also be competitive for such a measurement.

Another idea could be to use the decay $B^+ \to \tau^+ \nu_\tau$ which would produce polarized τ leptons [35]. Their spin can be precessed in a bent crystal and their final polarization can be measured through the angular distribution of the daughter lepton in the decays [35]. The channeling of a short-lived polarized particle through a bent crystal has already been tested successfully [36] to measure the magnetic moments of short-living baryons such as the Σ^+ hyperon [37]. The feasibility of this proposal at CEPC remains to be investigated.

Another idea to determine a_τ is to use $e^+e^- \to \tau^+\tau^-$. A determination of the dipole form factor that is directly proportional to a_τ can be obtained by studying the angular distributions of the decay products of the polarized taus [38, 39] using unpolarized electron beams.

Here as well the CEPC project has very interesting prospects to offer. A study has already been done for a future flavour factory showing that with 3×10^9 $\tau^+\tau^-$ pairs the estimated sensitivity is of order 10^{-6} [38]. Projecting such a result for CEPC we are expecting a similar sensitivity.

Electric Dipole Moment of the τ Since CP violation has been discovered in the 1960s, there has been experimental efforts to try to measure the electric dipole moments (EDMs) of leptons, neutron, atoms and molecules. As EDMs violate both parity and time reversal symmetries, their values yield a mostly model-independent measure (assuming CPT symmetry is valid) of CP-violation in nature. Therefore, values for these EDMs place strong constraints upon the scale of CP-violation that extensions of the SM may allow. New sources of CP violation is one essential ingredient to lead to a successful electroweak baryogenesis to account for the baryon asymmetry of the universe. Hence EDMs are very interesting quantities to study since if they are observed, that would be a clear indication of the existence of new sources of CP violation [40–44], the SM prediction being at an unobservable rate. Indeed, a fundamental EDM in the SM can only be generated at three loop level [45, 46].

While strong experimental limits have been placed on the electron [47] and muon [48] EDMs giving stringent constraints on ND [40–44, 49], the measurement of the tau EDM suffers the same difficulty as the measurement of its anomalous magnetic moment: the tau lifetime is too short! The best current limit comes from the Belle collaboration that

has searched for CP violating effects in the process $e^+e^- \to \gamma^* \to \tau^+\tau^-$ using triple momentum and spin correlations [50].

The upper limit sensitivity for the real part of d_τ has been estimated to be $\mathrm{Re}\,(d_\tau) \sim 3 \times 10^{-19}\ e \cdot \mathrm{cm}$ with 50 ab^{-1} at Belle II [51, 52]. We are expecting to reach a similar sensitivity with the CEPC project.

Weak Dipole Moments of the τ By analogy with the couplings to the photon, one can define two weak dipole moments of the τ lepton, the weak magnetic term a_τ^W and the CP-violating weak electric term d_τ^W, through the effective Z couplings [53]:

$$\mathcal{L}^Z_{\mathrm{wdm}} = -\frac{1}{2\,\sin\theta_W \cos\theta_W} Z_\mu \bar{\tau} \left[i a_\tau^W \frac{e}{2m_\tau} \sigma^{\mu\nu} q_\nu + d_\tau^W \sigma^{\mu\nu} \gamma_5 q_\nu \right] \tau\ . \tag{5.6}$$

Experimentally, some bounds have been derived considering the process $e^+e^- \to \tau^+\tau^-$ at LEP [54–56] and studying the correlations between the spins of the two τ in the final state as proposed in Refs. [57–60]. The current best experimental limits come from the ALEPH collaboration that has obtained at 95% confidence level [54]:

$$\begin{aligned} &\left|\mathrm{Re}\left(a_\tau^W\right)\right| < 1.1 \times 10^{-3}\ , \quad \left|\mathrm{Im}\left(a_\tau^W\right)\right| < 2.7 \times 10^{-3} \\ &\left|\mathrm{Re}\left(d_\tau^W\right)\right| < 0.5 \times 10^{-17} e \cdot \mathrm{cm}\ , \quad \left|\mathrm{Im}\left(d_\tau^W\right)\right| < 1.1 \times 10^{-17} e \cdot \mathrm{cm} \end{aligned} \tag{5.7}$$

Here also the experimental limits are well above the Standard Model prediction [57, 59] giving a lot of room for improvement on these limits at CEPC. This will allow to constrain ND appearing in these quantities. Moreover, by combining these constraints with the ones coming from the electroweak precision observables and the parity violation measurements, we will be able to constrain theories beyond the SM that predict new couplings of leptons to the Z boson such as the left-right symmetric models.

Similarly a weak magnetic coupling $W\tau\nu_\tau$ of the form [53]:

$$\mathcal{L}^W_{\mathrm{wdm}} = -\frac{g}{2\sqrt{2}} i \frac{\kappa_\tau^W}{2m_\tau} W_\mu \left[\bar{\tau}\sigma^{\mu\nu} q_\nu (1-\gamma_5)\nu_\tau\right] + \mathrm{h.c.}\ , \tag{5.8}$$

has also be studied by DELPHI collaboration [61] at LEP considering $e^+e^- \to \tau^+\tau^-$. The distribution of the final decay products has been fitted leading to the following limits at 90% confidence level for the anomalous tensor coupling κ_τ^W [61]: $-0.096 < \kappa_\tau^W < 0.037$. In the same analysis where within an effective field theory framework, various measurements ($e^+e^- \to \tau^+\tau^-$ cross section, the transverse τ polarization asymmetry and $\Gamma(W \to \tau\nu_\tau)$) from LEP, SLD and Tevatron have been considered to establish more stringent bounds on ND in a_τ, stronger bounds on κ_τ^W have also been derived at 95% confidence level [30]: $-0.003 < \kappa_\tau^W < 0.004$. For κ_τ^W as well the CEPC project should be able to improve significantly the bounds.

5.5 Charged Lepton Flavor Violation

Charged Lepton Flavor Violation (cLFV) processes are very interesting to study because if they are observed, that would be a clear indication of physics beyond the Standard Model. After the observation of neutrino oscillations and if we extend the SM to include the neutrino masses only, cLFV can only happen through the oscillations of the neutrinos

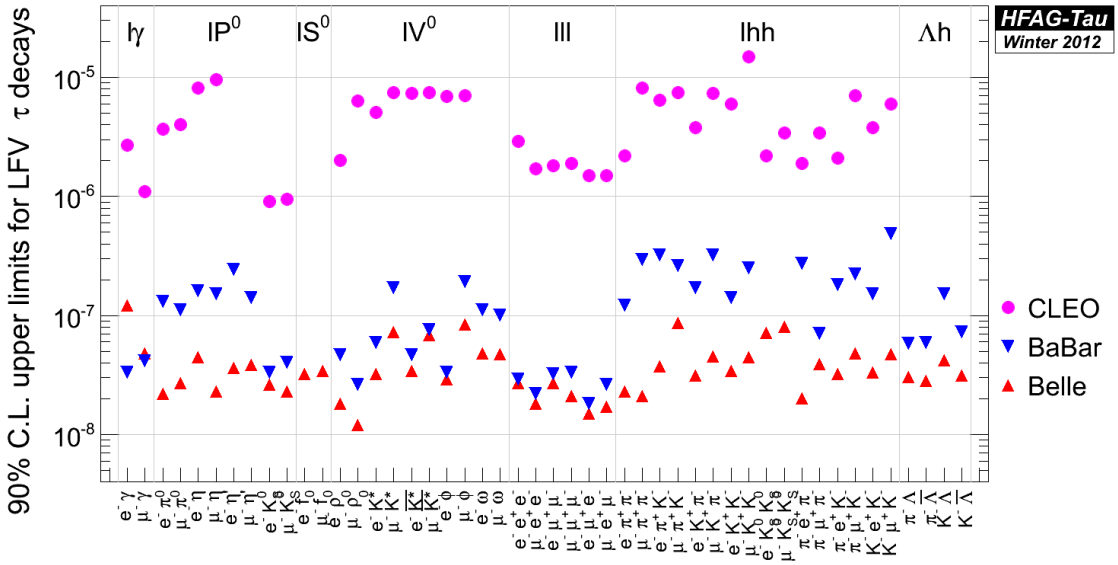

Figure 5.1 *Bounds on Tau Lepton Flavour Branching Ratios from CLEO, BaBar, Belle. Figure taken from HFAG [1]*

and due to GIM mechanism the prediction for the rates are at an unobservable level (e.g. $\sim 10^{-52}$ for $\mu \to e\gamma$ [62, 63]). However, many new physics scenarios predict LFV already at an observable level with decay rates of 10^{-10}-10^{-7} [64–69]. While stringent bounds already exist for μ-e for instance from MEG experiment $\mathrm{Br}(\mu^+ \to e^+\gamma) < 5.7 \times 10^{-13}$ (90% CL) [70], the bounds are much weaker in the case of τ-μ or τ-e and several new physics scenarios have emerged favoring large effects for this coupling. Moreover, recent studies within different new-physics scenarios find interesting correlations between μ and τ cLFV decays with $\mu \to e\gamma$ often expected to be close to the present exclusion limit. Hence new measurements of charged lepton flavor violation decays that could constrain the τ-ℓ coupling would be extremely interesting to have. The CPEC will allow us to study cLFV in τ, Z^0 and H^0 decays in different landscapes, the first two with a run of two years at Z^0 peak and the third one in five (or more) years at Z^0+ Higgs production. It will also allow us by combine these data to have a very interesting handle to discriminate between different new physics scenarios and their flavor structure.

Charged Lepton Flavor Violation in τ decays

τ decays offer a very interesting landscape to look for CLFV. The lepton τ is heavy enough to decay into hadrons and up to now 48 modes have been bounded at the level of 10^{-8} [1] as can be seen in Fig. 5.1. The B factories BaBar and Belle have improved by more than one order of magnitude [71–77] the previous CLEO bounds [78] on a significant list of modes. Some modes like $\tau \to \ell\omega$ have also been bounded for the first time. A similar improvement is expected with Belle-II [79]. LHCb has recently published a competitive limit on $\tau \to 3\mu$ [80].

The branching ratios expected from different new physics models can be as high as 10^{-10} - 10^{-7} [64–69], being at reach at the experimental facilities. CEPC offers very interesting prospects in improving the current bounds especially for the process $\tau \to \mu\gamma$

	$\tau \to 3\mu$	$\tau \to \mu\gamma$	$\tau \to \mu\pi^+\pi^-$	$\tau \to \mu K\bar{K}$	$\tau \to \mu\pi$	$\tau \to \mu\eta^{(\prime)}$
$O^{4\ell}_{S,V}$	✓	–	–	–	–	–
O_D	✓	✓	✓	✓	–	–
O^q_V	–	–	✓ (I=1)	✓(I=0,1)	–	–
O^q_S	–	–	✓ (I=0)	✓(I=0,1)	–	–
O_{GG}	–	–	✓	✓	–	–
O^q_A	–	–	–	–	✓ (I=1)	✓ (I=0)
O^q_P	–	–	–	–	✓ (I=1)	✓ (I=0)
$O_{G\tilde{G}}$	–	–	–	–	–	✓

Table 5.2 *Sensitivity of LFV τ decays to the different effective operators at tree-level. The symbol ✓ (–) denotes that the operator does (not) contribute at tree-level to a given process. For operators involving quark bilinears, the relevant isospin structure ($I = 0, 1$) probed by a given decay is also specified. Table taken from Ref. [84]*

where one expects to reach a sensitivity on the branching ratio of 10^{-9}, two orders of magnitude better than the current bound. One could expect a better sensitivity on this mode compared to Belle II where there is an irreducible background coming from the e^+e^- initial state radiation to $\mu^+\mu^-$ not present at CEPC.

Moreover the hadronic modes should not be neglected: indeed they offer the opportunity to directly test ND in the couplings between quarks and leptons. As can be seen from Table. 5.2, the hadronic tau LFV modes $\tau \to \ell P$ or $\tau \to \ell PP$ are sensitive to a large number of operators encoding the ND beyond the dipole one: scalar, pseudo scalar, vector, axial-vector, gluonic ones [66, 81]. Recent progress has been done to describe the hadronic part of $\tau \to \ell\pi\pi$ [82, 83] in a robust way allowing to set reliable bounds on LFV couplings from this decay. The hadronization of the quarks and gluons into two pions is obtained from a coupled channel ($\pi\pi$ and $K\bar{K}$) analysis taking into account FS interactions.

Studying all the tau LFV modes including the hadronic ones, their branching ratios but also their spectra [84, 85], will allow by combining them and looking at the correlations to unveil the underlying dynamics of New Physics. Some studies for specific models have already been performed, see e.g. [86]. For the study of the hadronic modes, the CEPC has also very good prospects to offer with an expected sensitivity of 10^{-9} on the branching ratios.

Charged Lepton Flavor Violation in Z^0 decays

If one just adds terms of the masses of the three neutrinos – and thus including the matrix U_{PMNS} due to established neutrino oscillations – to the SM, one predicts $\mathrm{BR}(Z \to e^\pm\mu^\mp) \sim \mathrm{BR}(Z \to e^\pm\tau^\mp) \sim 10^{-54}$ and $\mathrm{BR}(Z \to \mu^\pm\tau^\mp) \sim 10^{-60}$, respectively. On the other hand the current upper limits on $\mathrm{BR}(Z \to e^\pm\mu^\mp) < 1.7 \times 10^{-6}$, $\mathrm{BR}(Z \to e^\pm\tau^\mp) < 9.8 \times 10^{-6}$ and $\mathrm{BR}(Z \to \mu^\pm\tau^\mp) < 1.2 \times 10^{-5}$ from LEP [87–89]. Most recently, ATLAS Collaboration improved the upper limit of the $Z \to e^\pm\mu^\mp$ to be 7.5×10^{-7} [90].

At the CEPC a few times of 10^{11} Z^0 would be produced, and the sensitivities would be reached to 10^{-11}, which is much larger than the current experimental data. The detection of $Z^0 \to ll'$ would have established not only the existence of ND, but also about its features, in particular with the Inverse Seesaw (ISS) and "3+1" effective models which add to the particle content of the SM one or more sterile neutrinos [91]. It will be extremely interesting to look for rare LFV Z^0 decays at the CEPC, which will provide background free environment. Thus the CEPC with running at Z^0 peak will manifest power to probe LFV in the $e-\mu$ sector well beyond MEG reach [70] and will provide complimentary constraints on new physics in addition to $\mu - e$ conversion and $0\nu\beta\beta$ decay experiments – or would find it!

In addition, to identify the heavy Majorana Neutrinos [92–96], one could look for the rare lepton-number-violation (LNV) decays of $Z^0 \to l^+l^+\pi^-\pi^-(K^-K^-)$, which provide opportunity to direct search for the heavy Majorana Neutrinos on the mass of $l^+\pi^-(K^-)$ mass distribution. The Majorana Neutrinos can be also searched in the LNV decay processes in B, D mesons and τ lepton, which will be probed in the Z^0 factory, and for a detail review see Ref. [96].

Charged Lepton Flavor Violation in Higgs decays

The possibility of LFV in Higgs decays has been discussed some time ago [97, 97, 98]. Model-independent studies on LFV Higgs couplings have been given [83, 84, 99–104]. Special models have been suggested to produce sizable LFV Higgs decays with observable rates at the LHC [99–104]. Most of them are in conflict with limits from radiative lepton decays ($\mu \to e\gamma$ and $\tau \to \mu\gamma$). As a positive note: the most general 2HDM (the so-called Type-III version) can lead to $H \to ll'$ decay rates [105] thus becoming good scenario for Higgs induced flavor effects. It is especially interesting to search for $H \to \tau\mu/\tau e$ decays. Most recently, the CMS Collaboration reported a preliminary results: $\mathrm{BR}(H \to \tau\mu) < 1.57$ % (at 95% C.L.), which is translated into $\mathrm{BR}(H \to \tau\mu) = (0.89^{+0.40}_{-0.37})\%$ with 2.5 sigma significance [106]. LFV Higgs decays will be studied at the CEPC in $e^+e^- \to Z^0H$. With Z^0 tagging, about 1 million Higgs boson can be produced in a five-year running at the center-of-mass of 240-250 GeV. We expect to obtain a sensitivity of 10^{-4}. On the other hand, if you do not like challenges, you are in the wrong business.

5.6 Summary

The Z^0 factory with very high luminosity will produce about 10^{12} Z^0 decays, which provide unique opportunity for "extreme" heavy flavor experiments. The main points are:

- It is crucial to probe CP asymmetries in the decays of beauty & charm hadrons and τ in *many-body* FS with accuracy in the huge data.
- This Z^0 factory would produce excellent landscapes for baryons' decays with no competiton.
- It is crucial to measure FS with neutral hadrons, not just charged ones. Huge boosts at a Z^0 factory will help significantly in the competition with Belle II about the information for underlying dynamics.
- It is important to use correlations with the decays of different states on different levels.

- One can probe rare decays in beauty & charm hadrons (including baryons) and τ.
- To probe EMDs of the pair of τ leptons.

Unexpected events can happen like production of $Z^0 \to b\bar{s}/s\bar{b}$, $Z^0 \to c\bar{u}/u\bar{c}$ or cLFV τ decays or LFV productions of $Z^0 \to \tau l$ ($l = e, \mu$) or $H^0 \to \tau l$. Those are one of the best places.

References

[1] Heavy Flavor Averaging Group, Y. Amhis, et al., *Averages of B-Hadron, C-Hadron, and tau-lepton properties as of early 2012*, arXiv:1207.1158 [hep-ex].

[2] I. Bigi and A. Sanda, *CP Violation*. Cambridge University Press, Cambridge Monographs on Particle Physics, Nuclear Physics and Cosmology, second ed., 2009.

[3] The LHCb Collaboration, R. Aaij et al., *Measurement of CP violation in the phase space of $B^\pm \to K^\pm\pi^+\pi^-$ and $B^\pm \to K^\pm K^+ K^-$ decays*, Phys.Rev.Lett. **111** (2013) 101801, arXiv:1306.1246 [hep-ex].

[4] Z. Yang, X.-G. Wu, G. Chen, Q.-L. Liao, and J.-W. Zhang, *B_c Meson Production around the Z^0 Peak at a High Luminosity e^+e^- Collider*, Phys.Rev. **D85** (2012) 094015, arXiv:1112.5169 [hep-ph].

[5] D. Asner, T. Barnes, J. Bian, I. Bigi, N. Brambilla, et al., *Physics at BES-III*, Int.J.Mod.Phys. **A24** (2009) S1–794, arXiv:0809.1869 [hep-ex].

[6] X.-W. Kang et al., *Study of CP violation in Λ_c^+ decay*, Int.J.Mod.Phys. **A26** (2011) 2523–2535, arXiv:1003.5494 [hep-ph].

[7] The LHCb Collaboration, R. Aaij et al., *Test of lepton universality using $B^+ \to K^+\ell^+\ell^-$ decays*, Phys.Rev.Lett. **113** (2014) no. 15, 151601, arXiv:1406.6482 [hep-ex].

[8] C. Bobeth, G. Hiller, and G. Piranishvili, *Angular distributions of $\bar{B} \to K\bar{\ell}\ell$ decays*, JHEP **0712** (2007) 040, arXiv:0709.4174 [hep-ph].

[9] The HPQCD Collaboration, C. Bouchard, G. P. Lepage, C. Monahan, H. Na, and J. Shigemitsu, *Standard Model Predictions for $B \to K\ell^+\ell^-$ with Form Factors from Lattice QCD*, Phys.Rev.Lett. **111** (2013) no. 16, 162002, arXiv:1306.0434 [hep-ph].

[10] G. Hiller and F. Kruger, *More model independent analysis of $b \to s$ processes*, Phys.Rev. **D69** (2004) 074020, arXiv:hep-ph/0310219 [hep-ph].

[11] The LHCb Collaboration, R. Aaij et al., *Differential branching fraction and angular analysis of the $B^+ \to K^+\mu^+\mu^-$ decay*, JHEP **1302** (2013) 105, arXiv:1209.4284 [hep-ex].

[12] The LHCb Collaboration, R. Aaij et al., *Differential branching fractions and isospin asymmetries of $B \to K^{(*)}\mu^+\mu^-$ decays*, JHEP **1406** (2014) 133, arXiv:1403.8044 [hep-ex].

[13] C. Bobeth, G. Hiller, and D. van Dyk, *More Benefits of Semileptonic Rare B Decays at Low Recoil: CP Violation*, JHEP **1107** (2011) 067, arXiv:1105.0376 [hep-ph].

[14] C. Bobeth, G. Hiller, D. van Dyk, and C. Wacker, *The Decay $\bar{B} \to \bar{K}\ell^+\ell^-$ at Low Hadronic Recoil and Model-Independent Delta B = 1 Constraints*, JHEP **1201** (2012) 107, arXiv:1111.2558 [hep-ph].

[15] C. Bobeth, G. Hiller, and D. van Dyk, *General Analysis of $\bar{B} \to \bar{K}^{(*)}\ell^+\ell^-$ Decays at Low Recoil*, Phys.Rev. **D87** (2013) 034016, arXiv:1212.2321 [hep-ph].

[16] S. L. Glashow, D. Guadagnoli, and K. Lane, *Lepton Flavor Violation in B Decays?*, arXiv:1411.0565 [hep-ph].

[17] The BaBar Collaboration, K. Flood, *New results in radiative electroweak penguin decays at BaBar*, PoS **ICHEP2010** (2010) 234.

[18] F. Archilli, *Talk by F. Archilli at the 8th InternationalWorkshop on the CKM Unitarity Triangle*, ckm 2014, Vienna, Austria, 2014.

[19] C. Bobeth, M. Gorbahn, T. Hermann, M. Misiak, E. Stamou, et al., *$B_{s,d} \to \ell^+\ell^-$ in the Standard Model with Reduced Theoretical Uncertainty*, Phys.Rev.Lett. **112** (2014) 101801, arXiv:1311.0903 [hep-ph].

[20] S. Fajfer and S. Prelovsek, *Effects of littlest Higgs model in rare D meson decays*, Phys.Rev. **D73** (2006) 054026, arXiv:hep-ph/0511048 [hep-ph].

[21] L. Cappiello, O. Cata, and G. D'Ambrosio, *Standard Model prediction and new physics tests for $D^0 \to h_1^+ h_2^- \ell^+\ell^- (h = \pi, K; \ell = e, \mu)$*, JHEP **1304** (2013) 135, arXiv:1209.4235 [hep-ph].

[22] S. Fajfer and N. Kosnik, *Resonance catalyzed CP asymmetries in $D \to P\ell^+\ell^-$*, Phys.Rev. **D87** (2013) 054026, arXiv:1208.0759 [hep-ph].

[23] A. Paul, A. de La Puente, and I. I. Bigi, *Manifestations of Warped Extra Dimension in Rare Charm Decays and Asymmetries*, Phys.Rev. **D90** (2014) 014035, arXiv:1212.4849 [hep-ph].

[24] M. Jamin, A. Pich, and J. Portoles, *Spectral distribution for the decay $\tau \to \nu_\tau K\pi$*, Phys.Lett. **B640** (2006) 176–181, arXiv:hep-ph/0605096 [hep-ph].

[25] M. Antonelli et al., *An Evaluation of V_{us} and precise tests of the Standard Model from world data on leptonic and semileptonic kaon decays*, Eur.Phys.J. **C69** (2010) 399–424, arXiv:1005.2323 [hep-ph].

[26] L. Beldjoudi and T. N. Truong, *$\tau \to \pi K \nu$ neutrino decay and πK scattering*, Phys.Lett. **B351** (1995) 357–368, arXiv:hep-ph/9411423 [hep-ph].

[27] S. Eidelman and M. Passera, *Theory of the tau lepton anomalous magnetic moment*, Mod.Phys.Lett. **A22** (2007) 159–179, arXiv:hep-ph/0701260 [hep-ph].

[28] The DELPHI Collaboration, J. Abdallah et al., *Study of tau-pair production in photon-photon collisions at LEP and limits on the anomalous electromagnetic moments of the tau lepton*, Eur.Phys.J. **C35** (2004) 159–170, arXiv:hep-ex/0406010 [hep-ex].

[29] F. Cornet and J. I. Illana, *Tau pair production via photon-photon collisions at LEP*, Phys.Rev. **D53** (1996) 1181–1184, arXiv:hep-ph/9503466 [hep-ph].

[30] G. A. Gonzalez-Sprinberg, A. Santamaria, and J. Vidal, *Model independent bounds on the tau lepton electromagnetic and weak magnetic moments*, Nucl.Phys. **B582** (2000) 3–18, arXiv:hep-ph/0002203 [hep-ph].

[31] A. Billur and M. Koksal, *Probe of the electromagnetic moments of the tau lepton in gamma-gamma collisions at the CLIC*, Phys.Rev. **D89** (2014) no. 3, 037301, arXiv:1306.5620 [hep-ph].

[32] M. Fael, L. Mercolli, and M. Passera, *Towards a determination of the tau lepton dipole moments*, arXiv:1301.5302 [hep-ph].

[33] M. Laursen, M. A. Samuel, and A. Sen, *Radiation Zeros and a Test for the g Value of the τ Lepton*, Phys.Rev. **D29** (1984) 2652–2654.

[34] M. A. Samuel and G. Li, *Measuring the magnetic moment of the tau lepton at the Fermilab tevatron, the, SSC and the LHC*, Int.J.Theor.Phys. **33** (1994) 1471–1478.

[35] M. A. Samuel, G.-w. Li, and R. Mendel, *The Anomalous magnetic moment of the tau lepton*, Phys.Rev.Lett. **67** (1991) 668–670.

[36] I. J. Kim, *Magnetic Moment Measurement of Baryons With Heavy Flavored Quarks by Planar Channeling Through Bent Crystal*, Nucl.Phys. **B229** (1983) 251.

[37] The E761 Collaboration, D. Chen et al., *First observation of magnetic moment precession of channeled particles in bent crystals*, Phys.Rev.Lett. **69** (1992) 3286–3289.

[38] J. Bernabeu, G. Gonzalez-Sprinberg, J. Papavassiliou, and J. Vidal, *Tau anomalous magnetic moment form-factor at super B/flavor factories*, Nucl.Phys. **B790** (2008) 160–174, arXiv:0707.2496 [hep-ph].

[39] J. Bernabeu, G. Gonzalez-Sprinberg, and J. Vidal, *Tau spin correlations and the anomalous magnetic moment*, JHEP **0901** (2009) 062, arXiv:0807.2366 [hep-ph].

[40] J. Ginges and V. Flambaum, *Violations of fundamental symmetries in atoms and tests of unification theories of elementary particles*, Phys.Rept. **397** (2004) 63–154, arXiv:physics/0309054 [physics].

[41] M. Pospelov and A. Ritz, *Electric dipole moments as probes of new physics*, Annals Phys. **318** (2005) 119–169, arXiv:hep-ph/0504231 [hep-ph].

[42] M. Raidal et al., *Flavour physics of leptons and dipole moments*, Eur.Phys.J. **C57** (2008) 13–182, arXiv:0801.1826 [hep-ph].

[43] O. Lebedev, K. A. Olive, M. Pospelov, and A. Ritz, *Probing CP violation with the deuteron electric dipole moment*, Phys.Rev. **D70** (2004) 016003, arXiv:hep-ph/0402023 [hep-ph].

[44] T. Fukuyama, *Searching for New Physics beyond the Standard Model in Electric Dipole Moment*, Int.J.Mod.Phys. **A27** (2012) 1230015, arXiv:1201.4252 [hep-ph].

[45] J. F. Donoghue, *T Violation in SU(2)×U(1) Gauge Theories of Leptons*, Phys.Rev. **D18** (1978) 1632.

[46] E. Shabalin, *Electric Dipole Moment of Quark in a Gauge Theory with Left-Handed Currents*, Sov.J.Nucl.Phys. **28** (1978) 75.

[47] The ACME Collaboration, J. Baron et al., *Order of Magnitude Smaller Limit on the Electric Dipole Moment of the Electron*, Science **343** (2014) no. 6168, 269–272, arXiv:1310.7534 [physics.atom-ph].

[48] J. McNabb, Ronald Steven, *An improved limit on the electric dipole moment of the muon*, UMI-31-13195.

[49] J. Engel, M. J. Ramsey-Musolf, and U. van Kolck, *Electric Dipole Moments of Nucleons, Nuclei, and Atoms: The Standard Model and Beyond*, Prog.Part.Nucl.Phys. **71** (2013) 21–74, arXiv:1303.2371 [nucl-th].

[50] The Belle Collaboration, K. Inami, *Search for the electric dipole moment of the tau lepton*, eConf **C0209101** (2002) TU10, arXiv:hep-ex/0210035 [hep-ex].

[51] J. Bernabeu, G. Gonzalez-Sprinberg, and J. Vidal, *CP violation and electric-dipole-moment at low energy tau-pair production*, Nucl.Phys. **B701** (2004) 87–102, arXiv:hep-ph/0404185 [hep-ph].

[52] J. Bernabeu, G. Gonzalez-Sprinberg, and J. Vidal, *CP violation and electric-dipole-moment at low energy tau production with polarized electrons*, Nucl.Phys. **B763** (2007) 283–292, arXiv:hep-ph/0610135 [hep-ph].

[53] A. Pich, *Precision Tau Physics*, Prog.Part.Nucl.Phys. **75** (2014) 41–85, arXiv:1310.7922 [hep-ph].

[54] The ALEPH Collaboration, A. Heister et al., *Search for anomalous weak dipole moments of the tau lepton*, Eur.Phys.J. **C30** (2003) 291–304, arXiv:hep-ex/0209066 [hep-ex].

[55] The L3 Collaboration, M. Acciarri et al., *Measurement of the weak dipole moments of the tau lepton*, Phys.Lett. **B426** (1998) 207–216.

[56] The OPAL Collaboration, K. Ackerstaff et al., *Search for CP violation in $Z^0 \to \tau^+\tau^-$ and an upper limit on the weak dipole moment of the tau lepton*, Z.Phys. **C74** (1997) 403–412.

[57] W. Bernreuther, U. Low, J. Ma, and O. Nachtmann, *CP Violation and Z Boson Decays*, Z.Phys. **C43** (1989) 117.

[58] W. Bernreuther, O. Nachtmann, and P. Overmann, *The CP violating electric and weak dipole moments of the tau lepton from threshold to 500-GeV*, Phys.Rev. **D48** (1993) 78–88.

[59] J. Bernabeu, G. Gonzalez-Sprinberg, M. Tung, and J. Vidal, *The Tau weak magnetic dipole moment*, Nucl.Phys. **B436** (1995) 474–486, arXiv:hep-ph/9411289 [hep-ph].

[60] J. Bernabeu, G. Gonzalez-Sprinberg, and J. Vidal, *Normal and transverse single tau polarization at the Z peak*, Phys.Lett. **B326** (1994) 168–174.

[61] The DELPHI Collaboration, G. Gomez-Ceballos, *A study of the Lorentz structure in tau decays in DELPHI*, Int.J.Mod.Phys. **A16S1B** (2001) 551–554.

[62] T.-P. Cheng and L.-F. Li, *Muon Number Nonconservation Effects in a Gauge Theory with V A Currents and Heavy Neutral Leptons*, Phys.Rev. **D16** (1977) 1425.

[63] B. W. Lee and R. E. Shrock, *Natural Suppression of Symmetry Violation in Gauge Theories: Muon - Lepton and Electron Lepton Number Nonconservation*, Phys.Rev. **D16** (1977) 1444.

[64] J. R. Ellis and D. V. Nanopoulos, *Charged lepton flavor violation in the light of the Super-Kamiokande data*, Eur.Phys.J. **C14** (2000) 319–334, arXiv:hep-ph/9911459 [hep-ph].

[65] A. Dedes, J. R. Ellis, and M. Raidal, *Higgs mediated $B^0_{s,d} \to \mu\tau$, $e\tau$ and $\tau \to 3\mu$, $e\mu\mu$ decays in supersymmetric seesaw models*, Phys.Lett. **B549** (2002) 159–169, arXiv:hep-ph/0209207 [hep-ph].

[66] A. Brignole and A. Rossi, *Lepton flavor violating decays of supersymmetric Higgs bosons*, Phys.Lett. **B566** (2003) 217–225, arXiv:hep-ph/0304081 [hep-ph].

[67] G. Cvetic, C. Dib, C. Kim, and J. Kim, *On lepton flavor violation in tau decays*, Phys.Rev. **D66** (2002) 034008, arXiv:hep-ph/0202212 [hep-ph].

[68] C.-x. Yue, Y.-m. Zhang, and L.-j. Liu, *Nonuniversal gauge bosons Z-prime and lepton flavor violation tau decays*, Phys.Lett. **B547** (2002) 252–256, arXiv:hep-ph/0209291 [hep-ph].

[69] A. Masiero, S. K. Vempati, and O. Vives, *Seesaw and lepton flavor violation in SUSY SO(10)*, Nucl.Phys. **B649** (2003) 189–204, arXiv:hep-ph/0209303 [hep-ph].

[70] The MEG Collaboration, J. Adam et al., *New constraint on the existence of the $\mu^+ \to e^+\gamma$ decay*, Phys.Rev.Lett. **110** (2013) 201801, arXiv:1303.0754 [hep-ex].

[71] The BaBar Collaboration, B. Aubert et al., *Search for decays of $B^0 \to$ mesons into e^+e^-, $\mu^+\mu^-$, and $e^\pm\mu^\mp$ final states*, Phys.Rev. **D77** (2008) 032007, arXiv:0712.1516 [hep-ex].

[72] The BaBar Collaboration, B. Aubert et al., *Searches for Lepton Flavor Violation in the Decays $\tau^{\pm} \to e^{\pm}\gamma$ and $\tau^{\pm} \to \mu^{\pm}\gamma$*, Phys.Rev.Lett. **104** (2010) 021802, arXiv:0908.2381 [hep-ex].

[73] The Belle Collaboration, K. Abe et al., *Search for Lepton Flavor Violating τ^- Decays into $\ell^-\eta$, $\ell^-\eta'$ and $\ell^-\pi^0$*, arXiv:hep-ex/0609013 [hep-ex].

[74] The Belle Collaboration, Y. Miyazaki et al., *Search for Lepton-Flavor-Violating tau Decays into Lepton and f0(980) Meson*, Phys.Lett. **B672** (2009) 317–322, arXiv:0810.3519 [hep-ex].

[75] K. Hayasaka et al., *Search for Lepton Flavor Violating Tau Decays into Three Leptons with 719 Million Produced Tau+Tau- Pairs*, Phys.Lett. **B687** (2010) 139–143, arXiv:1001.3221 [hep-ex].

[76] The Belle Collaboration, Y. Miyazaki et al., *Search for Lepton-Flavor-Violating tau Decays into a Lepton and a Vector Meson*, Phys.Lett. **B699** (2011) 251–257, arXiv:1101.0755 [hep-ex].

[77] The Belle Collaboration, Y. Miyazaki et al., *Search for Lepton-Flavor-Violating and Lepton-Number-Violating $\tau \to \ell hh'$ Decay Modes*, Phys.Lett. **B719** (2013) 346–353, arXiv:1206.5595 [hep-ex].

[78] The CLEO Collaboration, A. Anastassov et al., *Update of the search for the neutrinoless decay $\tau \to \mu\gamma$*, arXiv:hep-ex/9908025 [hep-ex].

[79] The Belle-II Collaboration, T. Abe et al., *Belle II Technical Design Report*, arXiv:1011.0352 [physics.ins-det].

[80] The LHCb Collaboration, R. Aaij et al., *Searches for violation of lepton flavour and baryon number in tau lepton decays at LHCb*, Phys.Lett. **B724** (2013) 36–45, arXiv:1304.4518 [hep-ex].

[81] E. Arganda, M. Herrero, and J. Portoles, *Lepton flavour violating semileptonic tau decays in constrained MSSM-seesaw scenarios*, JHEP **0806** (2008) 079, arXiv:0803.2039 [hep-ph].

[82] J. Daub, H. Dreiner, C. Hanhart, B. Kubis, and U. Meissner, *Improving the Hadron Physics of Non-Standard-Model Decays: Example Bounds on R-parity Violation*, JHEP **1301** (2013) 179, arXiv:1212.4408 [hep-ph].

[83] A. Celis, V. Cirigliano, and E. Passemar, *Lepton flavor violation in the Higgs sector and the role of hadronic τ-lepton decays*, Phys.Rev. **D89** (2014) no. 1, 013008, arXiv:1309.3564 [hep-ph].

[84] A. Celis, V. Cirigliano, and E. Passemar, *The model-discriminating power of lepton flavor violating tau decays*, Phys.Rev. **D89** (2014) 095014, arXiv:1403.5781 [hep-ph].

[85] B. Dassinger, T. Feldmann, T. Mannel, and S. Turczyk, *Model-independent analysis of lepton flavour violating tau decays*, JHEP **0710** (2007) 039, arXiv:0707.0988 [hep-ph].

[86] C. Tarantino, *FCNC Processes in the LHT Model: A 2009 Look*, PoS **EPS-HEP2009** (2009) 185, arXiv:0909.0381 [hep-ph].

[87] The OPAL Collaboration, R. Akers et al., *Measurement of the $\tau^- \to h^- h^+ \nu_\tau$ and $\tau^- \to h^- h^+ h^- \leq 1\pi^0 \nu_\tau$ branching ratios*, Z.Phys. **C68** (1995) 555–568.

[88] The L3 Collaboration, O. Adriani et al., *Search for lepton flavor violation in Z decays*, Phys.Lett. **B316** (1993) 427–434.

[89] The DELPHI Collaboration, P. Abreu et al., *Search for lepton flavor number violating Z0 decays*, Z.Phys. **C73** (1997) 243–251.

[90] The ATLAS Collaboration, G. Aad et al., *Search for the lepton flavor violating decay $Z \to e\mu$ in pp collisions at $\sqrt{s}$ TeV with the ATLAS detector*, Phys.Rev. **D90** (2014) no. 7, 072010, arXiv:1408.5774 [hep-ex].

[91] A. Abada, V. De Romeri, and A. Teixeira, *Effect of steriles states on lepton magnetic moments and neutrinoless double beta decay*, JHEP **1409** (2014) 074, arXiv:1406.6978 [hep-ph].

[92] H. Georgi and S. Glashow, *Unity of All Elementary Particle Forces*, Phys.Rev.Lett. **32** (1974) 438–441.

[93] P. Minkowski, *$\mu \to e\gamma$ at a Rate of One Out of 1-Billion Muon Decays?*, Phys.Lett. **B67** (1977) 421.

[94] S. Weinberg, *Baryon and Lepton Nonconserving Processes*, Phys.Rev.Lett. **43** (1979) 1566–1570.

[95] R. N. Mohapatra and G. Senjanovic, *Neutrino Mass and Spontaneous Parity Violation*, Phys.Rev.Lett. **44** (1980) 912.

[96] A. Atre, T. Han, S. Pascoli, and B. Zhang, *The Search for Heavy Majorana Neutrinos*, JHEP **0905** (2009) 030, arXiv:0901.3589 [hep-ph].

[97] A. Pilaftsis, *Lepton flavor nonconservation in H0 decays*, Phys.Lett. **B285** (1992) 68–74.

[98] J. L. Diaz-Cruz and J. Toscano, *Lepton flavor violating decays of Higgs bosons beyond the standard model*, Phys.Rev. **D62** (2000) 116005, arXiv:hep-ph/9910233 [hep-ph].

[99] T. Han and D. Marfatia, *$h \to \mu\tau$ at hadron colliders*, Phys.Rev.Lett. **86** (2001) 1442–1445, arXiv:hep-ph/0008141 [hep-ph].

[100] A. Goudelis, O. Lebedev, and J.-h. Park, *Higgs-induced lepton flavor violation*, Phys.Lett. **B707** (2012) 369–374, arXiv:1111.1715 [hep-ph].

[101] G. Blankenburg, J. Ellis, and G. Isidori, *Flavour-Changing Decays of a 125 GeV Higgs-like Particle*, Phys.Lett. **B712** (2012) 386–390, arXiv:1202.5704 [hep-ph].

[102] R. Harnik, J. Kopp, and J. Zupan, *Flavor Violating Higgs Decays*, JHEP **1303** (2013) 026, arXiv:1209.1397 [hep-ph].

[103] S. Davidson and P. Verdier, *LHC sensitivity to the decay $h \to \tau^{\pm} mu^{\mp}$*, Phys.Rev. **D86** (2012) 111701, arXiv:1211.1248 [hep-ph].

[104] A. Falkowski, D. M. Straub, and A. Vicente, *Vector-like leptons: Higgs decays and collider phenomenology*, JHEP **1405** (2014) 092, arXiv:1312.5329 [hep-ph].

[105] D. A. Sierra, M. Dhen, C. S. Fong, and A. Vicente, *Dynamical flavor origin of $\mathbb{Z}_N$ symmetries*, arXiv:1412.5600 [hep-ph].

[106] The CMS Collaboration, *Search for Lepton Flavour Violating Decays of the Higgs Boson*, CMS-PAS-HIG-14-005, 2014.

CHAPTER 6

THE CEPC DETECTOR

6.1 Detector Overview

The CEPC conceptual detector design, as illustrated in Fig. 6.1, takes the ILC detector designs (e.g. ILD and SiD) [1–3] as a reference. It fulfils the requirement of the physics program at the lepton collider with precision measurements of the Higgs boson at $\sqrt{s} \sim 240$ GeV. For the preCDR initial study, the ILD detector has been chosen as the starting point for the CEPC detector design.

In order to accommodate the CEPC collision environment, some necessary changes have been made to the Machine Detector Interface (MDI, detailed in Section 6.8) and sub-detector design. The CEPC design, for instance, has a significantly shorter focal length L^* of 1.5 m than that of the ILC design (3.5 m), which indicates that the final focusing magnet QD0 will be placed inside the CEPC detector. In addition, unlike the ILC detectors, the CEPC detector will operate in continuous mode, which imposes special considerations on power consumption and subsequent cooling of the sub-detectors.

Another major change in the CEPC detector is that the thickness of magnetic field return yoke for both barrel and end-cap regions is reduced since the CEPC does not require the detector to operate in Push-Pull mode as designed for the ILC.

As illustrated in Fig. 6.1, the CEPC detector consists of the following sub-detectors:

- A vertex detector (VTX, detailed in Section 6.2) constructed with high spatial resolution pixel sensors. The vertex detector is placed very close to the interaction point (IP), with an inner radius of 16 mm. This vertex detector ensures excellent tagging capability of b-/c-quark jets and τ-leptons.
- A silicon tracker (Section 6.3) composed of Silicon Inner Tracker (SIT), Forward Tracking Disks (FTDs), Silicon External Tracker (SET) and End-cap Tracking Disks

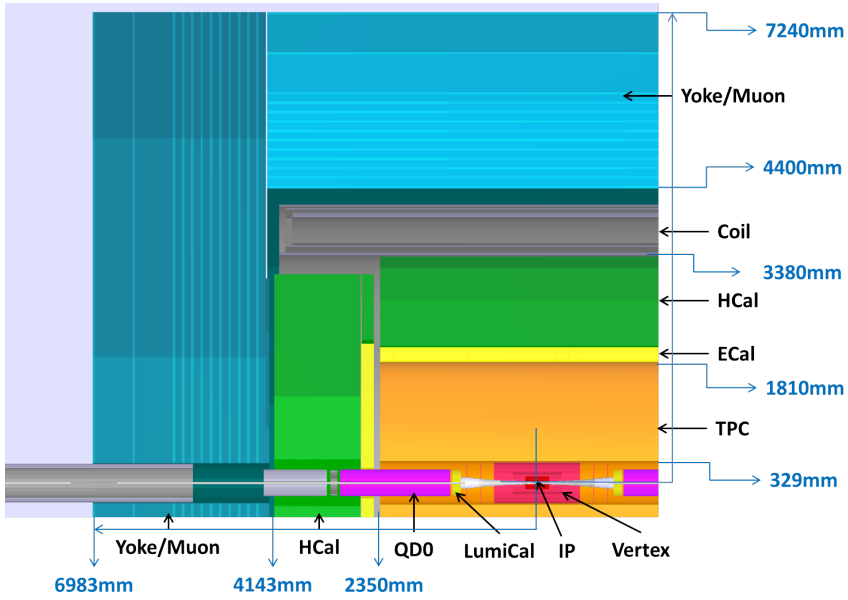

Figure 6.1 Overview of the CEPC detector.

(ETDs). The VTX and SIT provide excellent spatial measurements near the IP, crucial for vertex reconstruction and jet flavour tagging. The SET and ETD, on the other hand, provide excellent spatial resolution with the maximal possible track arm length, therefore improving the track momentum resolution of charged particles. The FTD significantly increases the geometric acceptance of the tracking system with coverage of $|\cos\theta| < 0.99$.

- A Time Projection Chamber (TPC, Section 6.4) with a half-length of 2.35 m and an outer radius of 1.8 m. The TPC provides a large number of spatial points ($\sim$200 hits per track) and spatial resolution in $r\phi$ plane better than 100 μm. It has excellent pattern recognition and track reconstruction efficiency (better than 97% for tracks with $p_{\mathrm{T}} > 1$ GeV).

- A calorimetry system (Section 6.5) consisting of Electromagnetic Calorimeter (ECAL) and Hadron Calorimeter (HCAL) with very fine granularity. The system plays an essential role in the Particle-Flow Algorithm (PFA) [4–7]), allowing excellent separation of showers from different particles, and provides jet energy resolution of 3 – 4%.

- A superconducting solenoid of 3.5 T (Section 6.7), surrounding the calorimetry system. The return yoke is placed outside the solenoid.

- A muon detector (in Section 6.6) with tracking layers installed in the return yoke.

The CEPC detector design is mainly driven by several selected benchmark physics processes as shown in Table 6.1. Precise measurements of the Higgs mass and cross section through the $Z \to \ell^+\ell^-$ recoil method requires high track momentum resolution provided by the tracking system. This also makes the measurement of the rare decay process of $H \to \mu^+\mu^-$ accessible. Measurements of $H \to b\bar{b}$, $c\bar{c}$, gg branching ratios imply excellent flavour-tagging capability for the vertex detector. In addition, many interesting

physics processes appear in multi-jet final states, requiring jet energy resolution of 3 – 4%. This can be achieved with the combination of the high granularity calorimetry system and the PFA algorithm.

Table 6.1 Required performance of the CEPC sub-detectors for critical benchmark Higgs processes.

Physics Process	Measured Quantity	Critical Detector	Required Performance
$ZH \to \ell^+\ell^- X$	Higgs mass, cross section	Tracker	$\Delta(1/p_{\mathrm{T}}) \sim 2 \times 10^{-5}$
$H \to \mu^+\mu^-$	BR($H \to \mu^+\mu^-$)		$\oplus 1 \times 10^{-3}/(p_{\mathrm{T}} \sin\theta)$
$H \to b\bar{b},\ c\bar{c},\ gg$	BR($H \to b\bar{b},\ c\bar{c},\ gg$)	Vertex	$\sigma_{r\phi} \sim 5 \oplus 10/(p \sin^{3/2}\theta)$ μm
$H \to q\bar{q},\ VV$	BR($H \to q\bar{q},\ VV$)	ECAL, HCAL	$\sigma_E^{\mathrm{jet}}/E \sim 3$ – 4%
$H \to \gamma\gamma$	BR($H \to \gamma\gamma$)	ECAL	$\sigma_E \sim 16\%/\sqrt{E} \oplus 1\%$ (GeV)

Details of the sub-detector baseline designs, technology options, expected performance, and critical R&D plans for further comprehensive studies and optimisation, are discussed in subsequent sections. The current detector design mainly aims for precision measurements of the Higgs properties. In order to accommodate precision measurements of the SM parameters and flavour physics at Z pole, some of the CEPC sub-detector design would need to be re-evaluated.

6.2 Vertex Detector

The identification of heavy-flavour (b- and c-) quarks and τ-leptons is essential for the CEPC physics program. It requires precise determination of the track parameters of charged particles in the vicinity of the interaction point (IP), permitting reconstruction of the displaced decay vertices of short-lived particles. This drives the need for a vertex detector with low material budget and high spatial resolution. The current design of the CEPC vertex detector adopts the same layout as the ILD vertex detector [2], but with special considerations for the sensor specifications.

6.2.1 Performance Requirements and Detector Challenges

As required for the precision physics program, the CEPC vertex detector is designed to achieve excellent impact parameter resolution, which in the $r\phi$ plane can be parameterised by:

$$\sigma(r\phi) = a \oplus \frac{b}{p(\mathrm{GeV})\sin^{3/2}\theta}\ \mu\mathrm{m} \tag{6.1}$$

where $\sigma(r\phi)$ denotes the transverse impact parameter resolution, p the track momentum and θ the polar track angle. The first term describes the intrinsic resolution of the vertex detector in the absence of multiple scattering and is independent of the track parameters, while the second term reflects the effects of multiple scattering. $a = 5$ and $b = 10$ are taken as the design values for the CEPC vertex detector. The main performance goals should comply with the following specifications on the system:

- Spatial resolution near the IP better than 3 μm;
- Material budget below 0.15% radiation length (X_0) per layer;
- First layer located as close as possible to the interaction point ($r = 16$ mm);
- Detector occupancy not exceeding 1%.

Unlike the ILD vertex detector, which operates in power-pulsing mode, the CEPC vertex detector will have to operate in continuous mode. The power consumption of the sensors and readout electronics should be kept below 50 mW/cm^2, if air cooling is intended inside the sensitive volume of the vertex detector. The readout time of the pixel sensor needs to be shorter than 20 μs, to minimise event accumulation from consecutive bunch crossings. The radiation tolerance requirements, which are critical for the innermost detector layer, are driven by the beam related backgrounds as described in Section 6.8. The annual values of the Total Ionising Does (TID) and Non-Ionising Energy Loss (NIEL) are estimated to be 300 kRad and 10^{12} 1 MeV n_{eq}/cm^2, respectively.

6.2.2 Baseline Design

The baseline layout of the CEPC vertex detector is exactly the same as that of the ILD detector. As shown in Fig. 6.2, it consists of three cylindrical and concentric double-layers mounted on ladders, which are the basic mechanical structure, with high spatial resolution pixel sensors on both sides. The CEPC vertex detector is designed to deliver six precise space-points for each charged particle traversing the detector, between radii of 16 mm

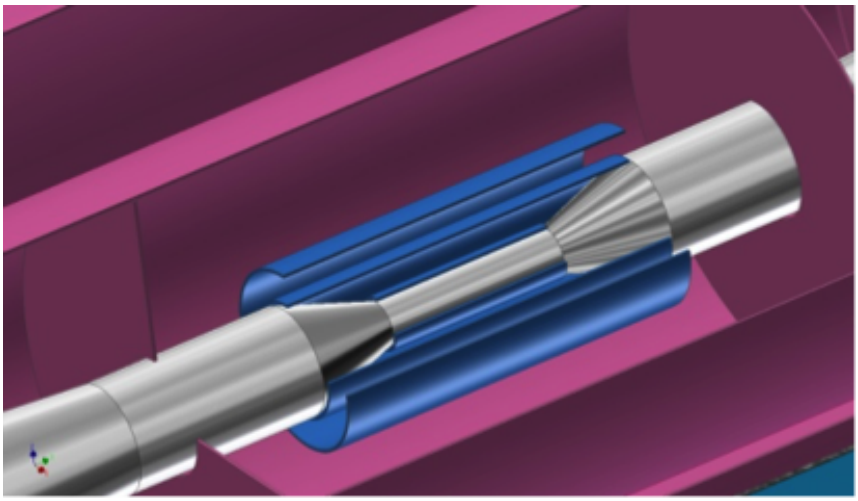

Figure 6.2 Schematic view of the vertex detector (in blue) around the beampipe (in silver).

to 60 mm with respect to the IP. The material budget of each detector layer amounts to $\sim 0.15\% X_0$. The main parameters of the CEPC vertex detector are summarised in Table 6.2.

Table 6.2 Main parameters of the CEPC vertex detector.

	R (mm)	$\|\mathbf{z}\|$ (mm)	$\|\cos\theta\|$	σ_{SP} (μm)	**Readout time** (μs)
Layer 1	16	62.5	0.97	2.8	20
Layer 2	18	62.5	0.96	2.8	20
Layer 3	37	125.0	0.96	4	20
Layer 4	39	125.0	0.95	4	20
Layer 5	58	125.0	0.91	4	20
Layer 6	60	125.0	0.90	4	20

6.2.3 Detector Performance

The identification of b/c-quark jets (called "flavour-tagging") plays an important role in physics analyses, where signal events with b/c-quark jets in the final state have to be separated from background events. Flavour-tagging typically relies on the reconstruction of the displaced vertex inside the jets and imposes stringent requirements on the precise determination of the impact parameters of the charged tracks embedded in the jets. For CEPC operation at the center-of-mass energy of $\sqrt{s} \sim 240$ GeV, those tracks are often of low momentum, for which the multiple scattering effect dominates the tracking performance as illustrated by Eq. 6.1.

The CEPC vertex detector layout has been fully implemented in the GEANT4-based simulation framework MOKKA [8]. In addition, as inspired by the detailed studies for the CLIC detectors [9], fast simulation with the LiC Detector Toy simulation and reconstruction framework (LDT) [10] has been used for detector performance evaluation and

layout optimisation. However, full assessment of the impact of the detector layout and material budget on the detector performance will be only possible with full simulation.

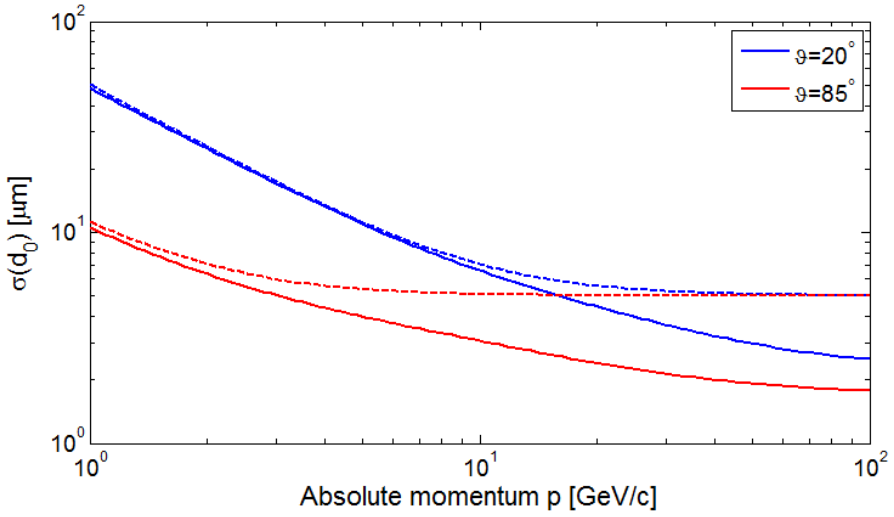

Figure 6.3 Resolution of the transverse impact parameter as a function of single muon track momentum estimated for the CEPC baseline design (solid lines) for polar angles of $\theta = 20°$ and $85°$, and compared to the analytical results obtained with Eq. 6.1 assuming $a = 5$ and $b = 10$ (dashed lines).

With the single-point resolution and material budget for each vertex detector layer, as listed in Table 6.2, the resolution of the transverse impact parameter has been estimated for the CEPC baseline design. As shown in Fig 6.3, the blue and red solid lines represent the resolution $\sigma_{r\phi}$ as a function of the muon track momentum for two polar angles, $\theta = 20°$ and $85°$. For comparison, the analytical results obtained with Eq. 6.1, assuming $a = 5$ and $b = 10$, are shown by the dashed lines. The results confirm that the required impact parameter resolution for the CEPC vertex detector can be achieved with the baseline design. In the following, performance changes corresponding to modifications in material budget, single-point resolution and distance to the IP are evaluated.

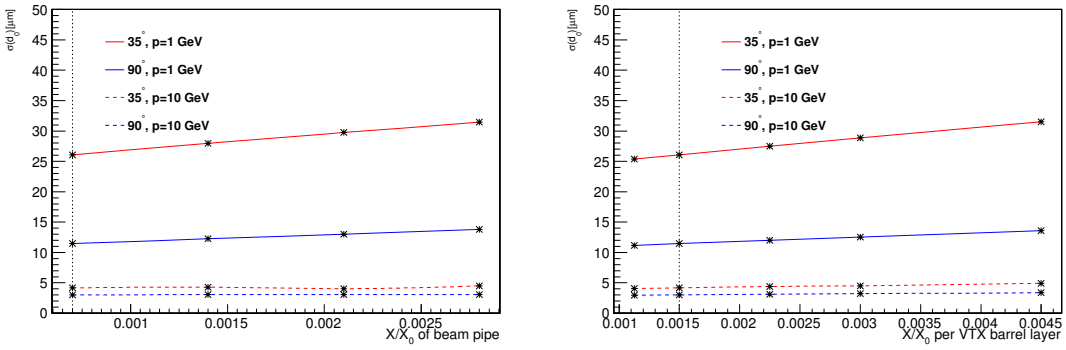

(a) (b)

Figure 6.4 Resolution of the transverse impact parameter as a function of material budget for (a) beampipe and (b) vertex detector layers. Resolution results are shown for $p = 1$ GeV muon tracks (solid lines) with polar angles of $\theta = 35°$ and $90°$. Results for muon tracks with $p = 10$ GeV are shown in dashed lines.

6.2.3.1 Material Budget

The baseline design requires a very low material budget for the beampipe and detector layers (pixel sensors and support structure), which might be difficult to meet in practice. Therefore it is important to assess thoroughly the performance sensitivity to additional materials. Figure 6.4(a) shows that resolution degrades when the beampipe material is increased. The effect is more prominent for tracks with lower momentum (which are more susceptible to the multiple scattering effect) and smaller polar angle (which transverse more material). Similar effects are also observed for increasing the material in the detector layers, as shown in Fig. 6.4(b).

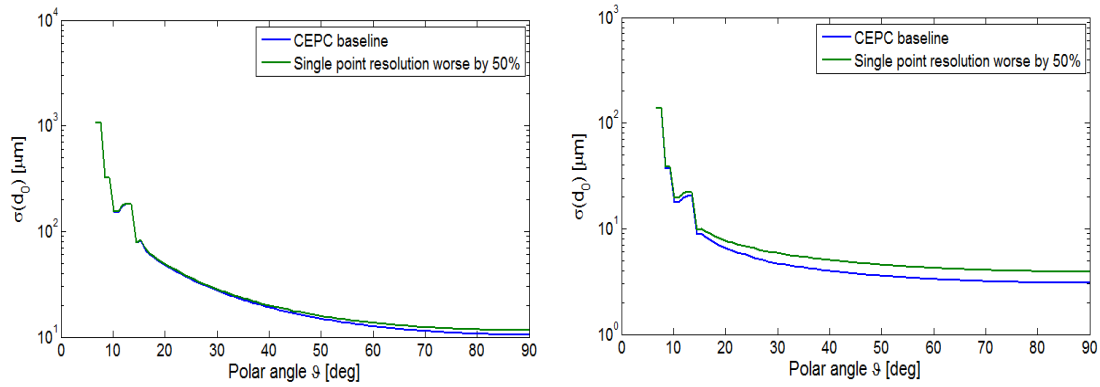

(a) (b)

Figure 6.5 Resolution of the transverse parameter as a function of polar angle θ with the default (in blue) and degraded (in green) single-point resolutions of the CEPC vertex detector. Results are shown for muon tracks with (a) $p = 1$ GeV and (b) $p = 10$ GeV.

6.2.3.2 Single-point Resolution

The impact of σ_{SP} on the transverse impact parameter resolution has been evaluated by decreasing σ_{SP} (or equivalently enlarging the pixel size for digital readout) by 50% with respect to the designed values as listed in Table 6.2. The resulting resolutions compared to the baseline design for high and low momentum tracks as a function of the polar angle θ are shown in Fig. 6.5. The resolution for the $p = 10$ GeV muon tracks degrades by approximately 30% in the barrel region, while for the $p = 1$ GeV muon track, for which multiple-scattering effects dominate the tracking performance, the resolution degrades by merely 10%. Fitting Eq. 6.1 to the degraded resolutions yields a term a which slightly exceeds the target value of 5 μm and a multiple scattering term b below 10 μm. This suggests that the single-point resolutions should be kept close to the designed values to achieve the expected performance. In addition, using worse single-point resolution or larger pixel size will possibly be restricted by the consequential higher detector occupancy caused by the beam-induced backgrounds (see Section 6.8) as well as the detector's capability to separate adjacent tracks in very dense jets.

6.2.3.3 Distance to the IP

The impact parameter resolution can be improved if the first vertex detector layer is moved closer to the IP to reduce the extrapolation uncertainty. Figure 6.6 compares the transverse impact parameter resolution at polar angle of $\theta = 90^\circ$ obtained with $r = 12$ mm

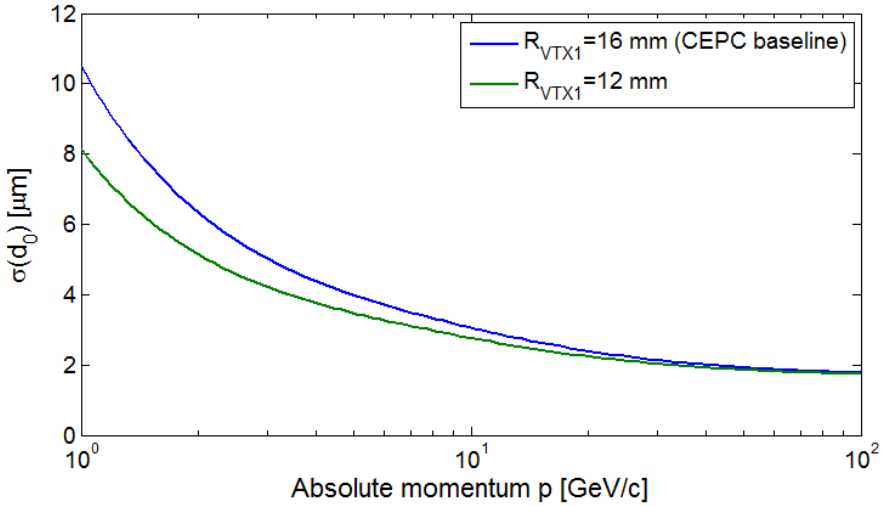

Figure 6.6 Resolution of the transverse impact parameter for muon tracks with polar angle of $\theta = 90°$ as a function of track momentum. Results are shown for the baseline design with the first detector layer positioned at $r = 16$ mm to the IP (in blue) and for a shorter distance of $r = 12$ mm (in green).

(beampipe radius reduced accordingly) and the CEPC baseline design of $r = 16$ mm. The gain is $\sim$20% for low track momentum ($p = 1$ GeV) but declines considerably for higher track momentum. On the other hand, the distance to the IP will be strongly constrained by the beam backgrounds, sensor radiation tolerance and mechanics feasibility, all of which require careful evaluation.

6.2.4 Sensor Options

The history of silicon pixel detectors can be traced back to the LEP era, when they were first introduced for the DELPHI experiment [11], and steady progress has been made over the last 20 years [12]. There has been a significant amount of R&D effort on pixel sensors for vertex detectors for future particle physics experiments [13], driven by the requirements of higher single point resolution and higher radiation hardness.

As outlined in Section 6.2.1, the detector challenges include high impact parameter resolution, low material budget, low detector occupancy and sufficient radiation tolerance (mild compared to the applications at the LHC or even the ILC, but not necessarily easy to achieve). To fulfil these system level requirements, the vertex detector must be constructed based on sensor technologies that push for fine pitch, low power consumption and fast readout. In particular, due to the absence of power-pulsing, which is allowed at the ILC [2] and CLIC [14], low power consumption is significantly more demanding for the CEPC vertex detector. Vertex detectors in other collider experiments, e.g. STAR [15], BELLE-II [16] and the ALICE upgrade [17], also operate in continuous mode, the same way as for the CEPC vertex detector, but they are typically much less demanding in terms of impact parameter resolution and material budget. At the time of drafting this conceptual design report, a sensor technology that satisfies all the requirements of the CEPC vertex detector does not yet exist. Nevertheless, there are several sensor technologies which have demonstrated potential and might in time, after extensive R&D, become suitable for construction of the CEPC vertex detector. Among the most promising technology

options are Depleted Field Effect Transistor (DEPFET) [18, 19], CMOS Pixel Sensors (CPS) [20, 21] and Silicon-on-insulator (SOI) [22].

DEPFET has a unique feature in that the main heat sources are located only at the ends of staves. As the thermal simulation of the BELLE-II staves shown in Fig. 6.7 indicates, power dissipation of 1 W for sensitive areas and another 1 W for switchers located within the acceptance area can be cooled down by a gentle air flow, while the major amount of heat (16 W in total) arising from the readout electronics, which are located outside the detector acceptance area, can be removed by massive CO_2 cooling. A prototype half stave for the BELLE-II experiment has achieved material budget as low as $0.21\%X_0$, and fast readout of 20 μs/frame. With a sensitive area of 64.4 mm$\times$12.5 mm, it might be applicable for the innermost layers of the CEPC vertex detector.

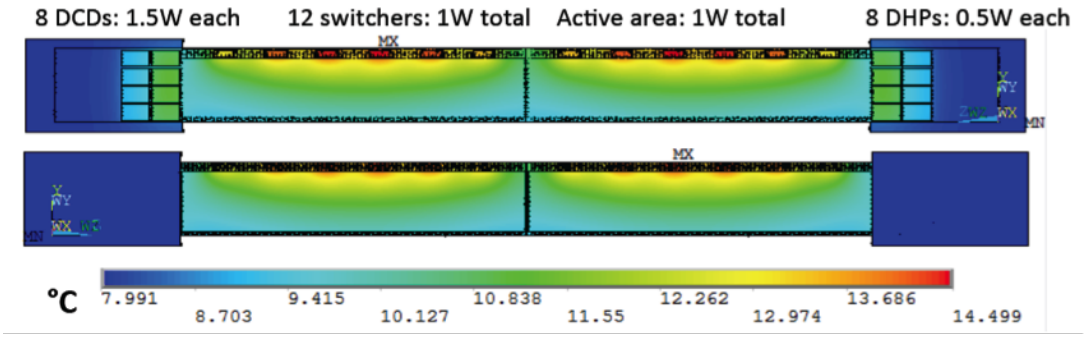

Figure 6.7 Thermal simulation of the BELLE-II staves, taken from [23].

CMOS sensor technology, in particular HR-CMOS, is gaining momentum from R&D for the ALICE ITS upgrade [17]. With successful operation and much experience learned from the MIMOSA-ULTIMATE CMOS sensor for the STAR PXL detector, and rapid progress achieved by the ALICE collaboration for the ALICE ITS upgrade, the HR-CMOS sensor is probably the closest to mature technology on the market. It has been demonstrated to meet almost every single aspect of the requirements for the CEPC vertex detector. However, it remains challenging to integrate all the specifications into a single functional chip. Intensive studies on circuit optimisation (e.g. in-pixel discrimination) and innovative readout schemes (e.g. column sparsification) are underway. Pushing the power consumption down to 50 mW/cm^2 or below will be a critical goal for its application to the CEPC vertex detector.

Sensors fabricated with the SOI technology are another important option. The critical issue of coupling between sensor and circuit has finally been well understood and addressed properly. This opens the door to a wide range of applications in astrophysics [24], material science [25] and particle physics [26], which have kept the Multi-Project Wafer (MPW) running steadily and continuously accessible. The SOI technology features fully depleted high resistive substrate, small feature size of 0.2 μm, full CMOS processing, and is suitable for 3D integration. A local group from IHEP has been actively involved in development of chips with fine pitch and complicated functions for over three years. Preliminary performance studies have demonstrated that making best use of high quality sensors and the SOI CMOS process could yield good signal-to-noise ratio, which may suggest an optimal solution for the demanding low power and fast readout. Similar to the HR-CMOS sensor technology described above, the power consumption needs to be capped at 50 mW/cm^2, keeping air-cooling feasible.

The criteria of being able to cope with continuous operation but retaining low power consumption have distinguished the three above-mentioned sensor options out of other technologies on the market. Other sensors like the Chronopixel [27] proposed for the SiD detector at the ILC and the CLICpix [28] for the CLIC detectors, in general consume a large amount of current in the pixels and have to rely heavily on the availability of power pulsing. HV-CMOS [29] sensor technology allows the implementation of simple electronics on top of the sensor and has been actively pursued by the ATLAS collaboration for their detector upgrade. It provides several promising features but might not be suitable for the CEPC vertex detector.

6.2.5 Mechanics and Integration

The design of the vertex detector is conceived as a barrel structure, consisting of six concentric layers. The geometric parameters of each detector layer are summarised in Table 6.2. The vertex detector covers the radial range from 16 mm to 60 mm. The two innermost layers extend to $|z|$=62.5 mm from the IP and the four outer layers to $|z|$=125.0 mm.

The detector will be realised with three double-layers, which are equipped with high spatial resolution pixel sensors on both sides and share a common support frame. In the azimuthal direction, each detector layer is segmented into ladders, which extend over the whole length of the layer. The ladders are the basic building blocks of the detector and contain all the structural and functional components, such as sensors, flex cable, support frame and cold plate, if it is necessary. Pixel sensors arranged in a row are connected to the flex cable with wire-bonding or other advanced bonding techniques. They are then glued to the support frame, which will be constructed from low Z materials (e.g. carbon fibre and silicon carbide), providing stable mechanical support. The other side of the support frame is equipped with another layer mounted with pixel sensors.

The design of the ladders should take into account the specifications of the vertex detector. On the one hand, the ladder mechanical structure needs to be built with lightweight material to minimise the effect of multiple scattering on the reconstruction of charged tracks; but on the other hand, it has to be constructed with the highest possible stiffness to control deformation from gravity and cooling forces imposed on the sensor. Much experience can be gained from other experiments facing the same challenges, e.g. the STAR pixel detector (PXL), and in future the ALICE ITS Upgrade and the BELLE-II PXD.

The ladder mechanical support will be inherently linked to the layout of the cooling system that will be adopted to remove the heat dissipated by the pixel sensors. The cooling system needs to be integrated into the mechanical structure. It remains the most critical issue for the cooling system design to properly balance the conflicting demands of efficient heat dissipation and minimal material budget. Therefore suitable cold plates, which are coupled with pixel sensors, with high thermal conductivity and low material budget, should be investigated. Table 6.3 summarises the applications and corresponding material budget of each detector layer in the aforementioned experiments. For the CEPC vertex detector, a suitable cooling method will be decided according to the sensor option chosen, and the power consumption and will be an important future R&D topic.

Simulation and module prototype studies should be carried out to find suitable designs that can meet the requirements for stability, cooling and performance of the vertex detector. For the design of the whole mechanical structure of the vertex detector, some criteria must be taken into account. Besides the aforementioned considerations on material bud-

Table 6.3 Vertex detector cooling method for various experiments.

Vertex detector	Power dissipation	Cooling method	Material budget requirement/layer
ALICE ITS	300 mW/cm^2	water	0.3%
STAR PXL	170 mW/cm^2	air	0.39%
ILD vertex	$<$120 mW/cm^2 (CPS and DEPFET)	air or N_2	0.15%
	35 W inside cryostat (FPCCD)	two-phase CO_2	
BELLE-II PXD	20 W for sensor and SWITCHER	air	0.2%
	180 W on each end	CO_2	

get, it should also ensure high accuracy in the relative positions of the detector sensors and provide an accurate position of the detector with respect to the TPC central tracker and the beam pipe. A mechanical connector or locating pin at each end of a ladder should be considered to allow the fixing and alignment of the ladder itself on the end rings. The cooling system should be arranged reasonably to ensure stable heat dissipation. It will be essential to reduce the dead region caused by the boundary of each ladder, so neighbouring ladders should be partially superimposed. In addition, the main mechanical support structures of the vertex detector should also meet the requirements of integration with the other detectors, such as the TPC and the forward tracking disks.

6.2.6 Critical R&D

As outlined above, the proposed vertex detector will be based on novel silicon pixel technologies, with low power consumption pixel sensors and low-mass mechanical structure, to meet the stringent performance requirements of the CEPC physics program. Since the technologies are not mature enough at this moment, it is necessary to evaluate emerging technologies, such as HR-CMOS, HV-CMOS, SOI and 3D integration, and carry out critical R&D effort to make them available for engineering construction.

6.2.6.1 Pixel sensors with low power consumption and high readout speed

From the viewpoint of circuit design, high readout speed and low power consumption are contradictory. However, moving column-shared discriminators into individual pixels would benefit readout speed and power reduction simultaneously in a conventional rolling shutter scheme. More efficient readout schemes can be implemented by in-pixel discrimination and column-coding to avoid periodical polling through the entire pixel array. Much of the improvements and optimisations at sensor level are related to such circuit design. Small pixel size is also a challenge to meet the single point resolution requirements for the innermost detector layers.

6.2.6.2 Mechanical design and cooling

Cooling, mechanical support and cabling within the acceptance region are critical engineering challenges. In order to build ladders with discrete chips of HR-CMOS or SOI, lightweight mechanical support and cabling are necessary with a material budget of less than $0.05\%X_0$ each. As for DEPFET all-silicon staves, the total material budget is expected to be as low as $0.15\%X_0$. Manufacturing and assembly of these ladders/staves has to

be fully verified. In addition, the vibration must be characterised carefully so as to obtain enough cooling capability and not degrade the impact parameter resolution. In the case of DEPFET, additional CO_2 cooling has to be introduced to cool the hot spots of the readout chips, which makes the system more complex.

6.2.6.3 Sensor thinning

Thinning sensors down to 50 μm has been demonstrated on MAPS chips/wafers, which do not require further processing on the back side of chips/wafers. Both DEPFET and SOI, however, require back side processing after thinning. DEPFET for BELLE-II has been successfully thinned down to 75 μm in the sensitive area [16] and is likely to be thinned to 50 μm without fundamental difficulties. SOI has already achieved 110 μm without any adverse effect observed [30]. However, the reliability and yield after thinning down to 50 μm have to be studied carefully.

6.2.6.4 Detector layout optimisation

It is very important to develop a full simulation of the vertex detector, and perform continuous optimisation studies, combined with the proposed tracking detector. With full simulation, more realistic studies of detector options with tight material budget requirement, for both pixel and microstrip layers, could be performed to evaluate the impact of CO_2 cooling instead of air cooling, if that is found to be necessary. In addition, it will be very helpful to carry out a study on an all-silicon tracker, comparing with the current baseline detector layout, for performance optimisation.

For all those R&D issues, it is vital to have worldwide effort to investigate the possible technologies, including the development of equipment and facilities to build and test detector modules, so as to realise the detector requirements under continuous operation.

6.2.7 Summary

The basic concepts of the ILD vertex detector, including the pixel sensor specifications required by the impact parameter resolution and radiation tolerance, the low-mass mechanical design, and the detector layout, are largely adapted to the baseline design of the CEPC vertex detector. However, as power-pulsing will not be an option at the CEPC, it will be crucial to develop pixel sensors with lower power consumption and fast readout electronics. Detailed designs for mechanical supports and cooling, cabling, and power conversion are also necessary. Furthermore, detector layout optimisation with full simulation should be studied. Most of these issues have to be resolved with future R&D work for the CEPC, exploiting synergies with other experiments which have similar requirements.

6.3 Silicon Tracker

In addition to the vertex detector (Section 6.2) and the TPC (Section 6.4), the CEPC tracking system also includes a silicon tracker, exploring a similar scenario to that adopted for the ILD detector design [2]. Complementary to the continuous tracking provided by the main tracker TPC, the CEPC silicon tracker, together with the vertex detector, provides several additional high-precision space-points on the track trajectory before and after the TPC, yet with sufficiently low material as to minimise the multiple-scattering effect. Such a tracking system, using a mixture of detector technologies, enables efficient and robust reconstruction of charged particles and precise determination of the particle momenta, with excellent resolution of

$$\sigma_{1/p_{\mathrm{T}}} = 2 \times 10^{-5} \oplus 1 \times \frac{10^{-3}}{p_{\mathrm{T}} \cdot \sin\theta.} \tag{6.2}$$

In addition, the silicon tracker provides the possibility to monitor possible field distortion in the TPC. It also contributes to the detector alignment and allows time-stamping for the separation between bunch crossings to suppress overlapping events.

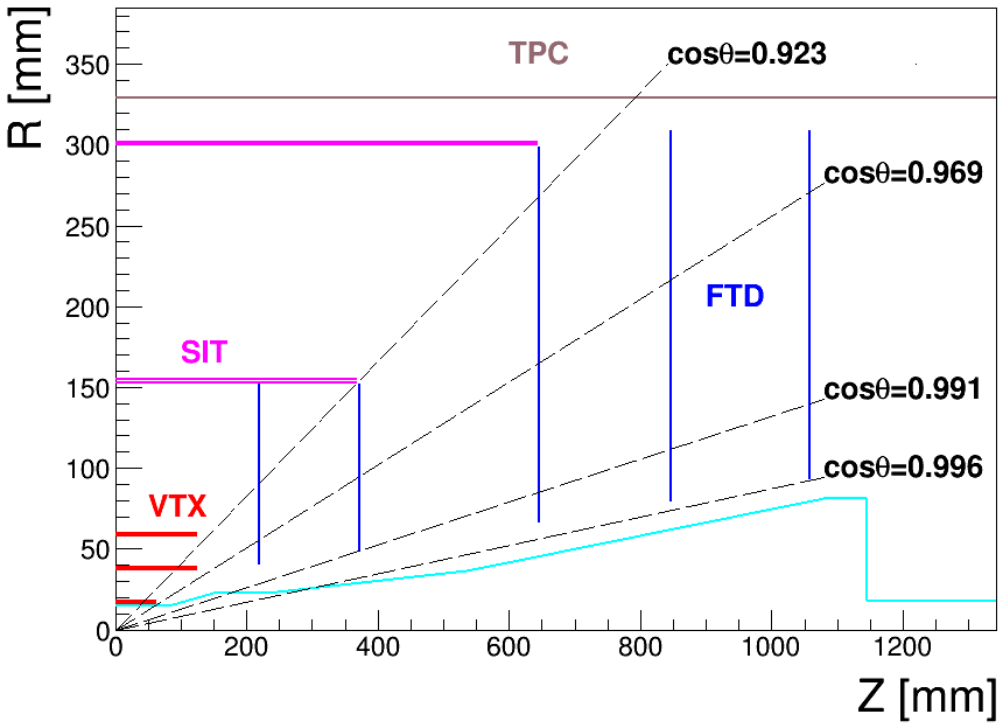

Figure 6.8 Preliminary layout of the CEPC silicon tracker. The red lines indicate the positions of the vertex detector layers and the blue lines the SIT and FTD for the silicon tracker. The SET and ETD, which sit outside the TPC, are not displayed.

6.3.1 Baseline Design

The baseline design for the CEPC silicon tracker adopts the same concept of "Silicon Envelope" [31] as for the ILD detector, but necessary modifications are made to cope

with the rather different CEPC interaction region design. In the central region, there are three detector layers mounted with double-sided silicon microstrip sensor modules, with two of them located between the vertex detector and the TPC to form the Silicon Internal Tracker (SIT) and the third just outside the TPC called the Silicon External Tracker (SET). The SIT enhances the matching efficiency between the vertex detector and the TPC, and improves the momentum resolution as well as the reconstruction of charged particles with low momenta. The SET delivers a precise entry point to the electromagnetic calorimeter after the TPC end wall. The SIT and the SET improve the overall tracking performance in the central region. In addition, they serve to monitor the distortion of the TPC and provide precise time-stamping for bunch separation.

Table 6.4 Main parameters of the CEPC silicon tracker.

Detector		Geometric dimensions			Material budget $[X/X_0]$
SIT	Layer 1:	$r = 153$ mm,		$z = 371.3$ mm	0.65%
	Layer 2:	$r = 300$ mm,		$z = 664.9$ mm	0.65%
SET	Layer 3:	$r = 1811$ mm,		$z = 2350$ mm	0.65%
FTD	Disk 1:	$r_{in} = 39$ mm,	$r_{out} = 151.9$ mm,	$z = 220$ mm	0.50%
	Disk 2:	$r_{in} = 49.6$ mm,	$r_{out} = 151.9$ mm,	$z = 371.3$ mm	0.50%
	Disk 3:	$r_{in} = 70.1$ mm,	$r_{out} = 298.9$ mm,	$z = 644.9$ mm	0.65%
	Disk 4:	$r_{in} = 79.3$ mm,	$r_{out} = 309$ mm,	$z = 846$ mm	0.65%
	Disk 5:	$r_{in} = 92.7$ mm,	$r_{out} = 309$ mm,	$z = 1057.5$ mm	0.65%
ETD	Disk:	$r_{in} = 419.3$ mm,	$r_{out} = 1822.7$ mm,	$z = 2420$ mm	0.65%

In the forward region, the End-cap Tracking Detector (ETD) is positioned between the TPC and the calorimeter, and the Forward Tracking Detector (FTD), which has five disks on each side, covers the low solid angle area. The ETD improves the momentum resolution for charged tracks in this particular region and increases the matching efficiency between the TPC and the calorimeter. The FTD is essential for charged particle reconstruction and momentum determination in the very forward region. To lower the detector occupancy due to high background rate and improve the angular resolution, it is foreseen to construct the two innermost disks with pixel detectors, and the remaining three disks with microstrip sensors. The preliminary layout of the CEPC silicon tracker is illustrated in Fig. 6.8 (SET and ETD not shown). The geometric parameters and material budget of the detector components are summarised in Table 6.4.

6.3.1.1 Silicon Microstrip Sensor

Silicon microstrip sensors bonded to front-end (FE) electronics will be the basic elements used to construct the CEPC silicon tracker. Pixel sensors for the two innermost FTD disks can be same as for the vertex detector as described in 6.2. The microstrip sensors will be fabricated with the cost-effective p^+-on-n technology and in large size wafers ($6''$ or even $8''$), featuring a large detection area of $10 \times 10\ \mathrm{cm}^2$ and a fine pitch size of $50\ \mu$m. The latter is essential to meet the stringent requirement on the single point resolution of $\sigma_{\mathrm{SP}} < 7\ \mu$m for high precision tracking. Thinned sensors with thickness below 200 μm are attractive to minimise the material and so the multiple-scattering effects. This can be achieved with

appropriate thinning techniques, e.g. mechanical thinning and silicon chemical etching. Slim-edge [32] is another attractive feature which can be used to minimise material excess due to sensor overlapping and simplify the detector construction.

Alternatively, it is possible to fabricate pixelated strip sensors based on CMOS technologies [33], as is being pursued by the ATLAS experiment for its detector upgrade toward the High Luminosity LHC. This has the clear advantage of fabricating large area sensors with significant reduction in production cost. Furthermore, it allows the development of active circuits on the sensor, which opens the possibility of generating additional spatial information or configurable grouping of strip channels.

6.3.1.2 Front-End Electronics

The FE electronics will be custom designed ASICs fabricated with deep sub-micron CMOS technology (preferably below 90 nm). The low noise readout chip, with similar functions to those provided by KPiX [34] and SiTRA [35] for the ILC tracking detectors, will allow full processing of the analogue signal, time stamping (required by the TPC time calibration), sparsification, digitisation and high-level digital processing, to relax the data-processing pressure on downstream electronics. In the absence of power-pulsing (continuous operation for the CEPC collider), it is critical to explore novel readout architectures to significantly reduce the power consumption of the readout electronics. The FE chip will be thinned down to below 200 μm and wire-bonded or bump-bonded to the silicon microstrip sensor. Other novel interconnection technologies, in particular 3D packaging-based Through Silicon Vias (TSV) [36], will be explored to make the design as compact as possible and to minimise material budget.

6.3.1.3 Powering and Cooling

Powering and cooling are a challenge for the CEPC silicon tracker. It is important to investigate the novel powering scheme based on DC-DC converters, which has been already actively pursued by the ATLAS and CMS experiments for silicon detector upgrades [37–39]. It allows significant reduction in material budget for the low-voltage power cables and gives less power dissipation in the delivery system. Cooling is another critical issue as power-pulsing will not be optional at the CEPC. Although cooling based on forced cooled gas flow might be still feasible to efficiently conduct away the heat generated by the sensors, ASICs and other electronics, it is important to look into other cooling techniques, such as silicon micro-channel cooling [40], which are being investigated by several other experiments. The technique chosen will have to provide sufficient cooling without compromising the detector performance.

6.3.1.4 Mechanics and Integration

There will always be additional challenging aspects of the mechanical design for a large area silicon tracker. A lightweight but stiff support structure can be built based on Carbonfibre Reinforced Plastic material [41]. The support structure, cable routing and electronics common to other sub-detectors need to be carefully designed to minimise the overall quantity of material and make easy construction and integration possible. Precise and quick system alignment might be achieved with dedicated laser monitoring systems, while the final alignment will be accomplished using tracks from well-understood physics events [42].

6.3.2 Tracker Performance

While the tracking performance in the central region, which features the same layout as the ILD detector, has been extensively studied [1, 2], the performance in the forward region, which has been re-designed to cope with the rather short L^*, requires additional careful evaluation. Figure 6.9 shows the estimated transverse momentum resolution for single muon tracks for two polar angles $\theta = 20°$ and $85°$ (solid lines), and the analytical results from Eq. 6.2 (dashed lines). Due the reduced lever arm of the tracks and fewer FTD disks in the forward region ($\theta = 20°$), the resolution is worse than the required performance.

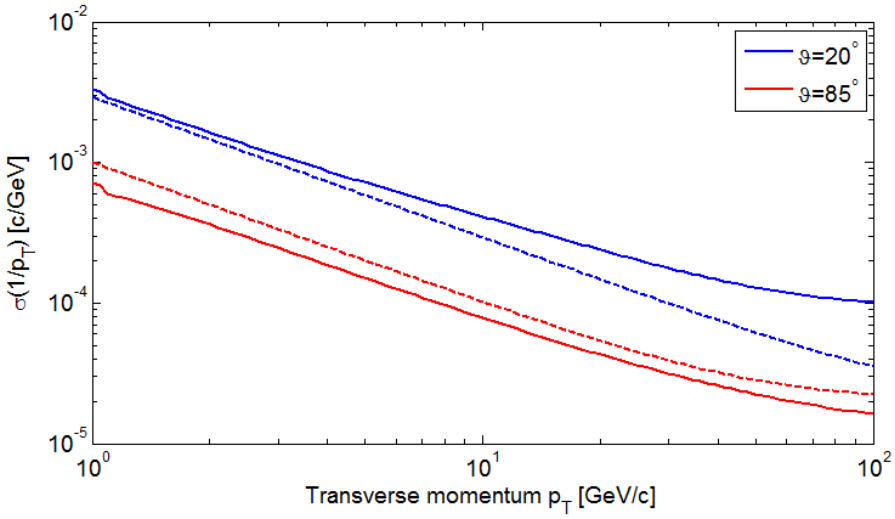

Figure 6.9 Resolution of the transverse momentum of single muon tracks as a function of the track momentum estimated for the CEPC baseline design (solid lines) compared to the analytical results obtained with Eq. 6.2 (dashed lines).

In addition, given its importance for heavy-flavour tagging, the impact parameter solution is assessed. As shown in Fig. 6.10, the transverse impact parameter resolution for the CEPC baseline design is clearly worse than the original ILD design in the forward region ($\theta < 10°$). Such a performance loss cannot recovered by inserting two more disks between the IP and the outermost FTD disk.

However, the impact parameter resolution in the very forward region ($\theta < 10°$) can be improved by extending the coverage of the innermost vertex detector. Figure 6.11 shows that either extending the first two barrel layers of the vertex detector from the current $z = 62.5$ mm to $z = 100$ mm or extending the inner radius of the first FTD disk down to $r = 22$ mm can improve the tracking performance. The feasibility of such a design will be largely constrained by the beam-induced background and requires detailed studies. Further optimisation of the detector layout can be only made once a more realistic design of mechanics and services becomes available.

6.3.3 Critical R&D

Silicon technology for large-area tracking detectors will continue to evolve over the next few years [43]. There are ongoing R&D activities conducted by the ATLAS and CMS experiments to develop advanced silicon detectors for the High Luminosity LHC as well as several pioneering R&D projects by the SiLC (Silicon tracking for the Linear Collider)

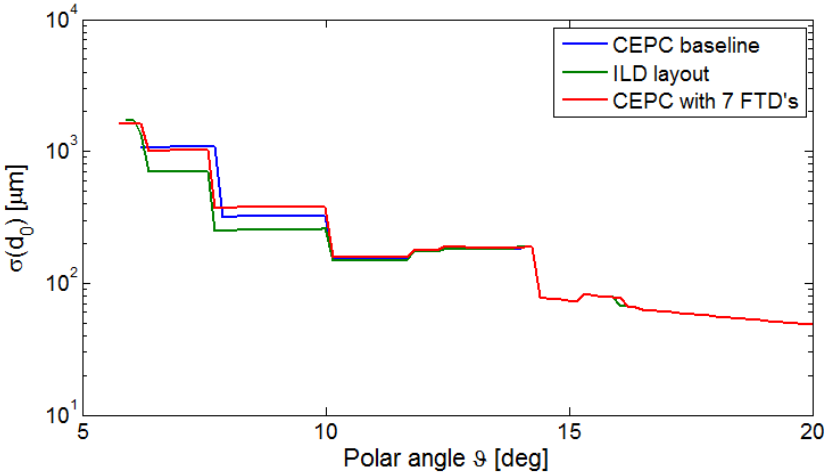

Figure 6.10 Impact parameter resolutions for muon tracks with momentum of $p = 1$ GeV as a function of polar angle, obtained for the baseline CEPC silicon tracker layout (in blue), the original ILD layout (in green) and the CEPC layout with seven FTD disks (in red).

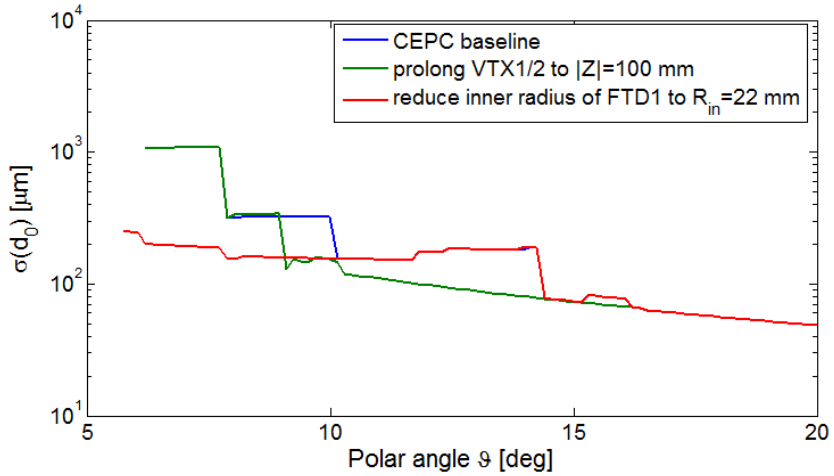

Figure 6.11 Impact parameter resolutions for muon tracks with momentum of $p = 1$ GeV as a function of polar angle obtained for the baseline CEPC silicon tracker layout (in blue), layout with the first two vertex detector layers extended (in green) and layout with the first FTD disk extending to smaller radius (in red).

collaboration. Despite the rather different operation conditions and requirements, it is always important to exploit synergies with existing R&D from other experiments to share expertise. During the preliminary studies, several critical R&D items have been identified for the CEPC silicon tracker. All of them, as listed below, will be pursued in the R&D phase of the CEPC project and made available for engineering construction.

- p^+-on-n silicon microstrip sensors with slim-edge structure and the alternative pixelated strip sensors with CMOS technologies;
- Front-end electronics with low power consumption and low noise, fabricated with CMOS technologies of small feature size;
- Efficient powering with low material budget and CO_2 cooling techniques;
- Lightweight but robust support structure and related mechanics;
- Detector layout optimisation, in particular in the forward region.

It will be vital to develop necessary instrumentation for the module assembly and to verify the detector module performance with beam tests. Prototypes of support structures, including cooling solutions, shall be also built for mechanical and thermal tests.

6.4 Main Tracking Detector – TPC

Time Projection Chamber (TPC) detectors have been widely used in high energy physics experiments, as listed in Table 6.6, thanks to their excellent tracking performance, low material budget and structural simplicity. The baseline design of the CEPC TPC detector takes exactly the same form as that of the ILD detector. It features a cylindrical chamber with inner and outer radii of 0.325 m and 1.8 m respectively, and a full length of 4.70 m. As the main tracker, the TPC provides nearly 200 three-dimensional (r, ϕ and z) space-points with $r\phi$ resolution of 100 μm along the track trajectory, and it covers the solid angle up to $\cos\theta \simeq 0.98$. This allows tracking efficiency of better than 97% for tracks with $p_{\mathrm{T}} > 1$ GeV. The detector will operate in a strong magnetic field of 3.5 T to achieve a track momentum resolution better than $\sigma(1/p_{\mathrm{T}}) = 10^{-4}$ GeV^{-1}. In addition, the low material thickness in the TPC detector allows optimal performance for the calorimeter behind. It also allows excellent particle identification using specific energy loss information ($\mathrm{d}E/\mathrm{d}x$). Overall, the TPC detector is designed to achieve robust tracking and easy maintenance during operation.

Table 6.5 Main specifications of TPC detectors in various experiments.

Experiment	**Magnetic field [T]**	**Momentum resolution [GeV^{-1}]**	$\sigma(\mathrm{r}\phi)$ [μm]	$\mathrm{d}E/\mathrm{d}x$
ALEPH [44]	1.5	1.2×10^{-3}	160 – 400	4.5%
PANDA [45]	0.5	2×10^{-3}	150	4%
STAR [46]	0.5	2×10^{-3}	500 – 2000	3%
T2K [47]	0.2	0.1	700	10%
HARP [48]	0.7	$0.02 - 0.25$	600 – 2400	16%
ALICE [49]	0.5	0.01	800 – 1100	5%

6.4.1 Design and Challenges

To meet the stringent requirements on momentum resolution, solid angle coverage, material budget and detection efficiency of the TPC detector, special consideration must be given to detector geometry, magnetic field, working gas, readout module and electronics, which are described in detail below. In addition, to realise the required space-point resolution, the CEPC TPC detector is designed to be read out with Micropattern Gaseous Detectors (MPGDs).

6.4.1.1 Structure

The basic ingredients of the TPC detector include a gaseous volume, in which the traversing particles create electron-ion pairs through collisions with the working gas atoms. An electric field is set up between a cathode and the end-plate to record the track information in the field cage. In the field cage, a chain of precision resistors with small current flow provides a uniform voltage drop in the z direction of the chamber, and non-uniformity due to the finite spacing of the strips falls into active regions. When the input electron signal is fed to the pre-amplifier electronics, and then to the shaping and discriminating circuit, the charge and time information will be obtained by the data acquisition (DAQ) system.

Such information is used to reconstruct the particle track. The structure of the ILD TPC detector is depicted in Fig. 6.12.

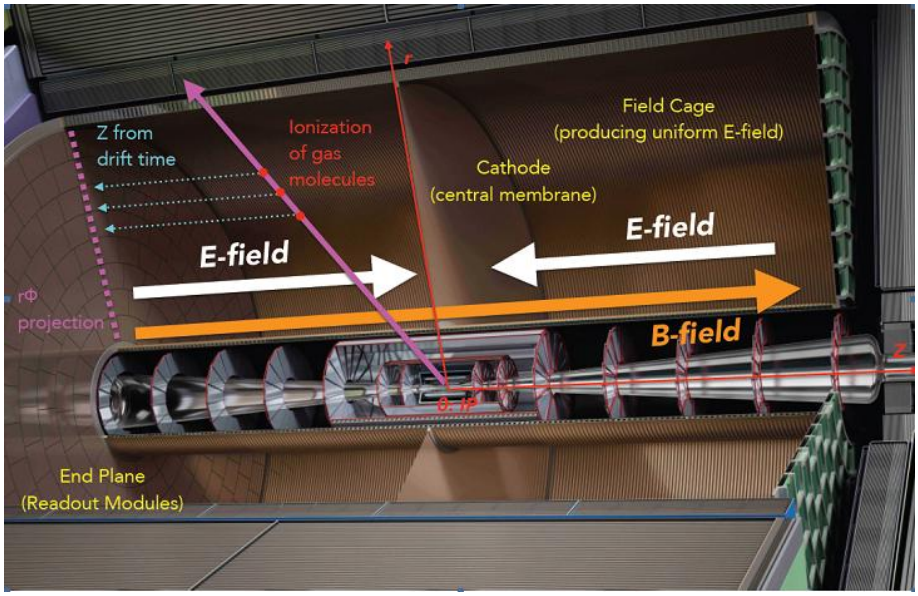

Figure 6.12 Sketch of the ILD TPC structure.

The mechanical structure of the TPC consists of a field cage, which is made with advanced composite materials, and two self-contained readout end-plates which include the gas amplification, readout electronics,high voltage system, and cooling. It will be challenging to design and build the TPC support structure with relatively light material but with sufficient rigidity. It is required to maintain accuracy, robustness in all directions, and stability over long periods of time. Due to the limited material budget, the field cage is not strong enough. This leaves the end-plates as the only viable option to which the support structure can be connected. In the current design, it has not yet been determined how to support the TPC end-plates. A promising solution is to suspend them from the solenoid, by a number of spokes which run radially along the faces of the calorimeter to the TPC end-plates. Load-bearing is not the most challenging issue; the main concerns are system accessibility and robustness against various accidental movements, especially in the longitudinal direction. The inner and outer silicon trackers might be supported by the TPC field cage. Although there are no major conceptual issues, such extra load requires a much stiffer structure, possibly at the cost of additional material. In addition, the supporting material should be non-magnetic, vibration absorbing, with a low thermal-expansion coefficient, and the ability to achieve a position precision of 100 μm. Given these requirements, carbon-fibre reinforced composite is considered the leading candidate.

In the following, main components of the CEPC TPC, including the chamber, the field cage and the end-plate, are described.

1. **Chamber**

   Large-scale TPC chambers have been successfully deployed in several collider experiments. They are typically cylindrical, filled with a working gas, and can operate under atmospheric pressure. Chambers in high magnetic field close to the centre of the magnet usually have higher occupancies due to the curling of charged particles with low momentum. Access for cables and services is limited in this region and the

material budget of the components inside the magnet must be kept low. In the active area, the added material due to the filled gas should be below $1\%X_0$. The chambers are attached to the end-plate from the inside to minimise the dead area between neighbouring chambers. A special mounting technique needs to be developed to allow rotation and tilting of the chambers.

2. **Field cage**

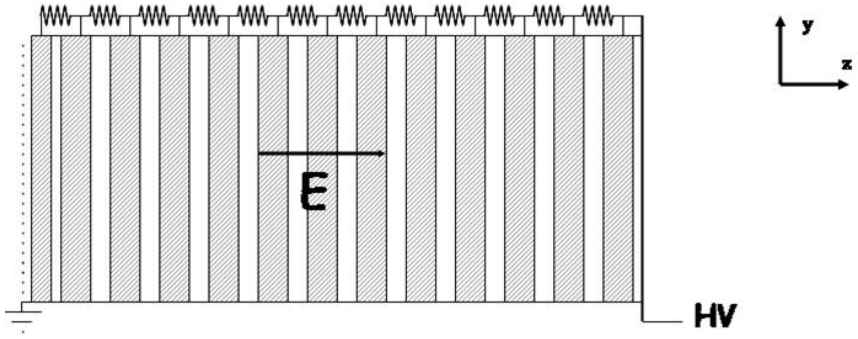

Figure 6.13 Sketch of the TPC field cage.

For the CEPC TPC detector, lightweight cylindrical inner and outer composite walls are designed to hold the field and form strips, which are attached to a resistor divider chain network as shown in Fig. 6.13. The resistors must be non-magnetic. A central cathode will be held at approximately 50 kV when the drift field is 300 V/cm, with the end-plates and other outer surfaces of the TPC at ground potential. This requires the composite walls to withstand the large potential of the central cathode. Narrow mirror strips will be arranged between the inner and outer walls to keep the electron field uniform over the whole active volume of the TPC.

3. **End-plate**

To obtain high position resolution, every end-plate is subdivided into many independent MPGD detector modules (standard GEM or Resistive Micromegas detector), which cover nearly the entire end-plate. Power cables, electronic connectors, cooling pipes, PCB boards and support brackets wall are also mounted on the end-plate. In case the detector modules are damaged by discharge or spark, they can be replaced and the end-plate should be kept stable during the replacement. In addition, the end-plate needs to be built with lightweight materials, so as not to compromise the jet energy resolution in the forward region. It should still be sufficiently rigid, however, such as to achieve stable positioning of the detector modules with a position precision better than 50 μm. The material budget of the mechanical structure accounts for $\sim 8\%X_0$. Additional material for the readout planes, front-end electronics and cooling are estimated to be $\sim 7\%X_0$, and up to $\sim 10\%X_0$ for the power cables and connector.

6.4.1.2 Detector Geometry

The TPC detector allows robust track reconstruction and precise momentum determination of charged particles. The tracking capability of the TPC can be characterised by its bending power, BL or BL^2, where B and L represent the magnetic field strength and the detector radius, respectively. Stronger B-field and larger detector volume will give

better separation and higher resolution. However, the detector size is typically limited by the construction cost, and strong B-field decreases the reconstruction efficiency for low momentum tracks. The resolution and separation of the charged tracks can be improved by having more space-points on the track and/or by improving the single-point spatial resolution.

For a track with specified incident angle and momentum, the measurement number is determined by the TPC geometry. At the same time, the detector geometry can also partly influence the point resolution due to the diffusion effect when electrons drift along the z direction. It is important to have efficient diffusion in the transfer and induction gaps while having as little diffusion as possible in the drift region. The diffusion constant in high B-field can be expressed as follows:

$$D(B) = \frac{D(B=0)}{\sqrt{1+(\omega\tau)^2}} \tag{6.3}$$

where $\omega \equiv eB/m$ and τ is the mean free time of electrons. In general, $\tau(E)$ is smaller in a higher electric field because of higher random velocity of electrons and larger cross sections of gas molecules. Therefore the influence of an axial magnetic field on the diffusion constant is relatively small in the high electric fields in the transfer/induction gaps of the detector.

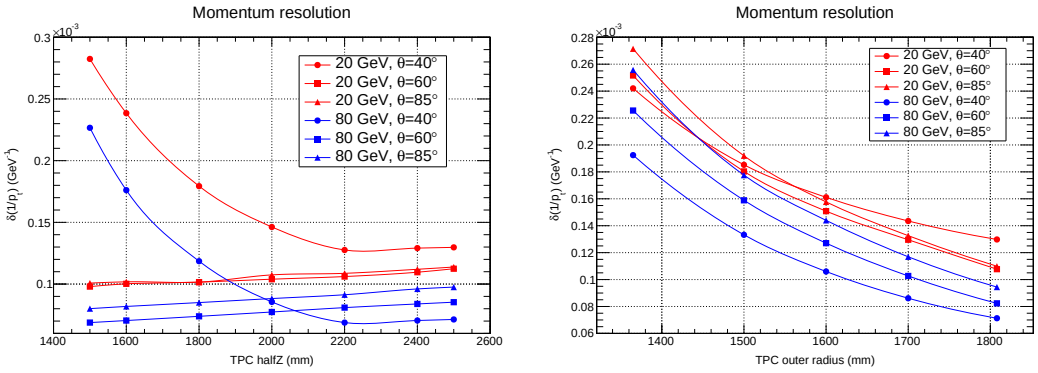

(a) (b)

Figure 6.14 Simulated results of track momentum resolution with different TPC geometries.

The transverse momentum resolution with different TPC half-lengths and outer radii is shown in Fig. 6.14. Better momentum resolution can be achieved for higher momentum tracks because they are less impacted by the multiple scattering effect. For small polar angles, the track momentum resolution improves rapidly as the TPC half-length increases, and stabilises beyond 2.2 m. But for large polar angles, the resolution performance improves slightly as the TPC half-length increases. The half-length of the CEPC TPC detector is designed to be 2.35 m. The momentum resolution as a function of the TPC outer radius is shown in Fig. 6.14(a). The resolution reaches the design value of 1.5×10^{-4} GeV^{-1} for $r > 1.7$ m. The outer radius of the CEPC TPC is designed to be 1808 mm, which is exactly the same as that of the ILD TPC. However, it requires further optimisation to balance the overall detector performance and cost.

6.4.1.3 Working Gas

In a given working gas and electric field, the drift velocity of electrons can be determined with:

$$\mu_e = f(\frac{E}{P}) \tag{6.4}$$

where E denotes the electric field vector, P the gas pressure and μ_e the electron drift velocity. After reaching saturation (nearly maximum), the electron drift velocity only depends slightly on the electric field. Figure 6.15 shows the drift velocity obtained for different gas mixtures. As the CEPC TPC is required to be sensitive to the longest possible track segments, the working gas should be selected in such way to achieve high velocity in low drift fields, to lower the high voltage over the whole drift length, with small transverse diffusion in the magnetic field to decrease the electron cluster size on the readout pads.

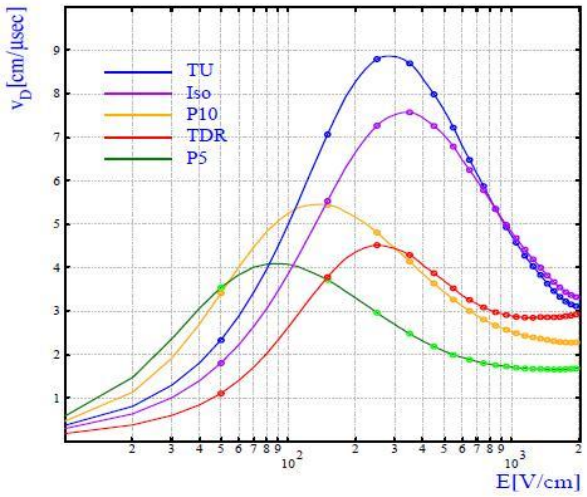

Figure 6.15 Drift velocity in different gas mixtures.

A gas mixture of Ar/CF_4/iC_4H_{10} (95%/3%/2%) has been used for the Large Prototype TPC Detector for ILD [50] and the TPC for the T2K experiment [47]. The saturated drift velocity of the mixed gas reaches nearly 8 cm/μs in a drift field of 300 V/cm. The gas has a large $\omega\tau$ parameter and transverse diffusion coefficient of 30 μm/$\sqrt{\text{cm}}$ in a drift field of 300 V/cm. In the B-field, a reasonable transverse diffusion coefficient could be realised at 100 V/cm of the drift field. A working gas with a higher saturated drift velocity than the T2K mixed gas should be considered. In addition, the gas gain needs to reach about 6000, but the signal attenuation due to electron attachment should be kept below 1%/m.

Detailed simulation studies will be carried out using the Garfield software package. The working gas must be carefully selected to accommodate the CEPC collision conditions. Gas with fast drift velocity shall be considered but consequent effects of electron accumulation and potentially more severe positive ion feedback need to be taken into account. Electron pile-up in the working gas will be simulated and its effects on benchmark physical measurements will be evaluated. It is possible to take the T2K working gas as the starting point and optimise it further for the CEPC TPC detector.

6.4.1.4 Readout Modules

The readout structure is designed to be modularised. Each module will consist of gas amplification system, readout pad plane and following electronics. High density electronics make it possible to integrate the electronics directly on the back of the readout pad plane. The readout module will then have to provide all necessary high and low voltages and cooling for heat dissipation, however, especially because power-pulsing will not be available at the CEPC. To achieve the required performance, an MPGD-based gas amplification system will be developed. The charge from the amplification system will be collected on a pad board. According to studies by the LCTPC collaboration, the pad size should be around $1 \times 6\ \mathrm{mm}^2$ to collect enough charge for high signal-to-noise ratio (SNR) and to achieve the expected point resolution. It has also been demonstrated that both amplification technologies combined with pad readout can be used to build modules, allowing coverage of a large detector area with little dead region.

1. **GEM+pad readout**

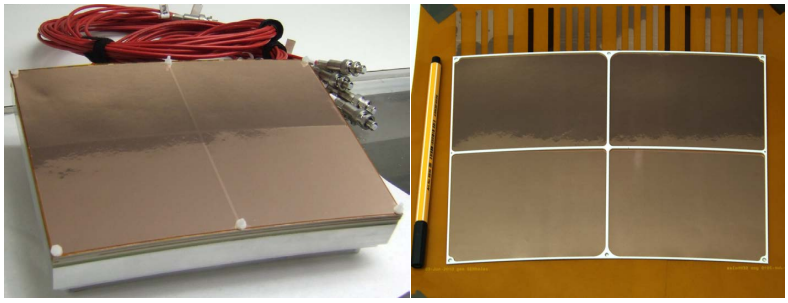

Figure 6.16 The design of double-GEM module with foils stretched between two bars at the top and bottom of the module (left) and GEM foil mounted on a ceramic grid to get the necessary support (right).

GEM has the advantages of high position resolution, good energy resolution, tolerance of high count rate, and easy assembly. Triple and quadruple GEM foils can be cascaded to build higher gain detectors. However, for cascaded GEM detectors, the last GEM foil near the readout plane can easily be damaged by sparks that are induced by the large number of electrons. To reduce the probability of sparks, two or three GEM foils are stacked up to provide the required gas gain. The de-focussing of multi-GEMs allows more than one pad per row to sample the charge, which makes it plausible to achieve good spatial resolution.

For multi-GEM systems, it is always challenging to provide the support structure, which has to keep the GEM surface flat and parallel without introducing dead space or adding too much material. Several methods have been developed and successfully deployed. Figure 6.16(left) shows the design of a double-GEM module with foils stretched between two bars at the top and bottom of the module, designed by the LCTPC Asian group. Figure 6.16(right) shows an alternative design by the DESY group, in which the GEM foil is mounted on a ceramic grid to get the necessary support.

2. **Micromegas+resistive pad readout**

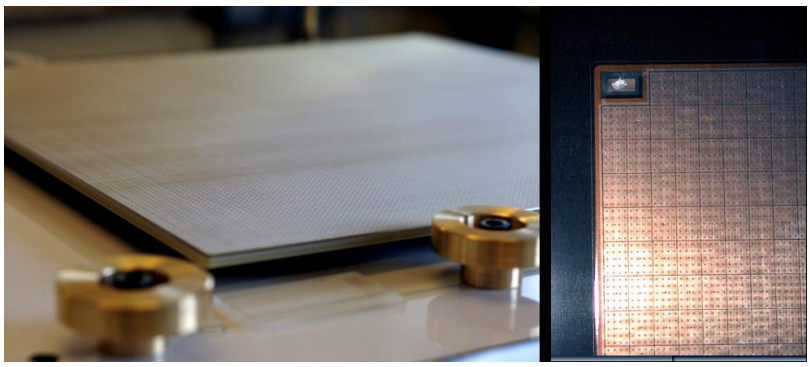

Figure 6.17 Readout with Micromegas detector.

Micromegas is a micro-pattern type of gaseous detector. Its typical structure consists of three electrodes: drift electrode, avalanche electrode and anode. The avalanche electrode is made of metallic micromesh and the anode is copper strips or pads on a glass fibre reinforced epoxy substrate. The gap between the drift electrode and avalanche electrode serves as the conversion region, and the gap between the micromesh and the anode is the avalanche region. In the conversion region, electron-ion pairs are produced by ionisation in the working gas. Electrons drift through the micromesh into the amplification gap following the electric force lines, and they are multiplied in the avalanche process. The distance between the avalanche electrode and anode can be maintained accurately by an array of tiny pillars using the "Bulk" technology [51].

The drawback of Micromegas is its vulnerability to sparks, especially in a high radiation environment. If a large number of electron-ion pairs are produced by avalanches in the amplification gap, they could lead to discharge between the mesh and the metal readout anode. Discharges will occur when the total number of generated electrons in the amplification region exceeds approximately 10^7 (Raether limit [52]). Additionally, in very high particle flux, Micromegas detectors are vulnerable to sparks because avalanches can so easily overlap each other in space and time, resulting in extremely high local electron density. In extreme cases, sparks can also damage the detector and electronics. One possible solution is to add a resistive layer to the anode surface to reduce sparks between the mesh and the readout electrode.

A Micromegas detector can provide enough amplification in a single structure, but the signals are very narrow on the readout plane. As well as reducing sparks, a resistive layer with appropriate resistivity can spread the signals induced on the readout strips or pad over a wider area, allowing the use of wider readout elements. Figure 6.17 shows a module with Micromegas amplification and a resistive layer on the pad plane for charge spreading and protection of the front-end electronics.

3. **THGEM+pad readout**

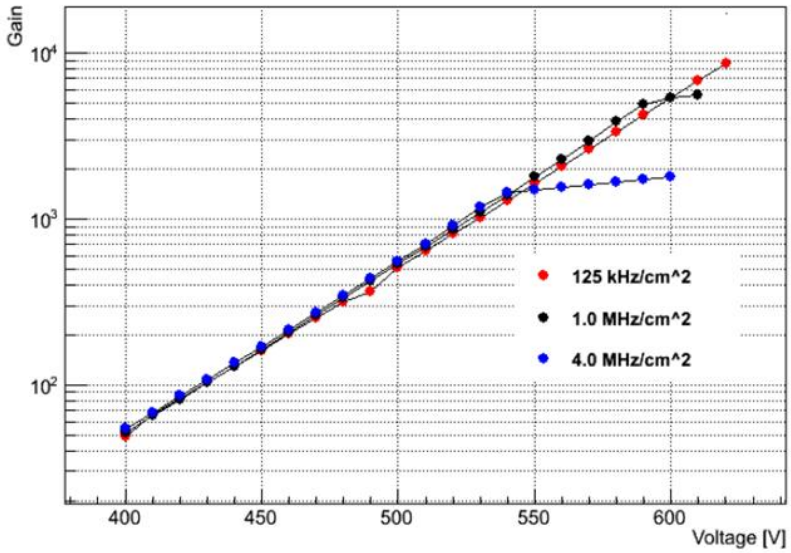

Figure 6.18 Thinner-THGEM gain behavior versus applied voltage under different X-ray rates.

The Thicker-GEM (THGEM) is a robust gaseous electron multiplier based on the principles of GEM, but with the geometrical parameters scaled up. THGEM can be fabricated with standard PCB mechanical drilling and global etching processes, which offer economical production of large numbers and large detector sizes. The geometrical parameters of THGEM spread over a wide range: the PCB thickness can vary from 0.2 to 1 mm, the hole diameter from 0.15 to 1 mm, and the hole pitch from 0.3 to 1.5 mm.

Thinner-THGEM has been also explored, with thickness of around 0.2 mm. The gain behaviour of thinner-THGEM as a function of applied voltage at different rates is shown in Fig. 6.18. The detector keeps a constant gain for up to 1.0 MHz/cm^2 and works well with different gas mixtures. Moreover, by using anode strips with width of 125 μm and pitch size of 250 μm, position resolution of $\sim$ 320 μm can be achieved [53].

6.4.1.5 Electronics

The CEPC TPC detector with MPGD readout requires a large number of rows of small-size pads (several mm^2). This is required to achieve high spatial and momentum resolution. There are no existing electronics readout systems that can fulfil all the requirements of such high density and very low power consumption. Selected readout electronics systems installed or under development for TPC detectors are listed in Table 6.6, including ALTRO for ALICE [54], AFTER for T2K [55] and Super-ALTRO for ILC [49, 55, 56]. In addition, the pixelated CMOS chip, Timepix [57], directly coupled to the gas amplification systems, is also listed, as it could be an alternative solution to the traditional pad-based readout systems. However, there are some outstanding issues for this technique in engineering large-sized structures.

Since the front-end electronics need to be mounted on the detector end-plate, developing a highly integrated ASIC with all functions mentioned above is necessary. A successive approximation ADC will be used, rather than a pipeline ADC, given its higher power efficiency. The buffered data are transmitted with high speed optical links to the DAQ system once a trigger is asserted. Without zero suppression the data size for one end-plate is estimated to be 20 – 40 Gb per event. Zero-suppression might not be necessary if the event

Table 6.6 Various TPC readout electronics systems.

	PASA/ALTRO	AFTER	Super-ALTRO	Timepix
TPC	ALICE	T2K	ILC	ILC
Pad size	$4 \times 7.5\ \mathrm{mm}^2$	$6.9 \times 9.7\ \mathrm{mm}^2$	$1 \times 6\ \mathrm{mm}^2$	$55 \times \mu\mathrm{m}^2$
Pad channels	5.7×10^5	1.25×10^5	$1 - 2 \times 10^6$	10^6
Max. drift time	92 μs	20 μs	46 μs	46 μs
Readout Chamber	MWPC	MicroMegas	GEM/MicroMegas	GEM/MicroMegas
Front-end				
Gain	12 mV/fC	18 mV/fC	12-27 mV/fC	2.64 mV/fC
Shaper	CR-(RC)^4	CR-(RC)^2	CR-(RC)^4	None
Peaking time	200 ns	100 ns	30-120 ns	90-180 ns
ENC	385e	1000e	520e	100e
Method	ADC	SCA	ADC	TOT
Sampling frequency	10 MSPS	25 MSPS	40 MSPS	
Dynamic range	10 bit	10 bit	10 bit	
Buffer depth	1k	511	1k	
Data reduction	Yes	No	Yes	Low data amount
Power consumption	32 mW/ch	6.2 – 7.5 mW/ch	1.76 mW/ch*	14 mW/ch
Radiation tolerance	160 kRad	No		200 krad
CMOS Process	250 nm	350 nm	130 nm	250 nm
Status	installed	installed	under development	under development

* with 0.5% duty cycle of power pulsing

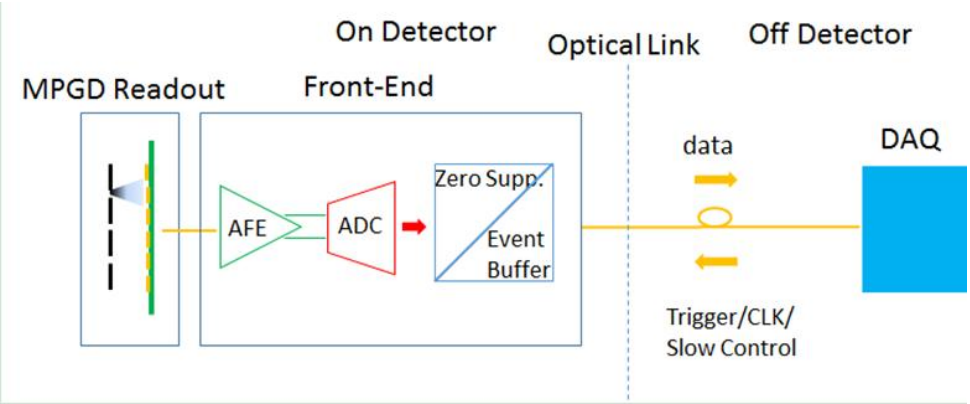

Figure 6.19 Proposed structure for the readout electronics.

Table 6.7 Main specifications of the end-plate front-end electronics.

Total number of channels	1 – 2 Million
AFE/ENC	500e
AFE/Gain	10 – 30 mV/fC, programmable
AFE/Peaking time	30 – 120 ns, programmable
ADC/Sampling rate	40 MSPS
ADC/Resolution	10 bit
Buffer latency	$\sim$50 μs
Data readout rate	20 – 40 Gb per event without zero suppression
Power consumption	$<$10 mW per channel
Area	$< 6\ \mathrm{mm}^2$ per channel, including cooling
Process	CMOS 65 nm

rate is below 1 kHz. Main specifications for the front-end electronics are summarised in Table 6.7.

The power consumption of the readout electronics for the ILC TPC can be reduced down to $\sim 100\ \mathrm{W/m}^2$ with so-called power pulsing(with a duty cycle of 0.5%). However this is not applicable for the CEPC detectors. Even with state-of-the-art technologies, the power density of the CEPC TPC could still be 5 – 10 time higher than that of the ILC TPC.

The TPC readout electronics are meters away from the interaction point and the radiation dose can be rather low ($<$1 kRad) at the CEPC, which might allow the use of standard but radiation-soft technologies. However energetic particles can always produce instantaneous failure (SEU or SEL) from time to time. Hence radiation tolerant design still needs to be considered to make sure that the overall system performance will not be affected or even irreversibly damaged by rare events.

6.4.1.6 Gas Supply and High Voltage

High purity of the working gas is essential for the TPC detector. A conventional recirculating gas system is necessary to remove atmospheric impurities. It has to maintain the pressure relative to atmosphere within a tight tolerance, to minimise the dynamic field distortions caused by flexing of the end-plate in the drift field. The TPC consists of the inner drift volume, enveloped by two tracking volumes. The drift volume contains approximately 41,500 litres of working gas. A total flow of $\sim$150 L/min will allow a complete five-volume change to purge insulating volumes in one day.

A working gas dominated by argon and mixed with several kinds of quenching gas at the few percent level might be feasible (Ar 95%, CF4 3%, and isobutane 2%), as used for the working gas for the TPC at the T2K experiment. To estimate the impact of the gas proportion uncertainties on the TPC performance, a theoretical calculation has been performed. The proportion of working gas should be kept stable at the level of 0.1%. Figure 6.20 shows that the drift velocity changes considerably in the working gas (Ar/CH_4=90/10%) with different ppm levels of H_2O. Therefore it is important to monitor and control the impurity content of O_2, H_2O and other contaminants, and maintain the flux for each gas

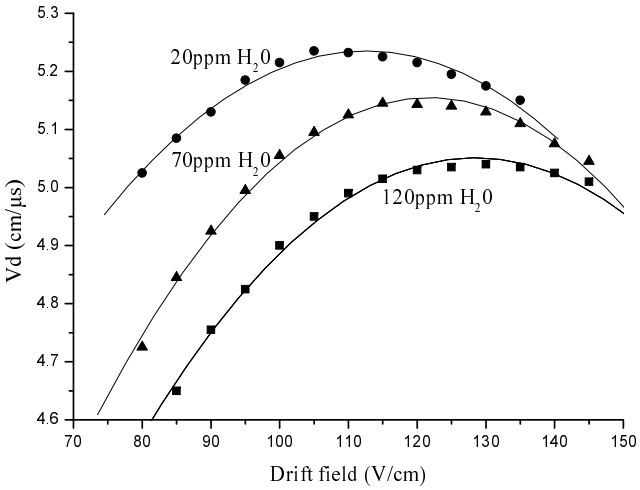

Figure 6.20 Drift velocity in the drift chamber with $Ar/CH_4(90/10\%)$ and H_2O.

composite at a high level of precision. The quality of the gas can be monitored with a gas chromatograph and the contamination by H_2O and O_2 with other dedicated devices. The gas monitoring and mixing system should be considered in the design of the gas supply system.

The impacts of varying temperature and pressure are estimated with a similar technique and the results suggest that they need to be controlled at the same level of precision. Thus, it is equally important to monitor and control the temperature and pressure, to keep the stability of the drift velocity in the working gas. However, as the TPC detector will be positioned between the silicon tracking detectors and calorimeter detectors, it has to face the unavoidable problem of temperature changes during operation.

A preliminary estimation of the high voltage precision and stability have been made based on the studies shown in Fig. 6.20. The typical strength of the drift field ranges between 200 – 300 V/cm with a maximum drift length of about 2 m. This implies the required high voltage to be a few tens of kilovolts, which can be delivered by commercial high-voltage supplies. However, a more concrete estimate of the maximum power of the high voltage system can only be made when the TPC count rate becomes available. In addition, low residual ripple and excellent long term stability (variation below 0.01%) are also necessary.

6.4.2 Alignment and Calibration

To achieve the unprecedented momentum resolution expected for the CEPC TPC detector, precise alignment and accurate calibration are required. It is necessary to minimise the shift and rotation of each detector element in the system. A typical precision of about 100 μm can be achieved with appropriate hardware alignment procedures. This can be further improved with track-based alignment (also called software alignment), which aims to reduce the misalignment uncertainties even below the intrinsic detector resolution[58]. Typically, tracks from cosmics and physics interactions are used for track-based align-

ment. Cosmic tracks can pass through different sub-detectors, making them suitable for relative alignment between different components of the detector system. Tracks from physics interactions are another important source. For instance, in the alignment of the ALEPH TPC[59], iterative track fitting was used to extract the alignment parameters of the TPC with respect to other sub-detectors, the Inner Tracking Chamber (ITC) and the Vertex Detector (VD), using muon tracks from $Z \to \mu^+\mu^-$ decays. In particular, a general algorithm called Millepede[42] has been developed for track-based alignment.

A dedicated laser system, to be installed inside the TPC, can provide another important handle for detector alignment. Tracks generated by the laser beam provide well-defined positions and times, allowing precise alignment of each readout pad of the TPC detector. The laser system can be also used for calibrating the measured tracks, which are formed by the electron drift through the imperfect electric and magnetic field. It thus enables the possibility of monitoring the drift property and even the operation conditions of the working gas. Implementing such a laser system is also an important topic in the TPC prototype studies. The LCTPC collaboration has been testing a photoelectron calibration system to measure track distortion in non-uniform electric and magnetic fields[60]. In this system, a fixed pattern of aluminium points is made on the cathode plane. When the laser hits the cathode, photoelectrons are released with a number of electrons close to that of the gas ionisation electrons generated by charged particles. The displacement can be derived from the difference between the position of the aluminium pattern and the measurement on the readout plane. A similar laser system with enhanced functionalities will be considered for the CEPC TPC prototype.

6.4.3 Critical R&D

The TPC designed following the ILD concept provides an excellent starting point for the CEPC TPC, but modifications are foreseen due to the different performance requirements and experimental conditions. Several critical issues have been identified and possible solutions have been suggested, which will have to be verified with prototypes in future development.

6.4.3.1 Ion Backflow

Ions generated from ionisation in the drift volume or from avalanche multiplication that find their way into the drift region will not only introduce field distortion but also degrade the TPC count rate capability. This so-called ion backflow should be fully suppressed in the TPC drift volume. With an average 300 eV required per ion-electron ionisation and 2 keV energy loss per mm, there will be roughly 12k primary electrons generated by a track with a typical length of 1.8 m in the TPC and there will be in total 240 k electrons in one event. With an electron drift velocity of 5 cm/μs, it takes ~ 40 μs for all the electrons to drift 2 m to reach the end-plate. With the expected bunch spacing of 3.6 μs at the CEPC, there will be about 11 events overlapping in the TPC volume. Therefore there will be 240k$\times 11/2 = 1.32$M electrons continuously drifting toward the end-plate. Ions, on the other hand, drift much more slowly than electrons, with a velocity of only 500 cm/s in an electric field of 500 V/cm. This leads to ions from 110,000 events overlapping in the TPC volume. If 1% of the ions are trapped by the gate and with the gas amplification factor assumed to be 10000, there will be 240k$\times 10000 \times 1\% \times 110,000 = 2.64$T ions

drifting back continuously. With the TPC volume of ∼20M cm^3, there will be on average 0.13M ions/cm^3.

Furthermore, ions from avalanche multiplication account for the largest contribution, because every incoming electron will cause G avalanche ions to be produced in the TPC. G denotes the gain of the detector. Thus there will be $G\varepsilon$ ions in the drift space, with ε being the fraction of ions that arrive in the drift space without being blocked. To estimate the size of the disturbing field in the drift volume, the total charge density ρ needs to be introduced:

$$\rho = \frac{eRGL\varepsilon}{v_I} \tag{6.5}$$

where e is the electron charge, $G\varepsilon$ the number of ions in the drift space for each electron, v_I the ion drift velocity, L the TPC drift region length and R the rate density. Assuming R to be homogeneous in the drift region and ρ to be a constant ρ_0, then for a TPC with inner radius r_1 and outer radius r_2, the electron distortion $E_r(r)$ can be expressed as:

$$E_r(r) = \frac{\rho_0}{2\varepsilon_0}(r - \frac{1}{2r}\frac{r_2^2 - r_1^2}{ln(r_2/r_1)}). \tag{6.6}$$

With the following values: $G = 4000$, $G\varepsilon = 0.25\%$ [61], $V_I = 1$ m/s@$E = 200$ V/m, L=2.35 m, $r_1 = 0.3$ m, $r_2 = 1.4$ m, and the electron distortion expected to be less than 1% ($Er(r) < 2$ V/m), the rate density R must be less than 5.3×10^6 s^{-1}m^{-3}. The cosmic ray and environmental radiation contributions can also be estimated by setting R to the sea level value of 2×10^6 s^{-1}m^{-3}. As shown in Fig. 6.21, the distortion is negative closer to the inner cage and positive near the outer cage.

Another important issue arises from the generation of ions inside the amplification regions. Those ions will introduce the space charge effect, thus affecting the detector performance in terms of gain, stability, etc. The GEM detector is being considered as the TPC amplification detector. Based on the reported counting rate of GEMs of 0.1 MHz/mm^2 [62] or even higher, the maximum tolerance of rate density R is estimated to be 4×10^{10} s^{-1}m^{-3}, with uniformity along the z direction assumed.

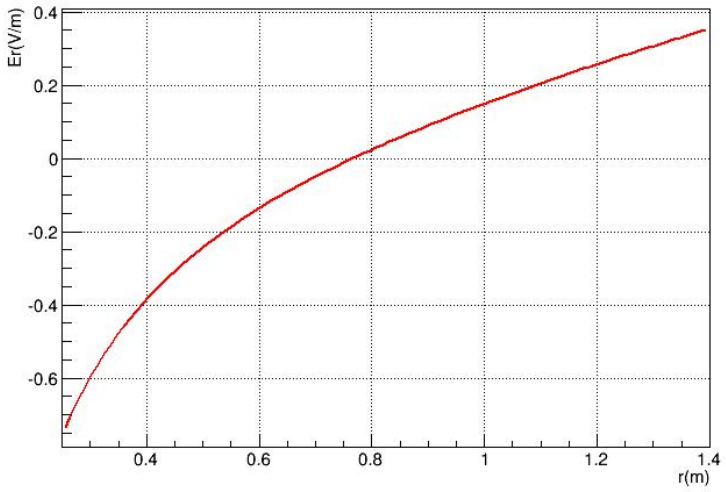

Figure 6.21 Radial distortion of electric field produced by a uniform charge distribution.

Ion backflow and feedback processes have been extensively studied in the development of GEM-based gaseous photomultipliers. Innovative structures and gating electrodes have been introduced with the aim of reducing ion-induced secondary processes [63]. The GEM structure has the innate potential to reduce the fractional ion backflow [64]. At 4 T, the fractional ion backflow has been found to be as low as 0.2% [65]. Despite being such a small value, the TPC operation even at moderate rates can still be affected by the accumulation of ions in the drift volume. Conventional wire grids with proper timing can be an option for ion gating, as was adopted and implemented in the large TPCs used at the LEP experiments, allowed by the time structure of the beams [66]. A mesh or GEM could be alternative options for ion gating, requiring proper gate timing.

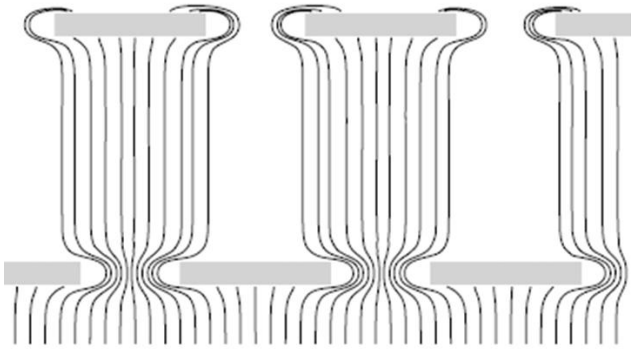

Figure 6.22 Staggered THGEM configuration.

For TPC operation in continuous mode, gating is not feasible. Studies have been made of different structures for gas multiplication detector. A four-layer GEM has been reported to suppress the fractional ion backflow to 0.5% [67]. THGEM is another option, as it has been reported that the ion backflow can be suppressed to 1% for staged triple-THGEM [68]. Suppression of ion backflow takes advantage of the difference in transverse diffusion between ions and electrons. For ions, the space diffusion is symmetric, independent of magnetic field and ion type [69, 70]; while for electrons, the diffusion is almost an order of magnitude higher than that of ions in a typical transfer field in GEM/THGEM (2 – 4 kV/cm). With a staggered configuration, as shown in Fig. 6.22, ions would be collected mostly by the facing electrode, while a good fraction of electrons would still drift in and avalanche. The effective gain will be affected [68] and a gain loss of about 30% is expected due to the staggered configuration.

Ion backflow has been studied with beam tests within the LC TPC collaboration [71]. Different hole sizes of the GEM detector and micro-grid size of the Micromegas detector were studied with the aim to increase the maximum possible electron/ion permeability but at the same reduce as much as possible the number of effective electrons in the transfer phase. To handle the increased rate of the electrons through the gating device, it might require additional material budget to strengthen the support structure to avoid instability or distortion of the electric field in the TPC.

The ageing behaviour of Micromegas detectors with GEM pre-amplification shall be also studied. A Micromegas detector is typically constructed with minimal insulation and its electric field is parallel with the application gap. Discharge or sparks can appear in the thin induction area of the final stage of a cascade GEM detector. By combining Micromegas with pre-amplification from GEM detectors, however, it is possible to achieve

similar gain as with the Micromegas alone, but with reduced voltage. A single GEM detector with multi-stage amplifier will reduce the risk of discharge and ensure stable detector operation. In addition, a GEM detector with pre-amplification can be used as the gating-control device, and will be investigated in further R&D.

6.4.3.2 $E \times B$ Effect in Readout Modules

Compared with the wire readout technology, MPGD readout promises smaller track distortion. However, according to the beam test results of the ILD prototype TPC (LP1), track distortion due to non-uniformity of electric field and resultant $E \times B$ effect remains a critical issue, which will affect the momentum resolution of the TPC. In addition, simulation results based on Garfield++ interfaced with Elmer [72, 73] have also shown track distortions, which are consistent with the test beam results. The simulation has also demonstrated significant electron loss near the gaps between segmented electrodes of the GEM foils because electrons can be pulled into the gap by the non-uniform electric field. The effect of electron loss was also observed in the beam test. Because of this effect, the track position obtained as the center of gravity of the collected electrons will deviate from the expected position, resulting in considerable track distortion.

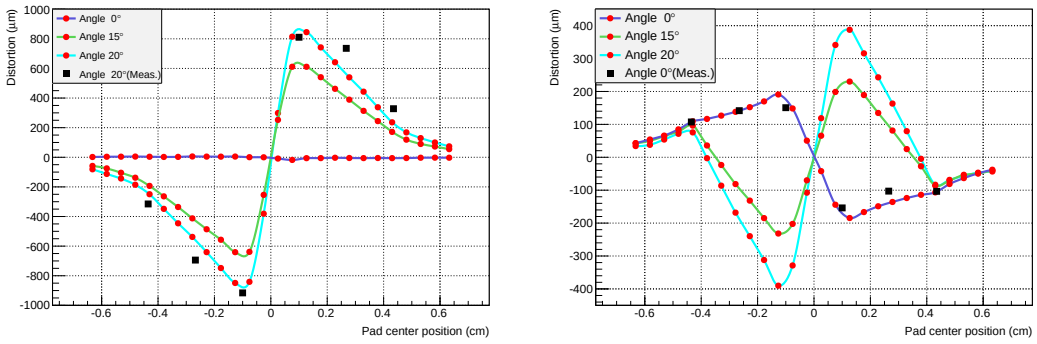

(a) (b)

Figure 6.23 Track distortion in segmented GEM module for (a) B = 0 and (b) B = 1 T.

In the magnetic field, the $E \times B$ effect is another important source of track distortion, and it actually causes real track distortion. The results of track distortion with magnetic field B=0 and 1 T are shown in Fig. 6.23(a) and Fig. 6.23(b), respectively. The track distortion depends on the track angle and the relative position between the GEM gap and the readout pads. For a pad height of 5.35 mm, the track distortion reaches a maximum around the pad position of 1 mm. At B=0, the distortion diminishes to zero for the track angle of $0°$. On the other hand, due to the $E \times B$ effect, it is nonzero in the case of $B = 1$ T and for other track angles the distortion from electron loss is overwhelming. Figure 6.23(b) shows that the region influenced by the $E \times B$ effect is smaller than that of electron loss, and the latter will dominate track distortion in the region outside 4.5 mm. Figure 6.23(a) and Figure 6.23(b) also show that the track distortion observed in the beam test can be well described by the simulation.

Simulation results indicate that using GEM foil without a gap on the front side facing the drift volume and narrow gaps on the back side can reduce the track distortion. Based on the simulation results, an interpolating function has been derived to correct for the observed distortion. Track distortion near the module boundary in the ϕ direction is shown

in Fig. 6.24(a) and Fig. 6.24(b). The gap between two nearby modules is in parallel with the radial direction of the modules, therefore electrons pulled toward the gap may cause real track distortion, which is shown in Fig. 6.24(a) for $B = 0$ T. For the track angle of $30°$, electron loss contributes significantly to the track distortion close to the gap. The $E \times B$ effect remains the dominant effect on track distortion for $B = 1$ T. In addition, zero track distortion presents in the region, where there is no hit recorded by the readout row because of electron loss. As expected, the width of this region increases with larger track angle.

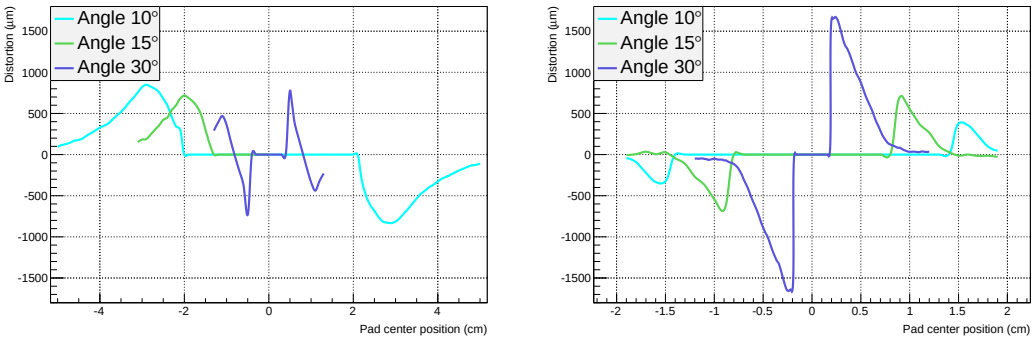

(a) (b)

Figure 6.24 Track distortion in the ϕ direction of module for (a) B = 0 and (b) B = 1 T.

6.4.3.3 Non-uniform Magnetic Field

The CEPC TPC has to face the critical issue of non-uniform magnetic field. Since the half-length of the TPC (2.5 m) is longer than the currently designed focal length of $L^* = 1.5$ m, the QD0 magnet will affect the magnetic field in the TPC region, even though shielding will be considered to minimise this effect. The magnetic field non-uniformity at a specific point can be parametrised as:

$$\begin{cases} B_x = B_0 kxz \\ B_y = B_0 kyz \\ B_z = B_0(1 - kz^2) \end{cases} \tag{6.7}$$

where $k = k_0/z_m r_m$, $B_0 = 3$ T, and $z_m = r_m = 3000$ mm. To study the impact of non-uniform magnetic field on track momentum measurement, tracks with $p = 10$ GeV, dip angle of 0.5 rad, and azimuth angle ϕ in $[0, 2\pi]$, are generated in this magnetic field. Tracks are then reconstructed with a uniform magnetic field of 3 T. The momentum bias of the reconstructed track as a function of non-uniformity is plotted in Figure 6.25. For a magnetic field change of 400 G, corresponding to a non-uniformity of $k_0 = 0.1$, the momentum bias is about 10^{-3} GeV^{-1}, which cannot be ignored. Fortunately, this study also suggests that the momentum resolution is only slightly degraded by the non-uniformity of the magnetic field.

The track momentum will not be accurate enough if the magnetic field non-uniformity is not properly taken into account in track reconstruction. Therefore it is necessary to develop an appropriate tracking algorithm and implement a precise map of the non-uniform magnetic field to improve the measurements. The non-uniformity effect can be corrected

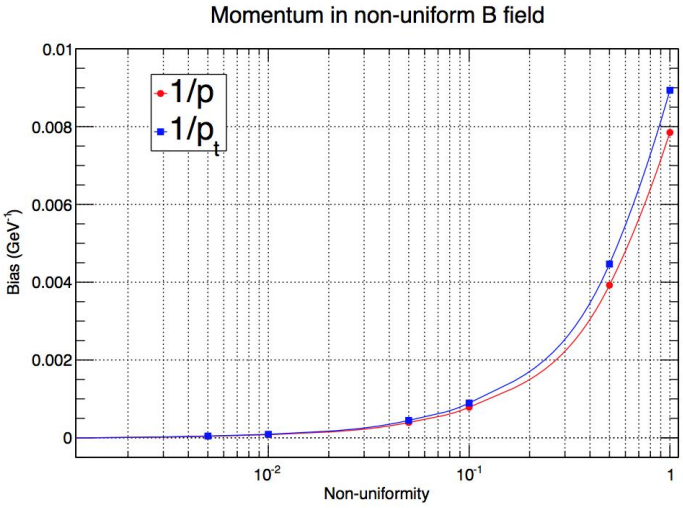

Figure 6.25 Momentum bias for different levels of magnetic field non-uniformity (k_0).

for in the tracking by accessing the magnetic field at each fitting step of the Kalman filter. An extension to the helical track model in uniform magnetic field has been made [74], and the basic concept for its propagation procedure is illustrated in Figure 6.26.

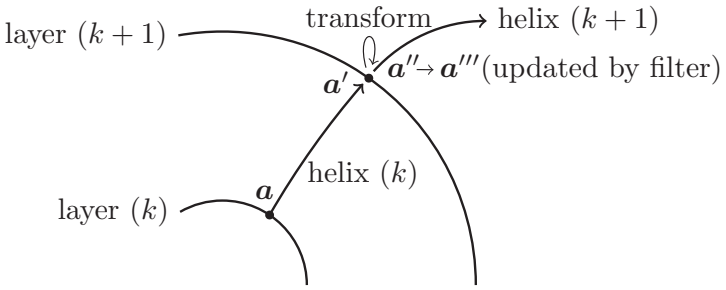

Figure 6.26 Basic idea for transforming the state vector a and the associated frame between two consecutive detector layers (k) and $(k+1)$.

In this segment helical track model, the non-uniformity of the magnetic field between two sites (a and a') is small enough so that the helical track model is still valid when the coordinate system is transformed using the magnetic field at the next site. Preliminary results suggest that the momentum bias can be eliminated if a proper tracking step size is chosen. The CPU time doubles with the new approach but is still more affordable than the traditional Runge-Kutta method. It should be pointed out that the non-uniformity of magnetic field will also influence the electron drift in the TPC volume. Therefore to obtain the precise TPC hit positions, this effect must be also corrected for.

6.4.3.4 Readout Options and Electronics

Critical R&D is needed to understand better the performance of the readout options described above. In addition, since gating is not possible, it is vital to investigate other methods to further suppress the ion backflow, with THGEM and GEM in different electrode patterns, as THGEM/GEM + pad readout might be the most promising readout method.

There is currently no working front-end electronics system that can meet all the requirements of the CEPC TPC, especially in terms of the high density but extremely low power

consumption. This requires significant R&D effort to address many of the critical issues. The proposed structure of the readout electronics is shown in Fig. 6.19, which is similar to that of the Super-ALTRO chip. Each individual channel of the front-end electronics consists of a preamplifier and a shaper as the analog front-end (AFE), a waveform sampling ADC, a zero-suppression unit and an event buffer with depth deep enough to cover the maximum drift time plus the trigger latency.

It is noted that the SAMPA readout chip [75], being developed for the ALICE TPC upgrade, can already provide several important features required for the CEPC TPC detector. It will be interesting to explore this synergy and even directly participate in the performance characterisation of the prototype chips through international cooperation. It shall be investigated whether it is possible to further enhance the chip performance or completely design a new readout chip to meet the requirements of the CEPC TPC detector.

6.4.3.5 Cooling

In the absence of power-pulsing at the CEPC, highly efficient cooling with little material budget is even more demanding. Two-phase CO_2 cooling is adopted for the ILC TPC detector to conduct away the heat generated by the front-end electronics and to keep the temperature of the TPC chamber stable at 20 °C. For the CEPC TPC, more efficient cooling methods such as micro-channel CO_2 cooling might be required and shall be explored. Effectiveness of the cooling techniques will be first evaluated with finite element studies, and optimisations will be also be pursued.

6.5 Calorimetery System

The CEPC calorimeters, including the high granularity electromagnetic calorimeter (ECAL) and the hadron calorimeter (HCAL), are designed for precise energy measurements of electrons, photons, taus and hadronic jets. The basic resolution requirements for the ECAL and HCAL are about $16\%/\sqrt{E(\mathrm{GeV})}$ and $50\%/\sqrt{E(\mathrm{GeV})}$, respectively. To fully exploit the physics potential of the Higgs, W, Z and related Standard Model processes 6.1, the jet energy resolution σ_E/E is required to reach 3 – 4%, or $30\%/\sqrt{E(\mathrm{GeV})}$ at energies below about 100 GeV. To achieve the required performance, a Particle Flow Algorithm (PFA) [76] -oriented calorimetry system is being considered as the baseline design.

The key idea of the PFA is to reconstruct each individual final state particle and measure its physical quantities in the most suitable sub-detectors. For instance, the momentum of a charged track is measured with the tracking system, photon energy with the ECAL, and neutral hadron energy with the combined ECAL and HCAL. On average, $\sim$65% of the energy of jets is carried by charged particles, $\sim$25% by photons and $\sim$10% by neutral hadrons. Significantly improved jet energy resolution can therefore be achieved with PFA compared to conventional measurement taken purely with calorimeters. In addition, PFA allows efficient and precise reconstruction of all the physics objects. To separate energy deposits from different incident particles, ultra-high granularity is vital for PFA-oriented calorimeters. Since neutral particles typically penetrate a certain depth before showering, an ideal PFA-oriented calorimeter should provide not only high transverse granularity but also sufficient longitudinal segmentation. This makes sampling calorimeters more suitable than homogeneous calorimeters.

The CALICE collaboration [77] has been coordinating R&D effort for PFA-oriented calorimeters for future lepton colliders. Figure 6.27 summarises the detector concepts being explored. The ECAL detector options include silicon-tungsten or scintillator-tungsten structures with analog readout, and MAPS-tungsten ECAL with digital readout, while the HCAL detector options have scintillator or gaseous detector (RPC, GEM or Micromegas) as the active sensor, and tungsten or iron as the absorber.

6.5.1 Electromagnetic Calorimeter

The particle flow paradigm has a tremendous impact on the design of the electromagnetic calorimeter. In order to separate close-by showers in the calorimeter, a detector with small Molière radius is required. A large ratio between interaction length and radiation length of the detector is advantageous to the separation between electromagnetic and hadronic showers. A small radiation length will make the electromagnetic shower start earlier in the calorimeter, while a large interaction length will reduce the fraction of hadronic showers starting in the calorimeter. Additionally, a calorimeter with a compact structure is favourable. These factors make tungsten the ideal choice for the absorber. In this section, two detector options are considered for the ECAL, which consists of layers of active sensors - silicon pads or pixels, or scintillator detector - interleaved with tungsten absorber plates.

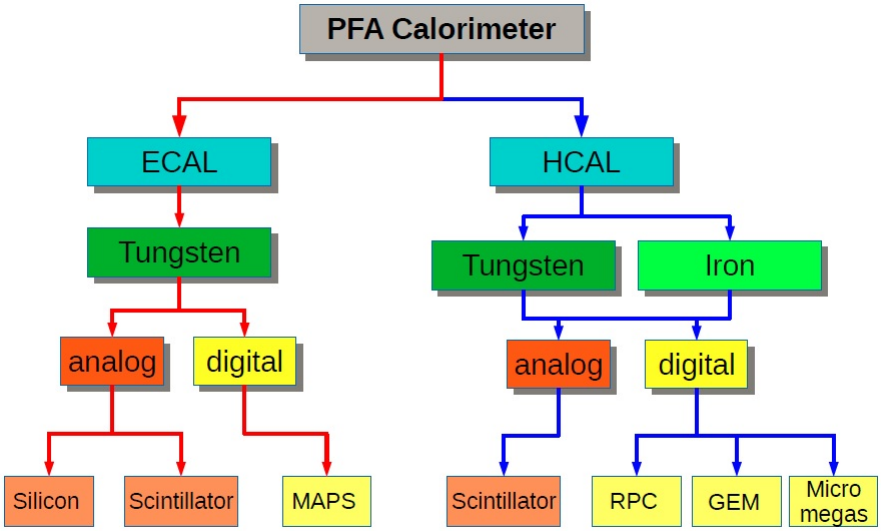

Figure 6.27 PFA: Overview of imaging calorimeters which are under development for future lepton colliders, with different absorber materials, readout technologies and active sensors.

6.5.1.1 Silicon-Tungsten-based ECAL (SiW ECAL)

The proposed ECAL design is based on the ILD detector, with modifications which are necessary to allow active cooling similar to that proposed for the High Granularity CALorimeter (HGCAL) [78] of the CMS end-cap Phase II upgrade. With granularity as high as 1×1 cm^2 pixels, clusters formed by hadronic jets can be well separated. Further optimisations of the ECAL dimensions, number of layers, granularity and possibly other parameters will be carried out in future.

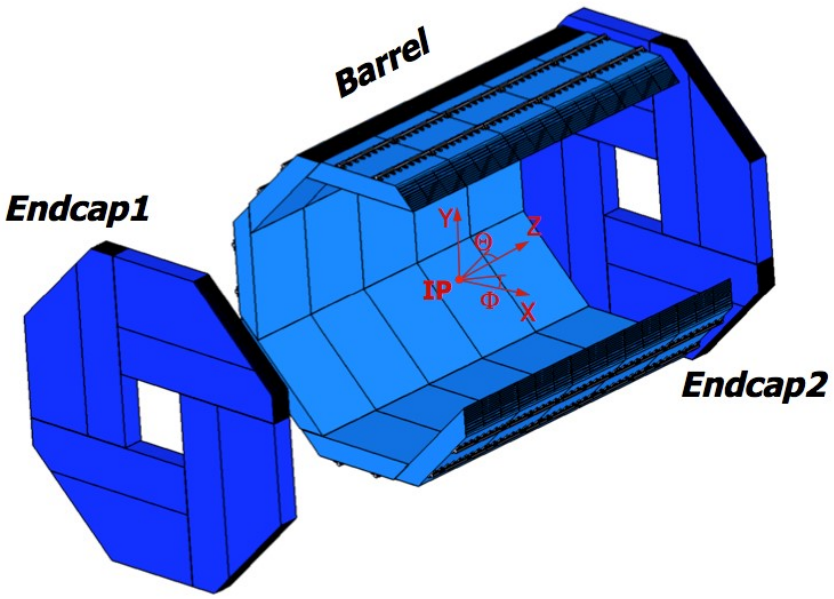

Figure 6.28 View of the SiW ECAL geometry. The barrel is segmented in 8 staves of 5 modules. Each barrel module incorporates 3 towers of 11 alveoli in which detector "slabs" are lodged. The end-caps are segmented in quadrants of 2 modules (with 2 and 3 towers).

The proposed ECAL octagonal geometry, as illustrated in Fig. 6.28, features the same design as for the ILD detector. Special attention is paid to reducing ECAL dead zones and avoiding projective placement that could degrade reconstruction of EM showers from the interaction point. The barrel octants ("staves") are divided into 5 modules, as shown in Fig. 6.29, each with 3 towers of 22 layers. An odd number of modules is chosen to avoid projective dead gaps in the middle of the barrel ($z = 0$). Every module tower has 11 tungsten layers and 11 alveoli, each housing a so-called detector "slab" with two sensitive layers separated by one tungsten layer. The slabs are slid into the alveoli during the final ECAL assembly. Such a design allows easy access to the detector during CEPC maintenance shutdowns. Eleven tungsten layers are glued inside the module to the Carbon Fibre Reinforced Polymer (CFRP) structure. The combination of these two materials provides excellent mechanical rigidity and precise placement of all tungsten layers. With the clearance of slabs inside alveoli being about 0.5 mm, such a design ensures a very compact structure with minimal dead space. The modules are attached to the HCAL by the outer rails.

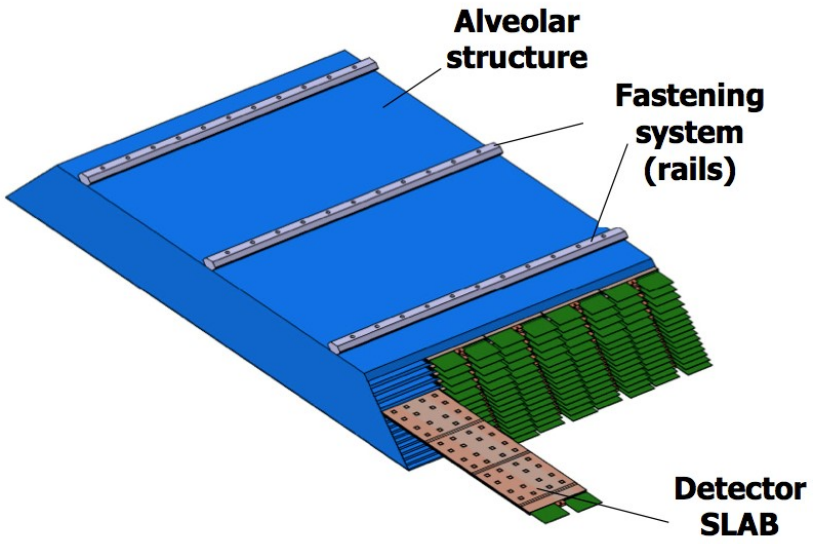

Figure 6.29 View of a barrel module (here with 5 towers as in the 2013 ILD design) of 15 alveoli. All services (cooling, power, interfacing electronics) are located at one side, on the outer rim of the ECAL. The modules are fastened to the HCAL by 2 or 3 rails. Services are provided between the rails.

The two end-caps are segmented in quadrants made of two modules, each with either two or three towers. The inner square holes of about 80×80 cm^2 may be partially covered, as in the ILD, by two independent small modules with circular holes for the beam pipe (so-called end-cap "rings"). Their design depends on the level of CEPC backgrounds in these regions, and is not yet elaborated.

The Very Front-End (VFE) readout electronics is embedded into the slabs. It performs amplification, auto-triggering, digitisation and zero-suppression, with local storage of data between the readout cycles. The digital signals are propagated to the slab ends, where dedicated boards send them outside the detector via cables running through the gaps between ECAL and HCAL or between the barrel and the end-caps.

A detector slab is shown in Fig. 6.30 and Fig. 6.31. It consists of a tungsten layer sandwiched between two detector layers. The former is glued in the middle of a CFRP H-

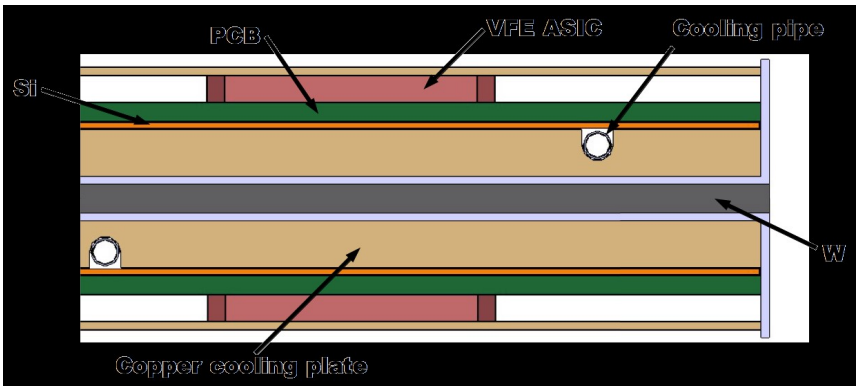

Figure 6.30 Transverse view of a slab, with one absorber and two active layers. The silicon sensors are glued to PCB which carries VFE chips, and are cooled by copper plates with CO_2 cooling pipes. The outer layer protects the slab and simplifies handling. The slab is inserted in the alveolus of the module.

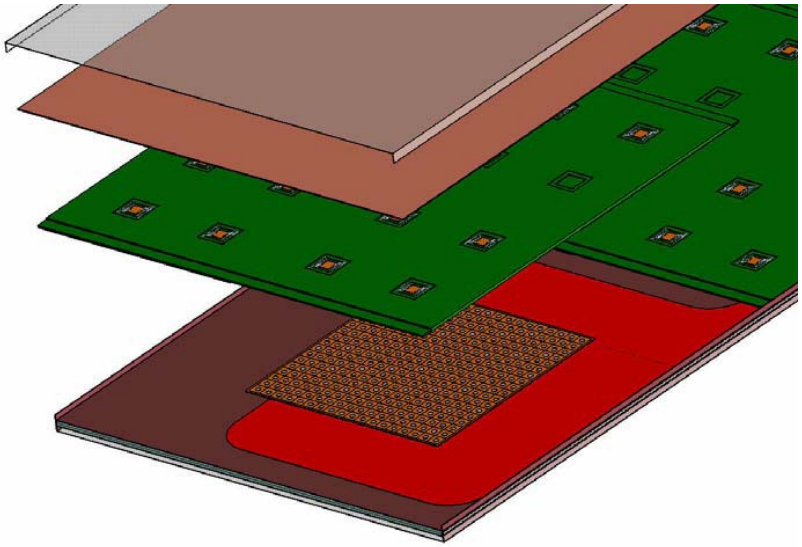

Figure 6.31 Exploded view of the detector slab end. Only the upper sensitive layer is shown; the bottom layer below the tungsten is identical. From bottom to top: tungsten/carbon fibre structure, Kapton high voltage cable (red), the silicon sensor (brown, four are glued to one PCB), square PCB with 16 VFE chips (green, other PCBs follow along the slab), copper cooling plate, thin protection plate.

shaped support structure. Each detector layer contains silicon sensors and printed circuit boards (PCB) holding the VFE readout chips, topped by a cooling plate. The sensors are highly resistive PIN diodes segmented into square pixels. Each of them is glued with conductive epoxy to a corresponding pad on the PCB. According to the ILD Letter of Intent (LoI) and more recent optimisation analyses, the shower separation and overall jet energy resolution improve when pixel size is decreased well below the Molière radius (20 mm in ILD LoI). The density of the channels is limited, however, by the VFE electronics and, to a lesser extent, by the capabilities of ILD passive cooling. The nominal ILD ECAL pixel size is therefore fixed at around 5×5 mm^2. Thicker sensors (e.g. 725 μm) are preferable as they provide better ECAL statistical energy resolution, higher signals and less capacitive noise.

The VFE chip foreseen for ILD, called SKIROC, was developed by the OMEGA laboratory from CNRS/Ecole Polytechnique in Palaiseau, France. The chip features 64 chan-

nels, a very low power consumption of 27 μW/channel in power-pulsed operation mode with 1% duty cycle, and a dynamic range ensuring a linear response for 1-1500 MIP signals. Recent cosmic, charge injection and beam tests of prototype slabs with about 1500 channels demonstrated the good performance of the chip. In its next version, it will implement full channel-wise zero-suppression.

To reduce the ECAL Molière radius, the thicknesses of BGA chip packaging and PCB are minimised. Special attention is paid to the PCB flatness, which should be sufficient for gluing the fragile silicon sensors.

Active Cooling Unlike the ILC, CEPC will operate continuously, so the VFE readout electronics cannot be power-pulsed. The energy consumption is, therefore, about two orders of magnitude higher and requires active cooling. Following the CMS-HGCAL design, this is done with evaporative CO_2 cooling pipes passing through 3 mm copper plates, as shown in Fig. 6.30.

Thanks to much more relaxed radiation constraints, the cooling requirements are less strict in CEPC: to reduce the silicon sensor leakage current due to radiation damage, the HGCAL is operated at very low temperatures (-30 °C) with a temperature gradient across the slab of less than 1-2 °C. In addition, the leakage currents produce extra power dissipation. The cooling design will, therefore, have to be re-optimised for CEPC. The cooling plate will be moved to the VFE chip side and will probably be thinner.

The OMEGA group have made a first preliminary estimation of the power consumption of the future VFE chip for the CEPC. The extrapolation to the CEPC conditions was done separately for analog and digital SKIROC parts. For continuous operation with 25 ns bunch crossings on average, the expected dissipation is 5 mW/channel. This may be compared to the active cooling heat extraction of 100 W per 0.3 m^2 alveolus or 33 mW/cm^2, as estimated for HGCAL CMS upgrade. It should allow operation with 0.6×0.6 cm^2 pixels with a safety margin of two.

Sensors Because of the large number of pixels, it is necessary to have a very stable detector insensitive to variations in operating conditions (temperature, bias voltage etc.). The calibration should also be as simple as possible (e.g. no complicated saturation effects). For good pattern recognition of hadron showers interacting in the ECAL, which is important for PFA, it should have a very good signal-to-noise ratio at the MIP level. Silicon PIN diodes, although expensive, fulfil all the requirements. The CALICE collaboration have been developing such a device for the last 10 years, so it is a mature and a well understood technology.

Expected Performance Recent (and preliminary) simulation studies have been made of a compact version of the ILD detector. The ECAL design is close to the what could be the CEPC ECAL: 20 to 30 sensor layers of 500 μm thick silicon, internal radius of 1.4 m, but no copper cooling layers, with a R_M of 20 mm against the $\sim$26 mm expected for a cooled version.

Using full reconstruction software (PandoraPFA) and the full calibration procedure (on fixed energy photons, and K_L, fine angular dependencies and HCAL/ECAL inter-calibration are folded-in), the performance has been estimated using *uds*-pair events at 91, 200, 360 and 500 GeV and a barrel ECAL of 20, 26 and 30 active layers (keeping the total amount of tungsten constant), respectively. As shown in Fig. 6.32, the relative Jet

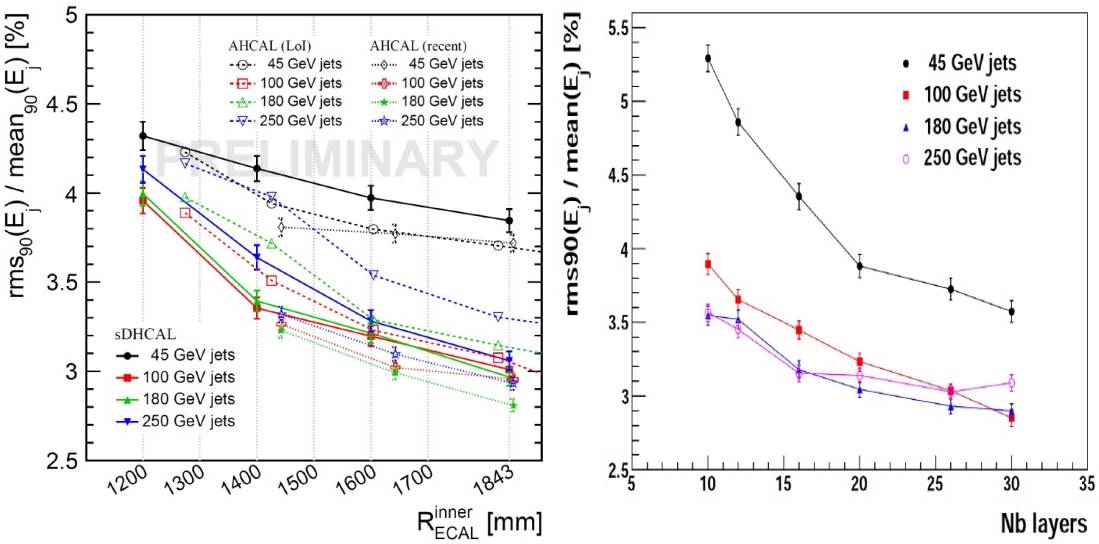

Figure 6.32 Examples of optimizations studies (from T.H. Hieu) for the JER using the full reconstruction chain on jets of 45, 100, 180, 250 GeV, as a function of (left) the ECAL internal radius and various HCAL options and (right) the number of layers [for a radius of 1.8 m].

Energy Resolution (JER) is found to be almost stable t around 3.5% (using RMS_{90}/E) for high-energy jets (above 100 GeV) for all ECAL configurations. For jets at 45 GeV, the relative JER increases almost linearly from 4.2% to 4.5% when the number of sensitive layers reduces from 30 to 20.

Although these numbers can only be purely indicative and the study has to be done again with the proper CEPC neighbouring detectors (especially trackers and HCAL), they hint that a compact version of the ECAL with a reduced number of sensitive layers offers a solution with sufficiently good performance. For low energy jets, as mostly expected at the CEPC, the difference in Molière radius should not affect the JER too much, the particles being rather well separated. Finally, the loss of performance in the JER is expected to be at least partially compensated by the use of thicker silicon sensors (725 μm instead of 500 μm).

Future R&D Plans R&D and optimisation of the ILC ECAL have already been performed for more than 10 years. The first ECAL prototype built by the CALICE collaboration proved the physical principles of PFA. Currently, the second prototype is under active development with an emphasis on challenging technological aspects. The CEPC ECAL may greatly profit from the similarities between the two projects.

The main difference is the beam time structure: at CEPC it is continuous while ILC operates with a duty cycle of the order of 1%. This allows the use of power pulsing and passive ECAL cooling. The power dissipation in the CEPC ECAL is about two orders of magnitude higher and requires active cooling. To keep the ECAL as compact as possible, the cooling should be implemented with the minimal amount of material. Both a detailed thermal simulation and a real prototype will be required to validate the future cooling technology. A similar cooling system will be developed for the CMS HGCAL, so there is synergy between the two projects.

The continuous bunch structure requires a new VFE chip and DAQ electronics. They should operate continuously and much faster than in the ILC ECAL. The ILC readout

scheme at 5 Hz (in the moments when the accelerator is idle) should also be modified. From the physics, the expected occupancy will be small and require only a light DAQ infrastructure.

The general ECAL design should be optimised for the lower CEPC energy. This will require an adaptation and a development of existing ILC software. In particular, at lower energies, the overlap between the clusters (so-called "confusion" in PFA shower pattern recognition) is much reduced. This increases the importance of the intrinsic resolution of the calorimeter.

6.5.1.2 Scintillator-Tungsten-based ECAL (ScW ECAL)

Alternatively, a sampling calorimeter with scintillator-tungsten structure is proposed. It can be built in a compact and cost effective way. The structure of the ScW ECAL is similar to the SiW ECAL, as shown in Fig. 6.28. The ScW ECAL consists of a cylindrical barrel system and two end-caps. In order to get adequate energy resolution, the ScW ECAL is longitudinally segmented into around 25 layers, and the tungsten plate may have different thicknesses to reduce the number of readout channels.

The active layers are plastic scintillators consisting of 5×45 mm^2 scintillator strips. The scintillator strips in adjacent layers are perpendicular to each other to achieve a 5×5 mm^2 effective transverse size. Each strip is covered by a reflector film to increase collection efficiency and improve uniformity of the scintillation light. Photons from each scintillator strip are read out by a very compact photo-sensor, SiPM, attached at the center of the strip. The compact photo-sensors (SiPM) and highly integrated readout electronics make the dead area in the ScW ECAL almost negligible.

Plastic scintillator is a robust material which has been used in many high energy physics experiments. Production of the scintillator strips can be performed at low cost by the extrusion method. Thanks to the strip structure, the number of readout channels can be significantly reduced. If the required granularity is used, the ScW ECAL has good energy resolution and linearity. The ScW ECAL consists of 25 super-layers. A super-layer is made of a tungsten plate (3 mm thick), scintillator strips (2 mm thick), and a readout/service layer (2 mm thick). The thickness of a super-layer is 7 mm. The total ScW ECAL thickness is 175 mm, and its radiation length is 21.4 X_0.

A physical prototype [79] of a scintillator ECAL has been built and exposed to test beam by the CALICE collaboration. The prototype consists of 30 active layers, each of which includes 72 scintillator strips read out by photo-sensors. The minimum detecting unit has a 45 mm long and 10 mm wide plastic scintillator and a SiPM. The thickness of the scintillator is 3 mm. The basic performance of the calorimeter has been tested with a hadron beam at Fermilab. The linearity of the system and the energy resolution are well understood. The results include a temperature correction calibrated using data for a temperature range between 19 to 28 °C. The deviation from linear behaviour is determined to be less than 2% and the energy resolution is found to be $12.9/\sqrt{E}$(GeV) $\oplus 1.2\%$ for 2-32 GeV electron beams.

Readout Electronics Silicon photomultipliers, which are used to read out the photons from the scintillator strips, are silicon single-photon sensitive devices built from an avalanche photodiode (APD) array on common Si substrate. Signals from about 80 SiPMs are fed into a readout chip through micro-strip lines. They are arranged on one identical flexible readout board (FPC). After shaping, digitisation and zero-suppression of the ana-

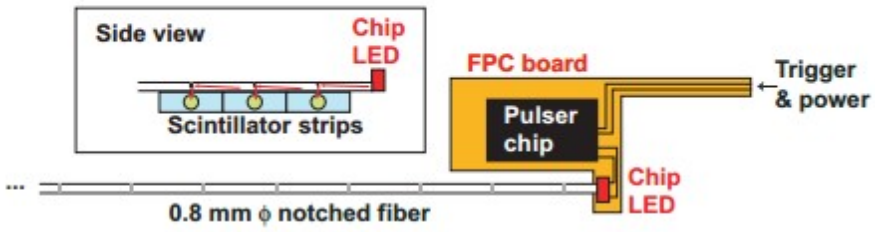

Figure 6.33 Schematics of the SiPM gain monitoring system with LED and notched fibre. Light pulses from the LED are scattered and distributed into each strip.

log signals on the chip, signals are taken out serially from the detector by a thin FPC cable through the detector gaps.

The dimension of each single APD can vary from 10 to 100 micrometers, and their density can be up to 10000/mm^2. Every APD in an SiPM operates in Geiger mode and is coupled with the others by a polysilicon quenching resistor. The supply voltage depends on the APD technology used, and typically varies between 20 V and 100 V, thus being 15 to 75 times lower than the voltage required for traditional photomultiplier tube (PMT) operation. In addition, SiPMs are insensitive to magnetic fields. The dynamic range of an SiPM is limited by the number of APD pixels. To satisfy the large dynamic range of the CEPC high energy electromagnetic showers, an SiPM with 10000 APD pixels in an area of 1 mm^2 is under study.

Calibration System The ScW ECAL consists of more than 8 million channels of scintillator strip units. The stability of the light output has to be monitored. A light distribution system is under study to monitor possible gain drifts of the SiPMs by monitoring photoelectron peaks. The system consists of a pulse generator, a chip LED, and a notched fibre. A schematic structure of the system is shown in Fig. 6.33. The pulse generator circuit and chip LED are arranged on a thin ($\sim$200 μm) FPC board. The chip LED is directly connected to the notched fibre to distribute light to $\sim$80 strips through its notches.

Future R&D For the ECAL readout with plastic scintillator strips, several critical issues need to be studied in detail. These include:

- Optimising the ECAL layout, thickness of scintillator strips, number of detection layers, segmentation within layers, cost-effectiveness etc;
- Extending the dynamic range of the SiPMs to improve detection performance;
- Developing methods to couple the scintillator strips and SiPMs efficiently;
- Designing an active cooling system as proposed for the "SiW ECAL" option.

6.5.2 Hadronic Calorimeter

A high-granularity hadronic calorimeter plays an essential role in PFA-based experiments such as CEPC. It allows separation of the energy deposits from charged and neutral hadrons. The contribution of the neutrals to the jet energy, around 10% on average, fluctuates over a wide range from event to event. The measurement accuracy of the neutral hadrons is the leading contribution to the jet energy resolution for jets with energy up to $\sim$100 GeV.

The HCAL is a sampling calorimeter with steel as the absorber and scintillator tiles or gaseous devices with embedded electronics. The moderate ratio of hadronic interaction length ($\lambda_I = 17$ cm) to electromagnetic radiation length ($X_0 = 1.8$ cm) of steel, allows a fine longitudinal sampling in terms of X_0 with a reasonable number of layers in λ_I, thus keeping the detector volume and readout channel count small. This fine sampling is beneficial for both the measurement of the sizeable electromagnetic energy part in hadronic showers and for the topological resolution of shower substructure, needed for particle separation. Compared to steel, using tungsten absorbers would lead to the number of hits being reduced by about 30%, so to extend the range of the linear response beyond 20 GeV, a finer segmentation of the readout would be required. This would need smaller readout pads and more readout channels. Moreover, steel allows the building of a self-supporting structure without auxiliary supports.

The active detector element has finely segmented readout pads of 1×1 cm^2 for the entire HCAL volume. Each pad is read out individually, pushing the readout channel density to approximately 4×10^5/m^3. For the entire HCAL ($\sim$100 m^3 in volume), the total number of channels reaches 4×10^7, which is one of the biggest challenges for the HCAL system. On the other hand, simulation results suggest that for a calorimeter with cell sizes as small as 1×1 cm^2, simple hit counting is already a good energy measurement for hadrons in the energy range of final state particles for the CEPC. As a result, the readout of each channel can be greatly simplified and just record "hit" or "no hit" according to a single threshold (equivalent to a "1-bit" ADC). A hadron calorimeter with only one threshold readout is called a Digital Hadron Calorimeter (DHCAL). In a DHCAL, each readout channel is used to register a "hit", instead of measuring energy deposition as used in traditional HCAL. In this context, gas detectors (such as RPC, GEM and Micromegas) become excellent candidates for the active element of a DHCAL.

The probability for more than one charged particle hitting the same readout pad increases for higher energy, especially in the central region of a shower. A more general calorimeter with multi-threshold readout (e.g. 3 thresholds) is therefore also considered, a so-called Semi-Digital Hadron Calorimeter (SDHCAL). Compared with the DHCAL, the SDHCAL records more detailed hit information for hadronic showers and has better energy resolution for jet energies above 40 GeV [80]. On the other hand, the energy calibration for the multi-threshold SDHCAL is more complicated compared to the DHCAL. In the following, the SDHCAL design as well as the DHCAL prototype are described.

For the CEPC HCAL, gaseous detectors have been proposed for the active layers: Resistive Plate Chambers (RPC) or Thick Gaseous Electron Multipliers (THGEM). Gaseous detectors provide high efficiency and excellent homogeneity, allowing fine lateral segmentation. Their cost-effectiveness and simplicity make them even more attractive for construction of a detector covering a large area.

6.5.2.1 RPC-based DHCAL

The proposed structure of glass RPC (GRPC) as an active layer for the CEPC HCAL is shown in Fig. 6.34. It is made of two glass plates of 0.7 mm and 1.1 mm in thickness. The thinner plate is used to form the anode while the thicker one forms the cathode. Ceramic balls (or cylindrical spacers) of 1.2 mm diameter are used as spacers between the glass plates. The gas volume is encapsulated by a 1.2 mm thick and 3 mm wide glass-fibre frame glued on both glass plates. The glue used for both the frame and spacers is required to be chemically passive and stable over a long period of time. The resistive coating on the glass plates is used to apply high voltage and thus to create the electric field in the gas volume. For GRPCs, the resistive coating is found to play important role in the pad multiplicity associated with a minimum ionising particle (MIP).

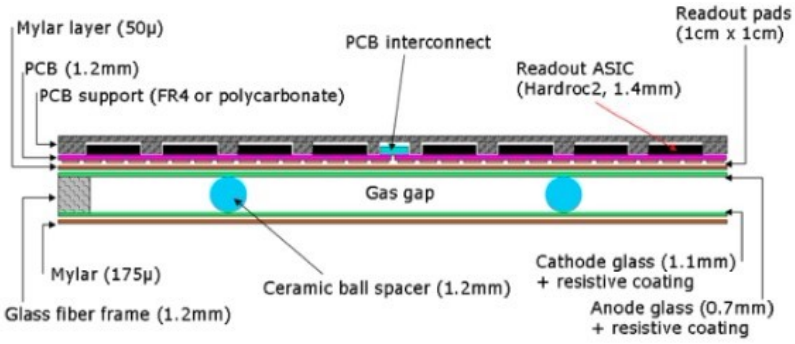

Figure 6.34 Cross-sectional view of an active layer with GRPC.

The GRPC and its associated electronics are housed in a special cassette, which protects the chamber and ensures that the readout board is in intimate contact with the anode glass. The cassette is a thin box consisting of 2.5 mm thick stainless steel plates separated by 6 mm wide stainless steel spacers. These plates are also part of the absorber. The electronics board is assembled with a polycarbonate spacer which is also used to fill the gaps between the readout chips and to improve the overall rigidity of the detector. The electronics board is fixed on the small plate of the cassette with tiny screws and this is then fixed to the other plate, which hosts the detector and the spacers. The whole width of the cassette is 11 mm of which only 6 mm correspond to the sensitive medium including the GRPC detector and the readout electronics.

To read out the SDHCAL GRPCs, an ASIC called HARDROC has been developed [81]. To solve the problem of connections related to the high number of electronics channels, the option of detector-embedded electronics using the daisy chain scheme was chosen and PCBs were developed for the readout of large detector GRPCs. The HARDROC chip implements a multi-threshold readout which integrates the functionalities of amplification, shaping, digitisation, internal triggering and local storage of the data. Each of its 64 channels consists of a fast low-impedance current preamplifier with 8-bit variable gain (in the [0,2] range) followed by 3 fast shapers (15 ns shaping time). A low-offset discriminator is present on each path and the three corresponding thresholds establish the multi-level readout. The thresholds are set using three integrated 10-bit Digital to Analog Converters (DACs). The outputs of the three discriminators are then encoded 3-to-2 bit and stored in an internal digital memory.

The electronics board hosts both the pick-up pads and the ASICs in addition to the connections linking the pads to the ASICs and those between the different ASICs. To ensure good transmission qualities and low cross-talk, an 8-layer PCB has been designed. The base pattern connects 64 pads arranged in a 8×8 matrix to the ASIC's pins. This is identical to the one used in the Active Sensor Unit (ASU) of the small GRPC chambers described in reference [82]. The rooting is designed so that two of the ASUs can be associated to form one slab hosting 48 ASICS. Each slab is then connected to one Detector InterFace board (DIF).

An SDHCAL prototype comprising 48 active layers was built by the IPNL group in collaboration with French, Belgian and Spanish groups. Each of these layers is made of 1 m^2 GRPC [83]. The GRPC signal is read out through 9216 pads of 1 cm^2 each. The pads are located on one face of an electronics board which hosts 144 HARDROC ASICs on its other side. Each electronics board is built by soldering three slabs, each covering a third of the detector surface.

Figure 6.35 Beam test of the 46-layer SDHCAL prototype.

The SDHCAL prototype was exposed to pions, muons and electrons from the CERN H2 beam line of the SPS in May 2012, and from the H6 beam line in August 2012. An important feature of the SDHCAL readout is the presence of three thresholds. Figure 6.35 shows the prototype during the beam test. The aim of using the threshold information is not to measure the energy deposited in each pad but an attempt to distinguish between pads crossed by few, many or too many charged particles. The information of three thresholds is coded in two bits. The threshold values were fixed to 114 fC, 5 pC and 15 pC respectively, the average MIP-induced charge being around 1.2 pC.

To fully exploit the data provided by the SDHCAL, the information related to the three thresholds can be used, which may help to better estimate the total number of tracks produced in a hadronic shower. Pads crossed by two particles during the same 200 ns time window, and separated by a distance larger than that of the avalanche, will on average have more charge than those crossed by one charged particle. Hadronic and electromagnetic showers at higher density of hits, with the second and third thresholds crossed, are observed as shown in the event displays of Fig. 6.36.

The thresholds information can be useful to understand the shower structure as suggested by these event displays. Nevertheless, here this will be used only to improve the energy measurement by expressing the energy of the hadronic shower as a weighted sum of:

$$E = aN_1 + bN_2 + cN_3. \tag{6.8}$$

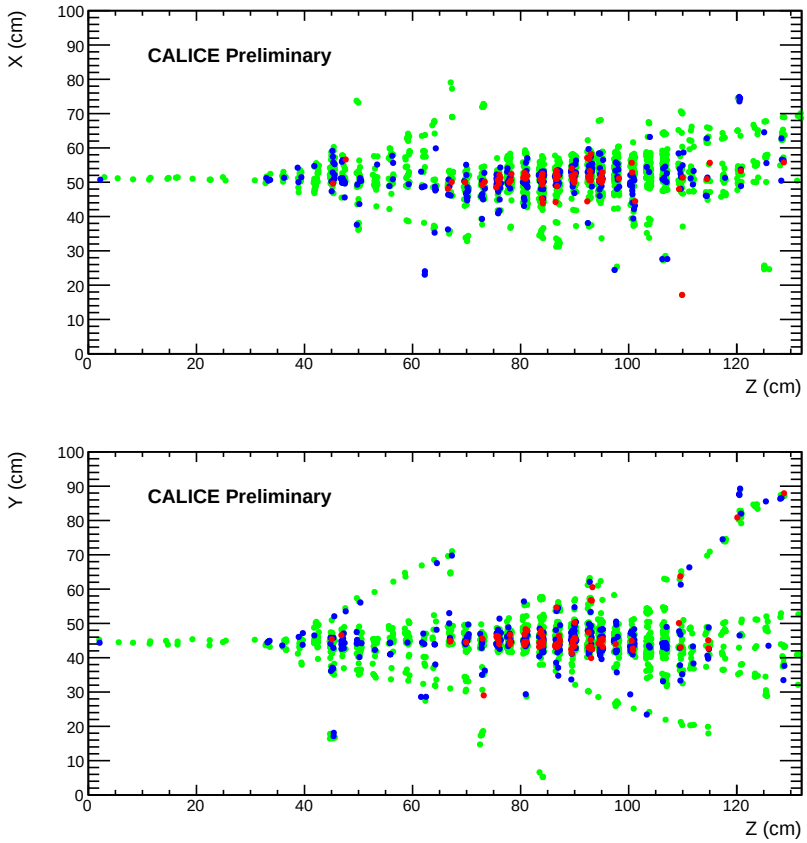

Figure 6.36 An 80 GeV pion event display with red indicating pads fired at the highest threshold, blue those at the middle threshold, and green those at the lowest threshold.

where N_1, N_2 and N_3 are the number of hits for which only the first threshold is crossed, the first and the second but not the third threshold is crossed, and the three thresholds are all crossed, respectively. a, b and c are the corresponding coefficients of the three terms. σ_E/E of the reconstructed pion energy E is a function of the beam energy. The reconstructed energy is computed using the three thresholds information (multi-threshold mode), and the distributions are fitted with a Crystal Ball function. The use of the three thresholds information has a very good impact on the energy resolution at energies higher than 40 GeV, as was predicted from our preliminary simulation studies [80]. Excellent linearity and energy resolution up to 80 GeV were obtained during the two periods of beam exposure at CERN, as shown in Fig. 6.37. Energy resolution of better than 8% at 80 GeV was obtained. These are encouraging results since the data used were collected without any gain correction to improve the homogeneity of the detector response.

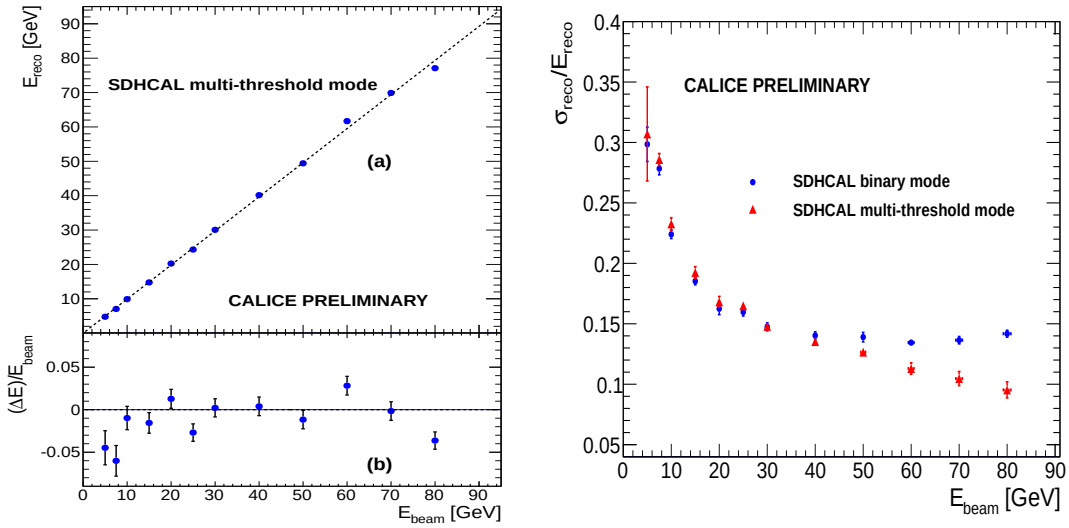

Figure 6.37 Linearity and energy resolution of the SDHCAL response to hadron beams in H2-SPS at CERN [83].

Optimisation of the SDHCAL Design Preliminary simulation results, without algorithm optimisation, show PFA performances comparable to the AHCAL reconstruction. An interesting aspect of the gaseous semi-digital HCAL is the simplicity with which the detector calibration is performed, if needed at all. The SDHCAL energy calibration requires 3 independent steps:

- First, inter-calibration of the ASIC charge thresholds: All ASICs will have to be tested and calibrated by injecting a precisely controlled charge, adapted for each of the thresholds, at the entrance of their final ASU/PCB pad. The variations can be compensated channel by channel in the ASIC by adjusting the channel gains.
- Second, calibration of the RPC multiplicity: The multiplicity response curve of the RPC to muons as a function of high voltage applied, thresholds, position and gas flow and atmospheric pressure can be measured on a cosmic test bench or muon beam and parameterised for each type of RPC.
- Third, physics calibration: The first two steps bring an absolute calibration at the level of the MIP, which can be cross-checked with cosmic muons or $Z \rightarrow \mu^+\mu^-$ events;

the final energy scale will be a complex interplay in the scope of the PFA analysis between the clustering algorithms, jet and particle energies and types.

The definition of the calibration procedure, and an estimation of the achievable precision, is part of the SDHCAL 1 m^3 programme. Other than the SDHCAL reconstruction algorithm optimisation, the cell size and the thickness of the absorber should also be optimised by simulations for the production.

The expertise acquired in the construction and the commissioning of the technological prototype and the results obtained can be used to implement a realistic simulation of the CEPC HCAL. Algorithms to linearise the calorimeter response and convert it to energy have been developed. They provide 3–4% precision when applied to the raw data. The multi-threshold capabilities of the SDHCAL at high energy (>40 GeV) clearly improve the energy resolution. This improvement, as shown in Fig. 6.37, is probably related to a better treatment of the saturation effect thanks to the information provided by the second and third thresholds. However, larger GRPCs are needed in the future SDHCAL, with the largest being 290×91 cm^2.

In parallel with the Semi-Digital HCAL R&D efforts, the Digital-HCAL (DHCAL) with a single threshold (0 or 1 output for each cell) has also been extensively studied. The first 1 m^3 digital hadronic calorimeter prototype with all front-end electronics embedded was built at Argonne National Laboratory (ANL) in 2010, as shown in Fig. 6.38 (left). The prototype has 54 layers with 1 m^2 area per layer, and each layer has 2 cm iron absorber (changed to tungsten in later beam tests). The first 38 layers have a uniform thickness of absorber, while the last 16 layers require a gradual increase of the absorber thickness from 2 cm to 10 cm, used as tail catcher for very high energy particles. The prototype has about half a million channels, with beam tests performed at Fermilab and CERN.

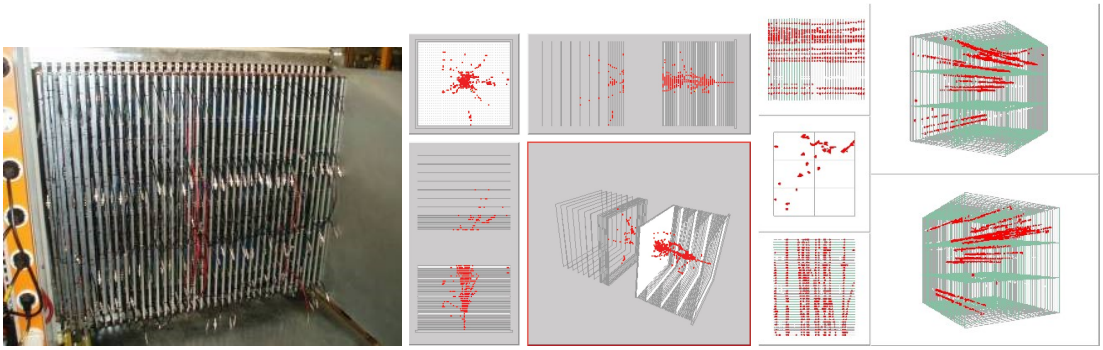

Figure 6.38 Left: 1 m^3 prototype of RPC-based DHCAL built at ANL; Middle: 60 GeV pion shower; Right: multi-muon tracks passing through the DHCAL in Fermilab test beams.

To first order the energy E of an incident particle is reconstructed as being proportional to the number N of pads hit. However, a non-vanishing noise rate and variations in the chamber efficiencies and average pad multiplicities need to be corrected for, such that the energy of an incident particle is reconstructed as:

$$E = \alpha_{sample} \times (\sum_{i=1}^{n} N_i \times \frac{\varepsilon_0}{\varepsilon_i} \times \frac{\mu_0}{\mu_i} - N_{noise}), \tag{6.9}$$

where the sum runs over all layers of the detector; α_{sample} is the sampling fraction, which may depend on particle energy; ε_0 and μ_0 are the average MIP detection efficiency and

the average pad multiplicity of the detector; ε_i and μ_i are the MIP detection efficiency and average pad multiplicity of layer i; and N_{noise} is the average contribution from noise. All these calibration parameters have been carefully measured and monitored over time during the test beam campaigns for the DHCAL prototype built at Argonne National Laboratory (ANL) [84–89]. The DHCAL responses for positrons and pions are measured at different beam momenta, and data analysis is still on-going.

Future R&D A proof-of-principle DHCAL prototype has been designed. R&D in several areas is still critical to demonstrate technical feasibility and optimise the design:

- With the advances of physics prototype test beam analysis, the unique characteristics of the imaging calorimeter are being revealed. On one hand, the calibration process becomes vastly different and significantly more difficult than traditional calorimeters, but on the other hand, the large amount of additional position information measured in the finely segmented DHCAL can greatly improve the energy resolution and pattern recognition capability. In the next stage of DHCAL R&D, it is necessary to fully explore the potential of a finely segmented DHCAL and to achieve or closely approach the ultimate energy resolution;

- For the running conditions at the CEPC, where separation between bunch crossings is only 3.5 μs, it is not feasible to implement power pulsing for the DHCAL front-end, as proposed for the ILC. The front-end of the DHCAL readout needs to have significantly reduced power consumption, in order to avoid or significantly reduce active cooling. Low power ASIC design techniques and cooling schemes are being considered to reduce the power dissipation by a factor of 100 or more;

- The digital part of the readout system needs to be optimised for better data concentration and reduced number of data connections without sacrificing reliability. Several ideas, including token ring passing and wireless data links, are being considered;

- A novel 1-glass RPC design is being developed [84], which features distinct advantages, such as an average pad multiplicity close to unity, a thinner chamber, a higher rate capability and a generous insensitivity to the surface resistivity of the resistive paint. The feasibility of larger chambers based on this design needs to be established;

- A high rate RPC could be a nice solution for the forward region of the DHCAL. The group is currently collaborating with several other institutes in developing low resistivity glass and Bakelite material for high rate RPCs;

- The group is pursuing the development of a realistic design for a DHCAL module. Several configurations are being considered;

- A high voltage distribution system is being developed which is capable of turning on/off, adjusting voltage values, and monitoring the current of individual chambers from a single high voltage input source;

- In order to operate a large DHCAL system at a future colliding beam experiment, a gas recirculation system is needed for both cost and environmental considerations. Initial development has started.

In order to continue the above-mentioned R&D, we are collaborating and setting up RPC test stands with the DHCAL physics prototype electronics to continue RPC development and long term stability tests, and are also focusing on design optimisation and next generation low-power front-end electronics development.

6.5.2.2 THGAM-based DHCAL

Thick Gaseous Electron Multipliers (THGEMs) can be built in large quantities at low cost, which might make them suitable for the large CEPC HCAL. THGEM detectors can provide flexible configurations, which allow small anode pads for high granularity. They are robust and fast, with only a few nano-seconds' rise time, and have a short recovery time which allows a higher rate capability compared to other detectors. They operate at a relatively low voltage across the amplification layer with stable high gain. The ionisation signal from charged tracks passing through the drift section of the active layer is amplified using a WELL THGEM layer structure. The amplified charge is collected at the anode layer with pads at zero volts. As the HCAL is located within the coil, WELL-THGEM, a new layer structure with thinner thickness, as shown in Fig. 6.39, can be considered as the sensitive medium, to keep the HCAL compact.

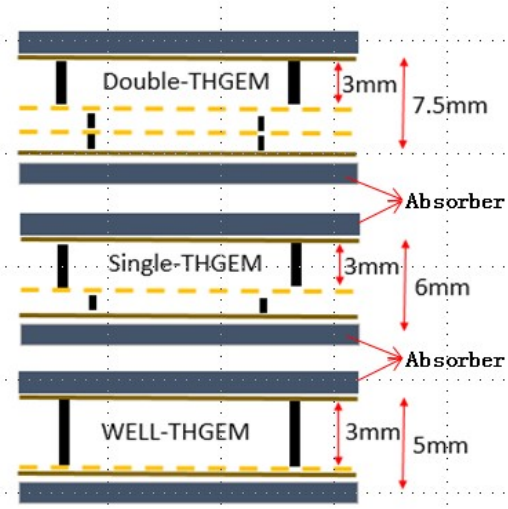

Figure 6.39 Structure of THGEM-based detector for DHCAL.

Digital readout has been proposed to limit the total amount of data, which simplifies the data treatment without comprising the energy resolution performance. The readout electronics of the DHCAL will be integrated into the sensitive layer of the system, thus minimising dead areas. Large electronics boards are assembled together to form extra-large boards before being attached to the THGEM. The board assembly will utilise a mechanical structure made of 4 mm stainless steel plate. In addition, to keep the HCAL as compact as possible, the fully equipped electronic boards are designed to be less than 2 mm thick in total.

A GEM/RPC based detector for DHCAL has been designed with 40 layers in total [1, 84]. Each layer contains 2.0 cm thick stainless steel, 0.8 cm thick RPC and readout electronics with 1×1 cm^2 readout pads. As THGEM production technology matures, the maximum area of THGEM is limited only by the size of the CNC drilling area. Its low price, robustness against occasional discharges, high gain and count rate capability

of up to 10MHz/cm^2 make THGEM very attractive for building the DHCAL. THGEM is cheaper and more robust than GEM, and has a higher counting rate capability than GRPC.

As illustrated in Fig. 6.39, the total thickness of the sensitive medium is 5 mm, which consists of 3 mm drift gap, 1 mm transfer gap and 1 mm induction gap. The absorber between the active layers is made of 20 mm thick stainless steel. The thickness of the readout electronics board is about 3 mm, and the total thickness of a single sensitive layer is less than 10 mm. Each layer corresponds to about 1.2 radiation length and 0.65 nuclear interaction length. The whole DHCAL detector is evenly divided into 40 layers, with a total stainless steel absorber thickness of 4.7 nuclear interaction lengths.

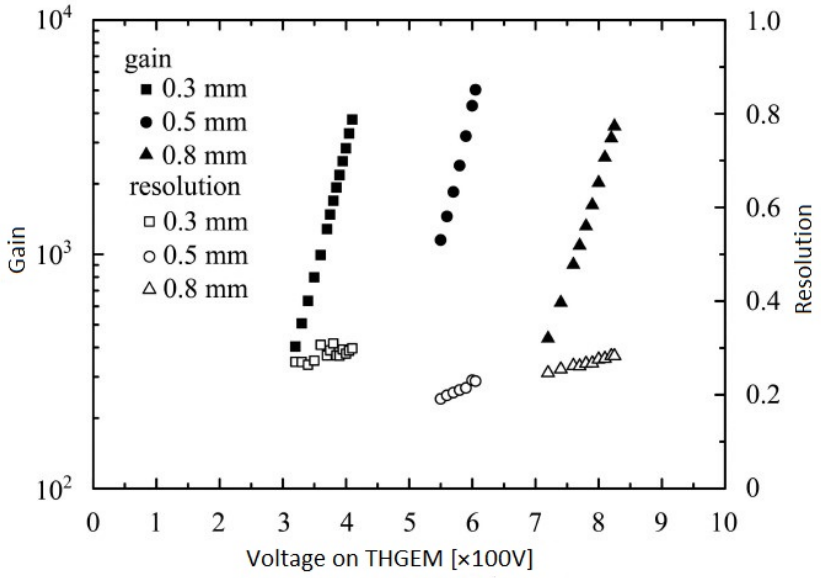

Figure 6.40 Gain and energy resolution of THGEM detector obtained with ^{55}Fe

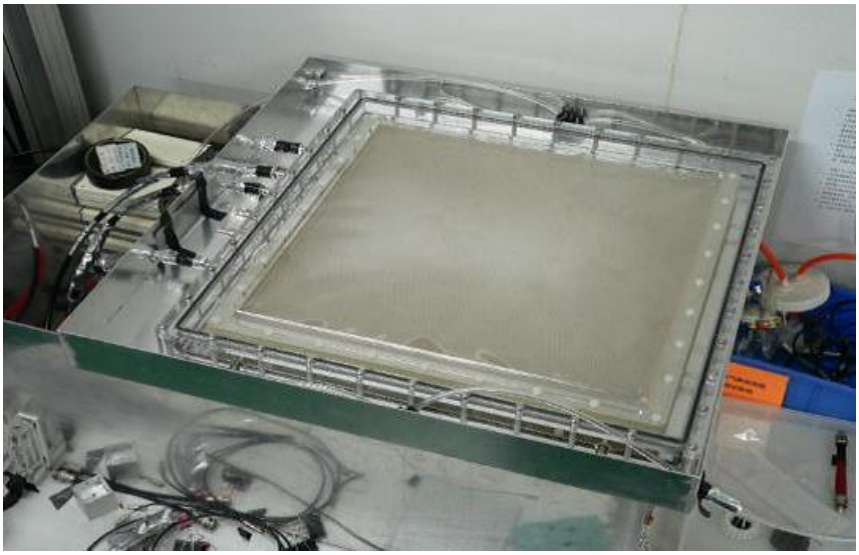

Figure 6.41 The maximum size of THGEM currently produced in China (40×40 cm^2).

THGEM was invented by Breskin in 2004 [86] and has been studied at IHEP since 2005. A THGEM with an area of 40×40 cm^2 has been successfully fabricated, as shown

in Fig. 6.41, and a gain of 2×10^5 has been achieved with a double THGEM, with an energy resolution of about 20%. The THGEM produced has the following features: 1) standard PCB processes are used, which keeps the cost low; 2) excellent performance in terms of energy resolution, gas gain and stability (as shown in Fig 6.40); 3) Rim around the hole formed by full-etching process, the size of which can be varied between 10 μm and 90 μm, as depicted in Fig.6.42 - this allows adjustment according to gas requirements.

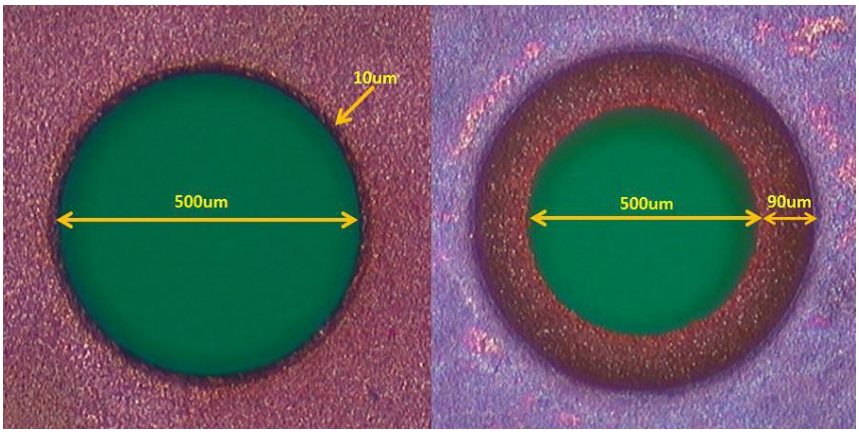

Figure 6.42 Micro-rim and large-rim THGEMs produced by IHEP, University of the Chinese Academy of Sciences (UCAS) and Guangxi University (GXU).

Research is being carried out on large THGEM detectors. Single THGEM detectors and Well-THGEM detectors are being developed to reduce detector instability and inefficiency. Gas recycling systems are built to lower gas consumption and pollution. The achieved THGEM detection rate of 1 MHz/cm^2 with efficiency greater than 95% already meets the CEPC requirements.

THGEM digital readout system A considerable effort has been made by the CALICE collaboration to standardise the readout of different types of calorimeter with embedded Very Front-End (VFE) electronics while minimising the space needed for the configuration distribution and data readout. Preliminary studies show a 1 cm$\times$1 cm readout pad is sufficient. Given the requirements for high channel count, small space, and low power, a custom application-specific integrated circuit (ASIC) has been developed for the front-end electronics. There are a given number of readout channels per ASIC chip, which performs all the front-end signal processing (amplification, shaping and discrimination). Each piece of ASIC event data consists of a time stamp (with a resolution of 100 ns) and a hit pattern.

The electronic readout system needs to be optimised for the readout of large numbers of channels. The readout system consists of front-end board, data concentrator, data collector, and timing and triggering module, as shown in Fig. 6.43. Once the ASIC chips in the front-end board acquire data, the data is read out serially from the front-end boards using "data push" into custom serial multiplexer cards called Data Concentrators (DCON) that reside on the outer edges of the detector. The serial streams are concatenated into high-speed serial streams, which are then sent to VME cards in the back-end system called the Data Collector (DCOL). The trigger system supplies the external trigger signal and the timing system supplies the synchronised clock signals. Such a system has been pursued by Argonne National Laboratory and Lyon University and joint effort is expected to develop a readout system with 55 million channels. Since the pad boards with ASIC chips

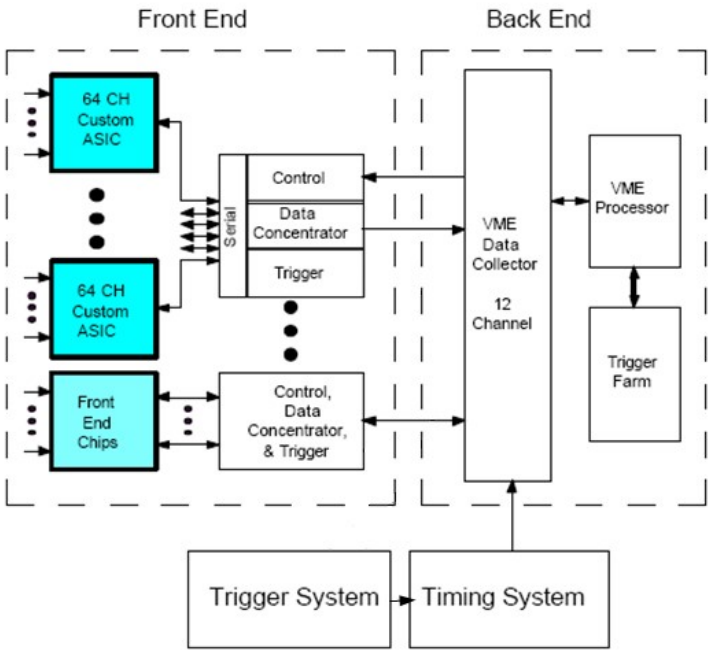

Figure 6.43 Conceptual block diagram of readout system.

are attached to the surface of the detectors and inserted into the narrow slots between the absorbers, the heating of the chips will be a big problem. Special cooling pipes are designed for the detector modules and material with excellent thermal conductivity will be used for the detector module box.

Future R&D

- Manufacture of an even larger THGEM with area of 60×100 cm^2 or even 100×200 cm^2 with WELL-THGEM. This is extremely important to construct the large DHCAL for the CEPC and minimise the dead area as much as possible. Gain homogeneity will be a very challenging issue for large area THGEM detectors.
- Construction of a DHCAL prototype with 40 layers covering an area of 1×1 m^2. A THGEM detector with a total thickness of 6 mm will be optimised to meet the DHCAL requirements, preferably with WELL-THGEM to reduce the detector thickness. It will be nontrivial to bring the total thickness, including the ASIC readout electronics, below 6 mm. The cooling system will be integrated into the system to verify the detector concept. The detector performance will be further studied with beam tests for this prototype.
- Development of readout electronics for the THGEM-based DHCAL prototype. It is important to understand the impacts of single-threshold and three-threshold electronics on the energy resolution. Even with the prototype, the number of readout channel comes to 10k per layer and 400k in total, assuming a readout pad size of 1×1 cm^2 and detector area of 1×1 m^2. This will be very challenging technically.

6.6 Muon System

The CEPC muon system acts as the muon identifier, the solenoid flux return yoke and the support structure for the whole spectrometer, following the same design as for the ILD detector [2]. High muon detection efficiency, low hadron mis-identification rate, modest position resolution and large coverage are the main concerns of the design. The muon system plays an important role in measuring physics processes involving muon final states, e.g. $e^+e^- \to ZH$ with $Z \to e^+e^-$ or $\mu^+\mu^-$. In addition, it compensates for leaking energetic showers and late showering pions from the calorimeters, which is important to improve the relative jet energy resolution [90].

6.6.1 Baseline Design

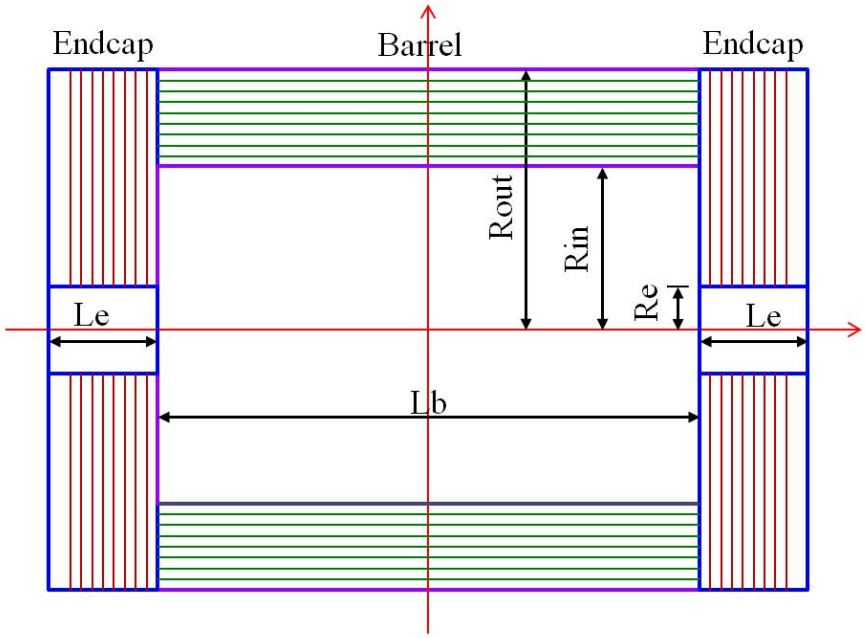

Figure 5.44 The layout of the muon system.

The muon system will be installed as the outermost component of the whole detector. Its main parameters are summarised in Table 6.8. The geometry and dimensions will have to be optimised together with the inner detectors, in particular the ECAL and the HCAL. In general, the muon system is divided into barrel and end-caps, as shown in Fig. 5.44. Both the barrel and end-caps are further segmented into modules arranged in an octagon, decagon or dodecagon, as adopted by several other experiments as shown in Fig. 5.45. The segmentation is constrained by the maximum sizes of the module and sensitive unit. More segments are required for a larger detector. For the CEPC muon system, dodecagon segmentation is selected for the baseline design. Detailed studies on the structure of the segments and modules will be carried out to minimise the dead area and to optimise the interface for routing, support and assembly.

The number of sensitive layers and the thickness of iron (or tungsten) in the absorbers are two critical parameters. Considering the center-of-mass energy of the CEPC ($\sqrt{s} \sim$

Table 6.8 The baseline design parameters of the CEPC muon system

Parameter	**Possible range**	**Baseline**
Lb/2 [m]	3.6 – 5.6	4.0
Rin [m]	3.5 – 5.0	4.4
Rout [m]	5.5 – 7.2	7.0
Le [m]	2.0 – 3.0	2.6
Re [m]	0.6 – 1.0	0.8
Segmentation	8/10/12	12
Number of layers	6 – 10	8 ($\sim$4 cm per layer)
Total thickness of iron	6 – 10λ ($\lambda = 16.77$ cm)	8 (136 cm) (8/8/12/12/16/16/20/20/24)
Solid angle coverage	0.94 – 0.98$\times 4\pi$	0.98
Position resolution [cm]	$\sigma_{r\phi}$: 1.5 – 2.5	2
	σ_z : 1 – 2	1.5
Average strip width [cm]	Wstrip: 2 – 4	3
Detection efficiency	92% – 98%	95%
Reconstruction efficiency ($E_\mu > 6$ GeV)	92% – 96%	94%
P($\pi \to \mu$)@30GeV	0.5% – 3%	$< 1\%$
Rate capability [Hz/cm^2]	50 – 100	$\sim$60
Technology	RPC	RPC (super module, 1 layer readout, 2 layers of RPC)
	Scintillating strip	
	Other	
Total area [m^2]	Barrel	$\sim$4450
	Endcap	$\sim$4150
	Total	$\sim$8660
Total channels	Barrel	26500
	Endcap	29000
	Total	$\sim 5.55 \times 10^4$ (3 cm strip width, 1-D readout, 2 ends for barrel, 1 end for end-cap)

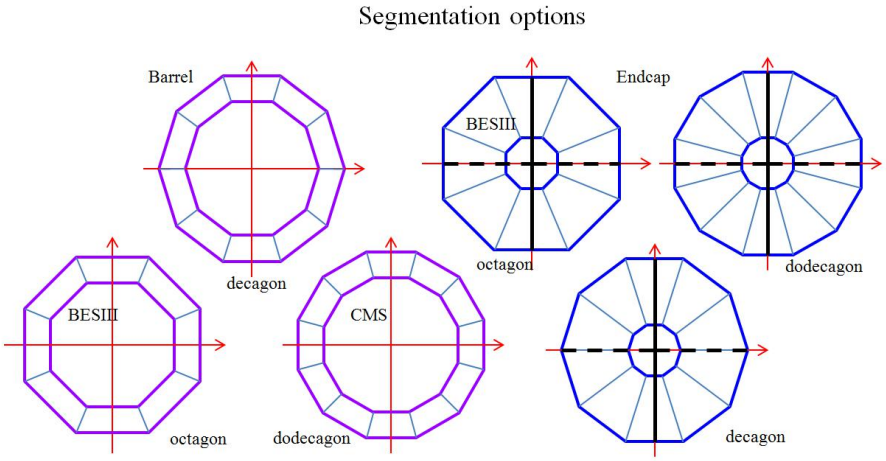

Figure 5.45 Segmentation options for the muon system.

240 GeV), the total thickness of iron absorber should not exceed 13 times the nuclear interaction length (λ) of iron. For the baseline design, it is chosen to be 8λ distributed in 8 layers, which should be sufficient for effective muon tracking. Gaps of 4 cm between neighbouring iron layers give adequate space for the sensors (RPC and scintillator strips).

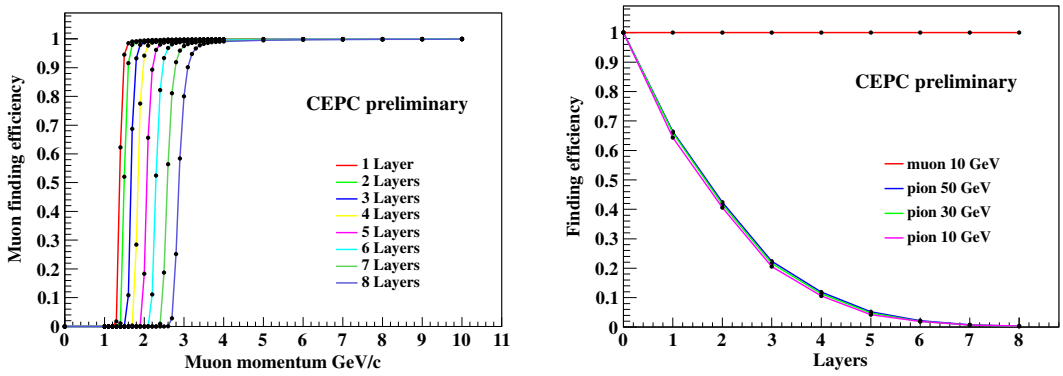

Figure 6.46 The muon detection efficiency as a function of momentum for different numbers of layers of muon detector (left), and the pion detection efficiency as a function of number of layers for different momenta (right).

Figure 6.46 (left) shows that for momentum larger than 4 GeV/c, the muon detection efficiency can still reach 95% even after penetrating 8 layers. This simulation result indicates that high detection efficiency might be still feasible for low energy muons. The cut-off momentum might be slightly above 4 GeV, after taking into account all the material in front of the muon system. Figure 6.46 (right) shows the detection efficiency for pions with energies of 10, 30, and 50 GeV, respectively. The results suggest that the pion detection efficiency is not sensitive to the pion energy itself, but rather to the number of detector layers. The efficiency decreases drastically with increasing number of layers and vanishes after 8 layers, which is the number chosen for the CEPC baseline design but which will undergo further study in future.

From the physics point of view, solid angle coverage, detection efficiency, spatial resolution, reconstruction efficiency and pion mis-identification rate are the fundamental concerns for the design. The solid angle coverage of the CEPC muon system should be up to $0.98 \times 4\pi$ in accordance with the TPC. Position resolutions of $\sigma_{r\phi} = 2.0$ cm and $\sigma_z = 1.5$ cm are also required. Detection efficiency of 95% is easy to achieve for small muon detectors but can be challenging for large size detector. It is even more challenging to keep all the modules efficient at 95% over 5 – 10 years of running, especially with the gas detector options.

Resistive Plate Chamber (RPC) and scintillating strips are adopted for the baseline design. Other options of Monitored Drift Tube (MDT), Cathode Strip Chamber (CSC) and Thin Gap Chamber (TGC) are also being considered but might be less suitable for the CEPC muon system. Based on the dimensions and segmentation of the baseline design, the total sensitive area of the muon system amounts to 8600 m^2. And assuming the strip width of 3 cm and with 1-D readout (2 ends for barrel and 1 end for the end-cap), the total number of electronic channels will be around 5.5×10^4.

6.6.2 Technologies

6.6.2.1 Resistive Plate Chamber (RPC)

RPC technology is suitable for building large area detectors with millimeter spatial resolution. It has been applied in muon systems for experiments including BaBar [91], Belle [92], CMS [93], ATLAS [94], BESIII [95] and Daya Bay [96]. It provides a common solution with the following advantages: low cost, robustness, easy construction of large areas, large signal, simple front-end electronics, good time resolution and good spatial resolution.

RPCs can be built with glass or Bakelite, and run in avalanche or streamer mode. Bakelite RPCs of about 1200 m^2 and 3200 m^2 were produced for the BESIII and Daya Bay muon systems, respectively. Compared with glass RPC, Bakelite RPC has the advantage of easier construction, lower density, larger cell size and lower cost, especially if the event rate is below 100 Hz/cm^2 as required by the CEPC muon system. The characteristics of Bakelite and glass RPCs are compared in Table 6.9. Further improvements are required for Bakelite RPCs, however, in terms of long-term stability, detection efficiency, readout technologies, lower resistivity ($< 10^{10}$) and higher rate capability.

6.6.2.2 Scintillator Strips

Scintillator strips are an attractive technology for muon systems. Plastic scintillator material can be extruded into strips longer than 5 m. The emission light of plastic scintillator (e.g. BC408) peaks at around 430 nm. Thus it is necessary to use wave-length shifting (WLS) fibres to shift the light spectrum to match the response of Si photo-diodes (SiPM) / multi pixel photo counters (MPPC), which peak at around 550 nm. With this technology, it is easy and convenient to construct compact and rigid modules with 1-D or 2D readout strip arrays. The required spatial resolution of 3 cm can be achieved with 1 cm thick, 3 cm wide and 2 – 5 m long scintillator strips.

Figure 6.47 shows a scintillator strip and its signal response with WLS and SiPM readout. The WLS fibre will be embedded in the scintillator strip during the extrusion process. It is also important that a layer of T_iO_2 should be co-extruded alongside the scintillator during the extrusion process. This layer of T_iO_2 will shield the light from outside and

Table 6.9 Comparison of Bakelite and glass RPC

Parameters		Bakelite	Glass
Bulk resistivity [$\Omega \cdot$ cm]	Normal	$10^{10} \sim 10^{12}$	$> 10^{12}$
	Developing	$10^8 \sim 10^9$	
Max unit size (2 mm thick) [m]		1.2×2.4	1.0×1.2
Surface flatness [nm]		< 500	< 100
Density [g/cm^3]		1.36	2.4∼2.8
Min board thickness [mm]		1.0	0.2
Mechanical performance		Tough	Fragile
Rate capability [Hz/cm^2]	Streamer	100@92% [97]	
	Avalanche	10K	100@95% [98]
Noise rate [Hz/cm^2]	Streamer	< 0.8	0.05 [99]

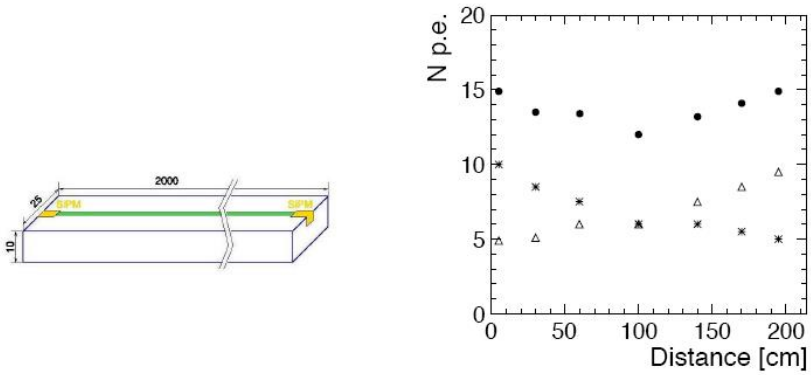

Figure 6.47 2 m long scintillator strip (left), and photon number as a function of distance read out by WLS and SiPM from both ends (right).

reflect the scintillating light. An SiPM will be glued at each end of the strip to read out the signals effectively.

6.6.3 Future R&D

The baseline design and most promising technologies for the CEPC muon system have been discussed. The next step will focus on future R&D, which could be accelerated by effective international cooperation in RPC and scintillator strip development. During initial studies, several critical R&D items have been identified, including:

- **Layout optimisation**: The total thickness and number of layers for the baseline design are based on the ILD design and further optimised with Monte Carlo simulation studies for CEPC. This requires further study and optimisation according to the CEPC physics program and operation conditions.
- **Bakelite RPC**: Improving the long-term stability, detection efficiency, readout technologies, resistivity ($< 10^{10}$) and rate capability of the Bakelite RPC.
- **Scintillator strips**: Extrusion techniques toward mass production, and SiPM signal readout electronics.

6.7 Detector Magnet System

The CEPC detector magnet system is designed to provide an axial magnetic field of about 3.5 T, homogeneous over the tracking volume (TV). The superconducting solenoid has a warm bore of 6.8 m in diameter and 8.05 m in length. The iron yoke consists of barrel and end-cap components. It provides the magnetic flux return, accommodates the installation space for the muon detector and serves as the main support structure for the CEPC detector.

6.7.1 General Design Considerations

The CEPC detector magnet follows the same design concepts as for the CMS and ILD magnets [100, 101], except for different geometrical dimensions. The magnet system consists of the solenoid coil and the iron yoke. Two options for the coil design can be considered:

- Option A: five modules with three long sectors (1.8 m) in the middle and another two short sectors (1 m) on either end, which are used for uniformity adjustment of the tracking volume (TV). The five modules are connected mechanically and electrically. With the thermal shields, they make up the cold mass, supported by several sets of tie-rods inside the vacuum tank.

- Option B: three modules of 2.7 m in length including an independent vacuum vessel. This reduces the risks in winding, impregnation, handling, testing and transport. The electromagnetic force between the coils, however, may increase the difficulty of designing the supporting rods and vacuum tank.

For both options, each module consists of four layers with indirect cooling. A nominal current of 18.575 kA is required for the design central field of 3.5 T. Option A has been adopted for the CEPC baseline design.

The iron yoke consists of the barrel with 3 rings (11 layers each) and the end-caps (11 layers each). They are laminated to house the muon detector. Figure 6.48 shows the 3D view and Fig. 6.49 shows the cross-sectional view of the magnet, respectively.

Table 6.10 Main parameters of the CEPC detector magnet.

Cryostat inner radius [mm]	3400	Barrel yoke outer radius [mm]	7240
Cryostat outer radius [mm]	4250	Yoke overall length [mm]	13966
Cryostat length [mm]	8050	Barrel weight [t]	5775
Cold mass weight [t]	165	End-cap weight [t]	6425
Barrel yoke inner radius [mm]	4400	Total yoke weight [t]	12200

The field map of the magnet system has been calculated with a 2D axisymmetric model, using the ANSYS magnetic vector potential formulation with the nodal-based method and infinite boundaries. All the gaps for the actual design of the yoke are taken into account, using an axisymmetric cylindrical simulation rather than the dodecagonal geometry. The

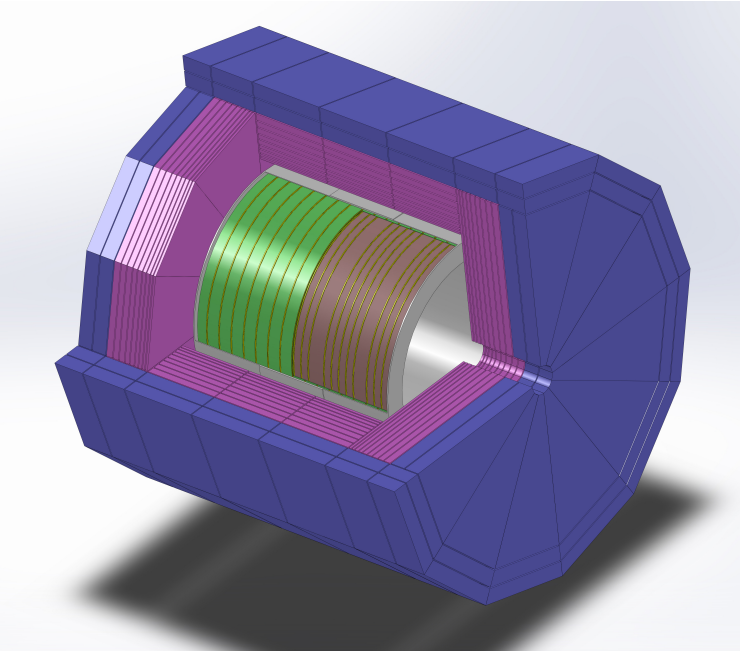

Figure 6.48 Structure of the coil and iron yoke

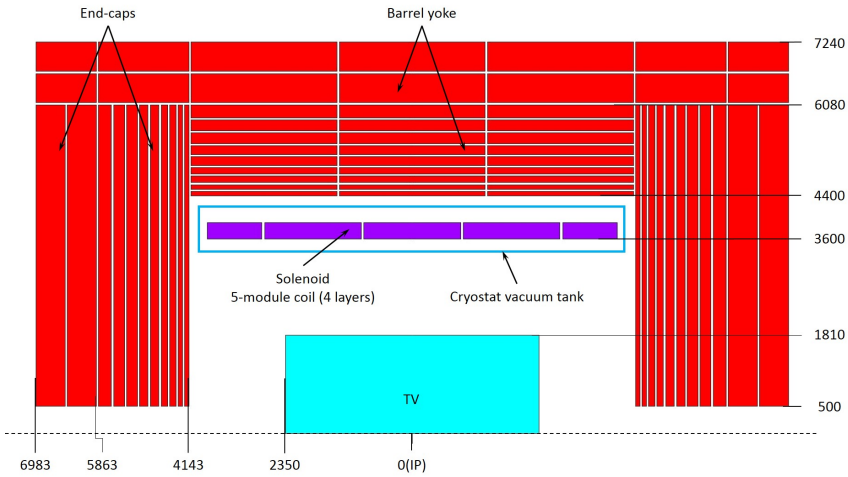

Figure 6.49 Schematic view of the CEPC detector magnet cross section.

$B - H$ curve for the iron in the yoke, as shown in Fig. 6.50, has been used for all the calculations.

Figures 6.51 and 6.52 respectively show the main component B_z of the field along the beam axis, and the field in various regions of the magnet with the central field 3.5 T.

6.7.2 Solenoid Design

6.7.2.1 Main Parameters

The main parameters of the CEPC solenoid are given in Table 6.11. The 7.4 m long CEPC detector coil is composed of 5 modules ("Option A"). This increases the ease of construction and reduces risks, including in superconducting wire selection, fabrication of the external support, winding and impregnation, transport and handling. The design enables

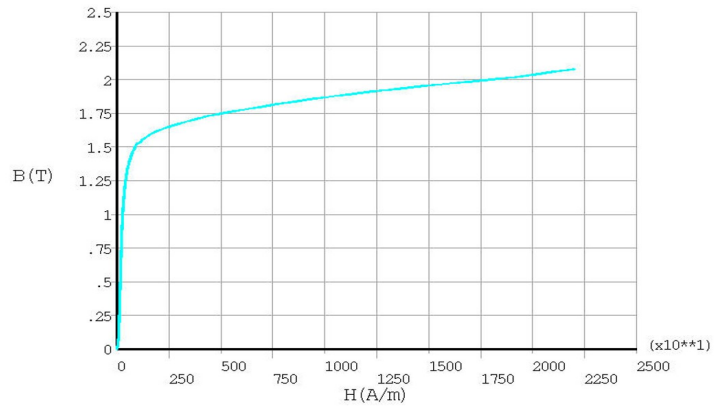

Figure 6.50 $B-H$ curve for the iron in the yoke.

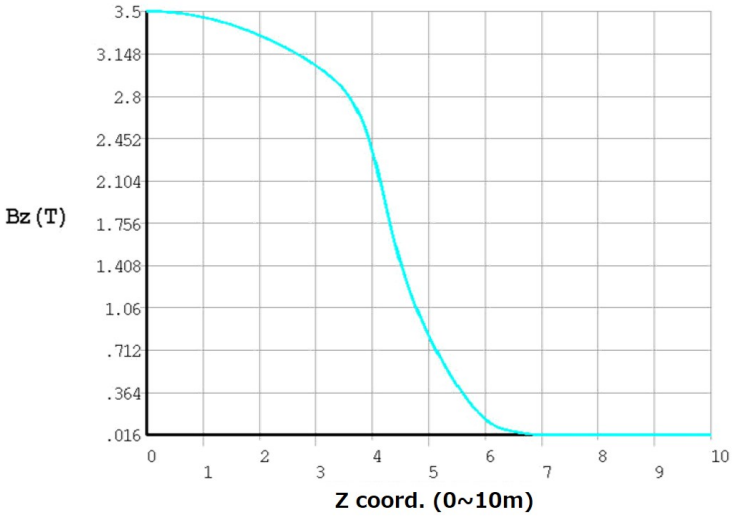

Figure 6.51 The calculated magnetic field B_z along the detector axis.

Table 6.11 Main parameters of the solenoid coil.

Solenoid central field [T]	3.5	Nominal current [kA]	18.575
Maximum field on conductor [T]	3.85	Total ampere-turns of solenoid [MAt]	23.925
Coil inner radius [mm]	3600	Inductance [H]	10.4
Coil outer radius [mm]	3900	Stored energy [GJ]	1.8
Coil length [mm]	7600	Stored energy per unit of cold mass [KJ/kg]	10.91

the possibility of using shorter unit lengths of superconducting conductor ($\sim$1.65 km) and allows them to be joined in known positions and in low field regions, on the outer radius of the solenoid. Another advantage is that the operating current density can be adjusted for the end modules, by using different dimensions of superconducting cable or changing the

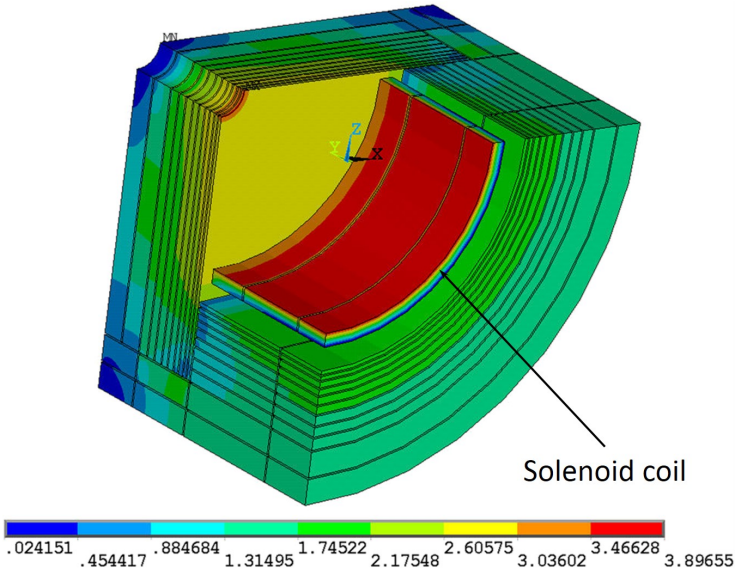

Figure 6.52 3D view of field (in T) in various regions of the CEPC detector magnet.

operating current between the middle and end modules, to improve the field homogeneity in the TV region.

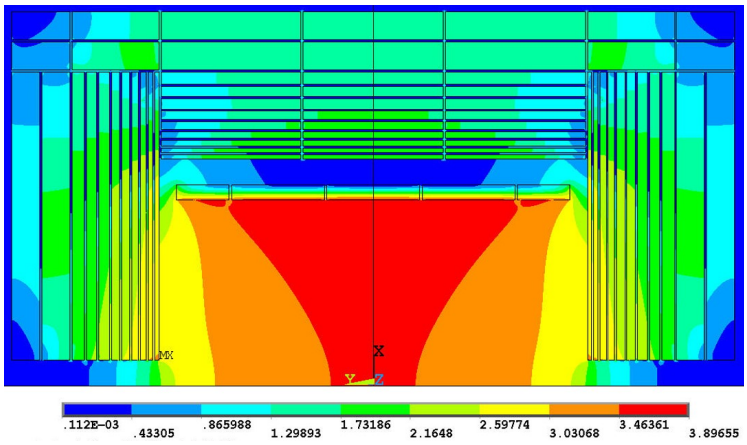

Figure 6.53 Field map of the magnet (T).

In addition, with an odd number of modules, the coil mid-plane ($Z = 0$ m), where the axial compressive forces are at a maximum, is not an interface between two modules. Such design limits the risk of delamination and heat deposit by friction in the module-to-module coupling region. This is particularly important for the innermost layer, where the field applied to the superconductor is at its maximum. Each middle module has 4 layers, with 78 turns per layer. Each end module also has 4 layers, but with 39 turns per layer. The nominal current is 18.575 kA for the design maximum central field of 3.5 T.

Figure 6.53 shows the magnetic flux density vector sum of the solenoid with the yoke. With the design field of 3.5 T at the interaction point, the field homogeneity in the TV region is about 10.2%. This can be improved by adjusting the relevant parameters of the end modules. The magnetic flux line distribution and field map are shown in Fig. 6.54 and Fig. 6.53, respectively. Fig. 6.55 shows the stray field distribution outside the magnet.

The range of magnetic field is from 50 G to 140 G with the 3.5 T central field. The 50 G line is at 14.8 m radial distance and 17.2 m axial distance with a total thickness of iron of 2.44 m both in the barrel and the two end-caps.

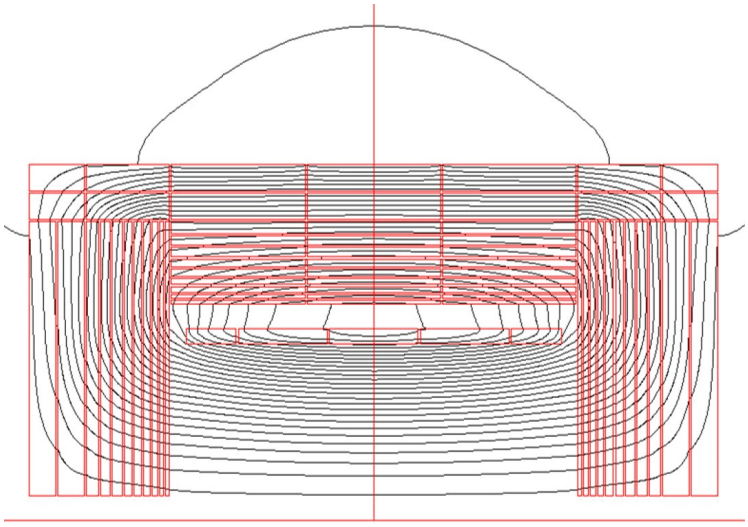

Figure 6.54 Magnetic flux line distribution of the magnet.

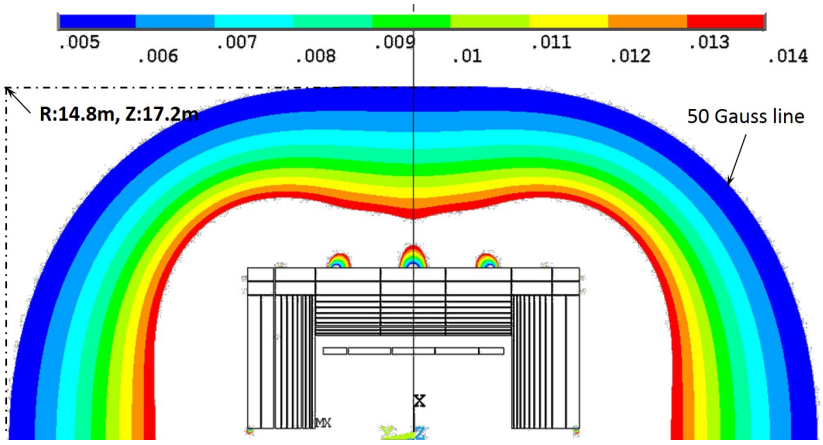

Figure 6.55 Stray field distribution outside the magnet (the field is given in T).

6.7.2.2 Coil Design

The coil has a 4-layer geometry to obtain the 3.5 T center field with a reasonable nominal current. The horizontal cryostat for the superconducting magnet consists of the vacuum tank and thermal shields (inner and outer) covered with multiple layer insulation (MLI). The stainless steel vacuum vessel is 8.05 m in length and has an outer radius of 4.25 m. Two service towers on top of the vessel are for the installation of current leads and phase separators. The vacuum tank is cantilevered from the central ring of the barrel yoke.

6.7.2.3 Coil Cooling Circuit

The superconducting coil in the cryostat requires cooling at liquid helium temperatures. The cold mass, which amounts to about 165 t, will be indirectly cooled by a network of

liquid helium (LHe) tubes. They are attached to the external coil wall and supplied in a thermosiphon circulating mode. Such a passive mode has already been successfully used in the ALEPH and CMS experiments. With this mode, the ΔT between the magnet hot spot and the source of cooling can be minimised. The thermosiphon cooling circuit is shown in Fig. 6.56.

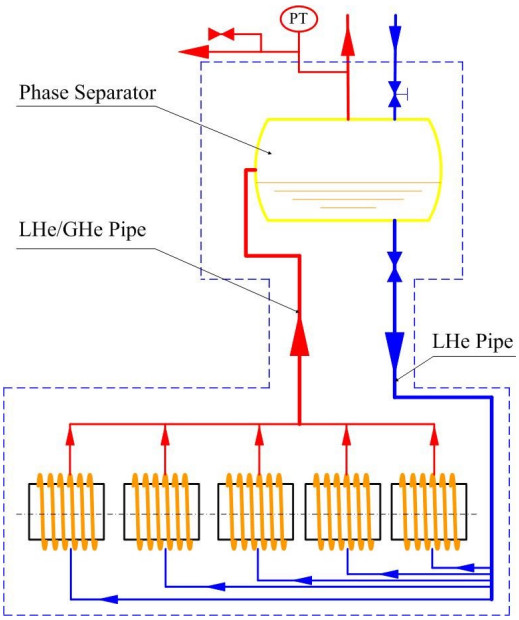

Figure 6.56 Coil cooling circuit.

6.7.2.4 Superconducting Conductor

The conductor design is similar to that of CMS [102]. As the forces induced in the conductor by the magnetic and thermal loads are beyond the yield stress of pure aluminium, a mechanical strengthening is envisaged. This consists of a superconducting Rutherford cable, which is sheathed in a stabiliser and mechanically reinforced. A cross-sectional view of the superconductor is shown in Fig. 6.57. Two aluminium alloy profiles are welded by electron beam to the central conductor stabiliser, which is made of high purity aluminium.

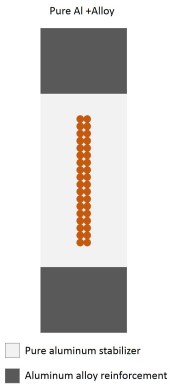

Figure 6.57 Cross section of solenoid conductor.

The Rutherford cable will be made with NbTi superconducting strands. It is proposed to use cables with similar characteristics to the CMS superconductor, but with a slightly increased number of strands in the cable.

Table 6.12 Superconductor characteristics

Superconducting strand in virgin state	
Strand diameter	1.28 mm
Cu/NbTi	1.1
SC strand critical current density	3300 A/mm^2 @4.2 K, 5 T
Rutherford cable	
Number of strands	36
Cable transposition pitch	185 mm
Final conductor	
Bare dimensions	75×23 mm^2
SC strand critical current density	>2970 A/mm^2 @4.2 K, 5 T
I_c degradation during manufacturing	<10%

6.7.2.5 Quench Protection

A quench protecting device should be installed to prevent magnet damage. As illustrated in Fig. 6.58, this device consists of magnet sensors, instrumentation modules, current line breakers and dump resistor.

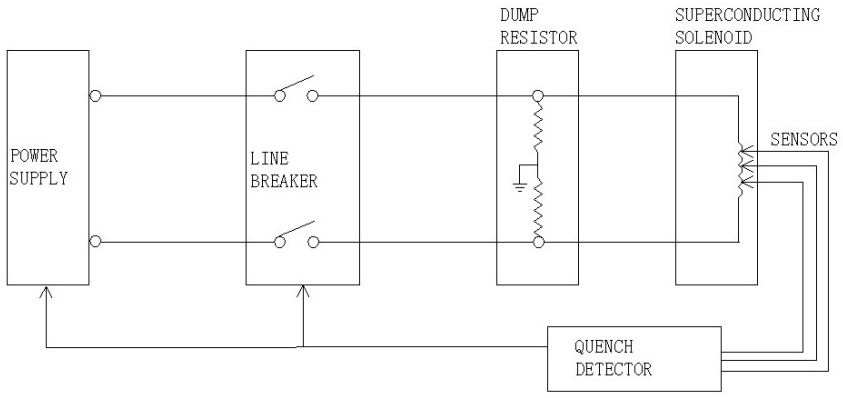

Figure 6.58 Electrical circuit of magnet with power supply and quench protection.

For safety reasons, two breakers that open both polarities of the power supply simultaneously are introduced. They are used to quickly separate the magnet from the power supply for easy inspection of the insulation, and protect the power supply against the high voltage developed during the energy dump.

6.7.3 Coil Manufacturing and Assembly

6.7.3.1 Coil Manufacturing

The coil winding will be based on the inner winding technique, as adopted for the BESIII detector magnet [103], where the supporting external cylinders are used as external mandrels. These mandrels will be built with aluminium alloy 5083 given its good welding and high mechanical strength. The cooling circuit will be designed to withstand possible deformations. To ensure good thermal conductivity, the helium tubes will be held on the surface of the mandrels before winding. Each module will be wound individually, and then vacuum impregnated. The layer-to-layer electrical joints are made after impregnation. The electrical connections will be attached on the external mandrels before being transferred to the magnet's final assembly location.

6.7.3.2 Coil Assembly

The proposed assembly procedure for the coil is similar to that used for CMS [104]. The modules will be stacked vertically for mechanical coupling. The joints between the modules will then be done and attached to the outer surface of the mandrels. After the installation of the thermal shields and the multilayer insulation on the coils, the cold mass will be swivelled to the horizontal position, and inserted into the outer cylinder of the vacuum tank. Finally the coil will be attached to the outer cylinder of the cryostat with several longitudinal and radial tie-rods.

6.7.4 Ancillaries

6.7.4.1 Power Supply

The power supply for the solenoid is DC stabilised current supply with low voltage and high current, which should be adjusted slowly and evenly. In order to have a steady field, the ripple of the power supply should be filtered. A high temperature superconductor (HTS) link is preferred over copper bus bars for the power lines, as HTS has less power dissipation and lower mass. HTS will also be used for the current leads.

6.7.4.2 Control and Safety Systems

The safety system and control system are independent, but exchange information between each other. The safety system measures the magnet status in order to prevent operation in dangerous conditions. The safety signals from the quench detectors and voltage taps are transferred directly to the main switch in the circuit and trigger a fast discharge of the magnet. As shown in Fig. 6.58, quench detectors are used to protect the bus bars and the current leads. In addition, a substantial amount of instrumentation is required to monitor the operational status of the magnet and to provide diagnostic data such as temperature, stress, position etc. The control system provides the controls needed to execute the automatic processes of the various running modes of the magnet system.

6.7.4.3 Cryogenic Design

A cryoplant with a capacity of 750 W at 4.5 K is under design for the operation of the superconducting facility. The normal role of the cryogenic system is to supply a mix of liquefaction and refrigeration at 4.5 K in varying proportions depending on the operating

mode. It shall also be able to extract the dynamic losses during the various magnet ramps or discharges.

The cryoplant includes the cold box, the compressors, the refrigeration control system and the infrastructure needed to power the refrigerator and cool the helium compressor. The helium liquefier will be in the underground area, supplying liquid helium to the coils and taking helium gas return back from the coils and power lines, possibly in a position close to the magnet compatible with the fringing field and the maintenance activities. For the thermosiphon refrigerating mode, the proximity cryogenics is on top of the magnet, including:

- a Dewar containing a spare volume of LHe to keep the magnet at nominal field in case of temporary disruption of LHe supply, and to allow the ramp down to zero field keeping the magnet in superconducting state;
- a valve box;
- a phase separator to feed the thermosiphon of the solenoid. Depending on the position of the cold box, a flexible vacuum line may be used to connect the liquefier to the proximity cryogenics.

In addition, the refrigerator shall be dimensioned, taking into account the acceptable cool-down time. Losses during ramping the magnet up and down and losses in the current leads must be taken into account for dimensioning the refrigeration plant, with some safety margin.

6.7.5 Magnet Tests and Field Mapping

A full test of the magnet at its nominal current is mandatory before being transported underground. This test will enable quality checking of the coil and magnet ancillaries at the nominal field and at a 110 percent nominal field. It is also necessary to make a complete field mapping of the magnet before the inner detectors are installed [105].

6.7.6 Iron Yoke Design

The magnet yoke is responsible for the return of the magnetic flux and reduction of the outside stray field to an acceptable level. The design of the yoke needs to meet several other requirements. It needs to provide mechanical support for the sub-detectors. Additionally, it will provide room for the muon detector, which will sit between layers of the yoke, and allow space for cables, cooling pipes, gas pipes etc. through the yoke. The magnet yoke is divided into a cylindrical barrel and two end-caps. Taking into account the mechanical performance and magnetic requirements, low carbon structural steel No. 10 (Chinese national standard) can be used as the yoke material. The preliminary design of the yoke is described below.

The barrel yoke is 8206 mm in length and has a dodecagonal shape. The inscribed circle diameters of the inner and outer dodecagon are 8800 mm and 14480 mm, respectively. The barrel yoke will be composed of 3 rings, each ring consisting of 11 layers. There will be two 40 mm gaps between the rings, which are designed to allow space for the data cables and services. From the inner to the outer layer, the layer thicknesses are 80 mm, 80 mm, 120 mm, 120 mm, 160 mm, 160 mm, 200 mm, 200 mm, 240 mm, 540 mm and 540 mm,

with a 40 mm space between yoke layers for the muon detector. Figure 6.59 shows the schematic view of the barrel yoke.

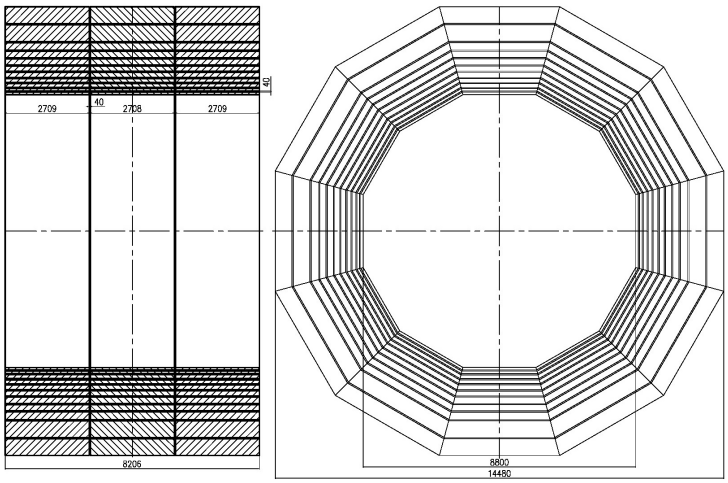

Figure 6.59 Schematic of the barrel yoke.

Figure 6.60 shows the schematic view of the end-cap yokes. The inscribed circle diameter of the outer dodecagon is 14480 mm and the total thickness of the end-cap is 2440 mm. Each end-cap yoke will consist of 11 layers and one pole tip. The thickness of the pole tip is 600 mm, and from the inner to the outer layer, the layer thicknesses are 80 mm, 80 mm, 120 mm, 120 mm, 160 mm, 160 mm, 200 mm, 200 mm, 240 mm, 540 mm and 540 mm. There will be a 40 mm space between layers for the end-cap muon detectors.

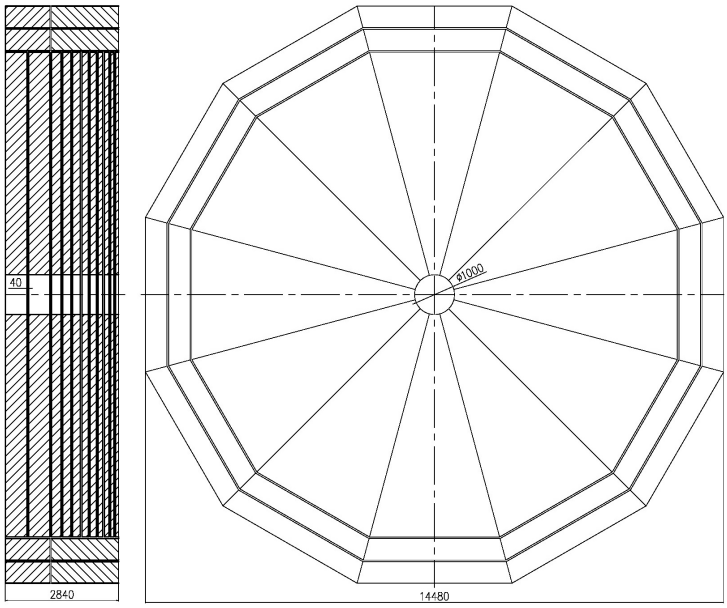

Figure 6.60 Schematic of the end-cap yoke.

The total weight of the yoke will be about 12200 tons. Each ring of the barrel yoke and each end-cap yoke will be composed of 12 segments. The maximum weight of the segments of the barrel yoke and end-cap yoke will no more than 100 and 200 tons, respectively. The yoke segments will be preassembled at the manufacturer. They will then

be transported to the experimental site as segments. If there is enough space, the yokes will be assembled in the IR hall. Otherwise they will be assembled in the surface building above the IR hall. The central ring of the barrel yoke will then be assembled underground together with the solenoid magnet, which is the biggest part to be lowered into the IR hall. Its weight will be about 3000 tons. A temporary gantry crane will be used. The time used for assembly in the IR hall will be longer than that of assembly in the surface building.

6.7.7 Future R&D

The future R&D of the large superconducting detector magnet will be in full swing in next five years, and then provide the technical reserves for engineering and manufacturing of the CEPC project. The detailed R&D plan is as following:

- The superconducting cable design and critical process: Large superconducting detector magnet generally has high current, large storage energy, and big coil aperture. And the aluminum stabilized superconducting Rutherford cable usually used to wind the coil in high energy experiments field. The critical process include mooring process of superconducting cables, high purity aluminum cladding processes and electron beam welding technology for the aluminum alloy. Compared with the original state, the attenuation of the critical current density of the finished cable should be less than 10%.
- Winding process and impregnation process of large inner coils: A dummy coil with a quarter length of the actual coil will be put up to look for the process parameters.
- Thermosyphon cooling design and technology: principle experiments and the 1/10 model experiments will be set up to explore the parameters of the cooling design.
- Power supply with high stability: The requirement is that maximum output current is 20 kA, and the maximum output voltage is 40 kV with a stability of 1/10000.
- Manufacturing and assembly of yokes: optimization of the connection structure of the polygon yokes and investigation of the domestic production and processing routes.

6.8 Machine-Detector Interface

The machine-detector interface (MDI) covers all aspects that are common to the collider and the detector. It is one of the most challenging areas of the CEPC project. The focus of this section is on the interaction region layout, detector backgrounds, luminosity instrumentation and mechanical integration. Further studies on most of these topics are required to achieve comprehensive understanding of the issues and to achieve the optimal overall collider and detector performance.

6.8.1 Interaction Region Layout

The interaction region (IR) of the CEPC consists of the beampipe, the surrounding silicon detectors, the luminosity calorimeter ("LumiCal"), and the interface to the two final focus quadrupoles (QD0 and QF1). The preliminary IR layout is depicted in Fig. 6.61. The current IR design features a rather short focal length of $L^* = 1.5$ m, defined as the distance between the QD0 and the interaction point (IP). On the one hand, such a short L^* will be essential to achieve high luminosity without exploding the chromaticity corrections; on the other hand, it imposes nontrivial constraints on the CEPC detector design and limits the detector coverage in the very forward region. To maximise the overall performance, it is necessary to fully evaluate the impacts of the short L^* on both the collider and the detector, and find the most optimal value for the CEPC.

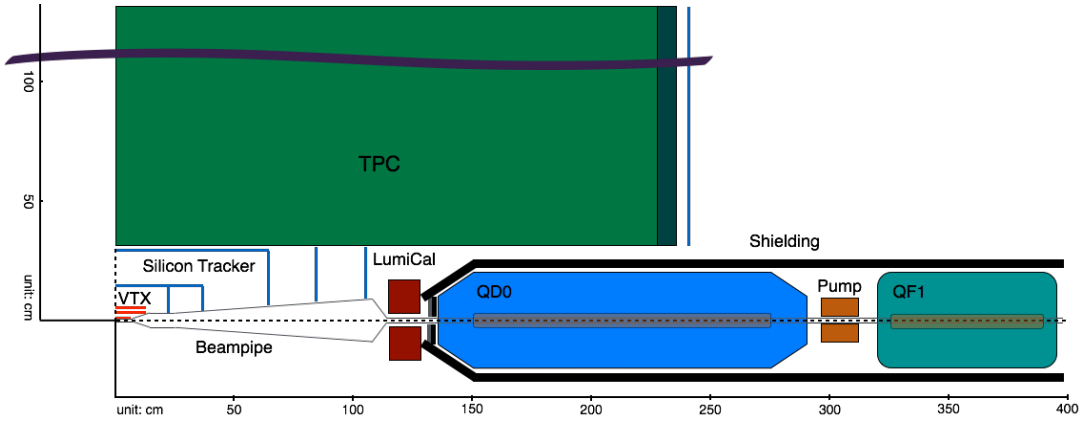

Figure 6.61 Preliminary layout of the interaction region for the CEPC project.

6.8.1.1 Final Focusing Magnets

The two final focusing quadrupoles, QD0 and QF1, end up inside the CEPC detector given the short focal length, and must operate in the background field of the detector solenoid. The preliminary conductor layout for the magnets is illustrated in Fig. 6.62, with the inner layer to provide the quadrupole focusing field and the outer layer to compensate for the detector solenoid field. Superconducting magnets are necessary to fulfil the strength requirements for the anti-solenoid ($\sim$6 T to compensate for the 3.5 T detector solenoid) and the quadrupole focusing magnet ($\sim$7 T). It is possible to build the magnets with NbTi [106], but Nb_3Sn [107] is probably more appropriate, as it has to take into account the efficiency loss and safe margins of operation. The design of cryogenics and mechanics is similar to the conceptual design for the TESLA final focusing magnets [108] but with

the diameters subject to the CEPC requirements. Detailed design of the two final focusing magnets can be found in Ref. [109].

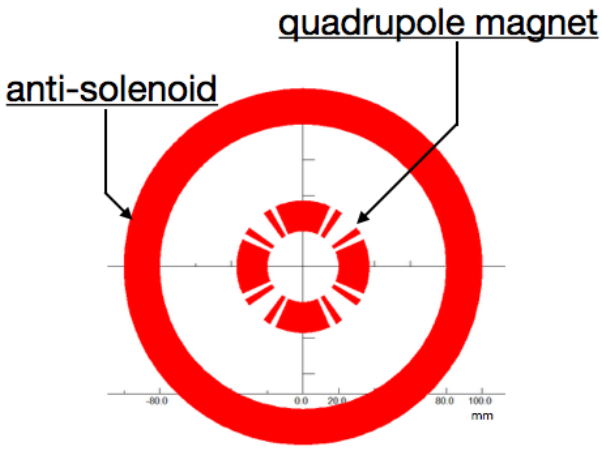

Figure 6.62 Preliminary conductor layout of the QD0.

6.8.1.2 Beampipe

The design of the beampipe foresees several constraints. In the central region, the radius should be small enough to optimise the measurement of the impact parameters but large enough not to interfere with the background. It will be made of beryllium to reduce photon conversions and hadronic interactions, but it has to be rigid enough (sufficient wall thickness) to withstand the vacuum pressure. In the forward region, it shall open conically away from the IP to allow enough space for the beam-induced background and can be built with stainless steel or other materials. The design of the beampipe will be based on detailed studies of the detector backgrounds, as well as the mechanical and thermal evaluations.

6.8.2 Detector Backgrounds

Backgrounds expected at the CEPC detector are among the most critical issues for the project. Different background sources can give rise to primary particles that can either enter the detector directly or generate secondary debris that ultimately reach the detector. It is desirable to achieve sufficient detector protection to prevent either excessive component occupancies or deterioration from radiation damage. The background sources and their impact on the detector components need to be evaluated thoroughly with Monte Carlo simulation, which will eventually provide guidance for detector and machine design optimisation. In the following, the main detector backgrounds from sources of synchrotron radiation, beam-gas interaction and beam-beam interactions are described.

6.8.2.1 Synchrotron Radiation

Synchrotron radiation (SR) photons are one of the most critical backgrounds for the CEPC detector. To prevent detector components being hit directly by the energetic SR photons, careful design of collimators and masks is needed, which is not yet implemented in the current straight-line section design. Preliminary simulation results, as shown in

Figs. 6.63(a) and 6.63(b), suggest that the main contribution arises from the bending of the last dipole magnets. Detailed studies with full detector simulation are envisaged to understand the impact on detector performance.

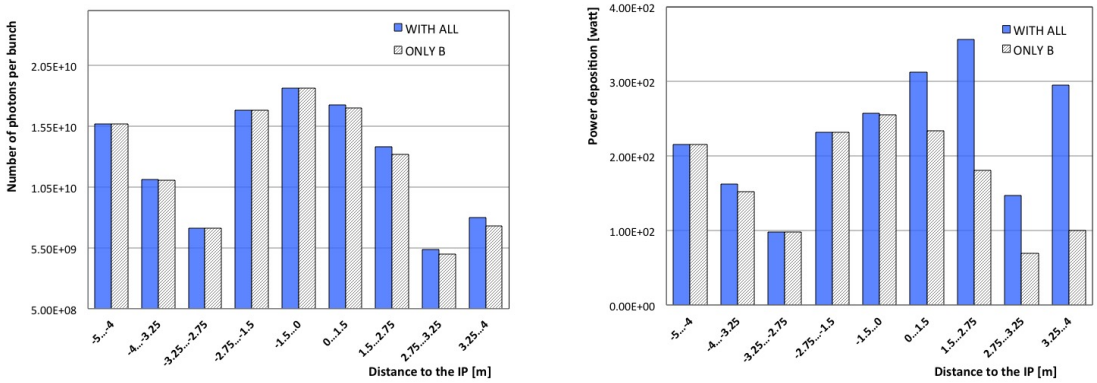

(a) Number of SR photons

(b) Power deposition

Figure 6.63 Number of synchrotron radiation photons and power deposition per bunch along the beam orbit. Grey hashed histograms represent the contributions induced by the bending of the last dipole before the IP, and blue histograms include contributions from all magnets along the ring.

6.8.2.2 Beam-Gas Interaction

Interactions between the electron/positron beam and the residual gas in the beam pipe, induced electromagnetic showers, production of secondary particles and their transport are simulated. The gas pressure is assumed to be 10^{-7} mbar, and the results obtained can be linearly rescaled for other pressures. The particles entering the interaction region are further interfaced to the full detector simulation, allowing for detailed evaluation of their impact on the detector backgrounds. Preliminary result suggests that detector background induced by beam-gas interaction is negligible. More detailed studies assuming different gas pressure levels are underway.

6.8.2.3 Beam-Beam Interactions

At the interaction point, two crossing bunches of opposite charge attract each other in the "pinch effect". The self-focusing effect during the process leads to higher luminosity for head-on collisions. However, the charged particles deflected by the strong forces will emit radiation called "beamstrahlung". The actual beam-beam effects can be estimated with Monte Carlo simulation, which will take into account dynamically changing bunch effects, reduced particle energies and their impact on the fields. For the CEPC beam-beam simulation, the program GUINEA-PIG [110] has been used and the input machine parameters are listed in Table 6.13. The backgrounds from beam-beam interactions, including beamstrahlung, electron-positron pair production, hadronic background and radiative B-habha events are described below.

Beamstrahlung

Due to the pinch effect in the beam-beam interaction, the trajectories of the particles in the bunches are bent, causing the emission of beamstrahlung. Beamstrahlung can have

Table 6.13 CEPC machine parameters input to GUINEA-PIG simulation.

Machine Parameters	Unit	Value
E_{cm}	GeV	240
Particles per bunch		3.7×10^{11}
Beam size σ_x/σ_y	μm	73.7/0.16
Beam size σ_z	μm	2260
Normalised Emittance $\varepsilon_x/\varepsilon_y$	mm·mrad	1595/4.8

potentially large impacts on the beam energy spread and the luminosity spectrum of the CEPC machine. However, as illustrated in Fig. 6.64, the beamstrahlung photons are dominantly produced with very low transverse momentum and small angle along the beam axis, hence they are almost negligible background for the CEPC detector.

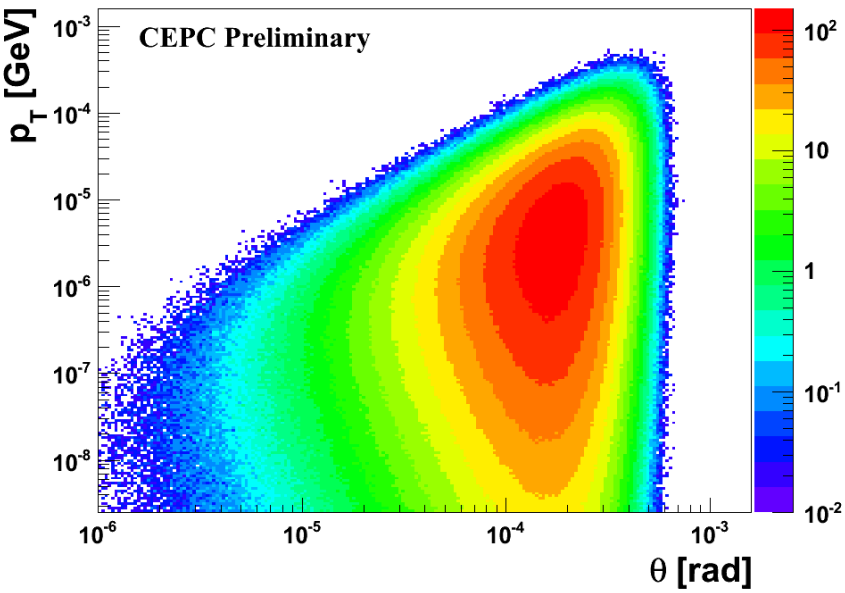

Figure 6.64 Transverse momentum distribution vs polar angle of beamstrahlung photons from the GUINEA-PIG simulation.

Electron-Positron Pair Production

Electron-positron pairs can be produced by both coherent and incoherent processes:

- Coherent Production: e^+e^- pairs are produced via the interaction of virtual or real photons (e.g. beamstrahlung photons) with the coherent field of the oncoming bunch. The particles can be highly energetic but are dominantly produced with small angle and confined in the beampipe.
- Incoherent Production: e^+e^- pairs can also be produced through interactions involving two real and/or virtual photons. Most of the particles are confined in the beampipe by the strong detector solenoid field. However, a small fraction of them are produced

with high transverse momentum and large polar angle. Incoherent pair production is considered one of the most important background sources for the CEPC detector.

Figure 6.65 shows the transverse momentum distribution versus polar angle of the incoherent e^+e^- pairs, after deflection through beam-beam interaction. It also shows the sharp kinematic edge (red band in the figure) developed by the pairs. Detector components, including the detector beampipe, must be placed away from the particles in that region. The hit density at the first vertex detector layer (r = 1.6 cm) amounts to $0.2/\mathrm{cm}^2/\mathrm{BX}$.

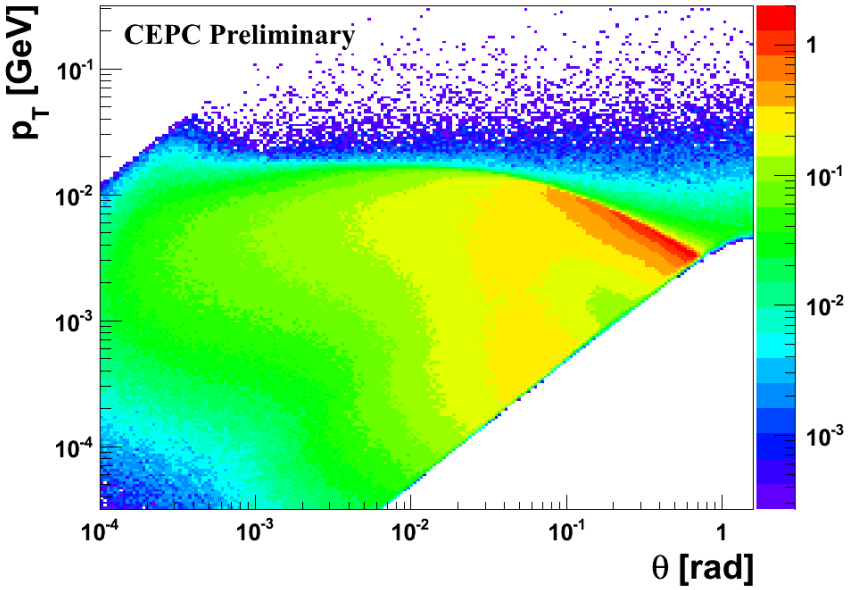

Figure 6.65 Transverse momentum distribution vs. polar angle for particles from incoherent e^+e^- pair production in bunch crossings.

Hadronic Background

The interaction of photons also produces quark pairs (e.g. the $\gamma\gamma \to q\bar{q}$ process), forming hadronic background events, but with a much smaller production rate than the dominant e^+e^- pair production. To evaluate the effects, energetic photons are generated with GUINEA-PIG with cross-section artificially inflated 10^5 times and passed to PYTHIA [111] for $\gamma\gamma \to q\bar{q}$ production followed by hadronisation. Preliminary studies show that most of the hadronic background events are of low energy and small polar angle, which makes them negligible background for the CEPC detector. Nevertheless, there can be a very small number of events forming jets with sufficiently large transverse momenta and polar angles (called "mini-jets"). These might affect the calorimeter performance and their impact will be evaluated with detailed detector simulation.

6.8.2.4 Radiative Bhabha Scattering

Radiative Bhabha scattering ($e^+e^- \to e^+e^-\gamma$) events are the dominant background for the Belle-II detector [112] at the SuperKEKB. They still represent the most important background for the CEPC detector. Radiative Bhabha scattering events with large angles are simulated with WHIZARD [113] and their contributions to the detector backgrounds are found to be negligible. On the other hand, radiative Bhabha events with small angles

are simulated with the dedicated BBBREM program [114]. Particle tracking with the outgoing electrons/positrons along the accelerator ring are performed with SAD [115]. Particles entering the IR and interacting with detector components, including the beampipe and final focusing magnets, are simulated with Geant4 [116]. Electrons/positrons emitting energetic photons (>2% of the beam energy as defined by the accelerator acceptance) can be kicked off their orbit and interact with accelerator and detector components. Preliminary results show that electrons/positrons re-entering the IR after the first turn contribute most significantly to the detector backgrounds. Figure 6.66(a) shows the average hit density at detector layers in the barrel region of the vertex detector and the silicon tracker. Additionally, Fig. 6.66(b) shows the average hit density along the z-direction at the first vertex detector layer ($r = 1.6$ cm), with the largest being ~ 7 hits/cm^2/BX at the ends of the layer.

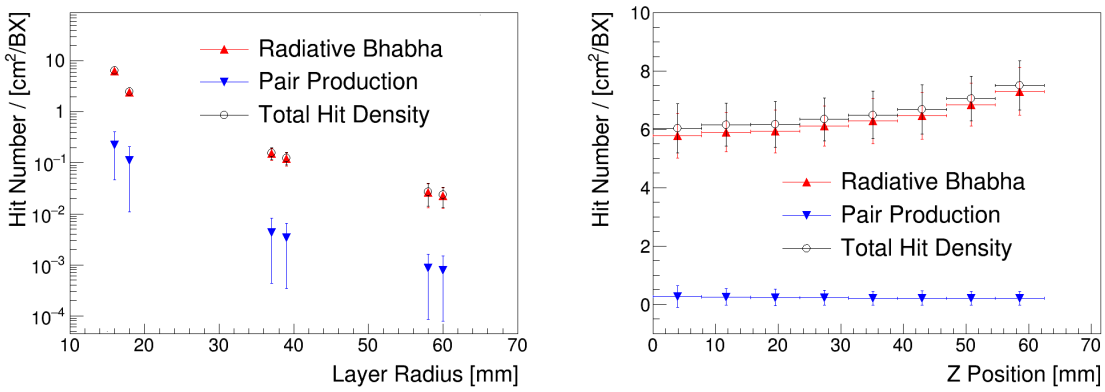

(a) (b)

Figure 6.66 Average hit density at detector layers (a) in the barrel regions and (b) along the z-direction at the first vertex detector layer.

6.8.2.5 Radiation Levels and Shielding

The radiation backgrounds can significantly degrade the detector performance, in particular the vertex detector, which is placed closest to the IP. Radiation damage induced in silicon detectors can be characterised as Total Ionisation Dose (TID) and Non-Ionising Energy Loss (NIEL), both of which need to be estimated reliably to guide the detector design. At the innermost vertex detector layer at $r = 1.6$ cm, the hit density, primarily induced by radiative Bhabha scattering events, can be up to $\sim 7/\mathrm{cm}^2/\mathrm{BX}$. The NIEL and TID distributions in the vertex detector are shown in Fig 6.67(a) and Fig 6.67(b), respectively. In particular, the corresponding annual NIEL and TID on the inner most layer are estimated to be 10^{12} $\mathrm{n}_{eq}/\mathrm{cm}^2$ and 300 kRad, respectively, with a safety factor of 5 taken into account. More detailed studies of all the detector background sources will be performed in future.

The detector shielding with the two final quadrupoles covered with tungsten masks, as illustrated in Fig. 6.61, demonstrates a basic way to prevent scattering particles entering the CEPC tracking detectors. A concrete design for the shielding shall be pursued to suppress the radiation backgrounds and eventually lower the radiation tolerance requirements on the silicon detectors.

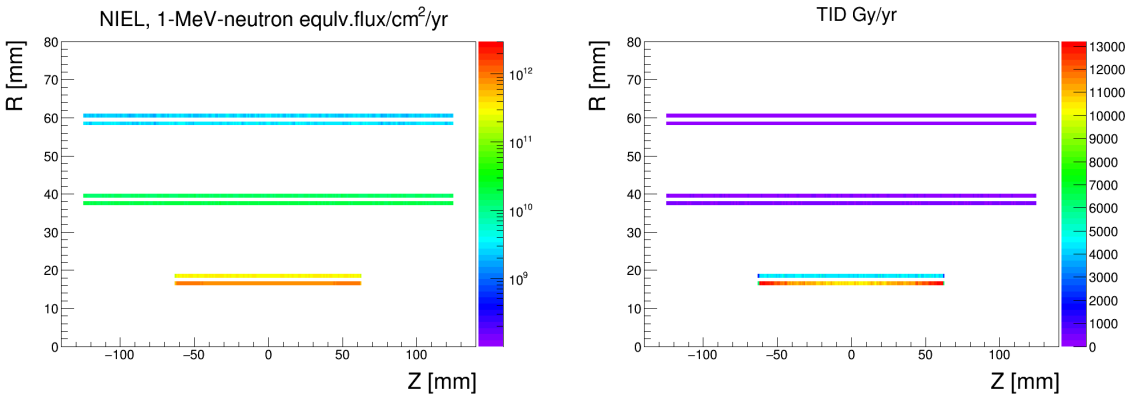

(a) (b)

Figure 6.67 NIEL (a) and TID (b) distributions in the vertex detector.

6.8.3 Luminosity Instrumentation

Precision measurements of the Higgs/Z physics program for the CEPC project requires a precision of 10^{-3} on the luminosity measurement. To meet such stringent requirements, a special cylindrical electromagnetic calorimeter with sensor-tungsten sandwich structure, called the "LumiCal", has been proposed to measure the luminosity by counting small angle radiative Bhabha scattering events. As shown in Fig. 6.61, it is positioned in the range of 115 – 128 cm away from the IP along the beam axis and covers the polar angle range between 60 – 90 mrad. It is essential to obtain sufficient polar angle resolution and at the same time keep the polar angle measurement bias as small as possible for fully contained electron showers.

Precise determination of the luminosity relies on full understanding of both the theoretical and experimental uncertainties. The theoretical uncertainty arises mainly from the unaccounted higher order corrections in the calculation of the small angle Bhabha process, which reached 5×10^{-4} for the LEP1 luminosity measurement in 2002 [117] and has been further improved after including the two-loop electroweak correction [118]. A precision of 5×10^{-4} can be conservatively assumed for the CEPC. The experimental uncertainty comes from different sources, including polar angle resolution ($\Delta\theta$), bias of polar angle, IP lateral position uncertainty, energy resolution, energy scale, beam polarisation, physics background subtraction and beamstrahlung. It is critical to control all the individual uncertainties to the level of 10^{-4}. Especially, since the Bhabha cross section is $\sigma \sim 1/\theta^3$, the luminosity precision related to the polar angle resolution can be expressed as

$$\frac{\Delta L}{L} = \frac{2\Delta\theta}{\theta_{\min}}$$

where $\theta_{\min} = 60$ mrad is the minimum polar angle of the fiducial region. The luminosity precision of 5×10^{-4} requires the polar angle to be measured with a precision of $\Delta\theta < 0.015$ mrad, which is a rigid constraint on the geometry/structure/material design. All the experimental uncertainties shall be evaluated carefully by Monte Carlo simulation with beam simulation included, followed by optimisation of all relevant design parameters.

Furthermore, the collider operation requires online monitoring of the luminosity in order to rapidly detect beam detuning at the IP and to provide fast feedback to re-tune the

beam delivery system. To serve this purpose, a dedicated beam monitor using radiation-hard sensor technologies (e.g. CVD diamond) has been suggested to determine the bunch-by-bunch luminosity by measuring radiative Bhabha events at zero photon scattering angle [119]. It will be placed downstream of the IP, at locations with event rates consistent with the aimed precision for online monitoring and small enough contamination by backgrounds from single-beam particle losses.

6.8.4 Mechanical Integration

Both QD0 and QF1 are located inside the detector, which drastically complicates the support and alignment of the detector and collider components in the interaction region. The two final focus magnets and the LumiCal will possibly be mounted on a dedicated support structure, extended from a pillar outside the detector and suspended from the solenoid cryostat. The beampipe and the silicon detectors will possibly be supported from a structure of carbon fibre reinforced plastic, which can hang at the flanges of the TPC field cage. It will require significant effort to realise a solid mechanical design and to define a reasonable procedure for detector assembly.

6.9 Detector Facilities at the Experiment Area

6.9.1 General Considerations

The requirements of the detector facility at the experimental area [120] are strongly dependent on the assembly procedure of the detector, which is mainly constrained by the construction and installation of the magnet, together with the necessity of providing adequate and safe working conditions during the fabrication, assembly and installation periods.

The total weight of the yoke will be around 10 kilotons. Carrying out the yoke assembly work in the underground cavern would require a large cavern with two cranes, one at each end of the cavern. To reduce the height of the cavern, large pieces should not be transferred over the detector. The superconducting solenoid components are fully assembled and tested on the surface and brought down into the experimental cavern with a minimum of further assembly work. The solenoid is then integrated with the yoke ring. This scheme will reduce the size and weight of the biggest and heaviest part to be lowered into the underground experiment hall.

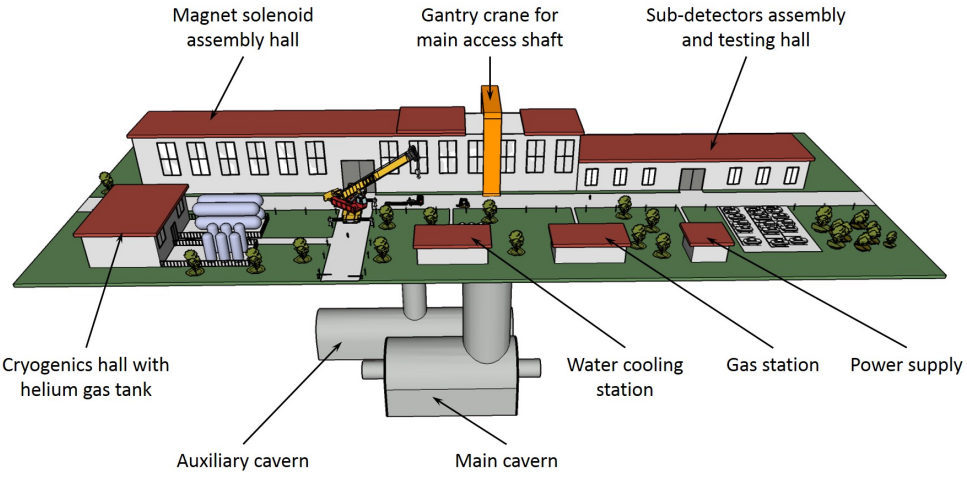

Figure 6.68 The CEPC detector experiment area.

However, several sub-detectors, such as the barrel and end-cap muon chambers, will be installed in the yoke in the underground cavern. Other sub-detector construction work can proceed in series on the surface as much as possible, while other sub-detectors can be assembled in the underground cavern. Moreover, assembling and testing some of detectors on the surface provides the additional advantages of convenience and the ability to rehearse risky operations. The experiment area, both surface buildings and underground caverns, is shown schematically in Fig. 6.68

6.9.2 Underground Caverns and Access

The criteria for the basic design for the integration of the CEPC detector underground caverns, where the beam level is situated at a depth of 100 m, are listed as following:

- A main cavern providing space for the withdrawal of the detector sections;
- One main access shaft, permitting successive installation of the large detector pieces from above ground;

- An auxiliary cavern with its access shaft, placed parallel to the main cavern, housing the counting room and the technical services, which should be accessible for maintenance work during data taking;
- The distance between the two caverns should allow the shortest possible routing of the cables while maintaining radiation safety;
- The auxiliary cavern should be integrated with the machine by-pass tunnel, if it is decided to have a by-pass tunnel in the interaction point area;
- One personnel access shaft serving both caverns;
- Survey galleries interconnecting the main cavern with the machine tunnel, located at beam height.

The main cavern is 30 m in width and height, 50 m long, and is equipped with two cranes, 60 and 300 tons, with an effective hook-span of 20 m. The main access shaft, 15 m in diameter, equipped with a 300 ton gantry crane, provides an opening for the installation of the magnet and the detector units. A second access shaft, 9 m in diameter, provides access for auxiliary cavern equipment installation. Several labyrinth tunnels are needed to run cables and services between the two caverns.

For the long term running stability of the detector, the ambient air in the main cavern must be kept at a low level of humidity. A system of air injection into the cavern which allows a high degree of temperature stability will also be designed. The auxiliary cavern has an overall diameter of 18 m and a total length of 80 m, which will be divided into three sections: counting room, gas distribution system and general detector services. A 9 m diameter auxiliary shaft will give access to the floors of all the sections. Both auxiliary shaft and auxiliary cavern are equipped with a lift which can carry several tons, which will ease the installation of all counting room equipment and provide direct installation access to the main cavern floor level. The counting room will house 200 to 300 electronics racks. The auxiliary cavern will also house the power supply and cryogenics system for the magnet, the quench protection system, and the cooling and ventilation distribution systems.

The design of the experimental area also includes facilities to provide for safe and efficient working conditions during the installation and maintenance periods. Access tunnels should connect the main cavern and auxiliary cavern with the bottom of the personnel shaft at different levels.

6.9.3 Surface Building and Facilities

6.9.3.1 Building Dimensions

The surface building requirements of the CEPC detector are dominated by the need to carry out a complete assembly and test of the magnet solenoid on the surface, which requires 18 m height under the crane hook. The construction of the magnet sub-assemblies requires a 150 m long, 20 m wide assembly hall, which will be linked by a double rail to the main access shaft for installation underground after testing. This hall will be equipped with two 80-ton overhead cranes. The sub-detector assembly hall is 80 m long, 20 m wide, and 10 m in lifting height, equipped with a 60-ton overhead crane. The main assembly work and some testing procedures for the DHCAL, ECAL, muon detector, TPC, Vertex

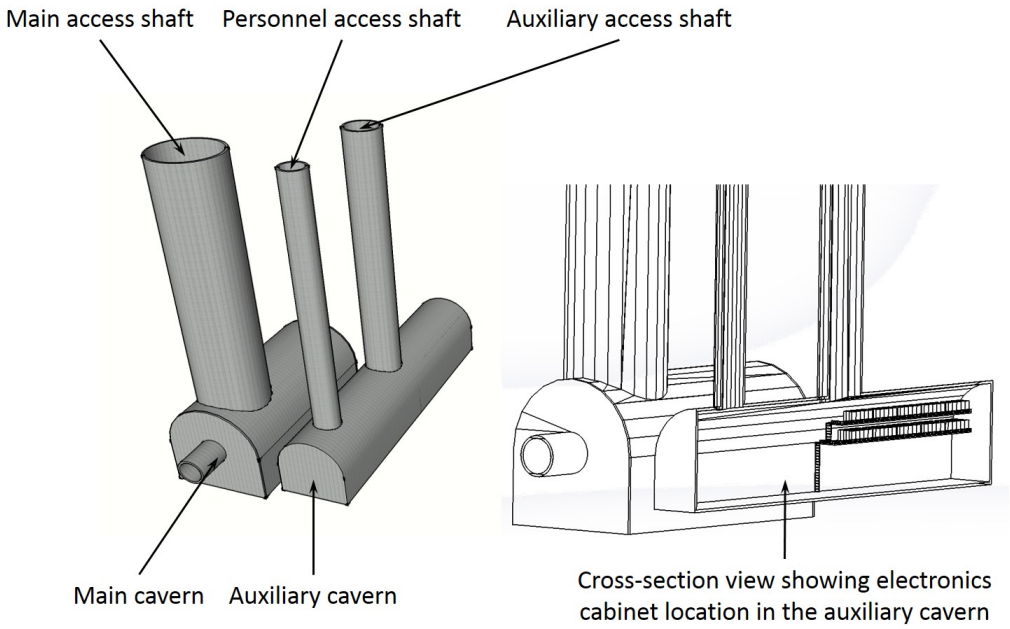

Figure 6.69 The CEPC detector underground cavern. Left: relative positions of main cavern, auxiliary cavern, main access shaft, personnel access shaft and auxiliary access shaft. Right: cross-section view showing electronics cabinet location in the auxiliary cavern.

and Si-tracker will be done in this hall. There is an area of overlap between the magnet assembly hall and sub-detector assembly hall, which can be accessed by cranes from both halls.

6.9.3.2 Cryogenics Infrastructure

The detector magnet is cooled by the thermal siphoning principle. Liquid helium is taken from a phase separator placed on top of the detector to the bottom of the solenoid, from where it is distributed over heat exchangers placed in contact with the cold mass. The thermal load creates helium gas in the heat exchangers and the hydrostatic pressure difference creates a driving force circulating the helium through the heat exchangers back to the phase separator. A 750 W at 4.5 K equivalent helium refrigerator then re-liquefies the gas and sends it to a intermediate storage dewar, which provides a buffer volume guaranteeing several hours' cooling period. This is sufficient for the slow ramp down of the magnet, even in the case of helium refrigerator failure. The cryogenics system installation should be designed to cool down the solenoid for the surface tests and, once the magnet has been lowered and reconnected, to provide cooling for cold tests in the underground experiment area.

6.9.3.3 Other Surface Facilities

During the construction phase of the magnet and during the assembly phase of the sub-detectors, a temporary surface basis is required for the storage, pre-assembly, and testing of the sub-detectors. Additional clean areas are required for the calorimeters, TPC and muon detector, and very clean areas are required for the Vertex and Si-tracker. Buildings for power supply, gas station and water cooling station are located round the auxiliary ac-

cess shaft. Some of the surface buildings should be equipped with heating and ventilation systems.

6.9.4 Safety Features

The design of the experimental area will incorporate several specific safety aspects, such as:

- Fixed gangways and staircases for easy access at all levels in the underground caverns;
- Emergency escape routes at each end of the main cavern;
- Smoke extraction, in case of fire;
- Fixed and mobile radiation shielding;
- A mobile shielding platform, providing protection beneath the main access shaft.

References

[1] T. Abe et al., *The International Large Detector: Letter of Intent*, arXiv:1006.3396 [hep-ex].

[2] T. Behnke et al., *The International Linear Collider Technical Design Report - Volume 4: Detectors*, arXiv:1306.6329 [physics.ins-det].

[3] T. Behnke et al., *The International Linear Collider Technical Design Report - Volume 1: Executive Summary*, arXiv:1306.6327 [physics.acc-ph].

[4] M. A. Thomson, *Particle Flow Calorimetry and PandoraPFA algorithm*, Nucl.Instrum.Meth. **A611** (2009) 25–40.

[5] M. Ruan and H. Videau, *Arbor, a new approach of the Particle Flow Algorithm*, AIDA-CONF-2014-002, CERN, Geneva, Apr, 2013.

[6] The CMS Collaboration, *Particle-Flow Event Reconstruction in CMS and Performance for Jets, Taus, and MET*, CMS-PAS-PFT-09-001, CERN, 2009. Geneva, Apr, 2009. http://cds.cern.ch/record/1194487.

[7] The CMS Collaboration, F. Beaudette, *The CMS Particle Flow Algorithm*, arXiv:1401.8155 [hep-ex].

[8] P. Mora de Freitas and H. Videau, *Detector simulation with MOKKA/GEANT4: Present and future*, LC-TOOL-2003-010 (2002) 623–627.

[9] D. Dannheim and M. Vos, *Simulation studies for the layout of the vertex and tracking regions of the CLIC detectors*, LCD-Note-2011-031 (2012) .

[10] M. Regler et al., *The LiC Detector Toy program*, J.Phys.Conf.Ser. **119** (2008) 032034.

[11] P. Chochula et al., *The DELPHI Silicon Tracker at LEP-2*, Nucl.Instrum.Meth. **A412** (1998) 304–328.

[12] F. Hartmann, *Evolution of Silicon Sensor Technology in Particle Physics*, Springer Tracts Mod.Phys. **231** (2009) 1–204.

[13] M. Battaglia et al., *R&D Paths of Pixel Detectors for Vertex Tracking and Radiation Imaging*, Nucl.Instrum.Meth. **A716** (2013) 29–45, arXiv:1208.0251 [physics.ins-det].

[14] L. Linssen, A. Miyamoto, M. Stanitzki, and H. Weerts, *Physics and Detectors at CLIC: CLIC Conceptual Design Report*, arXiv:1202.5940 [physics.ins-det].

[15] L. Greiner et al., *A MAPS based pixel vertex detector for the STAR experiment*, PoS **Vertex2012** (2013) 010.

[16] C. Marinas, *The Belle-II pixel vertex tracker at the SuperKEKB flavour factory*, Nucl. Instrum. Meth. **A628** (2011) 95–98.

[17] The ALICE Collaboration, B. Abelev et al., *Technical Design Report for the Upgrade of the ALICE Inner Tracking System*, J.Phys. **G41** (2014) 087002.

[18] O. Alonso et al., *DEPFET active pixel detectors for a future linear e^+e^- collider*, arXiv:1212.2160 [physics.ins-det].

[19] M. Vos et al., *DEPFET active pixel detectors*, PoS **VERTEX2009** (2009) 015.

[20] R. Turchetta et al., *A monolithic active pixel sensor for charged particle tracking and imaging using standard VLSI CMOS technology*, Nucl.Instrum.Meth. **A458** (2001) 677–689.

[21] I. Valin et al., *A reticle size CMOS pixel sensor dedicated to the STAR HFT*, JINST **7** (2012) C01102.

[22] Y. Onuki et al., *SOI detector developments*, PoS **VERTEX2011** (2011) 043.

[23] C. Lacasta, *THE PIXEL DETECTOR FOR BELLE-II AT SUPERKEKB*, 22nd International Workshop on Vertex Detectors (Vertex 2013) (2013) .

[24] S. Nakashima et al., *Development and characterization of the latest X-ray SOI pixel sensor for a future astronomical mission*, Nucl.Instrum.Meth. **A731** (2013) 74–78.

[25] T. Hatsui et al., *A direct-detection X-ray CMOS image sensor with 500 μm thick high resistivity silicon*, 2013 International Image Sensor Workshop (2013) .

[26] Y. Ono et al., *Development of the Pixel OR SOI detector for high energy physics experiments*, Nucl.Instrum.Meth. **A731** (2013) 266–269.

[27] C. Baltay et al., *Chronopixel Vertex Detectors for Future Linear Colliders*, arXiv:1109.2811 [physics.ins-det].

[28] D. Dannheim, *Vertex-Detector R&D for CLIC*, JINST **9** (2014) C03026, arXiv:1312.5774 [physics.ins-det].

[29] I. Peric, *Active pixel sensors in high-voltage CMOS technologies for ATLAS*, JINST **7** (2012) C08002.

[30] K. Shinsho et al., *Evaluation of monolithic Silicon-on-Insulator pixel devices thinned to 100 μm*, IEEE Nucl.Sci.Symp.Conf.Rec. (2010) 646–649.

[31] J. Augustin et al., *A silicon envelope for the TPC*, LC-DET-2003-013 (2003) .

[32] R. Mori et al., *Charge collection measurements on slim-edge microstrip detectors*, JINST **7** (2012) P05002.

[33] I. Peric et al., *Strip Technology and HVMAPS*, PoS **Vertex2012** (2013) 021.

[34] J. Brau et al., *KPiX - A 1,024 Channel Readout ASIC for the ILC*, IEEE Nucl.Sci.Symp.Conf.Rec. (2013) 1857–1860.

[35] T. Pham et al., *A 130-nm CMOS mixed mode front end readout chip for silicon strip tracking at the future linear collider*, Nucl.Instrum.Meth. **A623** (2010) 498–500.

[36] H.-G. Moser, *3D Interconnection with TSV*, PoS **Vertex2012** (2013) 024.

[37] A. Affolder et al., *DC-DC converters with reduced mass for trackers at the HL-LHC*, JINST **6** (2011) C11035.

[38] S. Diez, *System Implications of the Different Powering Distributions for the ATLAS Upgrade Strips Tracker*, Phys.Procedia **37** (2012) 960–969.

[39] K. Klein et al., *DC-DC conversion powering schemes for the CMS tracker at Super-LHC*, JINST **5** (2010) C07009.

[40] A. Nomerotski et al., *Evaporative CO2 cooling using microchannels etched in silicon for the future LHCb vertex detector*, JINST **8** (2013) P04004, arXiv:1211.1176 [physics.ins-det].

[41] The ATLAS Collaboration, A. Affolder, *Silicon Strip Detectors for the ATLAS HL-LHC Upgrade*, Phys.Procedia **37** (2012) 915–922.

[42] V. Blobel, *Software alignment for tracking detectors*, Nucl.Instrum.Meth. **A566** (2006) 5–13.

[43] A. Savoy-Navarro, *Large Area Silicon Tracking: New Perspectives*, arXiv:1203.0736 [physics.ins-det].

[44] W. Atwood et al., *Performance of the ALEPH time projection chamber*, Nucl.Instrum.Meth. **A306** (1991) 446–458.

[45] M. Ball et al., *Technical Design Study for the PANDA Time Projection Chamber*, arXiv:1207.0013 [physics.ins-det].

[46] M. Anderson et al., *The Star time projection chamber: A Unique tool for studying high multiplicity events at RHIC*, Nucl.Instrum.Meth. **A499** (2003) 659–678, arXiv:nucl-ex/0301015 [nucl-ex].

[47] N. Abgrall et al., *Time Projection Chambers for the T2K Near Detectors*, Nucl.Instrum.Meth. **A637** (2011) 25–46, arXiv:1012.0865 [physics.ins-det].

[48] E. Radicioni, *Characterization, calibration and performances of the TPC of the HARP experiment at the CERN PS*, IEEE Trans.Nucl.Sci. **52** (2005) 2986–2991.

[49] J. Alme et al., *The ALICE TPC, a large 3-dimensional tracking device with fast readout for ultra-high multiplicity events*, Nucl.Instrum.Meth. **A622** (2010) 316–367, arXiv:1001.1950 [physics.ins-det].

[50] LCTPC Collaboration, P. Schade and J. Kaminski, *A large TPC prototype for a linear collider detector*, Nucl.Instrum.Meth. **A628** (2011) 128–132.

[51] I. Giomataris et al., *Micromegas in a bulk*, Nucl.Instrum.Meth. **A560** (2006) 405–408.

[52] H. Raether, *Electron avalanches and breakdown in gases*. Butterworths, London, 1964. https://cds.cern.ch/record/102989.

[53] R. Chechik, A. Breskin, C. Shalem, and D. Mormann, *Thick GEM-like hole multipliers: Properties and possible applications*, Nucl.Instrum.Meth. **A535** (2004) 303–308, arXiv:physics/0404119 [physics].

[54] R. Esteve Bosch et al., *The ALTRO chip: A 16-channel A/D converter and digital processor for gas detectors*, IEEE Trans.Nucl.Sci. **50** (2003) 2460–2469.

[55] P. Baron et al., *AFTER, an ASIC for the readout of the large T2K time projection chambers*, IEEE Trans.Nucl.Sci. **55** (2008) 1744–1752.

[56] E. J. GARCÍA, *Novel Front-end Electronics for Time Projection Chamber Detectors*, PhD dissertation .

[57] X. Llopart et al., *Timepix, a 65k programmable pixel readout chip for arrival time, energy and/or photon counting measurements*, Nucl.Instrum.Meth. **A581** (2007) no. 1-2, 485 – 494.

[58] A. Strandlie and R. Fruhwirth, *Track and vertex reconstruction: From classical to adaptive methods*, Rev.Mod.Phys. **82** (2010) 1419–1458.

[59] ALEPH Collaboration, W. Wiedenmann, *Alignment of the ALEPH tracking devices*, Nucl.Instrum.Meth. **A323** (1992) 213–219.

[60] The LCTPC Collaboration, *Report to the DESY PRC 2010*, LC-DET-2012-067 (2010) .

[61] M. Ball et al., *Technical Design Study for the PANDA Time Projection Chamber*, arXiv:1207.0013 [physics.ins-det].

[62] I. Crotty et al., *High-rate, high-position resolution microgap RPCs for X-ray imaging applications*, Nucl.Instrum.Meth. **A505** (2003) 203–206.

[63] D. Mormann et al., *Operation principles and properties of the multi-GEM gaseous photomultiplier with reflective photocathode*, Nucl.Instrum.Meth. **A530** (2004) 258–274.

[64] K. Matsumoto et al., *Ion-Feedback Suppression for Gaseous Photomultipliers with Micro Pattern Gas Detectors*, Phys.Procedia **37** (2012) 499–505.

[65] A. Lyashenko et al., *Further progress in ion back-flow reduction with patterned gaseous hole-multipliers*, JINST **2** (2007) P08004, arXiv:0706.3606 [physics.ins-det].

[66] D. Cowen et al., *Gating in the ALEPH Time Projection Chamber*, Nucl.Instrum.Meth. **A252** (1986) 403–406.

[67] A. Bondar et al., *Study of ion feedback in multi GEM structures*, Nucl.Instrum.Meth. **A496** (2003) 325–332, arXiv:physics/0208017 [physics].

[68] M. Alexeev et al., *Ion backflow in thick GEM-based detectors of single photons*, JINST **8** (2013) P01021.

[69] E. W. McDaniel and E. A. Mason, *Mobility and diffusion of ions in gases*. Wiley series in plasma physics. Wiley, New York, NY, 1973.

[70] F. Sauli, *Principles of operation of multiwire proportional and drift chambers*, p. 92 p, CERN. CERN, Geneva, 1977. http://cds.cern.ch/record/117989. CERN, Geneva, 1975 - 1976.

[71] T. Matsuda, *Results of the first beam test of a GEM TPC large prototype*, JINST **5** (2010) P01010.

[72] R. Veenhof, *GARFIELD, recent developments*, Nucl.Instrum.Meth. **A419** (1998) 726–730.

[73] CSC-IT Center for Science, *Elmer Models Manual*, . www.nic.funet.fi/index/elmer/doc/ElmerModelsManual.pdf.

[74] B. Li, K. Fujii, and Y. Gao, *Kalman-filter-based track fitting in non-uniform magnetic field with segment-wise helical track model*, Comput.Phys.Commun. **185** (2014) 754–761, arXiv:1305.7300 [physics.ins-det].

[75] The ALICE Collaboration, P. Antonioli, A. Kluge, and W. Riegler, *Upgrade of the ALICE Readout & Trigger System*, . http://cds.cern.ch/record/1603472.

[76] J. Brient, *Improving the jet reconstruction with the particle flow method: An introduction*, in the Proceedings of 11th International Conference on Calorimetry in High-Energy Physics (Calor 2004) (2004) 445–451.

[77] CALICE Collaboration. twiki.cern.ch/twiki/bin/view/CALICE/CaliceCollaboration.

[78] The CMS Collaboration, B. Bilki, *CMS Forward Calorimeters Phase II Upgrade*, J.Phys.Conf.Ser. **587** (2015) no. 1, 012014.

[79] CALICE Collaboration, *First Stage Analysis of the Energy Response and Resolution of the Scintillator ECAL in the Beam Test at FNAL*, CAN-016 (2008) .

[80] S. Mannai, *Energy Reconstruction in GRPC Semi-Digital HCAL*, CALICE Collaboration Meeting (2009) .

[81] F. Dulucq et al., *HARDROC: Readout chip for CALICE/EUDET Digital Hadronic Calorimeter*, IEEE Nucl.Sci.Symp.Conf.Rec. (2010) 1678–1683.

[82] M. Bedjidian et al., *Performance of Glass Resistive Plate Chambers for a high granularity semi-digital calorimeter*, JINST **6** (2011) P02001, arXiv:1011.5969 [physics.ins-det].

[83] CALICE Collaboration, *First results of the CALICE SDHCAL technological prototype*, CAN-037 (2012) .

[84] G. Drake et al., *Resistive Plate Chambers for hadron calorimetry: Tests with analog readout*, Nucl.Instrum.Meth. **A578** (2007) 88–97.

[85] B. Bilki et al., *Environmental Dependence of the Performance of Resistive Plate Chambers*, JINST **5** (2010) P02007, arXiv:0911.1351 [physics.ins-det].

[86] B. Bilki et al., *Measurement of the Rate Capability of Resistive Plate Chambers*, JINST **4** (2009) P06003, arXiv:0901.4371 [physics.ins-det].

[87] B. Bilki et al., *Measurement of Positron Showers with a Digital Hadron Calorimeter*, JINST **4** (2009) P04006, arXiv:0902.1699 [physics.ins-det].

[88] B. Bilki et al., *Hadron Showers in a Digital Hadron Calorimeter*, JINST **4** (2009) P10008, arXiv:0908.4236 [physics.ins-det].

[89] B. Bilki et al., *Calibration of a digital hadron calorimeter with muons*, JINST **3** (2008) P05001, arXiv:0802.3398 [physics.ins-det].

[90] CALICE Collaboration, *Construction and performance of a silicon photomultiplier/extruded scintillator tail-catcher and muon-tracker*, JINST **7** (2012) P04015, arXiv:1201.1653 [physics.ins-det].

[91] BaBar Collaboration, B. Aubert et al., *The BaBar detector*, Nucl.Instrum.Meth. **A479** (2002) 1–116, arXiv:hep-ex/0105044 [hep-ex].

[92] A. Abashian et al., *The Belle Detector*, Nucl.Instrum.Meth. **A479** (2002) 117–232.

[93] The CMS Collaboration, *CMS, the Compact Muon Solenoid. Muon technical design report*, CERN-LHCC-97-32 (1997) . http://cds.cern.ch/record/343814.

[94] The ATLAS Collaboration, *ATLAS muon spectrometer: Technical design report*, CERN-LHCC-97-22, ATLAS-TDR-10 (1997) . http://cds.cern.ch/record/331068.

[95] Y. Xie et al., *First results of the RPC commissioning at BESIII*, Nucl.Instrum.Meth. **A599** (2009) 20–27.

[96] J.-L. Xu et al., *Design and preliminary test results of Daya Bay RPC modules*, Chi.Phys. **C35** (2011) 844–850.

[97] Y. Xie et al., *Performance Study of RPC Prototypes for the BESIII Muon Detector*, Chi.Phys. **C31** (2007) 70–75.

[98] C. Gustavino et al., *Performance of glass RPC operated in avalanche mode*, Nucl.Instrum.Meth. **A527** (2004) 471–477.

[99] Y. Hoshi et al., *Freonless gas mixtures for glass RPC operated in streamer mode*, Nucl.Instrum.Meth. **A508** (2003) 56–62.

[100] F. Kircher, *CMS coil design and assembly*, IEEE Trans. Appl. Superconductivity **Vol. 12** (2002) no. 1, 462–464.

[101] F. Kircher et al., *Conceptual Design of the ILD Detector Magnet System*, LC-DET-2012-081 .

[102] B. Blau et al., *The CMS Conductor*, IEEE Trans. Appl. Superconductivity **Vol. 12** (2002) no. 1, 345–348.

[103] B. Wang et al., *Development and Fabrication for BESIII Superconducting Muon Detector Solenoid*, IEEE Trans. Appl. Superconductivity **Vol. 15** (2005) no. 2, 1263–1266.

[104] P. Fabbricatore et al., *The Manufacture of Modules for CMS Coil*, IEEE Trans. Appl. Superconductivity **Vol. 16** (2006) no. 2, 512–516.

[105] J. Yan et al., *Magnetic field mapping in the BESIII solenoid*, IEEE Trans. Appl. Superconductivity **Vol. 20** (2010) no. 3, 324–327.

[106] O. S. Bruning et al., *LHC Design Report. 1. The LHC Main Ring*, CERN-2004-003 (2004) . http://cds.cern.ch/record/782076.

[107] A. Lietzke et al., *Test results for HD1, a Nb3Sn dipole magnet*, IEEE Trans. Appl. Superconduct. **14** (2004) no. 2, 345 – 348.

[108] A. Devred et al., *Conceptual design for the final focus quadrupole magnets for TESLA*, DAPNIA-STCM-01-03, DESY-TESLA-2001-17 (2001) .

[109] The CEPC-SPPC Study Group, *CEPC-SPPC Preliminary Conceptual Design Report, Volume II - Accelerator*, IHEP-CEPC-DR-2015-01, IHEP-AC-2015-01 (2015) .

[110] D. Schulte, *Beam-beam simulation with GUINEA-PIG*, In 5th International Computational Accelerator Physics Conference (1998) . CLIC-NOTE 387.

[111] T. Sjostrand, S. Mrenna, and P. Z. Skands, *PYTHIA 6.4 Physics and Manual*, JHEP **0605** (2006) 026, arXiv:hep-ph/0603175.

[112] M. Iwasaki et al., *Beam Background and MDI Design for SuperKEKB/Belle-II*, Conf.Proc. **C1205201** (2012) 1825–1827.

[113] W. Kilian, T. Ohl, and J. Reuter, *WHIZARD: Simulating Multi-Particle Processes at LHC and ILC*, Eur.Phys.J. **C71** (2011) 1742, arXiv:0708.4233 [hep-ph].

[114] R. Kleiss and H. Burkhardt, *BBBREM – Monte Carlo simulation of radiative Bhabha scattering in the very forward direction*, Comput.Phys.Commun. **81** (1994) no. 3, 372 – 380.

[115] SAD Home Page. http://acc-physics.kek.jp/SAD/.

[116] S. Agostinelli et al., *GEANT4: A simulation toolkit*, Nucl. Instrum. Meth. **A506** (2003) 250–303.

[117] S. Jadach, *Theoretical error of luminosity cross-section at LEP*, arXiv:hep-ph/0306083 [hep-ph].

[118] P. Khiem et al., *Full electroweak radiative corrections to at the ILC with GRACE-Loop*, Phys.Lett. **B740** (2015) 192–198.

[119] D. El Khechen et al., *Fast Luminosity Monitoring using Diamond Sensors for the Super Flavor Factory SuperKEKB*, IPAC-2014-THPME090 (2014) .

[120] L. Evans, *The Large Hadron Collider: A marvel technology*. 2009. ISBN-9781439804018.

CHAPTER 7

NEW PHYSICS SEARCHES AT SPPC

7.1 Supersymmetry

Introduction: SUSY at 100 TeV

The SppC, due to its large center-of-mass energy, clearly has the capability to discover new physics at a higher mass scale than the Large Hadron Collider. In the case of supersymmetry, there are compelling reasons to expect that even if the LHC makes the initial discoveries, the SppC would play a decisive role in understanding the physical implications of the LHC's results. In particular, the question of understanding the Higgs boson mass and couplings is likely to require the extra energy available at SppC. The reason is the well known fact that the tree-level Higgs boson mass in the MSSM is bounded above by the Z boson mass. In more detail, [1–6]

$$m_h^2 \approx m_Z^2 \cos^2(2\beta) + \frac{3m_t^4}{4\pi^2 v^2}\left(\log\frac{m_{\tilde{t};\mathrm{ave}}^2}{m_t^2} + \frac{X_t^2}{m_{\tilde{t};\mathrm{ave}}^2}\left(1 - \frac{X_t^2}{12m_{\tilde{t};\mathrm{ave}}^2}\right)\right). \tag{7.1}$$

The second term in the above equation results from loop corrections to the quartic coupling in the MSSM. The first term in parentheses is logarithmically sensitive to the average mass of the stops. The remaining terms are threshold corrections depending on the left-right stop mass mixing parameter X_t. In the context of supersymmetry, then, the rather large mass $m_h \approx 125\ \mathrm{GeV} > m_Z$ has one of the following three implications:

- If stops are unmixed, they must be quite heavy, with masses of several TeV. In this case, the approximation in Eq. 7.1 breaks down and it is necessary to resum logarithmic terms via renormalization group evolution of the Higgs quartic coupling in the effective theory below the stop mass scale.

- On the other hand, the stop mass scale can be lower—near one TeV—provided that the mixing parameter is large. The minimal MSSM tuning arises for values of X_t slightly below "maximal mixing," $X_t \lesssim \sqrt{6} m_{\tilde{t};\mathrm{ave}}$ [7].
- Finally, the above formula could be invalidated by the presence of other Higgs boson interactions beyond those included in the MSSM [8, 9].

The detailed computation of the stop mass scale needed to explain the Higgs boson mass depends on the precise scenario; for example, the RG equations are different in Split Supersymmetry [10–17] (where the gauginos are significantly lighter than the scalars) than in High-Scale Supersymmetry [18–21] (where the gaugino and scalar mass scales coincide). In any case it is clear that explaining the 125 GeV Higgs boson mass with unmixed stops requires them to be quite out of reach of the LHC—but, at least for large values of $\tan\beta$, within the range of the SppC.

The case of large mixing parameter X_t has received a great deal of attention as one of the most natural corners of MSSM parameter space [7, 22–26]. Because mixing tends to split mass eigenstates, it is common in this scenario for one stop to be light (well below a TeV) while the other is heavy. LHC measurements of the lighter stop eigenstate could potentially shed some light on the physics, but the SppC will likely be needed to produce the heavier stop eigenstate in abundance and pin down the mechanism of Higgs mass lifting. The measurement of transitions like $\tilde{t}_2 \to Z\tilde{t}_1, h\tilde{t}_1$ can provide estimates of the parameters appearing in Eq. 7.1. While the stops and their couplings to the Higgs boson are generically interesting targets for SppC, model-dependent physics that explains the requisite large values of X_t may also involve interesting strong dynamics, potentially at accessible energies [27, 28].

The final possibility is that supersymmetry exists but is nonminimal. In theories extending the MSSM, new interactions of the Higgs boson can lift its mass above the Z mass more efficiently than do loops of stops. The new contributions could arise at one-loop order, similar to the stop loop, from contributions of new vectorlike fermions [29–31]. In this case, the particles may be discovered at the LHC, although precision tests of their interactions with the Higgs could rely on the CEPC or SppC. However, the most efficient way to increase the Higgs boson mass is through new *tree-level* interactions beyond the MSSM [8]. Models of this type typically fall into two classes: those with new D-term contributions and those with new F-term contributions.

Theories where the Higgs boson mass is lifted by D-terms predict new gauge bosons that can be discovered at the scale of several TeV [32–36]. The underlying assumption is that the Higgs boson is charged under a new gauge group. If a $\mathrm{U}(1)_x$ gauge symmetry under which the two Higgs doublets have opposite charge is broken by scalar fields ϕ having supersymmetry-breaking soft mass m_ϕ^2, one obtains hard SUSY-breaking corrections to the MSSM potential of the form $\xi g_x^2(|H_u|^2 - |H_d|^2)^2$. Here $\xi = m_\phi^2/(M_{Z_x}^2 + 2m_\phi^2)$ is a measure of how badly SUSY is broken in the sector giving mass to the new gauge field. Because this is a form of hard SUSY breaking, we expect from fine-tuning considerations that $M_{Z_x} \lesssim 10$ TeV. This is a mass range that will not be fully covered by searches for Z' and W' gauge bosons at the LHC, but which is perfectly suited for SppC. Furthermore, even an initial discovery of a heavy Z' in the e^+e^- or $\mu^+\mu^-$ channel at the LHC would leave open the question of how the new particle couples to the Higgs and whether it could be responsible for such D-term corrections to the Higgs potential. This question could be a target for SppC studies.

New F-term contributions to the Higgs boson mass can come in several forms, but the paradigmatic example is the NMSSM or other singlet extension of the MSSM with a chiral superfield S coupling through $\lambda S H_u H_d$ in the superpotential [37–39]. Although in principle such an effective theory could remain weakly coupled up to large energy scales, small values of λ are fairly inefficient at lifting the Higgs mass. This is especially true since the $|\lambda H_u H_d|^2$ quartic is most effective at $\tan\beta \approx 1$, but then the MSSM tree-level contribution $m_Z^2 \cos^2(2\beta)$ is small. This has led to a focus on the λSUSY scenario of $\lambda \approx 2$ [40], leading to a Landau pole near 10 TeV. Various UV completions exist, such as the "Fat Higgs" theory [41]. Any scenario along these lines, with compositeness *and* supersymmetry at scales near 10 TeV, would provide dramatic and exciting new physics at SppC.

To summarize, in many of the supersymmetric scenarios that are still viable in light of the 125 GeV Higgs mass, there are key physics targets that are within reach of SppC but not of the LHC. In the MSSM itself, these are the stops (at least the heavier of the two, in the highly mixed case), which for most values of $\tan\beta$ would be discovered and have their properties measured at SppC. This could experimentally confirm our theoretical understanding of the Higgs mass in the MSSM. Alternatively, in D-term extensions of the MSSM, the discovery of new heavy gauge bosons—for example, a Z'—and the study of their couplings to Higgs bosons could be a crucial channel. F-term scenarios come in a wider variety, but in addition to an extended Higgs sector, also frequently predict strong coupling and possibly compositeness at the several TeV scale. Almost any scenario in which supersymmetry exists near the weak scale, then, would provide great opportunities for the SppC, going well beyond the capabilities of the LHC.

Summary of Simplified Model Results

The following sections summarize the work performed in [42, 43]. These were studies of the mass reach for various particles at future hadron colliders. The focus was on Simplified Models [44–46] that are motivated by Supersymmetry (SUSY). Simplified Models are by a Lagrangian field theory using a minimal number of new physics states. The goal is to isolate the particles that generate a particular signature of interest. Then the goal is to design a set of searches that cover the range of kinematic possibilities which can arise as a function of the particle masses. Based on our prejudice for which models should be prioritized, below we will present results for the following:

Simplified Model	Decay Channel	100 TeV reach
Gluino-neutralino (light flavor)	$\widetilde{g} \to q\,\overline{q}\,\widetilde{\chi}_1^0$	11 TeV
Squark-neutralino	$\widetilde{q} \to q\,\widetilde{\chi}_1^0$	8 TeV
Gluino-squark with a massless neutralino	$\widetilde{g} \to \left(q\,\overline{q}\,\widetilde{\chi}_1^0 / q\,\widetilde{q}^*\right)$; $\widetilde{q} \to \left(q\,\widetilde{\chi}_1^0 / q\,\widetilde{g}\right)$	15.5 TeV
Gluino-neutralino (heavy flavor)	$\widetilde{g} \to t\,\overline{t}\,\widetilde{\chi}_1^0$	6.4 TeV
Stop-neutralino	$\widetilde{t} \to t\,\widetilde{\chi}_1^0$	5.5 TeV

In this table, "100 TeV reach" corresponds to the maximum discovery potential at a future 100 TeV proton collider with 3000 fb^{-1} of integrated luminosity.

These models were chosen as they are expected to represent the most likely first signatures of SUSY at a hadron collider. The gluino-neutralino with light flavor decays,

squark-neutralino, and gluino-squark with a massless neutralino are classic examples of models that yield "jets + $E_{\mathrm{T}}^{\mathrm{miss}}$", where $E_{\mathrm{T}}^{\mathrm{miss}}$ is missing transverse energy. These models are motivated by their large production cross section which implies that a large regions of SUSY parameter space would yield this as the first signature. These will be followed by the gluino-neutralino with heavy flavor decays and stop-neutralino models, which are motivated by the expectation that they would represent the first manifestation of "natural SUSY" models.

Parton level events were generated using `Madgraph5` v1.5.10 [47]. All signals involve the pair production of SUSY particles and are matched using MLM matching up to 2 additional jets. The k_T-ordered shower scheme with a matching scale of `qcut=xqcut=100` GeV was used. Note that we do not account for any possible inadequacies inherent in the current Monte Carlo technology, *e.g.* electroweak gauge bosons are not included in the shower.

The gluinos and squarks were treated as stable at the parton level. These events were subsequently decayed and showered using `Pythia6` [48] and passed through the `Delphes` detector simulation [49] using the "Snowmass" detector parameter card [50]. Total production cross sections were computed at NLO using a modified version of `Prospino` v2.1 [51–53]. The stop cross sections were computed at NLL using [54].

Gluino-Neutralino with Light Flavor Decays

In the "gluino-neutralino model with light flavor decays", the gluino $\widetilde{g}$ is the only kinematically accessible colored particle. The squarks are completely decoupled and do not contribute to gluino production diagrams. The gluino undergoes a prompt three-body decay through off-shell squarks, $\widetilde{g} \to q\,\overline{q}\,\widetilde{\chi}_1^0$, where q is one of the light quarks and $\widetilde{\chi}_1^0$ is a neutralino LSP. The only two relevant parameters are the gluino mass $m_{\widetilde{g}}$ and the neutralino mass $m_{\widetilde{\chi}_1^0}$.

The background is dominated by W/Z + jets, with subdominant contributions from $t\,\bar{t}$ production. Single top events and W/Z events from vector boson fusion processes are negligible. In all cases, there are decay modes which lead to multi-jet signatures. The $E_{\mathrm{T}}^{\mathrm{miss}}$ can come from a variety of sources, such as neutrinos, jets/leptons which are lost down the beam pipe, and energy smearing effects.

The gluino-neutralino model with light flavor decays can be probed with an analysis inspired by the ATLAS analysis in [55]. After an event preselection, rectangular cuts on one or more variables are optimized at each point in parameter space to yield maximum signal significance. Specifically, we simultaneously scan a two-dimensional set of cuts on $E_{\mathrm{T}}^{\mathrm{miss}}$ and H_{T}, where $E_{\mathrm{T}}^{\mathrm{miss}}$ is the magnitude of the missing transverse momentum and H_{T} is defined as the scalar sum of jet p_{T} . Following a standard four jet pre-selection, the search strategy is given by

SEARCH STRATEGY: Simultaneous optimization over H_{T} and $E_{\mathrm{T}}^{\mathrm{miss}}$

- $E_{\mathrm{T}}^{\mathrm{miss}}/\sqrt{H_{\mathrm{T}}} > 15\ \mathrm{GeV}^{1/2}$
- The leading jet p_T must satisfy $p_T^{\mathrm{leading}} < 0.4\,H_{\mathrm{T}}$
- $E_{\mathrm{T}}^{\mathrm{miss}} > (E_{\mathrm{T}}^{\mathrm{miss}})_{\mathrm{optimal}}$
- $H_{\mathrm{T}} > (H_{\mathrm{T}})_{\mathrm{optimal}}$

These cuts are applied to our realistic simulated events. The discovery reach and limits for all four collider scenarios in the full $m_{\tilde{g}}$ versus $m_{\tilde{\chi}_1^0}$ plane can be seen in Fig. 7.1. The 14 TeV 300 fb^{-1} limit with massless neutralinos is projected to be at a gluino mass of 2.3 TeV (corresponding to 110 events), while the 14 TeV 3000 fb^{-1} limit is projected to be at 2.7 TeV (corresponding to 175 events). The 14 TeV LHC with 3000 fb^{-1} could discover a gluino as heavy as 2.3 TeV if the neutralino is massless, while for $m_{\tilde{\chi}_1^0} \gtrsim 500$ GeV the gluino mass reach rapidly diminishes. At a 33 TeV machine with 3000 fb^{-1}, the limit with massless neutralinos is projected to be 5.8 TeV (corresponding to 61 events). The 33 TeV proton collider with 3000 fb^{-1} could discover a gluino as heavy as 4.8 TeV if the neutralino is massless, while for $m_{\tilde{\chi}_1^0} \gtrsim 1$ TeV the gluino mass reach rapidly diminishes. Finally, for a 100 TeV collider with 3000 fb^{-1}, the limit with massless neutralinos is projected to be 13.5 TeV (corresponding to 60 events). The 100 TeV proton collider with 3000 fb^{-1} could discover a gluino as heavy as 11 TeV if the neutralino is massless, while for $m_{\tilde{\chi}_1^0} \gtrsim 1$ TeV the gluino mass reach rapidly diminishes.

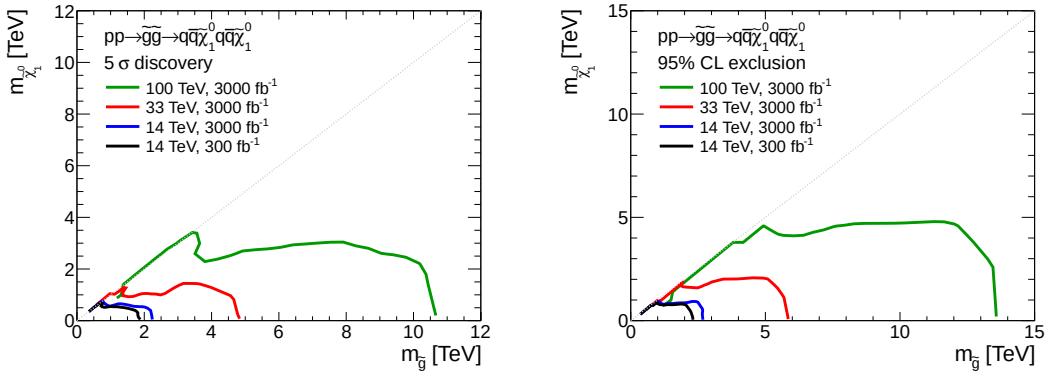

Figure 7.1 Results for the gluino-neutralino model with light flavor decays. The left [right] panel shows the $5\,\sigma$ discovery reach [95% CL exclusion] for the four collider scenarios studied here. A 20% systematic uncertainty is assumed and pileup is not included.

Compressed Strategy

This section is devoted to analyses which target the compressed region of parameter space for the gluino-neutralino with light-flavor decays Simplified Model where

$$m_{\tilde{g}} - m_{\tilde{\chi}_1^0} \equiv \Delta m \ll m_{\tilde{g}}. \tag{7.2}$$

For models with this spectrum, the search strategy of the previous section does not provide the optimal reach. With compressed spectra the gluino decays only generate soft partons, thereby suppressing the H_{T} signals and reducing the efficiency for passing the 4 jet requirement. A more effective strategy for compressed spectra searches relies instead on events with hard initial state radiation (ISR) jets to discriminate signal from background [56, 57].

The dominant background is the production of a Z boson in association with jets, where the Z boson decays into a pair of neutrinos ($Z \to \nu\nu$), leading to events with jets and a significant amount of missing transverse energy. Subleading backgrounds are the production of a W boson which decays leptonically $\left(W \to \ell\,\nu\right)$ in association with jets, where the charged lepton is not reconstructed properly. Finally, when considering events with a

significant number of jets, $t\bar{t}$ production in the fully hadronic decay channel $\left(t \to b\,q\,q'\right)$ can be relevant.

In this study, we will apply two different search strategies that are optimized for this kinematic configuration and will choose the one which leads to the most stringent bound on the production cross section for each point in parameter space. Some of the cuts chosen below are inspired by recent public results from ATLAS [58] and CMS [59] on monojet searches. Following a standard pre-selection, we rely on the following two strategies:

SEARCH STRATEGY 1: Leading jet based selection

- at most 2 jets
- leading jet must have $p_T > (\text{leading jet } p_{\mathrm{T}})_{\text{optimal}}$ and $|\eta| < 2.0$
- second jet is allowed if $\Delta\varphi(j_2, E_{\mathrm{T}}^{\mathrm{miss}}) > 0.5$
- $E_{\mathrm{T}}^{\mathrm{miss}} > \left(E_{\mathrm{T}}^{\mathrm{miss}}\right)_{\text{optimal}}$

where both $\left(E_{\mathrm{T}}^{\mathrm{miss}}\right)_{\text{optimal}}$ and $(\text{leading jet } p_{\mathrm{T}})_{\text{optimal}}$ are determined simultaneously by taking the values in the range $1 - 10$ TeV that yields the strongest exclusion.

SEARCH STRATEGY 2: $E_{\mathrm{T}}^{\mathrm{miss}}$ based selection without jet veto

- leading jet with $p_T > 110$ GeV and $|\eta| < 2.4$
- $E_{\mathrm{T}}^{\mathrm{miss}} > (E_{\mathrm{T}}^{\mathrm{miss}})_{\text{optimal}}$

with $E_{\mathrm{T}}^{\mathrm{miss}}$ varied in the range $(1, 10)$ TeV. No requirement is placed on a maximum number of jets. Note that for higher jet multiplicities the production of top quark pairs in the fully hadronic decay mode starts to dominate over W/Z + jets production.

The discovery reach and limits for all four collider scenarios in the full $m_{\tilde{g}}$ versus $m_{\tilde{\chi}_1^0}$ plane can be seen in Fig. 7.2. With 300 fb^{-1} of data this search can exclude gluino masses of up to approximately 900 GeV for a mass difference of 5 GeV, with reduced reach for larger mass differences. The limits increase to around 1 TeV with a factor of 10 more data. This improves the reach near the degenerate limit by roughly 200 GeV compared to the $H_{\mathrm{T}} + E_{\mathrm{T}}^{\mathrm{miss}}$-based analysis; the $H_{\mathrm{T}} + E_{\mathrm{T}}^{\mathrm{miss}}$-based searches do not begin to set stronger limits until $\Delta \gtrsim 50$ GeV. The discovery reach of this search is gluino masses up to 800 GeV near the degenerate limit. Unlike the exclusion reach, the discovery reach for this search is not a substantial improvement over the $H_{\mathrm{T}} + E_{\mathrm{T}}^{\mathrm{miss}}$-based analysis, even in the degenerate limit. This occurs because the signal efficiency using these searches is such that there are not enough events to reach 5σ confidence.

For a 33 TeV proton collider with 3000 fb^{-1} of data, the exclusion reach for a mass difference of 5 GeV covers gluino masses of up to approximately 1.8 TeV, with reduced reach for larger mass differences. For very small mass differences in the range of 5 to 50 GeV discoveries could be made for gluino masses up to 1.4 TeV. This search improves the exclusion (discovery) reach near the degenerate limit by roughly 800 GeV (400 GeV) compared to the $H_{\mathrm{T}} + E_{\mathrm{T}}^{\mathrm{miss}}$-based analysis; the $H_{\mathrm{T}} + E_{\mathrm{T}}^{\mathrm{miss}}$-based searches do not begin to set stronger limits until $\Delta \gtrsim 50$ GeV.

For a 100 TeV proton collider with 3000 fb^{-1} of data, the exclusion reach for a mass difference of 5 GeV covers gluino masses of up to approximately 5.7 TeV, with reduced reach for larger mass differences. For very small mass differences discoveries could be made for gluino masses up to 4.8 TeV. This search improves the exclusion (discovery)

reach near the degenerate limit by roughly 1.7 TeV (1.3 TeV) compared to the $H_{\mathrm{T}}+E_{\mathrm{T}}^{\mathrm{miss}}$-based analysis; the $H_{\mathrm{T}}+E_{\mathrm{T}}^{\mathrm{miss}}$-based searches do not begin to set stronger limits until $\Delta \gtrsim 500$ GeV.

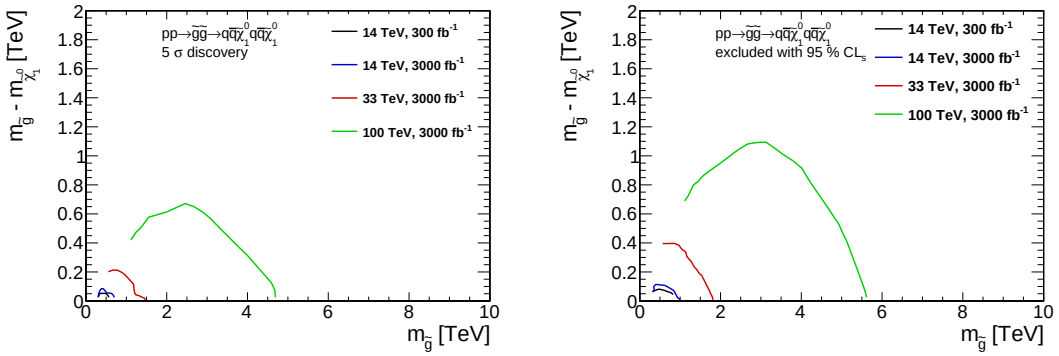

Figure 7.2 Results for the gluino-neutralino model with light flavor decays for the analyses that target the compressed region of parameter space. The left [right] panel shows the $5\,\sigma$ discovery reach [95% CL exclusion] for the four collider scenarios studied here. A 20% systematic uncertainty is assumed and pileup is not included.

Squark-Neutralino

In the "squark-neutralino model", the first and second generation squarks $\widetilde{q}$ are all allowed to be kinematically accessible. The squarks undergo prompt two-body decays, $\widetilde{q} \to q\,\widetilde{\chi}_1^0$, where t is the top quark and $\widetilde{\chi}_1^0$ is a neutralino LSP. The only two relevant parameters are the squark mass $m_{\widetilde{q}}$ and the neutralino mass $m_{\widetilde{\chi}_1^0}$.

The backgrounds are essentially identical to those that were relevant for the gluino-neutralino with light flavor decays model. Since the final state is two (or more) hard jets and missing energy, this model also serves to test the power of jets+$E_{\mathrm{T}}^{\mathrm{miss}}$ style analyses. The mass reach is not be nearly as high as in the gluino-neutralino light flavor decay model for two reasons: neglecting ISR and FSR, the final state has only two hard jets from the squark decays as opposed to four hard jets from the gluino decays, and cross section for producing squark pairs with the gluino completely decoupled is substantially lower than that for producing gluino pairs of the same mass. Note that we checked that the 4 jet requirement included in the jets+$E_{\mathrm{T}}^{\mathrm{miss}}$ preselection does not have a detrimental impact on the squark results presented below. These results are shown in Fig. 7.3.

The 14 TeV 300 fb^{-1} limit with massless neutralinos is projected to be 1.5 TeV (corresponding to 1022 events), while the 14 TeV 3000 fb^{-1} limit is projected to be 1.7 TeV (corresponding to 3482 events). Finally, we note that the 14 TeV LHC with 3000 fb^{-1} could discover a squark as heavy as 800 GeV if the neutralino is massless. The 33 TeV 3000 fb^{-1} limit with massless neutralinos is projected to be 3.4 TeV (corresponding to 3482 events). Finally, we note that the 33 TeV proton collider with 3000 fb^{-1} could discover a squark as heavy as 1.4 TeV if the neutralino is massless. The 100 TeV 3000 fb^{-1} limit with massless neutralinos is projected to be 8.0 TeV (corresponding to 849 events). Finally, we note that the 100 TeV proton collider with 3000 fb^{-1} could discover a squark as heavy as 2.4 TeV if the neutralino is massless. Compared to the 14 and 33 TeV searches, the squark reach degrades less rapidly as the neutralino mass is increased from the massless limit.

Given the large number of events for the masses that lie at the edge of the exclusion reach, it is prudent to explore if other strategies can be more effective than the $E_{\mathrm{T}}^{\mathrm{miss}}$-$H_{\mathrm{T}}$optimization. Following a CMS study [60], we separate events into bins of H_T, and we reconstruct the "stransverse mass" [61, 62], m_{T2}, from the $E_{\mathrm{T}}^{\mathrm{miss}}$and the two leading jets in each event. The m_{T2} variable is defined as an extension of the transverse mass, m_T, for events in which there are at least two invisible decay products. In this case, we define m_{T2} with the assumption that the invisible decay products are massless, which causes Standard Model backgrounds to be peaked at small values of m_{T2}, while signal distributions have a kinematic endpoint at the squark mass. We optimize cuts on m_{T2} for each H_T bin, and treat each bin as a separate signal region in a combined maximum likelihood fit. The results of this search at $\sqrt{s} = 100$ TeV with 3 ab^{-1} are shown as dashed lines in Fig. 7.3, where we see significant improvement in discovery potential relative to the jets+$E_{\mathrm{T}}^{\mathrm{miss}}$ strategy described above [63]. In particular, we are able to discover (exclude) squarks up to $\sim$ 8 TeV (10 TeV) using this more sophisticated strategy.

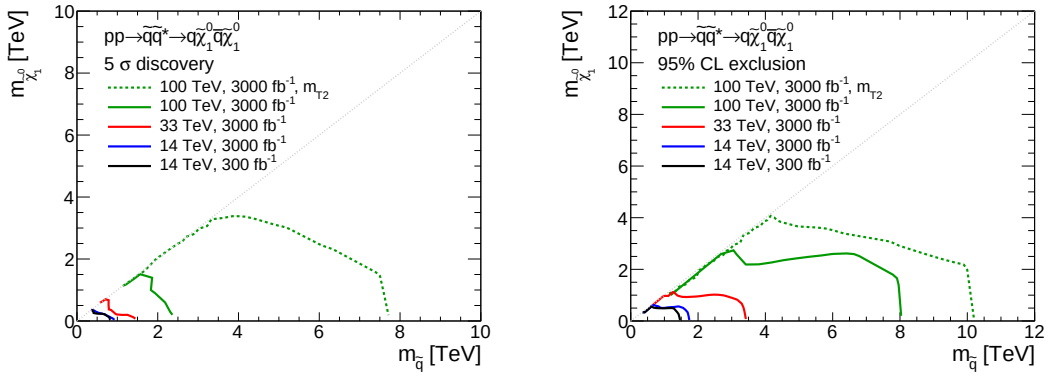

Figure 7.3 Results for the squark-neutralino model with light flavor decays. The left [right] panel shows the $5\,\sigma$ discovery reach [95% CL exclusion] for the four collider scenarios studied here. The solid lines represent a the results using the $H_{\mathrm{T}} + E_{\mathrm{T}}^{\mathrm{miss}}$-based strategy, while the dashed line relies on a more sophisticated approach based on m_{T2}. A 20% systematic uncertainty is assumed and pileup is not included.

Compressed Strategy

The results presented in the previous section were derived using a search which targeted the bulk of the squark-neutralino Simplified Model parameter space. In the compressed region where

$$m_{\tilde{q}} - m_{\tilde{\chi}_1^0} \equiv \Delta m \ll m_{\tilde{q}} \tag{7.3}$$

a different search strategy is required. For parameters in this range, the jets which result from the direct decays of the squark will be very soft and one has to rely on ISR jets to discriminate these models from background. These signatures will be very similar to those produced by the compressed gluino-neutralino model with light flavor decays, and therefore the backgrounds will be identical to the compressed gluino-neutralino with light flavor decay model. Therefore, we will use the same search strategies described above.

The results for the squark-neutralino model in the compressed region of parameter space are given in Fig. 7.4. For all four colliders, only the $E_{\mathrm{T}}^{\mathrm{miss}}$ based strategy will be relevant for this model. At a 14 TeV collider, it is possible to exclude (discover) squarks in the degenerate limit with mass less than $\sim$ 650 GeV (500 GeV) with 300 fb^{-1} of data. Increasing the integrated luminosity by a factor of 10 has a minimal impact on the

discovery reach for compressed squark models. This search improves the exclusion (discovery) reach near the degenerate limit by roughly $300\ \mathrm{GeV}(150\ \mathrm{GeV})$ compared to the $H_{\mathrm{T}} + E_{\mathrm{T}}^{\mathrm{miss}}$-based analysis described above; the $H_{\mathrm{T}} + E_{\mathrm{T}}^{\mathrm{miss}}$-based searches do not begin to set stronger limits until $\Delta \gtrsim 50\ \mathrm{GeV}$. Moving to 33 TeV, it is possible to exclude (discover) squarks in the degenerate limit with mass less than $\sim 1.2(0.7)\ \mathrm{TeV}$ with $3000\ \mathrm{fb}^{-1}$ of data. This does not substantially improves the discovery reach near the degenerate limit compared to the $H_{\mathrm{T}} + E_{\mathrm{T}}^{\mathrm{miss}}$-based analysis, but does improve the exclusion reach by roughly $200\ \mathrm{GeV}$ for $\Delta \lesssim 100\ \mathrm{GeV}$. Finally, for the 100 TeV collider, it is possible to exclude (discover) squarks in the degenerate limit with mass less than $\sim 4\ \mathrm{TeV}(3\ \mathrm{TeV})$ with $3000\ \mathrm{fb}^{-1}$ of data. This improves the exclusion (discovery) reach near the degenerate limit compared to the $H_{\mathrm{T}} + E_{\mathrm{T}}^{\mathrm{miss}}$-based analysis targeted at the non-compressed region described above by roughly $1.5\ \mathrm{TeV}(1.8\ \mathrm{TeV})$ for $\Delta \lesssim 200\ \mathrm{GeV}$.

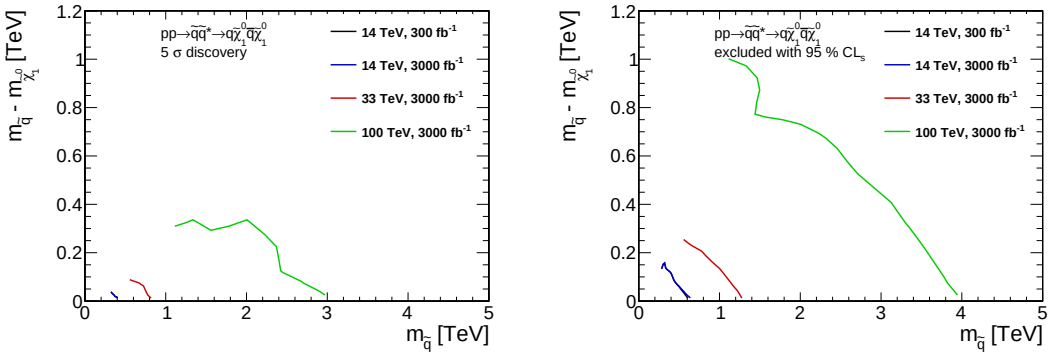

Figure 7.4 Results for the squark-neutralino model with light flavor decays for the analyses that target the compressed region of parameter space. The left [right] panel shows the $5\,\sigma$ discovery reach [95% CL exclusion] for the four collider scenarios studied here. A 20% systematic uncertainty is assumed and pileup is not included.

Gluino-squark with Massless Neutralino

In the "gluino-squark-neutralino model", the gluino $\widetilde{g}$ and the first and second generation squarks $\widetilde{q}$ are all allowed to be kinematically accessible. The only relevant parameters are the squark mass $m_{\widetilde{q}}$, which is taken to be universal for the first two generations, the gluino mass $m_{\widetilde{g}}$, and the neutralino mass $m_{\widetilde{\chi}^0}$. For this study we fix the neutralino mass $m_{\widetilde{\chi}^0} = 1\ \mathrm{GeV}$, which captures the relevant kinematics for $m_{\widetilde{g}}, m_{\widetilde{q}} \gg m_{\widetilde{\chi}^0}$. The decay mode is chosen depending on the mass hierarchy.

This model is a good proxy for comparing the power of searches which rely on the traditional jets and $E_{\mathrm{T}}^{\mathrm{miss}}$ style hadron collider search strategy to discriminate against background. The final state ranges from two to four (or more) hard jets from the decay (depending on the production channel) and missing energy. The current preliminary limits on this model using $20\ \mathrm{fb}^{-1}$ of 8 TeV data are $m_{\widetilde{g}} = 1750\ \mathrm{GeV}$ and $m_{\widetilde{q}} = 1600\ \mathrm{GeV}$ (ATLAS [64]) assuming a massless neutralino.

The results for the gluino-squark-neutralino model are given in Fig. 7.5. The $14\ \mathrm{TeV}$ $300\ \mathrm{fb}^{-1}$ limits are projected to be $m_{\widetilde{g}} = m_{\widetilde{q}} = 2.8\ \mathrm{TeV}$ (corresponding to 155 events); $m_{\widetilde{g}} = 2.4\ \mathrm{TeV}$ (corresponding to 43 events) and the squark mass is at the edge of the region simulated; $m_{\widetilde{q}} = 2.1\ \mathrm{TeV}$ (corresponding to 774 events) and the gluino mass is at the edge of the region simulated. The $14\ \mathrm{TeV}$ $3000\ \mathrm{fb}^{-1}$ limits are projected to be $m_{\widetilde{g}} =$

$m_{\widetilde{q}} = 3.2$ (corresponding to 293 events); $m_{\widetilde{g}} = 3.0$ TeV (corresponding to 23 events) and the squark mass is at the edge of the region simulated; $m_{\widetilde{q}} = 2.7$ TeV (corresponding to 953 events) and the gluino mass is at the edge of the region simulated. The 33 TeV 3000 fb^{-1} limits are projected to be $m_{\widetilde{g}} = m_{\widetilde{q}} = 6.8$ (corresponding to 132 events); $m_{\widetilde{g}} = 6.1$ TeV (corresponding to 21 events) and the squark mass is at the edge of the region simulated; $m_{\widetilde{q}} = 5.5$ TeV (corresponding to 473 events) and the gluino mass is at the edge of the region simulated. The 100 TeV 3000 fb^{-1} limits are projected to be $m_{\widetilde{g}} = m_{\widetilde{q}} = 16$ (corresponding to 136 events); $m_{\widetilde{g}} = 16$ TeV (corresponding to 13 events) and the squark mass is at the edge of the region simulated; $m_{\widetilde{q}} = 14$ TeV (corresponding to 169 events) and the gluino mass is at the edge of the region simulated. Clearly the search does better with light gluinos. Note that we find that we are closer to the ideal limit than in the 14 TeV and 33 TeV cases. Both of these facts are likely related to the four jet preselection requirement.

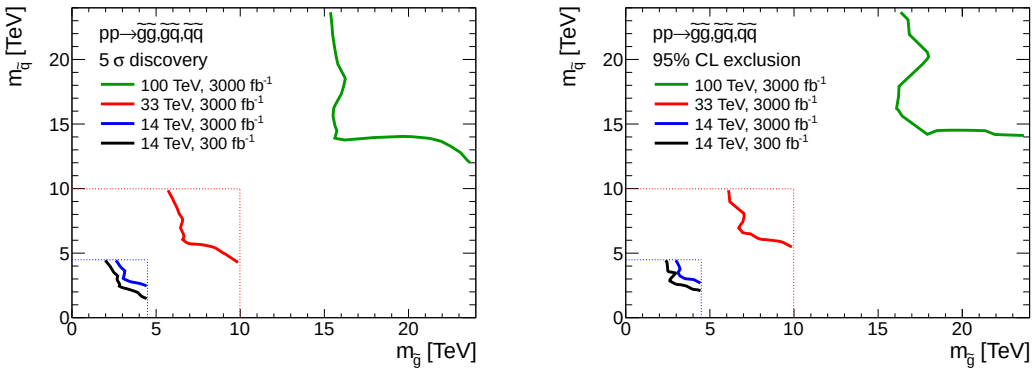

Figure 7.5 Results for the gluino-squark-neutralino model. The neutralino mass is taken to be 1 GeV. The left [right] panel shows the $5\,\sigma$ discovery reach [95% CL exclusion] for the four collider scenarios studied here. A 20% systematic uncertainty is assumed and pileup is not included.

Gluino-Neutralino with Heavy Flavor Decays

In the "gluino-neutralino model with heavy flavor decays", the gluino $\widetilde{g}$ is the only kinematically accessible colored particle. The squarks are completely decoupled and do not contribute to gluino production diagrams. The gluino undergoes a prompt three-body decay through off-shell stops, $\widetilde{g} \to t\,\bar{t}\,\widetilde{\chi}_1^0$, where t is the top quark and $\widetilde{\chi}_1^0$ is a neutralino LSP. The only two relevant parameters are the gluino mass $m_{\widetilde{g}}$ and the neutralino mass $m_{\widetilde{\chi}_1^0}$.

The model produces two $t\,\bar{t}$ pairs along with considerable $E_{\mathrm{T}}^{\mathrm{miss}}$ (away from the compressed region of parameter space), and therefore provides an interesting benchmark scenario for searches involving a combination of hadronic activity, leptonic signatures and b-tagging. A search which requires same-sign di-leptons (SSDL) is one viable approach to eliminating the SM background since this final state is highly suppressed in the SM. A SSDL pair is required and any remaining leptons are not allowed to form a Z-boson, inspired by the CMS collaboration in [65]. We note that this was the only channel explored in this scenario; it would be interesting to investigate how an all hadronic final state would perform at the higher energy machines.

The analysis used to derive the results below requires an SSDL pair, which is very efficient at eliminating backgrounds. The dominant background is top pair production, where both tops decay leptonically (the di-leptonic channel). There are subdominant backgrounds from $W\,b\,b$, which are accounted for by including the BJ Snowmass particle container [66]. All backgrounds simulated for Snowmass are included and their rates are found to be negligible. Since the SSDL requirement is very effective at suppressing backgrounds, only mild cut on $E_{\mathrm{T}}^{\mathrm{miss}}$ is necessary to observe this model. This implies that this search will also be very effective in the compressed regions of parameter space where $m_{\widetilde{g}} \simeq m_{\widetilde{\chi}_1^0}$.

After preselection, the following are used as discriminating variables. Eight model points, three with very low LSP mass, three with medium LSP mass, and two with high LSP mass are used to define eight signal regions, which rely on some combination of the following cuts.

SEARCH STRATEGY: Same-sign di-lepton based selection

- symmetric $M_{T2} > \left(\text{symmetric } M_{T2}\right)_{\text{optimal}}$
- $p_T > \left(p_T\right)_{\text{optimal}}$ for the hardest lepton
- $E_{\mathrm{T}}^{\mathrm{miss}} > \left(E_{\mathrm{T}}^{\mathrm{miss}}\right)_{\text{optimal}}$
- $N_{\text{jets}} > \left(N_{\text{jets}}\right)_{\text{optimal}}$
- $N_{b\text{-jets}} > \left(N_{b\text{-jets}}\right)_{\text{optimal}}$
- $M_{\text{eff}} > \left(M_{\text{eff}}\right)_{\text{optimal}}$
- $(H_{\mathrm{T}})_{\text{jets}} > \left((H_{\mathrm{T}})_{\text{jets}}\right)_{\text{optimal}}$

Symmetric M_{T2} is defined in the canonical way [61, 62, 67], where the SSDL pair is used for the visible signal and the invisible particle test mass is assumed to be zero; M_{eff} is defined as the scalar sum of the p_T of all visible objects and $E_{\mathrm{T}}^{\mathrm{miss}}$.

The results for the gluino-squark-neutralino model are given in Fig. 7.6. The $14\ \mathrm{TeV}$ $300\ \mathrm{fb}^{-1}$ limit is projected to be $1.9\ \mathrm{TeV}$ (corresponding to 73 events), and the $3000\ \mathrm{fb}^{-1}$ limit is projected to be $2.4\ \mathrm{TeV}$ (corresponding to 67 events). The $14\ \mathrm{TeV}$ LHC with $3000\ \mathrm{fb}^{-1}$ could discover a gluino (with $\widetilde{g} \to t\,\bar{t}\,\widetilde{\chi}_1^0$) as heavy as $2.0\ \mathrm{TeV}$ if the neutralino is massless. The $33\ \mathrm{TeV}$ $3000\ \mathrm{fb}^{-1}$ limit is projected to be $4.0\ \mathrm{TeV}$ (corresponding to 243 events). A $33\ \mathrm{TeV}$ proton collider with $3000\ \mathrm{fb}^{-1}$ could discover a gluino (with $\widetilde{g} \to t\,\bar{t}\,\widetilde{\chi}_1^0$) as heavy as $3.4\ \mathrm{TeV}$ if the neutralino is massless. The $100\ \mathrm{TeV}$ $3000\ \mathrm{fb}^{-1}$ limit is projected to be $8.8\ \mathrm{TeV}$ (corresponding to 224 events). A $100\ \mathrm{TeV}$ proton collider with $3000\ \mathrm{fb}^{-1}$ could discover a gluino (with $\widetilde{g} \to t\,\bar{t}\,\widetilde{\chi}_1^0$) as heavy as $6.4\ \mathrm{TeV}$ if the neutralino is massless. Note that due to the relatively weak cuts that can be placed on $E_{\mathrm{T}}^{\mathrm{miss}}$, the SSDL signal is robust against models with almost degenerate gluino and neutralino.

Stop-Neutralino

In the "stop-neutralino model", the stop $\widetilde{t}$ is the only kinematically accessible colored particle. The stop undergoes a prompt two-body decay, $\widetilde{t} \to t\,\widetilde{\chi}_1^0$, where t is the top quark and $\widetilde{\chi}_1^0$ is a neutralino LSP. The only two relevant parameters are the gluino mass $m_{\widetilde{t}}$ and the neutralino mass $m_{\widetilde{\chi}_1^0}$.

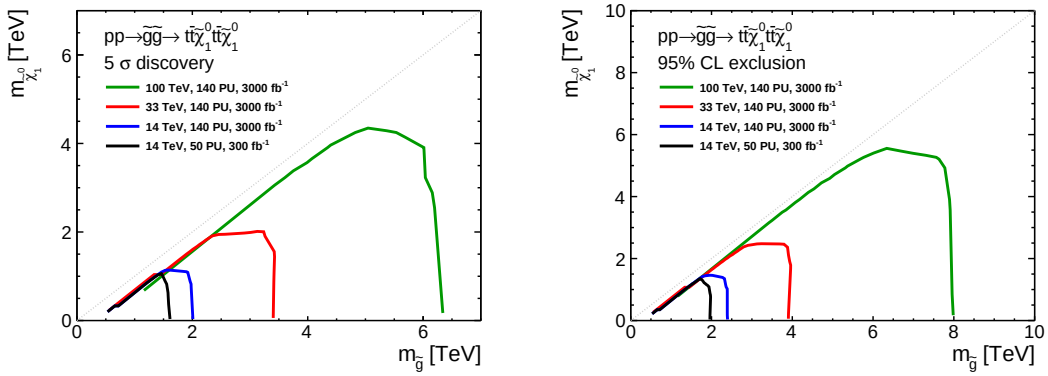

Figure 7.6 Results for the gluino-squark-neutralino model. The neutralino mass is taken to be 1 GeV. The left [right] panel shows the $5\,\sigma$ discovery reach [95% CL exclusion] for the four collider scenarios studied here. A 20% systematic uncertainty is assumed and pileup is included.

This section will only provide the reach for a 100 TeV collider. Since the stop masses that can be probed are quite large with respect to the weak scale, it is likely that the tops resulting from stops decays will be very boosted. The left panel of Fig. 7.7 shows the p_T distribution of the leading top quark for three different stop masses (assuming a massless neutralino). For stops with a mass of a few TeV or higher, the tops from the stop decay are highly boosted with $p_T \gg m_t$. The right panel of Fig. 7.7 shows the mean distance between the W boson and the b from the decay of the top as a function of $m_{\tilde{t}}$ and $m_{\tilde{\chi}^0_1}$.

Given that the jet radius chosen for this study is $\Delta R = 0.5$, the top will on average be contained within a single jet. Stop searches at a 100 TeV collider will therefore have to probe a kinematic regime not accessible to the 14 TeV LHC, where the top p_T relevant for most searches is less than a TeV.

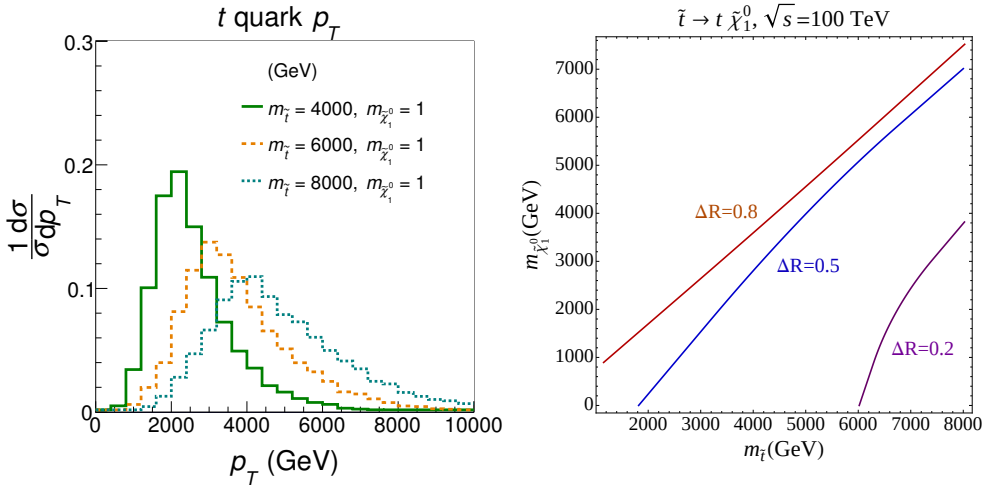

Figure 7.7 The p_T distribution of the leading top quark for $m_{\tilde{t}} = 2, 6, 10$ TeV assuming $m_{\tilde{\chi}^0_1} = 1$ GeV [left]. The average size of top jets from stop decays as a function of $m_{\tilde{t}}$ and $m_{\tilde{\chi}^0_1}$ [right].

Since we do not currently have a detailed detector design, we consider a strategy that is less sensitive to the detector response. When a highly-boosted top decays leptonically, or when the resulting b (or even c) quark decay yields a lepton, it is very likely that the lepton(s) will be collinear with the top jet. Requiring a hard lepton inside a jet can there-

fore be used to tag boosted tops [68]. Tagging a top jet by a muon is similar to leptonic b-tagging techniques implemented at the Tevatron [69–74] and at the LHC [75–78]. By definition these leptons will not be isolated from nearby tracks or calorimeter activity, removing a common handle for rejecting fake leptons. For simplicity we therefore only consider the case where a muon is collinear with a jet, and assume that a layered detector design similar to that employed by LHC experiments will provide adequate rejection of fake muons. Rejection of fake electrons without the use of an isolation requirement is more detector-dependent, and is not considered here. We make the following requirements:

SEARCH STRATEGY: Muon-inside-jet based selection

1. At least two anti-k_T jets [79] with cone parameter $\Delta R = 0.5$ and kinematic cuts: $|\eta| < 2.5$ and $p_T > 1000$ GeV.
2. At least one muon with $p_{T\mu} > 200$ GeV contained within a $\Delta R = 0.5$ cone centered around one of the leading two jets.
3. Events with at least one isolated lepton with $p_T > 35$ GeV and $|\eta| < 2.5$ are rejected. The isolation criterion demands the total p_T of all particles within a $\Delta R < 0.5$ cone around the lepton to be less than 10% of its p_T.
4. $\Delta\phi_{E_{\mathrm{T}}^{\mathrm{miss}}\,J} > 1.0$, where $\Delta\phi_{E_{\mathrm{T}}^{\mathrm{miss}}\,J}$ is the smallest $|\Delta\phi|$ between $E_{\mathrm{T}}^{\mathrm{miss}}$ and any jet with $p_T > 200$ GeV and $|\eta| < 2.5$.
5. $E_{\mathrm{T}}^{\mathrm{miss}} > 3$, 3.5 or 4 TeV. Out of the three choices, the cut is chosen for each mass point by optimizing the expected exclusion.

After imposing a muon-in-jet requirement on the background, the selected sample is composed mainly of boosted heavy quarks. The neutrinos and muons resulting from their decays will be highly collimated and the total $E_{\mathrm{T}}^{\mathrm{miss}}$ will tend to be aligned with the jet momenta. Therefore it is useful to impose an angular $\Delta\phi$ cut between the $E_{\mathrm{T}}^{\mathrm{miss}}$ and all the jets. For $q\bar{q}$, the maximum angle between each neutrino and the final q jet will be of order m_q/p_T. After a stringent $\Delta\phi$ cut, the remaining background is then boosted $t\bar{t} + X$ events. In particular, $t\bar{t} + W/Z$ is the dominant background in the signal region.

All of the results presented below have are obtained with very minimal cut-flows that do not rely on b-tagging or jet substructure techniques. Additional refinements should increase the search sensitivity, at the price of making assumptions on the future detector design.

As the neutralino mass approaches the stop mass, both the $E_{\mathrm{T}}^{\mathrm{miss}}$ and the top p_T are reduced. By relaxing some of the cuts discussed above and trading the muon-in-jet requirement for an isolated lepton requirement, sensitivity to this region of parameter space can be improved. Our cut-flow targeting the compressed region is:

SEARCH STRATEGY: Isolated lepton based selection

1. At least two anti-k_T jets with cone parameter $\Delta R = 0.5$. The kinematic requirements $|\eta| < 2.5$ and $p_T > 500$ GeV are imposed.
2. Two isolated leptons (either electrons or muons) with $p_{Tl} > 35$ GeV. A lepton satisfies the isolation cut when the total p_T of all particles in a cone of $\Delta R = 0.5$ around the lepton is less than 10% of its p_T.
3. $E_{\mathrm{T}}^{\mathrm{miss}} > 2$ TeV.

4. $\Delta\phi_{E_{\mathrm{T}}^{\mathrm{miss}}J,l} > 1.0$, where $\Delta\phi_{E_{\mathrm{T}}^{\mathrm{miss}}J,l}$ is the smallest $|\Delta\phi|$ between $E_{\mathrm{T}}^{\mathrm{miss}}$ and any jet with $p_T > 200$ GeV and $|\eta| < 2.5$, and any isolated lepton with $p_{Tl} > 35$ GeV and $|\eta| < 2.5$

These requirements yield increased sensitivity for $m_{\tilde{t}} \lesssim 3$ TeV close to the diagonal of the $(m_{\tilde{t}},\ m_{\tilde{\chi}_1^0})$ plane. Note that the $E_{\mathrm{T}}^{\mathrm{miss}} > 2$ TeV requirement implicitly relies on the presence of extra QCD radiation in association with the signal. This implies some uncertainty on initial-state radiation that we assume is covered by the systematic uncertainties applied on the signal samples. Note that this cut-flow is much more sensitive to detector and machine details than the previous one. We therefore present it only as a a proof of principle that going to higher energies does not necessarily imply sacrificing sensitivity to compressed, i.e. soft, physics.

Stops with masses up to ≈ 5.5 TeV can be discovered when the neutralino is massless, assuming $3000\ \mathrm{fb}^{-1}$ of integrated luminosity. The exclusion reach is ≈ 8 TeV, which corresponds to ~ 100 signal events before cuts. Note that this agrees with the estimate obtained by extrapolating the number of excluded signal events at $\sqrt{s} = 8$ TeV [80]. Since we optimized for exclusion as opposed to discovery, there is a gap between the discovery contours of the two different search strategies. The searches proposed here also have good discriminating power away from the massless neutralino limit. A 1.5 TeV stop could be discovered in the compressed region of parameter space. It is possible to exclude neutralino masses up to 2 TeV in most of the parameter space. Clearly a 100 TeV collider can have a significant impact on our understanding of this parameter space.

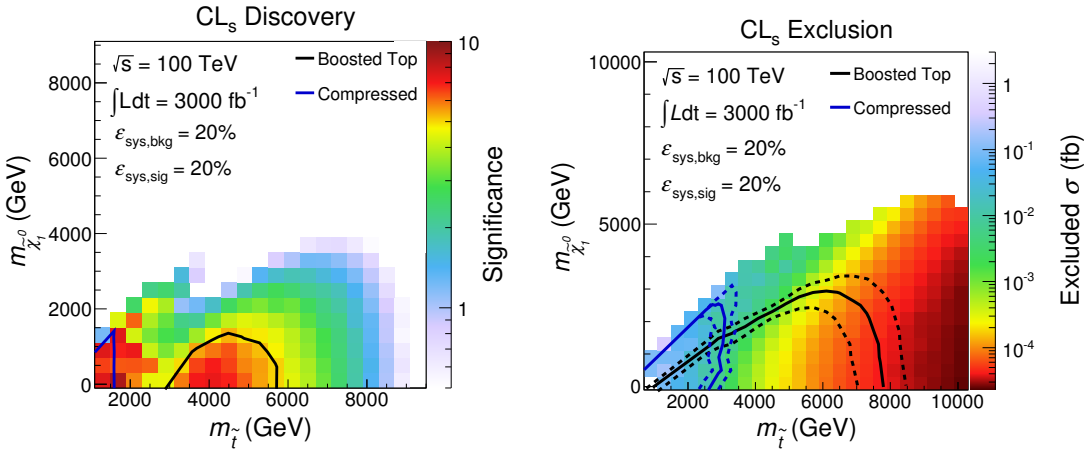

Figure 7.8 Projected discovery potential [left] and exclusion limits [right] for 3000 fb^{-1} of total integrated luminosity. At each signal point, the significance is obtained by taking the smaller CL$_s$ between the heavy stop and compressed spectra search strategies, and converting CL$_s$ to number of σ's. The blue and black contours (dotted) are the expected ($\pm 1\sigma$) exclusions/discovery contours using the heavy stop and compressed spectra searches.

7.2 New Resonances

Z'

Additional colorless vector gauge bosons (Z') occur in many extensions of the Standard Model (SM), in part because it is generically harder to break additional abelian $U(1)'$ factors than non-abelian ones[1]. The existence of a Z' could have many other possible implications, including an NMSSM-like solution to the μ problem (and the possibility of electroweak baryogenesis), new F and D term contributions to the lightest scalar mass, an additional Higgs singlet, additional neutralinos (with collider and dark matter consequences), new vector (under the SM) fermions for anomaly cancellation, and additional possibilities for neutrino mass. Other possibilities involve interactions with dark matter, the mediation of supersymmetry breaking, FCNC (for family non-universal couplings), associated charged W' s, and the production of superpartners and exotics. The Z' couplings could also give clues about a possible embedding of the $U(1)'$ into a more fundamental underlying theory. Although Z's can occur at any scale and with couplings ranging from extremely weak to strong, we concentrate here on TeV-scale masses with couplings not too different from electroweak, which might therefore be observable at the LHC or future colliders.

Following the notation in [81], we define the couplings of the SM and additional neutral gauge bosons to fermions by

$$-L_{NC} = eJ^{\mu}_{em}A_{\mu} + g_1 J^{\mu}_1 Z^0_{1\mu} + g_2 J^{\mu}_2 Z^0_{2\mu}, \tag{7.4}$$

with

$$J^{\mu}_{\alpha} = \sum_i \bar{f}_i \gamma^{\mu}[\epsilon^{\alpha i}_L P_L + \epsilon^{\alpha i}_R P_R] f_i. \tag{7.5}$$

The SM (Z^0_1) parameters are $g_1 = g/\cos\theta_W$ and $\epsilon^{1i}_L = t^i_{3L} - \sin^2\theta_W q^i$, $\epsilon^{1i}_R = -\sin^2\theta_W q^i$, where q^i is the electric charge of f_i in units of $|e|$ and $t^i_{3L} = \pm 1/2$ is the third component of weak isospin. We will absorb g_α into the chiral charges[2] by defining

$$g^{1i}_{L,R} \equiv g_1 \epsilon^{1i}_{L,R}, \qquad g^{2i}_{L,R} \equiv g_2 \epsilon^{2i}_{L,R}. \tag{7.6}$$

When it does not cause confusion we will drop the superscript 2 on $g^{2i}_{L,R}$. It will also be convenient to define the vector and axial couplings and the asymmetry parameters

$$g^i_{V,A} \equiv g^i_L \pm g^i_R, \qquad A_i \equiv \frac{g^{i\,2}_L - g^{i\,2}_R}{g^{i\,2}_L + g^{i\,2}_R} = \frac{2\, g^i_V g^i_A}{g^{i\,2}_V + g^{i\,2}_A}, \tag{7.7}$$

for $i = u, d, e, \nu, \cdots$. Analogous definitions hold for the $g^{1i}_{L,R}$.

We will assume as well that the $U(1)'$ charges commute[3] with $SU(2)$, so that there are only five relevant chiral charges,

$$g^u_L = g^d_L \equiv g^q_L, \quad g^u_R, \quad g^d_R, \quad g^e_L = g^\nu_L \equiv g^\ell_L, \quad g^e_R. \tag{7.8}$$

[1] For reviews, see [81–84]. Specific properties are reviewed in [85–91].

[2] The gauge coupling g_2 is not really a separate parameter, because it can be absorbed in the chiral couplings, as in (7.6). However, the separate extraction of g_2 would become meaningful if the charges were established to correspond to an embedding in a nonabelian group of some other model with well-defined normalization, such as the E_6 and LR models.

[3] One exception is the benchmark sequential model, in which $g^{2i}_{L,R} = g^{1i}_{L,R}$. This could possibly emerge from a diagonal embedding of the SM in a larger group, or for Kaluza-Klein excitations in an extra-dimensional theory.

	χ	ψ	η	LR	B-L	SSM	
D	$2\sqrt{10}$	$2\sqrt{6}$	$2\sqrt{15}$	$\sqrt{5/3}$	1	1	
$\hat{\epsilon}_L^q$	–1	1	–2	–0.109	1/6	$\hat{\epsilon}_L^u$	$\frac{1}{2}-\frac{2}{3}\sin^2\theta_W$
						$\hat{\epsilon}_L^d$	$-\frac{1}{2}+\frac{1}{3}\sin^2\theta_W$
$\hat{\epsilon}_R^u$	1	–1	2	0.656		$\hat{\epsilon}_R^u$	$-\frac{2}{3}\sin^2\theta_W$
$\hat{\epsilon}_R^d$	–3	–1	–1	–0.874		$\hat{\epsilon}_R^d$	$\frac{1}{3}\sin^2\theta_W$
$\hat{\epsilon}_L^l$	3	1	1	0.327	–1/2	$\hat{\epsilon}_L^\nu$	$\frac{1}{2}$
						$\hat{\epsilon}_L^e$	$-\frac{1}{2}+\sin^2\theta_W$
$\hat{\epsilon}_R^e$	1	–1	2	–0.438		$\hat{\epsilon}_R^e$	$\sin^2\theta_W$
$\hat{Q}_u$	2	–2	4	0.765	0	$-\frac{1}{2}$	
$\hat{Q}_d$	–2	–2	1	–0.765	0	—	

Table 7.1 Benchmark models and couplings, with $\epsilon_{L,R}^i \equiv \hat{\epsilon}_{L,R}^i/D$.

Ideally, one would like to determine these, as well as $M_{Z'}$ and $\Gamma_{Z'}$, in a model-independent way from collider as well as existing and future precision data. In practice, the existing limits are sufficiently stringent that we may have to resort to considering specific benchmark models. For illustration, we will consider the well known χ, ψ, and LR models, associated with the breakings $SO(10) \to SU(5) \times U(1)_\chi$, $E_6 \to SO(10) \times U(1)_\psi$, and $SU(2)_L \times SU(2)_R \times U(1)_{B-L} \to SU(2) \times U(1)_Y \times U(1)_{LR}$ (for $g_R = g$), respectively. We will also consider $Z_\eta = \sqrt{\frac{3}{8}} Z_\chi - \sqrt{\frac{5}{8}} Z_\psi$, associated with a certain compactification of the heterotic string, and the B-L model[4] with charge $(B-L)/2$. The charges for these benchmark models are listed in Table 7.1. For the E_6, LR, and B-L models we will take for the reference value of g_2 the GUT-normalized hypercharge coupling

$$g_2 = \sqrt{\frac{5}{3}}\, g \tan\theta_W \sim 0.46, \tag{7.9}$$

which is an approximation to the simplest E_6 prediction [92] for the GUT models and follows for $g_R = g$ in $SU(2)_L \times SU(2)_R \times U(1)_{B-L}$. We will also consider the sequential model with $g_2 = g_1$ and $\epsilon_{LR}^{2i} = \epsilon_{LR}^{1i}$.

There have been extensive studies of diagnostic possibilities[5] of the Z' couplings at the LHC utilizing the cross sections

$$\sigma^f \equiv \sigma[f\bar{f}] \equiv \sigma_{pp\to Z'\to f\bar{f}} = \sigma_{Z'} B(Z' \to f\bar{f}) \tag{7.10}$$

for decays into the final state $f\bar{f}$ for $f = \ell, \tau, t, b$ (with $\ell = e, \mu$), as well as forward-backward or charge asymmetries, rapidity distributions, and possible final state polarizations for $\tau^-\tau^+$ or $t\bar{t}$. Other possible probes include $\Gamma_{Z'}$ from the line shape, and various rare decay modes and associated productions.

[4]The $B-L$ charge usually occurs in a linear combination with $T_{3R} = Y - \frac{B-L}{2}$, where $Y = Q - T_{3L}$, as in the χ and LR models. Here we consider a simple $B-L$ charge as an example of a purely vector coupling.
[5]See, for example, [93–114]. Other studies are reviewed in [81, 84, 88].

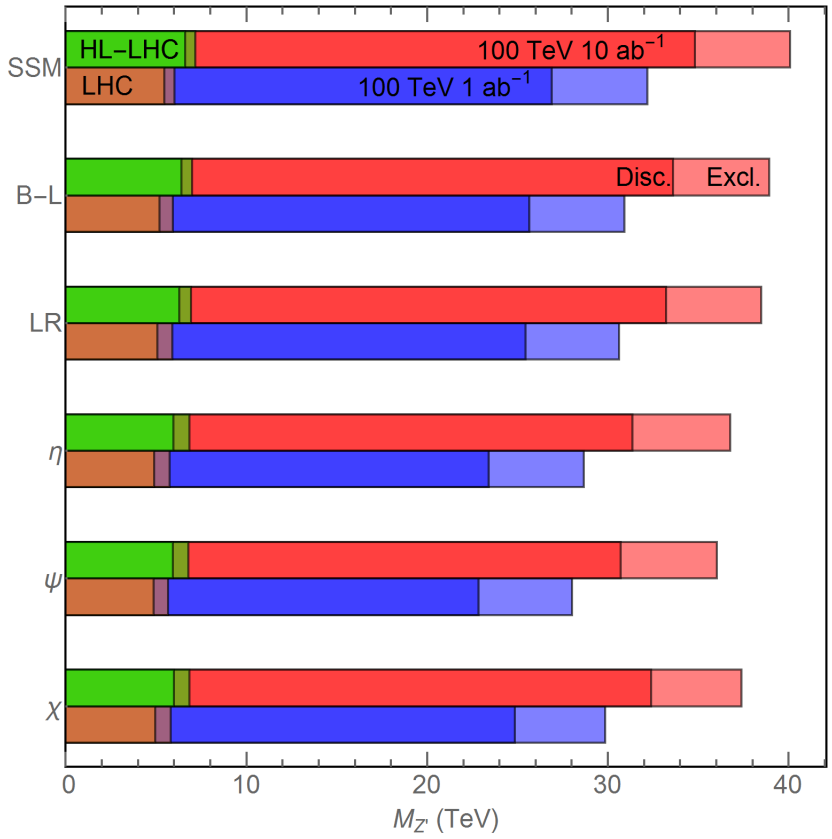

Figure 7.9 The discovery and exclusion reaches of Z' at SPPC 100 TeV at 1 ab^{-1} (blue) and 10 ab^{-1} (red) and LHC 14 TeV at 300 fb^{-1} (brown) and 3000 fb^{-1} (green) through dilepton (e, μ) channels.

To gain a sense of what might be achievable at the SPPC, we show the discovery and exclusion reach of the LHC and the SPPC in Fig. 7.9. We use Madgraph5 [47] for parton level event generation using models generated by FeynRules [115], showered by Pythia6.4 [48] and detector simulated by Delphes3 [116]. We choose CTEQ6.1 Parton Distribution Function (PDF) in five flavor scheme. We conservatively assume the detector of SPPC similar to the ATLAS detector, a common assumption recommended by the Snowmass. Typical Z' models with electroweak couplings should be observable[6] at the LHC as resonances in the dilepton channels for masses up to 4–6 (6–7) TeV for $\sqrt{s} = 14$ TeV and an integrated luminosity of 100 (3000) fb^{-1}. We can see that at 1 ab^{-1} the 100 TeV SPPC could discover (exclude) up to 23–26 (28–32) TeV Z' for various benchmark models. These discovery (exclusion) reach will increase to 30–34 (36–40) with a higher luminosity of 10 ab^{-1}. The great reach of the SPPC for Z' will provide valuable insights into BSM physics.

New Di-jet Resonances

The SPPC will have unprecedented reach for high mass as well as weakly coupled resonances in the two-jet final state. In addition, the increased energy reach of the SPPC will

[6]The reach is reduced if the dilepton branching ratios are significantly reduced due to BSM decay channels [99, 109].

probe new scales for evidence of quark compositeness. Such sensitivity studies are very useful not only to demonstrate the power of new machines, but also because they identify possible regions in the coupling vs. mass plane for resonance searches that, in order to be covered, impose minimum requirements on machine luminosity and the trigger system. The di-jet system, in particular, is of primary importance for calibrating detector response in the hadronic environment.

Aside from experimental motivations, many BSM theories predict new resonances in the two-jet final state. New gauge symmetries, for example, should have massive vector resonances to avoid strong constraints on new long-distance forces. Composite Higgs models also generally have new di-jet resonances at high masses as a part of the UV completion. We will focus on Z'_B and coloron resonances [117, 118], which are flavor-universal color singlet and color octet vector resonances, as well as level-2 Kaluza-Klein gluons in universal extra dimensions (UED) [119]. For sensitivity to Randall-Sundrum model gluons, see Ref. [120]. The Z'_B, coloron, and UED models only introduce two new parameters: the effective coupling of the new resonance to quarks and the resonance mass.

Finally, the di-jet final state can also be used to probe quark compositeness [121]. Here, the scale of quark compositeness is assumed to be too high to be seen directly, and so the scattering behavior of quarks is perturbed by new chiral exchange structures which manifest as angular correlations in high di-jet mass events. We focus on resonance searches in this contribution, but a discussion of the phenomena and corresponding reach for future machines can be found in Ref. [121].

QCD Background

We begin by presenting our simulation procedure for the di-jet final state for resonance searches at future high-energy proton-proton colliders. The quantum chromodynamic background for resonance searches is modeled in MadGraph 5 v.1.5.7 [47] with the CTEQ6L1 PDFs [122] interfaced with PYTHIA v6.4.20 [48] for parton showering and hadronization: we use MLM [123] matching between two-jet and three-jet final states. The event samples for $\sqrt{s}$ = 14 TeV, 33 TeV, and 100 TeV are generated in increasing bins of leading jet p_T, as shown in Table 7.2, similar to the procedure from Refs. [124, 125], in order to preserve large statistics at the high mass tail of the di-jet mass distribution. Events are clustered using FASTJET v.3.0.2 [126] by the anti-k_T algorithm [79] with distance parameter $R = 0.5$. We do not include any interference between signal and background for the resonance searches, and so the background sample is identical for each of the BSM searches. The di-jet invariant mass is constructed following the CMS analysis [127], where the two leading p_T jets are used as seed jets. Then, subleading jets within $\Delta R = 1.1$ are added to the closest seed jet to form two wide jets, whose invariant mass is shown for the background samples in Fig. 7.10.

Z'_B and Coloron Signal

Having constructed our background sample for the resonance searches, we now focus on the Z'_B and coloron signal models. Again, the Z'_B is a baryon-number coupled, color-singlet massive vector resonance, with a universal coupling to quarks given by

$$\mathcal{L} \supset \frac{g_B}{6} Z'_{B\mu} \bar{q} \gamma^\mu q \, . \tag{7.11}$$

p_T bin	14 TeV	33 TeV	100 TeV
1	$0.100 - 0.150$	$0.200 - 0.300$	$0.500 - 0.650$
2	$0.150 - 0.200$	$0.300 - 0.400$	$0.650 - 0.800$
3	$0.200 - 0.250$	$0.400 - 0.550$	$0.800 - 1.00$
4	$0.250 - 0.325$	$0.550 - 0.700$	$1.00 - 1.30$
5	$0.325 - 0.400$	$0.700 - 0.850$	$1.30 - 1.55$
6	$0.400 - 0.500$	$0.850 - 1.00$	$1.55 - 1.80$
7	$0.500 - 0.650$	$1.00 - 1.25$	$1.80 - 2.10$
8	$0.650 - 0.800$	$1.25 - 1.50$	$2.10 - 2.40$
9	$0.800 - 1.00$	$1.50 - 1.75$	$2.40 - 2.70$
10	$1.00 - 1.20$	$1.75 - 2.00$	$2.70 - 3.00$
11	$1.20 - 1.40$	$2.00 - 2.30$	$3.00 - 3.50$
12	$1.40 - 1.60$	$2.30 - 2.75$	$3.50 - 4.00$
13	$1.60 - 1.80$	$2.75 - 3.10$	$4.00 - 4.75$
14	$1.80 - 2.00$	$3.10 - 3.50$	$4.75 - 5.50$
15	$2.00 - 2.25$	$3.50 - 4.00$	$5.50 - 6.25$
16	$2.25 - 2.50$	$4.00 - 4.50$	$6.25 - 7.00$
17	$2.50 - 2.80$	$4.50 - 5.00$	$7.00 - 8.50$
18	$2.80 - 3.00$	$5.00 - 6.00$	$8.50 - 10.0$
19	$3.00 - 3.30$	$6.00 - 7.00$	$10.0 - 12.5$
20	$3.30 - 3.75$	$7.00 - 8.50$	$12.5 - 15.0$
21	$3.75 - 4.10$	$8.50 - 10.0$	$15.0 - 17.5$
22	$4.10 - 4.50$	$10.0 - 11.5$	$17.5 - 20.0$
23	$4.50 - 6.00$	$11.5 - 13.0$	$20.0 - 25.0$
24	$6.00+$	$13.0+$	$25.0+$

Table 7.2 Kinematic bins of leading jet p_T used in the QCD background production.

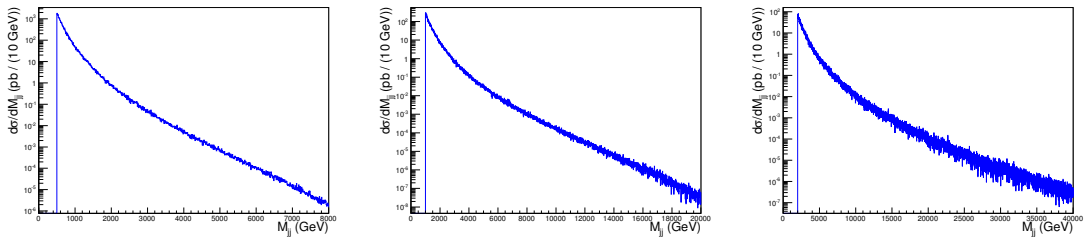

Figure 7.10 Background samples generated for QCD at (**left**) 14 TeV, (**middle**) 33 TeV, (**right**) 100 TeV as described in the text. Taken from Ref. [118].

As is well known, a gauged $U(1)_B$ baryon number requires new matter content in addition to the Standard Model, since global baryon number is anomalous in the Standard Model. Details of this model completion can be found in Ref. [117] and references therein.

We adopt the renormalizable coloron model [128] as the baseline framework for constructing a massive color octet resonance. The model begins with two parent $SU(3)$ gauge symmetries, where a bifundamental scalar field acquires a vacuum expectation value and breaks the $SU(3) \times SU(3)$ symmetry to the diagonal subgroup, which we identify as $SU(3)_c$. The SM quarks are all charged under one of the parent $SU(3)$ symmetries, lead-

ing to flavor universal couplings to the massive vector partner of the $SU(3)$ gluon, known as the coloron. The Lagrangian term between the coloron and the SM quarks is

$$\mathcal{L} \supset g_s \tan\theta \bar{q}\gamma^\mu T^a G'^a_\mu q \,, \tag{7.12}$$

with g_s as the strong coupling constant and $\tan\theta$ is the ratio of the two parent $SU(3)$ gauge couplings. The Z'_B and coloron are hence benchmark models for s-channel $q\bar{q}$ resonances that are probed via di-jet searches at hadron colliders.

We analyze the di-jet search sensitivity at the 14 TeV LHC, a possible 33 TeV pp collider, and a future 100 TeV pp collider. Signals are generated using MadGraph 5 with CTEQ6L1 PDFs interfaced with Pythia for showering and hadronization, and then passed through PGS v4 [129] for basic detector simulation.

Using our samples for QCD background and signal, we conduct a resonance search using a Crystal Ball fit on the signal distribution to identify the sharp Gaussian peak (cf. Appendix of [117]). To estimate the statistical significance $\sigma = N_S/\sqrt{N_S + N_B}$ of this signal peak, we compare the number of signal events within 3 standard deviations of the Gaussian center to the number of QCD events in the same mass window: we ignore systematic uncertainties, though these are certainly important when the resonance becomes very weakly coupled.

The results for the Z'_B resonance are shown in Fig. 7.11 for 5σ discovery sensitivity and 95% C.L. exclusion. We have reproduced the current exclusion limits from Ref. [117], which summarizes di-jet limits from Refs. [127, 130–137] as well as the latest ATLAS results [138]. The increasing reach to higher resonance masses is clear, but at the other end, we use dotted lines for each machine to indicate uncertainty about the extrapolation of the multijet trigger to lower mass thresholds. These thresholds essentially dictate the minimum resonance mass that future colliders will be able to probe, and hence motivate manifold considerations between detector design, triggers, and luminosity in order to ensure sensitivity gaps do not arise when we progress to the next machine.

We see that future hadron colliders have incredible reach for new, weakly-coupled di-jet resonances as well as heavy resonance states. For the 14 TeV LHC using 300 fb^{-1} luminosity, a Z'_B resonance as heavy as 4.5 (5.3) TeV or as weakly coupled as $g_B \sim 0.65$ (0.4) could be discovered (excluded), while using 3 ab^{-1} of integrated luminosity would push the mass reach to 5.5 (6.1) TeV and coupling reach to $g_B \sim 0.35$ (0.2) for discovery (exclusion). At a 33 TeV or a 100 TeV collider with 3 ab^{-1} of luminosity, the reach for discovery (exclusion) moves to 11.5 (13) TeV and 28 (34) TeV, respectively. Using 15 ab^{-1} at 100 TeV moves the discovery reach to 33 TeV and the exclusion reach to 38 TeV.

Similarly impressive results are obtained for the coloron model. We see that the 14 TeV LHC with 300 fb^{-1} can discover (exclude) colorons as heavy as 6.5 (7.5) TeV or couplings as small as $\tan\theta \sim 0.08$ (0.04), while increasing the luminosity to 3 ab^{-1} improves the discovery (exclusion) reach to 7.5 (8.5) TeV in mass and 0.045 (0.030) in $\tan\beta$. A $\sqrt{s} = 33$ TeV or $\sqrt{s} = 100$ TeV collider and 3 ab^{-1} dataset can push this sensitivity as high as 16 (18) TeV and 40 (44) TeV for discovery (exclusion), respectively. A 15 ab^{-1} dataset at 100 TeV can discover (exclude) a 43 (48) TeV resonance. These hugely impressive prospects lend strong support to the possibility of a future hadron collider at very high center of mass energy.

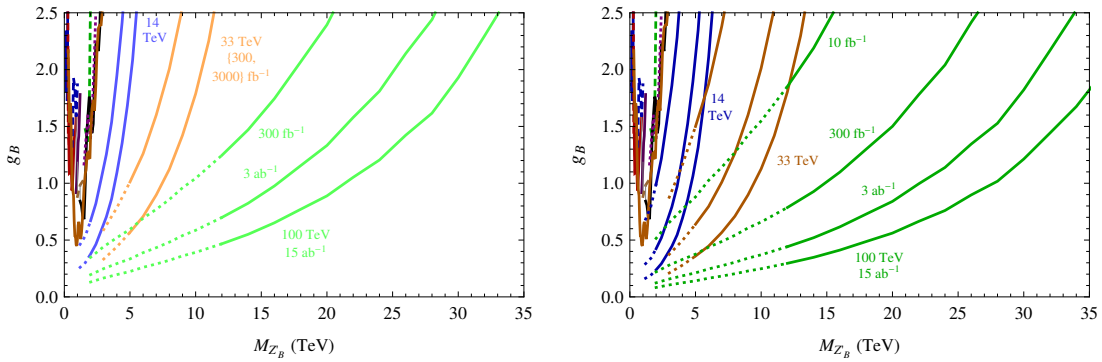

Figure 7.11 **Left**: Leading experimental limits and projected 5σ discovery sensitivity contours for 14 TeV (light blue solid), 33 TeV (light orange solid), and 100 TeV (light green solid). **Right**: Leading experimental limits and projected 95% C.L. exclusion contours for 14 TeV (dark blue solid), 33 TeV (dark brown solid), and 100 TeV (dark green solid) pp colliders in the coupling g_B versus mass $M_{Z'_B}$ plane for Z'_B resonances. The dotted continuation of each projection line to low masses indicates an extrapolation to low multijet trigger thresholds. Updated from Ref. [118].

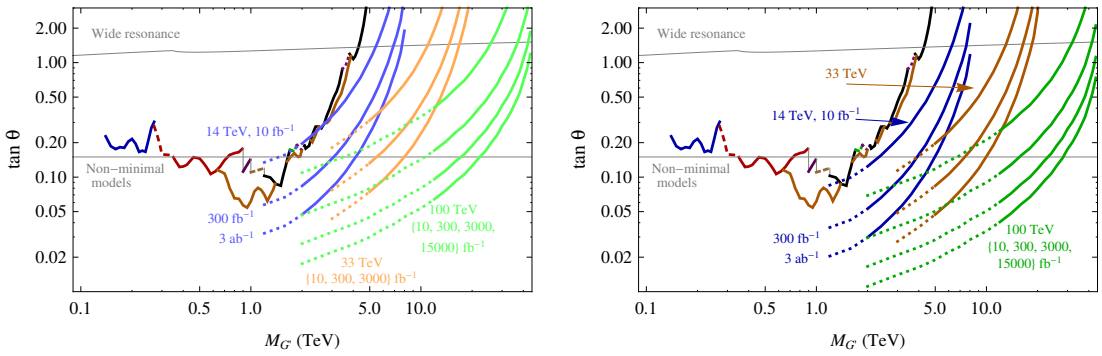

Figure 7.12 Leading experimental limits and (**left**) projected 5σ discovery sensitivity contours and (**right**) 95% C.L. exclusion contours for 14 TeV (blue solid), 33 TeV (brown solid), and 100 TeV (green solid) pp colliders in the coupling $\tan\theta$ versus mass $M_{G'}$ plane for coloron resonances. Values of $\tan\theta$ above each line are excluded at the 95% C.L. The dotted continuation of each projection line to low masses indicates an extrapolation to low multijet trigger thresholds. Updated from Ref. [118].

Kaluza-Klein Gluon

We now present results for di-jet resonances in models with extra dimensions. Universal Extra Dimensions (UED) models, introduced in [139], provide phenomenological connections between collider and dark matter. We consider a minimal UED model implementation that ascribes a coupling between the level-2 Kaluza Klein (KK) gauge boson to two SM fermions as a result of loop-induced effects from the level-1 KK particles. The resulting vertex for level-2 KK gluons and SM quarks [119, 140–142] is

$$ig_3\frac{\lambda^a}{2}\gamma^\mu\left[\frac{1}{\sqrt{2}}\frac{1}{16\pi^2}\ln\left(\frac{\Lambda R}{2}\right)^2\left(-\frac{11}{2}\right)g_3^2\right], \tag{7.13}$$

where λ^a are the Gell-Mann matrices, g_3 is the $SU(3)$ coupling constant, R is the radius of the extra dimension, and Λ is the cutoff scale. We see that R and Λ control the coupling and the mass of the resonance. Correspondingly, we present the discovery and exclusion

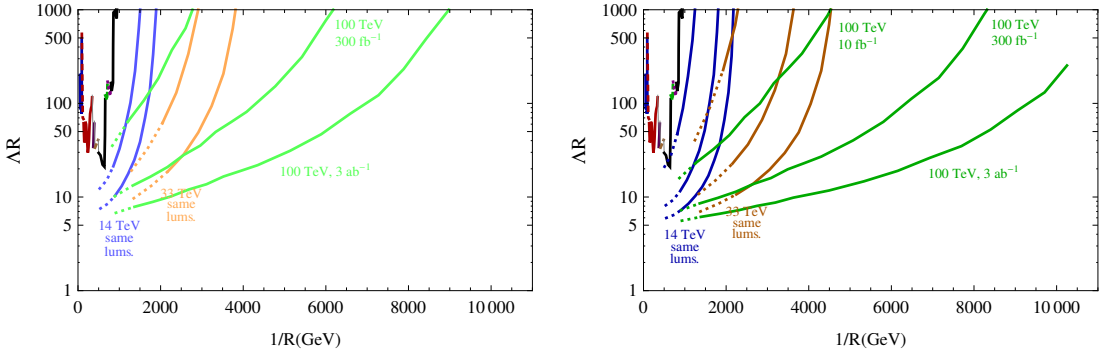

Figure 7.13 **(Left)** Current limits and projected 5σ discovery and **(right)** current limits and projected 95% C.L. exclusion limits for the level-2 KK gluon as a dijet resonance in MUED. The dotted continuation of each projection line indicates an extrapolation to low multijet trigger thresholds. Taken from Ref. [119].

contours for the level-2 KK gluon in the ΛR vs. R^{-1} plane in Fig. 7.13 for a future proton-proton collider. The current limit touches $\Lambda R \approx 20$, but future luminosity from the 14 TeV could push the exclusion reach to $\Lambda R \approx 6$. For higher masses, the 100 TeV machine has impressive reach into the multi-TeV range for R^{-1}. Prospects for more complicated model constructions, such as non-minimal UED models, can be found in Ref. [119].

A curious feature of UED models is the KK tower states that occurs at integer multiples of the lowest-lying resonances. Resonance searches that probe the KK gluon mass scale also constrain the cutoff scale in minimal UED, and if a new KK resonance is seen at the 14 TeV LHC, it is possible and intriguing to consider that higher modes will be accessible and discovered with a 100 TeV collider.

Summary

We have demonstrated that future proton-proton colliders will have clear discovery potential for high-mass resonances in the two-jet final state. In addition, the large integrated luminosity, if appropriately complemented by low multijet trigger thresholds, also provides unprecedented sensitivity to weakly coupled, light resonances.

Z' as Mediator between Dark Matter and the Standard Model

In this section we study the dark matter detectability at the future hadron colliders in the framework of a simplified Z' model [143]. Although the effective operator approach provides a simpler parameterization of the DM interaction with the SM particles [144, 145], its usefulness to guide collider studies is limited. First of all, at high energy colliders, generically, integrating out the mediator is not a good approximation. This is already questionable at LHC 7 and 8 TeV runs [146–148]. It will be much more problematic at higher energies, in particular at the SppC. Secondly, ignoring the details of DM interaction with the SM leads us to miss additional, and in many cases even the leading, signal of the models. A useful next step to go beyond the effective operator approach is to consider the simplified, and yet UV complete, models. One obvious possibility is to introduce simple mediators between the dark matter and the SM fields. Such simplified models do have more parameters than the effective operator approach. However, it is necessary to consider them in order to get a comprehensive coverage of possible signals of dark matter. In computing the direct detection constraints, it is straightforward to map the simplified models to the effective operators. However, the difference of the two approaches are in

the reach of the collider searches. In this section, we consider this in the context of high energy proton colliders.

Constraint for Generic Z' Models

As an example of the simplified mediator models, we consider the mediator to be a new Z' gauge boson [143, 147, 149–159]. In general, the couplings of Z' to quarks g_q may depend on quark flavors and should be determined by the details of UV models. For simplicity, we assume g_q is universal for all the quarks. The interactions can be described by

$$\mathcal{L}_{\rm FV} = \left(\sum_q g_q \bar{q}\gamma_\mu q + g_\chi \bar{\chi}\gamma_\mu \chi\right) Z'^\mu, \tag{7.14}$$

$$\mathcal{L}_{\rm FA} = \left(\sum_q g_q \bar{q}\gamma_\mu\gamma_5 q + g_\chi \bar{\chi}\gamma_\mu\gamma_5 \chi\right) Z'^\mu, \tag{7.15}$$

$$\mathcal{L}_{\rm SV} = \left(\sum_q g_q \bar{q}\gamma_\mu q + g_\chi \chi^* i\overleftrightarrow{\partial_\mu}\chi\right) Z'^\mu, \tag{7.16}$$

where the subscripts FV and FA denote Dirac fermionic DM with vector and axial vector mediator, respectively. $\mathcal{L}_{\rm SV}$ is the interaction between a complex scalar DM and the vector mediator. There are 4 parameters characterizing these models, i.e., m_χ, $m_{Z'}$, g_q, and g_χ. It should be noted that besides the monojet signature, dijet resonance searches could also set stringent constraints on g_q via the on-shell Z' production $q\bar{q} \to Z' \to q\bar{q}$ [147].

We investigate the monojet + $\not{E}_{\rm T}$ signature at a pp collider with $\sqrt{s} = 33$, 50 and 100 TeV, assuming an integrated luminosity of 3 $\rm ab^{-1}$. A set of parameters corresponding to the ATLAS detector are adopted for fast detector simulation. The jets are clustered using the anti-k_T algorithm with a distance parameter of $R = 0.4$. The following selection cuts have been imposed to suppress SM backgrounds for $\sqrt{s} = 33/50/100$ TeV:

- The leading jet j_1 is required to have $p_T > 800/1000/1600$ GeV and $|\eta| < 2.4$.
- No more than 2 jets with $p_T > 100$ GeV and $|\eta| < 4$ are rejected. A second jet j_2 is allowed if $\Delta\phi(j_1, j_2) < 2.5$.
- No any isolated e, μ, τ, or γ with $p_T > 20$GeV and $|\eta| < 2.5$.
- $\not{E}_{\rm T} > 800/1000/1600$ GeV.

For simplicity, we set $g_\chi = g_q$. The estimated 90% C.L. limits for $m_{Z'} = 1$ and 5 TeV in the m_χ-g_q plane are shown in Fig. 7.14.

The cross section for the DM production $pp \to \chi\bar{\chi}$ + jets depends significantly on whether the mediator Z' is on-shell or not. The momentum transfer Q^2 in the Z' propagator must be larger than $4m_\chi^2$ to produce a DM particle pair. When Z' is off-shell and $m_{Z'}^2 \ll Q^2$, the cross section scales as $(g_q g_\chi/Q^2)^2$. When Z' is off-shell and $m_{Z'}^2 \gg Q^2$, the cross section scales as $(g_q g_\chi/m_{Z'}^2)^2$ and can be matched to the cross section in the EFT approach with an effective energy scale of $\Lambda_{\rm eff} = m_{Z'}/\sqrt{g_q g_\chi}$. On the other hand, if Z' is on-shell produced and then decays into a pair of DM particles, the production cross section would be resonantly enhanced, and scale as $g_q^2 \cdot {\rm Br}(Z' \to \chi\bar{\chi})$ under the narrow width approximation. The sensitivities of the monojet search drop quickly when

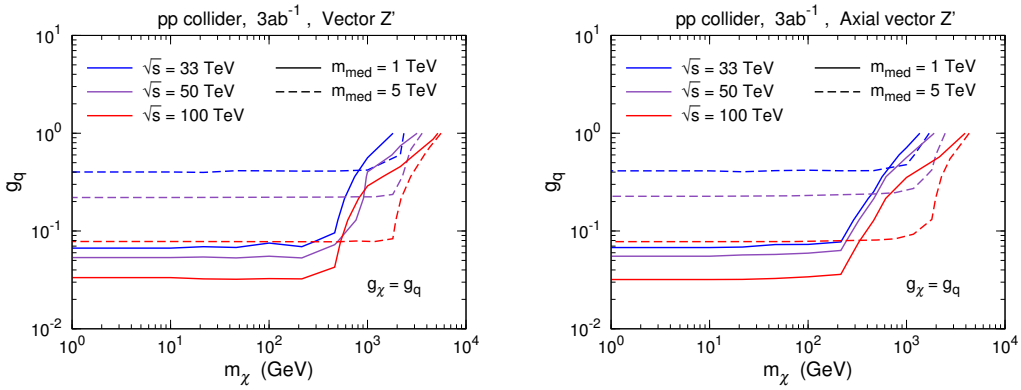

(a) Fermionic DM with vector Z'.

(b) Fermionic DM with axial vector Z'.

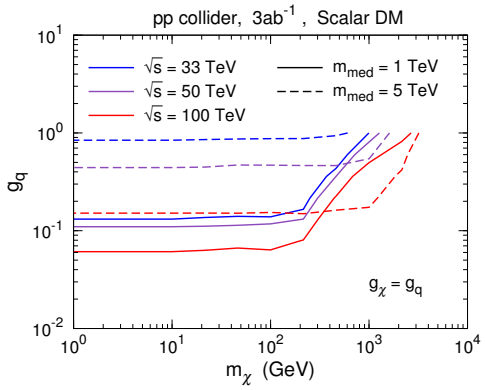

(c) Scalar DM with vector Z'.

Figure 7.14 Estimated 90% C.L. limits in the m_χ-g_q plane for the $\mathrm{monojet} + \not{E}_{\mathrm{T}}$ channel at a pp collider with $\sqrt{s} = 33$ TeV (blue lines), 50 TeV (purple lines) and 100 TeV (red lines), assuming an integrated luminosity of 3 ab^{-1}. The solid and dashed lines correspond to $m_{Z'} = 1$ TeV and 5 TeV, respectively. The regions above the curves are expected to be excluded. We have assumed $g_\chi = g_q$.

m_χ becomes larger than $m_{Z'}/2$ due to the Z' off-shell effect. As a result, for a large enough value of m_χ, the collider search can be more sensitive to a heavier on-shell Z' than a lighter off-shell Z'.

For fixed $m_{Z'}$, g_q, and g_χ, the production cross section of the scalar DM is much smaller than that of the fermionic DM. The reason is that the scalar DM particle has less helicity states and its pair production suffers a kinematic suppression in the angular distribution. Therefore, the SppC sensitivity for the scalar DM will be weaker than that for the fermionic DM.

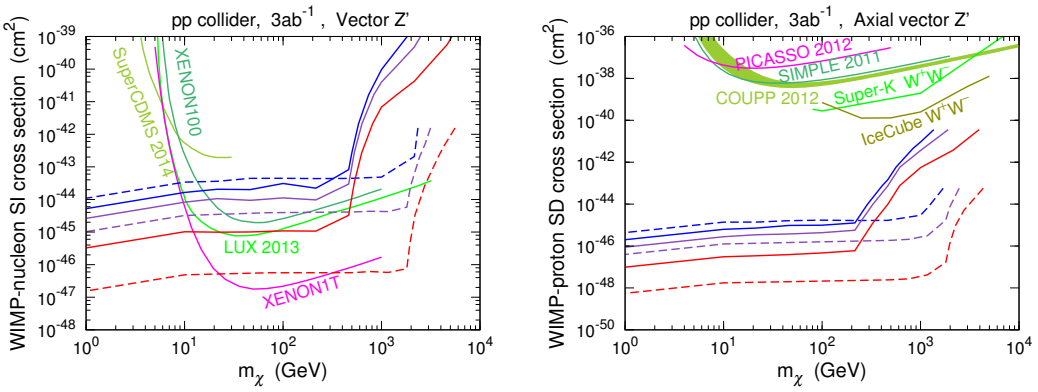

(a) Fermionic DM with vector Z', SI. (b) Fermionic DM with axial vector Z', SD.

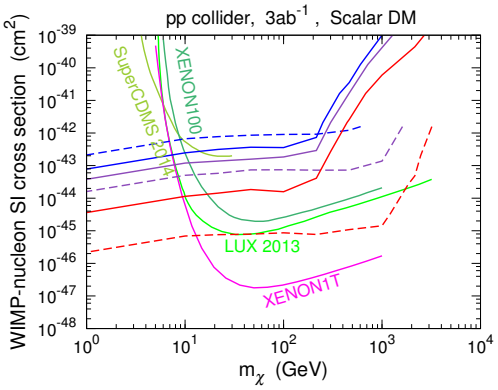

(c) Scalar DM with vector Z', SI.

Figure 7.15 Estimated 90% C.L. limits from the monojet search in the m_χ-$\sigma_{\chi N}$ plane. Blue/purple/red lines correspond to $\sqrt{s} = 33/50/100$ TeV. An integrated luminosity of 3 ab^{-1} is assumed. The cases for $m_{Z'} = 1$ TeV and $m_{Z'} = 5$ TeV are indicated by solid and dashed lines, respectively. For the SI scattering, the recent limits from direct detection experiments XENON100 [160], LUX [161], SuperCDMS [162], and the expected reach of XENON1T [163] are also shown. For the SD scattering, the limits from SIMPLE [164], PICASSO [165], and COUPP [166] are also shown, as well as the limits from neutrino detection experiments Super-K [167] and IceCube [168].

The vector and axial vector DM-quark interactions induce spin-independent (SI) and spin-dependent (SD) scatterings in direct detection experiments, respectively. The translated 90% C.L. limits from the monojet search in the m_χ-$\sigma_{\chi N}$ plane are shown in Fig. 7.15, where $\sigma_{\chi N}$ is the DM-nucleon scattering cross section. For the vector interaction, direct detection experiments have set stringent constraints. The SppC has a better capability to search for light DM with $m_\chi \lesssim 10$ GeV, where direct searches lose their sensitivity dra-

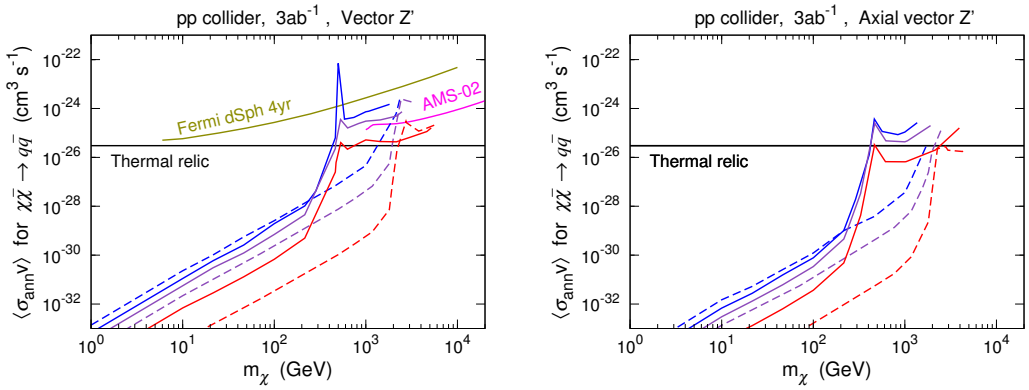

(a) Fermionic DM with vector Z'. (b) Fermionic DM with axial vector Z'.

Figure 7.16 Estimated 90% C.L. limits from the monojet search in the m_χ-$\langle\sigma_{\rm ann}v\rangle$ plane. The left (right) panel represents the limits on the fermionic DM interacting with a vector (axial vector) Z', whose mass is 1 TeV for solid lines and 5 TeV for dashed lines. Blue/purple/red lines correspond to $\sqrt{s} = 33/50/100$ TeV and an integrated luminosity of 3 $\rm ab^{-1}$. For the axial vector interaction, since the velocity dependent p-wave annihilation is important due to the helicity suppression in s-wave, we take the DM velocity dispersion as $\langle v^2\rangle = 0.24$ to calculate $\langle\sigma_{\rm ann}v\rangle$ at the freeze-out epoch [169]. For a comparison, also shown are the recent limits from the Fermi-LAT gamma-ray detections on the dwarf galaxies [170], and the expected limits from the CTA gamma-ray detection on the dwarf galaxy Segue 1 [171] and from the AMS-02 anti-proton detections.

matically. For the axial vector interaction, constraints from the direct detection are very weak. The monojet search at the SppC will significantly improve current limits by several orders of magnitude.

In Fig. 7.16, we show the translated 90% C.L. limits from the monojet search in the m_χ-$\langle\sigma_{\rm ann}v\rangle$ plane, where $\langle\sigma_{\rm ann}v\rangle$ is the thermal average DM annihilation cross section. The vector interaction leads to the s-wave DM annihilation and can be explored by gamma-ray [172] and cosmic-ray observations[173, 174]. The SppC could have a better sensitivity for $m_\chi \lesssim m_{Z'}/2 \lesssim \mathcal{O}(1)$ TeV. For the axial vector interaction, the DM annihilation is helicity suppressed in s-wave and highly depends on DM velocity dispersion in the Galaxy. Therefore, it cannot be explored by indirect detection experiments. At the SppC, it is possible to exclude the thermally produced DM with $m_\chi \lesssim m_{Z'}/2$.

For fixed g_q and g_χ, the estimated 90% C.L. limits can be expressed in the $m_{Z'}$-m_χ plane, as shown in Fig. 7.17 for $\sqrt{s} = 50$ TeV and an integrated luminosity of 3 $\rm ab^{-1}$. For large couplings as $g_q = g_\chi = 1$, the monojet search can explore the mass parameter space up to $m_{Z'} \sim 10$ TeV and $m_\chi \sim \mathcal{O}(\rm TeV)$. Limits from direct and indirect searches are also mapped into the $m_{Z'}$-m_χ plane, assuming $g_q = g_\chi = 0.5$. For the axial vector Z', direct and collider searches are complementary to each other, since they probe orthogonal directions in the mass parameter space [150].

Since the simplified model described by $\mathcal{L}_{\rm FA}$ involves a massive vector boson coupling to nonconserved currents, it has a dangerous UV behavior that leads to a quickly increasing of DM production cross section when the energy scale becomes much higher than $m_{Z'}$. Consequently, as shown in Fig. 7.17(b), the sensitivity for $g_q = g_\chi > 0.3$ is unusually improved for $m_{Z'} \lesssim 40$ GeV. In this region, the production process $q\bar{q} \to \chi\bar{\chi}$ may violate the perturbative unitarity. For $g_q = g_\chi = 1$, the unitary bound for this process with appropriate center-of-mass energy are demonstrated in Fig. 7.17(b) with the light red

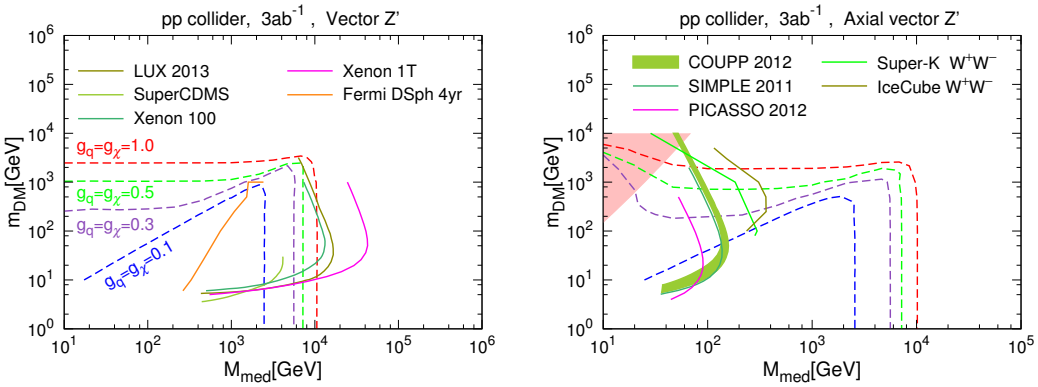

(a) Fermionic DM with vector Z'. (b) Fermionic DM with axial vector Z'.

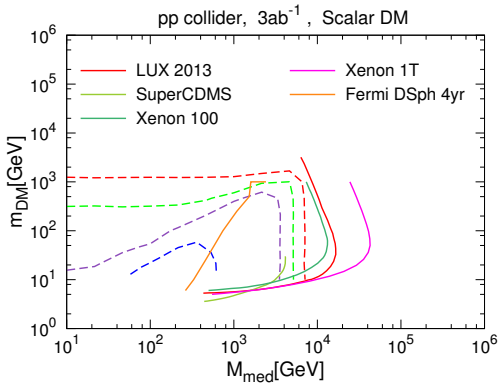

(c) Scalar DM with vector Z'.

Figure 7.17 Estimated 90% C.L. limits in the $m_{Z'}$-m_χ plane for the monojet + $\not{E}_{\rm T}$ channel at the SppC with $\sqrt{s} = 50$ TeV, assuming an integrated luminosity of 3 $\rm ab^{-1}$. Dashed blue/purple/green/red lines correspond to $g_q = g_\chi = 0.1/0.3/0.5/1.0$. Limits from direct and indirect searches assuming $g_q = g_\chi = 0.5$ are also shown. The light red region in the frame (b) indicates the unitarity violation region for $g_q = g_\chi = 1$.

color. In this case, the simplified model with only Z' is not sufficient. A full UV-complete model is needed.

7.3 New Phenomena of Standard Model Physics

Jets

At energies above about 1 GeV, quantum chromodynamics (QCD) is a weakly-coupled, asymptotically free gauge theory. Because of soft and collinear singularities that arise at every perturbative order, collimated streams of particles, called jets, are produced at high energies. Jets are ubiquitous in high energy proton collisions produced from QCD dynamics and are typically the dominant decay modes of electroweak-scale particles, the W, Z and H bosons and the top quark. Looking forward to a 100 TeV future proton collider, jets will be produced with even higher rates than at the Large Hadron Collider (LHC), and therefore, for both understanding QCD as well as searching for new physics, detailed analyses and understanding of jets will be absolutely necessary.

Jets, as experimental objects, require algorithms to be well-defined. The most widely used jet algorithms are sequential clustering algorithms, with the anti-k_T algorithm [79] the standard at the LHC. Sequential jet algorithms are defined by two features: the clustering metric and the recombination scheme. The clustering metric defines how close two particles (or whatever the inputs to the jet algorithm are), and whether or not they should be clustered and identified as coming from a common splitting. For the k_T-type algorithms, the clustering metric is

$$d_{ij} = \min[p_{Ti}^n, p_{Tj}^n] \frac{R_{ij}^2}{R_0^2}\,, \tag{7.17}$$

where p_{Ti} is the transverse momentum with respect to the beam of particle i, R_0 is the jet radius and R_{ij} is the distance between particle i and j in the rapidity-azimuth plane. The integer n defines the jet algorithm; $n = 1$ is the k_T algorithm [175, 176], $n = 0$ is the Cambridge/Aachen algorithm [177–179], and $n = -1$ is the anti-k_T algorithm. For all pairs of particles $\{i, j\}$ in the event, d_{ij} is calculated and the closest pair of particles are combined.

Once the pair of particles that are closest according to the clustering metric are found, how they are recombined still needs to be defined. The ubiquitous recombination scheme used at the LHC is the E-scheme [180] where the particles are clustered by simply adding their four-momentum. This has some desirable properties; for example, the jet axis from recombination coincides with the sum of the four-momenta of all of the jet's constituents. However, this recombination scheme has the undesirable feature that it is sensitive to contamination in the jet and this can result in significant displacement of the jet axis from the direction of the original high energy parton that generated the jet.

At a high luminosity proton collider, like the LHC or a proposed 100 TeV machine, there can be a significant number of secondary proton collisions per bunch crossing, in addition to the hard proton scattering. These secondary collisions are referred to as pile-up, and can deposit a significant amount of radiation in each even that is uncorrelated with and contaminates the physics of the hard process. At the end of Run 1 of the LHC, the number of pile-up interactions per bunch crossing was up to 30, while projections of the number pile-up interactions at a 100 TeV collider ranging up to 200 or more. Relevant for

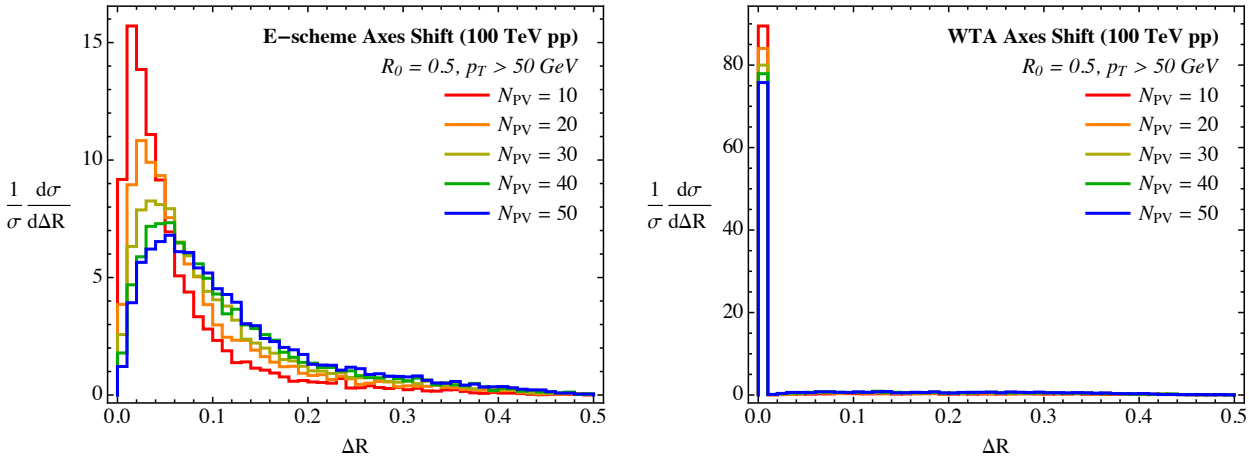

Figure 7.18 The angular shift of the jet axis due to pileup, comparing the standard E-scheme jet axis (left) to the WTA jet axis (right), sweeping the number of pileup vertices N_{PV}.

the reconstruction of jets, this pile-up radiation will in general be clustered into jets and affect both the energy and direction of the jets.

The jet axis direction is determined by both the clustering metric and the recombination scheme. Most importantly, the recombination scheme determines the response of the jet axis to the momenta of the particles in the jet. By definition, the jet axis as defined by the E-scheme is sensitive to the addition of contamination radiation in the jet, because this contamination will affect the net four momentum of the jet. This response, referred to as recoil [181–184], can significantly displace the jet axis from the direction of the hard particles, that are typically thought of as arising from the final-state parton shower of the initiating hard parton. This effect of recoil can be reduced or essentially eliminated by simply changing the recombination scheme of the jet algorithm. Instead of summing the four momenta of the particles at each stage in the clustering, we can define the Winner-Take-All (WTA) recombination scheme [185–187] for which the clustered particle's momenta aligns with the direction of the harder of the two particles in the clustering. That is, for particles i and j that are clustered, the momentum of the clustered particle J is defined as

$$\begin{aligned} p_{TJ} &= p_{Ti} + p_{Tj}, \\ \phi_J &= \begin{cases} \phi_i, & p_{Ti} > p_{Tj}, \\ \phi_j, & p_{Tj} > p_{Ti}, \end{cases} \\ \eta_J &= \begin{cases} \eta_i, & p_{Ti} > p_{Tj}, \\ \eta_j, & p_{Tj} > p_{Ti}. \end{cases} \end{aligned}$$

The WTA recombination scheme is insensitive to recoil and so the jet direction coincides with the direction of the hardest particle in the jet. This is essentially never contamination, so the WTA recombination scheme produces jets that are much less sensitive to contamination than the E-scheme axis.

To demonstrate the insensitivity of the WTA scheme to recoil, we can measure the angle between the jet axis before and after the addition of a number of pile-up vertices in Monte Carlo simulation. We have simulated events at a 100 TeV proton collider with PYTHIA 8.183 [48, 188] at Born-level only with no fixed-order corrections. Jet analyses are done with FASTJET 3.0.3 [126] at the particle level, with no detector simulation. The

WTA recombination scheme is implemented in the `Nsubjettiness` FASTJET contrib [189]. In Fig. 7.18, we plot the angle between the jet axis before and after the addition of pile-up with the traditional E-scheme and WTA scheme jet with a minimum transverse momentum of 50 GeV at a 100 TeV collider. The number of pile-up vertices ranges from 10 to 50, and the angle between the E-scheme axes significantly drift as the number of pile-up vertices increases, demonstrating the recoil-sensitivity. By contrast, even with 50 pile-up vertices, the WTA jet axis is amazingly robust, with the vast majority of jets with identical axes before and after the addition of pile-up.

Motivated by studies of jet substructure and boosted objects at the LHC, there have been numerous observables defined on jets for both the discrimination of QCD jets from boosted electroweak as well as studying QCD itself [190–192]. A potentially useful observable for both discrimination and studying QCD is the energy fraction of the softer particle in first branching as defined by a sequential jet algorithm. For relatively narrow QCD jets, the distribution of this energy fraction should be set by the splitting functions and so provides a direct probe into the universal collinear structure of QCD. However, such an observable is not infrared and collinear (IRC) safe, and so its distribution cannot be calculated order-by-order in perturbation theory. This property would seem to preclude any prediction of such an observable in QCD.

Nevertheless, there exist a class of IRC unsafe observables whose distributions are calculable when all-orders effects are included. Such observables are referred to as Sudakov safe [193], as the perturbative Sudakov factor exponentially suppresses the singular region of phase space, controlling divergences in perturbation theory and rendering these observables well-defined and finite. However, because these observables cannot be calculated order-by-order in perturbation theory, their distributions do not have analytic dependence on the coupling. Examples of Sudakov safe observables include ratios of IRC safe observables, whose distributions have an expansion in $\sqrt{\alpha_s}$, manifesting non-analyticity. Additionally, observables have been defined whose distributions are actually independent of α_s, at sufficiently high energies [194, 195].

The p_T fraction observable is another example of Sudakov safety. To be concrete, we will define the p_T fraction of the branching as follows, which effectively employs the modified mass drop tagger [196, 197] or soft drop groomer [194]. We recluster the jet with the Cambridge/Aachen algorithm, which angular orders the particles composing the jet. Then, beginning at the trunk of the Cambridge/Aachen branching tree, we step through the subsequent branches. At each branching, we demand that:

$$\frac{\min[p_{Ti}, p_{Tj}]}{p_{Ti} + p_{Tj}} > z_{\text{cut}} \,, \tag{7.18}$$

where i and j are the two branches and z_{cut} is some parameter. If this inequality is not satisfied, then the softer branch is thrown away, and one continues to the next branching. When the inequality of Eq. 7.18 is satisfied, the procedure terminates and we define

$$z_{\max} = \max_{\text{failed branches}} \frac{p_{T,\text{dropped}}}{p_{T,\text{dropped}} + p_{T,\text{kept}}}. \tag{7.19}$$

for the branches that fail the inequality. $z_{\max}$ is infrared safe, but not collinear safe, because the branches that fail could be exactly collinear, and yet $z_{\max}$ could take a non-trivial value.

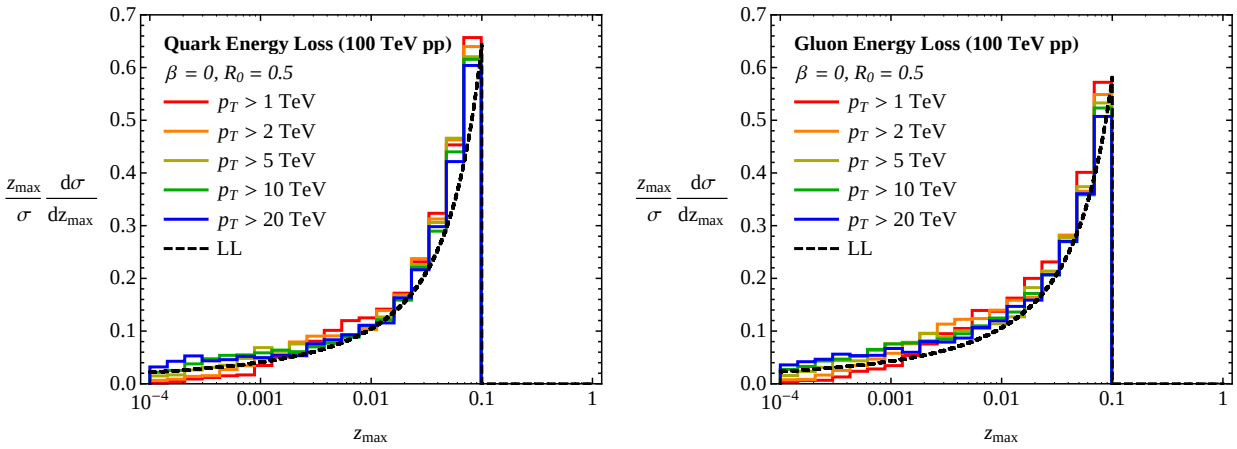

Figure 7.19 Distribution of the maximum fractional energy loss $z_{\rm max}$ for quark (left) and gluon (right) jets in the Monte Carlo sample with transverse momenta ranging from 1 to 20 TeV, compared to Eq. 7.20, in dashed black.

Nevertheless, the distribution of $z_{\rm max}$ can be calculated in perturbative QCD, with the calculation presented in [194]. At lowest order, one finds the distribution:

$$\frac{z_{\rm max}}{\sigma}\frac{d\sigma}{dz_{\rm max}} = \frac{\log\frac{1}{z_{\rm cut}} + B_i}{(\log\frac{1}{z_{\rm max}} + B_i)^2}\,, \tag{7.20}$$

where B_i are the subleading terms in the splitting functions ($B_q = -3/4$ for quarks, $B_g = -\frac{11}{12} + \frac{n_f}{6C_A}$ for gluons, where n_f is the number of light flavors). This distribution is independent of both α_s and the total jet color and only depends on the jet flavor through the subleading terms in the splitting function. In Fig. 7.19, we plot the $z_{\rm max}$ distribution in a sample of quark or gluon jets produced at a 100 TeV collider with transverse momenta ranging from 1 to 20 TeV and compare to this calculation. We have also set $z_{\rm cut} = 0.1$. The $z_{\rm max}$ distribution was determined using the implementation of the soft drop groomer in the `RecursiveTools` FastJet contrib [189]. As predicted by Eq. 7.20, the distribution of $z_{\rm max}$ is very weakly dependent on the jet p_T and is very similar between quarks and gluons. Sudakov safe observables like $z_{\rm max}$ are sensitive to very different dynamics of QCD at high energies and can directly probe physics that is obscured with traditional IRC safe observables.

W, *Z* Radiation

With access to energies significantly above the weak scale, the SPPC will probe electroweak interactions deep into their unbroken phase. Besides offering an interesting array of tests in hard electroweak interactions at multi-TeV energies, the soft/collinear structure of almost *any* multi-TeV process can become significantly altered, as the logarithmic enhancements familiar from QED and QCD will become active for electroweak emissions (see, e.g., [198–202]). Obtaining correct descriptions of the complete event structure when $E \gg m_W$ then becomes greatly facilitated by incorporating factorization and resummation, such as that provided by parton showering and parton distribution functions. In effect, we will begin to see weak bosons (including the Higgs boson) behaving as nearly-massless partons, in stark contrast to the conventional perspective in which they are viewed as "heavy" particles. Jets, whether initiated by QCD processes, electroweak

process, or new physics processes, will be found to contain electroweak splittings with probabilities at the $O(10\%)$ level. Similarly, weak bosons can usefully be thought of as collinear components of the protons, at the same level as gluons and photons.

To develop some intuition of the collinear splitting behavior of electroweak "partons," it is useful to first consider a conceptual limit with an unbroken $SU(2) \times U(1)$ gauge symmetry with massless gauge bosons and fermions, supplemented by a massless scalar doublet field ϕ without a VEV (the would-be Higgs doublet). In this limit, many processes are direct analogs of those in QED and QCD. Fermions with appropriate quantum numbers may emit (transverse) $SU(2)$ and $U(1)$ gauge bosons with both soft and collinear enhancements. The $SU(2)$ bosons couple to one another via their non-abelian gauge interactions, and undergo soft/collinear splittings of the schematic form $W \to WW$, similar to $g \to gg$. All of the electroweak gauge bosons may also undergo collinear-enhanced splittings into fermion pairs, similar to $g \to q\bar{q}$ or $\gamma \to f\bar{f}$. Beyond these, the major novelty is the introduction of the scalar degrees of freedom. First, the scalars may themselves radiate $SU(2)$ and $U(1)$ gauge bosons, with soft/collinear limits identical to their counterparts with fermionic sources. Second, the electroweak gauge bosons can split into a pair of scalars, again in close analog with splittings to fermion pairs. Third, fermions with appreciable Yukawa couplings to the scalar doublet can emit a scalar and undergo a chirality flip. Finally, the scalars can split into collinear fermion pairs.[7]

In the realistic case of spontaneously-broken symmetry, several important changes take place. Primarily, all of the soft and collinear divergences associated with the above splittings become physically regulated, effectively shutting off at $p_T \lesssim m_W$ (or m_h, m_t where appropriate). Roughly speaking, m_W plays a role similar to $\Lambda_{\rm QCD}$ in the QCD parton shower, albeit with far less ambiguity of the detailed IR structure since this regulation occurs at weak coupling. Another major difference is the mixing of the scalar doublet's Goldstone degrees of freedom into the W and Z gauge bosons, allowing for the appearance of longitudinal modes. In many cases, the longitudinal gauge bosons behave identically to the original scalars, as dictated by the Goldstone equivalence theorem [203, 204]. For example the splitting $W_T^+ \to W_L^+ Z_L$ is, up to finite mass effects, an exact analog of $W_T^+ \to \phi^+ {\rm Im}(\phi^0)$ in the unbroken theory. Similarly for longitudinal gauge boson emissions from heavy fermions, such the equivalence between $t_L \to Z_L t_R$ and $t_L \to {\rm Im}(\phi^0) t_R$.

But important exceptional cases now also occur for emissions near $p_T \sim m_W$. Most well known, even a massless fermion exhibits a kind of soft/collinear-enhanced emission of W_L and Z_L [205, 206]. These emissions have no Goldstone equivalent analog, and are highly power-suppressed for $p_T \gtrsim m_W$. But the overall population of emissions at the boundary between "broken" and "unbroken" behavior nonetheless grows logarithmically with the fermion energy. This is formally subdominant to the double-logarithmic growth of transverse emissions, but remains numerically important at multi-TeV energy scales. Emissions from massless quarks also cause the energetic initial-state protons to act as sources of longitudinal boson beams, allowing for studies of the high-energy interac-

[7] Splittings amongst the scalars, controlled by the quartic coupling in the scalar potential, would need to be of the $1 \to 3$ variety. These are still formally single-log divergent, but are expected to be rather highly numerically suppressed due to an additional $O(1/8\pi^2)$ phase space factor and the small value of the quartic required to match the known Higgs boson mass. With massive bosons, the available phase space volume further shrinks.

Process	$\mathcal{P}(p_T)$	$\mathcal{P}(1\text{ TeV})$	$\mathcal{P}(10\text{ TeV})$
$f \to V_T f$	$(3\times10^{-3})\left[\log\frac{p_T}{m_{\text{EW}}}\right]^2$	1.7%	7%
$f \to V_L f$	$(2\times10^{-3})\log\frac{p_T}{m_{\text{EW}}}$	0.5%	1%
$V_T \to V_T V_T$	$(0.01)\left[\log\frac{p_T}{m_{\text{EW}}}\right]^2$	6%	22%
$V_T \to V_L V_T$	$(0.01)\log\frac{p_T}{m_{\text{EW}}}$	2%	5%
$V_T \to f\bar{f}$	$(0.02)\log\frac{p_T}{m_{\text{EW}}}$	5%	10%
$V_T \to V_L h$	$(4\times10^{-4})\log\frac{p_T}{m_{\text{EW}}}$	0.1%	0.2%
$V_L \to V_T h$	$(2\times10^{-3})\left[\log\frac{p_T}{m_{\text{EW}}}\right]^2$	1%	4%

Table 7.3 An illustrative set of approximate total electroweak splitting rates in final-state showers [208].

tions of the effective Goldstone bosons through weak boson scattering (discussed further below). Similar types of emissions occur in the splittings of transverse bosons, such as $W_T^+ \to Z_L W_T^+ \,/\, Z_T W_L^+$.

The splittings of transverse neutral bosons present some additional subtleties, as neutral-current interference can be substantial. For example, it is tempting to generally allow splittings of the form $\gamma \to W^+W^-$ according to the W bosons' electric charge. However, suppose that the photon is produced from an interaction amongst right-handed chiral fermions. Then the corresponding diagram with the production and splitting of a Z boson would approximately cancel, as the exchanged boson is pure hypercharge when viewed in interaction basis. A correct description for general processes requires defining both the prompt production rates and the splitting rates within a density matrix formalism, very similar to the program begun by Nagy and Soper for the treatment of color and spin quantum numbers in QCD showers [207]. The electroweak case is further complicated by the nontrivial propagator structure as the Z pole is approached and the need to match onto QED. Ultimately, the final production rate of an exclusive (un-split) γ or Z state from any process at $E \gg m_Z$ can only be properly assessed after first evolving down from the hard process scale in this manner.

Table 7.3 provides a few estimates for total splitting rates of individual final-state particles, including approximate numerical values for particles produced at $p_T = 1$ TeV and 10 TeV. The $SU(2)$ self-interactions amongst transverse gauge bosons tend to give the largest rates, quickly exceeding 10% as the energy is raised above 1 TeV. This has significant impact on processes with prompt transverse boson production such as $W/Z/\gamma$+jets, and especially on multiboson production including transverse boson scattering. Generally, it is important to appreciate that *any* particle in an event, whether initial-state or final-state, or even itself produced inside of a parton shower, can act as a potential electroweak radiator. Consequently, the total rate for finding one or more electroweak splittings within a given event must be compounded, and can sometimes add up to $O(1)$.

Fig 7.20 summarizes the parton luminosities when electroweak bosons are included in the PDFs. One immediate observation from comparing the $W_T\gamma$ and W_TW_T luminosities is that transverse weak bosons begin to appear on the same footing as photons, as might have been anticipated. Ultimately, they must be folded into the full DGLAP evolution,

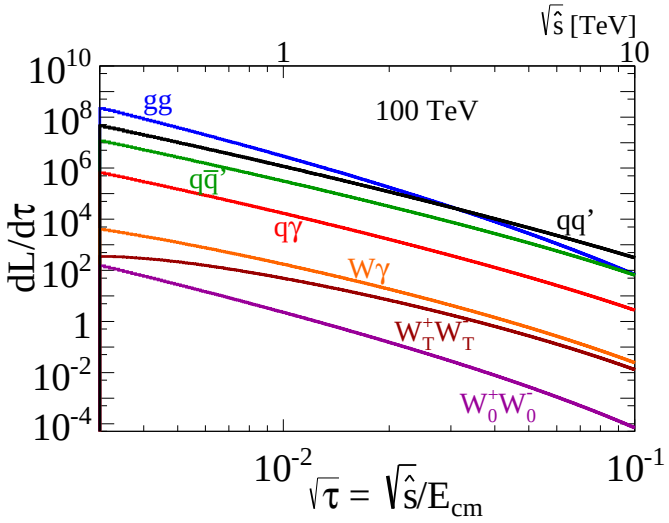

Figure 7.20 Partonic luminosities at the 100 TeV SPPC, illustrating the relative contributions from weak bosons when treated as partons in the PDFs [208].

though at SPPC energies the running effects are not yet sizable. The longitudinal bosons are sourced from the quarks as described above at $p_T \sim m_W$, with individual splitting rates $O(3\text{–}10)$ times smaller than their transverse counterparts at multi-TeV energies. This leads to $O(10\text{–}100)$ times smaller luminosities. For VBF process initiated by the longitudinal bosons, the PDF approach effectively integrates out the usual forward tagging jets, treating them as part of the "beam." This of course becomes a progressively more justifiable approach, as these jets with $p_T \sim m_W$ will appear at extremely high rapidities, and may anyway become a less distinctive feature to discriminate against backgrounds in the presence of copious QCD initial-state radiation at similar p_T. From a practical perspective, the ability to treat VBF as a $2 \to 2$ process rather than $2 \to 4$ would significantly reduce the computational burden for event simulation. The tagging jets can then be resolved using the usual initial-state radiation machinery, appropriately adapted for this unique electroweak splitting process.

W, Z Radiation in Decay of Heavy Resonances

The invisible and semi-invisible decays of a Z' and W' are difficult to probe directly. At large energies, neutrinos can emit W and Z bosons making missing energy visible.[8] The Sudakov enhancement of this process can make the three-body decays of a W' or Z' significant if the leptons are sufficiently boosted, e.g. $Z' \to \nu\bar{\nu}Z$ or $Z' \to \nu l^- W^+$.

The radiation of a W or Z from a neutrino has a soft collinear log enhancement, which is cut off by $m_{W,Z}$. If a Z boson is radiated, the collinear enhancement results in a strong tendency for the Z boson to be emitted parallel to the neutrino. Assuming that the Z boson lies completely parallel to the neutrino allows one to reconstruct the neutrino in its entirety. If a W boson is radiated, the neutrino becomes completely visible and tagging its origin as a neutrino is needed. If the W can be reconstructed (most likely in a hadronic

[8]The importance of heavy Z' three-body decays was first mentioned in Ref. [209] in the context of SSC and later in Ref. [202, 210] in context of a 100 TeV collider.

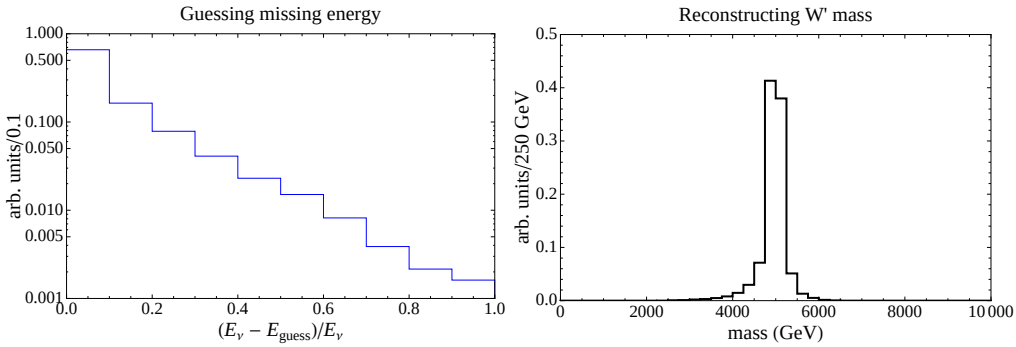

Figure 7.21 On the LHS plot we plot the difference between our "guess" about the energy of the neutrino and the actual neutrino energy. The "guess" for the neutrino energy comes from assuming that the neutrino is collinear with the leptonic Z. The reconstructed neutrino allows one to guess the real missing energy in an event as well as reconstruct the full mass peak of a W' particle (plot on the RHS). The mass resolution is smeared since the Z is not always collinear with the neutrino, but the peak is very clearly at the W' mass of 5 TeV.

decay mode), the small ΔR distance between it and the lepton allows one to tag the lepton as originating from a neutrino.

We illustrate the utility of leptonically decaying Sudakov emitted Z bosons in two examples. The first example is a heavy W' boson. When looking at events with an extra Z, the tendency of the Z to lie parallel with the neutrino allows for the reconstruction of missing energy rather than missing transverse energy. The reconstructed neutrino can then be used to find the mass of the decaying W' boson. We show that in this case a full reconstruction of the W' mass peak is possible.

We work at parton level assuming that the leptons and missing energy are measured perfectly. Madgraph5 [47, 211, 212] was used to generate the events. In this preliminary analysis, alongside with the standard acceptance criteria, we apply following cuts:

- Exactly three leptons (either e or μ) in the event
- $p_T > 0.5$ TeV for the leading lepton
- The invariant mass of the subleading leptons reconstructs the Z mass. 75 GeV $< m_{ll} < 105$ GeV
- Eta of all leptons and reconstructed Z obey $|\eta_{Z,l}| < 2.5$
- $\Delta\phi_{Z E_{\mathrm{T}}^{\mathrm{miss}}} < 0.5$
- $E_{\mathrm{T}}^{\mathrm{miss}} > 0.5$ TeV and $m_T(l, E_{\mathrm{T}}^{\mathrm{miss}}) > 0.5$ TeV

We present the results of the W' reconstruction in Fig. 7.21. In most of the cases, the missing energy can be reconstructed to the precision of $\sim 20\%$ or even better. The reconstructed mass peak (the same figure on the right) is a little smeared due to imperfect reconstruction of the neutrino, however the mass peak is still clearly visible. For a 5 TeV W', $\sigma \times Br \times \epsilon \sim 14$ fb. Thus for a rather reasonable integrated luminosity, we can obtain enough signal events to easily determine the mass of the W' through this method. The dominant background comes from WZZ which has a negligible cross section times efficiency.

Another example is a Z' boson. The magnitude of the invisible channel can be probed by the emission of a W or Z boson. Probing the invisible channel allows one to directly

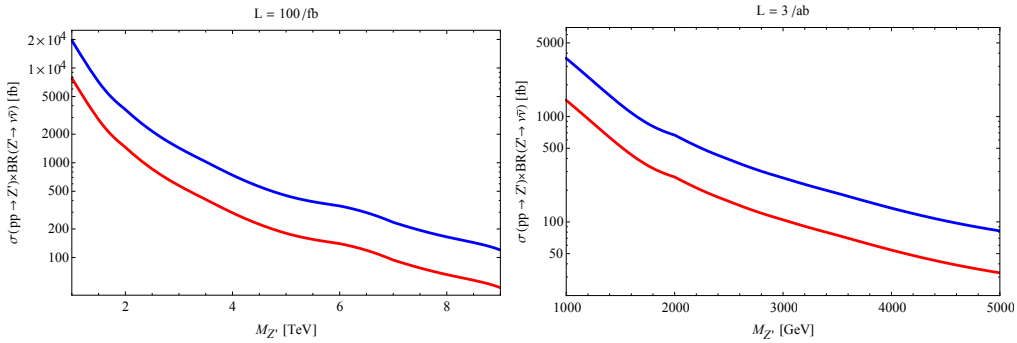

Figure 7.22 Reach of a 100 TeV collider to a Z' decaying invisibly for a luminosity of 100 fb^{-1} and 3000 fb^{-1}. The blue and red lines are the 5 and 2 σ results respectively.

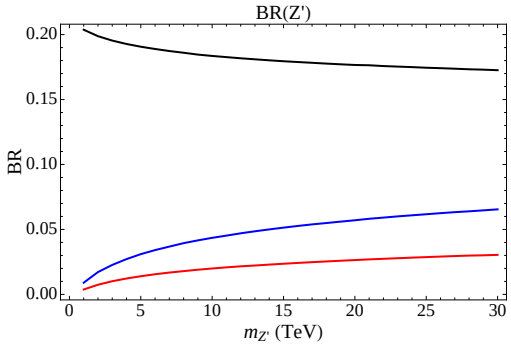

Figure 7.23 Branching ratios of a B-L gauge boson. We have the $\nu\bar{\nu}, \nu\bar{\nu}Z, \nu l^{\pm}W^{\mp}$ final states in black, red and blue respectively. We see that the 3-body branching ratios associated with an invisible decay mode of the Z' gauge boson can be as large as several percent so that finding the invisible channel through radiation of a Z or W is possible.

measure the Z's couplings to the left handed leptons. To illustrate this, we perform a simple cut-and-count search for leptonic Z recoiling against $E_{\mathrm{T}}^{\mathrm{miss}}$. We compare the rate of these events after acceptance cuts and a cut on $E_{\mathrm{T}}^{\mathrm{miss}}$ to the rate of the ZZ background to determine the possible reach of the 100 TeV machine. The results of this search are shown in Fig. 7.22. We phrase our results in terms of

$$\sigma(pp \to Z') \times BR(Z' \to \nu\bar{\nu}) \tag{7.21}$$

as the ratio is known for every given mass of the Z'. As we see from the figure, the future hadron collider can probe invisible decays of Z's with couplings of order $\mathcal{O}(0.1)$.

As shown in Fig. 7.23, the invisible decay channel of the Z' can be probed with Sudakov radiation without suffering too large of a hit from branching ratios. The 3-body branching ratios can be very large.

Next, we further pursue this approach showing how one can determine quantum numbers of new particles based on total EW gauge bosons emission. Particles which are not charged under $SU(2)_L \times U(1)_Y$ do not radiate W and Z bosons and can thus be distinguished from their charged counterparts.

We illustrate this effect in an example where we assume a "natural SUSY" - like spectrum at the TeV scale, namely a stop as an NLSP decaying into a neutralino LSP. SUSY with light third generation squarks is a well motivated [213, 214] and well studied scenario [215–217]. The left and right handed stops have different couplings to the Z. Due

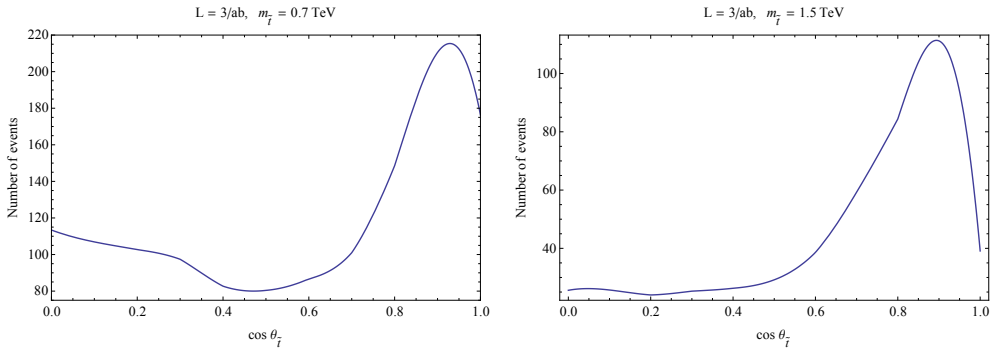

Figure 7.24 Number of events passing cuts as a function of $\cos\theta_{\tilde{t}}$ for three mass points. $\cos\theta_{\tilde{t}} = 0$ is a right handed stop.

to electroweak symmetry breaking, they mix so that the NLSP is an admixture of the two. We explore how electroweak Sudakov radiation of Zs can be used to bound the mixing angle of the NLSP stop.

At large masses, the chirality of the stops can be measured by the additional radiation of a Z or W in the event. The Sudakov enhancement for the radiation of Zs and Ws makes this measurement feasible at a 100 TeV machine. Note however that the radiation of the EW gauge bosons from the stop is only single log enhanced because the collinear singularity in this case is cut off by the mass of the emitting particle (the stop) and effectively does not lead to any enhancement. Meanwhile, both ISR and FSR have a Sudakov double log enhancement. Because both the decay products of the stop and the initial state quarks have the same chirality as the stop, the radiation strength provides a good measure of the chirality of the stop regardless of where the radiation came from.

To illustrate our point we choose two benchmark points: $m_{\tilde{t}} = 0.7$ TeV and $m_{\tilde{t}} = 1.5$ TeV, all decaying into a massless bino-like neutralino. Note that the first benchmark point can be easily discovered by the LHC while the second one is inaccessible even for the LHC14. We do not consider heavier stops as their cross section is too small.

To study the chirality of the NLSP stop, we propose analyzing the production of $\tilde{t}\tilde{t}^*$ decaying into $t\bar{t}\chi^0\chi^0$ accompanied by an emission of a Z at any stage of the process. We take advantage of an abundant semileptonic channel in $t\bar{t}$ final states and demand that the extra Z decays leptonically.

In order to remove backgrounds, we first reconstruct the leptonic Z in each of these events within a $m_Z \pm 15$ GeV window (if there is more than one candidate, we choose the candidate with the mass closest to m_Z). After that, we impose a transverse mass cut of 500 GeV between the non-Z lepton and $E_{\mathrm{T}}^{\mathrm{miss}}$ to remove missing energy that stems from a W. After this cut, the main background is $t\bar{t}WW$ with about 20 events at a luminosity of 3 ab^{-1} (taking into account standard isolation and acceptance cuts).

We show the predicted number of signal events as a function of mixing angle in Fig. 7.24. We define the mixing angle between the stops as follow:

$$\begin{pmatrix} \tilde{t}_1 \\ \tilde{t}_2 \end{pmatrix} = \begin{pmatrix} \cos\theta_{\tilde{t}} & \sin\theta_{\tilde{t}} \\ -\sin\theta_{\tilde{t}} & \cos\theta_{\tilde{t}} \end{pmatrix} \begin{pmatrix} \tilde{t}_R \\ \tilde{t}_L \end{pmatrix}, \tag{7.22}$$

such that $\theta = 0$ corresponds to the lightest stop being purely right-handed.

There are several clear features observable from these plots. The first is that there is a clear difference between $\cos\theta_{\tilde{t}} = 0$ and 1. Thus purely left and purely right handed stops can be distinguished. A more surprising point is that the maximum/minimum of these plots are at values of $\cos\theta_{\tilde{t}}$ which is not 0 or 1, which is due to the fact that the LSP was chosen to be a bino.

Top Quark as Parton

At the high collision energy of the SppC, $\sqrt{S} = 100\,\text{TeV}$, the Standard Model can be tested in its unbroken phase. All particles with masses around the electroweak scale appear as light as the bottom quark at the Tevatron collision energy of $\sqrt{S} = 2\,\text{TeV}$. In particular, the top-quark ultimately behaves as a massless parton inside the proton at very high energies. Processes with top-quarks in the initial state thus become important compared to gluon-initiated processes. When treating the top-quark as a parton, it is understood that the initial top-quark in the hard-scattering process originates from a gluon splitting into a top-antitop pair. If the process probes a very high energy scale Q, this splitting is dominantly collinear and generates a logarithmic enhancement of the cross section by $\alpha_s(Q)\log(Q^2/m_t^2)$. For $Q \sim 10\,\text{TeV}$, for instance, $\alpha_s(Q)\log(Q^2/m_t^2) \sim 0.6$, which makes a perturbative expansion of the hard process questionable. Defining a parton distribution function (PDF) for the top-quark inside the proton allows us to resum large collinear logarithms $\alpha_s^n(Q)\log^n(Q^2/m_t^2)$ to all orders n in perturbation theory. The applicability of perturbation theory for the hard process is thus restored, if we include top-initiated partonic processes. Initial heavy quarks have been studied in detail in the context of bottom-initiated processes [218, 219], and the main concepts can be adopted for the top-quark. The NNPDF collaboration has released a top-quark PDF as part of their NNPDF2.3 set [220], which facilitates the implementation. However, top-quark PDFs and the choice of the QCD factorization scale must be handled with care, especially in energy regions not far above the top-quark production threshold. We will discuss the details below, employing the example of top-antitop initiated production of a heavy neutral scalar resonance, $t\bar{t} \to H^0$ [221].

Top-quark parton luminosities at $\sqrt{S} = 100\,\text{TeV}$ can become competitive with light-parton luminosities. This is shown in Figure 7.25(a) for parton momentum fractions corresponding to the production of a heavy resonance with mass m_H. In particular, the $t\bar{t}$ luminosity reaches a few percent of the $b\bar{b}$ luminosity at scales $Q \sim 10\,\text{TeV}$. Compared to the LHC at $\sqrt{S} = 14\,\text{TeV}$, the top-quark luminosity at $100\,\text{TeV}$ is strongly enhanced, as can be seen in Figure 7.25(b). In the relevant mass range of $500\,\text{GeV}$ up to $4\,\text{TeV}$, the effect is as large as a factor of $10^3 - 10^5$. This enhancement facilitates the observability of top-quark initiated processes at the SppC. Phenomenologically, top-initiated processes are important in models that feature flavor-hierarchical couplings to quarks. A prominent example are Kaluza-Klein excitations of gauge bosons and the graviton in models with extra space dimensions, which couple dominantly to top-quarks [222–225]. These resonances are predicted to lie at the edge or beyond the mass reach of the LHC, but necessarily within the reach of the SppC. The discovery of Kaluza-Klein resonances in top-antitop fusion will give us valuable evidence of a solution to the electroweak hierarchy problem by gravitational redshifting. Other examples include heavy scalars from extended Higgs sectors or new vector bosons in models with strong dynamics. More generally, any new heavy particle produced from top-antitop or top-bottom fusion falls in the class of collinearly

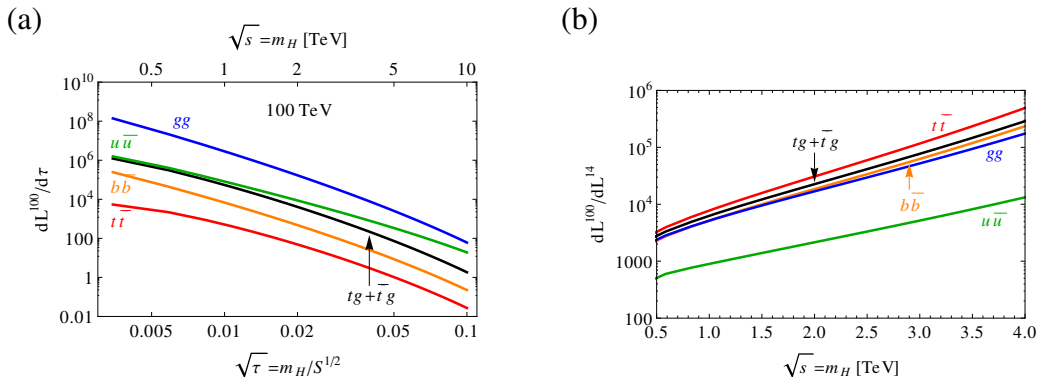

Figure 7.25 Parton luminosities at $\sqrt{S} = 100$ TeV (a) and the ratio between luminosities at 100 TeV and 14 TeV (b), for $t\bar{t}$ (red), $tg + \bar{t}g$ (black), $b\bar{b}$ (orange), $u\bar{u}$ (green) (including the initial-state interchange), and gg (blue).

enhanced processes and thus benefits from resummation by using PDFs for heavy quarks.

Implementation of Top-quark PDFs

As described above, the use of top-quark PDFs is particularly interesting in processes where the top plays an important role in the production of heavy new physics states. A simple example is found in the production of new Higgs-like scalars, whose couplings to fermions are proportional to the standard model Yukawa couplings in many models. Estimates of the inclusive production cross section at $\sqrt{S} = 100$ TeV have been made for charged Higgs via $t\bar{b} \to H^+$ and for neutral scalars via $t\bar{t} \to H^0$ [221, 226]. In the very high energy limit these processes should be considered the leading order contributions to inclusive production, as in Figure 7.26(c). This is also the limit in which the top-quark mass can be generally neglected and the top quark behaves very much like a parton in the proton. On the other hand, for scales near and below the top mass threshold a partonic treatment is inappropriate and the top PDFs should not be employed. Then the leading order (LO) process in the neutral scalar case is Figure 7.26(a) (and related gluon-gluon initiated graphs).

Typically the top-quark PDF is set to be zero below the mass threshold and it is evolved to non-zero values at higher scales as a function of the lighter parton densities. Thus in principle one could begin using top PDFs at the top mass threshold and $t\bar{t} \to H^0$ would seem to be the leading process. However a comparison of this LO 6-flavor calculation with the LO 5-flavor calculation (as in Figure 7.26(a)) shows order-of-magnitude differences for a 'natural' choice of factorization scale around the mass of the heavy state, $\mu_F = m_{H^0}$. The dependence on the choice of factorization scale is also very large for the 6-flavor LO calculation, because the top PDFs grow rapidly near the threshold region.

Similar issues were noted historically in the treatment of the b quark [227–229]. These can be addressed with so-called General Mass Variable Flavor Number schemes, which effectively interpolate between the 5-flavor results at the heavy-quark threshold and 6-flavor results in the high-energy limit. Such formalisms include the ACOT scheme and its derivatives [230, 231], the FONLL scheme [232], and the TR scheme [233]. These schemes enable a smooth transition across the top mass threshold and up to very high energies. Near the mass threshold one must consider all three graphs of Figure 7.26 (and

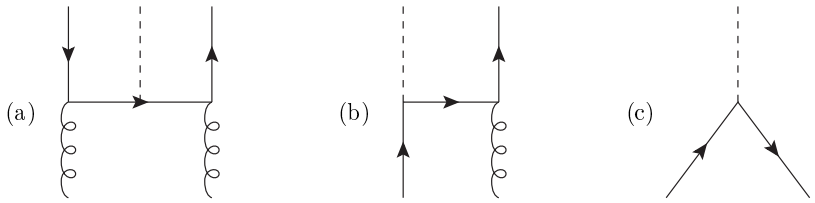

Figure 7.26 Representative tree-level graphs relevant to the inclusive production of a heavy color-singlet neutral particle (dashed line). (a) The 5-flavor LO process from gg fusion; (b) The 6-flavor process involving only one initial top (solid line) in tg fusion; (c) The 6-flavor process initiated by $t\bar{t}$ fusion.

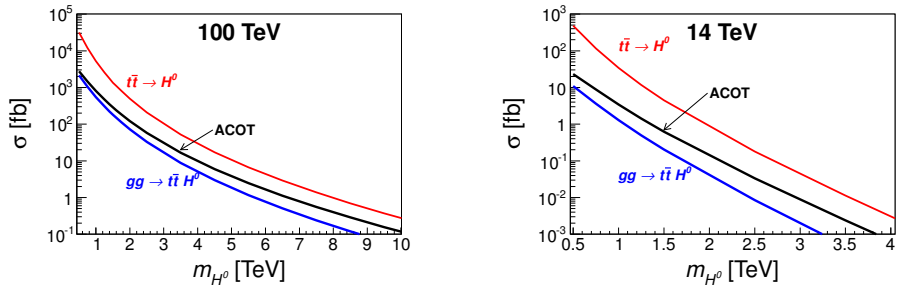

Figure 7.27 Inclusive cross section for H^0 production with Yukawa coupling $y = 1$ at 100 TeV (left panel) and 14 TeV (right panel) versus its mass m_{H^0}, in the 5-flavor scheme (bottom blue), the 6-flavor scheme (upper red), and the ACOT scheme (middle black).

similar tree-level graphs) to have a stable LO calculation of the inclusive rate for H^0 production.

Figure 7.27 shows a comparison of calculations in the 5-flavor, massless 6-flavor, and ACOT schemes for inclusive H^0 production at the 14 TeV LHC and a 100 TeV machine. The ACOT scheme shows the desired behavior of interpolating between the region near the top threshold and the very high energy limit. The ACOT scheme includes the effect of top-quark PDFs which resum potentially large collinear logarithms at all orders, while the 5-flavor LO calculation includes only the lowest-order logarithm. For masses in the multi-TeV range the resummed logarithms give a significant enhancement which may be as large as a factor of $2 - 3$ as the relevant scale approaches 10 TeV. At the same time one can see that the simplest LO 6-flavor calculation is likely unreliable except for masses above 10 TeV.

As mentioned, however, the size of the LO 6-flavor cross section estimate is very sensitive to the choice of factorization scale. Based on a careful comparison of the phase space integration in a 5-flavor scheme and the LO expansion of the PDF in the 6-flavor scheme, one can choose an effective scale μ_{eff} which provides a better matching of the two calculations near the top threshold [221, 234]. This scale is in general much lower than the mass of the heavy state $\mu_{\text{eff}} < m_{H^0}$. In Figure 7.28, left panel, this suppression relative to m_{H^0} is shown. Using such an effective scale for the LO 6-flavor calculation turns out to match the ACOT calculation using all graphs of Figure 7.26 rather well. The 6-flavor scheme thus gives a good estimate of the cross section at LO, if the factorization scale is lowered down to the effective scale of collinear parton splitting. This is shown

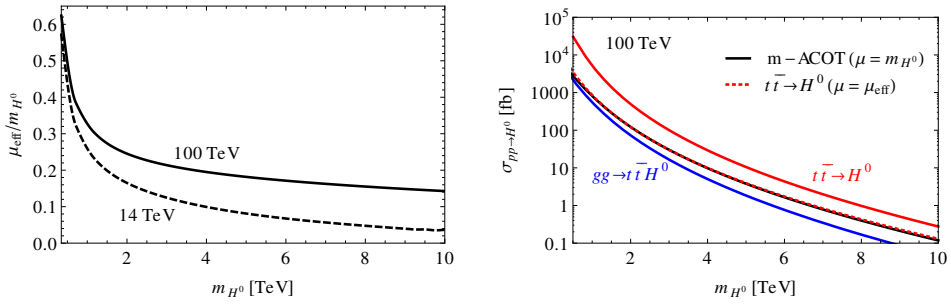

Figure 7.28 Left: Effective factorization scale $\mu_{\rm eff}$ divided by m_{H^0} for $\sqrt{S} = 100$ TeV (solid) and $\sqrt{S} = 14$ TeV (dashed). Right: The LO total cross section $\sigma_{pp\to H^0}$ at $\sqrt{S} = 100$ TeV as a function of m_{H^0} in the massless 6-flavor scheme using the effective factorization scale $\mu = \mu_{\rm eff}$ (dotted red), compared with the default scale choice $\mu = m_{H^0}$ in the massless 6-flavor scheme (solid red), the 5-flavor scheme (blue) and ACOT (black).

in the right panel of Figure 7.28. In contrast to the LO 6-flavor calculation however, the ACOT calculation is less scale dependent.

In the ACOT and 5-flavor calculations it is possible to look at distributions for semi-inclusive observables such as H^0 plus one or more final state tops. A comparison of these distributions reflects the overall cross section enhancement from resummation in the ACOT case versus the LO 5-flavor result, but distribution shapes are relatively unchanged. The largest effect is a mild enhancement of the p_T distribution of H^0 at lower values of p_T.

Although the examples above were calculated for a Higgs-like scalar, the general implementation of top-quark PDFs is applicable to any process at a high-energy machine which might receive contributions from initial-state tops. Similar considerations on implementing an appropriate active flavor number scheme and choices of scale will apply.

7.4 Running Electroweak Couplings as a Probe of New Physics

The SPPC will provide remarkable opportunities, not only for the production of new heavy particles, but also for the performance of high precision tests of Standard Model (SM) processes across a wide range of energies. Future measurements can constrain the energy dependence of SM parameters, which evolve according to the renormalization group. For example, measurements of ElectroWeak (EW) processes at $\sqrt{s} = 100$ TeV can be used to constrain the energy dependence of the $SU(2) \times U(1)$ gauge couplings, $\alpha_{1,2}(Q)$ [235].

In the SM, α_2 is asymptotically free and therefore gets weaker with energy, while α_1 gets stronger with energy. At 1 (10) TeV, α_1 is predicted to increase by 2.7 (5.5)% relative to its value at m_Z, while α_2 is predicted to decrease by 3.9 (7.4)%. If new states beyond the SM have EW quantum numbers, the β functions of $\alpha_{1,2}$ shift at the mass thresholds of the new states, changing the energy evolution of $\alpha_{1,2}$ at higher energies. Percent-level measurements of $\alpha_{1,2}$ at multi-TeV energies will provide nontrivial checks of the SM, and will allow for model-independent constraints on new EW states, analogous to the model-independent limits on colored states resulting from measurements of the energy dependence of α_3 [236, 237].

In order for an EW process to allow for a precise measurement of running $\alpha_{1,2}(Q)$, it should meet several criteria. First, the process should have high cross section at large energies, allowing for small statistical uncertainties. Second, the process should be theoret-

ically well-understood, allowing for small theoretical uncertainties. Finally, the process should be experimentally clean, minimizing experimental uncertainties. Two processes that meet the above criteria are neutral current Drell-Yan (DY), $pp \to Z^*/\gamma^* \to \ell^+\ell^-$, and charged current DY, $pp \to W^{\pm *} \to \ell^\pm \nu$ [238]. The impact of radiative corrections from superpartners on DY has been studied by Refs. [238–240].

Running $\alpha_{1,2}(Q)$ can be constrained with neutral current DY by measuring the shape of the dilepton invariant mass spectrum, since the dilepton mass sets the scale where the weak couplings are evaluated,

$$\frac{\mathrm{d}\sigma}{\mathrm{d}M_{\ell\ell}}(pp \to Z^*/\gamma^* \to \ell^+\ell^-) \equiv \frac{\mathrm{d}\sigma^{Z/\gamma}}{\mathrm{d}M_{\ell\ell}}\big(\alpha_{1,2}(M_{\ell\ell})\big). \tag{7.23}$$

Charged current DY constrains $\alpha_2(Q)$, which impacts the shape of the transverse mass spectrum,

$$\frac{\mathrm{d}\sigma}{\mathrm{d}M_T}(pp \to W^* \to \ell\nu) \equiv \int_{M_T}^{\infty} \mathrm{d}M_{\ell\nu} \frac{\mathrm{d}\sigma^{W^\pm}}{\mathrm{d}M_T \mathrm{d}M_{\ell\nu}}\big(\alpha_2(M_{\ell\nu})\big). \tag{7.24}$$

The precision with which running $\alpha_{1,2}(Q)$ can be extracted from DY measurements depends on the size of statistical, theoretical, and experimental uncertainties (we refer the reader to Ref. [235] for a detailed discussion). The cross section sets the size of statistical uncertainties. Assuming 3 ab^{-1} at 100 TeV, statistical uncertainties are below 1% for $M_{\ell\ell}, M_T \lesssim 3$ TeV. Theoretical uncertainties include scale uncertainties and PDF uncertainties. Drell-Yan has been computed to NNLO QCD and NLO EW order. Scale and PDF uncertainties are found to be $\lesssim 1-2\%$ at relevant energies when evaluated using the DYNNLO and FEWZ generators [241–246] and the NNPDF2.3 PDF set [220]. Neutral current DY has been measured at 7/8 TeV center of mass energies [247–249], with experimental uncertainties that are uncorrelated across different invariant mass bins

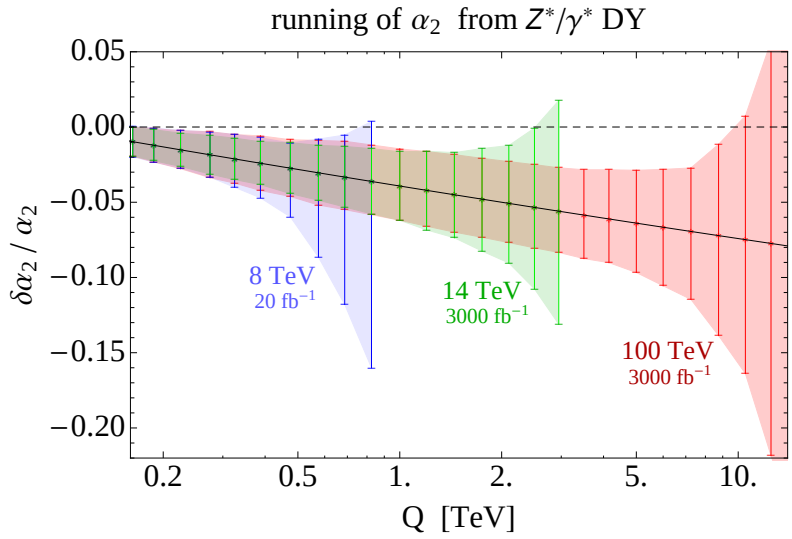

Figure 7.29 The projected reach to measure $\alpha_2(Q)$ with future Z^*/γ^* measurements, assuming α_1 runs according to the SM prediction. Blue, green, red show the reach with 8, 14, and 100 TeV, assuming luminosities of 20, 3000, and 3000 fb^{-1}. The error bars are 1σ. The SM prediction (solid,black) is well-separated from the case that α_2 does not run above m_Z (dashed, black). Figure from Ref. [235].

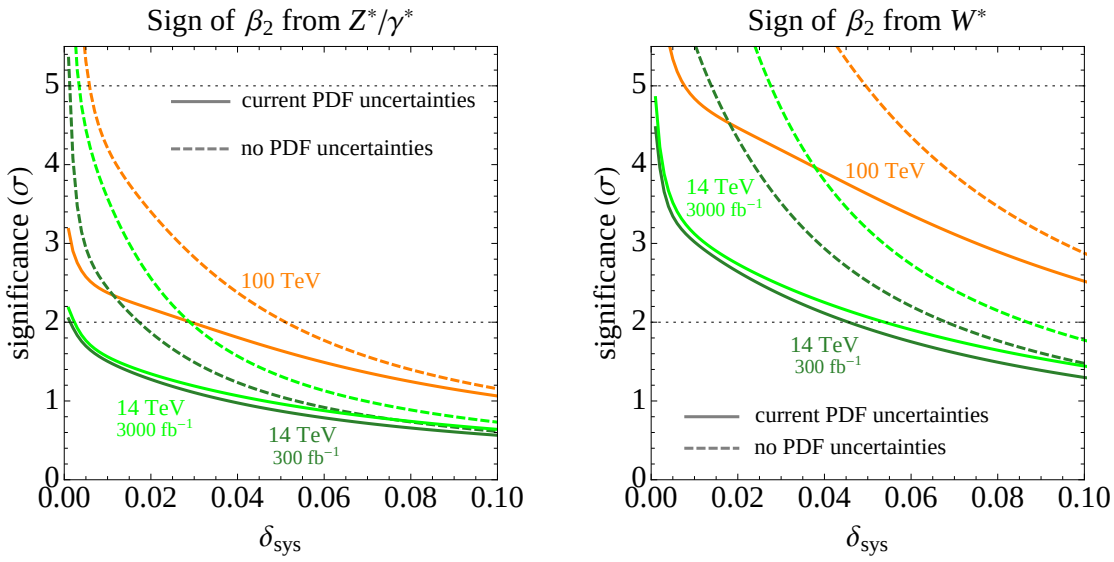

Figure 7.30 Projected exclusion of the no running hypothesis of α_2 in Z^*/γ^* (left) and W^* (right) Drell-Yan, as a function of the size of uncorrelated systematic uncertainties. Expected limits are shown assuming present level PDF uncertainties (solid curves) as well as negligible ones (dashed curves), for 14 TeV (green) and 100 TeV (orange). Figure from Ref. [235].

at the $\sim 1-2\%$ level. We optimistically assume that a future 100 TeV collider can achieve comparable experimental precision, and we leave the study of experimental uncertainties for future work.

Figure 7.29 shows the expected precision with which $\alpha_2(Q)$ can be measured with neutral current DY at $\sqrt{s} = 8, 14, 100$ TeV. Statistical, scale, and PDF uncertainties are included and (uncorrelated) experimental uncertainties are assumed to be 1%. If $\alpha_2(Q)$ decreases with energy according to the SM prediction, it will be possible for a 100 TeV collider to detect the $\alpha_2(Q)$ running by rejecting the constant hypothesis $\alpha_2(Q) = \alpha_2(M_Z)$. Figure 7.30 shows the significance at which constant α_2 can be rejected at $\sqrt{s} = 14$ and 100 TeV, as a function of the ultimate size of experimental uncertainties that are uncorrelated across different bins of $M_{\ell\ell}, M_T$. At 100 TeV, constant α_2 can be rejected with 5 (3) σ significance assuming experimental uncertainties of 1 (7)%.

The SPPC can probe running EW coupling measurements to set powerful model-independent limits on new states with EW quantum numbers. Figure 7.31 shows the reach of a 100 TeV collider to constrain new states as a function of their mass and the size of the shift of the EW gauge coupling β functions. Figure 7.32 shows the reach to constrain higgsinos, winos, or **5**-plets of $SU(2)$ using charged current DY measurements. The SPPC will thus have the reach to detect winos lighter than ~ 1.5 TeV, independently of how they decay.

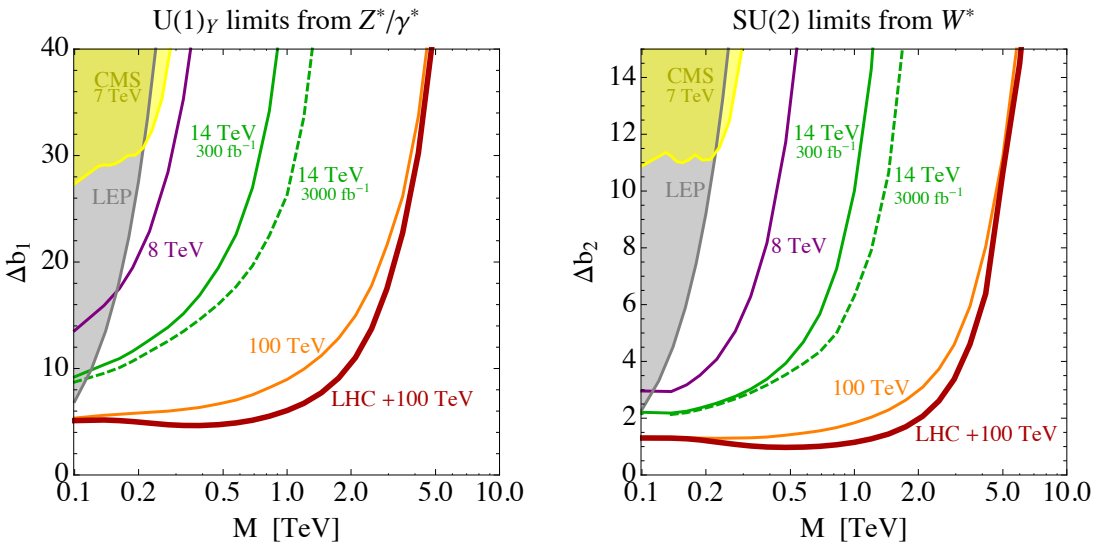

Figure 7.31 The reach to BSM contributions to the EW beta function coefficients, Δb_1 (left) and Δb_2 (right), as a function of the mass of the new states, M. Neutral (charged) current DY is used to derive the limit on the left (right). Current limits from LEP and 7 TeV DY at CMS are indicated by shaded regions. Projected reach is shown for 8 TeV (purple), 14 TeV (green), 100 TeV (orange), and LHC+100 TeV (red). Figures from Ref. [235].

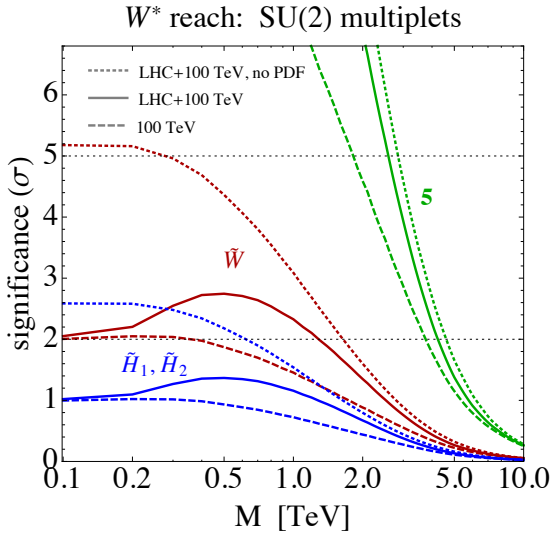

Figure 7.32 W^* expected exclusion (in standard deviations) as a function of mass for various SU$(2)_L$ representations. Sensitivity is shown at 100 TeV and LHC+100 TeV for a pair of Higgsinos (blue), a wino (red) and a 5-plet of SU$(2)_L$ (green). Figure from Ref. [235].

7.5 B+L Violation at High Energies

The electroweak interactions in the Standard Model are described by the $SU(2)_W \times U(1)_Y$ gauge theory spontaneously broken to the electromagnetic $U(1)_{\rm em}$ by the vacuum expectation value (vev) of the Higgs field. The coupling constants for both gauge groups are much smaller than one, hence the electroweak sector is weakly coupled. For this rea-

son essentially all of the theoretical predictions and computations performed in the electroweak sector and relevant to the electroweak phenomenology at particle colliders have been carried out in perturbation theory. However, even at weak coupling, $\alpha_W << 1$, particle collisions at sufficiently high energies can produce high multiplicity final states with the number of particles $n \gtrsim 1/\alpha_W$. This kinematic regime is beyond the scope of ordinary weakly-coupled perturbation theory.

The $SU(2)_W$ gauge theory is weakly coupled but *non-Abelian*, which results in a topologically non-trivial vacuum structure. Perturbation theory ignores the possibility of quantum tunneling or over-the-barrier transitions between different vacua—the effect of which would result in the non-conservation of the baryon (B) and lepton (L) numbers in the Standard Model.

A new fundamental energy scale $E_{\rm sph}$ emerges in the theory which represents the minimum height of the barrier separating topologically distinct vacua in the electroweak theory. The energy of the sphaleron solution [250] in the EW sector is $E_{\rm sph} = c_{\rm sph}\frac{M_W}{\alpha_W} \approx 10\,\text{TeV}$. A quintessential feature of quantum theory is the possibility of quantum tunneling. These process are forbidden in classical physics and neither they can be computed to any order in perturbation theory. In vacuum the probability of tunneling is exponentially suppressed, $\sigma^{\rm inst} \propto e^{-4\pi/\alpha_W} \simeq 5 \times 10^{-162}$ which makes these processes unobservable in normal circumstances. However by now it is a theoretically well-established fact that in the conditions which existed in the early Universe at high temperature, such processes with baryon and lepton number non-conservation were unsuppressed and have occurred frequently [251].

A natural question to ask is whether similar conditions can be recreated in ultra-high energy collisions at the next generation of proton colliders where energies available for triggering these quantum tunneling effects can easily approach and exceed the sphaleron energy. Our aim is to address and resolve this fascinating and long-standing open problem. The role of very-high-particle-multiplicity external states in this case is crucial for reducing and lifting the exponential suppression. First semi-classical calculations based on a perturbative expansion around the instanton configuration at non-zero energies were carried out and discussed in [252–256] for the high-final-state-multiplicity process $q + q \to 7\bar{q} + 3\bar{l} + n_W W + n_Z Z + n_h H$.

At ultra-high energies, 100 TeV hadron colliders open an entirely new challenge. Gaining a detailed understanding of the ultra-high-energy regime is of fundamental importance to our understanding of Nature. The current state of the art amounts to perturbation theory techniques applied in the perturbative or in the instanton background, and it has been established that these methods are insufficient to solve the problem. New computational methods and techniques are needed and we aim to develop them based on the experience gained in developing the current state of the art and on combining the existing techniques and ideas with new semi-classical and quantum analytical and numerical approaches.

The expected novel high-multiplicity scattering events are not restricted only to the intrinsically non-perturbative $(B + L)$-violating processes. On the contrary, it is likely that new non-perturbative effects will appear in both (B+L)-violating as well as (B+L)-conserving events. Some of the non-perturbative processes can violate Baryon plus Lepton particle number at ultra high energies—this would be a far-reaching discovery, but $B + L$ violation is not a necessary requirement for all or even most of the multi-particle events of interest. The common feature of these events is that they do not follow rules

of the well-established standard weakly-coupled description, and if observed, will have a clean experimental signature—a fireball production of 30-50 electroweak jets with an optimistic estimate for cross sections in the $\sim$ pb regime—with a negligible traditional Standard Model background.

There is a close analogy and complementarity between these genuinely non-perturbative processes which violate baryon and lepton numbers and the simpler but equally mysterious B+L conserving purely 'perturbative' electroweak processes with high multiplicity. The common origin of these phenomena is linked to the existence of a new fundamental energy scale in the theory—the sphaleron mass $E_{\rm sph} \sim M_W/\alpha_W \approx 10\,{\rm TeV}$, and to the high particle multiplicities $n \gg 1/\alpha_W$ produced in the final states in both cases. For $(B+L)$ non-conserving non-perturbative processes at high energies the role of high-multiplicity external states is crucial for reducing the exponential suppression. The inter-vacua transitions involving $n \gg 1/\alpha_W$ particles in both initial and final states, (many $\to$ many interactions) are known to be unsuppressed and these reactions play an important role in our understanding of the evolution of $B+L$ and the matter-anti-matter asymmetry in the early Universe. The non-perturbative scattering processes of the type few $\to$ many still present a open problem. These processes are of particular importance as they can be tested experimentally at the next generation of hadron colliders with up to a 100 TeV energy reach. Theoretical understanding and the possibility of experimental observation of these effect will amount to a remarkable breakthrough: this will be the first manifestation of quantum tunneling in particle physics.

As we have already noted, particle collisions at very high energies kinematically allow for a production of high-multiplicity final states with n particles where the value of n can reach and exceed the value set by the inverse coupling constant. In this weak-coupling high multiplicity regime at high energy collisions we have $n \gg 1/\alpha \gg 1$ and $\alpha \ll 1$. In this case the long-standing problem of the factorial factorial growth affecting perturbative series [257] becomes critical. The key point is that for the n-point scattering amplitudes $\mathcal{A}_n$ the factorial growth of perturbation theory at large n affects already the leading order tree-level result, $\mathcal{A}_n^{\rm tree} \sim \alpha^{n/2}\, n! \gg 1$ (rather than the less relevant asymptotically high orders of perturbation theory). The factorial growth can arise from the large number of Feynman diagrams contributing to the scattering amplitude $\mathcal{A}_n$ at large n. This leads to the factorial growth of the cross section, $\sigma_n^{\rm tree} \sim \alpha^n\, n! \times f_n({\rm kinematics})$, in violation of unitarity and signals the breakdown of perturbative description of these observables for $n \gtrsim 1/\alpha$. Perturbation theory explodes and we loose the means to a quantitative understanding of the theory in this regime. These conclusions were reached in simple models of massive scalar field theory studied in 1990's [258, 259] and more recently were generalized to the realistic case of spontaneously broken gauge-Higgs theory in [260–262]. Scattering processes with n Higgs bosons and m massive W and Z bosons were computed for high multiplicities near their kinematic mass threshold, and found to grow factorially $A_{n+m} \sim n!\, m!$ thus providing first concrete evidence for breakdown of perturbation theory in the electroweak sector.

The breakdown of the weakly-coupled perturbative technique is extremely interesting both from the theoretical point of view, and for phenomenological implications and new possibilities at future high energy colliders. Since these processes are essentially free from the traditional Standard Model backgrounds, the observability of the rate can be always settled experimentally. These high-multiplicity processes with and without $(B+$

L)-violation provide a physics programme which is completely unique to the very high energy pp machine. These experimental studies cannot be done anywhere else.

In conclusion we note that there is an obvious complementarity between the fundamental need to find new fundamental physics beyond the Standard Model and the challenge to understand the minimal Standard Model at very high electroweak multiplicities. The searches for beyond the Standard Model physics at the next generation of hadron colliders will rely on predictions for final states involving multiple leptons and missing energy. Hence it is essential to have a robust theoretical control of the Standard Model backgrounds with the same final states. These would arise from a multiple vector boson production, which are precisely the type of processes we are dealing with. The breakdown of perturbation theory at high energies and multiplicities clearly signals a change in the qualitative behavior of the SM and its discovery would be a huge step forward in our understanding of the SM itself, but one may even speculate that the problem goes even deeper and signals the onset of new physics at energies that will be tested in the next generation of colliders.

7.6 Higgs and New Physics

Extended Higgs Sector

Introduction

Many well-motivated candidates for physics beyond the Standard Model feature extensions of the minimal Higgs sector. Well known examples include the Minimal Supersymmetric Standard Model (MSSM) [263–265], Next-to-Minimal Supersymmetric Standard Model (NMSSM) [37, 266], and Two Higgs Doublet Models (2HDM) [267–270], etc. In addition to a SM-like Higgs boson in these models, the low energy spectrum typically includes extra neutral CP-even and CP-odd Higgses, as well as charged ones.

The discovery of the non-SM Higgses would provide unambiguous evidence for new physics beyond the SM. The search for these extra Higgses, however, is typically challenging at the LHC. For the extra neutral Higgses, most of the current searches at the LHC focus on the conventional Higgs search channels of WW, ZZ, $\gamma\gamma$, $\tau\tau$ and bb channel [271–277]. The production of the extra Higgses is usually suppressed compared to that of the SM Higgs, either due to its larger mass or its suppressed couplings to the SM particles. The decay of the heavy neutral Higgses to the WW and ZZ is absent for the CP-odd Higgs, and could be highly suppressed for the non-SM like CP-even Higgs. The decay modes of $\tau\tau$ or bb suffer from either suppressed signal or large SM backgrounds, and are therefore only relevant for regions of the parameter space with an enhanced bb or $\tau\tau$ coupling. The search for the charged Higgs at the LHC is even more difficult. For $m_{H^\pm} > m_t$, the cross section for the dominant production channel of $tbH^\pm$ is typically small. The dominant decay mode $H^\pm \to tb$ is hard to identify given the large tt and $ttbb$ background, while the subdominant decay of $H^\pm \to \tau\nu$ has suppressed branching fraction. In the MSSM, even at the end of the LHC running, there is a "wedge region" in the $m_A - \tan\beta$ plane for $\tan\beta \sim 7$ and $m_A \gtrsim 300$ GeV in which only the SM-like Higgs can be covered at the LHC. Similarly, the reach for the non-SM Higgses is limited in models with an extended Higgs sector.

In addition to their decays to the SM particles, non-SM Higgses can decay via exotic modes, e.g., heavier Higgs decays into two light Higgses, or one light Higgs plus one SM

gauge boson. Examples include $H^0 \to H^+H^-$, $H^0 \to AA$, $H^0 \to AZ$, $A \to H^\pm W^\mp$, and $H^\pm \to AW$, etc. These channels typically dominate once they are kinematically open. The current limits on the beyond the SM Higgs searches are therefore weakened, given the suppressed decay branching fractions into SM final states. Furthermore, these additional decay modes could provide new search channels for the non-SM Higgs, complementary to the conventional search modes. Recent studies on exotic Higgs decays can be found in Refs. [278–289].

A 100 TeV pp collider offers great opportunity for probing non-SM Higgses. The production cross sections can be enhanced by about a factor of 30–50 for gluon fusion and bb associated production, and about a factor of 90 for the charged Higgs for Higgs mass of about 500 GeV, and even more for heavier Higgses. In the new mass domain accessible to the machine, the decays of $H^0/A \to tt$ and $H^\pm \to tb$ are easily allowed kinematically. In the former case, the branching fraction becomes sizable for intermediate $\tan\beta$ and dominant for low $\tan\beta$. The channels of $pp \to H^0/A, bbH^0/A$ with $H^0/A \to \tau\tau, bb, tt$ provide full coverage of the $\tan\beta$ domain. In the latter case, $H^\pm \to tb$ becomes dominant over the whole $\tan\beta$ domain if exotic decay modes are not present. New kinematics of these signal events at a 100 TeV pp collider also bring new handles. For example, the top quark appearing in the decay could be highly boosted. Looking into its internal structure (though a finer granularity of both ECAL and HCAL is typically required) or requiring an extremely hard lepton in top decays can efficiently suppress the relevant backgrounds. In addition, exotic Higgs decays can provide alternative search channels at the 100 TeV pp collider when the conventional decays are suppressed.

In this subsection, we summarize the production and decay of heavy non-SM Higgses at a 100 TeV pp collider, and highlight the main search channels for H^0, A^0 and $H^\pm$ and its potential reach. Note that while it is a viable possibility for the light CP-even Higgs h^0 to be non-SM like, and the heavy CP-even Higgs H^0 to be SM-like (the so-called H^0-125 case with $\sin(\beta-\alpha) \sim 0$) [290], we will here focus on the conventional case of h^0 being the SM-like Higgs of 125 GeV with a heavy non-SM H^0. For simplicity, the results presented in the following sections are for the alignment limit of $\cos(\beta-\alpha) = 0$, even though regions of $\cos(\beta-\alpha)$ away from zero can still be accommodated by the current experimental Higgs search results [290].

Our discussion is organized as follows. In Sec. 7.6, we briefly introduce the Type II 2HDM with its particle content and relevant couplings. In Sec. 7.6, we present the dominant production cross sections for H^0, A^0 and $H^\pm$ at the 100 TeV pp collider. In Sec. 7.6, we discuss the decay modes for heavy Higgses. In Sec. 7.6, we present the reach for heavy Higgses at a 100 TeV pp collider using the conventional decay modes into SM fermions. In Sec. 7.6, we discuss the prospect for heavy Higgs discovery via exotic decay modes to light Higgses or one light Higgs plus a SM gauge boson. In Sec. 7.6, we conclude.

Type II 2HDM

In the 2HDM[9], we introduce two $\mathrm{SU}(2)$ doublets Φ_i, $i = 1, 2$:

$$\Phi_i = \begin{pmatrix} \phi_i^+ \\ (v_i + \phi_i^0 + iG_i)/\sqrt{2} \end{pmatrix}, \tag{7.25}$$

where v_1 and v_2 are the vacuum expectation values of the neutral components which satisfy the relation: $v = \sqrt{v_1^2 + v_2^2} = 246$ GeV after electroweak symmetry breaking. Assuming a discrete $\mathcal{Z}_2$ symmetry imposed on the Lagrangian, we are left with six free parameters, which can be chosen as four Higgs masses (m_h, m_{H^0}, m_A, $m_{H^\pm}$), the mixing angle α between the two CP-even Higgses, and the ratio of the two vacuum expectation values, $\tan\beta = v_2/v_1$. In the case in which a soft breaking of the $\mathcal{Z}_2$ symmetry is allowed, there is an additional parameter m_{12}^2.

The mass eigenstates contain a pair of CP-even Higgses: h^0, H^0, one CP-odd Higgs A and a pair of charged Higgses $H^\pm$:

$$\begin{pmatrix} H^0 \\ h^0 \end{pmatrix} = \begin{pmatrix} \cos\alpha & \sin\alpha \\ -\sin\alpha & \cos\alpha \end{pmatrix} \begin{pmatrix} \phi_1^0 \\ \phi_2^0 \end{pmatrix}, \quad \begin{aligned} A &= -G_1 \sin\beta + G_2 \cos\beta \\ H^\pm &= -\phi_1^\pm \sin\beta + \phi_2^\pm \cos\beta \end{aligned}. \tag{7.26}$$

Two types of couplings that are of particular interest are the couplings of a Higgs to two gauge bosons, as well as the couplings of a SM gauge boson to a pair of Higgses. Both are determined by the gauge coupling structure and the mixing angles. The H^0VV and h^0VV couplings are [291]:

$$g_{H^0VV} = \frac{m_V^2}{v}\cos(\beta-\alpha), \quad g_{h^0VV} = \frac{m_V^2}{v}\sin(\beta-\alpha). \tag{7.27}$$

The couplings for a SM gauge boson with a pair of Higgses are [291]:

$$g_{AH^0Z} = -\frac{g\sin(\beta-\alpha)}{2\cos\theta_w}(p_{H^0} - p_A)^\mu, \qquad g_{Ah^0Z} = \frac{g\cos(\beta-\alpha)}{2\cos\theta_w}(p_{h^0} - p_A)^\mu, \tag{7.28}$$

$$g_{H^\pm H^0 W^\mp} = \frac{g\sin(\beta-\alpha)}{2}(p_{H^0} - p_{H^\pm})^\mu, \qquad g_{H^\pm h^0 W^\mp} = \frac{g\cos(\beta-\alpha)}{2}(p_{h^0} - p_{H^\pm})^\mu, \tag{7.29}$$

$$g_{H^\pm A W^\mp} = \frac{g}{2}(p_A - p_{H^\pm})^\mu, \tag{7.30}$$

with g being the $\mathrm{SU}(2)$ coupling, θ_w being the Weinberg angle and p_μ being the incoming momentum of the corresponding particle. Note that A and $H^\pm$ always couple to the non-SM-like Higgs more strongly, while the $H^\pm AW^\mp$ coupling is independent of the mixing parameters.

In the Type II 2HDM, one Higgs doublet Φ_1 provides masses for the down-type quarks and charged leptons, while the other Higgs doublet Φ_2 provides masses for the up-type quarks. The couplings of the CP-even Higgses h^0, H^0 and the CP-odd Higgs A to the SM gauge bosons and fermions are scaled by a factor ξ relative to the SM value, as presented in Table 7.4.

In addition, the $H^\pm tb$ coupling is

$$g_{H^\pm tb} = \frac{g}{2\sqrt{2}m_W}\left[(m_b\tan\beta + m_t\cot\beta) \pm (m_b\tan\beta - m_t\cot\beta)\gamma_5\right], \tag{7.31}$$

[9]For more details about the 2HDM, see Ref. [267].

$\xi_{h^0}^{VV}$	$\sin(\beta-\alpha)$	$\xi_{H^0}^{VV}$	$\cos(\beta-\alpha)$	ξ_{A}^{VV}	0
$\xi_{h^0}^{u}$	$\cos\alpha/\sin\beta$	$\xi_{H^0}^{u}$	$\sin\alpha/\sin\beta$	ξ_{A}^{u}	$\cot\beta$
$\xi_{h^0}^{d,l}$	$-\sin\alpha/\cos\beta$	$\xi_{H^0}^{d,l}$	$\cos\alpha/\cos\beta$	$\xi_{A}^{d,l}$	$\tan\beta$

Table 7.4 The multiplicative factors ξ by which the couplings of the CP-even Higgses and the CP-odd Higgs to the gauge bosons and fermions scale with respect to the SM value. The superscripts u, d, l and VV refer to the up-type quarks, down-type quarks, leptons, and WW/ZZ respectively.

which is enhanced at both small and large $\tan\beta$. The $H^{\pm}\tau\nu$ has similar enhancement at large $\tan\beta$ as well.

Production Cross Sections

The dominant production processes for the neutral Higgses are gluon fusion $gg \to H^0/A$ with dominant top and bottom (for large $\tan\beta$) loops, as well as bbH^0/A associated production. ttH^0/A associated production could be important as well. The dominant production process for the charged Higgses is $tbH^{\pm}$ associated production. Production cross sections at 100 TeV pp collider for A^0, H^0 and $H^{\pm}$ are shown in Fig. 7.33. For H^0, we have assumed the alignment limit of $\cos(\beta-\alpha)=0$ in which the light CP-even Higgs is the SM-like one, and the couplings of the heavy CP-even Higgs H^0 to the SM particles is the same in amplitude as that of the CP-odd Higgs A, but differs in the relative sign of the couplings to the up type quarks comparing to that of the down type quarks. For charged Higgs production, corrections from resumming top logarithms may play a role at 100 TeV [221, 226], but are not expected to significantly affect the general features of the results [226, 297]. For neutral Higgses, gluon fusion production dominates at low $\tan\beta$ while bbH^0/A associated production dominates at large $\tan\beta$. The $tbH^{\pm}$ production cross section gets enhanced at both small and large $\tan\beta$.

Comparing to the 14 TeV LHC, the production rates can be enhanced by about a factor of $30-50$ for gluon fusion and bb associated production, and about a factor of 90 for the charged Higgs for Higgs mass if about 500 GeV, and even more for heavier Higgses, resulting in great discovery potential for heavy Higgses at a 100 TeV pp colliders.

Heavy Higgs Decays

Conventional decay modes for heavy Higgses are $H^0 \to tt/bb/\tau\tau/WW/ZZ/\gamma\gamma$, $A \to tt/bb/\tau\tau$ and $H^{\pm} \to tb/\tau\nu/cs$. Note that for h^0 being SM-like, H^0 decays to WW and ZZ are highly suppressed given that $\cos(\beta-\alpha)\sim 0$ is preferred. The branching fractions for a heavy H^0, A, and $H^{\pm}$ are shown in the dashed curves in Fig. 7.34, assuming exotic decay modes are kinematically forbidden.

Five main exotic decay categories for Higgses of the Type II 2HDM are shown in Table 7.5. Once these decay modes are kinematically open, they typically dominate over the conventional decay channels, as shown in Fig. 7.34 for H^0 (left panel), A (middle panels), and $H^{\pm}$ (right panel). Note that in the alignment limit of $\cos(\beta-\alpha)=0$, the branching fraction of $H^0 \to h^0h^0$ is zero. The branching fractions for heavy A are similar to those of H^0, except that the decay modes of H^0H^0 and H^+H^- are absent.

Note that the current experimental searches for the non-SM Higgs always assume the absence of exotic decay modes. Once there are light Higgs states such that these exotic

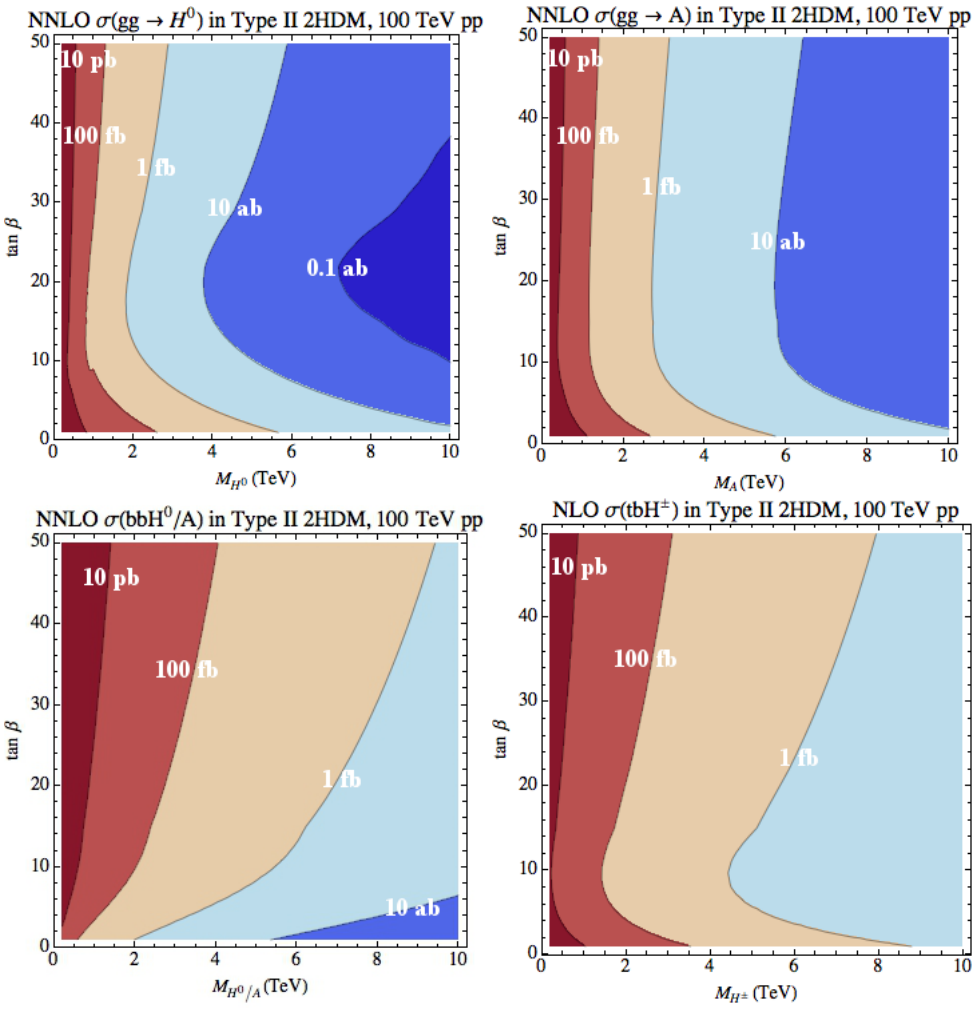

Figure 7.33 Dominant production cross sections for non-SM like Higgses in the type II 2HDM at the 100 TeV pp collider: NNLO cross section for $gg \to H^0$ or A (top left and top right panel, calculated using HIGLU [292] with the NNPDF2.3 parton distribution functions [220]), NNLO cross section for bottom-associated production bbH^0/A (lower left panel, calculated using SusHi [293–295]. bbH^0 and bbA cross sections are the same in the alignment limit), NLO cross section for $tbH^\pm$ (lower right panel, calculated in Prospino [51, 296]).

modes are kinematically open, the current search bounds can be greatly relaxed [279, 281, 283].

Conventional Search Channels

At a 100 TeV pp collider, new mass domains for both neutral and charged Higgs bosons become accessible, given the enhanced production cross sections and the dominance of decays to final states with top quarks (at small $\tan\beta$ for neutral Higgses and at both small and large $\tan\beta$ for charged Higgses), as well as novel kinematic features of the decay products. Combining production processes and decay channels, the main search channels to cover various $\tan\beta$ regions are summarized in Table 7.6.

The top quarks from the heavy Higgs can decay either hadronically or leptonically. The hard leptons produced from top decay products, together with the boosted top jets, can efficiently suppress the backgrounds, including the irreducible backgrounds of tt and $ttbb$.

	Decay	Final States	Channels
Neutral Higgs H^0, A	HH type	$(bb/\tau\tau/WW/ZZ/\gamma\gamma)(bb/\tau\tau/WW/ZZ/\gamma\gamma)$	$H^0 \to AA$, ...
	HZ type	$(\ell\ell/qq/\nu\nu)(bb/\tau\tau/WW/ZZ/\gamma\gamma)$	$H^0 \to AZ, A \to H^0$
	H^+H^- type	$(tb/\tau\nu/cs)(tb/\tau\nu/cs)$	$H^0 \to H^+H^-$, ...
	$H^\pm W^\mp$ type	$(\ell\nu/qq')(tb/\tau\nu/cs)$	$H^0/A \to H^\pm W^\mp$, ..
Charged Higgs	$HW^\pm$ type	$(\ell\nu/qq')(bb/\tau\tau/WW/ZZ/\gamma\gamma)$	$H^\pm \to H^0W, AW$, .

Table 7.5 Exotic Decay modes for Higgses in the 2HDM. H in column two refers to any of the neutral Higgs h^0, H^0 or A.

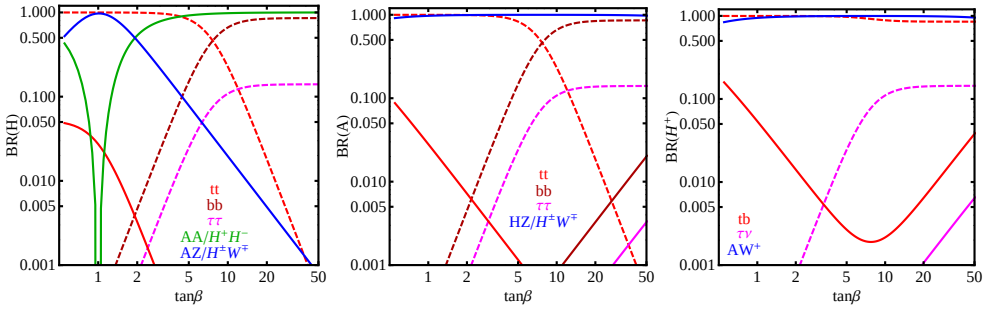

Figure 7.34 Branching fractions for H^0 (left panel), A (middle panel) and $H^\pm$ (right panel). The parent and daughter Higgs masses are chosen to be 2 TeV and 800 GeV, respectively. Note that in the $H^0(A)$ decay, we have assumed either light A (H^0) *or* light $H^\pm$, but not both. Dashed curves are the branching fractions when exotic decay modes are kinematically forbidden. All decay branching fractions are calculated using the program 2HDMC [298].

	$\tan\beta$	Channels
Neutral Higgs H^0, A	High	$pp \to bbH^0/A \to bb\tau\tau, bbbb$
	Intermediate	$pp \to bbH^0/A \to bbtt$
	Low	$pp \to H^0/A \to tt$
Charged Higgs $H^\pm$	High	$pp \to tbH^\pm \to tbtb, tb\tau\nu_\tau$
	Low	$pp \to tbH^\pm \to tbtb$

Table 7.6 Main conventional search channels for non-SM Higgses to cover various $\tan\beta$ regions [299] at a 100 TeV pp collider.

For final states with taus, either large transverse mass for the signal events or hard leptons from tau decays can efficiently distinguish the signal and backgrounds. The choices made in the illustrative analyses below (see caption of Fig. 7.35) also benefit the reconstruction of the heavy Higgs resonance. In addition, the large rapidity of the two non-top b-jets in $pp \to bbH^0/A \to bbtt$ and $pp \to tbH^\pm \to tbtb$ can be used to further suppress the backgrounds; this kinematic feature has not been applied for the H^0/A and $H^\pm$ searches at the LHC.

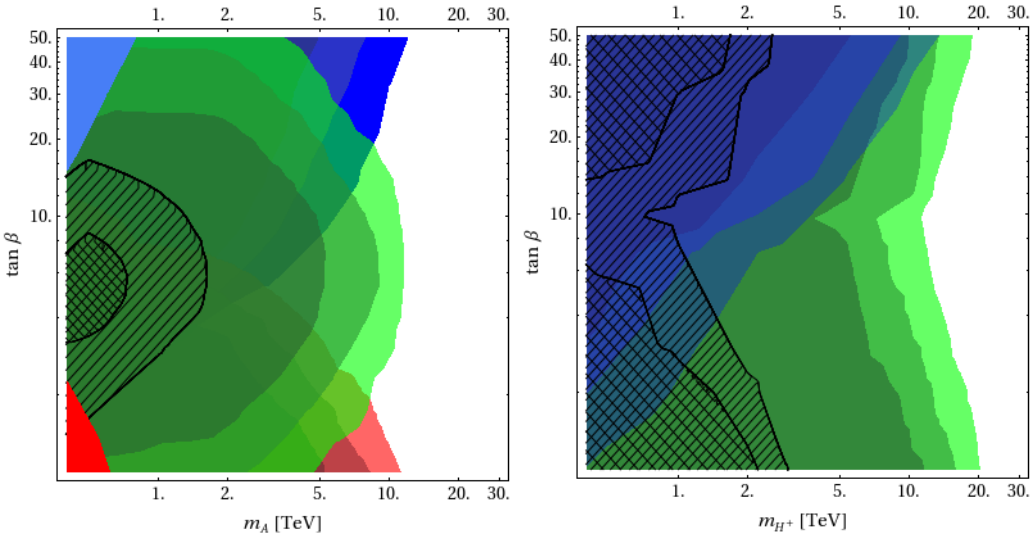

Figure 7.35 95% C. L. Exclusion limits for the MSSM Higgs bosons at a 100 TeV pp collider [299]. The three regions with the same color and different opacities are excluded by assuming a luminosity of 0.3 ab^{-1}, 3 ab^{-1}, and 30 ab^{-1}, respectively. Left: neutral Higgs bosons (H/A). The blue, green and red regions are excluded by the channels $pp \to bbH/A \to bb\tau_h\tau_l$, $pp \to bbH/A \to bbt_ht_l$ and $pp \to H/A \to t_ht_l$, respectively. The blue and red regions in the upper left and lower left corners are the current exclusion limits of $pp \to bbH/A \to bb\tau_h\tau_l$ and $pp \to H/A \to t_ht_l$ at the LHC. Right: charged Higgs bosons ($H^\pm$). The blue and green regions are excluded by the channels $pp \to tbH^\pm \to tb\tau_h\nu_\tau$ and $pp \to tbH^\pm \to t_hbt_lb$, respectively. The cross-hatched and backward diagonal hatched regions are the predicted exclusion contours for associated Higgs production at the LHC for 0.3 ab^{-1}, and 3 ab^{-1} of data, respectively.

To fully utilize the kinematic features of the signal events, a Boosted Decision Tree method may be used to search for heavy Higgses decaying to semileptonic tops or taus [299]. The 95% C.L. exclusion limits yielded by these channels are presented in Fig. 7.35, with various luminosities (0.3 ab^{-1}, 3 ab^{-1}, and 30 ab^{-1}) and an ATLAS-type detector assumed. The exclusion limits for both the neutral and charged Higgs bosons are pushed from the $\mathcal{O}(1)$ TeV scale at the LHC to the $\mathcal{O}(10)$ TeV scale at a 100 TeV pp collider for the whole range of $\tan\beta$. In particular, the wedge region for the netral Higgs searches ($\tan\beta \sim 7$) and the low $\tan\beta$ region are fully covered by the channels $pp \to bbH^0/A \to bbtt$ and $pp \to tbH^\pm \to tbtb$, respectively.

Exotic Search Channels

Other than decays into conventional searches channels as mentioned in Sec. 7.6, exotic Higgs decays to final states with two light Higgses or one Higgs plus one SM gauge boson provide complementary search channels. Here, we list such exotic Higgs decays and consider potential search strategies.

- $H^0 \to AA$

With one final state Higgs decay via bb, and the other decay via $\gamma\gamma$, the $bb\gamma\gamma$ channel has been shown to be sensitive to the di-Higgs final states [300], in particular, with resonant enhancement of the production cross section. Final states involve taus might also be useful in probing this decay. Associated production with bb can enhance the reach further at large $\tan\beta$.

- $H^0 \to AZ$ or $A \to H^0 Z$

With $Z \to \ell\ell$ and $H^0/A \to bb, \tau\tau$, the final states of $bb\ell\ell$, $\tau\tau\ell\ell$ can be obtained with gluon fusion production, or in the bb associated production with two additional b jets [278–280]. In parameter regions where $\mathrm{Br}(A \to H^0 Z) \times \mathrm{Br}(H^0 \to ZZ)$ is not completely suppressed, ZZZ final states with two Z decaying leptonically and one Z decaying hadronically can also be useful [279]. Other channels with top final states could be explored as well.

- $H^0 \to H^+ H^-$

With both $H^\pm$ decaying via $\tau\nu$ final states, the signal of $\tau\tau\nu\nu$ can be separated from the SM W^+W^- background since the charged tau decay product in the signal typically has a hard spectrum compared to that of the background [283]. Utilizing the top identification strategy as mentioned in Sec. 7.6, $ttbb$ or $tb\tau\nu$ final states could also be useful.

- $H^0/A \to H^\pm W^\mp$

Similar to the H^+H^- case, $H^\pm \to \tau\nu, tb$ and $W \to \ell\nu$ with $\ell\tau\nu\bar{\nu}$ or $tb\ell\nu$ could be used to search for $H^0/A \to H^\pm W^\mp$. Note that for the CP-even Higgs H^0, the branching fraction of $H^0 \to H^\pm W^\mp$ is mostly suppressed comparing to $H^0 \to H^+H^-$ as long as the latter process is kinematically open and not accidentally suppressed (see Fig. 7.34) [283]. However, for the CP-odd Higgs A, this is the only decay channel with a charged Higgs in the decay products.

- $H^\pm \to H^0 W, AW$

This is the only exotic decay channel for the charged Higgs in the 2HDM. Given the associated production of $tbH^\pm$, and the decay of H^0, A into the bb or $\tau\tau$ channel, $\tau\tau bbWW$ or $bbbbWW$ can be used to probe this channel [281]. $H^0/A \to t\bar{t}$ could also be used given the boosted top in the high energy environment.

Conclusion

Discovery of the non-SM Higgs bosons in an extended Higgs sector would provide clear evidence for new physics beyond the SM. At the 14 TeV LHC, the conventional search channels for neutral and charged Higgses leave a wedge region open around intermediate $\tan\beta \sim 7$ and $m_A \gtrsim 300$ GeV in which only the SM Higgs is detected. Exotic decays of heavy Higgses into two light Higgses or one light Higgs and one SM gauge boson provide complementary search channels once they are kinematically open.

A 100 TeV pp collider offers great discovery potential for non-SM heavy Higgses. In this write-up, we summarized the reach at the 100 TeV pp collider for conventional search modes, in particular, via the $H^0/A \to t\bar{t}$ and $H^\pm \to tb$ channels. The whole range of $\tan\beta$ can be probed for masses up to about 10 TeV when various channels are combined. We also outline the possible search channels for exotic decays when the branching fractions for conventional channels are suppressed. Combinations of those channels can greatly extend the reach of the non-SM Higgs at a 100 TeV pp collider.

Higgs Decay to Light Flavor Quarks

Introduction

The first run of the LHC was very successful not only because of the Higgs discovery but also because it has in addition provided us with a rather strong qualitative test of several aspects of the Higgs mechanism: it shows that the Higgs plays a dominant in inducing the masses to the EW gauge bosons and that its coupling are consistent with taming of the longitudinal WW scattering rates up to high energies. However, in the SM minimalistic way of EWSB the Higgs plays an additional, second important role, namely inducing masses to all the SM charged fermions. It leads to a sharp prediction, free of input parameters, regarding the Higgs-fermion coupling strength

$$y_f \simeq \sqrt{2}\,\frac{m_f}{v}\,, \tag{7.32}$$

where $f = u, c, t, d, s, b, e, \mu, \tau$ and v that holds to a very good accuracy. This additional function of the Higgs was not yet tested directly in a strong way, thus far. The best information currently available is on the Higgs couplings to the third generation charge fermions

$$\mu_{ht\bar{t}} = 2.41 \pm 0.81,\ \mu_{b\bar{b}} = 0.71 \pm 0.31,\ \mu_{\tau\bar{\tau}} = 0.97 \pm 0.23\,, \tag{7.33}$$

where in the above we averaged over the results of ATLAS and CMS for the Higgs signal strength to fermions $\mu_{f\bar{f}} \equiv \frac{\sigma}{\sigma_{\rm SM}}\,\frac{{\rm BR}_{f\bar{f}}}{{\rm BR}^{\rm SM}_{f\bar{f}}}$ with σ stands for the production cross section, ${\rm BR}_{f\bar{f}} = {\rm BR}(h \to f\bar{f})$ and the SM script stands for the SM case. The results are consistent with the SM expectations at the 2σ CL, but of course with a noticeable large errors. Our current knowledge regarding the Higgs couplings to the first two generation, light, fermions, is significantly poorer. In fact at this point we only have a rather weak (95% CL) upper bound on the corresponding signal strengths of the muons and electrons [301, 302]

$$\mu_{\mu^+\mu^-} \leq 7, \qquad \mu_{e^+e^-} \leq 4 \cdot 10^5\,. \tag{7.34}$$

Such an information does not exist at present regarding the Higgs light quark couplings.

Measuring these Higgs-light couplings is interesting from the following three reasons. First, the light quarks Yukawa coupling is a parameter of the SM and as such it merit a measurement. The second is that due to the success of the indirect and direct tests of the SM it is now expected that the EW gauge bosons and the top quark dominantly acquire there masses due to the Higgs mechanism this is less obvious for the case of the first two generation quarks. The light quark masses could be in principle induced by other subdominant sources of EWSB, say from a technicolor-like condensate, and hence have suppressed or even vanishing Yukawa couplings to the Higgs. In fact, based on current knowledge, we could just add bare mass terms to the first two generation fermions and think about the SM as an effective theory that is valid up to some fairly high scale, were "unitarity" or the SM weakly coupled description would breakdown. This is somewhat similar to what was the status of the EW gauge sector prior to the first run of the LHC. Deciding whether the fermion-EW system is valid up to energies far above the TeV scale is a very well defined target for future collider. The third argument, following probably an opposite reasoning, is that with new physics it is actually pretty easy to obtain an enhancement in the Higgs-light quark interaction strength. Furthermore, as the Higgs is rather light its only open decay channels are to particles that very weakly interact with

it. The dominant decay mode of the Higgs is to bottom pair, with the bottom Yukawa coupling is $\mathcal{O}(0.02)$. Any deformation of the Higgs couplings to the lighter SM particles, say the charm quarks (for possibly relevant discussions see [303–311]), could in principle compete with the Higgs-bottom coupling and would lead to a dramatic change of the Higgs phenomenology at collider [312].

Recent theoretical and experimental progress allowed to open a window towards studying the Higgs coupling to light quarks at future colliders as follows. On the theoretical frontier, it was demonstrated in [312] that using inclusive charm-tagging would enable the LHC experiments to search for the decay of the Higgs into pair of charm jets. Furthermore in [313] it was shown that the charm-Higgs coupling could be probed by looking at exclusive decay modes involving a $c - \bar{c}$ meson and a photon. A similar mechanism, based on exclusive final state with light quark states and vector bosons (photon as well as EW ones) was shown to yield a potential access to the light quark-Higgs couplings in [314] (see also [315] for study of exclusive EW gauge boson decays). On the experimental frontier in the last year or so ATLAS has published two papers on SUSY searches which are based on charm-tagging to identify stop to charm final state, in a compressed scenario [316] and scharm to charm decay model in non-degenerate-squarks SUSY models [317]. Furthermore on the exclusive frontier in [318] ATLAS has searched for Higgs and Z Boson Decays to charmonia and a photon final states. The above works provide a proof of principle that in the future we may be able to test the Higgs mechanism of mass generation even for the light quarks. In this subsection we shall attempt to give a brief summary of the current knowledge. Our emphasis is on the hadronic machine where most of the recent progress was made, however for completeness we also discuss the reach of electron-positron circular machines.

Current Status, Preliminary Studies at the LHC

At present there is no official experimental bound on the size of the Higgs-charm couplings. However, [319] introduced four different types of data-driven analyses with different level of robustness that constrain the size of the Higgs-charm Yukawa couplings, κ_c, (measured in units of the Standard Model (SM) charm Yukawa)

$$\kappa_x = y_x / y_x^{\mathrm{SM}} \,. \tag{7.35}$$

We shall here briefly describe the method that we have applied to obtain the bound. More details can be found in [319].

Direct Bound via Recast of $Vh(b\bar{b})$

We recast the, vector associated higgs, Vh, production analysis that search for bottom final states. We use this mode to directly and model independently constrain the higgs to charm coupling, We can recast the analysis of $h \to b\bar{b}$ to study $h \to c\bar{c}$. In this case, the signal strength is modified,

$$\mu_b \;\; \to \;\; \frac{\sigma \cdot \mathrm{Br}_b \cdot \epsilon_{b_1}\epsilon_{b_2} + \sigma \cdot \mathrm{Br}_c \cdot \epsilon_{c_1}\epsilon_{c_2}}{\sigma_{SM} \cdot \mathrm{Br}_b^{SM} \cdot \epsilon_{b_1}\epsilon_{b_2}} = \mu_b + \frac{\mathrm{Br}_c^{SM}}{\mathrm{Br}_b^{SM}} \frac{\epsilon_{c_1}\epsilon_{c_2}}{\epsilon_{b_1}\epsilon_{b_2}} \mu_c \,, \tag{7.36}$$

where $\epsilon_{b_{1,2}}$ and $\epsilon_{c_{1,2}}$ are efficiencies to tag jets originating from bottom and charm quark, respectively. μ_c is normalized to be 1 in a case of the SM.If the charm tagging rates, $\epsilon_{c_{1,2}}$,

are larger, we will be more sensitive to charm final states, μ_c. However, this is not enough because one criterion of b-tagging only constraints a linear combination of μ_b and μ_c. In order to disentangle the degeneracy, we need at least two tagging criteria with different ratios, $\epsilon_{c/b} \equiv (\epsilon_{c_1}\epsilon_{c_2})/(\epsilon_{b_1}\epsilon_{b_2})$. The ATLAS and CMS have different tagging working points and hence μ_c is extracted, giving a bound. If no new production mechanism is assumed than the resulting bound is too weak to yield a non-trivial bound on κ_c (as branching ratio larger than one is formally allowed at two sigma). However as shown in Fig. 7.36 when κ_c (or more generally $\kappa_{u,d,s,c}$) becomes big then new contributions to Vh final states becomes important and the "runaway" to arbitrarily large Yukawa is eliminated. Including the new

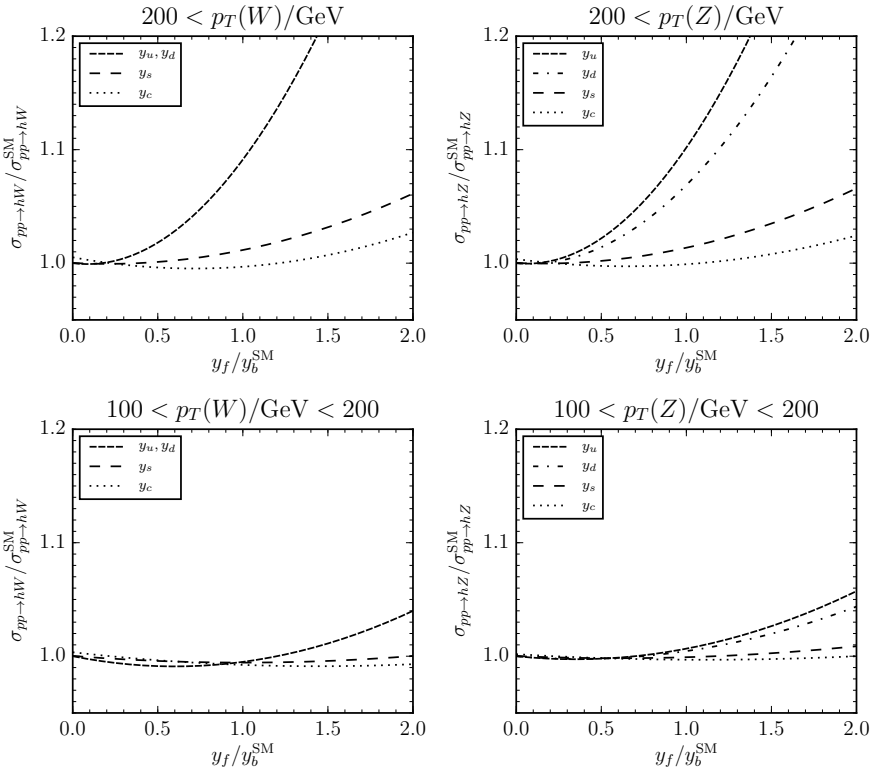

Figure 7.36 The cross section of the new production mode to associated Wh (Zh) modes is shown on the left (right) for various p_T cuts for various quark-Higgs Yukawa couplings (in units of the bottom Yukawa) normalised to the SM value.

production mechanism and combining the data form ATLAS and CMS multi-working-points study of $Vh(b\bar{b})$ yield the following bound

$$\kappa_c \lesssim 250\,. \tag{7.37}$$

Direct Bound via Recast of $h \to J/\psi\gamma$

Recently, ATLAS put the first bound on the Higgs exclusive decay to $J/\psi\gamma$ [318]

$$\sigma(pp \to h) \times \mathrm{BR}_{h\to J\psi\gamma} < 33\,\mathrm{fb}\,, \tag{7.38}$$

under the assumption of SM Higgs production this can be interpreted as bound of $\mathrm{BR}(h \to J/\psi\gamma) < 1.5 \times 10^{-3}$. The partial width of $h \to J/\psi\gamma$ is given by [313, 320]

$$\begin{aligned}\Gamma_{h\to J/\psi\gamma} =& \left|(11.9 \pm 0.2)\kappa_\gamma - (1.04 \pm 0.14)\kappa_c\right|^2 \cdot 10^{-10}\,\mathrm{GeV} \\ =& 1.42\,(\kappa_\gamma - 0.087\kappa_c)^2 \cdot 10^{-8}\,\mathrm{GeV}\,,\end{aligned} \tag{7.39}$$

where $m_h = 125.9 \pm 0.4\,\mathrm{GeV}$ is assumed.

The dependence on the production mechanism and the Higgs total width can be canceled to a good approximation in the ratio between the bound (or measurement in the future) of the $pp \to h \to J/\psi\gamma$ rate and one of the other Higgs rate measurements with inclusive production, for example $h \to ZZ^* \to 4\ell$. We define

$$R_{J/\psi,Z} = \frac{\sigma(pp\to h)\times \mathrm{BR}_{h\to J/\psi\gamma}}{\sigma(pp\to h)\times \mathrm{BR}_{h\to ZZ^*\to 4\ell}} = \frac{\Gamma_{h\to J/\psi\gamma}}{\Gamma_{h\to ZZ^*\to 4\ell}} = 2.79\frac{(\kappa_\gamma - 0.087\kappa_c)^2}{\kappa_V^2}\cdot 10^{-2}\,, \tag{7.40}$$

where perfect cancellation of the production is assumed (correct for leading order) and $\mathrm{BR}^{\mathrm{SM}}_{h\to ZZ^*\to 4\ell} = 1.26 \cdot 10^{-4}$. By using Eq. (7.38) and the ZZ^* signal strength $\mu_{ZZ^*} = 1.44^{+0.40}_{-0.33}$ [321] we can extract

$$R_{J/\psi,Z} = \frac{33\,\mathrm{fb}}{\mu_{ZZ^*}\sigma^{\mathrm{SM}}\mathrm{BR}^{\mathrm{SM}}_{h\to ZZ^*\to 4\ell}} < 9.32\,. \tag{7.41}$$

Combine the last with Eq. (7.40) leads to

$$-210\kappa_V + 11\kappa_\gamma < \kappa_c < 210\kappa_V + 11\kappa_\gamma\,. \tag{7.42}$$

Indirect Bound from the Total Bound on the Higgs Width

The measurement of the total width yield Both ATLAS and CMS give model independent bound on the Higgs total width from the invariant mass distribution of $h \to 4\ell$ and $h \to \gamma\gamma$. These bounds are limited by the experimental resolution of around 1 GeV. Under the assumption of no interference with the background the upper limits by ATLAS [322] are

$$\begin{aligned}&\Gamma_h < 5.0\,\mathrm{GeV}\ \text{from}\ h \to \gamma\gamma\,, \\ &\Gamma_h < 2.6\,\mathrm{GeV}\ \text{from}\ h \to ZZ^* \to 4\ell\,.\end{aligned} \tag{7.43}$$

The corresponding CMS bounds are [323]

$$\begin{aligned}&\Gamma_h < 2.4\,\mathrm{GeV}\ \text{from}\ h \to \gamma\gamma\,, \\ &\Gamma_h < 3.4\,\mathrm{GeV}\ \text{from}\ h \to ZZ^* \to 4\ell\,, \\ &\Gamma_h < 1.7\,\mathrm{GeV}\ \text{combined}\,,\end{aligned} \tag{7.44}$$

comparing to the SM prediction of $\Gamma_h^{\mathrm{SM}} = 4.07\,\mathrm{MeV}$ [324] for $m_h = 125.0\,\mathrm{GeV}$.

We can use the above upper bound on the total width to bound the charm Yukawa by assuming that the entire Higgs width is saturated by it

$$\kappa_c^2\,\mathrm{BR}^{\mathrm{SM}}_{h\to c\bar{c}}\Gamma_h^{\mathrm{SM}} = 1.18 \times 10^{-4}\kappa_c^2\,\mathrm{GeV} < \Gamma_h \tag{7.45}$$

where $\mathrm{BR}^{\mathrm{SM}}_{h\to c\bar{c}} = 2.90 \cdot 10^{-2}$. This finally gives:

$$\kappa_c \lesssim 150\,(\mathrm{ATLAS}),\ 120\,(\mathrm{CMS})\,. \tag{7.46}$$

Indirect Bound from Global Fit to Higgs Couplings

A global fit to the Higgs signal strength, in particular a comparison with the vector boson fusion (VBF) channel that is predominantly independent of new physics contamination yields a bound (obtained in [319])

$$\kappa_c \lesssim 6\,. \tag{7.47}$$

Constraining Non-universality

A comparison with the data from $t\bar{t}h$ data allows us to show that current data eliminates the possibility that the Higgs couples to quark in a universal way, as is consistent with the SM prediction. naive average of $\mu_{t\bar{t}h}$ from ATLAS [325] and CMS [326], $\mu_{t\bar{t}h}^{\rm avg} = 2.41 \pm 0.81$ see Eq. (7.33), leads to lower bound on the top Yukawa

$$|\kappa_t| > 0.9\sqrt{\frac{\mathrm{BR}^{\rm SM}_{h\to\text{relevant modes}}}{\mathrm{BR}_{h\to\text{relevant modes}}}} > 0.9\,, \tag{7.48}$$

where $\mathrm{BR}_{h\to\text{relevant modes}}$ stands for the relevant final state in the $t\bar{t}h$ measurements. Note that the last equality valid in case that the Higgs to charm pairs is the dominant partial width. This bound in case of universal coupling is translated to an upper bound on the charm Yukawa $\kappa_c \gtrsim 280$. We summarise the current situation in Fig. 7.37 (taken from [319])

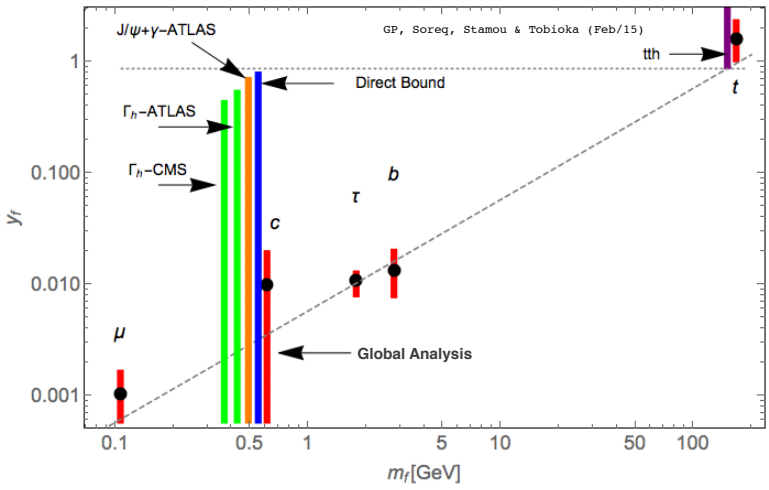

Figure 7.37 Summary of current constraints on the Higgs couplings to fermions including the new bounds on the charm Yukawa, taken from [319].

We point for two new production mechanisms, related to Vh and VBF processes, that become important when the first two generation quarks have enhanced couplings to the Higgs. In conjunction with a future measurement at electron-positron collider (linear or circular) the former mechanism is sensitive to the Higgs-light-quarks couplings. We finally demonstrate that if the experimentalists will use other working point for charm tagging (already used in SUSY searches) they can improve our direct bound by roughly order of magnitude using currently available data.

Projections for the Future, Going beyond the LHC

HL-LHC

We also extrapolate this analysis to future reach. Expected error for 3000 fb^{-1} at 14 TeV, based on a medium working point, is $\Delta\mu_b = 0.14$, based on the ATLAS high luminosity study [325]. Following the analysis steps described in 7.6 and using the ATLAS tight working point to remove the flat direction we obtain the future reach of μ_c, which is shown as the black ellipses in the $\mu_b - \mu_c$ plane in Fig. 7.38.

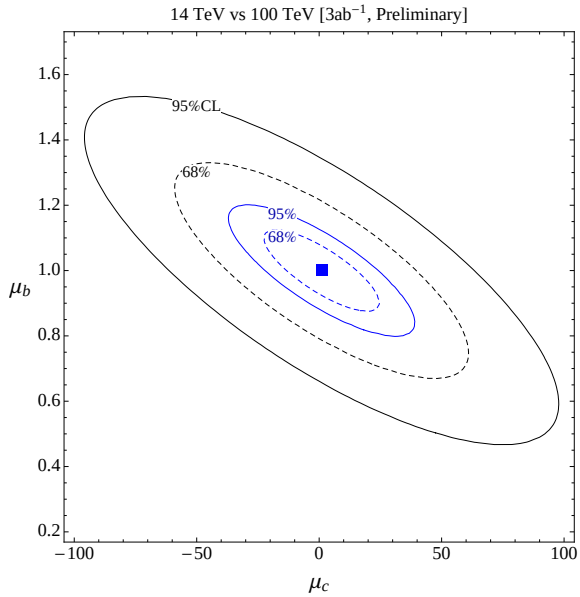

Figure 7.38 Projections for constraining the signal strength of $h \to b\bar{b}$ and $h \to c\bar{c}$ based on charm tagging: The black curves corresponds to a 3 ab^{-1} 14 TeV LHC while the blue ones corresponds to a 100 TeV future collider. The SM expectation is $\mu_x = 1$.

Circular Electron-Positron Colliders

Following the preliminary analysis of [327] and followups the reach is based on working point with $2 \cdot 10^6$ Higgses (with potential increase of one extra order or magnitude) in associate production, which implies the following fantastic accuracies on the relevant signal strengths (assuming SM central values):

$$\delta\mu_{b\bar{b}} = 0.2\% \,,\ \delta\mu_{c\bar{c}} = 1.2\%,\ \delta\mu_{\tau\bar{\tau}} = 0.7\% \,,\ \delta\mu_{\mu\bar{\mu}} = 13\% \,, \tag{7.49}$$

and, furthermore, there is ongoing discussion whether it would be possible also to run precisely on the Higgs resonance and being able to measure the electron Higgs Yukawa couplings (see link for a very recent discussion). The above information is based on inclusive approach to particle identification. As one cannot apply u, d, s-jet-tagging with a reasonable efficiencies no direct information can be extracted on the Higgs coupling to these light quark states. However, using exclusive decay modes, following the proposal of [314] there is some moderate sensitivity to the Higgs Yukwa couplings to the up and down quarks that is summarised in Tab. 7.7.

An additional less direct information regarding the light quark-Higgs couplings can be extracted from the modification to the production cross section. As already discussed in

Fig. 7.36 when $\kappa_{u,d,s,c}$ deviates from the SM prediction then new contributions to Vh final states could become important. As the production in lepton collider is unaffected by these modifications and is measured to a fantastic subpercentage accuracy a simple comparison of the Vh rates at the LHC (or other hadronic machine) with the leptonic one can yield a new type of constraints on the light-quark-Higgs couplings. For completeness we show in Fig. 7.39 the corresponding enhancement to production modes that passes the VBF selection cuts. Similarly, comparison between different colliders/center-of-masses could provide another indirect constraints on the light-quark-Higgs couplings. Finally, there are

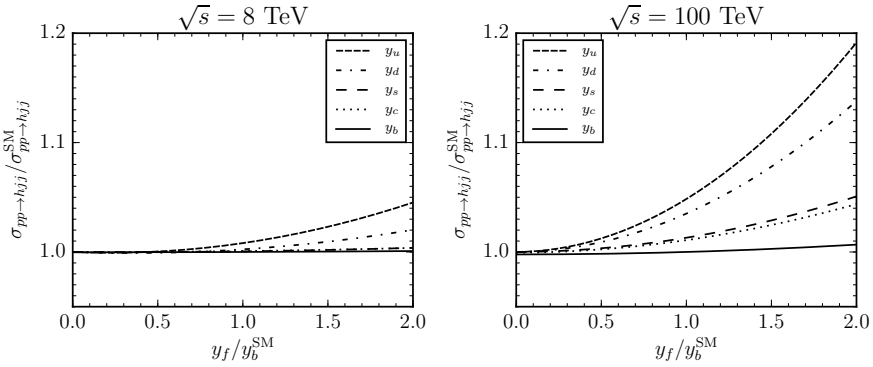

Figure 7.39 The cross section of the new production modes that passes the VBF selection cuts is shown on the left (right) for the 8 TeV LHC (100 TeV future collider) for various quark-Higgs Yukawa couplings (in units of the bottom Yukawa) normalised to the SM value.

also modification to the quark-anti-quark fusion Higgs production (these dominates over the virtual contributions to the ggh effective coupling, see *e.g.* [312, 314]). The SM Higgs production cross section for 100 TeV pp collider is (taken from the HXSECWG of the European Strategy)

$$\sigma^{100}_{ggF} = 740.3\,\text{pb}\,, \tag{7.50}$$
$$\sigma^{100}_{\text{VBF}} = 82.0\,\text{pb}\,, \tag{7.51}$$
$$\sigma^{100}_{WH} = 15.90\,\text{pb}\,, \tag{7.52}$$
$$\sigma^{100}_{ZH} = 11.26\,\text{pb}\,, \tag{7.53}$$
$$\sigma^{100}_{t\bar{t}H} = 37.9\,\text{pb}\,, \tag{7.54}$$
$$\sigma^{100}_{b\bar{b}H} = 8.64\,\text{pb}\,, \tag{7.55}$$
$$\sigma^{100}_{gg\to HH} = 1.42\,\text{pb}\,, \tag{7.56}$$
$$\sigma^{100}_{H,\text{inclusive}} = 896.0\,\text{pb}\,, \tag{7.57}$$

where $\sigma_{H,\text{inclusive}}$ does not include the $gg \to HH$ process.

We can estimate the $q\bar{q} \to h$ production base on the calculation of [294] for $b\bar{b} \to h$ at NLO, where we use the MSTW parton distribution function [328]. The production via

$q\bar{q} \to h$ in pp with 8TeV are

$$\sigma^8_{u\bar{u}\to h} = \left(\frac{y_u}{y_b^{\rm SM}}\right)^2 9.4\,{\rm pb}\,, \qquad \frac{\sigma^8_{u\bar{u}\to h}}{\sigma^8_{ggF}} = 0.49\left(\frac{y_u}{y_b^{\rm SM}}\right)^2, \tag{7.58}$$

$$\sigma^8_{d\bar{d}\to h} = \left(\frac{y_d}{y_b^{\rm SM}}\right)^2 6.4\,{\rm pb}\,, \qquad \frac{\sigma^8_{d\bar{d}\to h}}{\sigma^8_{ggF}} = 0.33\left(\frac{y_d}{y_b^{\rm SM}}\right)^2, \tag{7.59}$$

$$\sigma^8_{s\bar{s}\to h} = \left(\frac{y_s}{y_b^{\rm SM}}\right)^2 1.7\,{\rm pb}\,, \qquad \frac{\sigma^8_{s\bar{s}\to h}}{\sigma^8_{ggF}} = 0.089\left(\frac{y_s}{y_b^{\rm SM}}\right)^2, \tag{7.60}$$

$$\sigma^8_{c\bar{c}\to h} = \left(\frac{y_c}{y_b^{\rm SM}}\right)^2 0.86\,{\rm pb}\,, \qquad \frac{\sigma^8_{c\bar{c}\to h}}{\sigma^8_{ggF}} = 0.045\left(\frac{y_c}{y_b^{\rm SM}}\right)^2, \tag{7.61}$$

where $\sigma^8_{ggF} = 19.27\,{\rm pb}$. The production via $q\bar{q} \to h$ in pp with 100 TeV are

$$\sigma^{100}_{u\bar{u}\to h} = \left(\frac{y_u}{y_b^{\rm SM}}\right)^2 94\,{\rm pb}\,, \qquad \frac{\sigma^{100}_{u\bar{u}\to h}}{\sigma^{100}_{ggF}} = 0.13\left(\frac{y_u}{y_b^{\rm SM}}\right)^2, \tag{7.62}$$

$$\sigma^{100}_{d\bar{d}\to h} = \left(\frac{y_d}{y_b^{\rm SM}}\right)^2 76\,{\rm pb}\,, \qquad \frac{\sigma^{100}_{d\bar{d}\to h}}{\sigma^{100}_{ggF}} = 0.10\left(\frac{y_d}{y_b^{\rm SM}}\right)^2, \tag{7.63}$$

$$\sigma^{100}_{s\bar{s}\to h} = \left(\frac{y_s}{y_b^{\rm SM}}\right)^2 39\,{\rm pb}\,, \qquad \frac{\sigma^{100}_{s\bar{s}\to h}}{\sigma^{100}_{ggF}} = 0.052\left(\frac{y_s}{y_b^{\rm SM}}\right)^2, \tag{7.64}$$

$$\sigma^{100}_{c\bar{c}\to h} = \left(\frac{y_c}{y_b^{\rm SM}}\right)^2 27\,{\rm pb}\,, \qquad \frac{\sigma^{100}_{c\bar{c}\to h}}{\sigma^{100}_{ggF}} = 0.036\left(\frac{y_c}{y_b^{\rm SM}}\right)^2. \tag{7.65}$$

Once more, modification to the production cross section at different colliders or center-of-mass energies would allow one in the future to constrain indirectly the light-quark-Higgs couplings.

100 TeV Collider

In this section we preform naive estimation of the future hadron collider sensitivity to probe the charm and strange Yukawa's at future 100TeV collider.

Inclusive, Charm Tagging

We begin with describing the sensitivity to the charm-Higgs couplings using our charm tagging analysis. We can follow the logic presented in section 7.6, however as we have no information at present on how the background will change with the different center of mass and type of cuts, and furthermore as we prefer not to speculate on the charm tagging efficiencies of an unknown detector we simply project the sensitivity based on the improve of the number of Higgs produced relative to the HL LHC case. This is expected to be at least order of magnitude and thus naively we rescale the significance by roughly a factor of three assuming $\Delta\mu_b = 0.05$. The resulting sensitivity is shown as the blue ellipses in the $\mu_b - \mu_c$ plane in Fig. 7.38.

7.6.0.1 Exclusive Modes

We estimate the reach in $\bar{\kappa}_s = y_s/y_b^{\rm SM}$ and $\bar{\kappa}_c = y_c/y_b^{\rm SM}$ that can be obtained, given the current theoretical uncertainties and the expected statistical errors. For simplicity,

$\bar{\kappa}_q$	$\sqrt{s}$ [TeV]	$\int \mathcal{L}\, dt$ [fb^{-1}]	# of events (SM)	$\bar{\kappa}_q > (<)$	$\bar{\kappa}_q^{\text{stat.}} > (<)$
$\bar{\kappa}_u$	e^+e^-	$2 \cdot 10^6 \cdot H$'s	$\mathcal{O}(40)$	$1.1\,(-1.5)$	$0.88\,(-1.2)$
$\bar{\kappa}_d$	e^+e^-	$2 \cdot 10^6 \cdot H$'s	$\mathcal{O}(40)$	$1.2\,(-1.4)$	$0.96\,(-1.1)$
$\bar{\kappa}_s$	14	3000	770	$0.56\,(-1.2)$	$0.27\,(-0.81)$
$\bar{\kappa}_s$	33	3000	1380	$0.54\,(-1.2)$	$0.22\,(-0.75)$
$\bar{\kappa}_s$	100	3000	5920	$0.54\,(-1.2)$	$0.13\,(-0.63)$
$\bar{\kappa}_c$	14	3000	45	$0.56\,(-5.7)$	$0.54\,(-5.4)$
$\bar{\kappa}_c$	33	3000	81	$0.49\,(-4.7)$	$0.47\,(-4.4)$
$\bar{\kappa}_c$	100	3000	348	$0.39\,(-3.6)$	$0.35\,(-3.3)$

Table 7.7 Three future hadron colliders with expected center of mass energies, integrated luminosities, number of $h \to \phi\gamma, J/\psi\gamma$ events for $\bar{\kappa}_{s,c} = \bar{\kappa}_{s,c}^{\text{SM}} = m_{s,c}/m_b$, the minimal (maximal) values of $\bar{\kappa}_{s,c}$ that can be probed with present (4th column) and negligible (last column) theory error, see text.

we assume $\kappa_\gamma = 1$ as in the SM. The significance of a deviation in the measured value of $\text{BR}_{h\to\phi\gamma}$ with respect to its SM prediction can be quantified by $\mathcal{S} = |\text{BR}_{h\to V\gamma} - \text{BR}^{\text{SM}}_{h\to V\gamma}|/(\delta\text{BR}_{h\to V\gamma})$, where $(\delta\text{BR}_{h\to V\gamma})^2 = \text{BR}_{h\to V\gamma}/(\sigma_h \mathcal{L} A_g) + (\delta\text{BR}^{\text{th}}_{h\to V\gamma})^2$ is the estimated uncertainty. The first term is the statistical uncertainty (σ_h is the total Higgs production cross section, $A_g \approx 0.75$ is the geometrical acceptance and $\mathcal{L}$ is the integrated luminosity), while the second term is the theoretical one, $\delta\text{BR}^{\text{th}}_{h\to\phi\gamma} \approx 3.0 \cdot 10^{-7}$ and $\delta\text{BR}^{\text{th}}_{h\to J/\psi\gamma} \approx 1.2 \cdot 10^{-7}$ for $\kappa_\gamma = 1$. In addition for the $J/\psi\gamma$ mode we also consider $\text{BR}(J/\psi \to \mu^+\mu^-) = 5.961\,\%$ [329]. Our criterion for a large-enough deviation from the SM prediction is $\mathcal{S} \geq 3$. Our results are summarized in Table 7.7.

Higgs Portal

Introduction

The Higgs portal [330–334] – the marginal coupling of Standard Model-singlet states to the Higgs field – represents a challenging and strongly motivated scenario for physics beyond the Standard Model. This portal is motivated from a purely bottom-up perspective as one of only two marginal couplings allowed between the SM and SM-singlet states, as well as from the top-down by a wide range of beyond-the-SM scenarios including dark matter, electroweak naturalness, and electroweak baryogenesis. Exploration of the Higgs portal is a high priority at the LHC and future colliders.

Here we consider the possible collider probes of a scalar Higgs portal of the form

$$\mathcal{L} = \mathcal{L}_{SM} - \frac{1}{2}\partial_\mu\phi\partial^\mu\phi - \frac{1}{2}M^2\phi^2 - c_\phi|H|^2\phi^2 \tag{7.66}$$

where H is the SM-like Higgs doublet and ϕ is a real scalar neutral under the Standard Model. In Higgs portals motivated by baryogenesis, dark matter, or naturalness, the dimensionless Higgs portal coupling is expected to be $\mathcal{O}(1)$. The most experimentally challenging scenario is one in which the theory respects a Z_2 symmetry, $\phi \to -\phi$, in which case there is no mixing between the Higgs and ϕ. In this case the theory at the weak scale

is

$$\mathcal{L} = \mathcal{L}_{SM} - \frac{1}{2}\partial_\mu\phi\partial^\mu\phi - \frac{1}{2}m_\phi^2\phi^2 - c_\phi v h\phi^2 \tag{7.67}$$

where $m_\phi^2 = M^2 + c_\phi v^2$ with $v = 246$ GeV. The sole means of producing ϕ at colliders is via the Higgs boson We will assume that ϕ has no SM decay modes, consistent with the Z_2 symmetry, and appears solely as missing energy at colliders. Consequently, the primary signatures at hadron colliders involve associated production modes of an off-shell Higgs in conjunction with missing energy. The most promising associated production channels include vector boson fusion, gluon fusion with an associated jet, and top pair associated production. Production in association with a W or Z boson may also be useful, but the relatively small cross sections for these processes at 100 TeV renders them less promising.

If $m_\phi < m_h/2$, the Higgs can decay into ϕ pairs and the Higgs portal may be constrained by bounds on the non-SM Higgs width. When $m_\phi > m_h/2$, however, such decays are kinematically forbidden and ϕ pair production instead proceeds solely via an off-shell Higgs, $pp \to h^* + X \to \phi\phi + X$. The rate for this process is suppressed relative to decays of an on-shell Higgs by both an additional factor of $|c_\phi|^2$ and two-body phase space, leading to a small rate and poor prospects at the LHC. In this respect a high-energy, high-luminosity hadron collider such as SPPC is ideally suited to probe the Higgs portal.

Searching for the Higgs Portal at the SPPC

We study the Higgs portal model of (7.67) in various associated production channels at $\sqrt{s} = 14$ & 100 TeV to both estimate sensitivity at the SPPC and compare to possible reach in the LHC era. In this section we describe our collider simulation for searches involving vector boson fusion, monojet, and $t\bar{t}$ associated production.

To simulate signal we implement the model in `FeynRules` with $m_h = 125$ GeV and generate events at leading order in `MadGraph5 v1.5.8` [47], fixing $c_\phi = 1$ and varying values of m_ϕ. We infer results for $c_\phi \neq 1$ by rescaling the signal cross section by $|c_\phi|^2$. We also simulate primary backgrounds in `MadGraph5`. Signal and background events are showered and hadronized using `Pythia 8.186` [188], tune 4C. Detector simulation is performed using `Delphes v3.1.2` with the default CMS detector card (for the LHC) and the Snowmass detector card [50] (for the SPPC). Jets are clustered using the anti-k_T algorithm [79] in `FastJet v3.0.6` [126] with $R = 0.5$. We require all jets to satisfy $p_{Tj} > 30$ GeV. We apply a minimal p_T cut of 10 GeV to all leptons and define lepton isolation in `Delphes` as `RelIso` $\equiv p_T^{\rm cone}/p_{T\ell} < 0.1$, where $p_T^{\rm cone}$ is the sum of hadronic p_T within a cone of $R = 0.3$ of the lepton.

The Higgs Portal in $\boldsymbol{E_{\rm T}^{\rm miss}}$ + Vector Boson Fusion

We first study $\phi\phi$ production in vector boson fusion of an off-shell Higgs. The final state is $\phi\phi jj$ with forward jets. The primary backgrounds are Z+jets, W+jets, $t\bar{t}$ + jets, and QCD multijets. We simulate Zjj and Wjj matched up to one additional jet and $t\bar{t}$ matched up to two additional jets. We do not simulate QCD multijets but adopt a cut flow designed to minimize these backgrounds.

We require at least two jets in the event and apply the baseline cuts

$$p_{Tj_{1(2)}} > 50\,\text{GeV} \qquad |\eta_{j_{1(2)}}| < 4.7 \tag{7.68}$$

$$\eta_{j_1}\eta_{j_2} < 0 \qquad |\eta_{j_1} - \eta_{j_2}| > 4.2 \tag{7.69}$$

We veto events containing an isolated $e^{\pm}$ or $\mu^{\pm}$ and apply a central-jet veto by vetoing events containing a third jet with $p_{Tj} > 30$ GeV and $\min \eta_{j_{1,2}} < \eta_{j3} < \max \eta_{j_{1,2}}$. We impose a cut on the azimuthal angle between $E_{\rm T}^{\rm miss}$ and jets by demanding $|\Delta\phi_{E_{\rm T}^{\rm miss},j}| > 0.5$ to ensure that QCD backgrounds are sufficiently suppressed in realistic scenarios. We distinguish signal from background with both a dijet invariant mass cut and a $E_{\rm T}^{\rm miss}$ cut:

$$\sqrt{(p_{j_1} + p_{j_1})^2} > M_{jj}^* \qquad E_{\rm T}^{\rm miss} > \not{E}_T^* \tag{7.70}$$

Here M_{jj}^* and $\not{E}_T^*$ are partially optimized values for the dijet invariant mass and $E_{\rm T}^{\rm miss}$ cuts chosen at each value of m_ϕ to maximize $S/\sqrt{B}$.

The Higgs Portal in $E_{\rm T}^{\rm miss} + j$ Associated Production

Next we consider searches in the $j + E_{\rm T}^{\rm miss}$ channel via gluon fusion with an associated jet. The primary backgrounds are Z+jets, W+jets, $t\bar{t}$ + jets, and QCD multijets. We simulate Zj and Wj matched up to one additional jet and $t\bar{t}$ matched up to two additional jets, and again do not simulate QCD multijets but adopt a cut flow to minimize this background.

As $\sqrt{s} \gg 2m_t$ for most signal events, the HEFT calculation of $gg \to gh^* \to g\phi\phi$ is invalid. We account for this with a p_T-dependent re-weighting of signal events generated using the HEFT in `MadGraph5`. We determine the re-weighting factor by calculating the differential cross section for $gg \to g\phi\phi$ from the cross section for $gg \to gh^*$ using the factorization of phase space across the Higgs propagator,

$$\frac{d\sigma^{L,EFT}_{gg\to g\phi\phi}(m_\phi)}{dp_T} = \int_{4m_\phi^2}^{\infty} \frac{c_\phi^2}{8\pi^2} \frac{v^2}{(\tilde{s} - m_h^2)^2} \sqrt{1 - \frac{4m_\phi^2}{\tilde{s}}} \frac{d\sigma^{L,EFT}_{gg\to gh^*}}{dp_T} d\sqrt{\tilde{s}} \ , \tag{7.71}$$

where the superscripts 'L' and 'EFT' denote the one loop and EFT cross sections, respectively. We convolve these cross sections with MSTW PDFs [328] to determine the proton-proton differential cross section and define the re-weighting factor in a given p_T-bin as

$$R(p_T^{\rm min}, p_T^{\rm max}, m_\phi) = \frac{\int_{p_T^{\rm min}}^{p_T^{\rm max}} dp_T \frac{d\sigma^{L}_{pp\to g\phi\phi}(m_\phi)}{dp_T}}{\int_{p_T^{\rm min}}^{p_T^{\rm max}} dp_T \frac{d\sigma^{EFT}_{pp\to g\phi\phi}(m_\phi)}{dp_T}} \tag{7.72}$$

We calculate the EFT cross section $\sigma^{EFT}_{gg\to gh^*}$ using the results of [335, 336] and the cross section incorporating the full loop functions, $\sigma^{L}_{gg\to gh^*}$, using the FEYNARTS, FORMCALC, and LOOPTOOLS packages [337, 338].

To estimate the sensitivity at the LHC and SPPC we require at least one jet in the event and apply the cuts

$$p_{Tj_1} > 110\,{\rm GeV} \qquad |\eta_{j_1}| < 2.4 \qquad E_{\rm T}^{\rm miss} > 300\,{\rm GeV} \tag{7.73}$$

To ensure rejection of QCD backgrounds we include an additional jet veto similar to the veto applied in CMS monojet searches [339]. A second jet with $p_{Tj_2} > 30$ GeV is allowed as long as $\Delta R_{j_1,j_2} < 2.4$ and vetoed otherwise. Events containing additional jets with $p_{Tj} > 30$ GeV are vetoed. We emphasize that even with this additional jet veto the QCD multi-jet backgrounds at the SPPC may favor harder $E_{\rm T}^{\rm miss}$ cuts than those applied here.

The Higgs Portal in $E_{\mathrm{T}}^{\mathrm{miss}} + t\bar{t}$ Associated Production

Finally, we consider the searches in the $t\bar{t} + E_{\mathrm{T}}^{\mathrm{miss}}$ channel. The dominant backgrounds in this channel are $t\bar{t}$+jets and W+jets. We simulate semi-leptonic and di-leptonic decays for the $t\bar{t}$ background matched up to two additional jets, while we simulate leptonic Wjj matched up to two additional jets. We apply the selection cuts

$$n_{\mathrm{jet}} \geq 4 \qquad |\eta_{j_{1,2,3,4}}| < 2.4 \qquad E_{\mathrm{T}}^{\mathrm{miss}} > 300 \tag{7.74}$$

In addition, we require exactly one isolated $e^{\pm}/\mu^{\pm}$ with

$$P_T^{\ell} > 10 \text{ GeV}$$

and at least one b-tag among the leading four jets. We require that the transverse mass between the lepton and $E_{\mathrm{T}}^{\mathrm{miss}}$ satisfy $m_T > 200$ GeV and that $M_{T2}^W > 300\,\mathrm{GeV}$ [340].

Results and Discussion

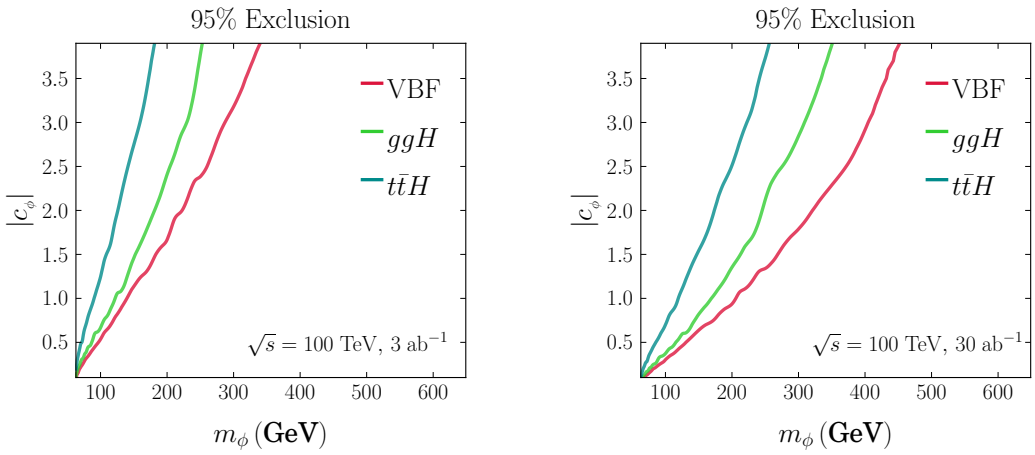

Figure 7.40 Left: The 95% exclusion sensitivity in vector boson fusion, gluon fusion with associated jet, and top pair associated production channels at the SPPC with 3 ab^{-1} integrated luminosity, determined from $S/\sqrt{S+B} = 1.96$ with purely statistical errors. Right: the 95% exclusion sensitivity at the SPPC with 30 ab^{-1} integrated luminosity.

We perform a simple cut and count analysis on the vector boson fusion, gluon fusion plus associated jet, and top pair associated production channels following the searches outlined above. For $\sqrt{s} = 14$ TeV we assume an integrated luminosity of 3 ab^{-1}. For $\sqrt{s} = 100$ TeV we consider scenarios with 3 ab^{-1} and 30 ab^{-1}, respectively. We compute the significance of each search in terms of the number of signal events S and background events B passing cuts as $S/\sqrt{S+B}$ for exclusion and $S/\sqrt{B}$ for discovery, neglecting systematic uncertainties in the signal and background estimates. We note that S/B is small for our optimized cuts at 100 TeV, so that systematic uncertainties in background determination could in principle have a substantial impact on sensitivity. However, we expect in practice that data-driven determination of the primary Z+jets background will substantially lower the relevant systematic uncertainties by the SPPC era.

Results for exclusion in the VBF, monojet, and $t\bar{t}$ searches at the SPPC are presented in Fig. 7.40, while results for discovery in the same channel are presented in Fig. 7.41. The reach of the VBF search is in good agreement with the simplified analysis in [341].

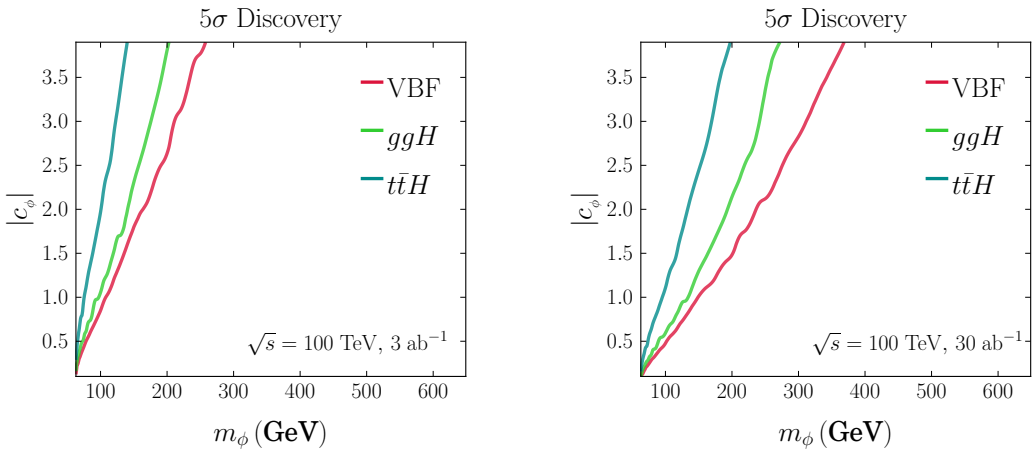

Figure 7.41 Left: The 5σ discovery reach in vector boson fusion, gluon fusion with associated jet, and top pair associated production channels at the SPPC with 3 ab^{-1} integrated luminosity, determined from $S/\sqrt{B} = 5$ with purely statistical errors. Right: the 5σ discovery reach at the SPPC with 30 ab^{-1} integrated luminosity.

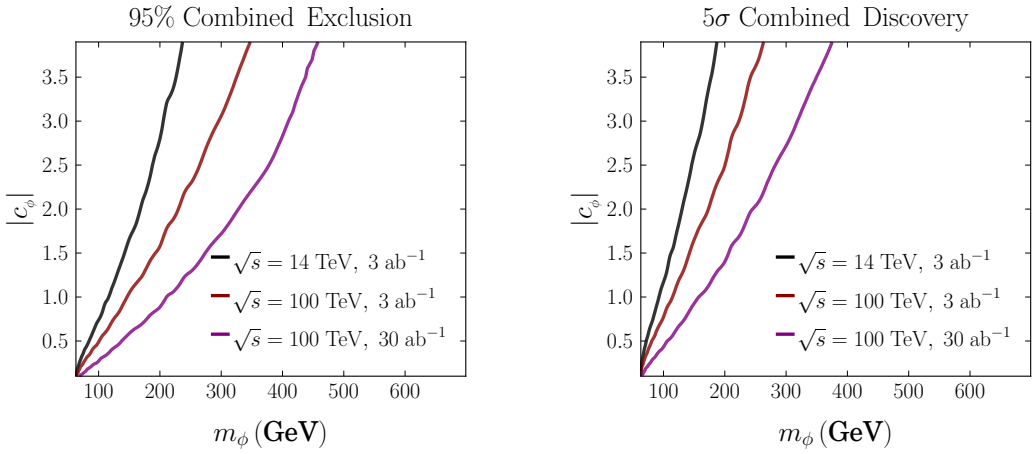

Figure 7.42 Left: The approximate 95% exclusion reach from the combination of vector boson fusion, gluon fusion with associated jet, and top pair associated production channels at the LHC and SPPC determined from $S/\sqrt{B} = 1.96$ with purely statistical errors, neglecting possible correlations. Right: The approximate 5σ discovery reach from the same combination at the SPPC and LHC.

The monojet search exhibits comparable sensitivity for $m_\phi \lesssim 200$ GeV, due to gluon PDF luminosity and the relatively low jet p_T cuts of our analysis. Some of this sensitivity is due to our fixed-order calculation for the monojet signal and omission of QCD multijet backgrounds, but on the other hand we have not included a compensating K-factor for the signal cross section that would increase sensitivity. Our results suggest that the monojet channel may be useful at the SPPC in conjunction with the VBF channel, and warrants further study taking into account QCD multijet backgrounds and NLO corrections to the signal cross section and differential distribution. Finally, the $t\bar{t}$ associated production search exhibits the least sensitivity of the three search channels, though there is room for improvement of the analysis using more sophisticated discriminating variables.

Ultimately, the optimized reach for Higgs portal states at the SPPC will involve the combination of available search channels. In Fig. 7.42 we present the combined reach of VBF, monojet, and $t\bar{t}$ searches at the SPPC, which we determine by adding the significance of the three channels in quadrature. This combination neglects possible correlations but provides a reasonable benchmark for combined reach. For the sake of comparison, we include the approximate combined reach at the LHC.

Implications for BSM Scenarios

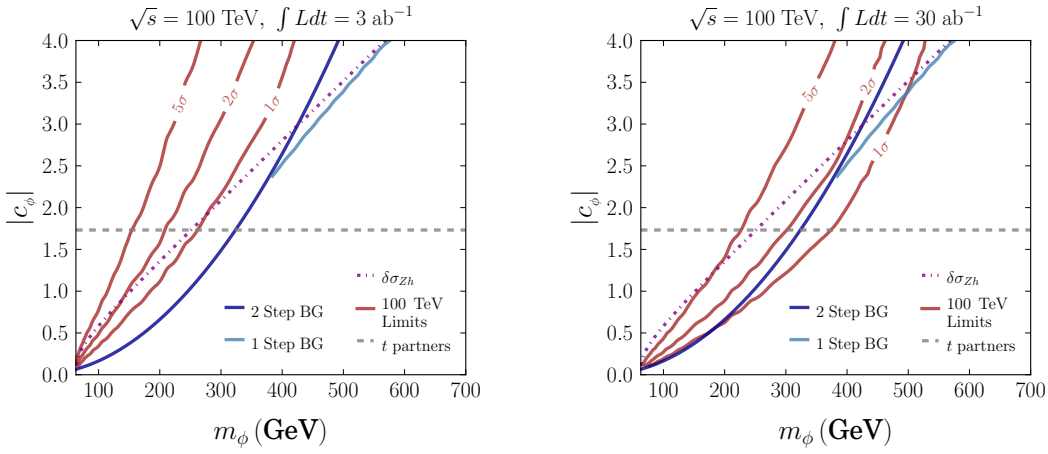

Figure 7.43 The combined reach of direct Higgs portal searches at SPPC with 3 ab^{-1} (left) and 30 ab^{-1} (right) compared to parameter spaces for motivated Higgs portal scenarios. In each case the red lines denote the $1, 2\sigma$ exclusion and 5σ discovery reach from direct searches at SPPC. The region to the left of the dark blue line indicates the possible parameter space for two-step singlet-assisted electroweak baryogenesis [341], while the region between the light blue and dark blue lines indicates the possible parameter space for one-step singlet-assisted baryogenesis [341]. The purple line indicates the 2σ contour for $\delta\sigma_{Zh}$ at CEPC. The dashed gray line indicates the effective coupling due to SM-neutral scalar top partners.

It is useful to compare the reach of the SPPC to the range of masses and couplings motivated by BSM scenarios with Higgs portal couplings. In Fig. 7.43 we show the combined reach at the SPPC at 3 ab^{-1} and 30 ab^{-1} relative to both the reach of precision Higgs coupling measurements at the CEPC and the parameter space for singlet-assisted electroweak baryogenesis (as described in [341]) and neutral naturalness (as described in [342]). In the case of singlet-assisted electroweak baryogenesis, the combined 95% exclusion reach at the SPPC at 30 ab^{-1} covers nearly the entire region of a two-step electroweak phase transition and a significant portion of the parameter space for a one-step transition. While our

analysis cannot decisively exclude some parts of the two-step phase transition or entirely cover the single-step phase transition, there is clearly sensitivity throughout the region of viable electroweak baryogenesis. It is likely that optimized searches can conclusively exclude (or possibly discover) this challenging scenario at the SPPC.

In the case of neutral naturalness where the weak scale is stabilized by SM-neutral scalar top partners, the combined 2σ exclusion reach extends out to $m_\phi \sim 210$ GeV at the SPPC with 3 ab^{-1} and $m_\phi \sim 300$ GeV with 30 ab^{-1}. This provides a robust test of the most experimentally-challenging possible manifestation of naturalness.

Finally, we highlight the complementarity between direct searches for Higgs portal states at the SPPC and indirect searches at the CEPC via shifts in the Zh production cross section. The leading shift to the Zh production cross section due to (real) Higgs portal scalars is [342, 343]

$$\delta\sigma_{Zh} = \frac{|c_\phi|^2}{8\pi^2}\frac{v^2}{m_h^2}\left(1 + \frac{1}{4\sqrt{\tau_\phi(\tau_\phi-1)}}\log\left[\frac{1-2\tau_\phi-2\sqrt{\tau_\phi(\tau_\phi-1)}}{1-2\tau_\phi+2\sqrt{\tau_\phi(\tau_\phi-1)}}\right]\right) \tag{7.75}$$

where $\tau_\phi = m_h^2/4m_\phi^2$ and $\delta\sigma_{Zh} = (\sigma_{Zh} - \sigma_{Zh}^{\rm SM})/\sigma_{Zh}^{\rm SM}$. In Fig. 7.43 we compare the 2σ reach at the future CEPC $e+e-$ collider to the 2σ exclusion reach and 5σ discovery reach at SPPC to demonstrate the complementarity of the two probes. The 2σ exclusion reach of the SPPC at 30 ab^{-1} exceeds the equivalent reach at CEPC throughout the parameter space under consideration. Compellingly, the 5σ discovery reach at SPPC also exceeds the 2σ reach at CEPC up to $m_\phi \sim 200$ GeV, so that the SPPC is a powerful tool for direct discovery of the Higgs portal in the event of suggestive hints at CEPC. Moreover, it implies that for $m_\phi \lesssim 200$ GeV, the SPPC can discover a high-mass Higgs portal even without suggestive deviations at CEPC.

Exotic Higgs Decay

Overview and Motivation

As has been repeatedly emphasized, the detailed experimental characterization of the only elementary scalar in the SM is vital to establish the nature of electroweak symmetry-breaking, and will either confirm the predictions of the SM or discover BSM physics. This program has three main directions:

1. High-precision determination of the couplings of the Higgs to SM particles, including itself.
2. The search for Higgs production in the decay of BSM particles.
3. The search for production of BSM particles through decays of the Higgs boson.

Among these directions, the search for *exotic Higgs decays* is uniquely sensitive to very small couplings between the Higgs sector and new physics (see [344] for an extensive discussion). This sensitivity arises in part because of the fortunate coincidence that $m_h < 2m_W$, allowing the small bottom Yukawa coupling $y_b \approx 0.02$ to dominate the tiny SM Higgs decay width of $\Gamma_h \approx 4.07$ MeV. A BSM fermion (boson) X with a Higgs coupling $g_{hXX} \sim 10^{-2}$ ($\sim 10^{-2}v$) can therefore give rise to exotic Higgs decays with $\sim 10\%$ branching fractions. Such branching fractions are too small to be indirectly excluded by the measurement of SM-like Higgs couplings [345, 346], and lead to large numbers of

exotic Higgs decay events at hadron colliders, as we discuss in more detail below. Direct searches for BSM particle production in decays of the Higgs therefore provide the primary discovery channel in a broad class of possible theories beyond the SM.

There are good theoretical reasons to expect new physics to show up in exotic Higgs decays. The operator $|H|^2$ is the lowest-dimension total-singlet operators that can be constructed from of SM fields, and therefore is one of only a few possible candidates to mediate the leading interactions with hidden-sector matter that is neutral under all SM gauge groups (see e.g. [330, 333, 347–349]). In the case of a BSM scalar S, we can have the "Higgs portal" coupling described in the previous subsection

$$\Delta\mathcal{L} = \kappa|S|^2|H|^2 \,. \tag{7.76}$$

Super-renormalizable couplings of the Higgs to hidden-sector particles can arise through mixing of h with S after spontaneous symmetry breaking. For the case of a BSM fermion ψ, the operator

$$\Delta\mathcal{L} = \frac{\mu}{\Lambda^2}|H|^2\bar{\psi}\psi \tag{7.77}$$

yields $\mathrm{Br}(h \to \bar{\psi}\psi) \sim 10\%$ for $\mu v/\Lambda^2 \sim 10^{-2}$. Of course, if some of the BSM states carry electroweak charge then operators linear in H are possible, as arise e.g. in the MSSM. Many theories beyond the SM can give rise to exotic Higgs decays via such interactions, such as the NMSSM and models of hidden sector dark matter; see [344] for a survey and a discussion of the signature space in related simplified models.

A 100 TeV proton-proton collider can offer unmatched discovery reach for new physics produced in Higgs decays. Already at the 14 TeV LHC with 300 fb^{-1}, a 10% branching fraction gives rise to $\sim 10^6$ exotic Higgs decay events. Searches at a 100 TeV collider would be sensitive to rare Higgs decay modes and their associated signals that are statistics-limited at the LHC. The gluon-fusion Higgs production cross section at $\sqrt{s} = 100$ TeV is about 740 pb, ~ 15 times larger than at the LHC and corresponding to about 10^9 produced Higgs bosons per ab^{-1} of integrated luminosity. This gives a spectacular sensitivity to exotic decay modes, which can reach the level of $Br \sim 10^{-8}$ for clean, low-background final states like $h \to 2X \to 4\ell$ [350].

There is great complementarity between future lepton and hadron colliders in searching for exotic Higgs decays. The large event rates at a hadron collider make it superior in searching for spectacular but very rare decays. However, the clean environment of a lepton collider is *a priori* better-suited for exotic Higgs decays resulting in final states with poor mass resolution and/or high background (at hadron machines), such as $h \to 4b$ or $h \to E_{\mathrm{T}}^{\mathrm{miss}}$.

Below we demonstrate the excellent sensitivity of a 100 TeV collider to a simple example of a hidden sector: a theory containing a dark photon and optionally a dark Higgs boson. These results originally appeared in [350], which also draws upon the studies by [351–353], and provide a useful demonstration of the expected sensitivity to clean exotic Higgs decay modes. This study also underlines some of the challenges of these Higgs-related searches at a future 100 TeV collider, most pertinently the need to identify and reconstruct relatively soft Higgs decay products with $p_T \lesssim 20$ GeV.

We make a final remark on the subject of triggers. At the LHC, triggering is often a limiting factor on the sensitivity to exotic Higgs decays, especially for hadronic, high multiplicity, or largely invisible decays. By the time detectors for a 100 TeV collider are built, it is not unreasonable to expect much more sophisticated high-level triggering mechanism-

s due to advances in data acquisition and processing. This might allow events to be fully reconstructed before deciding whether to write them to permanent storage [354]. Such a capability would be enormously helpful for exotic Higgs decay searches, since difficult low-p_T final states resulting from high-multiplicity, displaced, and/or hadronic decays could be searched for in real-time to ensure high signal acceptance. That being said, the dark photon study presented here conservatively assumes triggers similar to those adopted by ATLAS and CMS in LHC Run I.

Searches for Dark Photons

We consider the compelling possibility of a spontaneously broken "dark" $U(1)_D$ gauge symmetry, mediated by a vector boson Z_D called the "dark photon". The dark photon's only renormalizable interaction with the SM is through kinetic mixing with the hypercharge gauge boson [351–353]. In addition, if a dark Higgs mechanism is responsible for the spontaneous breaking of the $U(1)_D$ gauge symmetry, the dark Higgs boson will in general have a renormalizable coupling to the 125 GeV SM-like Higgs, resulting in a mixing between the two physical scalar states. In this simplified model, the two operators mediating interactions between the dark sector and the SM are

$$\mathcal{L}_{int} = -\frac{1}{2}\frac{\epsilon}{\cos\theta}\,\hat{Z}_{D\mu\nu}\,\hat{B}^{\mu\nu} - \kappa|S|^2|H|^2, \tag{7.78}$$

which we refer to as the hypercharge portal interaction and the Higgs portal interaction respectively. The hypercharge portal interaction can mediate the decay $h \to Z^{(*)}Z_D$ through Z-Z_D mixing and enables the Z_D to decay to the SM. It also allows for single Z_D production in Drell-Yan (DY)-like events $q\bar{q} \to Z_D \to \ell\ell$, and contributes to electroweak precision observables. The Higgs portal interaction can mediate the decay $h \to Z_D Z_D$ through mixing between the Higgs and the scalar S, after spontaneous symmetry breaking in both sectors. Crucially, the Z_D couplings to SM fermions depend on gauge couplings, rather than Yukawa couplings, making the Z_D comparatively leptophilic: even above the $b\bar{b}$ threshold, $\mathrm{Br}(Z_D \to ee + \mu\mu) \sim 30\%$. This makes Z_D production a relatively conspicuous signal at hadron colliders.

In [350], a detailed analysis was performed to compare the potential reach of future colliders for this simple hidden sector. A 100 TeV pp collider has by far the best discovery reach (we assume an integrated luminosity of 3 ab^{-1}). Fig. 7.44 shows the sensitivity to the hypercharge portal coupling from exotic Higgs decays $h \to Z^{(*)}Z_D$ (left) and resonant production of Z_D (right), which used the studies by [248, 355–357]. The latter offers somewhat higher sensitivity, but both searches probe $\epsilon \sim 10^{-3} - 10^{-2}$ and surpass the reach of the model independent electroweak precision tests at current and future colliders. If a signal is discovered in the DY spectrum, an observation of the corresponding exotic Higgs decay mode will be an indispensable diagnostic for distinguishing the kinetically mixed dark photon from other possibilities, such as a weakly coupled sequential Z'.

The hypercharge portal can be probed much more deeply if the Higgs portal coupling provides the leading interaction with the dark sector. In that case, the spectacular exotic Higgs decay $h \to Z_D Z_D \to 4\ell$ can be probed for branching fractions as low as $\sim 10^{-8}$ if the Z_D decays promptly, see Fig. 7.45. Prompt Z_D decay requires $\epsilon \gtrsim 10^{-5} - 10^{-3}$, so any observation of $h \to Z_D Z_D \to 4\ell$ not only gives information about the Higgs portal coupling (which sets the production cross section), but is sensitive to smaller values of ϵ than either resonant production of Z_D or $h \to Z^{(*)}Z_D$.

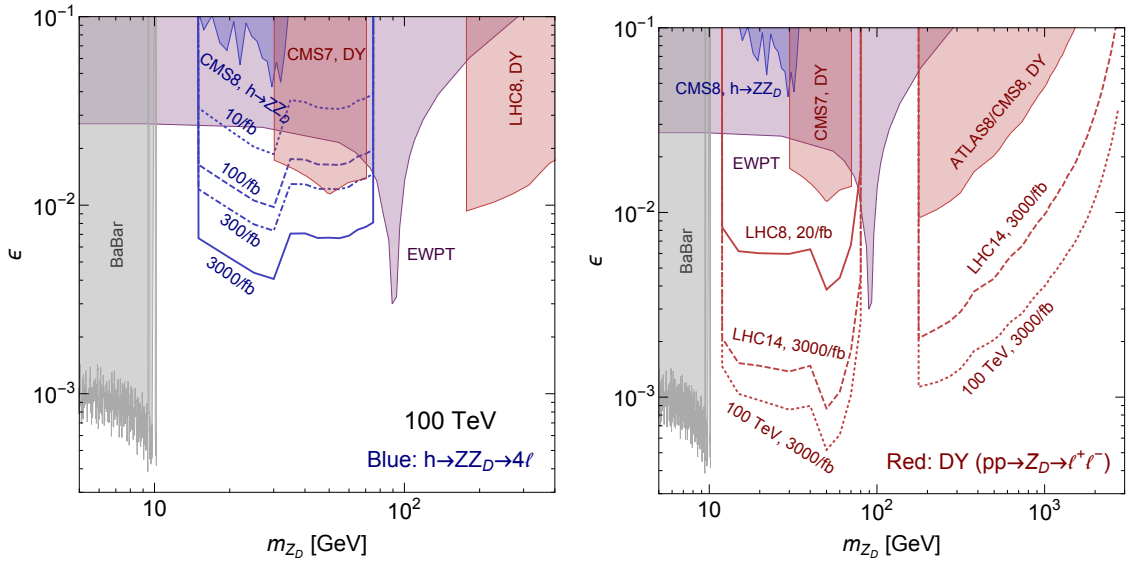

Figure 7.44 Left: The blue lines show expected 95% CLs limits on ϵ from $h \to Z_D Z^{(*)} \to 4\ell$ at a 100 TeV pp collider. Limits shown correspond to integrated luminosities of 10 (dotted), 100 (dashed), 300 (dot-dashed), and 3000 fb^{-1} (solid). Right: Prospects for Z_D searches from DY production (red lines) at LHC8 (20 fb^{-1}, solid), LHC14 (3000 fb^{-1}, dashed), and a 100 TeV pp collider (3000 fb^{-1}, dotted), with limits from existing recasts shown in shaded red (from [248, 355–357] and rescalings to higher luminosities, see [350] for details). A recast [344] of a CMS8 analysis [358] sensitive to $h \to ZZ_D$ is shown in the blue shaded region. The purple region shows the current EWPT constraints [350], while the gray region is a limit from BaBar [359]. The red regions are the bounds from Drell-Yan production of Z_D [248, 355–357].

At even smaller values of ϵ, displaced $h \to Z_D Z_D \to 4\ell$ searches give sensitivity to $\epsilon \sim 10^{-7} - 10^{-5}$ if these events are produced through the Higgs portal at the 100 TeV collider, as shown in Fig. 7.46. However, even more spectacular sensitivity is possible if the majority of dark photons decay outside of the detector. This would allow $\mathrm{Br}(h \to Z_D Z_D)$ to be as large as 0.5% without being constrained by invisible Higgs branching ratio measurements at future lepton colliders [345, 346]. In that case, ϵ values as low as $10^{-10} - 10^{-7}$ can be probed by looking for highly displaced dark photon decays (see green contours in Fig. 7.46). Such spectacular sensitivity is only possible due to the high Higgs production rate at a future 100 TeV machine.

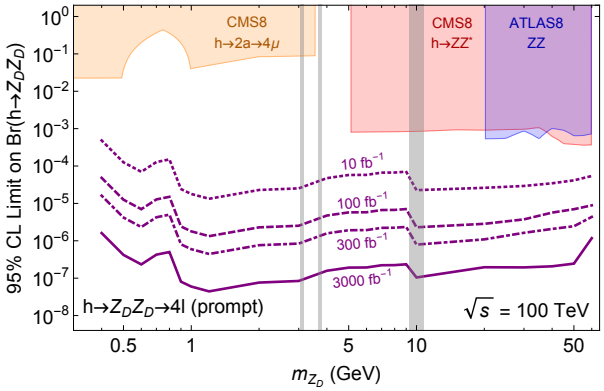

Figure 7.45 Expected 95% CLs limits on the total exotic Higgs decay branching ratio, $\mathrm{Br}(h \to Z_D Z_D)$, at a 100 TeV pp collider. Gray bands correspond to regions where quarkonium background may invalidate the analysis of [350]. The limits obtained in [344] from a recast of LHC Run 1 results are shown in red ($h \to ZZ^* \to 4\ell$ search by CMS [358]) and blue (ATLAS ZZ cross section measurement [360]) shaded regions. The limit from the CMS 8 TeV $h \to 2a \to 4\mu$ search [361] is shaded in orange, assuming equal efficiencies for pseudoscalar and dark photon decay to muons.

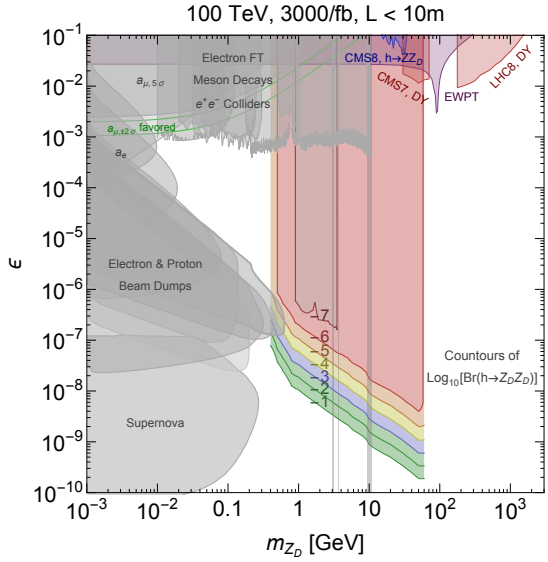

Figure 7.46 Estimate of expected 95% CLs limits on ϵ for different $\mathrm{Br}(h \to Z_D Z_D)$ at a 100 TeV collider, assuming a displaced lepton jet search has the same sensitivity to decays within a distance L from the interaction point as a prompt $Z_D Z_D$ search (see Fig. 7.45). A detector size L of 10 m is assumed. Gray shaded regions show current constraints [362].

References

[1] R. Barbieri, M. Frigeni, and F. Caravaglios, *The Supersymmetric Higgs for heavy superpartners*, Phys.Lett. **B258** (1991) 167–170.

[2] H. E. Haber and R. Hempfling, *Can the mass of the lightest Higgs boson of the minimal supersymmetric model be larger than m(Z)?*, Phys.Rev.Lett. **66** (1991) 1815–1818.

[3] J. Casas, J. Espinosa, M. Quiros, and A. Riotto, *The Lightest Higgs boson mass in the minimal supersymmetric standard model*, Nucl.Phys. **B436** (1995) 3–29, arXiv:hep-ph/9407389 [hep-ph].

[4] M. S. Carena, J. Espinosa, M. Quiros, and C. Wagner, *Analytical expressions for radiatively corrected Higgs masses and couplings in the MSSM*, Phys.Lett. **B355** (1995) 209–221, arXiv:hep-ph/9504316 [hep-ph].

[5] M. S. Carena, M. Quiros, and C. Wagner, *Effective potential methods and the Higgs mass spectrum in the MSSM*, Nucl.Phys. **B461** (1996) 407–436, arXiv:hep-ph/9508343 [hep-ph].

[6] H. E. Haber, R. Hempfling, and A. H. Hoang, *Approximating the radiatively corrected Higgs mass in the minimal supersymmetric model*, Z.Phys. **C75** (1997) 539–554, arXiv:hep-ph/9609331 [hep-ph].

[7] C. Wymant, *Optimising Stop Naturalness*, Phys.Rev. **D86** (2012) 115023, arXiv:1208.1737 [hep-ph].

[8] J. Casas, J. Espinosa, and I. Hidalgo, *The MSSM fine tuning problem: A Way out*, JHEP **0401** (2004) 008, arXiv:hep-ph/0310137 [hep-ph].

[9] M. Dine, N. Seiberg, and S. Thomas, *Higgs physics as a window beyond the MSSM (BMSSM)*, Phys.Rev. **D76** (2007) 095004, arXiv:0707.0005 [hep-ph].

[10] J. D. Wells, *Implications of supersymmetry breaking with a little hierarchy between gauginos and scalars*, arXiv:hep-ph/0306127 [hep-ph].

[11] N. Arkani-Hamed and S. Dimopoulos, *Supersymmetric unification without low energy supersymmetry and signatures for fine-tuning at the LHC*, JHEP **0506** (2005) 073, arXiv:hep-th/0405159 [hep-th].

[12] G. Giudice and A. Romanino, *Split supersymmetry*, Nucl.Phys. **B699** (2004) 65–89, arXiv:hep-ph/0406088 [hep-ph].

[13] N. Arkani-Hamed, S. Dimopoulos, G. Giudice, and A. Romanino, *Aspects of split supersymmetry*, Nucl.Phys. **B709** (2005) 3–46, arXiv:hep-ph/0409232 [hep-ph].

[14] J. D. Wells, *PeV-scale supersymmetry*, Phys.Rev. **D71** (2005) 015013, arXiv:hep-ph/0411041 [hep-ph].

[15] G. Kane, P. Kumar, R. Lu, and B. Zheng, *Higgs Mass Prediction for Realistic String/M Theory Vacua*, Phys.Rev. **D85** (2012) 075026, arXiv:1112.1059 [hep-ph].

[16] A. Arvanitaki, N. Craig, S. Dimopoulos, and G. Villadoro, *Mini-Split*, JHEP **1302** (2013) 126, arXiv:1210.0555 [hep-ph].

[17] N. Arkani-Hamed et al., *Simply Unnatural Supersymmetry*, arXiv:1212.6971 [hep-ph].

[18] G. F. Giudice and A. Strumia, *Probing High-Scale and Split Supersymmetry with Higgs Mass Measurements*, Nucl.Phys. **B858** (2012) 63–83, arXiv:1108.6077 [hep-ph].

[19] G. Degrassi et al., *Higgs mass and vacuum stability in the Standard Model at NNLO*, JHEP **1208** (2012) 098, arXiv:1205.6497 [hep-ph].

[20] P. Draper, G. Lee, and C. E. M. Wagner, *Precise Estimates of the Higgs Mass in Heavy SUSY*, Phys.Rev. **D89** (2014) 055023, arXiv:1312.5743 [hep-ph].

[21] E. Bagnaschi, G. F. Giudice, P. Slavich, and A. Strumia, *Higgs Mass and Unnatural Supersymmetry*, JHEP **1409** (2014) 092, arXiv:1407.4081 [hep-ph].

[22] R. Kitano and Y. Nomura, *A Solution to the supersymmetric fine-tuning problem within the MSSM*, Phys.Lett. **B631** (2005) 58–67, arXiv:hep-ph/0509039 [hep-ph].

[23] R. Dermisek and H. D. Kim, *Radiatively generated maximal mixing scenario for the Higgs mass and the least fine tuned minimal supersymmetric standard model*, Phys.Rev.Lett. **96** (2006) 211803, arXiv:hep-ph/0601036 [hep-ph].

[24] R. Dermisek and I. Low, *Probing the Stop Sector and the Sanity of the MSSM with the Higgs Boson at the LHC*, Phys.Rev. **D77** (2008) 035012, arXiv:hep-ph/0701235 [HEP-PH].

[25] M. Perelstein and C. Spethmann, *A Collider signature of the supersymmetric golden region*, JHEP **0704** (2007) 070, arXiv:hep-ph/0702038 [hep-ph].

[26] M. Carena, S. Gori, N. R. Shah, and C. E. Wagner, *A 125 GeV SM-like Higgs in the MSSM and the $\gamma\gamma$ rate*, JHEP **1203** (2012) 014, arXiv:1112.3336 [hep-ph].

[27] S. Knapen and D. Shih, *Higgs Mediation with Strong Hidden Sector Dynamics*, JHEP **1408** (2014) 136, arXiv:1311.7107 [hep-ph].

[28] A. Basirnia, D. Egana-Ugrinovic, S. Knapen, and D. Shih, *125 GeV Higgs from Tree-Level A-terms*, arXiv:1501.00997 [hep-ph].

[29] K. Babu, I. Gogoladze, M. U. Rehman, and Q. Shafi, *Higgs Boson Mass, Sparticle Spectrum and Little Hierarchy Problem in Extended MSSM*, Phys.Rev. **D78** (2008) 055017, arXiv:0807.3055 [hep-ph].

[30] S. P. Martin, *Extra vector-like matter and the lightest Higgs scalar boson mass in low-energy supersymmetry*, Phys.Rev. **D81** (2010) 035004, arXiv:0910.2732 [hep-ph].

[31] P. W. Graham, A. Ismail, S. Rajendran, and P. Saraswat, *A Little Solution to the Little Hierarchy Problem: A Vector-like Generation*, Phys.Rev. **D81** (2010) 055016, arXiv:0910.3020 [hep-ph].

[32] H. E. Haber and M. Sher, *Higgs Mass Bound in $E(6)$ Based Supersymmetric Theories*, Phys.Rev. **D35** (1987) 2206.

[33] M. Drees, *Comment on 'Higgs Boson Mass Bound in $E(6)$ Based Supersymmetric Theories.'*, Phys.Rev. **D35** (1987) 2910–2913.

[34] L. Randall, *talk at The 10th International Conference on Supersymmetry and Unification of Fundamental Interactions (SUSY02), Hamburg, Germany, 17-23 Jun 2002*, unpublished (2002) .

[35] P. Batra, A. Delgado, D. E. Kaplan, and T. M. Tait, *The Higgs mass bound in gauge extensions of the minimal supersymmetric standard model*, JHEP **0402** (2004) 043, arXiv:hep-ph/0309149 [hep-ph].

[36] A. Maloney, A. Pierce, and J. G. Wacker, *D-terms, unification, and the Higgs mass*, JHEP **0606** (2006) 034, arXiv:hep-ph/0409127 [hep-ph].

[37] M. Drees, *Supersymmetric Models with Extended Higgs Sector*, Int.J.Mod.Phys. **A4** (1989) 3635.

[38] J. Espinosa and M. Quiros, *On Higgs boson masses in nonminimal supersymmetric standard models*, Phys.Lett. **B279** (1992) 92–97.

[39] U. Ellwanger, C. Hugonie, and A. M. Teixeira, *The Next-to-Minimal Supersymmetric Standard Model*, Phys.Rept. **496** (2010) 1–77, arXiv:0910.1785 [hep-ph].

[40] R. Barbieri, L. J. Hall, Y. Nomura, and V. S. Rychkov, *Supersymmetry without a Light Higgs Boson*, Phys.Rev. **D75** (2007) 035007, arXiv:hep-ph/0607332 [hep-ph].

[41] R. Harnik, G. D. Kribs, D. T. Larson, and H. Murayama, *The Minimal supersymmetric fat Higgs model*, Phys.Rev. **D70** (2004) 015002, arXiv:hep-ph/0311349 [hep-ph].

[42] T. Cohen, T. Golling, M. Hance, A. Henrichs, K. Howe, et al., *SUSY Simplified Models at 14, 33, and 100 TeV Proton Colliders*, arXiv:1311.6480 [hep-ph].

[43] T. Cohen and others., *Boosting Stop Searches with a 100 TeV Proton Collider*, JHEP **1411** (2014) 021, arXiv:1406.4512 [hep-ph].

[44] J. Alwall, M.-P. Le, M. Lisanti, and J. G. Wacker, *Model-Independent Jets plus Missing Energy Searches*, Phys.Rev. **D79** (2009) 015005, arXiv:0809.3264 [hep-ph].

[45] J. Alwall, P. Schuster, and N. Toro, *Simplified Models for a First Characterization of New Physics at the LHC*, Phys.Rev. **D79** (2009) 075020, arXiv:0810.3921 [hep-ph].

[46] LHC New Physics Working Group Collaboration, D. Alves et al., *Simplified Models for LHC New Physics Searches*, J.Phys. **G39** (2012) 105005, arXiv:1105.2838 [hep-ph].

[47] J. Alwall, M. Herquet, F. Maltoni, O. Mattelaer, and T. Stelzer, *MadGraph 5 : Going Beyond*, JHEP **1106** (2011) 128, arXiv:1106.0522 [hep-ph].

[48] T. Sjöstrand, S. Mrenna, and P. Z. Skands, *PYTHIA 6.4 Physics and Manual*, JHEP **0605** (2006) 026, arXiv:hep-ph/0603175 [hep-ph].

[49] J. de Favereau, C. Delaere, P. Demin, A. Giammanco, V. Lema卯tre, et al., *DELPHES 3, A modular framework for fast simulation of a generic collider experiment*, arXiv:1307.6346 [hep-ex].

[50] J. Anderson, A. Avetisyan, R. Brock, S. Chekanov, T. Cohen, et al., *Snowmass Energy Frontier Simulations*, arXiv:1309.1057 [hep-ex].

[51] W. Beenakker, R. Hopker, and M. Spira, *PROSPINO: A Program for the production of supersymmetric particles in next-to-leading order QCD*, arXiv:hep-ph/9611232 [hep-ph].

[52] W. Beenakker, R. Hopker, M. Spira, and P. Zerwas, *Squark and gluino production at hadron colliders*, Nucl.Phys. **B492** (1997) 51–103, arXiv:hep-ph/9610490 [hep-ph].

[53] W. Beenakker et al., *Stop production at hadron colliders*, Nucl.Phys. **B515** (1998) 3–14, arXiv:hep-ph/9710451 [hep-ph].

[54] C. Borschensky et al., *Squark and gluino production cross sections in pp collisions at $\sqrt{s}$ = 13, 14, 33 and 100 TeV*, arXiv:1407.5066 [hep-ph].

[55] The ATLAS Collaboration, *Searches for Supersymmetry at the high luminosity LHC with the ATLAS Detector*, ATL-PHYS-PUB-2013-002, CERN, Geneva, Feb, 2013.

[56] J. Alwall, M.-P. Le, M. Lisanti, and J. G. Wacker, *Searching for Directly Decaying Gluinos at the Tevatron*, Phys.Lett. **B666** (2008) 34–37, arXiv:0803.0019 [hep-ph].

[57] J. L. Feng et al., *Discovering supersymmetry at the Tevatron in wino LSP scenarios*, Phys.Rev.Lett. **83** (1999) 1731–1734, arXiv:hep-ph/9904250 [hep-ph].

[58] The ATLAS Collaboration, *Search for New Phenomena in Monojet plus Missing Transverse Momentum Final States using 10fb-1 of pp Collisions at $\sqrt{s}$=8 TeV with the ATLAS detector at the LHC*, ATLAS-CONF-2012-147, CERN, Geneva, Nov, 2012.

[59] The CMS Collaboration, *Search for new physics in monojet events in pp collisions at $sqrts = 8$ TeV*, CMS-PAS-EXO-12-048, CERN, Geneva, 2013.

[60] The CMS Collaboration, *Search for supersymmetry in hadronic final states using MT2 with the CMS detector at $sqrts = 8$ TeV*, CMS-PAS-SUS-13-019, CERN, Geneva, 2014.

[61] C. Lester and D. Summers, *Measuring masses of semiinvisibly decaying particles pair produced at hadron colliders*, Phys.Lett. **B463** (1999) 99–103, arXiv:hep-ph/9906349 [hep-ph].

[62] A. Barr, C. Lester, and P. Stephens, *m(T2): The Truth behind the glamour*, J.Phys. **G29** (2003) 2343–2363, arXiv:hep-ph/0304226 [hep-ph].

[63] M. Hance, *Simplified Strong SUSY at future hadron colliders*, Exploring the Physics Frontier with Circular Colliders at Aspen Center for Physics, 2015. https://indico.cern.ch/event/336571/session/7/contribution/31.

[64] The ATLAS Collaboration, *Search for squarks and gluinos with the ATLAS detector in final states with jets and missing transverse momentum and 20.3 fb^{-1} of $\sqrt{s} = 8$ TeV proton-proton collision data*, ATLAS-CONF-2013-047, CERN, Geneva, May, 2013.

[65] The CMS Collaboration, S. Chatrchyan et al., *Search for new physics in events with same-sign dileptons and b jets in pp collisions at $\sqrt{s} = 8$ TeV*, JHEP **1303** (2013) 037, arXiv:1212.6194 [hep-ex].

[66] A. Avetisyan et al., *Methods and Results for Standard Model Event Generation at $\sqrt{s}$ = 14 TeV, 33 TeV and 100 TeV Proton Colliders (A Snowmass Whitepaper)*, arXiv:1308.1636 [hep-ex].

[67] M. Burns, K. Kong, K. T. Matchev, and M. Park, *Using Subsystem MT2 for Complete Mass Determinations in Decay Chains with Missing Energy at Hadron Colliders*, JHEP **0903** (2009) 143, arXiv:0810.5576 [hep-ph].

[68] J. Thaler and L.-T. Wang, *Strategies to Identify Boosted Tops*, JHEP **0807** (2008) 092, arXiv:0806.0023 [hep-ph].

[69] CDF Collaboration, D. Acosta et al., *Measurement of the $t\bar{t}$ production cross section in $p\bar{p}$ collisions at $\sqrt{s} = 1.96$ TeV using lepton plus jets events with semileptonic B decays to muons*, Phys.Rev. **D72** (2005) 032002, arXiv:hep-ex/0506001 [hep-ex].

[70] D0 Collaboration, V. Abazov et al., *A Search for anomalous heavy-flavor quark production in association with W bosons*, Phys.Rev.Lett. **94** (2005) 152002, arXiv:hep-ex/0411084 [hep-ex].

[71] CDF Collaboration, A. Abulencia et al., *Search for anomalous semileptonic decay of heavy flavor hadrons produced in association with a W boson at CDF II*, Phys.Rev. **D73** (2006) 051101, arXiv:hep-ex/0512065 [hep-ex].

[72] CDF Collaboration, T. Aaltonen et al., *First measurement of the production of a W boson in association with a single charm quark in $p\bar{p}$ collisions at $\sqrt{s}$ = 1.96-TeV*, Phys.Rev.Lett. **100** (2008) 091803, arXiv:0711.2901 [hep-ex].

[73] CDF Collaboration, T. Aaltonen et al., *Measurement of the $t\bar{t}$ Production Cross Section in 2 fb^{-1} of $p\bar{p}$ Collisions at $\sqrt{s} = 1.96$ TeV Using Lepton Plus Jets Events with Soft Muon b-Tagging*, Phys.Rev. **D79** (2009) 052007, arXiv:0901.4142 [hep-ex].

[74] CDF Collaboration, T. Aaltonen et al., *Measurement of the $t\bar{t}$ Production Cross Section in $p\bar{p}$ Collisions at sqrt(s)=1.96 TeV using Soft Electron b-Tagging*, Phys.Rev. **D81** (2010) 092002, arXiv:1002.3783 [hep-ex].

[75] The ATLAS Collaboration, G. Aad et al., *Expected Performance of the ATLAS Experiment - Detector, Trigger and Physics*, arXiv:0901.0512 [hep-ex].

[76] The ATLAS Collaboration, *Soft muon tagging and Dstar/mu correlations in 7 TeV collisions with ATLAS*, ATLAS-CONF-2010-100, CERN, Geneva, Dec, 2010. http://cds.cern.ch/record/1316469.

[77] The CMS Collaboration, S. Chatrchyan et al., *Identification of b-quark jets with the CMS experiment*, JINST **8** (2013) P04013, arXiv:1211.4462 [hep-ex].

[78] The ATLAS Collaboration, *Search for pair-produced top squarks decaying into a charm quark and the lightest neutralinos with 20.3 fb^{-1} of pp collisions at $\sqrt{s} = 8$ TeV with the ATLAS detector at the LHC*, ATLAS-CONF-2013-068, CERN, Geneva, Jul, 2013.

[79] M. Cacciari, G. P. Salam, and G. Soyez, *The Anti-k(t) jet clustering algorithm*, JHEP **0804** (2008) 063, arXiv:0802.1189 [hep-ph].

[80] G. Salam and A. Weiler. http://collider-reach.web.cern.ch.

[81] P. Langacker, *The Physics of Heavy Z' Gauge Bosons*, Rev.Mod.Phys. **81** (2009) 1199–1228, arXiv:0801.1345 [hep-ph].

[82] M. Cvetic and S. Godfrey, *Discovery and identification of extra gauge bosons*, arXiv:hep-ph/9504216 [hep-ph].

[83] J. L. Hewett and T. G. Rizzo, *Low-Energy Phenomenology of Superstring Inspired E(6) Models*, Phys.Rept. **183** (1989) 193.

[84] A. Leike, *The Phenomenology of extra neutral gauge bosons*, Phys.Rept. **317** (1999) 143–250, arXiv:hep-ph/9805494 [hep-ph].

[85] M. Cvetic and P. Langacker, *Z-prime physics and supersymmetry*, arXiv:hep-ph/9707451 [hep-ph].

[86] J. Erler, P. Langacker, S. Munir, and E. Rojas, *Improved Constraints on Z-prime Bosons from Electroweak Precision Data*, JHEP **0908** (2009) 017, arXiv:0906.2435 [hep-ph].

[87] P. Langacker, *The Physics of New U(1)-prime Gauge Bosons*, AIP Conf.Proc. **1200** (2010) 55–63, arXiv:0909.3260 [hep-ph].

[88] P. Nath et al., *The Hunt for New Physics at the Large Hadron Collider*, Nucl.Phys.Proc.Suppl. **200-202** (2010) 185–417, arXiv:1001.2693 [hep-ph].

[89] J. Jaeckel and A. Ringwald, *The Low-Energy Frontier of Particle Physics*, Ann.Rev.Nucl.Part.Sci. **60** (2010) 405–437, arXiv:1002.0329 [hep-ph].

[90] F. del Aguila, J. de Blas, and M. Perez-Victoria, *Electroweak Limits on General New Vector Bosons*, JHEP **1009** (2010) 033, arXiv:1005.3998 [hep-ph].

[91] R. Diener, S. Godfrey, and I. Turan, *Constraining Extra Neutral Gauge Bosons with Atomic Parity Violation Measurements*, Phys.Rev. **D86** (2012) 115017, arXiv:1111.4566 [hep-ph].

[92] R. Robinett and J. L. Rosner, *Mass Scales In Grand Unified Theories* , Phys.Rev. **D26** (1982) 2396.

[93] P. Langacker, R. W. Robinett, and J. L. Rosner, *New Heavy Gauge Bosons in p p and p anti-p Collisions*, Phys.Rev. **D30** (1984) 1470.

[94] A. Czarnecki, M. Jezabek, and J. H. Kuhn, *Lepton Spectra From Decays Of Polarized Top Quarks* , Nucl.Phys. **B351** (1991) 70–80.

[95] F. del Aguila, M. Cvetic, and P. Langacker, *Determination of Z-prime gauge couplings to quarks and leptons at future hadron colliders*, Phys.Rev. **D48** (1993) 969–973, arXiv:hep-ph/9303299 [hep-ph].

[96] F. Del Aguila and M. Cvetic, *Diagnostic power of future colliders for Z-prime couplings to quarks and leptons: e+ e- versus p p colliders*, Phys.Rev. **D50** (1994) 3158–3166, arXiv:hep-ph/9312329 [hep-ph].

[97] F. Del Aguila, M. Cvetic, and P. Langacker, *Reconstruction of the extended gauge structure from Z-prime observables at future colliders*, Phys.Rev. **D52** (1995) 37–43, arXiv:hep-ph/9501390 [hep-ph].

[98] M. Dittmar, A.-S. Nicollerat, and A. Djouadi, *Z-prime studies at the LHC: An Update*, Phys.Lett. **B583** (2004) 111–120, arXiv:hep-ph/0307020 [hep-ph].

[99] J. Kang and P. Langacker, *Z' discovery limits for supersymmetric E(6) models*, Phys.Rev. **D71** (2005) 035014, arXiv:hep-ph/0412190 [hep-ph].

[100] M. S. Carena, A. Daleo, B. A. Dobrescu, and T. M. Tait, *Z' gauge bosons at the Tevatron*, Phys.Rev. **D70** (2004) 093009, arXiv:hep-ph/0408098 [hep-ph].

[101] LHC/LC Study Group Collaboration, G. Weiglein et al., *Physics interplay of the LHC and the ILC*, Phys.Rept. **426** (2006) 47–358, arXiv:hep-ph/0410364 [hep-ph].

[102] F. Petriello and S. Quackenbush, *Measuring Z' couplings at the CERN LHC*, Phys.Rev. **D77** (2008) 115004, arXiv:0801.4389 [hep-ph].

[103] S. Godfrey and T. A. Martin, *Identification of Extra Neutral Gauge Bosons at the LHC Using b- and t-Quarks*, Phys.Rev.Lett. **101** (2008) 151803, arXiv:0807.1080 [hep-ph].

[104] P. Osland, A. Pankov, A. Tsytrinov, and N. Paver, *Spin and model identification of Z' bosons at the LHC*, Phys.Rev. **D79** (2009) 115021, arXiv:0904.4857 [hep-ph].

[105] Y. Li, F. Petriello, and S. Quackenbush, *Reconstructing a Z-prime Lagrangian using the LHC and low-energy data*, Phys.Rev. **D80** (2009) 055018, arXiv:0906.4132 [hep-ph].

[106] R. Diener, S. Godfrey, and T. A. Martin, *Discovery and Identification of Extra Neutral Gauge Bosons at the LHC*, arXiv:0910.1334 [hep-ph].

[107] R. Diener, S. Godfrey, and T. A. Martin, *Unravelling an Extra Neutral Gauge Boson at the LHC using Third Generation Fermions*, Phys.Rev. **D83** (2011) 115008, arXiv:1006.2845 [hep-ph].

[108] S. Gopalakrishna et al., *Chiral Couplings of W' and Top Quark Polarization at the LHC*, Phys.Rev. **D82** (2010) 115020, arXiv:1008.3508 [hep-ph].

[109] C.-F. Chang, K. Cheung, and T.-C. Yuan, *Supersymmetric Decays of the Z' Boson*, JHEP **1109** (2011) 058, arXiv:1107.1133 [hep-ph].

[110] J. Erler, P. Langacker, S. Munir, and E. Rojas, *Z' Bosons at Colliders: a Bayesian Viewpoint*, JHEP **1111** (2011) 076, arXiv:1103.2659 [hep-ph].

[111] E. L. Berger, Q.-H. Cao, C.-R. Chen, and H. Zhang, *Top Quark Polarization As A Probe of Models with Extra Gauge Bosons*, Phys.Rev. **D83** (2011) 114026, arXiv:1103.3274 [hep-ph].

[112] C.-W. Chiang, N. D. Christensen, G.-J. Ding, and T. Han, *Discovery in Drell-Yan Processes at the LHC*, Phys.Rev. **D85** (2012) 015023, arXiv:1107.5830 [hep-ph].

[113] E. Accomando, D. Becciolini, A. Belyaev, S. Moretti, and C. Shepherd-Themistocleous, *Z' at the LHC: Interference and Finite Width Effects in Drell-Yan*, arXiv:1304.6700 [hep-ph].

[114] E. L. Berger, Q.-H. Cao, J.-H. Yu, and H. Zhang, *Measuring Top-Quark Polarization in Top-Pair + Missing Energy Events*, arXiv:1305.7266 [hep-ph].

[115] N. D. Christensen and C. Duhr, *FeynRules - Feynman rules made easy*, Comput.Phys.Commun. **180** (2009) 1614–1641, arXiv:0806.4194 [hep-ph].

[116] S. Ovyn, X. Rouby, and V. Lemaitre, *DELPHES, a framework for fast simulation of a generic collider experiment*, arXiv:0903.2225 [hep-ph].

[117] B. A. Dobrescu and F. Yu, *Coupling-mass mapping of dijet peak searches*, Phys.Rev. **D88** (2013) no. 3, 035021, arXiv:1306.2629 [hep-ph].

[118] F. Yu, *Di-jet resonances at future hadron colliders: A Snowmass whitepaper*, arXiv:1308.1077 [hep-ph].

[119] K. Kong and F. Yu, *Discovery potential of Kaluza-Klein gluons at hadron colliders: A Snowmass whitepaper*, arXiv:1308.1078 [hep-ph].

[120] K. Agashe et al., *Constraining RS Models by Future Flavor and Collider Measurements: A Snowmass Whitepaper*, arXiv:1310.1070 [hep-ph].

[121] L. Apanasevich et al., *Sensitivity of potential future pp colliders to quark compositeness*, arXiv:1307.7149 [hep-ex].

[122] J. Pumplin et al., *New generation of parton distributions with uncertainties from global QCD analysis*, JHEP **0207** (2002) 012, arXiv:hep-ph/0201195 [hep-ph].

[123] M. L. Mangano et al., *ALPGEN, a generator for hard multiparton processes in hadronic collisions*, JHEP **0307** (2003) 001, arXiv:hep-ph/0206293 [hep-ph].

[124] S. Esen and R. M. Harris, *Jet Triggers and Dijet Mass*, CMS-NOTE-2006-069, CERN, Geneva, May, 2006. http://cds.cern.ch/record/962023.

[125] K. Gumus, N. Akchurin, S. Esen, and R. M. Harris, *CMS Sensitivity to Dijet Resonances*, CMS-NOTE-2006-070, CERN, Geneva, May, 2006. http://cds.cern.ch/record/962025.

[126] M. Cacciari, G. P. Salam, and G. Soyez, *FastJet User Manual*, Eur.Phys.J. **C72** (2012) 1896, arXiv:1111.6097 [hep-ph].

[127] The CMS Collaboration, *Search for Narrow Resonances using the Dijet Mass Spectrum with 19.6fb-1 of pp Collisions at sqrts=8 TeV*, CMS-PAS-EXO-12-059, CERN, Geneva, 2013. https://cds.cern.ch/record/1519066.

[128] Y. Bai and B. A. Dobrescu, *Heavy octets and Tevatron signals with three or four b jets*, JHEP **1107** (2011) 100, arXiv:1012.5814 [hep-ph].

[129] J. Conway, *Pretty Good Simulation of high energy collisions*, , 2012. http://physics.ucdavis.edu/~conway/research/software/pgs/pgs4-general.htm.

[130] UA2 Collaboration, J. Alitti et al., *A Search for new intermediate vector mesons and excited quarks decaying to two jets at the CERN $\bar{p}p$ collider*, Nucl.Phys. **B400** (1993) 3–24.

[131] CDF Collaboration, F. Abe et al., *Search for new particles decaying to dijets at CDF*, Phys.Rev. **D55** (1997) 5263–5268, arXiv:hep-ex/9702004 [hep-ex].

[132] CDF Collaboration, T. Aaltonen et al., *Search for new particles decaying into dijets in proton-antiproton collisions at s**(1/2) = 1.96-TeV*, Phys.Rev. **D79** (2009) 112002, arXiv:0812.4036 [hep-ex].

[133] The CMS Collaboration, *Search for Narrow Resonances using the Dijet Mass Spectrum in pp Collisions at $sqrts$ of 7 TeV*, CMS-PAS-EXO-11-094, CERN, Geneva, 2012. https://cds.cern.ch/record/1461223.

[134] The ATLAS Collaboration, G. Aad et al., *Search for New Physics in the Dijet Mass Distribution using 1 fb^{-1} of pp Collision Data at $\sqrt{s} = 7$ TeV collected by the ATLAS Detector*, Phys.Lett. **B708** (2012) 37–54, arXiv:1108.6311 [hep-ex].

[135] The CMS Collaboration, S. Chatrchyan et al., *Search for narrow resonances using the dijet mass spectrum in pp collisions at $\sqrt{s}$=8 TeV*, Phys.Rev. **D87** (2013) no. 11, 114015, arXiv:1302.4794 [hep-ex].

[136] The CMS Collaboration, S. Chatrchyan et al., *Search for narrow resonances and quantum black holes in inclusive and b-tagged dijet mass spectra from pp*

collisions at $\sqrt{s} = 7$ *TeV*, JHEP **1301** (2013) 013, arXiv:1210.2387 [hep-ex].

[137] The ATLAS Collaboration, *Search for New Phenomena in the Dijet Mass Distribution updated using 13.0 fb*$^{-1}$ *of pp Collisions at* $sqrts = 8$ *TeV collected by the ATLAS Detector*, ATLAS-CONF-2012-148, CERN, Geneva, Nov, 2012. http://cds.cern.ch/record/1493487.

[138] The ATLAS Collaboration, G. Aad et al., *Search for new phenomena in the dijet mass distribution using* $p - p$ *collision data at* $\sqrt{s} = 8$ *TeV with the ATLAS detector*, Phys.Rev. **D91** (2015) no. 5, 052007, arXiv:1407.1376 [hep-ex].

[139] T. Appelquist, H.-C. Cheng, and B. A. Dobrescu, *Bounds on universal extra dimensions*, Phys.Rev. **D64** (2001) 035002, arXiv:hep-ph/0012100 [hep-ph].

[140] H.-C. Cheng, K. T. Matchev, and M. Schmaltz, *Radiative corrections to Kaluza-Klein masses*, Phys.Rev. **D66** (2002) 036005, arXiv:hep-ph/0204342 [hep-ph].

[141] H.-C. Cheng, K. T. Matchev, and M. Schmaltz, *Bosonic supersymmetry? Getting fooled at the CERN LHC*, Phys.Rev. **D66** (2002) 056006, arXiv:hep-ph/0205314 [hep-ph].

[142] A. Datta, K. Kong, and K. T. Matchev, *Minimal Universal Extra Dimensions in CalcHEP/CompHEP*, New J.Phys. **12** (2010) 075017, arXiv:1002.4624 [hep-ph].

[143] Q.-F. Xiang et al., *Searches for dark matter signals in simplified models at future hadron colliders*, arXiv:1503.02931 [hep-ph].

[144] Z.-H. Yu et al., *Constraining the interaction strength between dark matter and visible matter: II. scalar, vector and spin-3/2 dark matter*, Nucl.Phys. **B860** (2012) 115–151, arXiv:1112.6052 [hep-ph].

[145] J.-M. Zheng et al., *Constraining the interaction strength between dark matter and visible matter: I. fermionic dark matter*, Nucl.Phys. **B854** (2012) 350–374, arXiv:1012.2022 [hep-ph].

[146] P. J. Fox, R. Harnik, R. Primulando, and C.-T. Yu, *Taking a Razor to Dark Matter Parameter Space at the LHC*, Phys.Rev. **D86** (2012) 015010, arXiv:1203.1662 [hep-ph].

[147] H. An, X. Ji, and L.-T. Wang, *Light Dark Matter and* Z' *Dark Force at Colliders*, JHEP **1207** (2012) 182, arXiv:1202.2894 [hep-ph].

[148] O. Buchmueller, M. J. Dolan, and C. McCabe, *Beyond Effective Field Theory for Dark Matter Searches at the LHC*, JHEP **1401** (2014) 025, arXiv:1308.6799 [hep-ph].

[149] N. Zhou et al., *Sensitivity of future collider facilities to WIMP pair production via effective operators and light mediators*, arXiv:1307.5327 [hep-ex].

[150] O. Buchmueller, M. J. Dolan, S. A. Malik, and C. McCabe, *Characterising dark matter searches at colliders and direct detection experiments: Vector mediators*, JHEP **1501** (2015) 037, arXiv:1407.8257 [hep-ph].

[151] J. Abdallah et al., *Simplified Models for Dark Matter and Missing Energy Searches at the LHC*, arXiv:1409.2893 [hep-ph].

[152] P. Harris, V. V. Khoze, M. Spannowsky, and C. Williams, *Constraining Dark Sectors at Colliders: Beyond the Effective Theory Approach*, arXiv:1411.0535 [hep-ph].

[153] F. J. Petriello, S. Quackenbush, and K. M. Zurek, *The Invisible Z' at the CERN LHC*, Phys.Rev. **D77** (2008) 115020, arXiv:0803.4005 [hep-ph].

[154] S. Chang, R. Edezhath, J. Hutchinson, and M. Luty, *Effective WIMPs*, Phys.Rev. **D89** (2014) no. 1, 015011, arXiv:1307.8120 [hep-ph].

[155] H. An, L.-T. Wang, and H. Zhang, *Dark matter with t-channel mediator: a simple step beyond contact interaction*, Phys.Rev. **D89** (2014) no. 11, 115014, arXiv:1308.0592 [hep-ph].

[156] Y. Bai and J. Berger, *Fermion Portal Dark Matter*, JHEP **1311** (2013) 171, arXiv:1308.0612 [hep-ph].

[157] A. Alves, S. Profumo, and F. S. Queiroz, *The dark Z' portal: direct, indirect and collider searches*, JHEP **1404** (2014) 063, arXiv:1312.5281 [hep-ph].

[158] G. Busoni et al., *On the Validity of the Effective Field Theory for Dark Matter Searches at the LHC, Part II: Complete Analysis for the s-channel*, JCAP **1406** (2014) 060, arXiv:1402.1275 [hep-ph].

[159] M. Papucci, A. Vichi, and K. M. Zurek, *Monojet versus the rest of the world I: t-channel models*, JHEP **1411** (2014) 024, arXiv:1402.2285 [hep-ph].

[160] XENON100 Collaboration, E. Aprile et al., *Dark Matter Results from 225 Live Days of XENON100 Data*, Phys.Rev.Lett. **109** (2012) 181301, arXiv:1207.5988 [astro-ph.CO].

[161] LUX Collaboration, D. Akerib et al., *First results from the LUX dark matter experiment at the Sanford Underground Research Facility*, Phys.Rev.Lett. **112** (2014) no. 9, 091303, arXiv:1310.8214 [astro-ph.CO].

[162] SuperCDMS Collaboration, R. Agnese et al., *Search for Low-Mass Weakly Interacting Massive Particles with SuperCDMS*, Phys.Rev.Lett. **112** (2014) no. 24, 241302, arXiv:1402.7137 [hep-ex].

[163] XENON1T Collaboration, E. Aprile, *The XENON1T Dark Matter Search Experiment*, Springer Proc.Phys. **C12-02-22** (2013) 93–96, arXiv:1206.6288 [astro-ph.IM].

[164] M. Felizardo et al., *Final Analysis and Results of the Phase II SIMPLE Dark Matter Search*, Phys.Rev.Lett. **108** (2012) 201302, arXiv:1106.3014 [astro-ph.CO].

[165] PICASSO Collaboration, S. Archambault et al., *Constraints on Low-Mass WIMP Interactions on ^{19}F from PICASSO*, Phys.Lett. **B711** (2012) 153–161, arXiv:1202.1240 [hep-ex].

[166] COUPP Collaboration, E. Behnke et al., *First Dark Matter Search Results from a 4-kg CF_3I Bubble Chamber Operated in a Deep Underground Site*, Phys.Rev. **D86** (2012) no. 5, 052001, arXiv:1204.3094 [astro-ph.CO].

[167] Super-Kamiokande Collaboration, T. Tanaka et al., *An Indirect Search for WIMPs in the Sun using 3109.6 days of upward-going muons in Super-Kamiokande*, Astrophys.J. **742** (2011) 78, arXiv:1108.3384 [astro-ph.HE].

[168] IceCube Collaboration, R. Abbasi et al., *Multi-year search for dark matter annihilations in the Sun with the AMANDA-II and IceCube detectors*, Phys.Rev. **D85** (2012) 042002, arXiv:1112.1840 [astro-ph.HE].

[169] P. J. Fox, R. Harnik, J. Kopp, and Y. Tsai, *Missing Energy Signatures of Dark Matter at the LHC*, Phys.Rev. **D85** (2012) 056011, arXiv:1109.4398 [hep-ph].

[170] Fermi-LAT Collaboration, M. Ackermann et al., *Dark matter constraints from observations of 25 Milky Way satellite galaxies with the Fermi Large Area Telescope*, Phys.Rev. **D89** (2014) 042001, arXiv:1310.0828 [astro-ph.HE].

[171] CTA Collaboration, M. Doro et al., *Dark Matter and Fundamental Physics with the Cherenkov Telescope Array*, Astropart.Phys. **43** (2013) 189–214, arXiv:1208.5356 [astro-ph.IM].

[172] X. Huang et al., *Constraints on the dark matter annihilation scenario of Fermi 130 GeV γ-ray line emission by continuous gamma-rays, Milky Way halo, galaxy clusters and dwarf galaxies observations*, JCAP **1211** (2012) 048, arXiv:1208.0267 [astro-ph.HE].

[173] S.-J. Lin, Q. Yuan, and X.-J. Bi, *Quantitative study of the AMS-02 electron/positron spectra: Implications for pulsars and dark matter properties*, Phys.Rev. **D91** (2015) no. 6, 063508, arXiv:1409.6248 [astro-ph.HE].

[174] Q. Yuan et al., *Implications of the AMS-02 positron fraction in cosmic rays*, Astropart.Phys. **60** (2014) 1–12, arXiv:1304.1482 [astro-ph.HE].

[175] S. Catani, Y. L. Dokshitzer, M. Seymour, and B. Webber, *Longitudinally invariant K_t clustering algorithms for hadron hadron collisions*, Nucl.Phys. **B406** (1993) 187–224.

[176] S. D. Ellis and D. E. Soper, *Successive combination jet algorithm for hadron collisions*, Phys.Rev. **D48** (1993) 3160–3166, arXiv:hep-ph/9305266 [hep-ph].

[177] Y. L. Dokshitzer, G. Leder, S. Moretti, and B. Webber, *Better jet clustering algorithms*, JHEP **9708** (1997) 001, arXiv:hep-ph/9707323 [hep-ph].

[178] M. Wobisch and T. Wengler, *Hadronization corrections to jet cross-sections in deep inelastic scattering*, arXiv:hep-ph/9907280 [hep-ph].

[179] M. Wobisch, *Measurement and QCD analysis of jet cross-sections in deep inelastic positron proton collisions at* $\sqrt{s} = 300$ *GeV*, DESY-THESIS-2000-049 (2000) .

[180] G. C. Blazey et al., *Run II jet physics*, arXiv:hep-ex/0005012 [hep-ex].

[181] S. Catani, G. Turnock, and B. Webber, *Jet broadening measures in* e^+e^- *annihilation*, Phys.Lett. **B295** (1992) 269–276.

[182] Y. L. Dokshitzer, A. Lucenti, G. Marchesini, and G. Salam, *On the QCD analysis of jet broadening*, JHEP **9801** (1998) 011, arXiv:hep-ph/9801324 [hep-ph].

[183] A. Banfi, G. P. Salam, and G. Zanderighi, *Principles of general final-state resummation and automated implementation*, JHEP **0503** (2005) 073, arXiv:hep-ph/0407286 [hep-ph].

[184] A. J. Larkoski, G. P. Salam, and J. Thaler, *Energy Correlation Functions for Jet Substructure*, JHEP **1306** (2013) 108, arXiv:1305.0007 [hep-ph].

[185] D. Bertolini, T. Chan, and J. Thaler, *Jet Observables Without Jet Algorithms*, JHEP **1404** (2014) 013, arXiv:1310.7584 [hep-ph].

[186] A. J. Larkoski, D. Neill, and J. Thaler, *Jet Shapes with the Broadening Axis*, JHEP **1404** (2014) 017, arXiv:1401.2158 [hep-ph].

[187] G. Salam, *Unpublished*, .

[188] T. Sjostrand, S. Mrenna, and P. Z. Skands, *A Brief Introduction to PYTHIA 8.1*, Comput.Phys.Commun. **178** (2008) 852–867, arXiv:0710.3820 [hep-ph].

[189] http://fastjet.hepforge.org/contrib/. FastJet Contrib.

[190] A. Abdesselam et al., *Boosted objects: A Probe of beyond the Standard Model physics*, Eur.Phys.J. **C71** (2011) 1661, arXiv:1012.5412 [hep-ph].

[191] A. Altheimer, S. Arora, L. Asquith, G. Brooijmans, J. Butterworth, et al., *Jet Substructure at the Tevatron and LHC: New results, new tools, new benchmarks*, J.Phys. **G39** (2012) 063001, arXiv:1201.0008 [hep-ph].

[192] A. Altheimer et al., *Boosted objects and jet substructure at the LHC. Report of BOOST2012, held at IFIC Valencia, 23rd-27th of July 2012*, Eur.Phys.J. **C74** (2014) 2792, arXiv:1311.2708 [hep-ex].

[193] A. J. Larkoski and J. Thaler, *Unsafe but Calculable: Ratios of Angularities in Perturbative QCD*, JHEP **1309** (2013) 137, arXiv:1307.1699 [hep-ph].

[194] A. J. Larkoski, S. Marzani, G. Soyez, and J. Thaler, *Soft Drop*, JHEP **1405** (2014) 146, arXiv:1402.2657 [hep-ph].

[195] A. J. Larkoski and J. Thaler, *Aspects of Jets at 100 TeV*, arXiv:1406.7011 [hep-ph].

[196] J. M. Butterworth, A. R. Davison, M. Rubin, and G. P. Salam, *Jet substructure as a new Higgs search channel at the LHC*, Phys.Rev.Lett. **100** (2008) 242001, arXiv:0802.2470 [hep-ph].

[197] M. Dasgupta, A. Fregoso, S. Marzani, and G. P. Salam, *Towards an understanding of jet substructure*, JHEP **1309** (2013) 029, arXiv:1307.0007 [hep-ph].

[198] S. Moretti, M. Nolten, and D. Ross, *Weak corrections to four-parton processes*, Nucl.Phys. **B759** (2006) 50–82, arXiv:hep-ph/0606201 [hep-ph].

[199] G. Bell, J. Kuhn, and J. Rittinger, *Electroweak Sudakov Logarithms and Real Gauge-Boson Radiation in the TeV Region*, Eur.Phys.J. **C70** (2010) 659–671, arXiv:1004.4117 [hep-ph].

[200] S. Dittmaier, A. Huss, and C. Speckner, *Weak radiative corrections to dijet production at hadron colliders*, JHEP **1211** (2012) 095, arXiv:1210.0438 [hep-ph].

[201] J. R. Christiansen and T. Sjöstrand, *Weak Gauge Boson Radiation in Parton Showers*, arXiv:1401.5238 [hep-ph].

[202] A. Hook and A. Katz, *Unbroken $SU(2)$ at a 100 TeV collider*, arXiv:1407.2607 [hep-ph].

[203] B. W. Lee, C. Quigg, and H. Thacker, *Weak Interactions at Very High-Energies: The Role of the Higgs Boson Mass*, Phys.Rev. **D16** (1977) 1519.

[204] M. S. Chanowitz and M. K. Gaillard, *The TeV Physics of Strongly Interacting W's and Z's*, Nucl.Phys. **B261** (1985) 379.

[205] G. L. Kane, W. Repko, and W. Rolnick, *The Effective $W^{\pm}$, Z^0 Approximation for High-Energy Collisions*, Phys.Lett. **B148** (1984) 367–372.

[206] S. Dawson, *The Effective W Approximation*, Nucl.Phys. **B249** (1985) 42–60.

[207] Z. Nagy and D. E. Soper, *Parton Showers with Quantum Interference*, JHEP **0709** (2007) 114, arXiv:0706.0017 [hep-ph].

[208] J. Chen, T. Han, R. Ruiz, and B. Tweedie. In preparation.

[209] M. Cvetic and P. Langacker, *Rare decays as diagnostics for Z-prime gauge couplings at hadron colliders*, Phys.Rev. **D46** (1992) R14–R18.

[210] T. G. Rizzo, *Fun with New Gauge Bosons at 100 TeV*, Phys.Rev. **D89** (2014) 095022, arXiv:1403.5465 [hep-ph].

[211] T. Stelzer and W. Long, *Automatic generation of tree level helicity amplitudes*, Comput.Phys.Commun. **81** (1994) 357–371, arXiv:hep-ph/9401258 [hep-ph].

[212] F. Maltoni and T. Stelzer, *MadEvent: Automatic event generation with MadGraph*, JHEP **0302** (2003) 027, arXiv:hep-ph/0208156 [hep-ph].

[213] S. Dimopoulos and G. Giudice, *Naturalness constraints in supersymmetric theories with nonuniversal soft terms*, Phys.Lett. **B357** (1995) 573–578, arXiv:hep-ph/9507282 [hep-ph].

[214] A. G. Cohen, D. Kaplan, and A. Nelson, *The More minimal supersymmetric standard model*, Phys.Lett. **B388** (1996) 588–598, arXiv:hep-ph/9607394 [hep-ph].

[215] C. Brust, A. Katz, S. Lawrence, and R. Sundrum, *SUSY, the Third Generation and the LHC*, JHEP **1203** (2012) 103, arXiv:1110.6670 [hep-ph].

[216] R. Essig, E. Izaguirre, J. Kaplan, and J. G. Wacker, *Heavy Flavor Simplified Models at the LHC*, JHEP **1201** (2012) 074, arXiv:1110.6443 [hep-ph].

[217] M. Papucci, J. T. Ruderman, and A. Weiler, *Natural SUSY Endures*, JHEP **1209** (2012) 035, arXiv:1110.6926 [hep-ph].

[218] R. M. Barnett, H. E. Haber, and D. E. Soper, *Ultraheavy Particle Production from Heavy Partons at Hadron Colliders*, Nucl.Phys. **B306** (1988) 697.

[219] F. I. Olness and W.-K. Tung, *When Is a Heavy Quark Not a Parton? Charged Higgs Production and Heavy Quark Mass Effects in the QCD Based Parton Model*, Nucl.Phys. **B308** (1988) 813.

[220] R. D. Ball, , et al., *Parton distributions with LHC data*, Nucl.Phys. **B867** (2013) 244–289, arXiv:1207.1303 [hep-ph].

[221] T. Han, J. Sayre, and S. Westhoff, *Top-Quark Initiated Processes at High-Energy Hadron Colliders*, arXiv:1411.2588 [hep-ph].

[222] A. L. Fitzpatrick, J. Kaplan, L. Randall, and L.-T. Wang, *Searching for the Kaluza-Klein Graviton in Bulk RS Models*, JHEP **0709** (2007) 013, arXiv:hep-ph/0701150 [hep-ph].

[223] H. Davoudiasl, J. Hewett, and T. Rizzo, *Experimental probes of localized gravity: On and off the wall*, Phys.Rev. **D63** (2001) 075004, arXiv:hep-ph/0006041 [hep-ph].

[224] T. Han, J. D. Lykken, and R.-J. Zhang, *On Kaluza-Klein states from large extra dimensions*, Phys.Rev. **D59** (1999) 105006, arXiv:hep-ph/9811350 [hep-ph].

[225] G. F. Giudice, R. Rattazzi, and J. D. Wells, *Quantum gravity and extra dimensions at high-energy colliders*, Nucl.Phys. **B544** (1999) 3–38, arXiv:hep-ph/9811291 [hep-ph].

[226] S. Dawson, A. Ismail, and I. Low, *A Redux on "When is the Top Quark a Parton?"*, Phys.Rev. **D90** (2014) no. 1, 014005, arXiv:1405.6211 [hep-ph].

[227] D. A. Dicus and S. Willenbrock, *Higgs Boson Production from Heavy Quark Fusion*, Phys.Rev. **D39** (1989) 751.

[228] D. Dicus, T. Stelzer, Z. Sullivan, and S. Willenbrock, *Higgs boson production in association with bottom quarks at next-to-leading order*, Phys.Rev. **D59** (1999) 094016, arXiv:hep-ph/9811492 [hep-ph].

[229] F. Maltoni, Z. Sullivan, and S. Willenbrock, *Higgs-boson production via bottom-quark fusion*, Phys.Rev. **D67** (2003) 093005, arXiv:hep-ph/0301033 [hep-ph].

[230] M. Aivazis, J. C. Collins, F. I. Olness, and W.-K. Tung, *Leptoproduction of heavy quarks. 2. A Unified QCD formulation of charged and neutral current processes from fixed target to collider energies*, Phys.Rev. **D50** (1994) 3102–3118, arXiv:hep-ph/9312319 [hep-ph].

[231] J. C. Collins, *Hard scattering factorization with heavy quarks: A General treatment*, Phys.Rev. **D58** (1998) 094002, arXiv:hep-ph/9806259 [hep-ph].

[232] S. Forte, E. Laenen, P. Nason, and J. Rojo, *Heavy quarks in deep-inelastic scattering*, Nucl.Phys. **B834** (2010) 116–162, arXiv:1001.2312 [hep-ph].

[233] R. Thorne and R. Roberts, *An Ordered analysis of heavy flavor production in deep inelastic scattering*, Phys.Rev. **D57** (1998) 6871–6898, arXiv:hep-ph/9709442 [hep-ph].

[234] F. Maltoni, G. Ridolfi, and M. Ubiali, *b-initiated processes at the LHC: a reappraisal*, JHEP **1207** (2012) 022, arXiv:1203.6393 [hep-ph].

[235] D. S. M. Alves, J. Galloway, J. T. Ruderman, and J. R. Walsh, *Running Electroweak Couplings as a Probe of New Physics*, arXiv:1410.6810 [hep-ph].

[236] D. E. Kaplan and M. D. Schwartz, *Constraining Light Colored Particles with Event Shapes*, Phys.Rev.Lett. **101** (2008) 022002, arXiv:0804.2477 [hep-ph].

[237] D. Becciolini et al., *Constraining new colored matter from the ratio of 3 to 2 jets cross sections at the LHC*, Phys.Rev. **D91** (2015) no. 1, 015010, arXiv:1403.7411 [hep-ph].

[238] D. Rainwater and T. M. Tait, *Testing Grand Unification at the (S)LHC*, Phys.Rev. **D75** (2007) 115014, arXiv:hep-ph/0701093 [hep-ph].

[239] S. Dittmaier and M. Huber, *Radiative corrections to the neutral-current Drell-Yan process in the Standard Model and its minimal supersymmetric extension*, JHEP **1001** (2010) 060, arXiv:0911.2329 [hep-ph].

[240] S. Brensing, S. Dittmaier, M. Kramer, and A. Muck, *Radiative corrections to W^- boson hadroproduction: Higher-order electroweak and supersymmetric effects*, Phys.Rev. **D77** (2008) 073006, arXiv:0710.3309 [hep-ph].

[241] S. Catani and M. Grazzini, *An NNLO subtraction formalism in hadron collisions and its application to Higgs boson production at the LHC*, Phys.Rev.Lett. **98** (2007) 222002, arXiv:hep-ph/0703012 [hep-ph].

[242] S. Catani et al., *Vector boson production at hadron colliders: a fully exclusive QCD calculation at NNLO*, Phys.Rev.Lett. **103** (2009) 082001, arXiv:0903.2120 [hep-ph].

[243] K. Melnikov and F. Petriello, *Electroweak gauge boson production at hadron colliders through O(alpha(s)**2)*, Phys.Rev. **D74** (2006) 114017, arXiv:hep-ph/0609070 [hep-ph].

[244] R. Gavin, Y. Li, F. Petriello, and S. Quackenbush, *FEWZ 2.0: A code for hadronic Z production at next-to-next-to-leading order*, Comput.Phys.Commun. **182** (2011) 2388–2403, arXiv:1011.3540 [hep-ph].

[245] R. Gavin, Y. Li, F. Petriello, and S. Quackenbush, *W Physics at the LHC with FEWZ 2.1*, Comput.Phys.Commun. **184** (2013) 208–214, arXiv:1201.5896 [hep-ph].

[246] Y. Li and F. Petriello, *Combining QCD and electroweak corrections to dilepton production in FEWZ*, Phys.Rev. **D86** (2012) 094034, arXiv:1208.5967 [hep-ph].

[247] The ATLAS Collaboration, G. Aad et al., *Measurement of the high-mass Drell–Yan differential cross-section in pp collisions at sqrt(s)=7 TeV with the ATLAS detector*, Phys.Lett. **B725** (2013) 223–242, arXiv:1305.4192 [hep-ex].

[248] The CMS Collaboration, S. Chatrchyan et al., *Measurement of the differential and double-differential Drell-Yan cross sections in proton-proton collisions at* $\sqrt{s} = 7$ *TeV*, JHEP **1312** (2013) 030, arXiv:1310.7291 [hep-ex].

[249] The CMS Collaboration, V. Khachatryan et al., *Measurements of differential and double-differential Drell-Yan cross sections in proton-proton collisions at* $\sqrt{s} = 8$ *TeV*, arXiv:1412.1115 [hep-ex].

[250] N. Manton, *Topology in the Weinberg-Salam Theory*, Phys.Rev. **D28** (1983) 2019.

[251] V. Kuzmin, V. Rubakov, and M. Shaposhnikov, *On the Anomalous Electroweak Baryon Number Nonconservation in the Early Universe*, Phys.Lett. **B155** (1985) 36.

[252] A. Ringwald, *High-Energy Breakdown of Perturbation Theory in the Electroweak Instanton Sector*, Nucl.Phys. **B330** (1990) 1.

[253] V. V. Khoze and A. Ringwald. Nucl. Phys. B **355** (1991) 351; Phys. Lett. B **259** (1991) 106.

[254] V. A. R. S. Y. Khlebnikov and P. G. Tinyakov. Nucl. Phys. B **350** (1991) 441.

[255] A. H. Mueller. Phys. Rept. **214** (1992) 159; V.A. Rubakov and M.E. Shaposhnikov, Phys.Usp. 39 (1996) **461**, hep-ph/9603208.

[256] M. P. Mattis. Nucl. Phys. B **348** (1991) 310, Nucl. Phys. B **353** (1991) 44.

[257] F. J. Dyson. Phys. Rev. **85** (1952) 631.

[258] M. B. Voloshin. Phys. Rev. **85** (1952) 631.

[259] D. T. S. M. V. Libanov, V. A. Rubakov and S. V. Troitsky. Phys. Rev. D **50** (1994) 7553 [hep-ph/9407381]; D. T. Son, Nucl. Phys. B **477** (1996) 378

[hep-ph/9505338]; M. V. Libanov, V. A. Rubakov and S. V. Troitsky, Phys. Part. Nucl. **28** (1997) 217.

[260] V. V. Khoze, *Multiparticle Higgs and Vector Boson Amplitudes at Threshold*, JHEP **1407** (2014) 008, arXiv:1404.4876 [hep-ph].

[261] V. V. Khoze, *Perturbative growth of high-multiplicity W, Z and Higgs production processes at high energies*, arXiv:1411.2925 [hep-ph].

[262] J. Jaeckel and V. V. Khoze, *An upper limit on the scale of new physics phenomena from rising cross sections in high multiplicity Higgs and vector boson events*, arXiv:1411.5633 [hep-ph].

[263] H. P. Nilles, *Supersymmetry, Supergravity and Particle Physics*, Phys.Rept. **110** (1984) 1–162.

[264] H. E. Haber and G. L. Kane, *The Search for Supersymmetry: Probing Physics Beyond the Standard Model*, Phys.Rept. **117** (1985) 75–263.

[265] R. Barbieri, *Looking Beyond the Standard Model: The Supersymmetric Option*, Riv.Nuovo Cim. **11N4** (1988) 1–45.

[266] J. R. Ellis et al., *Higgs Bosons in a Nonminimal Supersymmetric Model*, Phys.Rev. **D39** (1989) 844.

[267] G. Branco et al., *Theory and phenomenology of two-Higgs-doublet models*, Phys.Rept. **516** (2012) 1–102, arXiv:1106.0034 [hep-ph].

[268] H. Haber, G. L. Kane, and T. Sterling, *The Fermion Mass Scale and Possible Effects of Higgs Bosons on Experimental Observables*, Nucl.Phys. **B161** (1979) 493.

[269] L. J. Hall and M. B. Wise, *FLAVOR CHANGING HIGGS - BOSON COUPLINGS*, Nucl.Phys. **B187** (1981) 397.

[270] J. F. Donoghue and L. F. Li, *Properties of Charged Higgs Bosons*, Phys.Rev. **D19** (1979) 945.

[271] The ATLAS Collaboration, G. Aad et al., *Search for neutral Higgs bosons of the minimal supersymmetric standard model in pp collisions at* $\sqrt{s}$ *= 8 TeV with the ATLAS detector*, JHEP **1411** (2014) 056, arXiv:1409.6064 [hep-ex].

[272] The CMS Collaboration, *Search for charged Higgs bosons with the H+ to tau nu decay channel in the fully hadronic final state at* $\sqrt{s}$ *=8 TeV*, CMS-PAS-HIG-14-020, CERN, Geneva, 2014. http://cds.cern.ch/record/1950346.

[273] The CMS Collaboration, S. Chatrchyan et al., *Search for a Higgs boson decaying into a b-quark pair and produced in association with b quarks in proton-proton collisions at 7 TeV*, Phys.Lett. **B722** (2013) 207–232, arXiv:1302.2892 [hep-ex].

[274] The ATLAS Collaboration, G. Aad et al., *Search for Higgs bosons in Two-Higgs-Doublet models in the* $H \to WW \to e\nu\mu\nu$ *channel with the ATLAS detector*, ATLAS-CONF-2013-027, CERN, Geneva, Mar, 2013.

[275] The CMS Collaboration, V. Khachatryan et al., *Searches for heavy Higgs bosons in two-Higgs-doublet models and for t to ch decay using multilepton and diphoton final states in pp collisions at 8 TeV*, Phys.Rev. **D90** (2014) no. 11, 112013, arXiv:1410.2751 [hep-ex].

[276] The ATLAS Collaboration, *Search for charged Higgs bosons in the τ+jets final state with pp collision data recorded at $\sqrt{s} = 8$ TeV with the ATLAS experiment*, ATLAS-CONF-2013-090, CERN, Geneva, Aug, 2013.

[277] The CMS Collaboration, S. Chatrchyan et al., *Higgs to tau tau (MSSM)*, CMS-PAS-HIG-13-021, CERN, Geneva, 2013.

[278] B. Coleppa, F. Kling, and S. Su, *Exotic Higgs Decay via AZ/HZ Channel: a Snowmass Whitepaper*, arXiv:1308.6201 [hep-ph].

[279] B. Coleppa, F. Kling, and S. Su, *Exotic Decays Of A Heavy Neutral Higgs Through HZ/AZ Channel*, JHEP **1409** (2014) 161, arXiv:1404.1922 [hep-ph].

[280] E. Brownson et al., *Heavy Higgs Scalars at Future Hadron Colliders (A Snowmass Whitepaper)*, arXiv:1308.6334 [hep-ex].

[281] B. Coleppa, F. Kling, and S. Su, *Charged Higgs search via $AW^{\pm}/HW^{\pm}$ channel*, JHEP **1412** (2014) 148, arXiv:1408.4119 [hep-ph].

[282] F. Kling, A. Pyarelal, and S. Su, *Light Charged Higgs Bosons in Single-Top and Top-Pair Production with decay to AW*, to appear.

[283] L. Tong and S. Su, *Exotic Higgs Decay Via Charged Higgs*, to appear.

[284] U. Maitra et al., *Searching for an elusive charged Higgs boson at the Large Hadron Collider*, Phys.Rev. **D89** (2014) no. 5, 055024, arXiv:1401.1775 [hep-ph].

[285] L. Basso et al., *Probing the charged Higgs boson at the LHC in the CP-violating type-II 2HDM*, JHEP **1211** (2012) 011, arXiv:1205.6569 [hep-ph].

[286] R. Dermisek, J. P. Hall, E. Lunghi, and S. Shin, *A New Avenue to Charged Higgs Discovery in Multi-Higgs Models*, JHEP **1404** (2014) 140, arXiv:1311.7208 [hep-ph].

[287] B. Mohn, N. Gollub, and K. A. Assamagan, *The ATLAS discovery potential for a heavy Charged Higgs boson in a large mass splitting MSSM scenario*, ATL-PHYS-PUB-2005-017. ATL-COM-PHYS-2005-021. CERN-ATL-COM-PHYS-2005-021, CERN, Geneva, 2005.

[288] K. Assamagan, *Signature of the charged Higgs decay $H^{\pm} \to W h^0$ with the ATLAS detector*, Acta Phys.Polon. **B31** (2000) 881–893.

[289] K. A. Assamagan, Y. Coadou, and A. Deandrea, *ATLAS discovery potential for a heavy charged Higgs boson*, Eur.Phys.J.direct **C4** (2002) 9, arXiv:hep-ph/0203121 [hep-ph].

[290] B. Coleppa, F. Kling, and S. Su, *Constraining Type II 2HDM in Light of LHC Higgs Searches*, JHEP **1401** (2014) 161, arXiv:1305.0002 [hep-ph].

[291] J. F. Gunion, H. E. Haber, G. L. Kane, and S. Dawson, *The Higgs Hunter's Guide*, Front.Phys. **80** (2000) 1–448.

[292] M. Spira, *HIGLU: A program for the calculation of the total Higgs production cross-section at hadron colliders via gluon fusion including QCD corrections*, arXiv:hep-ph/9510347 [hep-ph].

[293] R. V. Harlander, S. Liebler, and H. Mantler, *SusHi: A program for the calculation of Higgs production in gluon fusion and bottom-quark annihilation in the Standard Model and the MSSM*, Comput.Phys.Commun. **184** (2013) 1605–1617, arXiv:1212.3249 [hep-ph].

[294] R. V. Harlander and W. B. Kilgore, *Higgs boson production in bottom quark fusion at next-to-next-to leading order*, Phys.Rev. **D68** (2003) 013001, arXiv:hep-ph/0304035 [hep-ph].

[295] R. V. Harlander and W. B. Kilgore, *Next-to-next-to-leading order Higgs production at hadron colliders*, Phys.Rev.Lett. **88** (2002) 201801, arXiv:hep-ph/0201206 [hep-ph].

[296] T. Plehn, *Charged Higgs boson production in bottom gluon fusion*, Phys.Rev. **D67** (2003) 014018, arXiv:hep-ph/0206121 [hep-ph].

[297] M. Flechl et al., *Improved cross-section predictions for heavy charged Higgs boson production at the LHC*, arXiv:1409.5615 [hep-ph].

[298] D. Eriksson, J. Rathsman, and O. Stal, *2HDMC: Two-Higgs-Doublet Model Calculator Physics and Manual*, Comput.Phys.Commun. **181** (2010) 189–205, arXiv:0902.0851 [hep-ph].

[299] J. Hajer, Y. Li, T. Liu, and J. Shiu, *to appear*, .

[300] U. Baur, T. Plehn, and D. L. Rainwater, *Probing the Higgs selfcoupling at hadron colliders using rare decays*, Phys.Rev. **D69** (2004) 053004, arXiv:hep-ph/0310056 [hep-ph].

[301] The ATLAS Collaboration, G. Aad et al., *Search for the Standard Model Higgs boson decay to $\mu^+\mu^-$ with the ATLAS detector*, Phys.Lett. **B738** (2014) 68–86, arXiv:1406.7663 [hep-ex].

[302] The CMS Collaboration, V. Khachatryan et al., *Search for a standard model-like Higgs boson in the $\mu^+\mu^-$ and $\mathrm{e}^+\mathrm{e}^-$ decay channels at the LHC*, arXiv:1410.6679 [hep-ex].

[303] C. Delaunay, C. Grojean, and G. Perez, *Modified Higgs Physics from Composite Light Flavors*, JHEP **1309** (2013) 090, arXiv:1303.5701 [hep-ph].

[304] C. Delaunay et al., *Light Non-degenerate Composite Partners at the LHC*, JHEP **1402** (2014) 055, arXiv:1311.2072 [hep-ph].

[305] M. Blanke et al., *Flavoured Naturalness*, JHEP **1306** (2013) 022, arXiv:1302.7232 [hep-ph].

[306] R. Mahbubani et al., *Light Nondegenerate Squarks at the LHC*, Phys.Rev.Lett. **110** (2013) no. 15, 151804, arXiv:1212.3328 [hep-ph].

[307] A. L. Kagan, G. Perez, T. Volansky, and J. Zupan, *General Minimal Flavor Violation*, Phys.Rev. **D80** (2009) 076002, arXiv:0903.1794 [hep-ph].

[308] A. Dery et al., *Higgs couplings to fermions: 2HDM with MFV*, JHEP **1308** (2013) 006, arXiv:1304.6727.

[309] G. F. Giudice and O. Lebedev, *Higgs-dependent Yukawa couplings*, Phys.Lett. **B665** (2008) 79–85, arXiv:0804.1753 [hep-ph].

[310] L. Da Rold, C. Delaunay, C. Grojean, and G. Perez, *Up Asymmetries From Exhilarated Composite Flavor Structures*, JHEP **1302** (2013) 149, arXiv:1208.1499 [hep-ph].

[311] A. Dery et al., *Model building for flavor changing Higgs couplings*, Phys.Rev. **D90** (2014) no. 11, 115022, arXiv:1408.1371 [hep-ph].

[312] C. Delaunay, T. Golling, G. Perez, and Y. Soreq, *Enhanced Higgs boson coupling to charm pairs*, Phys.Rev. **D89** (2014) no. 3, 033014, arXiv:1310.7029 [hep-ph].

[313] G. T. Bodwin, F. Petriello, S. Stoynev, and M. Velasco, *Higgs boson decays to quarkonia and the $H\bar{c}c$ coupling*, Phys.Rev. **D88** (2013) no. 5, 053003, arXiv:1306.5770 [hep-ph].

[314] A. L. Kagan et al., *An Exclusive Window onto Higgs Yukawa Couplings*, arXiv:1406.1722 [hep-ph].

[315] Y. Grossmann, M. König, and M. Neubert, *Exclusive Radiative Decays of W and Z Bosons in QCD Factorization*, arXiv:1501.06569 [hep-ph].

[316] The ATLAS Collaboration, G. Aad et al., *Search for pair-produced third-generation squarks decaying via charm quarks or in compressed supersymmetric scenarios in pp collisions at $\sqrt{s} = 8$ TeV with the ATLAS detector*, Phys.Rev. **D90** (2014) no. 5, 052008, arXiv:1407.0608 [hep-ex].

[317] The ATLAS Collaboration, G. Aad et al., *Search for Scalar-Charm Pair Production in pp Collisions at $\sqrt{s} = 8$ TeV with the ATLAS Detector*, arXiv:1501.01325 [hep-ex].

[318] The ATLAS Collaboration, G. Aad et al., *Search for Higgs and Z Boson Decays to $J/\psi\gamma$ and $\Upsilon(nS)\gamma$ with the ATLAS Detector*, arXiv:1501.03276 [hep-ex].

[319] G. Perez, Y. Soreq, E. Stamou, and K. Tobioka. to appear.

[320] G. T. Bodwin et al., *Relativistic corrections to Higgs boson decays to quarkonia*, Phys.Rev. **D90** (2014) no. 11, 113010, arXiv:1407.6695 [hep-ph].

[321] The ATLAS Collaboration, G. Aad et al., *Measurements of Higgs boson production and couplings in the four-lepton channel in pp collisions at*

center-of-mass energies of 7 and 8 TeV with the ATLAS detector, Phys.Rev. **D91** (2015) 012006, arXiv:1408.5191 [hep-ex].

[322] The ATLAS Collaboration, G. Aad et al., *Measurement of the Higgs boson mass from the $H \to \gamma\gamma$ and $H \to ZZ^* \to 4\ell$ channels with the ATLAS detector using 25 fb^{-1} of pp collision data*, Phys.Rev. **D90** (2014) no. 5, 052004, arXiv:1406.3827 [hep-ex].

[323] The CMS Collaboration, V. Khachatryan et al., *Precise determination of the mass of the Higgs boson and tests of compatibility of its couplings with the standard model predictions using proton collisions at 7 and 8 TeV*, arXiv:1412.8662 [hep-ex].

[324] LHC Higgs Cross Section Working Group Collaboration, S. Heinemeyer et al., *Handbook of LHC Higgs Cross Sections: 3. Higgs Properties*, arXiv:1307.1347 [hep-ph].

[325] The ATLAS Collaboration. Search for the $b\bar{b}$ decay of the Standard Model Higgs boson in associated $(W/Z)H$ production with the ATLAS detector, 2014.

[326] The CMS Collaboration, V. Khachatryan et al., *Search for the associated production of the Higgs boson with a top-quark pair*, JHEP **1409** (2014) 087, arXiv:1408.1682 [hep-ex].

[327] TLEP Design Study Working Group Collaboration, M. Bicer et al., *First Look at the Physics Case of TLEP*, JHEP **1401** (2014) 164, arXiv:1308.6176 [hep-ex].

[328] A. Martin, W. Stirling, R. Thorne, and G. Watt, *Parton distributions for the LHC*, Eur.Phys.J. **C63** (2009) 189–285, arXiv:0901.0002 [hep-ph].

[329] Particle Data Group Collaboration, K. Olive et al., *Review of Particle Physics (RPP)*, Chin.Phys. **C38** (2014) 090001.

[330] V. Silveira and A. Zee, *SCALAR PHANTOMS*, Phys.Lett. **B161** (1985) 136.

[331] J. McDonald, *Gauge singlet scalars as cold dark matter*, Phys.Rev. **D50** (1994) 3637–3649, arXiv:hep-ph/0702143 [HEP-PH].

[332] C. Burgess, M. Pospelov, and T. ter Veldhuis, *The Minimal model of nonbaryonic dark matter: A Singlet scalar*, Nucl.Phys. **B619** (2001) 709–728, arXiv:hep-ph/0011335 [hep-ph].

[333] B. Patt and F. Wilczek, *Higgs-field portal into hidden sectors*, arXiv:hep-ph/0605188 [hep-ph].

[334] V. Barger et al., *LHC Phenomenology of an Extended Standard Model with a Real Scalar Singlet*, Phys.Rev. **D77** (2008) 035005, arXiv:0706.4311 [hep-ph].

[335] R. K. Ellis, I. Hinchliffe, M. Soldate, and J. van der Bij, *Higgs Decay to tau+ tau-: A Possible Signature of Intermediate Mass Higgs Bosons at the SSC*, Nucl.Phys. **B297** (1988) 221.

[336] S. Dawson, *Radiative corrections to Higgs boson production*, Nucl.Phys. **B359** (1991) 283–300.

[337] T. Hahn, *Generating Feynman diagrams and amplitudes with FeynArts 3*, Comput.Phys.Commun. **140** (2001) 418–431, arXiv:hep-ph/0012260 [hep-ph].

[338] T. Hahn and M. Perez-Victoria, *Automatized one loop calculations in four-dimensions and D-dimensions*, Comput.Phys.Commun. **118** (1999) 153–165, arXiv:hep-ph/9807565 [hep-ph].

[339] The CMS Collaboration, V. Khachatryan et al., *Search for dark matter, extra dimensions, and unparticles in monojet events in proton-proton collisions at* $\sqrt{s}$ = *8 TeV*, arXiv:1408.3583 [hep-ex].

[340] Y. Bai, H.-C. Cheng, J. Gallicchio, and J. Gu, *Stop the Top Background of the Stop Search*, JHEP **1207** (2012) 110, arXiv:1203.4813 [hep-ph].

[341] D. Curtin, P. Meade, and C.-T. Yu, *Testing Electroweak Baryogenesis with Future Colliders*, arXiv:1409.0005 [hep-ph].

[342] N. Craig, C. Englert, and M. McCullough, *New Probe of Naturalness*, Phys.Rev.Lett. **111** (2013) no. 12, 121803, arXiv:1305.5251 [hep-ph].

[343] C. Englert and M. McCullough, *Modified Higgs Sectors and NLO Associated Production*, JHEP **1307** (2013) 168, arXiv:1303.1526 [hep-ph].

[344] D. Curtin et al., *Exotic Decays of the 125 GeV Higgs Boson*, arXiv:1312.4992 [hep-ph].

[345] S. Dawson, A. Gritsan, H. Logan, J. Qian, C. Tully, et al., *Working Group Report: Higgs Boson*, arXiv:1310.8361 [hep-ex].

[346] M. E. Peskin, *Estimation of LHC and ILC Capabilities for Precision Higgs Boson Coupling Measurements*, arXiv:1312.4974 [hep-ph].

[347] T. Binoth and J. van der Bij, *Influence of strongly coupled, hidden scalars on Higgs signals*, Z.Phys. **C75** (1997) 17–25, arXiv:hep-ph/9608245 [hep-ph].

[348] R. Schabinger and J. D. Wells, *A Minimal spontaneously broken hidden sector and its impact on Higgs boson physics at the large hadron collider*, Phys.Rev. **D72** (2005) 093007, arXiv:hep-ph/0509209 [hep-ph].

[349] M. J. Strassler and K. M. Zurek, *Echoes of a hidden valley at hadron colliders*, Phys.Lett. **B651** (2007) 374–379, arXiv:hep-ph/0604261 [hep-ph].

[350] D. Curtin, R. Essig, S. Gori, and J. Shelton, *Illuminating Dark Photons with High-Energy Colliders*, arXiv:1412.0018 [hep-ph].

[351] B. Holdom, *Two U(1)'s and Epsilon Charge Shifts*, Phys.Lett. **B166** (1986) 196.

[352] P. Galison and A. Manohar, *Two Z's or Not Two Z's?*, Phys.Lett. **B136** (1984) 279.

[353] K. R. Dienes, C. F. Kolda, and J. March-Russell, *Kinetic mixing and the supersymmetric gauge hierarchy*, Nucl.Phys. **B492** (1997) 104–118, arXiv:hep-ph/9610479 [hep-ph].

[354] D. Whiteson and M. Klute, *Detectors for Future Colliders*, Slides presented at Aspen Winter Workshop "Exploring the Physics Frontier with Circular Colliders", January, 2015.

[355] I. Hoenig, G. Samach, and D. Tucker-Smith, *Searching for dilepton resonances below the Z mass at the LHC*, arXiv:1408.1075 [hep-ph].

[356] J. M. Cline, G. Dupuis, Z. Liu, and W. Xue, *The windows for kinetically mixed Z'-mediated dark matter and the galactic center gamma ray excess*, arXiv:1405.7691 [hep-ph].

[357] The ATLAS Collaboration, *Search for high-mass dilepton resonances in 20 fb^{-1} of pp collisions at $\sqrt{s} = 8$ TeV with the ATLAS experiment*, ATLAS-CONF-2013-017, CERN, Geneva, Mar, 2013. http://cds.cern.ch/record/1525524.

[358] The CMS Collaboration, *Properties of the Higgs-like boson in the decay H to ZZ to 4l in pp collisions at $\sqrt{s} = 7$ and 8 TeV*, CMS-PAS-HIG-13-002, CERN, Geneva, 2013. https://cds.cern.ch/record/1523767.

[359] BaBar Collaboration, J. Lees et al., *Search for a dark photon in e+e- collisions at BABAR*, arXiv:1406.2980 [hep-ex].

[360] The ATLAS Collaboration, *Measurement of the total ZZ production cross section in proton-proton collisions at $\sqrt{s} = 8$ TeV in 20 fb^{-1} with the ATLAS detector*, ATLAS-CONF-2013-020, CERN, Geneva, Mar, 2013. http://cds.cern.ch/record/1525555.

[361] The CMS Collaboration, *Search for a non-standard-model Higgs boson decaying to a pair of new light bosons in four-muon final states*, CMS-PAS-HIG-13-010, CERN, Geneva, 2013. http://cds.cern.ch/record/1563546.

[362] R. Essig, J. A. Jaros, W. Wester, et al., *Dark Sectors and New, Light, Weakly-Coupled Particles*, arXiv:1311.0029 [hep-ph].

CHAPTER 8

FUTURE HEAVY-ION AND ELECTRON-ION COLLISION PROGRAM

8.1 Introduction

The fundamental theory of strong interactions among quarks and gluons is Quantum Chromodynamics (QCD). Because of the non-Abelian nature of the strong interaction due to the SU(3) gauge symmetry in QCD, quarks and gluons are confined within the realm of hadrons which are the only stable vacuum excitations. The approximate chiral symmetry among light quarks are spontaneously broken to give rise to none-zero quarks condensate in vacuum and light mesons as Goldstone bosons. The approximate conformal symmetry is also broken by quantum interactions leading to the non-vanishing gluon condensate in vacuum and running strong coupling constant. Under extreme high temperature and density, one expects the boundary between hadrons would disappear and quark and gluon degrees of freedom are freed to form a new state of matter called quark gluon plasma (QGP). According to the lattice numerical study of the QCD (LQCD) [1], there is indeed a rapid cross-over phase transition from a hadronic gas to QGP at a critical temperature $T_c \approx 151 \pm 3$ MeV and zero baryon chemical potentials. Below T_c in the form of a hadronic gas, quarks and gluons confined in color-neutral hadrons. These hadrons would melt during the deconfinement phase transition and quarks and gluons can roam freely at a temperature above T_c in a volume much larger than a nucleon size. The deconfinement phase transition is caused by breaking of Z_3-symmetry (symmetry in the limit of pure gauge QCD) at high temperature accompanied by a rapid change of the corresponding order parameter, the expectation value of the Polyakov loop. The chiral symmetry is also approximately restored at these high temperatures above T_c.

Such a new state of matter in an environment of very high temperatures and densities was prevailing in the early Universe as the quark epoch from 10^{-12} to 10^{-6} seconds after

the Big Bang. It might still exist in some compact stellar objects such as neutron stars. In order to create such a new state of matter in a laboratory, one can also accelerate two heavy nuclei to close to the speed of light and collide them head-on. Through such high-energy heavy-ion collisions, one can convert a fraction of the colliding energy into an initial matter at extremely high temperatures and densities beyond the phase transition point to form a QGP. There are two major such collider facilities for high-energy heavy-ion collision experiments being operated today, the Relativistic Heavy-Ion Collider (RHIC) at the Brookhaven National Laboratory (BNL) and the Large Hadron Collider (LHC) at the European Organization for Nuclear Research (CERN). Before November of 2010, RHIC had been the highest-energy heavy-ion collider in the world since 2000. In 2010 the LHC took the lead in colliding energy and became the heavy-ion collider running at the highest energy.

Remarkable discoveries have been made at RHIC since its operation in 2000 [2–4] with evidences pointing to the formation of a strongly coupled QGP in Au+Au collisions at the highest energy at RHIC. One surprising discovery is that the hot and dense QCD matter created in relativistic heavy-ion collisions has strong collective flow characteristic of a strongly-coupled liquid, rather than the weakly-coupled gas of quarks and gluons as expected before. In fact, the shear viscosity to entropy density ratio extracted from comparisons between experimental data and viscous hydrodynamic calculations is so low [5] that it has been termed "the perfect liquid". The second discovery at RHIC is the observation of substantial jet quenching [6], indicating that the matter is virtually opaque to energetic quarks and gluons. Differences in the yields and flow of baryons versus mesons indicate that hadron formation at intermediate transverse momenta proceeds via constituent quark coalescence, providing the evidence for partonic collectivity in the final hadron spectra [3]. STAR experiment has also identified anti-hypertriton and anti-alpha production in Au+Au collisions, the first ever observation of an anti-hypernucleus and anti-alpha [7].

With more than one order of magnitude higher colliding energy, many of the proposed signals for the QGP become much stronger and easier to observe at LHC [8]. The dense matter created in heavy-ion collisions at the LHC is much hotter and has longer lifetime during its dynamical evolution. The QGP matter has also much smaller net baryon density as compared to that at RHIC. With increased colliding energy, rates of hard processes are much higher than at RHIC making them much better and easily accessible probes of the QGP matter. Recent experimental data from heavy-ion collisions at LHC unambiguously confirmed all experimental evidences of QGP as first observed at RHIC [9]. The collective phenomena as manifested in anisotropic flows and the ridge structure with the large pseudo-rapidity gap even in the most central Pb+Pb collisions point to a QGP at high temperatures with small specific shear viscosity. Jet quenching phenomena are clearly observed with jet energy up to hundreds of GeV both in the single inclusive hadron spectra and reconstructed jets. The mass dependence of the quark energy loss is observed for the first time according to high p_T suppression of charm mesons and non-prompt J/ψ. The centrality dependence of J/ψ suppression clearly show the increasing fraction of J/ψ production from recombination in the QGP medium. There are also strong evidence for collectivity in recent data on p+Pb collisions at the LHC.

In the near future, the focus of heavy-ion collisions at RHIC and LHC will be on quantitative characterization of the strongly coupled QGP using rare probes such as large transverse momentum jets, heavy flavor particles, real and virtual photons and quarkonia s-

tates. Study of collective phenomena using detailed multiple particle correlations can also provide more precision constraints on the bulk transport coefficients of the QGP. Since existing RHIC and LHC data have already provided interesting hints on the weakening of the interaction strength both among bulk partons [10, 11] and between hard probes and bulk medium [12], it will be extremely interesting to see whether such trend continues at future higher collider energies and eventually reach the weakly interacting scenario as predicted by pQCD.

The proposed Circular Electron-positron and Proton-proton Collider (CEPC) consist of two major phases. The first phase is the e^+e^- collider at the center-of-mass energy 240 GeV as a Higgs factory which can carry out many precise measurements on properties of the Higgs particle and its coupling to other Standard model particles. In the second phase, the e^+e^- collider can be converted to a proton-proton collider facility with center-of-mass collision energy up to 50-90 TeV, which is about 5 times of the maximum LHC energy. Between these two phases, an electron-proton or electron-ion collider with 120 GeV electrons scattering on 25-45 TeV protons or heavy nuclei with similar energy per nucleon, can be built to study hadronic physics and nuclear physics at the highest colliding energies. Extracting medium properties of QGP in heavy-ion collisions depends largely on the hydrodynamic evolution and then on the initial state of the colliding nuclei. At extremely high energies, the initial state is mainly determined by nonlinear gluon dynamics and can lead to a phenomenon known as gluon saturation or color-glass condensate (CGC), which can be studied in electron-ion collisions or even manifests itself in electron-proton collisions at ultra-high energies. The proposed electron-proton and electron-ion collision experiments are closely related and complimentary to the physics in heavy-ion collisions. They constituent two modern pillars of high-energy nuclear physics in quest for the nature of strong interaction at unprecedented small length scales.

One can address many important questions in future heavy-ion collision experiments in the energy range of tens or even hundreds of TeV. They include:

(a) What is the effective equation of state (EoS) for the strongly interacting matter at high temperatures? Can one start to see effect of charm quarks in the EoS?

(b) What is the thermalization mechanism and how the thermalization time depend on the colliding energy?

(c) What are the transport properties of strongly interacting matter at such high temperatures as probed by high-energy jets and collective phenomena? Are they approaching the weak coupling values at higher temperature as predicted by perturbative QCD?

(d) What is the nature of the initial state and its fluctuation in nuclear collisions?

(e) Can we find other exotic hadrons or nuclei such as light multi-Λ hyper-nuclei, bound states of $(\Lambda\Lambda)$ or the H di-baryon ?

In future electron-proton and electron-ion collision experiments, some of the key questions to answer are:

(a) What is the partonic structure of nucleons and nuclei in very small-x regime?

(b) What is the role of gluons and gluonic self-interactions in hadrons and nuclei?

(c) What is the role of parton distributions in nuclei in the initial state for heavy ion collisions?

(d) Can one observe unambiguous signals of the gluon saturation in protons and nuclei?

(e) Can the nature of color confinement be revealed in electron-proton and electron-ion collisions at TeV scale?

The answers to these important questions in strong interaction rely on both theoretical advances and experimental programs of high-energy electron-nuclei (proton) and heavy-ion collisions at future high-energy collider facilities. In this report, we will give a brief review of the physics potentials of electron-nucleus (proton) and heavy-ion collision at tens or hundreds of TeV energy scale. The scope of this report is limited only to a few selected topics list above. A more comprehensive report will need much more concerted and dedicated efforts.

8.2 QCD and Strong Interaction Matter

The Quantum chromodynamics (QCD), as a non-Abelian quantum gauge field theory, has been very successful in describing the strong interaction among quarks and gluons that are the fundamental constituents of visible matter in nature. The asymptotic freedom behavior of QCD at short distances render the possibility of calculating hard processes by perturbative methods. On the other hand, its non-perturbative features at long distances are only systematically computable using numerical simulations in a path integral representation of QCD. Many of our current theoretical understanding of properties of dense matter at high temperature and baryon density are based on lattice QCD. Though experiments at RHIC and LHC have confirmed the existence of a new form of matter, strongly coupled Quark Gluon Plasma (sQGP), in relativistic heavy-ion collisions, its properties is not yet fully understood quantitatively. This requires future efforts from both experimental and theoretical studies. Lattice QCD calculations can provide crucial inputs to phenomenological studies of QGP properties.

Lattice QCD is a discretized version of QCD in Euclidean space and time which reproduces QCD in the continuum limit when the lattice spacing goes to zero. Most lattice QCD calculations which are relevant to heavy-ion collisions have been performed using non-chiral fermions which recover the flavor or chiral symmetry of QCD only in the continuum limit, e.g. staggered and Wilson fermions. Chiral fermions are generally much more expensive to work with. However, owing to Moore's law, currently these actions are also used and start to produce interesting results in QCD thermodynamics, e.g. the confirmation of the value of the crossover temperature T_c [13] and investigations of the restoration of $U(1)_A$ symmetry [14–16].

The equation of state (EoS) of QCD matter contains information on the change of degrees of freedom in different temperature and baryon density regimes. It is one of the important ingredients to model the evolution of the fireball produced in heavy-ion collisions through classical hydrodynamic equations. The computation of the QCD EoS has been one of the major goals in the lattice QCD community since 1980 [17]. At zero baryon number density it has been shown very recently with lattice calculations of $N_f = 2+1$ that QCD equation of state obtained from the HotQCD and Wuppertal-Budapest collaborations by using two different discretization schemes agree very well [18, 19]. Shown in Fig. 8.1 are energy density, entropy density and pressure as functions of temperature from the HotQCD Collaboration [18] (shaded bands). There is apparently a rapid transition from low to high temperature. It has been established from the analysis of chiral condensates that this transition in QCD with its physical mass spectrum at zero baryon density is a rapid crossover. The pseudo critical temperature of the QCD transition is confirmed to be $T_c \simeq 155$ MeV [13, 20, 21]. Below and around this crossover, the EoS can be described well by a hadron resonance gas model (solid lines).

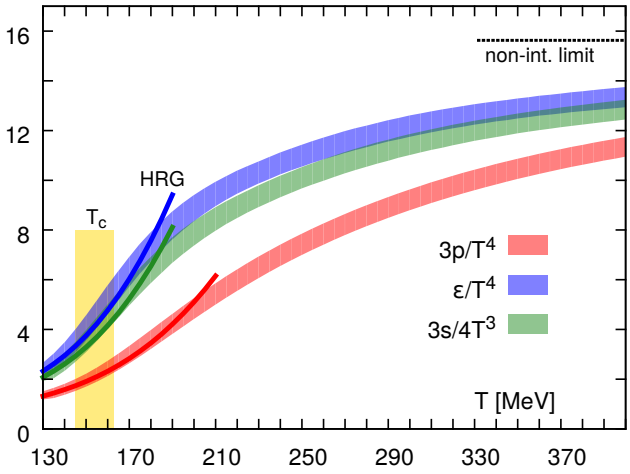

Figure 8.1 The pressure, energy and entropy density (scaled by T^4) as functions of the temperature from lattice QCD calculation by the HotQCD Collaboration [18] (shaded bands) as compared to hadron resonance gas (HRG) model results (solid lines).

There is also some evidence that 2- or 2+1-flavor QCD in the "chiral" limit, i.e. in the limit of vanishing light quark masses with the strange quark mass being at its physical value, is second-order and belongs to the universality class of the three-dimensional $O(N)$ spin models [22, 23]. If confirmed, this would be in accordance with the picture of Pisarski and Wilczek [24]. However, the existing $O(N)$ scaling studies have been performed on rather coarse lattices with staggered fermion actions that are no longer state-of-the-art. They lead to large taste violations. Therefore the order of the QCD phase transition in the chiral limit is still under debate and arguments in favor of a first-order transition have been put forward [25]. The inclusion of charm quarks gives some small effects to the QCD equation of state which might be noticeable at the higher temperatures reached in heavy-ion collisions at 100 TeV scale.

The properties of light meson (e.g. ρ) and heavy quarkonia (e.g. J/ψ and Υ) as measured via the dilepton channel can serve as useful probes for the chiral symmetry restoration and deconfinement transition in the QCD medium, respectively. Theoretical study of these hadron properties at finite temperature requires the computation of two-point correlation function on the lattice and extraction of the hadron spectral functions. These hadron spectral functions are directly related to thermal dilepton rates, the dissociation of quarkonia states as well as the transport properties of the medium, e.g. electrical conductivity, heavy quark diffusion coefficients.

The most current lattice QCD study of hadron spectral functions suggests that all charmonia dissociate at $T \gtrsim 1.5\ T_c$ in gluonic plasma [26]. Very recent lattice QCD studies including dynamic quarks on screening mass and spectral functions suggest the same picture [27, 28]. Due to the large value of heavy quark mass, the direct study of bottomonia is very hard on the lattice since the lattice spacing a has to be much smaller than the inverse of the heavy quark mass. Effective theories, e.g. Non-Relativistic QCD (NRQCD), have been put on the lattice to study the properties of bottomonia. It has been found that all the S wave states exist at temperatures up to at least 2 T_c and P wave states melts just above T_c [29–33]. However, a different observation is found in Ref. [34] that P waves states might stay bounded at higher temperatures above T_c by using a new inversion method. It has

also been realized that the potential of static quarks in the medium is complex [35–37] whose computation on the lattice has been carried out [38–41].

The fate of heavy-light mesons or baryons also reflects the change of relevant degrees of freedom in strong interaction matter. For instance, the abundance of strange hadrons is considered as one of the signals for the formation of QGP. By investigating fluctuations and correlations of electrical charge and baryon number with strangeness and charm it was found that both open strange and open charm hadrons start to dissociate in the chiral crossover temperature region [42–44].

As proposed recently in Ref. [45] the freeze-out temperatures and baryon chemical potentials can be determined by matching the lattice QCD computations with those measured in heavy-ion collisions. An upper band of freeze-out temperature is found to be 148 ± 4 MeV [46]. An indirect evidence of experimentally yet unobserved open strange and open charm hadrons has been found [43, 47]. These unobserved hadrons brings down the freeze-out temperature in the strange hadron sector by $\sim 5-8$ MeV [47].

Transport properties of the hot QCD medium are also the focus of future experimental studies through collective phenomena of both light and heavy flavor hadrons and electromagnetic emissions. Currently there are only a limited number of results on transport coefficients from lattice-QCD calculations with dynamical quarks. Most calculations have been performed in the quenched limit at vanishing net-baryon number density [48–50]. It proves difficult to extract transport coefficients directly from imaginary-time two-point correlation functions. Currently, the Maximum Entropy Method is a commonly used technique to achieve this goal [51]. The determination of the electrical conductivity and the heavy-quark diffusion coefficient in full QCD is rather straightforward and mainly limited by computational resources. However, the determination of fluid-dynamical transport coefficients, e.g. viscosities, is hampered by large noise-to-signal ratios. For QCD in the quenched approximation, noise reduction techniques are known and are applied while for full QCD computations such algorithms still need to be developed.

Electrical conductivity has been computed in the continuum limit in quenched QCD at three temperatures above T_c [52, 53]. Recently the computation has also been performed on the lattice with dynamic quarks [54–56]. The charm-quark diffusion coefficient has been obtained at one value of the lattice cutoff and three temperatures in the deconfined phase [48]. Currently, there are no lattice results on bottom-quark diffusion coefficients which are very important in heavy-quark physics at LHC energies and beyond. The heavy-quark diffusion coefficients have been studied on the lattice by measuring proposed observables by heavy-quark effective theory [57]. Results on heavy-quark diffusion coefficients obtained in this approach are close to the charm-quark diffusion coefficients [58–60]. However, most of these results are also obtained at a finite lattice cutoff, so a reliable extraction of diffusion coefficients needs to be performed.

Shear and bulk viscosities have been calculated a few years ago on rather coarse and small lattices, without a continuum extrapolation[61, 62]. In order to obtain better results, the number of gauge field configurations needs to be increased by an order of magnitude. However, algorithms like multi-level updates to improve the signal-to-noise ratio [63] of two-point correlators of the energy-momentum tensor as currently used in the quenched approximation are not applicable in full QCD. Recently, there have been efforts made in Refs. [64–66] which provide an opportunity to determine some of the 2nd-order transport coefficients from a first-principles calculation.

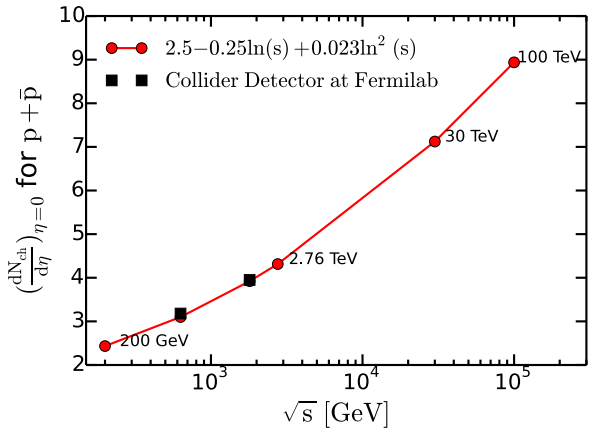

Figure 8.2 The charged multiplicity for $p + p(\bar{p})$ collisions as a function of the colliding energy, as extrapolated from experimental data at Fermilab Tevatron, BN RHIC and CERN LHC.

8.3 Bulk Properties of Matter in Heavy-ion Collisions

In the study of QGP properties in high-energy heavy-ion collisions, the space-time evolution of the bulk matter underpins all experimental and phenomenological since it will affect all the expected final observables from which one extracts medium properties of the QGP. Whether it is an effective theory such as relativistic hydrodynamics or a Monte Carlo model for parton and hadron transport, one always needs the basic information of initial parton production. The initial parton production determines the initial energy density or temperature at the thermalization time and its fluctuation in both transverse area and longitudinal direction. Given these initial conditions, one can then use the hydrodynamical model or parton-hadron transport model for the space-time evolution of the bulk medium. Through comparisons between hydrodynamic or transport results and experimental data on the final hadron spectra and their azimuthal anisotropy or multiple hadron correlations, one can extract values of the bulk transport coefficients such as shear and bulk viscosity. For the study of other hard and electromagnetic signals, one also has to reply on the space-time evolution of the bulk medium to understand the experimental measurements and extract medium properties such as initial temperature, flow velocity and jet transport coefficients.

Multiplicity

The mechanism of initial parton production has been one of the fundamental problems in heavy-ion collisions and strong interaction in general. It is determined by the properties of strong interaction at high energy where non-linear aspects of QCD are at play and it is also the focus of research at the future electron-ion colliders (EIC). Shown in Fig. 8.2 is the charged hadron multiplicity in $p + p(\bar{p})$ collisions as a function of the colliding energy as extrapolated from experimental data at Fermilab Tevatron [67], BNL RHIC [68] and CERN LHC [69] to very high energies. This extrapolation is also consistent with HIJING calculations [70] in which the rise of the multiplicity in the central rapidity region at high colliding energy is mainly caused by the increase of gluonic mini-jet production as the initial gluon distribution inside the beam proton increases at smaller momentum fraction.

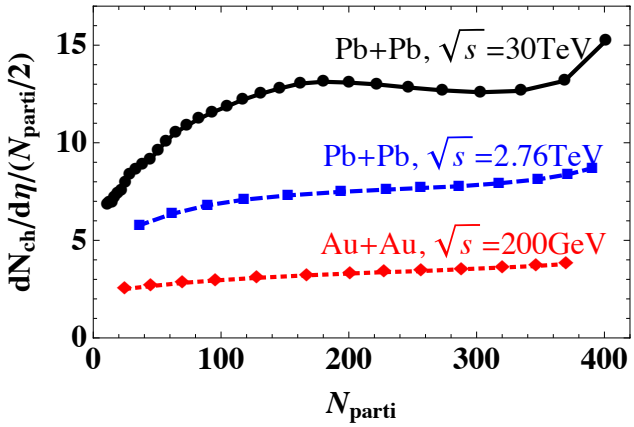

Figure 8.3 Rapidity density of charged hadrons in the central rapidity per participant pair as functions of the number of participant nucleons in $Au + Au$ collisions at RHIC, $Pb + Pb$ collisions at LHC and at $\sqrt{s} = 30$ TeV, from HIJING Monte Carlo simulations.

There are currently two types of pQCD based models for the description of initial parton production in heavy-ion collisions. One of these models, HIJING Monte Carlo model [70–72] employs the Glauber model for multiple interaction in high-energy nucleon-nucleus and nucleus-nucleus collisions. It includes both the incoherent hard and semi-hard parton scattering that are described by pQCD and the coherent soft interaction via excitation of remanent strings between valence quark and diquarks. Initial parton production from incoherent hard or semi-hard parton scatterings is proportional to the number of binary nucleon-nucleon collisions $N_{\rm coll}$ while the soft parton production from string excitation is proportional to the number of participant nucleons $N_{\rm part}$ in a given centrality of heavy-ion collisions. One should also take into account the impact-parameter-dependent nuclear modification of parton distributions in a nucleus in the semi-hard parton interaction. This is will introduce additional impact-parameter dependence of the parton production in the hard or semi-hard parton scattering. The final centrality dependence of the initial parton multiplicity from both soft and semi-hard processes will therefore be a linear combination of $N_{\rm part}$ and $N_{\rm coll}$.

The average number of participant nucleons or wounded nucleons $N_{\rm part}$ in heavy-ion collisions as a function of the impact-parameter can be calculated within the Glauber model in terms the overlapping functions of two nuclei [73] which can reach to the limit of the total number of nucleons within the overlap region of two colliding nuclei. It therefore has a very weak energy dependence in very high energies. The number of binary collisions depends almost linearly on the total inelastic cross section and therefore has a strong energy dependence. Correspondingly, the final hadron multiplicity in heavy-ion collisions per participant pair should increase faster as a function of energy as compared to $p + p$ collisions. Similarly, the final hadron multiplicity in the central rapidity region per participant pair at fixed colliding energy should increase with $N_{\rm part}$ towards more central collisions as shown by the HIJING simulations in Fig. 8.3. The exact behavior of the final hadron multiplicity per participant pair as a function of the centrality or $N_{\rm part}$ is controlled mainly by the impact-parameter dependence of the parton shadowing in heavy nuclei which in turn could also be addressed by experiments in high energy electron-ion at a future high energy EIC.

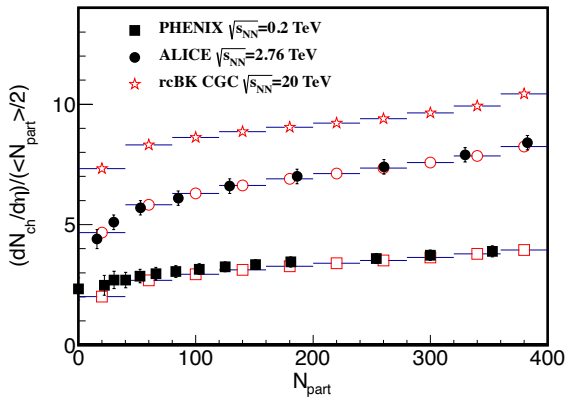

Figure 8.4 Centrality dependences of charged particle multiplicity at $\sqrt{s_{NN}} = 0.2$, 2.76 and 20 TeV, respectively from the rcBK model [78–81].

The second type of models for initial particle production is based on the approach of interacting semi-classical gluonic fields or the Color Glass Condensate model [74]. There are many variants of models including KLN [75–77], rcBK [78–81] and IP-Glasma [82–84]. One can calculate initial gluon multiplicity in heavy-ion collisions and assume parton-hadron duality to calculate the final hadron multiplicity which is proportional to the initial gluon multiplicity. The IP-Glasma model combines the impact parameter-dependent saturaration model for high energy nucleon and nuclear wave function with classical Yang-Mills dynamics of Glasma fields in heavy ion collisions. It can be used to estimate the initial energy density event-by-event. In the rcBK model, the k_T-factorization is assumed which involves an integral over unintegrated gluon distributions whose evolution can be obtained by solving the nonlinear Balitisky-Kovchegov (BK) equation with the running coupling kernel (rcBK) [78–81].

Shown in Fig. 8.4 is the centrality dependence of charged particle multiplicity at three collision energies using the rcBK model (open symbols) which can reproduce experimental results well at RHIC and LHC energies (solid symbols). The hadron multiplicity in the most central Pb+Pb collisions at $\sqrt{s} = 20$ TeV from rcBK estimate is comparable to the HIJING estimate (shown in Fig. 8.3 is for $\sqrt{s} = 30$ TeV). Notice that a cross section parameter of hard valence charges is assumed as energy-independent ($\sigma_0 = 4.2$ fm^2). If an energy-dependent cross section parameter is used, one will get a flatter curve for the centrality dependence. The mechanism and consequences of gluon saturation is also one of the main topics in high-energy electron-ion collider.

Together with the transverse distribution of participant nucleons and binary collisions, the above models for initial particle production can provide the initial energy density distributions which can fluctuate from event to event. These fluctuating initial energy density distributions in turn will provide the initial conditions for hydrodynamic or transport evolution of the bulk matter in heavy-ion collisions. Assuming an initial thermalization time $\tau_0 = 0.6$ fm/c, the initial energy density and temperature at the center of heavy-ion collisions are listed in Table 8.1.

$\sqrt{s_{NN}}\ [TeV]$	$T_0\ [MeV]$	$\tau_0\ [fm]$	$dN_{\rm ch}/d\eta$
0.20 (Au+Au)	360	0.6	720
2.76 (Pb+Pb)	470	0.6	1600
30 (Pb+Pb)	560	0.6	2700

Table 8.1 The initial energy density ε_0, temperature T_0 at the center of heavy-ion collisions, thermalization time τ_0 and the final charge hadron rapidity density at different colliding energies.

Collective Expansion and Anisotropic Flow

One of the evidences for the formation of sQGP in heavy-ion collisions at RHIC and LHC is the observation of strong anisotropic flow due to collective expansion driven by the initial high energy density and pressure in the overlapped region of the collisions [2, 3]. During the last decade of both experimental and theoretical exploration of such phenomenon, a rather detailed picture of the collective expansion of the anisotropic fireball in heavy-ion collisions emerges. During the early stage of high-energy heavy-ion collisions, parton production are approximately localized in the transverse plane of the two colliding nuclei. The local transverse energy density is governed by the initial wave functions of the colliding nuclei, the interaction strength of beam partons and the quantum process of parton production from the collision. These different aspects of initial parton production determine the event-by-event transverse as well as longitudinal energy density distributions during the early stage of the heavy-ion collisions. Due to the thermalization processes whose mechanism is still under intense theoretical investigation [85], these initial state of fluctuating energy density distribution achieves local equilibrium and the subsequent collective expansion can be approximately described by relativistic viscous hydrodynamic equations with an effective EoS as parametrization of the lattice QCD results [86]. After hydrodynamic expansion over a finite period of time, the spatial anisotropies of the initial energy density distributions are converted into anisotropies of the final hadron spectra in momentum space [87]. One can characterize the momentum anisotropies in terms of the Fourier coefficients of the final hadron azimuthal distribution or two-particle azimuthal correlation in each event. One normally refers to these Fourier coefficients as anisotropic flows v_n with the corresponding order n of the Fourier expansion. Comparisons of the experimental measurements of the anisotropic flows at RHIC and results from viscous hydrodynamic model simulations point to rather small values of the shear viscosity to entropy density ratio η/s [88, 89] that is very close to the quantum mechanics bound [90].

Shown in Fig. 8.5 are the calculated anisotropic flows from the state of art 2+1D viscous hydrodynamic simulations [11] that employs IP-Glasma model for initial gluon production with both event-by-event geometric fluctuations in nucleon positions and the sub-nucleon color-charge fluctuations. Hydrodynamic results describe extreme well the experimental data on the anisotropic flows up to the fifth order in heavy-ion collisions at both RHIC and LHC. There is also an indication that the shear viscosity to entropy ratio decreases slightly from RHIC to LHC. This points to the direction of theoretical estimate that the QGP at higher temperatures might transit from a strongly coupled to weakly coupled one as described by pQCD calculations. Heavy-ion collisions at the very high energy region can reach even higher initial temperatures (see Table 8.1) and therefore approach closer to such a weakly coupling limit.

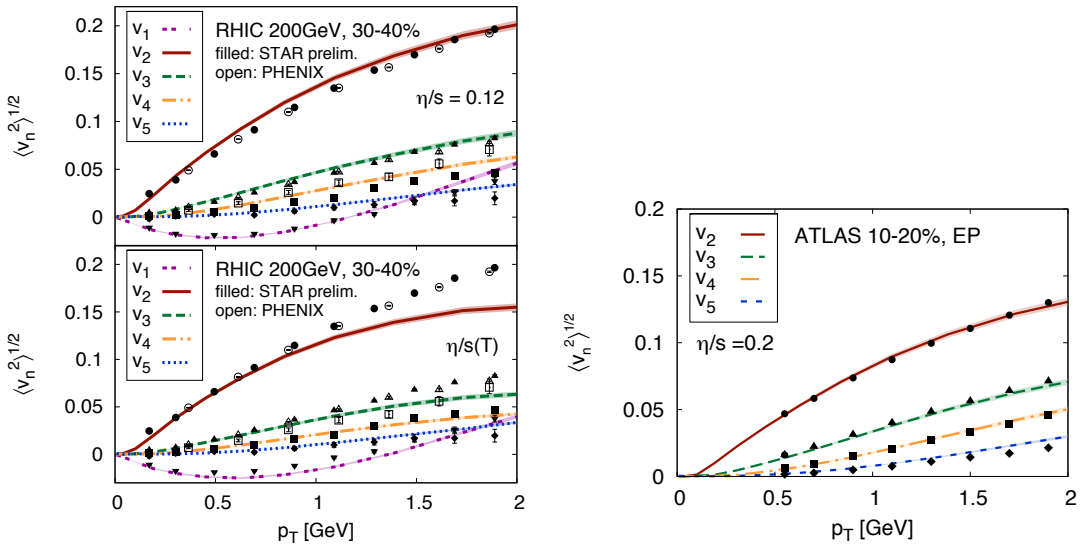

Figure 8.5 Anisotropic flows as functions of p_T from viscous hydrodynamic model simulations with event-by-event fluctuating initial condition from IP-Glasma model [11] as compared to experimental data from PHENIX [91] and STAR [92] at RHIC and ATLAS [93] at LHC.

Assuming the same values of shear viscosity to entropy density ratio as in heavy-ion collisions at the LHC, the differential anisotropic flows at $\sqrt{s} = 20 - 30$ TeV should remain roughly the same. However, due to increased radial flow and the flattening of the transverse momentum spectra, the integrated anisotropic flows should continue to increase with the colliding energy. Shown in Fig. 8.6 are differential anisotropic flows calculated from 3+1D ideal hydrodynamic simulations [94] with fluctuating initial conditions from HIJING [70–72] and AMPT [95] model for 20-30% central Pb+Pb collisions at 30 TeV. For over all normalization of the final hadron multiplicity we have rescaled the initial energy density from the AMPT model by a factor so that the multiplicity in 20-30% central Pb+Pb collisions at 30 TeV is close to most central Pb+Pb collisions at $\sqrt{s_{NN}} = 2.76$ TeV. In these initial conditions fluctuations in the longitudinal direction are also considered that should affect the final state anisotropic flow in the central rapidity region [94]. Harmonic flow coefficients v_n show a normal ordering that decreases with the order of harmonics at the same p_T. Precision measurements of these anisotropic flows at future very high energy heavy-ion collisions can shed light on the temperature dependence of the shear viscosity to entropy ratio and whether one is approaching a weakly coupling limit as given by pQCD at higher colliding energies.

8.4 Jet Quenching in Heavy-ion Collisions

In high-energy heavy-ion collisions, hard scattering of beam partons can produce energetic partons with very large transverse momentum. These energetic partons will fragment into large transverse momentum hadrons and appear in the detector as clusters of collimated hadrons which can be reconstructed as jets in experimental measurements. These initial energetic partons are produced in the very early stage of heavy-ion collisions and will certainly interact with soft partons from the bulk QGP that is formed over large volume of space. The interaction between jet partons and the QGP medium will lead to elastic and

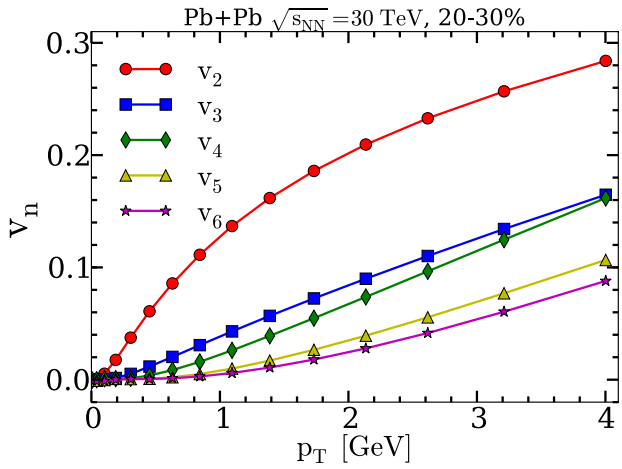

Figure 8.6 Anisotropic flows v_n for 20-30% central Pb+Pb collisions at $\sqrt{s_{NN}} = 30$ TeV from 3+1D ideal hydrodynamic simulations with full fluctuating initial conditions from HIJING and AMPT model.

radiative energy loss and therefore suppression of the final state jets or large transverse momentum hadrons. These phenomena of jet quenching was originally proposed as one of the signatures of the QGP matter in high-energy heavy-ion collisions [96] which were first observed in heavy-ion collisions at RHIC [97]. After more than a decade of both theoretical and experimental studies at RHIC and LHC [9], jet quenching has become a powerful tool to study properties of the dense medium in heavy-ion collisions such as the jet transport parameter, defined as the averaged transverse momentum broadening squared per unit length which is also related to the local gluon number density,

$$\hat{q} = \frac{4\pi^2\alpha_s C_R}{N_c^2-1}\int\frac{dy^-}{\pi}\langle F^{\sigma+}(0)F_\sigma^+(y)\rangle = \frac{4\pi^2\alpha_s C_R}{N_c^2-1}\rho_A x G_N(x)|_{x\to 0}. \tag{8.1}$$

Temperature Dependence of Jet Transport Parameter

Since the hot bulk QGP medium is transient with a very short life-time and rapid expansion, the dynamical evolution of the bulk medium has to be taken into account for accurate descriptions of jet quenching phenomena. The hydrodynamical models as discussed in the previous section become necessary for jet quenching studies. One therefore needs a framework for the study that combines bulk medium evolution and jet quenching for extraction of jet transport parameter. A recent effort has been carried out by the JET topical collaboration to create a comprehensive Monte Carlo package which combines the most advanced model for bulk medium evolution, up-to-date models for parton propagation in medium and final hadronization of jet shower partons and jet-induced medium excitation. A comprehensive study has been carried out that surveyed five different approaches to parton energy loss combined with bulk medium evolution from 2+1D and 3+1D hydrodynamic models that have been constrained by the bulk hadron spectra [12]. Through χ^2-fitting of the single inclusive hadron spectra at both RHIC and LHC with five different approaches to parton energy loss: GLV [98] and its recent CUJET implementation [99], the high-twist (HT) approaches (HT-BW and HT-M) [100, 101] and the MARTINI [102] and McGill-AMY [103] model, one obtained the most up-to-date constraints on the values of the jet transport parametersas shown in Fig. 8.7 [12]. Analyses of RHIC and LHC data with the YaJEM model [104] give similar constraints as shown

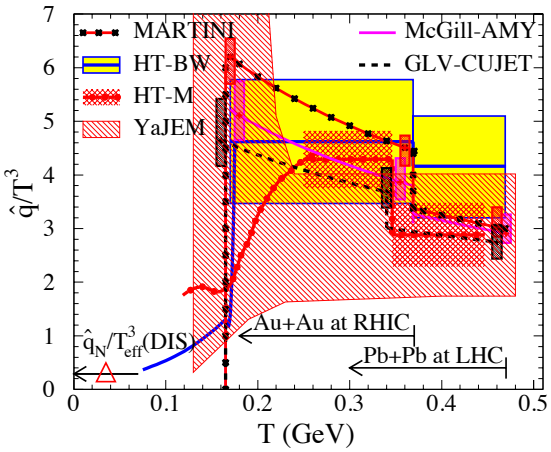

Figure 8.7 Scaled jet transport parameter $\hat{q}/T^3$ for an initial quark jet with energy $E = 10$ GeV at the center of the most central A+A collisions at an initial time $\tau_0 = 0.6$ fm/c constrained from recent analysis by the JET Collaboration [12] with χ^2 fits to the suppression factors of single inclusive hadron spectra at RHIC and LHC. Errors from the fits are indicated by filled boxes at three separate temperatures at RHIC and LHC, respectively. The arrows indicate the range of temperatures at the center of the most central A+A collisions. The triangle indicates the value of $\hat{q}_N/T^3_{\text{eff}}$ in cold nuclei from DIS experiments.

in Fig. 8.7. The jet transport parameter extracted from these analyses are $\hat{q} \approx 1.2 \pm 0.3$ and 1.9 ± 0.7 GeV^2/fm in the center of the most central Au+Au collisions at $\sqrt{s} = 200$ GeV and Pb+Pb collisions at $\sqrt{s} = 2.67$ TeV, respectively, at an initial time $\tau_0 = 0.6$ fm/c for a quark jet with an initial energy of 10 GeV/c. When scaled by T^3, the natural scale in a QGP at high temperature, $\hat{q}/T^3$ represents the interaction strength between jets and the medium. Current values at RHIC and LHC indicate a gradual weakening toward higher colliding energies where the initial temperatures are also higher. At $\sqrt{s} = 30$ TeV, one expects to reach even higher initial temperatures in the center of Pb+Pb collisions and further weakening of the jet-medium interaction. Shown in Fig. 8.8 as open boxes with question marks are the predicted values of $\hat{q}$ this energy, higher LHC energy and lower energies of the beam energy scan program at RHIC. Together with the current values at the LHC and RHIC energy, one can obtain a temperature dependence of $\hat{q}/T^3$.

Suppression of Single Hadron Spectra

For an estimate of the suppression of single inclusive hadron spectra in heavy-ion collisions at very high future collider energy, we use both the higher-twist (HT) [100] and McGill-AMY [103] model.

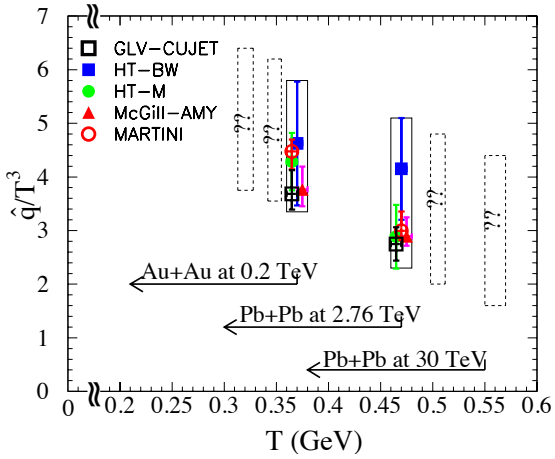

Figure 8.8 Scaled jet transport parameter $\hat{q}/T^3$ for an initial quark jet with energy $E = 10$ GeV at the center of the most central A+A collisions at an initial time $\tau_0 = 0.6$ fm/c constrained from recent analysis by the JET Collaboration [12]. The dashed boxes indicate expected values in A+A collisions at $\sqrt{s} = 0.063, 0.130$, 5.5 and 30 TeV/n, assuming the initial entropy is proportional to the final measured charged hadron rapidity density. The arrows indicate the range of temperatures at the center of the most central A+A collisions at different colliding energies.

Within the HT approach, the effect of parton energy on the final hadron spectra is implemented through effective medium-modified fragmentation functions (FF) [105–107],

$$D_{h/c}(z_c, \Delta E_c, \mu^2) = (1 - e^{-\langle N_g^c \rangle}) \left[\frac{z_c'}{z_c} D^0_{h/c}(z_c', \mu^2) + \langle N_g^c \rangle \frac{z_g'}{z_c} D^0_{h/g}(z_g', \mu^2) \right] + e^{-\langle N_g^c \rangle} D^0_{h/c}(z_c, \mu^2), \tag{8.2}$$

where $z_c' = p_T/(p_{Tc} - \Delta E_c)$, $z_g' = \langle L/\lambda \rangle p_T/\Delta E_c$ are the rescaled momentum fractions, ΔE_c is the radiative parton energy loss and $\langle N_g^c \rangle$ is the average number of induced gluon emissions. The FFs in vacuum $D^0_{h/c}(z_c, \mu^2)$ is given by the AKK08 parameterizations [108]. The total parton energy loss within the HT approach in a finite and expanding medium can be expressed as [109],

$$\frac{\Delta E_a}{E} = C_A \frac{\alpha_s}{2\pi} \int dy^- \int_0^{Q^2} \frac{dl_T^2}{l_T^4} \int dz [1 + (1-z)^2] \times \hat{q}_a(y) 4 \sin^2 \left[\frac{y^- l_T^2}{4Ez(1-z)} \right], \tag{8.3}$$

in terms of the jet transport parameter $\hat{q}_a$ for a jet parton a. The jet transport parameter for a gluon is $9/4$ times of a quark and therefore the radiative energy loss of a gluon jet is also $9/4$ times larger than that of a quark jet. According to the definition of jet transport parameter, we can assume that it is proportional to the local parton density in a QGP medium. In a dynamical evolving medium, it can be expressed in general as

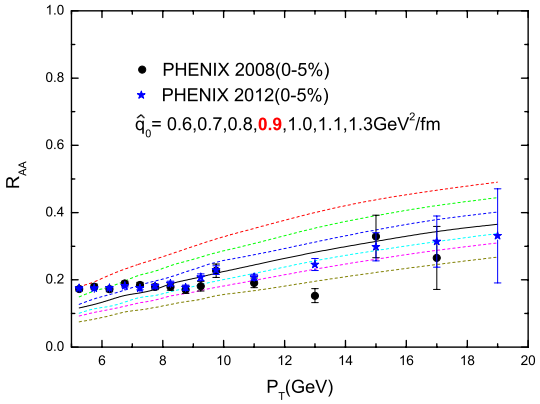

Figure 8.9 Nuclear modification factor at mid-rapidity for π^0 spectra in $0-5\%$ central Au+Au collisions at $\sqrt{s_{NN}} = 200$ GeV with a range of values of initial quark jet transport parameter $\hat{q}_0$ at $\tau_0 = 0.6$ fm/c in the center of the most central collisions (from top to bottom), as compared to PHENIX data [114, 115] at RHIC.

[100, 110, 111],

$$\hat{q}(\tau, r) = \hat{q}_0 \frac{\rho_{QGP}(\tau, r)}{\rho_{QGP}(\tau_0, 0)} \cdot \frac{p^\mu u_\mu}{p_0}, \tag{8.4}$$

In our calculation, we use a full (3+1)D ideal hydrodynamics [94, 112] to describe the space-time evolution of the local temperature and flow velocity in the bulk medium along the jet propagation path in heavy-ion collisions. Here $\rho_{QGP}(\tau, r)$ is the parton density in an ideal gas, and $\rho_{QGP}(\tau_0, 0)$ is the initial parton density at the time $\tau_0 = 0.6$ fm/c in the center of the hot system, p^μ is the four momentum of the jet and u^μ is the four flow velocity in the collision frame, $\hat{q}_0$ denotes the jet transport parameter at the center of the bulk medium in the QGP phase at the initial time τ_0.

The averaged number of gluon emissions $\langle N_g^a \rangle$ from the propagating parton ($a = q, g$) within the high-twist approach of parton energy loss [113] is given by,

$$\begin{aligned} \langle N_g^a(\mu^2) \rangle &= C_A \frac{\alpha_s}{2\pi} \int dy^- \int_0^{Q^2} \frac{dl_T^2}{l_T^4} \int \frac{dz}{z} [1 + (1-z)^2] \\ &\quad \times \hat{q}_a(y) 4 \sin^2 \left[\frac{y^- l_T^2}{4Ez(1-z)} \right]. \end{aligned} \tag{8.5}$$

Using the above medium modified FFs with the collinear next-to-leading order (NLO) pQCD parton model [118, 119] and the CTEQ5 parameterization of parton distributions, one can calculate the final hadron spectra in both heavy-ion and p+p collisions. Shown in Fig. 8.9 and Fig. 8.10 are the nuclear modification factors,

$$R_{AA} = \frac{d\sigma_{AA}/dp_T^2 dy}{\int d^2b\, T_{AA}(\mathbf{b}) d\sigma_{NN}/dp_T^2 dy}, \tag{8.6}$$

for the charged hadron spectra as compared to the RHIC/LHC data on central collisions with different values for the jet transport parameter. The values of $hatq$ from best χ^2 fits are $\hat{q}_0 = 0.7 - 1.0$ GeV^2/fm at RHIC energy and $\hat{q}_0 = 1.3 - 2.0$ GeV^2/fm at LHC. This is consistent with HIJING 2.0 prediction [70] and the JET analyses [12].

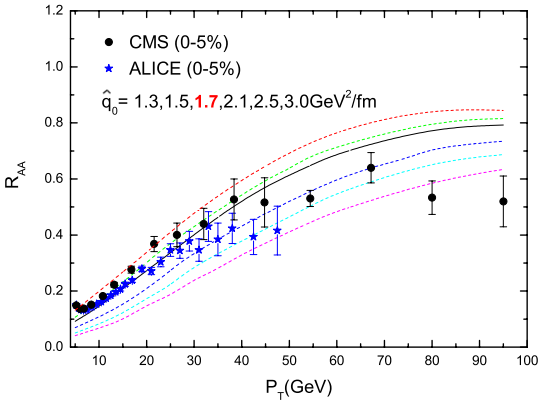

Figure 8.10 Nuclear modification factor at mid-rapidity for changed hadron spectra in $0-5\%$ central Pb+Pb collisions at $\sqrt{s_{NN}} = 2.76$ TeV/n with a range of values of initial quark jet transport parameter $\hat{q}_0$ at $\tau_0 = 0.6$ fm/c in the center of the most central collisions(from top to bottom), as compared to ALICE [116] and CMS data [117] at LHC.

Since the jet transport parameter $\hat{q}_0$ is proportional to the initial parton number density which in turn is proportional to the final charged hadron multiplicity, we can assume $\hat{q}_0 = 2.6 - 4.0$ GeV^2/fm for a quark jet in central $Pb + Pb$ collisions at $\sqrt{s_{NN}} = 30$ TeV which is about 2 times that at LHC energy according to Table 8.1. Shown in Fig. 8.11 is the nuclear modification factor at mid-rapidity for charged hadron spectra in $0-5\%$ central Pb+Pb collisions at $\sqrt{s_{NN}} = 30.0$ TeV with a range of values of initial quark jet transport parameter $\hat{q}_0 = 2.6 - 4.0$ GeV^2/fm at $\tau_0 = 0.6$ fm/c in the center of the most central collisions(from top to bottom), as compared to Pb+Pb collisions at $\sqrt{s_{NN}} = 2.76$ TeV with the value of $\hat{q}_0 = 1.3 - 2.0$ GeV^2/fm and ALICE [116] and CMS data [117] at LHC as shown in Fig. 8.10. Over the range of $p_T = 10 - 100$ GeV/c, the hadron spectra are significantly more suppressed at $\sqrt{s} = 30$ TeV than at LHC due to larger initial values of jet transport parameter. The difference becomes smaller at high transverse momentum due to different initial jet spectra at two different energies.

In the McGill-AMY approach [103, 120], nuclear modification of hadron spectra in nucleus-nucleus collisions can be calculated by first solving a set of coupled transport rate equations for the hard jet energy/momentum distributions $f(p,t) = dN(p,t)/dp$ in the hot nuclear medium. The coupled rate equations for quark and gluon jets may generically be written as the following form:

$$\frac{df_j(p,t)}{dt} = \sum_{ab} \int dk \left[f_a(p+k,t) \frac{d\Gamma_{a\to j}(p+k,k)}{dkdt} - P_j(k,t) \frac{d\Gamma_{j\to b}(p,k)}{dkdt} \right], \tag{8.7}$$

In the above equation, $d\Gamma_{j\to a}(p,k)/dkdt$ represents the transition rate for the process $j \to a$, with p the initial jet energy and k the momentum lost in the process. The transition rates for radiative processes are taken from Refs. [121–123], and for the collisional processes, the drag and the diffusion contributions are incorporated following Refs. [103, 120]. The contributions from energy gain processes are taken into account by the $k < 0$ integral.

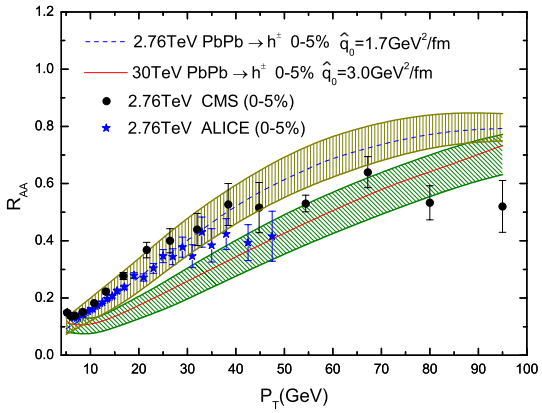

Figure 8.11 Nuclear modification factor at mid-rapidity for changed hadron spectra in $0-5\%$ central Pb+Pb collisions at $\sqrt{s_{NN}} = 30.0$ TeV with a range of values of initial quark jet transport parameter $\hat{q}_0 = 2.6 - 4.0$ GeV^2/fm at $\tau_0 = 0.6$ fm/c in the center of the most central collisions(from top to bottom), as compared to Pb+Pb collisions at $\sqrt{s_{NN}} = 2.76$ TeV with the value of $\hat{q}_0$ is from 1.3 GeV^2/fm to 2.0 GeV^2/fm and ALICE [116] and CMS data [117] at LHC as shown in Fig. 8.10.

After solving the above coupled rate equations, one may obtain the medium-modified fragmentation function as follows:

$$\tilde{D}_{h/j}(z, \vec{r}_\perp, \phi_p) = \sum_{j'} \int dp_{j'} \frac{z'}{z} D_{h/j'}(z') P(p_{j'}|p_j, \vec{r}_\perp, \phi_p), \tag{8.8}$$

where $z = p_h/p_j$ and $z' = p_h/p_{j'}$, with p_h the momentum of the hadron h and $p_j(p_{j'})$ the initial (final) jet momentum. $D_{h/j}(z)$ is the vacuum fragmentation function, and $P(p_{j'}|p_j, \vec{r}_\perp, \phi)$ represents the differential probability for obtaining a parton j' with momentum $p_{j'}$ from a given parton j with momentum p_j. This probability distribution depends on the path traveled by the parton and the local medium profiles such as the temperature and flow along that path. Therefore, $P(p_{j'}|p_j, \vec{r}_\perp, \phi_p)$ depends on the initial jet production location $\vec{r}_\perp$ and the propagation direction ϕ_p. Jets are decoupled from the medium when the local temperature of the nuclear medium is below the transition temperature $T_c = 160$ MeV.

By convoluting the medium-modified fragmentation function with the initial jet momentum distribution computed from perturbative QCD, one may obtain the final medium-modified hadron spectra:

$$\frac{d\sigma_{AB\to hX}}{d^2p_T^h dy} = \int d^2\vec{r}_\perp \mathcal{P}_{AB}(\vec{r}_\perp) \sum_j \int \frac{dz}{z^2} \tilde{D}_{h/j}(z, \vec{r}_\perp, \phi_p) \frac{d\sigma_{AB\to jX}}{d^2p_T^j dy}. \tag{8.9}$$

In the above equation, $\mathcal{P}_{AB}(b, \vec{r}_\perp)$ is the probability distribution of the initial jet production position $\vec{r}_\perp$, and is determined from binary collision distribution simulated by the Glauber model. One may fix the propagation direction ϕ_p or average over a certain range.

Putting the above ingredients together, one may obtain the hadron yield after medium modification and calculate the nuclear modification factor R_{AA}.

In Fig. 8.12, we show the comparison of the calculated nuclear modification factor R_{AA} from McGill-AMY approach as a function of p_T for: central 0-5% Au-Au collisions

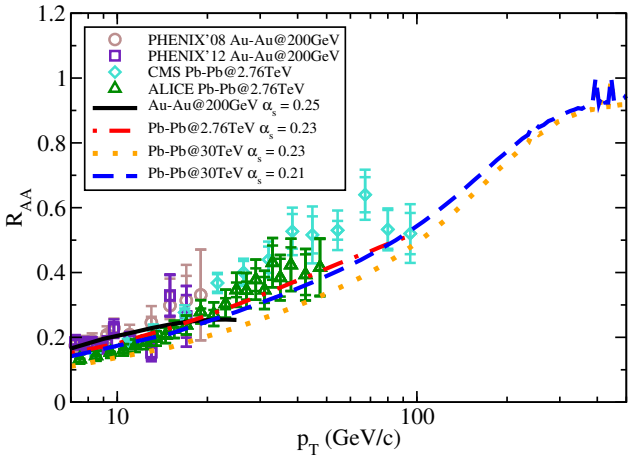

Figure 8.12 (Color online) The nuclear modification factor R_{AA} as a function of p_T for central Au-Au collisions at 200 AGeV at RHIC, for central Pb-Pb collisions at 2.76 ATeV at the LHC, and for central Pb-Pb collisions at 30 ATeV.

at 200 AGeV at RHIC, central 0-5% Pb-Pb collisions at 2.76 ATeV at the LHC, and central 0-5% Pb-Pb collisions at 30 ATeV. Note that in the McGill-AMY model, the model parameter is the strong coupling constant α_s which is usually fitted to the experimental data. For RHIC Au-Au collisions it is obtained as $\alpha_s = 0.25$ by fitting to PHENIX data, and for the LHC $\alpha_s = 0.23$ using CMS and ALICE data. The decreasing of α_s from RHIC to the LHC may be understood as originating from the increasing of the average temperature (or the energy density) of the hot nuclear media produced at RHIC and LHC. To account for such effect when moving from 2.76 ATeV Pb-Pb collisions to 30 ATeV Pb-Pb collisions, we decrease the strong coupling constant from $\alpha_s = 0.23$ to $\alpha_s = 0.21$. One may consider the calculation for 30 ATeV Pb-Pb collisions using $\alpha_s = 0.23$ as the lower reference bound for the nuclear modification factor R_{AA}.

Medium Modification of Reconstructed Jets

The jet quenching or parton energy loss in hot and dense QGP can affect not only hadron suppression but also in jet modifications in high-energy nuclear collisions [124, 125]. The study of fully reconstructed jet production in relativistic heavy-ion collisions plays a very important role in probing the properties of the QGP formed in Pb+Pb reactions at the LHC [126]. Full jets in experiments are reconstructed from hadronic energies measured either through tracking or calorimetric detectors or both with a given jet -inding algorithm [127]. The jet production cross section with the same jet-finding algorithm can also be calculated within the next-to-leading (NLO) pQCD, using Monte Carlo packages such as MEKS [128]. Inclusive differential jet production cross sections in p+p collisions at NLO accuracy provide the baseline to calculate inclusive jet productions in heavy-ion collisions [125],

$$\frac{1}{\langle N_{\rm bin}\rangle}\frac{d\sigma^{AA}(R)}{dydE_T} = \int_{\epsilon=0}^{1} d\epsilon \sum_{q,g} P_{q,g}(\epsilon)\frac{1}{1-(1-f_{q,g})\cdot\epsilon}\frac{d\sigma^{pp}_{q,g}(CNM)}{dydE'_T}. \quad (8.10)$$

In the above expression for jet production cross section in heavy-ion collisions, several cold nuclear matter effects (shadowing, anti-shadowing and EMC effect) are taken into account through the EPS09 [129] parameterization of nuclear parton distribution functions

(nPDF). The parameter $f_{q,g}$ is the part of the fractional energy loss that is redistributed inside the jet cone, it can be calculated form the angular distribution of medium induced gluon radiation [125, 130], $P_{q,g}(\epsilon)$ is the probability that a jet loses energy fraction $\epsilon E'_T$, here $E'_T = E_T/[1-(1-f_{q,g})\cdot\epsilon]$ [125].

Shown in Fig. 8.13 are the nuclear modification factors of inclusive jet production,

$$R_{AA}^{\text{jet}} = \frac{d\sigma^{AA}/dydE_T}{\langle N_{\text{bin}}\rangle d\sigma^{pp}/dydE_T}, \tag{8.11}$$

in central Pb+Pb collisions for different jet radius $R = 0.3$,0.4,0.5 at $\sqrt{s_{NN}} = 20$ TeV. One-dimension longitudinal Bjorken expansion of the QGP fireball with Glauber transverse distribution and a highest initial temperature T_0 =570 MeV is assumed. The calculated jet suppression factors increase with jet transverse energy for all three different jet radii. The suppression factor for a larger jet cone size is slightly less because more radiated gluon remain inside the jet cone and thus less effective energy loss for the reconstructed jet. These calculated suppression factors for reconstructed jets at $\sqrt{s} = 20$ TeV are somewhat similar to that measured at the current LHC energy [131, 132] event though the initial parton energy density or the jet transport parameter is almost a factor of 2 larger. This indicates that the jet suppression factor is less sensitive to the properties of the medium as compared to the single inclusive hadrons. It is therefore helpful to explore other observables such as jet shape or profile functions.

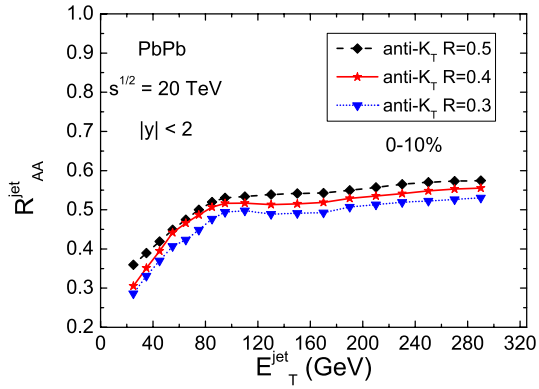

Figure 8.13 Nuclear modification factor R_{AA} for inclusive jet production as a function of jet transverse energy for different jet radius in central Pb+Pb collisions at $\sqrt{s_{NN}} = 20$ TeV.

Jet shape, also called jet energy profile, is the internal energy distribution of a jet. Medium modification of the jet shape in heavy-ion collisions due to multiple scattering and induced radiation relative to hadron-hadron reactions has shown to be sensitive to jet-medium interaction [124, 125]. The differential jet shape is defined as

$$\rho(r) = \frac{1}{\Delta r}\frac{1}{N^{\text{jet}}}\sum_{\text{jets}}\frac{P_T(r-\Delta r/2, r+\Delta r/2)}{P_T(0,R)}, \qquad \Delta r/2 \le r \le R-\Delta r/2 \tag{8.12}$$

Jet shapes in hadronic collisions have been studied recently in the framework of QCD resummation at NLO [133, 134], which give a decent description of jet profiles in p+p collisions and provide the baseline for investigating jet shape modification in high-energy

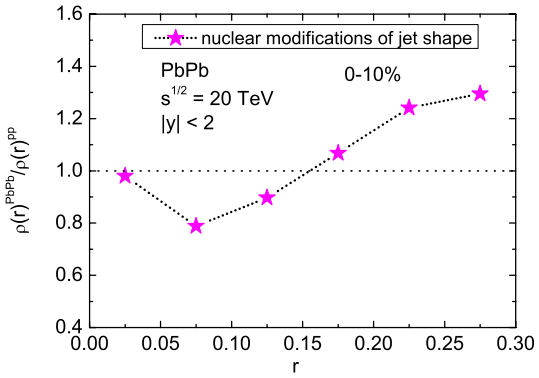

Figure 8.14 Nuclear modification $R_{AA}^{\text{jet-shape}}$ for differential jet shapes with $R = 0.3$ in central Pb+Pb collisions at $\sqrt{s} = 20$ TeV.

nuclear colliisons. In heavy-ion reactions, the jet energy consists of two parts: the energy of quenched leading parton (E_p) and the redistributed energy of radiated gluon (E_g) inside the jet cone. The total jet energy should be their sum, $E^{\text{jet}} = E^g + E^p$. Thus jet shapes in heavy-ion collisions can be calculated as follows

$$\rho^{AA}(r, E_{\text{jet}}) = \frac{E_g}{E_{\text{jet}}}\rho^{\text{medium}}(r, E_g) + \frac{E_p}{E_{\text{jet}}}\rho^{pp}(r, E_p), \tag{8.13}$$

where $\rho^{\text{medium}}(r, E_g)$ is calculated from the angular spectra of medium induced gluon radiation. Furthermore we define the nuclear modification ratio of jet shapes as

$$R_{AA}^{\text{jet-shape}} = \frac{\rho^{AA}(r, E_{\text{jet}})}{\rho^{pp}(r, E_{\text{jet}})}. \tag{8.14}$$

Shown in Fig. 8.14 is the calculated the nuclear modifications of jet shapes in central Pb+Pb collisions at $\sqrt{s} = 20$ TeV. One can see a considerable enhancement of jet shapes in heavy-ion collisions relative to those in p+p in the region when $r \to R$ due to induced gluon radiation while there is some depletion of jet energy distribution at intermediate r due to fixed total jet energy. Such a feature has been observed in heavy-ion collisions at LHC [135] and should provide information on jet-medium interaction at future high-energy heavy-ion colliders.

8.5 Medium Nodification of Open Heavy Mesons

An alternative candidate of hard probe of the QGP properties is heavy flavor meson. Since the large mass of heavy quarks effectively suppresses their thermal production from the bulk matter, the majority of them are produced at the primordial stage of nuclear collisions through hard scatterings. After that, they propagate through the hot QGP matter with their flavor conserved and therefore serve as a clean probe of the whole evolution history of the QGP fireballs. In this section, we adopt an improved Langevin approach [136, 137] to simulate the in-medium energy loss of open heavy quarks. The hadronization into heavy mesons is simulated using a hybrid model of fragmentation and coalescence developed in Ref. [137].

In the limit of small momentum transfer in each interaction, multiple scatterings of heavy quarks inside a thermalized medium can be described using the Langevin equation. Apart from the collisional energy loss due to these quasi-elastic scatterings, heavy quarks may also lose energy via medium-induced gluon radiation. We modify the classical Langevin equation as follows to simultaneously incorporate these two energy loss mechanisms:

$$\frac{d\vec{p}}{dt} = -\eta_D(p)\vec{p} + \vec{\xi} + \vec{f}_g. \tag{8.15}$$

The first two terms on the right-hand side of Eq.(8.15) are inherited from the original Langevin equation, describing the drag force and thermal random force exerted on heavy quarks when they scatter with light partons in the medium background. We assume that the fluctuation-dissipation theorem is still hold between these two terms $\eta_D(p) = \kappa/(2TE)$, in which κ is known as the momentum-space diffusion coefficient of heavy quarks: $\langle \xi^i(t)\xi^j(t')\rangle = \kappa\delta^{ij}\delta(t-t')$. The third term $\vec{f}_g$ in Eq.(8.15) is introduced to describe the recoil force heavy quarks experience when they radiate gluons. The probability of gluon radiation within the time interval $[t, t+\Delta t]$ can be evaluated according to the number of radiated gluons,

$$P_{\rm rad}(t,\Delta t) = \langle N_{\rm g}(t,\Delta t)\rangle = \Delta t \int dx dk_\perp^2 \frac{dN_{\rm g}}{dx dk_\perp^2 dt}, \tag{8.16}$$

as long as Δt is chosen sufficiently small so that $P_{\rm rad}(t,\Delta t) < 1$ is always satisfied. In our study, the distribution of the medium-induced gluon radiation is taken from the high-twist approach to parton energy loss [138–140]:

$$\frac{dN_{\rm g}}{dx dk_\perp^2 dt} = \frac{2C_A\alpha_s P(x)\hat{q}}{\pi k_\perp^4}\sin^2\left(\frac{t-t_i}{2\tau_f}\right)\left(\frac{k_\perp^2}{k_\perp^2 + x^2M^2}\right)^4, \tag{8.17}$$

where x is the fractional energy taken from the heavy quark by the radiated gluon, $k_\perp$ is the gluon transverse momentum, $P(x)$ is the quark splitting function and $\tau_f = 2Ex(1-x)/(k_\perp^2 + x^2M^2)$ is the gluon formation time. In Eq.(8.17), a quark transport coefficient $\hat{q}$ is utilized, which is related to the diffusion coefficient κ by adding the factor of dimension in our work $\hat{q} = 2\kappa$. With this assumption, only one free parameter remains in the modified Langevin equation [Eq.(8.15)]. As shown in the earlier work [137], $\hat{q}/T^3 = 5.0$ is chosen to best describe the experimental data of heavy flavor meson at high $p_{\rm T}$ at RHIC and LHC.

With this improved Langevin approach, we may simulate the evolution of heavy quarks in relativistic nuclear collisions. The dense QCD medium produced in these collisions is simulated with a (3+1)-dimensional ideal hydrodynamic model [94, 112]. This hydrodynamic calculation provide the space-time evolution of the local temperature and fluid velocity of the QGP fireballs. With these information, for every time step, we boost each heavy quark into the local rest frame of the fluid cell through which it propagates and then update its energy and momentum according to our modified Langevin equation. After that, the heavy quark is boosted back to the global center of mass frame and stream freely until its interaction with the medium for next time step. Before the hydrodynamical evolution commences (at $\tau_0 = 0.6$ fm/c), heavy quarks are initialized with a MC-Glauber model for their spatial distribution and a leading order pQCD calculation together with the CTEQ5 parton distribution functions [141] for their momentum distribution. The nuclear shadowing effect in the initial state of nucleus-nucleus collisions is taken into account by using the EPS09 parameterization [129]. With these initializations, heavy quarks evolve inside

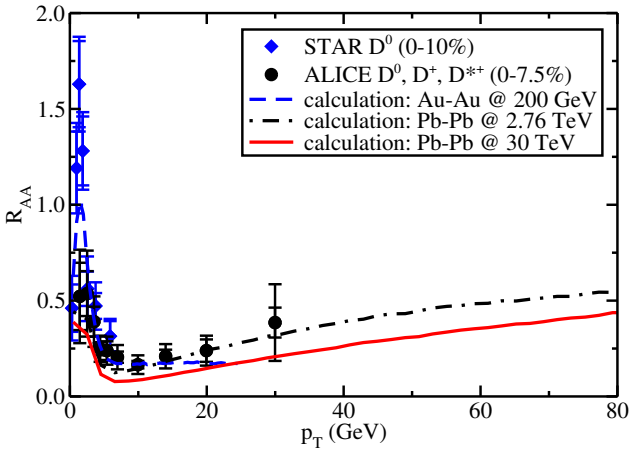

Figure 8.15 (Color online) The nuclear modification factor $R_{\rm AA}$ of D mesons, compared between in central Au-Au collisions at 200 AGeV, in central Pb-Pb collisions at 2.76 ATeV, and in central Pb-Pb collisions at 30 ATeV.

the QGP matter until they reach fluid cells with local temperature below $T_{\rm c}$ (165 MeV). Then they hadronize into heavy flavor hadrons within a hybrid model of fragmentation and coalescence. The relative probability of fragmentation and heavy-light quark coalescence is calculated with the Wigner functions in an instantaneous coalescence model [142]. If a heavy quark is chosen to combine with a thermal parton from the medium, the momentum distribution of the produced hadron is calculated directly with the coalescence model itself. On the other hand, if the heavy quark is chosen to fragment, its fragmentation process is simulated with PYTHIA 6 [143] in which the Peterson fragmentation function is used.

In Fig.8.15, the suppression factors for D meson $R_{\rm AA}$ are shown for different collisional energies. For central Au-Au collisions at 200 AGeV, a bump structure in the D meson $R_{\rm AA}$ can be observed around 1-2 GeV. This is contributed by the coalescence mechanism in heavy quark hadronization process, which combines low $p_{\rm T}$ heavy quarks and light thermal partons and enhances the production of D mesons at medium $p_{\rm T}$. Such a bump is significantly suppressed in Pb-Pb collisions at 2.76 ATeV and 30 ATeV due to the strong nuclear shadowing effect for these collisional energies at low $p_{\rm T}$. At higher $p_{\rm T}$, the D meson $R_{\rm AA}$ is relatively flat between 10 and 20 GeV in Au-Au collisions at 200 AGeV, but starts to increase with $p_{\rm T}$ in 2.76 and 30 ATeV Pb-Pb collisions. This probably results from the harder initial $p_{\rm T}$ spectra of charm quarks produced at the RHIC energy than at the LHC energies. In addition, we observe that D mesons are more suppressed in 30 ATeV than in 2.76 ATeV Pb-Pb collisions, since larger collisional energy leads to higher initial temperature and longer lifetime of the QGP fireballs and therefore increases the total in-medium energy loss of heavy quarks.

8.6 J/ψ Production

The suppression of J/ψ in hot medium has been considered as a probe of the QGP created in the early stage of heavy ion collisions [144]. The nuclear modification factor $R_{AA} \sim 0.3$ in central Au+Au collisions at RHIC [145] goes up to about 0.5 in central Pb+Pb collisions at $\sqrt{s_{NN}} = 2.76$ TeV at the LHC [146] due to the increasing contribution

of charmonium regeneration [147–149]. One can similarly investigate the behavior of nuclear modification factor R_{AA} of J/ψ at tens of TeV, e.g. $\sqrt{s_{NN}} = 20$ TeV in the framework of transport approach [150–153].

Considering that charmonium is so heavy and difficult to be thermalized in heavy-ion collisions, one can use the classical transport equation to describe the charmonium motion in the medium,

$$\frac{\partial f_\Psi}{\partial t} + \frac{\mathbf{p}}{E_\Psi} \cdot \nabla f_\Psi = -\alpha_\Psi f_\Psi + \beta_\Psi, \tag{8.18}$$

where $f_\Psi(\mathbf{x}, \mathbf{p}, t)$ are the charmonium distribution functions in phase space for $\Psi = J/\psi, \psi', \chi_c$. Considering the fact that J/ψ's in the final state come from direct production and decay from excited states ψ' and χ_c, one needs the distributions of ψ' and χ_c. The charmonium energy is denoted by $E_\Psi = \sqrt{m_\Psi^2 + \mathbf{p}^2}$, and α_Ψ and β_Ψ are the charmonium dissociation and regeneration rates. Taking the gluon dissociation $g + \Psi \to c + \bar{c}$ as the main dissociation process at high temperature, the loss term α_Ψ can be expressed as,

$$\begin{aligned} \alpha_\Psi(\mathbf{x}, \mathbf{p}, t|\mathbf{b}) &= \frac{1}{2E_\Psi} \int \frac{d^3\mathbf{k}}{(2\pi)^3} \frac{1}{2E_g} W_{g\Psi}^{c\bar{c}}(\mathbf{p}, \mathbf{k}) f_g(\mathbf{x}, \mathbf{k}, t) \\ &\quad \times \Theta\left(T(\mathbf{x}, t|\mathbf{b}) - T_c\right), \end{aligned} \tag{8.19}$$

with impact parameter $\mathbf{b}$ describing the centrality of collisions, gluon energy E_g, the thermal gluon distribution f_g and the dissociation probability $W_{g\Psi}^{c\bar{c}}$. The dissociation probability is determined by the dissociation cross section from gluons whose vacuum value $\sigma_\Psi(0)$ is calculated through the operator production expansion [154, 155]. Temperature dependent cross section $\sigma_\Psi(T)$ can be estimated by taking into account the geometry relationship between the cross section and the size of J/ψ, $\sigma_\Psi(T) = \sigma_\Psi(0)\langle r_\Psi^2\rangle(T)/\langle r_\Psi^2\rangle(0)$. The charmonium size $\langle r_\Psi^2\rangle(T)$ can be calculated in the potential model [156]. The step function Θ means that we considered here only the dissociation (and regeneration) in the deconfined phase with T_c being the critical temperature for the deconfinement phase transition. Considering the strong interaction between charm quarks and the high-temperature medium at colliding energy $\sqrt{s_{NN}} = 20$ TeV, one can approximately take thermal charm quark distribution f_c in calculating the regeneration rate. Since the regeneration process is the inverse process of the gluon dissociation, the regeneration probability $W_{c\bar{c}}^{g\Psi}$ can be obtained via the detailed balance between the two processes. In the above transport approach, we have neglected elastic collisions between charmonium and the medium, since its effect on the momentum integrated R_{AA} is rather small [157].

The local temperature $T(\mathbf{x}, t)$ and medium velocity $u_\mu(\mathbf{x}, t)$ appeared in the thermal gluon and charm quark distributions f_g and f_c are given by equations of ideal hydrodynamics, $\partial_\mu T^{\mu\nu} = 0$, where $T_{\mu\nu}$ is the energy-momentum tensor of the medium. While the charm quarks are assumed to be thermalized, they do not reach chemical equilibrium. The space-time evolution of the charm quark density $n_c(\mathbf{x}, \tau|\mathbf{b})$ satisfies the conservation $\partial_\mu(n_c u^\mu) = 0$, with the initial density determined by the nuclear thickness functions $n_c(\mathbf{x}, \tau_0|\mathbf{b}) = [d\sigma_{NN}^{c(\bar{c})}/dy] T_A(\mathbf{x} - \mathbf{b}/2) T_B(\mathbf{x} + \mathbf{b}/2)$.

The shadowing effect becomes extremely important at small x or high colliding energy $\sqrt{s_{NN}}$. In our calculation we use the EKS98 package [158] to take into account of the shadowing factor $R(x)$. Its value in the dominant kinematic region for charm quark production at $\sqrt{s_{NN}} = 20$ TeV is around 0.8, which leads to a strong suppression for the regeneration: the charmonium nuclear modification factor is reduced to $\sim 64\%$ due to

the shadowing effect! The other cold nuclear matter effects like Cronin effect [159] and nuclear absorption can also be included in the initial condition of the transport equation [153].

The initial thermodynamic conditions for the hydrodynamic evolution is determined by fitting the extrapolated multiplicity of charged hadrons at $\sqrt{s_{NN}} = 20$ TeV. We take the initial thermalization time $\tau_0 = 0.6$ fm/c and the initial temperature at the center of the fireball $T_0 = 540$ MeV for central Pb+Pb collisions [160]. The critical temperature is chosen as $T_c = 165$ MeV.

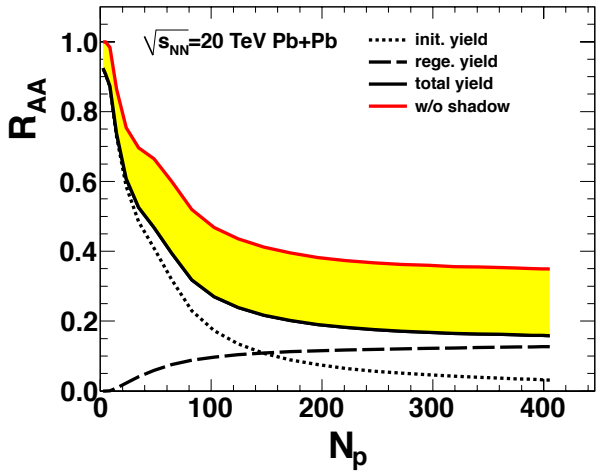

Figure 8.16 The prompt J/ψ nuclear modification factor as a function of centrality at mid-rapidity $|y| < 1$ in $\sqrt{s_{NN}} = 20$ TeV Pb+Pb collisions. The dotted, dashed and solid lines are the initial production, regeneration and full result, respectively. The upper limit of the band is the full result without shadowing effect.

The initial charmonium distribution is in principle fixed by the corresponding p+p data, modified by the cold nuclear matter effects [153]. Since there are not yet p+p data at $\sqrt{s_{NN}} = 20$ TeV, we use the simulator PYTHIA [161] to extract the J/ψ and charm quark production cross sections in central rapidity region $|y| < 1$,

$$\frac{d\sigma_{NN}^{J/\psi}}{p_t dp_t} = A\frac{n-1}{\langle \bar{p}_t^2 \rangle_{NN}} \left(1 + \frac{p_t^2}{\langle \bar{p}_t^2 \rangle_{NN}}\right)^{-n} \tag{8.20}$$

and $\frac{d\sigma_{NN}^{c\bar{c}}}{dy} = 1.4$ mb, where $\langle \bar{p}_t^2 \rangle_{NN} = \langle p_t^2 \rangle_{NN} + a_{gN} l$ is the J/ψ averaged transverse momentum square modified by the Cronin effect with $\langle p_t^2 \rangle_{NN} = 22.69(\text{GeV/c})^2$, $a_{gN} = 0.2$ GeV^2/fm, $A = 2.011 \times 1.68 \times (10)^{-2}$ mb, $n = 3.164$, and l being the averaged traveling length of the two gluons before they fuse into a J/ψ.

The prediction of the nuclear modification factor R_{AA} for J/ψ at $\sqrt{s_{NN}} = 20$ TeV is shown in Fig.8.16. The initially produced J/ψ's are almost totally dissolved in central collisions due to the high temperature at mid rapidity. Because of the strong shadowing effect which reduces the charm quark number by a factor of 80% and the regenerated J/ψ number by a factor of about 64%, the charmonium regeneration is largely suppressed, and the full result is only about 15% in central collisions. Considering the uncertainty of the calculation of the shadowing effect, the maximum R_{AA} without considering the shadowing effect can reach 35%, see the upper limit of the band in Fig. 8.16.

8.7 Summary

Since the discovery of the strongly coupled QGP at RHIC about a decode ago, experimental and theoretical efforts in high-energy nuclear physics have been focused on the quantitative study of the properties of the sQGP at extremely high temperatures,. These include the extraction of the shear viscosity to entropy density ratio of the bulk QGP medium and the jet transport parameter for energetic jets propagating inside the QGP medium in high-energy heavy-ion collisions at both RHIC and LHC. The future frontier of heavy-ion collisions will be in both lower and very high colliding energy regime. At lower colliding energies such as that in the beam energy scan (BES) region of RHIC and FAIR, one expects to reach higher baryon density in heavy-ion collisions and looks for signals of the critical end-point of the QCD phase transition in the exploration of the phase structure of QCD matter. In the very high energy regime, one expects to reach the higher initial temperature than currently possible at RHIC and LHC in the center of two colliding nuclei. At such higher initial temperatures, properties of QGP medium might approach that of weakling interacting quarks and gluons. The shear viscosity to entropy ratio should increase and the jet transport parameter scaled by T^3 should instead decrease as predicted by the pQCD.

Using HIJING and CCG model, we have estimated the final charged hadron multiplicity in central Pb+Pb collisions at $\sqrt{s} = 30$ TeV to be about twice of that at the current LHC energy ($\sqrt{s} = 2.67$ TeV). The corresponding initial temperature of a thermalized QGP will be about $T_0 \approx 560$ MeV. Assuming initial thermalization to about the same as at LHC, $\tau_0 = 0.6$ fm/c, we estimated the anisotropic flow of charged hadrons using an event-by-event 3+1D ideal hydrodynamic model with fluctuating initial conditions. One should expect see strong signals of higher harmonic flow which should provide stringent constraints on shear viscosity. We also calculated the suppression factors for large transverse momentum charged hadrons in central Pb+Pb collisions at $\sqrt{s} = 30$ TeV within two different approaches to energy loss. The estimated suppression factor is shown to continue decrease over large range of transverse momentum, and thus provides an enough sensitivity to determine the jet transport at such initial high temperature. Though the suppression of full jet production is not as sensitive to the increased initial temperature, the jet profile function is found to significantly modified and should provide additional constraints on the properties of the QGP medium. The final J/ψ yield in Pb+Pb collisions at $\sqrt{s} = 30$ TeV is still completely dominated by regeneration mechanism from recombination of initially produced charm quarks because of the complete suppression of the initially produced J/ψ. The final J/ψ suppression factor is however smaller than that at LHC because of the suppression of initial charm quark production by the gluon nuclear shadowing. One therefore should determined such gluon shadowing from p+A and e+A collisions in order to unambiguously determined the J/ψ's regenerated from QGO medium through recombination. A systematic study of these experimental observables at a future very high energy heavy-ion collider should provide us an opportunity to determine the properties of the dense QGP and shed light on the weakly interacting limit of QGP at very high temperature.

8.8 Physcis Perspective at Future Electron-Proton or Electron-Ion Colliders

Introduction

An electron-hadron (protons and heavy nuclei) collider with 120 GeV electrons scattering on 25-45 TeV protons (or heavy nuclei with similar energy per nucleon) can be built to study the frontier of hadronic physics as an extension of the proposed CEPC program.

There have been substantial conceptual design and physics studies for building the Electron Ion Collider (EIC) [162, 163] in the US and the Large Hadron electron Collider (LHeC) [164–166] at CERN. The square of the center-of-mass colliding energy of the proposed CEPC is about 10 times of that at the LHeC and over 600 times of that at EIC. The CEPC will become the most powerful electron-hadron collider in the near future.

Deep inelastic scattering (DIS) between high energy lepton and hadron, as illustrated in the left figure of Fig. 8.17, provides us the most direct and precise probe of target hadrons. At the CEPC, we can obtain unprecedented knowledge of the internal landscape of the nucleons. Especially, by going to extremely high energy, one can access the partonic structure of nucleons and nuclei in very small-x regime, hence determine the role of gluons and gluon self-interactions in hadrons. The kinematic coverage of CEPC as compared to HERA and some other past electron-hadron colliders is shown in the right plot of Fig. 8.17. DIS can be studied in a significantly enlarged kinematical range at CEPC, which will offer us new insights into QCD low-x physics and multi-dimensional tomography of hadrons as well as electroweak physics and new physics beyond standard model.

For the first time, we will be able to precisely probe the structure of protons and other hadrons with the finest resolution of order $10^{-19}-10^{-20}$m, and we will have the capability to discover new physics if there is any at that scale in the high Q^2 and high x regime. In the low x regime with not too large Q^2, we can study the non-linear gluon dynamics and nuclear structure at extremely high density. According to Quantum Chromodynamics (QCD) and the small-x model calculation [167], one can define an empirical saturation line as indicated in the red (for gold nuclei) and black (for protons) solid lines in the right figure of Fig. 8.17 to separate the dilute linear dynamical regime from the dense non-linear regime. Below the saturation line, where the gluon density is of order $\frac{1}{\alpha_s}$, the non-linear gluonic dynamics becomes very important and eventually could lead to the so-called gluon saturation phenomenon, which is characterised by the existence of one new form of dense nuclear matter, namely the colour glass condensate (CGC).

One of the most interesting open question in physics is the QCD colour confinement. Although there have been no analytical proof, we have never been able to observe a free quark or gluon, but only hadrons, such as mesons and baryons, that are built upon them. It is generally accepted that the peculiar non-linear gluon dynamics at strong coupling limit is responsible for this phenomenon. By studying the gluonic dynamics under extreme conditions may shed light on this problem and help us understand the underlying mechanism. Ever since the discovery of the Higgs boson with mass 126GeV by ATLAS [168] and CMS [169], precise measurements of various properties of the newly found Higgs boson, especially its coupling to other known fundamental particles, become the main objective of high energy experimental study. By doing so, we can conduct crucial precise test of standard model in particle physics and further determine the possibility of discoveries for other new particles.

Figure 8.17 Left: Generic illustration of a typical event in DIS. Right: Kinematical coverage of ep scattering at the CEPC with $x_{\mathrm{Bj}} \equiv \frac{Q^2}{ys}$. Q^2, which is defined as the virtuality of the intermediate photon, is the measure of resolution power of the scattering. s represents the center of mass energy of the ep system and $y \equiv \frac{P\cdot q}{P\cdot k}$ is the measure of inelasticity. The kinematical coverage of the CEPC is the area between the dotted lines, which has never been studied in any past experiments.

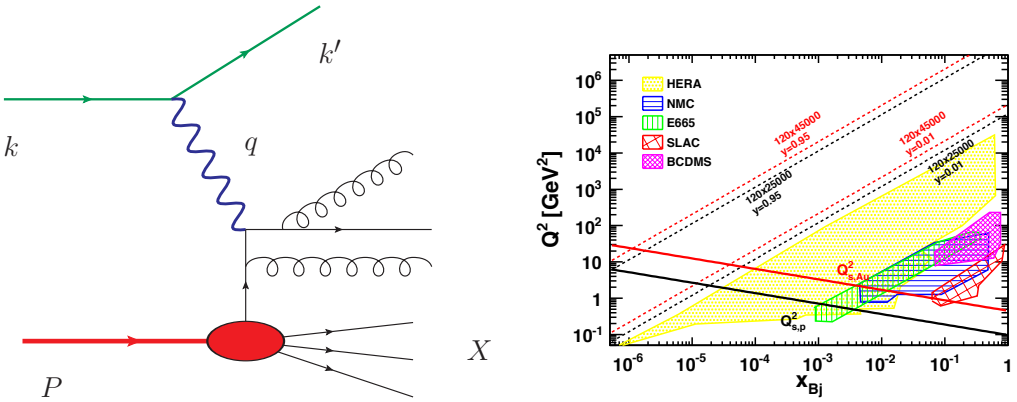

Since the LHC is a hadron-hadron collider, as we have learnt so far, it suffers from relatively large uncertainties mostly due to the imperfect knowledge of parton distribution functions, especially the gluon distribution function. The CEPC can provide us with precise measurement of parton distribution functions for Q^2 as large as $10^6\,\mathrm{GeV}^2$ and for x_{Bj} as low as 10^{-7}. This would substantially reduce the uncertainties for all measurements in proton-proton collisions and impose significant implications on the studies of properties of Higgs boson and the searches of other new particle, thus improve the discovery capabilities of future proton-proton colliders.

The bottom line is that the CEPC has a very interesting and diverse physics program of its own, which includes studies of extreme QCD matter, precise measurements in Higgs physics and new physics search. It shall play an very important role complementary to the inclusive circular electron-positron and proton-proton collider.

Large Q^2 Regime and Parton Distributions

Ever since the birth of QCD in 1960s, the quest for better understanding of the internal structure of protons and nuclei has been one of the primary goal in high energy nuclear physics. DIS is a very clean and ideal process for the purpose of probing the internal landscape and dynamics of protons and nuclei. By measuring outgoing electron momentum k', one can reconstruct two important signature quantities of the intermediate virtual photon for this process, namely x_{Bj} and Q^2. According to the QCD factorization theorem, the total cross section as functions of x_{Bj} and Q^2 can be written as

$$\sigma_{\mathrm{tot}}(x_{\mathrm{Bj}}, Q^2) = \int_{x_{\mathrm{Bj}}}^{1} \frac{dz}{z} \sum_f \mathcal{H}_f\left(z, \alpha_s(Q^2)\right) f(\frac{x_{\mathrm{Bj}}}{z}, Q^2), \tag{8.21}$$

where $f(\frac{x_{\mathrm{Bj}}}{z}, Q^2)$ stands for the parton distribution functions and $\mathcal{H}_f\left(z, \alpha_s(Q^2)\right)$ is the perturbative calculable hard part, which can be written as power expansion of α_s. For relatively large x_{Bj}, one can increase the resolution of the virtual photon probe by increasing Q^2. The evolution of parton distributions with respect to Q^2 is governed by the well known Dokshitzer-Gribov-Lipatov-Altarelli-Parisi (DGLAP) evolution equation [170–172]. The

DGLAP evolution can be carried out with great precision which enables us to describe all the available DIS data with impressive agreement. For the moment, parton distributions, especially the gluon distribution at small-x, have large uncertainty which limits the discovery power of hadron-hadron colliders. The state of art global fit of parton distributions, such as CTEQ [173] and MSTW [174], relies primarily on the DIS data due to its accuracy. With the CEPC, we can significantly improve the uncertainty of parton distributions which is vital for various physics studies at hadron-hadron colliders.

Besides the substantial physics interest of its own, parton distributions are indispensable inputs for searches of new physics, such as gluino and other beyond standard model particles. Furthermore, by pushing up to extremely large Q^2, we can increase the resolution of hard probes to measure hadron structures at smaller scale, which allows us to search for the possible substructure of partons and leptons as well as extra-dimensions. Also, the standard model Higgs boson can be produced via both the neutral current ($ZZ \to h \to b\bar{b}$) and charged current ($W^+W^- \to h \to b\bar{b}$) channels in DIS. These events can be easily reconstructed and help us explore the electro-weak physics and the coupling between Higgs and heavy quarks.

In addition, DIS processes can help us access different aspects of QCD dynamics. Instead of evolving along the horizontal Q^2 line, as shown in the left diagram of Fig. 8.18, we can also consider the evolution along the x axis with fixed Q^2 when x is small. Here x is the longitudinal momentum faction of a certain parton with respect to its parent hadron. In DIS, x can be identified as x_{Bj} approximately. The small-x evolution is known to be governed by the famous Balitskii, Fadin, Kuraev, and Lipatov (BFKL) equation [175, 176], which effectively resums the small-x logarithms of $\left(\alpha_s \ln \frac{1}{x}\right)^n$. DIS is also an ideal process to probe the small-x dynamics which is main topic of the next section.

Low-x Physics and Gluon Saturation

Small-x physics provides us the QCD description of dense parton densities at high energy limit when the longitudinal momentum fraction x of partons is small. Due to the enhancement of the Bremsstrahlung radiations of small-x gluons, gluon density is expected to rise rapidly as x decreases, which has been observed at HERA. The rise of gluon density can be seen from the solution of BFKL evolution equation which increases as $Y = \ln 1/x$ increases. The important feature of BFKL evolution is that the resulting cross section grows as $e^{(\alpha_P - 1)Y}$, with $\alpha_P - 1 = \frac{4\alpha_s N_c}{\pi} \ln 2$ at leading order. This behaviour essentially is the same as the exchange of Pomeron, thus sometimes the rise of gluon density and cross sections is attributed to the so-called BFKL Pomeron. In addition, it is conceivable that multiple interactions and recombinations of overlapping gluons $gg \to g$ become important when gluon density is of order $\mathcal{O}(\frac{1}{\alpha_s})$. As a result, the rapid growth of gluon distribution is tamed due to the gluon recombination. This triggers the onset of the gluon saturation phenomenon [74, 177–179] as a result of nonlinear QCD dynamics when the gluon density is high.

To incorporate the non-linear recombination effect, which reflects the nature of the non-Abelian QCD dynamics, Balitsky and Kovchegov independently derived the non-linear extension of the BFKL evolution equation, which now is normally referred as the BK evolution equation [78, 79]. In practice, as indicated in the left diagram of Fig. 8.18, one can define the so-called saturation scale $Q_s^2(Y)$ to separate the nonlinear saturated dense regime from the linear dilute regime. From HERA, we have learnt that the low-x inclu-

sive DIS data exhibits the so-called geometrical scaling behaviour [180] for all data with $x_{\rm Bj} < 0.01$. Instead of being functions of both $x_{\rm Bj}$ and Q^2, it was found that the inclusive cross section can be cast into a single variable function which only depends on $\tau \equiv \frac{Q^2}{Q_s^2(Y)}$ with $Q_s^2(x_{\rm Bj}) = \left(\frac{x_{\rm Bj}}{x_0}\right)^{\lambda}$ GeV^2 and $x_0 = 3.04\times10^{-3}$ and $\lambda = 0.288$. It was demonstrated in Refs. [181, 182] that the geometrical scaling behaviour of DIS data can be easily derived from the traveling wave type solution of the non-linear BK evolution. The remarkable geometrical scaling and its natural interpretation as the solution of the BK equation has been considered as one of most interesting evidence for saturation physics. Another interesting experimental evidence for gluon saturation phenomenon is the suppression of the forward rapidity back-to-back dihadron correlations in central deuteron-gold collisions [183–188]. It indicates that the saturation momentum $Q_s(x)$ can be large enough in the low-x regime to cause sizable deflection to the produced back-to-back dijets when they interact with the dense gluons in the heavy nucleus target.

In terms of scattering amplitudes, the saturation phenomenon is equivalent to the unitarity constraint of scattering matrix which is exactly encoded in the BK equation due to the presence of the non-linear term. The core ingredients of saturation physics are the multiple interactions and the non-linear small-x evolution. As compared to the collinear parton landscape of hadrons provided by the DGLAP type formalism, the small-x formalism provides the unique opportunity to probe the nonlinear QCD dynamics when parton density is high.

It seems conceptually obvious that the parton saturation phenomenon is an inevitable consequence of QCD dynamics in high energy scatterings. Central to this subject is the search for the signatures of gluon saturation in high energy experiments.

As mentioned in the conceptual design reports of EIC and LHeC, one of the key golden measurements to study saturation physics is the dijet (dihadron) correlations in DIS along the virtual photon direction. One can use leading hadrons in jets as surrogates of jets to do the study as well. This process can be viewed as a virtual photon scattering on dense nuclear target and producing two final state back-to-back $q\bar{q}$ jets, $\gamma^* + A(g) \to q(k_1) + \bar{q}(k_2) + X$. This process is the dominant channel in small x limit, since the gluon distribution is much larger than quark distributions inside hadron at high energy. In the back-to-back correlation limit, the transverse momentum imbalance of produced dijet is much smaller than each individual momentum:$q_\perp = |k_{1\perp} + k_{2\perp}|\ell^+\ell^- P_\perp$, with $P_\perp$ defined as $(k_{1\perp} - k_{2\perp})/2$. At partonic level, the cross section of this process can be cast into [189, 190]

$$\sigma^{\gamma^*\to 2\,\text{Jets}} = \int d^2R_\perp \mathcal{H}_{\rm tot}(z, k_{1\perp}, k_{2\perp}, Q^2) \exp\left[-S_{\rm sud}(\alpha_s, P_\perp, R_\perp)\right] S_{\rm WW}(x_g, R_\perp) e^{-iq_\perp\cdot R_\perp} \tag{8.22}$$

where $\mathcal{H}_{\rm tot}(z, k_{1\perp}, k_{2\perp})$ is the perturbative calculable hard part, $S_{\rm sud}$ is the Sudakov factor for this particular process [191, 192] and $S_{\rm WW}(x_g, R_\perp)$ is the Fourier transform of the Weizsacker-Williams gluon distribution function, which is the genuine unintegrated gluon density function at small-x. Through this process, the CEPC can provide us the vital opportunity to access the Weizsacker-Williams gluon distribution function and its evolution at high energy for the first time, as well as the associated gluon saturation effects.

Due to multiple scatterings between the probe and highly evolved dense gluons inside target protons and nuclei, the produced $q\bar{q}$ dijet tends to receive large total transverse

Figure 8.18 Left: Illustration of QCD evolutions and the idea of saturation physics. Right: Dihadron correlations $C(\Delta\phi) \equiv \frac{\sigma^{\gamma^* \to 2\text{ Jets}}(\Delta\phi)}{\sigma^{\text{Trigger Jet}}}$ at CEPC where $\Delta\phi$ is defined as the azimuthal angle difference between the leading trigger hadron and the associate hadron in the opposite direction. Here $C(\Delta\phi)$ is normalised by the single inclusive cross section of trigger jet production $\sigma^{\text{Trigger Jet}}$. The original study is done for EIC conceptual design[193]. This plot is generated later for the designed energy at CEPC.

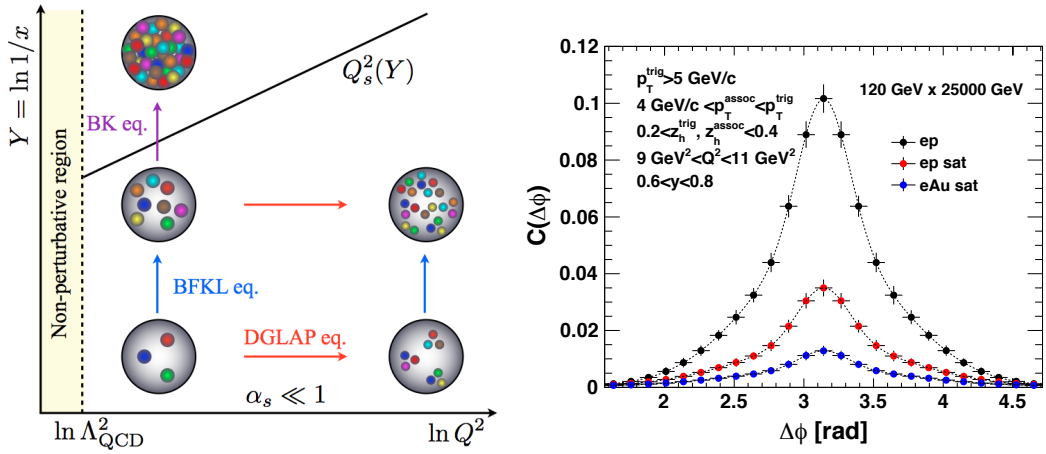

momentum $q_\perp$ which causes the $q\bar{q}$ dijet to deflect from the back-to-back configuration. This will result in the suppression of the back-to-back dijet (dihadron) correlation in eA collisions as compared to ep collisions with or without the saturation effect, as shown in the right figure of Fig. 8.18. The observation of the projected suppression in this measurement could become the smoking gun evidence for the saturation phenomenon and lead to the discovery of a new form of dense matter, namely CGC.

Of course, there are a lot of other interesting physics which can be studied at the CEPC. Here is an incomplete list of other key measurements in DIS.

- Through three dimensional imaging of internal structure of protons and nuclei, we expect to understand how gluons and quarks move and distribute in colour neutral hadrons. By measuring the transverse momentum dependent parton distributions [194] and generalised parton distributions [195–197] in DIS, we can gain additional knowledge of how partons are distributed in a confined hadron with respect to their longitudinal and transverse momenta as well as their transverse positions. The goal is to extract and understand the tomographic images of protons and nuclei.

- Diffractive processes, which are unique events characterised by rapidity gaps in particle productions, are very sensitive to gluon distributions in high energy limit. By measuring the diffractive cross section, due to different small-x evolution behaviour in diffractive cross sections as compared to the total cross section, we can study the small-x evolution as well as saturation effects from a different perspective, and compare with results from conventional collinear approaches. In particular, by comparing between the diffractive meson productions in eA and ep collisions, exclusive diffractive vector meson and heavy quarkonium productions, can be used to distinguish the saturation model [198, 199] from other models without saturation effects. Since light vector mesons are relatively less likely to be produced due to the presence of dense gluonic matter in the heavy nuclei, we can use this process to search the onset of saturation effects by measuring the productions of different mesons, such as $\phi(s\bar{s})$,

$J/\Psi(c\bar{c})$ and $\Upsilon(b\bar{b})$. In addition, diffractive processes can also help us understand better the role of QCD Pomerons exchanges in DIS.

Summary

To summarize, let us begin with comments on the intimate relations between the $ep(eA)$ collider and e^+e^- as well as hadron-hadron colliders which essentially can be realised in the same comprehensive and integrated high energy program. Generally speaking, from the e^+e^- collider program to the $ep(eA)$ collider, we gain higher centre of mass energy which renders more discovery power, and we can obtain the most accurate parton distributions which lays the important foundation for new physics searches at the following hadron-hadron collider. In the meantime, the $ep(eA)$ collider can help us clarify some of the most interesting QCD problems and may lead to the discovery of new form of dense gluon matter. Last but not least, the $ep(eA)$ program is also complementary to the pA and AA sub-program of the hadron-hadron collider for the purpose of investigations on the high energy and high density QCD matter.

The designed circular electron-proton collider, not only can provide substantial amount of information about nucleons and nuclei at very high energy with great precision and discovery possibilities, but also can help us study Higgs physics and beyond standard model physics more precisely. It can become the most powerful and superior high energy physics machine in 21st century that enables mankind to precisely explore unknown secrets of nature at the deepest level and the smallest scale.

References

[1] Y. Aoki, Z. Fodor, S. Katz, and K. Szabo, *The QCD transition temperature: Results with physical masses in the continuum limit*, Phys.Lett. **B643** (2006) 46–54, arXiv:hep-lat/0609068 [hep-lat].

[2] PHENIX Collaboration, K. Adcox et al., *Formation of dense partonic matter in relativistic nucleus-nucleus collisions at RHIC: Experimental evaluation by the PHENIX collaboration*, Nucl.Phys. **A757** (2005) 184–283, arXiv:nucl-ex/0410003 [nucl-ex].

[3] STAR Collaboration, J. Adams et al., *Experimental and theoretical challenges in the search for the quark gluon plasma: The STAR Collaboration's critical assessment of the evidence from RHIC collisions*, Nucl.Phys. **A757** (2005) 102–183, arXiv:nucl-ex/0501009 [nucl-ex].

[4] P. Jacobs and X.-N. Wang, *Matter in extremis: Ultrarelativistic nuclear collisions at RHIC*, Prog.Part.Nucl.Phys. **54** (2005) 443–534, arXiv:hep-ph/0405125 [hep-ph].

[5] U. Heinz and R. Snellings, *Collective flow and viscosity in relativistic heavy-ion collisions*, Ann.Rev.Nucl.Part.Sci. **63** (2013) 123–151, arXiv:1301.2826 [nucl-th].

[6] X.-N. Wang, *Discovery of jet quenching and beyond*, Nucl.Phys. **A750** (2005) 98–120, arXiv:nucl-th/0405017 [nucl-th].

[7] STAR Collaboration, B. Abelev, *Observation of an Antimatter Hypernucleus*, Science **328** (2010) 58–62, arXiv:1003.2030 [nucl-ex].

[8] N. Armesto et al., *Heavy Ion Collisions at the LHC - Last Call for Predictions*, J.Phys. **G35** (2008) 054001, arXiv:0711.0974 [hep-ph].

[9] B. Muller, J. Schukraft, and B. Wyslouch, *First Results from Pb+Pb collisions at the LHC*, Ann.Rev.Nucl.Part.Sci. **62** (2012) 361–386, arXiv:1202.3233 [hep-ex].

[10] H. Song, S. A. Bass, and U. Heinz, *Elliptic flow in 200 A GeV Au+Au collisions and 2.76 A TeV Pb+Pb collisions: insights from viscous hydrodynamics + hadron cascade hybrid model*, Phys.Rev. **C83** (2011) 054912, arXiv:1103.2380 [nucl-th].

[11] C. Gale et al., *Event-by-event anisotropic flow in heavy-ion collisions from combined Yang-Mills and viscous fluid dynamics*, Phys.Rev.Lett. **110** (2013) 012302, arXiv:1209.6330 [nucl-th].

[12] JET Collaboration, K. M. Burke et al., *Extracting the jet transport coefficient from jet quenching in high-energy heavy-ion collisions*, Phys.Rev. **C90** (2014) no. 1, 014909, arXiv:1312.5003 [nucl-th].

[13] T. Bhattacharya et al., *QCD Phase Transition with Chiral Quarks and Physical Quark Masses*, Phys.Rev.Lett. **113** (2014) no. 8, 082001, arXiv:1402.5175 [hep-lat].

[14] G. Cossu et al., *Finite temperature study of the axial U(1) symmetry on the lattice with overlap fermion formulation*, Phys.Rev. **D87** (2013) no. 11, 114514, arXiv:1304.6145 [hep-lat].

[15] HotQCD Collaboration, A. Bazavov et al., *The chiral transition and $U(1)_A$ symmetry restoration from lattice QCD using Domain Wall Fermions*, Phys.Rev. **D86** (2012) 094503, arXiv:1205.3535 [hep-lat].

[16] M. I. Buchoff et al., *QCD chiral transition, U(1)A symmetry and the dirac spectrum using domain wall fermions*, Phys.Rev. **D89** (2014) no. 5, 054514, arXiv:1309.4149 [hep-lat].

[17] J. Engels, F. Karsch, H. Satz, and I. Montvay, *High Temperature SU(2) Gluon Matter on the Lattice*, Phys.Lett. **B101** (1981) 89.

[18] HotQCD Collaboration, A. Bazavov et al., *Equation of state in (2+1)-flavor QCD*, Phys.Rev. **D90** (2014) no. 9, 094503, arXiv:1407.6387 [hep-lat].

[19] S. Borsanyi et al., *Full result for the QCD equation of state with 2+1 flavors*, Phys.Lett. **B730** (2014) 99–104, arXiv:1309.5258 [hep-lat].

[20] A. Bazavov et al., *The chiral and deconfinement aspects of the QCD transition*, Phys.Rev. **D85** (2012) 054503, arXiv:1111.1710 [hep-lat].

[21] Wuppertal-Budapest Collaboration, S. Borsanyi et al., *Is there still any T_c mystery in lattice QCD? Results with physical masses in the continuum limit III*, JHEP **1009** (2010) 073, arXiv:1005.3508 [hep-lat].

[22] S. Ejiri et al., *On the magnetic equation of state in (2+1)-flavor QCD*, Phys.Rev. **D80** (2009) 094505, arXiv:0909.5122 [hep-lat].

[23] H.-T. Ding et al., *Chiral phase transition of N_f=2+1 QCD with the HISQ action*, PoS **LATTICE2013** (2014) 157, arXiv:1312.0119 [hep-lat].

[24] R. D. Pisarski and F. Wilczek, *Remarks on the Chiral Phase Transition in Chromodynamics*, Phys.Rev. **D29** (1984) 338–341.

[25] S. Aoki, H. Fukaya, and Y. Taniguchi, *Chiral symmetry restoration, eigenvalue density of Dirac operator and axial U(1) anomaly at finite temperature*, Phys.Rev. **D86** (2012) 114512, arXiv:1209.2061 [hep-lat].

[26] H. Ding et al., *Charmonium properties in hot quenched lattice QCD*, Phys.Rev. **D86** (2012) 014509, arXiv:1204.4945 [hep-lat].

[27] A. Bazavov et al., *In-medium modifications of open and hidden strange-charm mesons from spatial correlation functions*, arXiv:1411.3018 [hep-lat].

[28] S. Borsanyi, , et al., *Charmonium spectral functions from 2+1 flavour lattice QCD*, JHEP **1404** (2014) 132, arXiv:1401.5940 [hep-lat].

[29] G. Aarts et al., *Bottomonium above deconfinement in lattice nonrelativistic QCD*, Phys.Rev.Lett. **106** (2011) 061602, arXiv:1010.3725 [hep-lat].

[30] G. Aarts et al., *Melting of P wave bottomonium states in the quark-gluon plasma from lattice NRQCD*, JHEP **1312** (2013) 064, arXiv:1310.5467 [hep-lat].

[31] G. Aarts et al., *S wave bottomonium states moving in a quark-gluon plasma from lattice NRQCD*, JHEP **1303** (2013) 084, arXiv:1210.2903 [hep-lat].

[32] G. Aarts et al., *The bottomonium spectrum at finite temperature from N_f = 2 + 1 lattice QCD*, JHEP **1407** (2014) 097, arXiv:1402.6210 [hep-lat].

[33] G. Aarts et al., *What happens to the Upsilon and η_b in the quark-gluon plasma? Bottomonium spectral functions from lattice QCD*, JHEP **1111** (2011) 103, arXiv:1109.4496 [hep-lat].

[34] S. Kim, P. Petreczky, and A. Rothkopf, *Lattice NRQCD study of S- and P-wave bottomonium states in a thermal medium with $N_f = 2 + 1$ light flavors*, arXiv:1409.3630 [hep-lat].

[35] M. Laine, O. Philipsen, P. Romatschke, and M. Tassler, *Real-time static potential in hot QCD*, JHEP **0703** (2007) 054, arXiv:hep-ph/0611300 [hep-ph].

[36] A. Beraudo, J.-P. Blaizot, and C. Ratti, *Real and imaginary-time Q anti-Q correlators in a thermal medium*, Nucl.Phys. **A806** (2008) 312–338, arXiv:0712.4394 [nucl-th].

[37] N. Brambilla, J. Ghiglieri, A. Vairo, and P. Petreczky, *Static quark-antiquark pairs at finite temperature*, Phys.Rev. **D78** (2008) 014017, arXiv:0804.0993 [hep-ph].

[38] Y. Burnier, O. Kaczmarek, and A. Rothkopf, *Static quark-antiquark potential in the quark-gluon plasma from lattice QCD*, arXiv:1410.2546 [hep-lat].

[39] Y. Burnier and A. Rothkopf, *Bayesian Approach to Spectral Function Reconstruction for Euclidean Quantum Field Theories*, Phys.Rev.Lett. **111** (2013) 182003, arXiv:1307.6106 [hep-lat].

[40] A. Rothkopf, T. Hatsuda, and S. Sasaki, *Complex Heavy-Quark Potential at Finite Temperature from Lattice QCD*, Phys.Rev.Lett. **108** (2012) 162001, arXiv:1108.1579 [hep-lat].

[41] Y. Burnier and A. Rothkopf, *Disentangling the timescales behind the non-perturbative heavy quark potential*, Phys.Rev. **D86** (2012) 051503, arXiv:1208.1899 [hep-ph].

[42] A. Bazavov et al., *Strangeness at high temperatures: from hadrons to quarks*, Phys.Rev.Lett. **111** (2013) 082301, arXiv:1304.7220 [hep-lat].

[43] A. Bazavov et al., *The melting and abundance of open charm hadrons*, Phys.Lett. **B737** (2014) 210–215, arXiv:1404.4043 [hep-lat].

[44] R. Bellwied et al., *Is there a flavor hierarchy in the deconfinement transition of QCD?*, Phys.Rev.Lett. **111** (2013) 202302, arXiv:1305.6297 [hep-lat].

[45] A. Bazavov et al., *Freeze-out Conditions in Heavy Ion Collisions from QCD Thermodynamics*, Phys.Rev.Lett. **109** (2012) 192302, arXiv:1208.1220 [hep-lat].

[46] S. Borsanyi et al., *Freeze-out parameters from electric charge and baryon number fluctuations: is there consistency?*, Phys.Rev.Lett. **113** (2014) 052301, arXiv:1403.4576 [hep-lat].

[47] A. Bazavov et al., *Additional Strange Hadrons from QCD Thermodynamics and Strangeness Freezeout in Heavy Ion Collisions*, Phys.Rev.Lett. **113** (2014) no. 7, 072001, arXiv:1404.6511 [hep-lat].

[48] H. Ding et al., *Heavy Quark diffusion from lattice QCD spectral functions*, J.Phys. **G38** (2011) 124070, arXiv:1107.0311 [nucl-th].

[49] H.-T. Ding, *In-medium hadron properties from lattice QCD*, EPJ Web Conf. **36** (2012) 00008, arXiv:1207.5187 [hep-lat].

[50] H.-T. Ding, *Hard and thermal probes of QGP from the perspective of Lattice QCD*, arXiv:1404.5134 [hep-lat].

[51] M. Asakawa, T. Hatsuda, and Y. Nakahara, *Maximum entropy analysis of the spectral functions in lattice QCD*, Prog.Part.Nucl.Phys. **46** (2001) 459–508, arXiv:hep-lat/0011040 [hep-lat].

[52] H.-T. Ding et al., *Thermal dilepton rate and electrical conductivity: An analysis of vector current correlation functions in quenched lattice QCD*, Phys.Rev. **D83** (2011) 034504, arXiv:1012.4963 [hep-lat].

[53] H.-T. Ding, O. Kaczmarek, and F. Meyer, *Vector spectral functions and transport properties in quenched QCD*, arXiv:1412.5869 [hep-lat].

[54] B. B. Brandt, A. Francis, H. B. Meyer, and H. Wittig, *Thermal Correlators in the ρ channel of two-flavor QCD*, JHEP **1303** (2013) 100, arXiv:1212.4200 [hep-lat].

[55] G. Aarts et al., *Electrical conductivity and charge diffusion in thermal QCD from the lattice*, arXiv:1412.6411 [hep-lat].

[56] A. Amato et al., *Electrical conductivity of the quark-gluon plasma across the deconfinement transition*, Phys.Rev.Lett. **111** (2013) 172001, arXiv:1307.6763 [hep-lat].

[57] S. Caron-Huot, M. Laine, and G. D. Moore, *A Way to estimate the heavy quark thermalization rate from the lattice*, JHEP **0904** (2009) 053, arXiv:0901.1195 [hep-lat].

[58] A. Francis, O. Kaczmarek, M. Laine, and J. Langelage, *Towards a non-perturbative measurement of the heavy quark momentum diffusion coefficient*, PoS **LATTICE2011** (2011) 202, arXiv:1109.3941 [hep-lat].

[59] D. Banerjee, S. Datta, R. Gavai, and P. Majumdar, *Heavy Quark Momentum Diffusion Coefficient from Lattice QCD*, Phys.Rev. **D85** (2012) 014510, arXiv:1109.5738 [hep-lat].

[60] O. Kaczmarek, *Continuum estimate of the heavy quark momentum diffusion coefficient κ*, arXiv:1409.3724 [hep-lat].

[61] H. B. Meyer, *A Calculation of the shear viscosity in SU(3) gluodynamics*, Phys.Rev. **D76** (2007) 101701, arXiv:0704.1801 [hep-lat].

[62] H. B. Meyer, *A Calculation of the bulk viscosity in SU(3) gluodynamics*, Phys.Rev.Lett. **100** (2008) 162001, arXiv:0710.3717 [hep-lat].

[63] H. B. Meyer, *The Yang-Mills spectrum from a two level algorithm*, JHEP **0401** (2004) 030, arXiv:hep-lat/0312034 [hep-lat].

[64] G. D. Moore and K. A. Sohrabi, *Kubo Formulae for Second-Order Hydrodynamic Coefficients*, Phys.Rev.Lett. **106** (2011) 122302, arXiv:1007.5333 [hep-ph].

[65] G. D. Moore and K. A. Sohrabi, *Thermodynamical second-order hydrodynamic coefficients*, JHEP **1211** (2012) 148, arXiv:1210.3340 [hep-ph].

[66] G. Denicol, H. Niemi, E. Molnar, and D. Rischke, *Derivation of transient relativistic fluid dynamics from the Boltzmann equation*, Phys.Rev. **D85** (2012) 114047, arXiv:1202.4551 [nucl-th].

[67] CDF Collaboration, F. Abe et al., *Pseudorapidity distributions of charged particles produced in $\bar{p}p$ interactions at $\sqrt{s} = 630$ GeV and 1800 GeV*, Phys.Rev. **D41** (1990) 2330.

[68] PHOBOS Collaboration, R. Nouicer et al., *Pseudorapidity distributions of charged particles in d + Au and p + p collisions at s(NN)**(1/2) = 200-GeV*, J.Phys. **G30** (2004) S1133–S1138, arXiv:nucl-ex/0403033 [nucl-ex].

[69] The ALICE Collaboration, K. Aamodt et al., *First proton-proton collisions at the LHC as observed with the ALICE detector: Measurement of the charged particle pseudorapidity density at s**(1/2) = 900-GeV*, Eur.Phys.J. **C65** (2010) 111–125, arXiv:0911.5430 [hep-ex].

[70] W.-T. Deng, X.-N. Wang, and R. Xu, *Hadron production in p+p, p+Pb, and Pb+Pb collisions with the HIJING 2.0 model at energies available at the CERN Large Hadron Collider*, Phys.Rev. **C83** (2011) 014915, arXiv:1008.1841 [hep-ph].

[71] X.-N. Wang and M. Gyulassy, *HIJING: A Monte Carlo model for multiple jet production in p p, p A and A A collisions*, Phys.Rev. **D44** (1991) 3501–3516.

[72] M. Gyulassy and X.-N. Wang, *HIJING 1.0: A Monte Carlo program for parton and particle production in high-energy hadronic and nuclear collisions*, Comput.Phys.Commun. **83** (1994) 307, arXiv:nucl-th/9502021 [nucl-th].

[73] P. F. Kolb, J. Sollfrank, and U. W. Heinz, *Anisotropic transverse flow and the quark hadron phase transition*, Phys.Rev. **C62** (2000) 054909, arXiv:hep-ph/0006129 [hep-ph].

[74] L. D. McLerran and R. Venugopalan, *Computing quark and gluon distribution functions for very large nuclei*, Phys.Rev. **D49** (1994) 2233–2241, arXiv:hep-ph/9309289 [hep-ph].

[75] D. Kharzeev and M. Nardi, *Hadron production in nuclear collisions at RHIC and high density QCD*, Phys.Lett. **B507** (2001) 121–128, arXiv:nucl-th/0012025 [nucl-th].

[76] D. Kharzeev and E. Levin, *Manifestations of high density QCD in the first RHIC data*, Phys.Lett. **B523** (2001) 79–87, arXiv:nucl-th/0108006 [nucl-th].

[77] H.-J. Drescher and Y. Nara, *Effects of fluctuations on the initial eccentricity from the Color Glass Condensate in heavy ion collisions*, Phys.Rev. **C75** (2007) 034905, arXiv:nucl-th/0611017 [nucl-th].

[78] I. Balitsky, *Operator expansion for high-energy scattering*, Nucl.Phys. **B463** (1996) 99–160, arXiv:hep-ph/9509348 [hep-ph].

[79] Y. V. Kovchegov, *Small x F(2) structure function of a nucleus including multiple pomeron exchanges*, Phys.Rev. **D60** (1999) 034008, arXiv:hep-ph/9901281 [hep-ph].

[80] J. L. ALbacete and A. Dumitru, *A model for gluon production in heavy-ion collisions at the LHC with rcBK unintegrated gluon densities*, arXiv:1011.5161 [hep-ph].

[81] J. L. Albacete, A. Dumitru, H. Fujii, and Y. Nara, *CGC predictions for p+Pb collisions at the LHC*, Nucl.Phys. **A897** (2013) 1–27, arXiv:1209.2001 [hep-ph].

[82] B. Schenke, P. Tribedy, and R. Venugopalan, *Fluctuating Glasma initial conditions and flow in heavy ion collisions*, Phys.Rev.Lett. **108** (2012) 252301, arXiv:1202.6646 [nucl-th].

[83] B. Schenke, P. Tribedy, and R. Venugopalan, *Event-by-event gluon multiplicity, energy density, and eccentricities in ultrarelativistic heavy-ion collisions*, Phys.Rev. **C86** (2012) 034908, arXiv:1206.6805 [hep-ph].

[84] B. Schenke, P. Tribedy, and R. Venugopalan, *Multiplicity distributions in p+p, p+A and A+A collisions from Yang-Mills dynamics*, Phys.Rev. **C89** (2014) 024901, arXiv:1311.3636 [hep-ph].

[85] F. Gelis, *Initial state in relativistic nuclear collisions and Color Glass Condensate*, Nucl.Phys. **A931** (2014) 73–82, arXiv:1412.0471 [hep-ph].

[86] P. Huovinen and P. Petreczky, *QCD Equation of State and Hadron Resonance Gas*, Nucl.Phys. **A837** (2010) 26–53, arXiv:0912.2541 [hep-ph].

[87] J.-Y. Ollitrault, *Anisotropy as a signature of transverse collective flow*, Phys.Rev. **D46** (1992) 229–245.

[88] P. Romatschke and U. Romatschke, *Viscosity Information from Relativistic Nuclear Collisions: How Perfect is the Fluid Observed at RHIC?*, Phys.Rev.Lett. **99** (2007) 172301, arXiv:0706.1522 [nucl-th].

[89] H. Song et al., *200 A GeV Au+Au collisions serve a nearly perfect quark-gluon liquid*, Phys.Rev.Lett. **106** (2011) 192301, arXiv:1011.2783 [nucl-th].

[90] G. Policastro, D. T. Son, and A. O. Starinets, *The Shear viscosity of strongly coupled N=4 supersymmetric Yang-Mills plasma*, Phys.Rev.Lett. **87** (2001) 081601, arXiv:hep-th/0104066 [hep-th].

[91] PHENIX Collaboration, A. Adare et al., *Measurements of Higher-Order Flow Harmonics in Au+Au Collisions at* $\sqrt{s_{NN}} = 200$ *GeV*, Phys.Rev.Lett. **107** (2011) 252301, arXiv:1105.3928 [nucl-ex].

[92] STAR Collaboration, Y. Pandit, *Beam Energy Dependence of First and Higher Order Flow Harmonics from the STAR Experiment at RHIC*, Nucl.Phys. **A904-905** (2013) 357c–360c, arXiv:1210.5315 [nucl-ex].

[93] The ATLAS Collaboration, G. Aad et al., *Measurement of the azimuthal anisotropy for charged particle production in* $\sqrt{s_{NN}} = 2.76$ *TeV lead-lead collisions with the ATLAS detector*, Phys.Rev. **C86** (2012) 014907, arXiv:1203.3087 [hep-ex].

[94] L. Pang, Q. Wang, and X.-N. Wang, *Effects of initial flow velocity fluctuation in event-by-event (3+1)D hydrodynamics*, Phys.Rev. **C86** (2012) 024911, arXiv:1205.5019 [nucl-th].

[95] B. Zhang, C. Ko, B.-A. Li, and Z.-w. Lin, *A multiphase transport model for nuclear collisions at RHIC*, Phys.Rev. **C61** (2000) 067901, arXiv:nucl-th/9907017 [nucl-th].

[96] X.-N. Wang and M. Gyulassy, *Gluon shadowing and jet quenching in A + A collisions at s**(1/2) = 200-GeV*, Phys.Rev.Lett. **68** (1992) 1480–1483.

[97] PHENIX Collaboration, K. Adcox et al., *Suppression of hadrons with large transverse momentum in central Au+Au collisions at $\sqrt{s_{NN}}$ = 130-GeV*, Phys.Rev.Lett. **88** (2002) 022301, arXiv:nucl-ex/0109003 [nucl-ex].

[98] M. Gyulassy, P. Levai, and I. Vitev, *Reaction operator approach to nonAbelian energy loss*, Nucl.Phys. **B594** (2001) 371–419, arXiv:nucl-th/0006010 [nucl-th].

[99] A. Buzzatti and M. Gyulassy, *Jet Flavor Tomography of Quark Gluon Plasmas at RHIC and LHC*, Phys.Rev.Lett. **108** (2012) 022301, arXiv:1106.3061 [hep-ph].

[100] X.-F. Chen et al., *Suppression of high p_T hadrons in $Pb + Pb$ Collisions at LHC*, Phys.Rev. **C84** (2011) 034902, arXiv:1102.5614 [nucl-th].

[101] A. Majumder and C. Shen, *Suppression of the High p_T Charged Hadron R_{AA} at the LHC*, Phys.Rev.Lett. **109** (2012) 202301, arXiv:1103.0809 [hep-ph].

[102] B. Schenke, C. Gale, and S. Jeon, *MARTINI: An Event generator for relativistic heavy-ion collisions*, Phys.Rev. **C80** (2009) 054913, arXiv:0909.2037 [hep-ph].

[103] G.-Y. Qin et al., *Radiative and collisional jet energy loss in the quark-gluon plasma at RHIC*, Phys.Rev.Lett. **100** (2008) 072301, arXiv:0710.0605 [hep-ph].

[104] T. Renk, *Physics probed by the P_T dependence of the nuclear suppression factor*, Phys.Rev. **C88** (2013) no. 1, 014905, arXiv:1302.3710 [hep-ph].

[105] X.-N. Wang, *High p(T) hadron spectra, azimuthal anisotropy and back to back correlations in high-energy heavy ion collisions*, Phys.Lett. **B595** (2004) 165–170, arXiv:nucl-th/0305010 [nucl-th].

[106] H. Zhang, J. Owens, E. Wang, and X.-N. Wang, *Dihadron tomography of high-energy nuclear collisions in NLO pQCD*, Phys.Rev.Lett. **98** (2007) 212301, arXiv:nucl-th/0701045 [nucl-th].

[107] H. Zhang, J. Owens, E. Wang, and X.-N. Wang, *Tomography of high-energy nuclear collisions with photon-hadron correlations*, Phys.Rev.Lett. **103** (2009) 032302, arXiv:0902.4000 [nucl-th].

[108] S. Albino, B. Kniehl, and G. Kramer, *AKK Update: Improvements from New Theoretical Input and Experimental Data*, Nucl.Phys. **B803** (2008) 42–104, arXiv:0803.2768 [hep-ph].

[109] W.-t. Deng and X.-N. Wang, *Multiple Parton Scattering in Nuclei: Modified DGLAP Evolution for Fragmentation Functions*, Phys.Rev. **C81** (2010) 024902, arXiv:0910.3403 [hep-ph].

[110] X.-F. Chen et al., *Bulk matter evolution and extraction of jet transport parameter in heavy-ion collisions at RHIC*, Phys.Rev. **C81** (2010) 064908, arXiv:1002.1165 [nucl-th].

[111] J. Casalderrey-Solana and X.-N. Wang, *Energy dependence of jet transport parameter and parton saturation in quark-gluon plasma*, Phys.Rev. **C77** (2008) 024902, arXiv:0705.1352 [hep-ph].

[112] L. Pang, Q. Wang, and X.-N. Wang, *Relics of Minijets amid Anisotropic Flows in High-energy Heavy-ion Collisions*, Phys.Rev. **C89** (2014) 064910, arXiv:1309.6735 [nucl-th].

[113] N.-B. Chang, W.-T. Deng, and X.-N. Wang, *Initial conditions for the modified evolution of fragmentation functions in the nuclear medium*, Phys.Rev. **C89** (2014) no. 3, 034911, arXiv:1401.5109 [nucl-th].

[114] PHENIX Collaboration, A. Adare et al., *Suppression pattern of neutral pions at high transverse momentum in Au + Au collisions at s(NN)**(1/2) = 200-GeV and constraints on medium transport coefficients*, Phys.Rev.Lett. **101** (2008) 232301, arXiv:0801.4020 [nucl-ex].

[115] PHENIX Collaboration, A. Adare et al., *Neutral pion production with respect to centrality and reaction plane in Au+Au collisions at* $\sqrt{s_{NN}}$*=200 GeV*, Phys.Rev. **C87** (2013) no. 3, 034911, arXiv:1208.2254 [nucl-ex].

[116] The ALICE Collaboration, B. Abelev et al., *Centrality Dependence of Charged Particle Production at Large Transverse Momentum in Pb–Pb Collisions at* $\sqrt{s_{\rm NN}} = 2.76$ *TeV*, Phys.Lett. **B720** (2013) 52–62, arXiv:1208.2711 [hep-ex].

[117] The CMS Collaboration, S. Chatrchyan et al., *Study of high-pT charged particle suppression in PbPb compared to pp collisions at* $\sqrt{s_{NN}} = 2.76$ *TeV*, Eur.Phys.J. **C72** (2012) 1945, arXiv:1202.2554 [nucl-ex].

[118] N. Kidonakis and J. Owens, *Effects of higher order threshold corrections in high E(T) jet production*, Phys.Rev. **D63** (2001) 054019, arXiv:hep-ph/0007268 [hep-ph].

[119] B. Harris and J. Owens, *The Two cutoff phase space slicing method*, Phys.Rev. **D65** (2002) 094032, arXiv:hep-ph/0102128 [hep-ph].

[120] G.-Y. Qin et al., *Jet energy loss, photon production, and photon-hadron correlations at RHIC*, Phys.Rev. **C80** (2009) 054909, arXiv:0906.3280 [hep-ph].

[121] P. B. Arnold, G. D. Moore, and L. G. Yaffe, *Photon emission from ultrarelativistic plasmas*, JHEP **0111** (2001) 057, arXiv:hep-ph/0109064 [hep-ph].

[122] P. Arnold, G. D. Moore, and L. G. Yaffe, *Photon and gluon emission in relativistic plasmas*, JHEP **06** (2002) 030, arXiv:hep-ph/0204343.

[123] S. Jeon and G. D. Moore, *Energy loss of leading partons in a thermal QCD medium*, Phys. Rev. **C71** (2005) 034901, arXiv:hep-ph/0309332.

[124] I. Vitev, S. Wicks, and B.-W. Zhang, *A Theory of jet shapes and cross sections: From hadrons to nuclei*, JHEP **0811** (2008) 093, arXiv:0810.2807 [hep-ph].

[125] I. Vitev and B.-W. Zhang, *Jet tomography of high-energy nucleus-nucleus collisions at next-to-leading order*, Phys.Rev.Lett. **104** (2010) 132001, arXiv:0910.1090 [hep-ph].

[126] W. Dai, I. Vitev, and B.-W. Zhang, *Momentum imbalance of isolated photon-tagged jet production at RHIC and LHC*, Phys.Rev.Lett. **110** (2013) 142001, arXiv:1207.5177 [hep-ph].

[127] M. Cacciari, G. P. Salam, and G. Soyez, *FastJet User Manual*, Eur.Phys.J. **C72** (2012) 1896, arXiv:1111.6097 [hep-ph].

[128] J. Gao et al., *MEKS: a program for computation of inclusive jet cross sections at hadron colliders*, Comput.Phys.Commun. **184** (2013) 1626–1642, arXiv:1207.0513 [hep-ph].

[129] K. Eskola, H. Paukkunen, and C. Salgado, *EPS09: A New Generation of NLO and LO Nuclear Parton Distribution Functions*, JHEP **0904** (2009) 065, arXiv:0902.4154 [hep-ph].

[130] I. Lokhtin and A. Snigirev, *A Model of jet quenching in ultrarelativistic heavy ion collisions and high-p(T) hadron spectra at RHIC*, Eur.Phys.J. **C45** (2006) 211–217, arXiv:hep-ph/0506189 [hep-ph].

[131] The ATLAS Collaboration, G. Aad et al., *Measurements of the Nuclear Modification Factor for Jets in Pb+Pb Collisions at* $\sqrt{s_{\mathrm{NN}}} = 2.76$ *TeV with the ATLAS Detector*, arXiv:1411.2357 [hep-ex].

[132] S. Aiola, *Measurement of jet spectra and in pp and Pb-Pb collisions at with the ALICE detector*, Nuclear Physics A **931** (2014) no. 0, 382 – 387.

[133] H.-n. Li, Z. Li, and C.-P. Yuan, *QCD resummation for jet substructures*, Phys.Rev.Lett. **107** (2011) 152001, arXiv:1107.4535 [hep-ph].

[134] H.-n. Li, Z. Li, and C.-P. Yuan, *QCD resummation for light-particle jets*, Phys.Rev. **D87** (2013) 074025, arXiv:1206.1344 [hep-ph].

[135] Y. Mao, *Jet shape and fragmentation function measurements with {CMS}*, Nuclear Physics A **932** (2014) no. 0, 88 – 92.

[136] S. Cao and S. A. Bass, *Thermalization of charm quarks in infinite and finite QGP matter*, Phys.Rev. **C84** (2011) 064902, arXiv:1108.5101 [nucl-th].

[137] S. Cao, G.-Y. Qin, and S. A. Bass, *Heavy-quark dynamics and hadronization in ultrarelativistic heavy-ion collisions: Collisional versus radiative energy loss*, Phys.Rev. **C88** (2013) no. 4, 044907, arXiv:1308.0617 [nucl-th].

[138] X.-f. Guo and X.-N. Wang, *Multiple scattering, parton energy loss and modified fragmentation functions in deeply inelastic e A scattering*, Phys.Rev.Lett. **85** (2000) 3591–3594, arXiv:hep-ph/0005044 [hep-ph].

[139] A. Majumder, *Hard collinear gluon radiation and multiple scattering in a medium*, Phys.Rev. **D85** (2012) 014023, arXiv:0912.2987 [nucl-th].

[140] B.-W. Zhang, E. Wang, and X.-N. Wang, *Heavy quark energy loss in nuclear medium*, Phys.Rev.Lett. **93** (2004) 072301, arXiv:nucl-th/0309040 [nucl-th].

[141] CTEQ Collaboration, H. Lai et al., *Global QCD analysis of parton structure of the nucleon: CTEQ5 parton distributions*, Eur.Phys.J. **C12** (2000) 375–392, arXiv:hep-ph/9903282 [hep-ph].

[142] Y. Oh, C. M. Ko, S. H. Lee, and S. Yasui, *Heavy baryon/meson ratios in relativistic heavy ion collisions*, Phys.Rev. **C79** (2009) 044905, arXiv:0901.1382 [nucl-th].

[143] T. Sjostrand, S. Mrenna, and P. Z. Skands, *PYTHIA 6.4 Physics and Manual*, JHEP **0605** (2006) 026, arXiv:hep-ph/0603175 [hep-ph].

[144] T. Matsui and H. Satz, J/ψ *Suppression by Quark-Gluon Plasma Formation*, Phys.Lett. **B178** (1986) 416.

[145] PHENIX Collaboration, A. Adare et al., J/ψ *Production vs Centrality, Transverse Momentum, and Rapidity in Au+Au Collisions at* $\sqrt{s_{NN}} = 200$ *GeV*, Phys.Rev.Lett. **98** (2007) 232301, arXiv:nucl-ex/0611020 [nucl-ex].

[146] The ALICE Collaboration, L. V. Palomo, *Charmonium production measurements in Pb-Pb collisions with ALICE at the LHC*, J.Phys.Conf.Ser. **509** (2014) 012111.

[147] P. Braun-Munzinger and J. Stachel, *(Non)thermal aspects of charmonium production and a new look at J / psi suppression*, Phys.Lett. **B490** (2000) 196–202, arXiv:nucl-th/0007059 [nucl-th].

[148] R. Thews and M. Mangano, *Momentum spectra of charmonium produced in a quark-gluon plasma*, Phys.Rev. **C73** (2006) 014904, arXiv:nucl-th/0505055 [nucl-th].

[149] L. Grandchamp and R. Rapp, *Charmonium suppression and regeneration from SPS to RHIC*, Nucl.Phys. **A709** (2002) 415–439, arXiv:hep-ph/0205305 [hep-ph].

[150] X.-l. Zhu, P.-f. Zhuang, and N. Xu, *J/psi transport in QGP and p(t) distribution at SPS and RHIC*, Phys.Lett. **B607** (2005) 107–114, arXiv:nucl-th/0411093 [nucl-th].

[151] L. Yan, P. Zhuang, and N. Xu, *Competition between J / psi suppression and regeneration in quark-gluon plasma*, Phys.Rev.Lett. **97** (2006) 232301, arXiv:nucl-th/0608010 [nucl-th].

[152] Y.-p. Liu, Z. Qu, N. Xu, and P.-f. Zhuang, *J/psi Transverse Momentum Distribution in High Energy Nuclear Collisions at RHIC*, Phys.Lett. **B678** (2009) 72–76, arXiv:0901.2757 [nucl-th].

[153] K. Zhou, N. Xu, Z. Xu, and P. Zhuang, *Medium Effects on Charmonium Production at ultrarelativistic energies available at the CERN Large Haron Collider*, Phys.Rev. **C89** (2014) 054911, arXiv:1401.5845 [nucl-th].

[154] M. E. Peskin, *Short Distance Analysis for Heavy Quark Systems. 1. Diagrammatics*, Nucl.Phys. **B156** (1979) 365.

[155] G. Bhanot and M. E. Peskin, *Short Distance Analysis for Heavy Quark Systems. 2. Applications*, Nucl.Phys. **B156** (1979) 391.

[156] H. Satz, *Colour deconfinement and quarkonium binding*, J.Phys. **G32** (2006) R25, arXiv:hep-ph/0512217 [hep-ph].

[157] B. Chen, K. Zhou, and P. Zhuang, *Mean Field Effect on J/ψ Production in Heavy Ion Collisions*, Phys.Rev. **C86** (2012) 034906, arXiv:1202.3523 [nucl-th].

[158] K. Eskola, V. Kolhinen, and C. Salgado, *The Scale dependent nuclear effects in parton distributions for practical applications*, Eur.Phys.J. **C9** (1999) 61–68, arXiv:hep-ph/9807297 [hep-ph].

[159] S. Gavin and M. Gyulassy, *Transverse Momentum Dependence of J/psi Production in Nuclear Collisions*, Phys.Lett. **B214** (1988) 241–246.

[160] U. W. Heinz, H. Song, and A. K. Chaudhuri, *Dissipative hydrodynamics for viscous relativistic fluids*, Phys.Rev. **C73** (2006) 034904, arXiv:nucl-th/0510014 [nucl-th].

[161] T. Sjostrand et al., *High-energy physics event generation with PYTHIA 6.1*, Comput.Phys.Commun. **135** (2001) 238–259, arXiv:hep-ph/0010017 [hep-ph].

[162] D. Boer et al., *Gluons and the quark sea at high energies: Distributions, polarization, tomography*, arXiv:1108.1713 [nucl-th].

[163] A. Accardi et al., *Electron Ion Collider: The Next QCD Frontier - Understanding the glue that binds us all*, arXiv:1212.1701 [nucl-ex].

[164] LHeC Study Group Collaboration, J. Abelleira Fernandez et al., *A Large Hadron Electron Collider at CERN: Report on the Physics and Design Concepts for Machine and Detector*, J.Phys. **G39** (2012) 075001, arXiv:1206.2913 [physics.acc-ph].

[165] LHeC Study Group Collaboration, J. Abelleira Fernandez et al., *On the Relation of the LHeC and the LHC*, arXiv:1211.5102 [hep-ex].

[166] J. Abelleira Fernandez et al., *A Large Hadron Electron Collider at CERN*, arXiv:1211.4831 [hep-ex].

[167] K. J. Golec-Biernat and M. Wusthoff, *Saturation effects in deep inelastic scattering at low Q**2 and its implications on diffraction*, Phys.Rev. **D59** (1998) 014017, arXiv:hep-ph/9807513 [hep-ph].

[168] The ATLAS Collaboration, G. Aad et al., *Observation of a new particle in the search for the Standard Model Higgs boson with the ATLAS detector at the LHC*, Phys.Lett. **B716** (2012) 1–29, arXiv:1207.7214 [hep-ex].

[169] The CMS Collaboration, S. Chatrchyan et al., *Observation of a new boson at a mass of 125 GeV with the CMS experiment at the LHC*, Phys.Lett. **B716** (2012) 30–61, arXiv:1207.7235 [hep-ex].

[170] V. Gribov and L. Lipatov, *Deep inelastic e p scattering in perturbation theory*, Sov.J.Nucl.Phys. **15** (1972) 438–450.

[171] G. Altarelli and G. Parisi, *Asymptotic Freedom in Parton Language*, Nucl.Phys. **B126** (1977) 298.

[172] Y. L. Dokshitzer, *Calculation of the Structure Functions for Deep Inelastic Scattering and e+ e- Annihilation by Perturbation Theory in Quantum Chromodynamics.*, Sov.Phys.JETP **46** (1977) 641–653.

[173] J. Gao et al., *CT10 next-to-next-to-leading order global analysis of QCD*, Phys.Rev. **D89** (2014) no. 3, 033009, arXiv:1302.6246 [hep-ph].

[174] A. Martin, W. Stirling, R. Thorne, and G. Watt, *Uncertainties on alpha(S) in global PDF analyses and implications for predicted hadronic cross sections*, Eur.Phys.J. **C64** (2009) 653–680, arXiv:0905.3531 [hep-ph].

[175] I. Balitsky and L. Lipatov, *The Pomeranchuk Singularity in Quantum Chromodynamics*, Sov.J.Nucl.Phys. **28** (1978) 822–829.

[176] E. Kuraev, L. Lipatov, and V. S. Fadin, *The Pomeranchuk Singularity in Nonabelian Gauge Theories*, Sov.Phys.JETP **45** (1977) 199–204.

[177] L. Gribov, E. Levin, and M. Ryskin, *Semihard Processes in QCD*, Phys.Rept. **100** (1983) 1–150.

[178] A. H. Mueller and J.-w. Qiu, *Gluon Recombination and Shadowing at Small Values of x*, Nucl.Phys. **B268** (1986) 427.

[179] L. D. McLerran and R. Venugopalan, *Gluon distribution functions for very large nuclei at small transverse momentum*, Phys.Rev. **D49** (1994) 3352–3355, arXiv:hep-ph/9311205 [hep-ph].

[180] A. Stasto, K. J. Golec-Biernat, and J. Kwiecinski, *Geometric scaling for the total gamma* p cross-section in the low x region*, Phys.Rev.Lett. **86** (2001) 596–599, arXiv:hep-ph/0007192 [hep-ph].

[181] S. Munier and R. B. Peschanski, *Geometric scaling as traveling waves*, Phys.Rev.Lett. **91** (2003) 232001, arXiv:hep-ph/0309177 [hep-ph].

[182] S. Munier and R. B. Peschanski, *Traveling wave fronts and the transition to saturation*, Phys.Rev. **D69** (2004) 034008, arXiv:hep-ph/0310357 [hep-ph].

[183] C. Marquet, *Forward inclusive dijet production and azimuthal correlations in p(A) collisions*, Nucl.Phys. **A796** (2007) 41–60, arXiv:0708.0231 [hep-ph].

[184] STAR Collaboration, E. Braidot, *Two Particle Correlations at Forward Rapidity in STAR*, Nucl.Phys. **A854** (2011) 168–174, arXiv:1008.3989 [nucl-ex].

[185] E. Braidot, *Two-particle azimuthal correlations at forward rapidity in STAR*, arXiv:1102.0931 [nucl-ex].

[186] PHENIX Collaboration, A. Adare et al., *Suppression of back-to-back hadron pairs at forward rapidity in d+Au Collisions at* $\sqrt{s_{NN}} = 200$ *GeV*, Phys.Rev.Lett. **107** (2011) 172301, arXiv:1105.5112 [nucl-ex].

[187] J. L. Albacete and C. Marquet, *Azimuthal correlations of forward di-hadrons in d+Au collisions at RHIC in the Color Glass Condensate*, Phys.Rev.Lett. **105** (2010) 162301, arXiv:1005.4065 [hep-ph].

[188] A. Stasto, B.-W. Xiao, and F. Yuan, *Back-to-Back Correlations of Di-hadrons in dAu Collisions at RHIC*, Phys.Lett. **B716** (2012) 430–434, arXiv:1109.1817 [hep-ph].

[189] F. Dominguez, B.-W. Xiao, and F. Yuan, k_t*-factorization for Hard Processes in Nuclei*, Phys.Rev.Lett. **106** (2011) 022301, arXiv:1009.2141 [hep-ph].

[190] F. Dominguez, C. Marquet, B.-W. Xiao, and F. Yuan, *Universality of Unintegrated Gluon Distributions at small x*, Phys.Rev. **D83** (2011) 105005, arXiv:1101.0715 [hep-ph].

[191] A. Mueller, B.-W. Xiao, and F. Yuan, *Sudakov Resummation in Small-x Saturation Formalism*, Phys.Rev.Lett. **110** (2013) 082301, arXiv:1210.5792 [hep-ph].

[192] A. Mueller, B.-W. Xiao, and F. Yuan, *Sudakov double logarithms resummation in hard processes in the small-x saturation formalism*, Phys.Rev. **D88** (2013) no. 11, 114010, arXiv:1308.2993 [hep-ph].

[193] L. Zheng, E. Aschenauer, J. Lee, and B.-W. Xiao, *Probing Gluon Saturation through Dihadron Correlations at an Electron-Ion Collider*, Phys.Rev. **D89** (2014) 074037, arXiv:1403.2413 [hep-ph].

[194] J. C. Collins, D. E. Soper, and G. F. Sterman, *Transverse Momentum Distribution in Drell-Yan Pair and W and Z Boson Production*, Nucl.Phys. **B250** (1985) 199.

[195] D. Muller et al., *Wave functions, evolution equations and evolution kernels from light ray operators of QCD*, Fortsch.Phys. **42** (1994) 101–141, arXiv:hep-ph/9812448 [hep-ph].

[196] X.-D. Ji, *Gauge-Invariant Decomposition of Nucleon Spin*, Phys.Rev.Lett. **78** (1997) 610–613, arXiv:hep-ph/9603249 [hep-ph].

[197] A. Radyushkin, *Nonforward parton distributions*, Phys.Rev. **D56** (1997) 5524–5557, arXiv:hep-ph/9704207 [hep-ph].

[198] H. Kowalski and D. Teaney, *An Impact parameter dipole saturation model*, Phys.Rev. **D68** (2003) 114005, arXiv:hep-ph/0304189 [hep-ph].

[199] H. Kowalski, L. Motyka, and G. Watt, *Exclusive diffractive processes at HERA within the dipole picture*, Phys.Rev. **D74** (2006) 074016, arXiv:hep-ph/0606272 [hep-ph].

CHAPTER 9

SUMMARY

The physics studies of this volume of the preCDR have shown that the CPEC and SPPC colliders have great physics potential. The preliminary designs of the CEPC collider, run as a Higgs factory, of the detector, similar in design to the ILD, and of the experimental facility are also outlined.

Based on the preliminary simulation studies presented here, the experiments at the CEPC are expected to measure the couplings of the Higgs to Standard Model particles to a precision significantly beyond what is achievable at the LHC, in some cases down to the sub-percent level. Moreover, the physics program at the Z pole remains a highly attractive option for the CEPC collider.

Theoretical explorations of the physics at a 100 TeV pp collider have also been summarized in this report. Such a collider will vastly extend the energy frontier and enhance our capability of directly searching for new particles. The examples presented here include searches for supersymmetry, new resonances, extended Higgs sectors, and WIMP dark matter.

It has been argued that such an improvement in physics capabilities will allow us to make significant progress in addressing, in some cases even conclusively, the most important questions in particlar physics. In particular, it will dramatically improve our understanding of the Higgs boson, the first spin zero elementary particle ever discovered. A better understanding of the Higgs will help reveal the nature of the electroweak phase transition. The CEPC and SPPC will also perform significantly more stringent tests on the notion of naturalness. For example, at these colliders one can perform a much more comprehensive search for top partners, beyond the reach of the LHC. Additionally, the SPPC will also explore a significant portion of, and in some cases completely cover, the

parameter space of WIMP dark matter. Finally, it is worth emphasizing that the precision measurements at the CEPC and the direct searches at the SPPC complement other beautifully. The combination of these two machines will provide a powerful and fruitful physics program for decades to come.

The results in the areas of detector design and simulation tools have benefited from the progress made through the global effort on the ILC and ILD. Further developments and improvements in the detector optimization, as well as software and simulation tools will be achieved in the future. The preCDR has identified areas and technologies critical to the success of the CEPC program and immediate R&D efforts have been recommended.

We note that the results reported in this volume are based on preliminary studies which serve as the starting points of much more detailed analyses. Nevertheless, the broad-brushed picture painted here has already revealed the inspiring physics prospects at the CEPC and SPPC.

APPENDIX A

INTERNATIONAL REVIEW

There were two reviews of this CEPC-SPPC Preliminary Conceptual Design Report: Volume-I Physics & Detector. The review on the physics part was by an International Committee chaired by Dr. Michelangelo Mangano (CERN) from Feburary 18 to March 1, 2015 at IHEP in Beijing, China.

International Review Committee Members:

Michelangelo Mangano (chair), CERN (Switzerland)	michelangelo.mangano@cern.ch
Kuang-Ta Chao, Peking U. (China)	ktchao@pku.edu.cn
He-Sheng Chen, IHEP (China)	chenhs@ihep.ac.cn
David J. Gross, UCSB (USA)	gross@kitp.ucsb.edu
Xiang-Dong Ji, SJTU (China)	xdji@sjtu.edu.cn
Luciano Maiani, Rome U. (Italy)	luciano.maiani@cern.ch
Raman Sundrum, U. Maryland (USA)	raman@umd.edu
Henry Tye, HKUST (China)	iastye@ust.hk
Yue-Liang Wu, UCAS (China)	ylwu@ucas.ac.cn

A seperate review on the detector part was by another International Committee chaired by Prof. Harry Weerts (ANL) between March 11-12, 2015 also at IHEP. The Committee issued a report on March 23, 2015 and gave permission to publish the executive summary of the report as an appendix of the preCDR.

A.1 Report of Review of CEPC-SppC Detector preCDR

A.1.1 Introduction

A review of the CEPC-SPPC Preliminary Conceptual Design Report for a detector at the CEPC was held at the Institute for High-Energy Physics in Beijing on March 11 and 12, 2015. The committee received two separate documents prior to the meeting titled "CEPC-SppC, Preliminary Conceptual Design Report: Physics and Detector", one describing the physics goals and the physics performance of the proposed detector and the other providing technical details of the detector subsystems. The review was organized around a series of overview talks covering aspects of the experimental program, the detector and all its subsystems.

The committee reviewed the preliminary Conceptual Design Report (preCDR) of a detector concept for a circular ∼240 – 250 GeV e^+e^- collider (Higgs factory), where Higgs production is dominated by the ZH final state. The overall accelerator strategy uses a circular tunnel (currently ∼54 km in circumference) that would originally house an electron-positron Higgs factory (CEPC) with later installation of a proton-proton collider (SPPC). The design foresees two IPs for the CEPC, and two additional ones for future pp collisions.

The starting point for study of a CEPC detector is the ILD detector concept, which has been used for ILC and CLIC studies and has been extensively studied in simulations and has associated R&D collaborations for sub-detectors. The ILD concept was adapted to the proposed Higgs factory. The ILD software framework is used for simulation and reconstruction at the full simulation and fast simulation level. The local team has been working on this for a little over 1 year. The stated CEPC physics goals are to accumulate 10^6 Higgs bosons with two experiments over a running period of 10 years. This will also result in roughly 10^7 ZZ and 10^8 W^+W^- events.

A.1.2 Observations

The assembled, local team was well organized, young, focused and enthusiastic with excellent leadership and vision. They made excellent, effective use of existing studies and the software framework resulting in an impressive achievement, given the short time scale. They are also either part of existing R&D collaborations (LCTPC) or associated with them (CALICE). Optimizing for the study on Higgs final states in a limited center-of-mass energy region has helped focus the effort. The proposed R&D program based on the current preCDR, resulting in a CDR in the next 5 years, followed by a TDR which enables a construction start in 2021 seems challenging but feasible.

A.1.3 Addressing the questions in the charge

Does the committee view the CEPC-SppC as well aligned with the future of China's and world's HEP program?

> The proposed physics program and strategy (CEPC Higgs factory followed by ∼100 TeV class pp collider) is well aligned with the worldwide program as expressed in European and U.S. strategic plans. This program will position China as a world leader in the accelerator based HEP program, and addressing and answering its challenges will have broad benefits to Chinese society.

Do the design goals appear well defined and credible?

The proposed ∼240-250 GeV e^+e^- collider with a goal of precision measurements of the Higgs boson provides an appropriate focus for the detector design. The design is based on the ILD detector concept, which has been well studied and simulated in previous global studies. The proponents presented a "CEPC-adapted" design, which we call CEPC-ILD, and simulated its response for the Higgs factory. The presented CEPC detector design is credible and can achieve the physics goals as demonstrated through presented simulation results.

Are the detector issues addressed adequately?

The proposed and current CEPC-ILD design is based on a well-simulated concept. The CEPC-ILD concept already includes a shorter L^*. CEPC would run with about 3.5 μsec between crossings without large gaps with continuous injection. One consequence is that electronics cannot be power pulsed. This implies that worldwide efforts in this direction cannot be used. The proposed R&D recognizes this and will address this in the future.

Do the technical system designs appear effective to reach the performance goals?

The Particle Flow Algorithm (PFA) approach is used to identify physics objects together with other algorithms. The proponents are using the standard PANDORA PFA, but are also developing a new approach based on an algorithm called ARBOR. Using these algorithms, the designs of the current vertex, tracking, calorimeter, magnetic field, luminosity monitor and muon system are such that the performance goals can be met or exceeded. Of course R&D remains to be done to go from designs to real systems.

What are the primary technical risks and potential impacts? What mitigation measures should be taken?

The CEPC-ILD design is based on the ILD concept, which has been studied, but never built, therefore many technical risks remain. The team has identified technical risks including feature size of pixels, Si readout electronics, ion back flow in the TPC, the need for cooling in the tracking systems, areas where material needs to be minimized, effects due to non-uniform magnetic field and compensation solenoids. An initial (long) list of R&D areas has been identified by the team and presented at the review. This R&D program would address many of the risks.

For completeness the committee lists suggested higher priority R&D topics in Appendix A.2.

Is the R&D program identified correctly?

The team has identified areas of R&D. Several of them are inherent in the ILD concept and they have added CEPC-ILD specific ones. The initial list seems adequate, but there are so many that this would need a more detailed examination, including setting of priorities for future R&D. Such an R&D program will produce prototypes, which will need to be put in testbeams; parts will require testing for radiation hardness in irradiation facilities and ultimately realistic detector slices will have to be tested in test beams. This has not been addressed yet.

How can the design be improved?

The current CEPC-ILD design is based on the ILD concept for ILC, which is designed to address a much broader spectrum of final states over an extended energy region (250 GeV to at least 1000 GeV), with some CEPC specific adjustments (for example, shorter L^*). The committee **strongly** recommends that the CEPC-ILD design be optimized for running in the 240 – 250 GeV region. This should include realistic machine backgrounds, physics backgrounds, as well as developing calibration and alignment procedures. The current emphasis is appropriately on the ZH-channel. Other channels such as Higgs production through WW-fusion ($ee \to \nu\nu H$ where $H \to bb$) are already very important at this center of mass energy to the total width measurement. The committee recommends that the optimization include all relevant final states. This optimization process may have a strong impact on the choice for some of the detector subsystems and therefore on the future R&D program. Ultimately it would be beneficial to do an optimization, which balances best physics performance and cost.

Overall findings & recommendations

- The committee encourages the development of a detector concept for the second IP for CEPC over the next 5 years. This would enable a complementary detector design.
- The committee encourages expanding involvement in the international community in the R&D and physics studies and exploring synergies with either ongoing or future R&D for other facilities. This will be of mutual benefit.
- Progress could be accelerated on the detector optimization, R&D and areas where the detector and accelerator interface (MDI), by bringing in experience (from previous colliders) & expertise from the rest of the world.
- Measurement of the beam energy will be a fundamental component of the CEPC Higgs precision program. The committee did not hear about this and realizes that this is a responsibility of the accelerator team, but wants to point out its critical importance.
- A polarized electron source is in the current CEPC design. However no other information about how it would be preserved and/or used in the collider was provided. Even if polarization cannot be preserved at operating energy, a measurement of the beam energy by resonant depolarization at lower energy could be of interest.
- *The committee did not review the layout of the IP, size of the cavern, access routes etc. However it was noted there was only one personnel access shaft for both caverns.*

A.2 R&D topics suggested by the Committee

Silicon

- It is noted that the R&D plan presented in the pre-CDR builds to a great extent on improvements of existing technologies. Emerging technologies, such as HR-CMOS, HV-CMOS and 3D tiered silicon, could have a significant impact on the detector

performance. A judicious evaluation of R&D in these new technologies compared to further development of existing technologies is recommended.

- Study of an all-silicon tracker is suggested. Study of longitudinal segmentation of the silicon envelope should be carried out.
- It is important to develop a full simulation of the silicon detectors. With this, continue layout optimization studies of the present tracker proposal. The simulation should include a digitization model for charge deposits in the pixels and strips. With full simulation, more realistic studies of detector options with $>0.15\%$ radiation lengths per pixel layer, and $> 0.5 \sim 0.65\%$ radiation lengths for microstrip layers could be performed to evaluate the impact of CO_2 cooling instead of air cooling, if that is found to be necessary.
- As explained in some detail in the report, it is vital to investigate pixel technology choices: DEPFET, CMOS or SOI, in collaboration with other groups. This includes developing the equipment to build and test modules, with particular emphasis on pixel feature size, readout speed and power consumption in continuous operation. To minimize material, investigate the limits of detector thinning.
- Similarly, investigations are needed of sensor choices for the silicon microstrip tracker layers, including slim-edge technology, thinning, and possibly pixelated CMOS options.
- Development is also essential for front-end readout ASICs for the microstrip detector, aiming to reduce power consumption to run in continuous readout mode, and with thinning.
- To minimize material, DC-DC powering schemes should be investigated for the strips.
- Together with module tests, it is recommended to build prototypes of support structures including cooling solutions for mechanical and thermal tests of both the vertex and tracker detectors.

TPC

- Ion backflow in the TPC in continuous operation might cause a significant problem. The current design calls for a single technology, either GEM or MicroMegas, to be deployed. It is suggested that R&D be carried out for a hybrid design; for example, several GEM stages combined with a last stage MicroMegas amplification region could provide a path to significantly lower the ion backflow. Study of the use of different hole pitches in the GEM foils, which could also suppress the ion backflow, is recommended. Clear specifications on the ion backflow and the dE/dx resolution should be developed.
- The effect of both the electric and magnetic field distortions could have a sizeable impact on the track momentum and impact parameter resolution. Careful evaluation and parametrization of the impact of inhomogeneities of the magnetic field need to be studied.
- Studies of alternative, faster gas mixtures, should be undertaken to mitigate pile-up and ion backflow.

- Exploring the possible use of the SAMPA chip for the TPC readout, under development for the ALICE TPC upgrade, is suggested.
- Finite element studies of the impact of cooling requirements for the TPC endplate on the added material budget are recommended.

Calorimeters

- The choice of technologies for the electromagnetic and hadron calorimeter is very well aligned with technologies being pursued by the CALICE Calorimeter R&D collaboration. They include a Silicon-Tungsten and Scintillator-Tungsten electromagnetic calorimeter, as well as a glass RPC based pure digital hadron calorimeter (DHCAL), a glass RPC based semi-digital hadron calorimeter (SDHCAL) and possibly a DHCAL based on Thick Gas electron Multipliers (THGEM) technology. The THGEM is being produced in China and has been tested at an IHEP beam. An extensive R&D program for all these technologies is described and again is very much aligned with the CALICE R&D program.
- The need for active cooling in the CEPC environment, where power pulsing is not possible, is clearly recognized and identified as a high priority R&D item for all calorimeter systems, because all of them require embedded electronics.
- Because of the many options being pursued, the R&D program is extensive and it is not clear whether all technologies should be pursued or can even be pursued, because they require a large number of resources.
- An optimization of the overall detector design, as recommended by the Committee, might have a big impact on the design and performance requirements of the calorimeter, especially if the jet energy resolution requirement can be relaxed. It is recommended that such an optimization be done to better guide the future calorimeter R&D.

Magnet

- The magnet design is based on the CMS solenoid. To make use of the material and design development over the course of the last decade, studies to optimize on the current design, either through the use of new materials or variations of the cable, are recommended.

MDI

- Rates and radiation dose of the detector are determined not by the physics events but by the backgrounds. During the review updated results on the rate of radiative Bhabha events were presented, which were significantly larger than the results from the pre-CDR. Detailed studies of all sources of background and their impact on all detector subsystems as well as physics performance cannot be overemphasized.

Muon

- Further improvement of large, high-rate RPC detectors in terms of detection efficiency and long-term stability is recommended. Suggest R&D collaboration with INO.

Experimental area and detector facility

- The detector assembly procedure needs careful consideration.
- The experimental hall design is still quite premature.

A.3 Committee members

Members of the International Review Committee:

Hendrik J. (Harry) Weerts (Chair), ANL (USA)	weerts@anl.gov
Marcel Demarteau, ANL (USA)	demarteau@anl.gov
Young-Kee Kim, University of Chicago (USA)	ykkim@hep.uchicago.edu
Rick Van Kooten, Indiana University (USA)	rvankoot@indiana.edu [remote participation]
HitoshiYamamoto, Tohoku University (Japan)	yhitoshi@epx.phys.tohoku.ac.jp
Phillippa Wells, CERN (Switzerland)	Pippa.Wells@cern.ch
Zheng Li, Xiang Tan University (China)	lizheng@xtu.edu.cn